High impact technologies for endovascular treatment of chronic total occlusions

Sakes, Aimée

Important note
To cite this publication, please use the final published version (if applicable).
Please check the document version above.

High Impact Technologies for
Endovascular Treatment
of Chronic Total Occlusions

Aimée Sakes

High Impact Technologies for Endovascular Treatment of Chronic Total Occlusions

Aimée Sakes

High Impact Technologies for Endovascular Treatment of Chronic Total Occlusions

Proefschrift

ter verkrijging van de graad van doctor

aan de Technische Universiteit Delft,

op gezag van de Rector Magnificus prof.dr.ir. T.H.J.J. van der Hagen;

voorzitter van het College voor Promoties,

in het openbaar te verdedigen op dinsdag 15 mei 2018 om 12:30 uur

door

Aimée SAKES

werktuigkundig ingenieur

geboren te Woerden, Nederland.

Dit proefschrift is goedgekeurd door de promotoren:
Prof.dr. J. Dankelman
Prof.dr.ir P. Breedveld

Samenstelling promotiecommissie:

Rector Magnificus	Technische Universiteit Delft, Voorzitter
Prof.dr. J. Dankelman	Technische Universiteit Delft, Promotor
Prof.dr.ir P. Breedveld	Technische Universiteit Delft, Promotor
Ir. J.W. Spronck	Technische Universiteit Delft

Onafhankelijke commissieleden:

Prof.dr.ir. M. Wisse	Technische Universiteit Delft
Prof.dr.ir. A.F.W. van der Steen	Erasmus Medisch Centrum
Prof.dr. R. de Winter	Academisch Medisch Centrum Amsterdam
Prof.dr.ir. J. van der Sloten	Katholieke Universiteit Leuven
Prof.dr. H.E.J. Veeger	Technische Universiteit Delft, reservelid

Title: High Impact Technologies for Endovascular Treatment of Chronic Total Occlusions
Author: Aimée Sakes (aimee_sakes@hotmail.com)
Cover design: Aimée Sakes & AgileColor
Printing: Ridderprint

SUMMARY

Summary

As of today, Chronic Total Occlusions (CTOs) are considered the most technically challenging occlusion type that cardiovascular interventionist face. CTOs are characterized as heavily calcified complete occlusions in the coronaries with a strong blood vessel wall connection of over three months old. The preferred treatment method of CTOs is the so-called Percutaneous Coronary Intervention (PCI). In the PCI, the CTO is reached by inserting a small catheter into the vasculature at the groin or wrist. Once arrived at the occlusion, a small Ø0.36–0.40 mm guidewire is used to cross the CTO. Finally, a balloon-stent catheter is guided over the guidewire and subsequently inflated to compress the plaque material against the blood vessel wall and as such reopen the coronary artery.

PCIs of CTOs remain challenging for even the most expert operators, which is evidenced not only by the low success rate in comparison to acute occlusions, but also by the high referral rate and considerably longer procedure time. The main challenge during PCI of CTOs is successfully crossing the guidewire through the CTO into the distal true lumen. Crossing is challenging as the CTO is heavily calcified and is thus able to resist large compressive forces. As a result, the small guidewire can buckle, which can eventually result in procedural failure if the CTO cannot be crossed. Furthermore, buckling is also unwanted as it can cause guidewire entrapment and blood vessel perforation if the tip suddenly changes position while applying a compressive load. Another major factor that complicates CTO crossing is the inability to actively steer the guidewire. Guidewire deflection by calcification, for example, cannot be actively corrected, which can result in blood vessel wall damage, subintimal crossing in which the guidewire crosses the CTO via the blood vessel wall, creating the false impression of a successful crossing procedure, and even perforation of the pericardium that can lead to hear failure. Finally, once the CTO is successfully crossed it can be challenging to reopen the blood vessel, as the calcified regions are able to resist large radial compressive forces.

The main goal of this thesis is to develop innovative prototypes that can aid the interventionist in steering towards and through the CTO, as well as puncture heavily calcified CTOs. In order to achieve this goal, solutions will be provided for the three main, device-related, challenges of PCIs of CTOs: (1) the ability to actively steer during the navigational phase and crossing procedure, while preventing unwanted guidewire deflection and damage to the blood vessel wall, (2) the ability to move through resistant calcified regions in the CTO without buckling, and (3) the ability to recreate the original lumen of the coronary artery by removing plaque material. For each challenge an overview of the state of the art is given. Furthermore, to get inspiration for the innovative steering and crossing mechanisms, biological mechanisms, such as the tongue shooting mechanism of the chameleon and the spines of hedgehogs, were researched. Other application areas, such as laparoscopy, bronchoscopy, and biopsy, are also discussed that will benefit from technical improvements by the addition of steerability or an improved ability to remove tissues.

Summary

Successfully crossing the CTO means active control of the crossing path, which allows for compensating of deflective forces, navigating tortuous CTOs, and choosing the most feasible route with the least amount of calcification. In order to allow for active control of the crossing path, an eight Degrees Of Freedom (DOF) miniature Ø2 mm steerable tip was developed. This "multisteerable" tip allows for forming complex curves and can actively counteract deflective forces. In a first experiment, this tip was successfully combined with an Optical Shape Sensing (OSS) fiber and forward-looking IntraVascular UltraSound (IVUS) transducer to visualize and reconstruct a 3D wire frame in front of the tip. This configuration can in future be used to determine the most feasible entry point, ensure correct intraluminal passage, and prevent blood vessel damage. Next to the multisteerable instrument, an additional steerable device has been developed for laparoscopy; a 2-DOF Ø5 mm electrosurgical grasper for use during laparoscopy.

Buckling during the penetration process is a result of the small diameter and flexibility requirement of the guidewire in combination with the high penetration forces of the CTO. Penetration forces for CTOs are approximately 1.7 N, which is in between 6 to 200 times higher than the critical buckling load of dedicated CTO guidewires. In order to find innovative buckling prevention strategies that can improve the critical load of the crossing tool, solutions from nature have been studied. It became apparent that using a high-speed crossing tool could have merit as it increases the buckling load of the crossing tool without the need to enlarge the diameter and can potentially decrease the penetration load of the CTO. In nature, smart use of elastic structures allows for generating extremely high accelerations and takeoff velocities. Based on these inspiring elastically-enhanced mechanisms found in nature, several high-speed crossing tools were developed. First, a spring-loaded device inspired by the chameleon tongue was developed that allows for delivering high force impacts up to 19 N onto the CTO. This rigid spring-loaded prototype was, subsequently, developed into a flexible version that allows for navigating through the vasculature towards the CTO. Next to the spring-loaded devices, two other ways of transporting and applying high-force impulses onto the CTO were developed. The first prototype uses a Newton's cradle inspired mechanism in which the impulse is transferred through a series of balls. In a feasibility experiment, we successfully illustrated that we could transfer a high-force impulse of up to 6 N over a curved path with a mean efficiency of 35%. In the second prototype, the balls were replaced by a fluidic medium and the impulse was transferred via a hydraulic pressure wave. The prototype was able to transfer high-force impulses up to 43 N through a flexible catheter, with an efficiency of over 80% without illustrating any shape dependency. In addition, the prototype was very effective in piercing CTO models. Therefore, we are convinced that with further development, this prototype can dramatically increase the success rate of PCI of CTOs.

After successfully crossing the CTO, the most challenging part of the PCI has been completed, but the final step of the PCI, the reopening of the coronary artery, can be

challenging in heavily calcified CTOs. Currently there are a lot of different devices available for the removal, conversion, and compression of plaque material. Unfortunately, CTOs are very resistant to compression and conversion using balloon catheter and thrombolytic agents, respectively. It is, therefore, preferred to, at least partially, remove the plaque material. Even though we have not developed a removal tool specifically designed for PCI of CTOs, we do propose two innovative miniature removal tools that function in a similar medical environment and can potentially be developed further for PCIs of CTOs in future. First, we have developed a flexible Ø5 mm endovascular morcellator for the surgical removal of pituitary tumors in horses using the vascular system, a procedure that had never been attempted before. Next, an ultrathin Ø1.2 mm biopsy needle was developed for the removal of breast tumors via the milk ducts during a ductoscopy procedure. Additionally, we would also like to suggest that the hammer tools developed for the penetration of the CTO could also be used to fragment the CTO during the reopening process.

The proposed tools have shown potential to improve the success rates of PCIs of CTOs in future. Buckling is no longer an issue using the high-speed hammer prototypes that are able to deliver up to 43 N onto the CTO, while the multisteerable instruments give the surgeon full control of the crossing path, which in turn prevents blood vessel wall damage. Specifically, the simple but versatile hydraulic pressure wave catheter has merit, as it allows for high-force delivery through a flexible shaft under any angle. However, in order to illustrate the added values of this, and the other, prototypes, as well as get definitive answers on their effectiveness, it is a necessity to perform *ex-vivo* and, subsequent, *in-vivo* experiments in future. Furthermore, we will look into ways of combining the three main functionalities of the prototypes as described above, as well as the ability to ensure correct intraluminal passage using FL-IVUS and OSS, into one miniature tool to improve the chances of a successful PCI for even the less experienced interventionist in future.

Summary

SAMENVATTING

Chronische Totale Occlusies (CTO's) worden beschouwd als de meest technisch uitdagende laesies waar cardiovasculaire interventionisten mee worden geconfronteerd. CTO's worden gekenmerkt als zwaar verkalkte volledige occlusies van een (krans)slagader van ten minste drie maanden oud. De voorkeursbehandeling van de CTO is de zogenaamde Percutane Coronaire Interventie (PCI), ook wel bekend als de dotter behandeling. In de PCI wordt de CTO bereikt door een kleine katheter in het bloedvatstelsel in te brengen bij de lies of pols en deze vervolgens naar de CTO te geleiden. Eenmaal aangekomen bij de occlusie wordt een kleine geleidedraad (Ø0.36–0.40 mm) gebruikt om de CTO te doorboren. Vervolgens wordt een ballonkatheter in combinatie met een stent over de geleidedraad geleid en opgeblazen om de occlusie tegen de bloedvatwand te drukken en zo de kransslagader te heropenen.

PCI's van CTO's blijven uitdagend voor zelfs de meest deskundige interventionisten, wat blijkt uit het lage slagingspercentage in vergelijking met acute occlusies, de hogere doorverwijzingsaantallen en de aanzienlijk langere proceduretijd. De grootste uitdaging tijdens de PCI van CTO's is het succesvol doorboren en passeren van de CTO met de geleidedraad. Het doorboren van de CTO is een complexe procedure door de zware verkalking van de CTO, hetgeen resulteert in hoge benodigde penetratiekrachten. Helaas is de kracht die benodigd is voor het doorboren van CTO's in vele gevallen hoger dan de kritische knikbelasting van de kleine geleidedraad, waardoor deze gaat knikken. Knik van de geleidedraad is ongewenst aangezien het kan leiden tot een onsuccesvolle behandeling als de CTO niet kan worden gepasseerd, met een open hart operatie als gevolg. Daarnaast is knik ook ongewenst omdat de geleidedraad kan wegslippen en zo perforatie van de bloedvatwand kan veroorzaken. Een andere belangrijke factor die het doorboren van CTO's compliceert is het niet in staat zijn om de geleidedraad actief te kunnen richten en sturen wanneer de tip van de geleidedraad door de verkalkingen wordt afgebogen. Dit kan leiden tot bloedvatwand schade, subintimale passage van de CTO (waarbij de geleidedraad via de bloedvatwand de CTO's passeert, wat de indruk kan wekken van een succesvolle procedure) en ernstige complicaties zoals bloedingen en perforatie van het pericardium. Tenslotte is het vaak uitdagend om de kransslagader succesvol te heropenen omdat de verkalkte gebieden van de CTO grote radiale compressie krachten kunnen weerstaan.

Het hoofddoel van dit proefschrift is om de slaagkans van PCI van CTO's te verhogen door het aandragen van innovatieve oplossingen. Om dit doel te bereiken, zullen wij oplossingen aandragen om de drie meest voorkomende instrument-gerelateerde problemen tijdens PCI van CTO's op te lossen. (1) Om de kans op een succesvolle navigatie en passeer procedure te verhogen, moet de geleidedraad actief kunnen worden gestuurd zodat ongewenste uitwijkingen van de tip en schade aan de bloedvatwand kunnen worden voorkomen. (2) Daarnaast moet het instrument in staat zijn om (zwaar) verkalkte gebieden in de CTO te kunnen doorboren zonder te knikken. (3) Tot slot, moet het oorspronkelijke lumen weer worden hersteld door het (gedeeltelijk)

verwijderen van plaque materiaal. Elk van de drie deeloplossingen wordt voorafgegaan met een overzicht van de state-of-the-art. Hiernaast zal inspiratie uit de natuur worden gehaald om tot innovatieve oplossing te komen om de drie hoofdfuncties te vervullen en met name de knikresistentie te verhogen. Naast het hoofdonderwerp; PCI van CTO's, worden drie andere medische toepassingsgebieden belicht: laparoscopie, bronchoscopie en biopsie. Om deze toepassingsgebieden verder door te ontwikkelen en de behandeling van moeilijk bereikbare gebieden mogelijk te maken, is het noodzakelijk om extra functionaliteit, zoals stuurbaarheid, toe te voegen aan het huidige instrumentarium.

De kans op een succesvolle passeerprocedure van een CTO kan aanzienlijk worden vergroot door de interventionist algehele controle over de passeerprocedure te geven, zodat deze tip deflecties kan compenseren, door kronkelige CTOs kan navigeren en de meest haalbare route kan selecteren om zo calcificaties te ontwijken. Om actieve besturing tijdens het navigatie en passeer proces te bewerkstelligen is een miniatuur "multistuurbaar" instrument (Ø2 mm) ontwikkeld. Dit multistuurbare instrument is in staat complexe (S-)bochten te vormen, actief het pad door de CTO te bepalen en tip deflecties te compenseren. Deze tip is succesvol gecombineerd met een optische vorm sensor fiber en intravasculair ultrasound probe om een 3D draadframe te visualiseren en reconstrueren. Deze toevoegingen maken het mogelijk om in de toekomst het meest haalbare (minst gecalcificeerde) passeer punt te kiezen, de gehele passeer procedure te visualiseren en subintimale passage te voorkomen. Naast de multistuurbare tip, is er een stuurbare elektrochirurgische grijper voor laparoscopische procedures ontwikkeld.

Het knikken van de geleidedraad tijdens het doorboren van de CTO wordt veroorzaakt door de lage buigstijfheid van de geleidingsdraad in combinatie met de hoge penetratiekracht van de CTO. De benodigde kracht voor het doorboren van CTO's is ongeveer 1.7 N, wat ongeveer 6 tot 200 keer hoger is dan de kritische knikbelasting van gespecialiseerde CTO geleidedraden. Om zwaar verkalkte CTO's te kunnen passeren zonder te knikken, zijn innovatieve knik preventiestrategieën uit de natuur bestudeerd. Van alle knik preventiestrategieën toegepast in de natuur, is het gebruik van een high-speed, op stoot-impuls gebaseerd, passeer instrument het meest veelbelovend aangezien een dynamische belasting de kritieke kracht waarop knik optreedt verhoogd en mogelijk ook de benodigde kracht voor penetratie verminderd. Om deze reden is een tweede onderzoek gestart naar schietmechanismen in de natuur. In de natuur wordt slim gebruik gemaakt van elastische structuren om zeer hoge versnellingen en snelheden te realiseren. Geïnspireerd op deze biologische mechanismen zijn er verschillende high-speed instrumenten ontwikkeld. Als eerste wordt een veer-geactueerd instrument geïnspireerd door de kameleon tong beschreven, dat in staat is hoge krachten tot wel 19 N op de CTO uit te oefenen zonder te knikken. Dit rigide prototype is vervolgens doorontwikkeld tot een flexibele versie, die het mogelijk maakt om door het bloedvatstelsel naar de CTO te navigeren. Naast deze veer-geactueerde instrumenten, zijn twee andere instrumenten ontwikkeld die in staat zijn om een stoot te transporteren door een flexibele schacht en

deze vervolgens uit te oefenen op de CTO. Het eerste prototype maakt gebruik van een Newton's wieg geïnspireerd mechanisme waarin de stoot wordt doorgegeven door een reeks van kogels. In een haalbaarheidsstudie, hebben we aangetoond dat het mogelijk is om hoge krachten, tot wel 6 N, door een reeks van kogels te vervoeren, met een gemiddelde efficiëntie van 35%. In het tweede prototype, zijn de kogels vervangen door een fluïde medium en wordt de stoot via een hydraulische drukgolf doorgegeven. Dit prototype vertoonde een zeer hoog rendement, welke niet werd beïnvloed door de vorm van de katheter en slechts minimaal door de katheter flexibiliteit, en was in staat om hoge piekkrachten tot 43 N te vervoeren (1.5–1.7 N benodigd om CTO's te doorboren). Daarnaast was het prototype zeer effectief in het doorboren van CTO modellen, en zijn wij overtuigd dat bij verdere doorontwikkeling dit instrument de slaagkans van PCI van CTO's drastisch kan verhogen.

Na het succesvol passeren van de CTO is het meest uitdagende deel van de PCI voltooid, maar de laatste stap, de heropening van de kransslagader, kan nog steeds uitdagend zijn in zwaar gecalcificeerde CTO's. Momenteel zijn er verschillende apparaten beschikbaar voor de heropening van (krans)slagaderen. Aangezien de CTO zeer resistent is tegen compressie en omzetting (middels trombolytische middelen), ligt de voorkeur bij het (gedeeltelijk) verwijderen van het plaquemateriaal. Ondanks dat we geen instrumenten hebben ontwikkeld voor het verwijderen van plaque materiaal in PCI van CTO's, hebben we wel twee innovatieve instrumenten ontwikkeld voor andere medische toepassingen. Deze instrumenten functioneren in een vergelijkbare omgeving en kunnen dus in de toekomst worden doorontwikkeld voor toepassing in PCI van CTO's. Eerst wordt een flexibele morcellator beschreven die is ontwikkeld voor de operatieve verwijdering van de hypofyse tumoren bij paarden via het bloedvatstelsel; een procedure die nooit eerder is uitgevoerd. Hiernaast, wordt een ultradunne biopsienaald (Ø1.2 mm) besproken die is ontwikkeld voor het verwijderen van borsttumoren via de melkkanalen in de zogenoemde ductoscopie procedure. Naast deze twee prototypes, is het ook mogelijk de eerder besproken hamer prototypes te gebruiken voor het fragmenteren van de CTO om zo de kransslagader te heropenen.

De voorgestelde instrumenten bieden een oplossing voor één van de drie meest voorkomende uitdagingen tijdens PCI's van CTO's. Knik is geen issue meer door het uitoefenen van een stoot op de CTO en de multistuurbare instrumenten geven de interventionist volledige controle over de gevolgde route door de CTO. Met name de eenvoudige en veelzijdige hydraulische drukgolf katheter, die in staat is om hoge krachten op de CTO uit te oefenen onafhankelijk van de vorm van de schacht, is zeer veelbelovend. Om de toegevoegde waarde van dit prototype en de andere prototype te illustreren zullen in de toekomst *ex-vivo* en de hier opvolgende *in-vivo* experimenten worden uitgevoerd. Hiernaast zullen we ons focussen op het integreren van de drie belangrijkste functionaliteiten van de voorgestelde instrumenten in één multifunctioneel

instrument dat zelfs de minder ervaren interventionist in staat stelt om een PCI van een CTO succesvol uit te voeren.

TABLE OF CONTENT

Table of Content

Chapter 1. Introduction

Part I. Improving Dexterity

Part II. High Impact Technologies

Chapter 5. Buckling Prevention in Nature – a Review

Chapter 6. Shooting Mechanisms in Nature – a Review **151**

Part III. Tissue Removal Technologies

Chapter 11. Applying Force for Recanalization – a Review

Chapter 14. Discussion

1

CHAPTER 1

INTRODUCTION

1

1

1.1. Chronic Total Occlusions (CTOs)

Chronic Total Occlusions (CTOs) are often considered the final frontier in cardiovascular interventions, substantiated by the low success rate of in between 55–90% depending on operator experience and CTO characteristics [1, 2]. CTOs are found in more than 20% of patients suffering from coronary artery disease [3]. Recanalization of CTOs by Percutaneous Coronary Intervention (PCI), using guidewires in combination with a balloon catheter to provide flow restoration of the occluded vessel, has been widely used since the 1990s (Figure 1.1). During a PCI, a cardiovascular interventionist inserts a small catheter in the inguinal femoral artery (located in the groin) or radial artery (located in the wrist) and feeds this catheter towards the CTO (Figure 1.1A) under X-ray guidance, also known as angiography. Once arrived at the lesion, a small guidewire is guided through the catheter (Figure 1.1B). A twisting motion with the guidewire is performed to engage, puncture, and cross the CTO. Subsequently, a balloon catheter is guided over the guidewire for the revascularization of the blood vessel by compressing the occlusion against the blood vessel wall (Figure 1.1C). Finally, a stent is placed as a blood vessel wall scaffold to prevent blood vessel collapse.
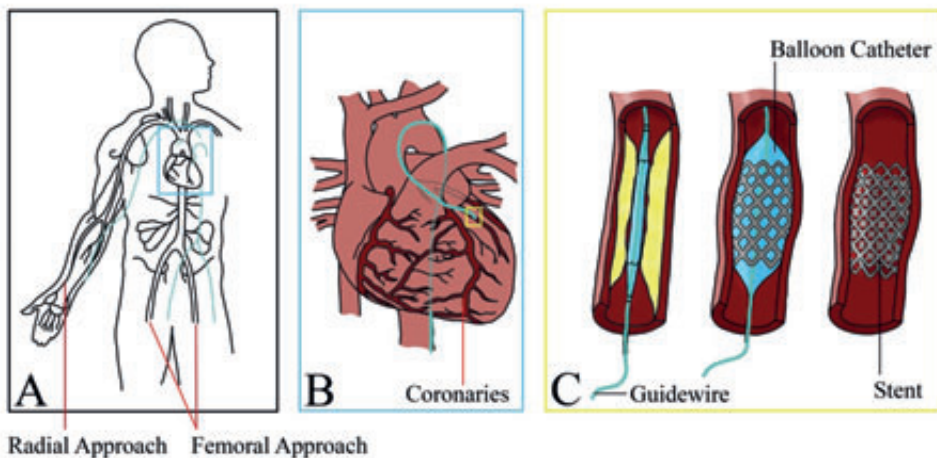
Figure 1.1— Percutaneous Coronary Intervention of CTOs. A: The vasculature is entered via the radial artery or femoral artery. B: the occlusion in the coronaries is entered using a guidewire. C: The occlusion is crossed with the guidewire. Subsequently, a balloon catheter with a stent is guided over the guidewire. Finally, the balloon catheter is inflated and the coronary is reopened.

1

1.2. CTO DEVELOPMENT AND PROPERTIES

A clear understanding of CTO histopathology is important to understand current challenges during PCI of CTOs, improve the success rate, and develop new devices. The initial event leading to the development of a CTO is on many occasions rupture of fatty build up in the coronary, also known as atherosclerotic plaque, in combination with a blood clot [4]. Subsequently, three distinct phases of CTO development can be distinguished (see Figure 1.2) [5]. In the **early stage** from 0 to 2 weeks, an acute inflammatory response causes thrombus formation on the blood vessel wall (Figure 1.2A). The thrombus will subsequently change into organized thrombus that grows in a bidirectional manner. At this stage, the occlusion is still low in collagen content and thus relatively easy to cross. In the **intermediate stage** from 6 to 12 weeks, microvessels appear within the atherosclerotic plaque (Figure 1.2B). Finally, in the **advanced stage** from 18 to 24 weeks, the collagen content of the CTO increases, with the highest concentration within the proximal cap, and the number of microvessels decrease (Figure 1.2D). Furthermore, the increase of calcification, due to cell differentiation and the recruitment of osteoblasts and osteoblast-like cells, makes the lesion more and more difficult to cross. Increased calcification is thus a predictor for technical and procedure failure. In the worst case scenario the fibrous cap of the CTO is also calcified, making this cap a distinct physical barrier complicating the crossing procedure.
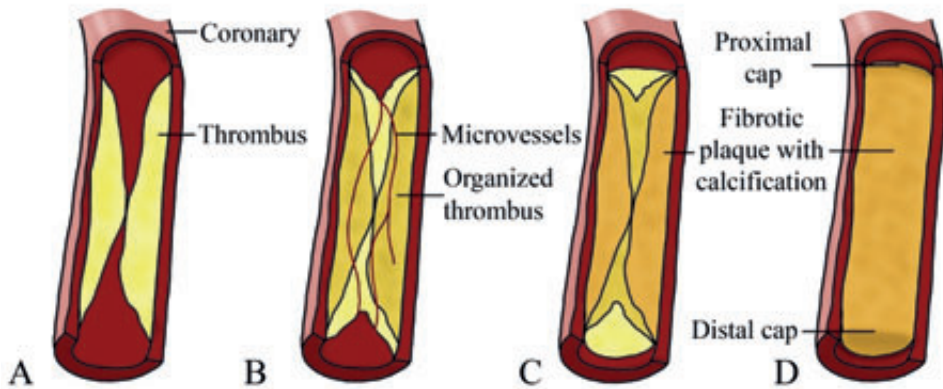
Figure 1.2— Development of a Chronic Total Occlusion (CTO). (A) Obstruction of the artery (0 to 2 weeks) with fresh thrombus. (B) Thrombus formation develops proximally and distally. The original thrombus changes in structure and becomes organized thrombus (6 to 12 weeks). (C) The thrombus develops further with the originally occluded area turning into fibrotic plaque (collagen) with calcified lesions (12 to 18 weeks). (D) Aged CTO (18 to 24 weeks) with fibrotic plaque and calcified lesions. The proximal and distal caps form a tough physical barrier during PCI of CTOs.

1

1.3. CURRENT CHALLENGES IN PERCUTANEOUS CORONARY INTERVENTIONS

1.3.1. Puncturing the CTO using a Guidewire

Since a CTO is classified to be at least three months old, the treatment usually takes place at the advanced stage of CTO maturation (Figure 1.2D). At this stage of development, the tough fibrous, and often calcified, proximal cap and calcified regions of the CTO are able to resist high compressive forces (Figure 1.3). Unfortunately, the required compressive force to puncture the CTO often exceeds the force that can be delivered by the flexible guidewire, resulting in buckling (Figure 1.3A); accounting for approximately 60% of the failure cases [6]. Buckling of the guidewire ultimately results in procedural failure if the CTO cannot be crossed and thus not be reopened. In turn, a sudden change in position of the guidewire tip due to buckling can cause blood vessel wall damage, such as dissection and perforation (Figure 1.3B).

1.3.2. Passive Steering towards and through the CTO

Another major challenge during PCI of CTOs is related to the inability to actively compensate for tip deflection and choose the most feasible crossing route during the crossing procedure. The guidewires and catheters used during PCI of CTOs are usually passive and can thus not be actively steered [7, 8]. This limited control of the instruments greatly impairs the dexterity of the surgeon, especially when navigating through tight arteries [7, 8] or tortuous heavily calcified occlusions. Furthermore, interventionists rely on angiographic visualization in 2D to determine their position in 3D. This can lead to incorrect interpretation of the guidewire position and can cause damage to the blood vessel wall and false lumen creation, in which the guidewire crosses the CTO via the blood vessel wall (in between the intima and adventitia, see Figure 1.3C).

1.3.3. Reopening the Coronary with a Balloon

Even if crossing is successful, reopening the coronary artery is sometimes challenging, because the calcified regions are able to resist high compressive forces and, therefore, complicate balloon catheter crossing and subsequent dilation of the lesion in about 2% of the cases (Figure 1.3D) [6].

1.4. STATE OF THE ART CTO DEVICES

According to a group of expert cardiovascular interventionists, the ideal CTO device should allow for precise steering during navigation and crossing, move through the most heavily calcified regions without buckling, and ensure correct intraluminal passage [1]. As of today, numerous devices have been developed to address these requirements, many of which have failed [1]. Multifunctional CTO devices are only sparsely available. An

1
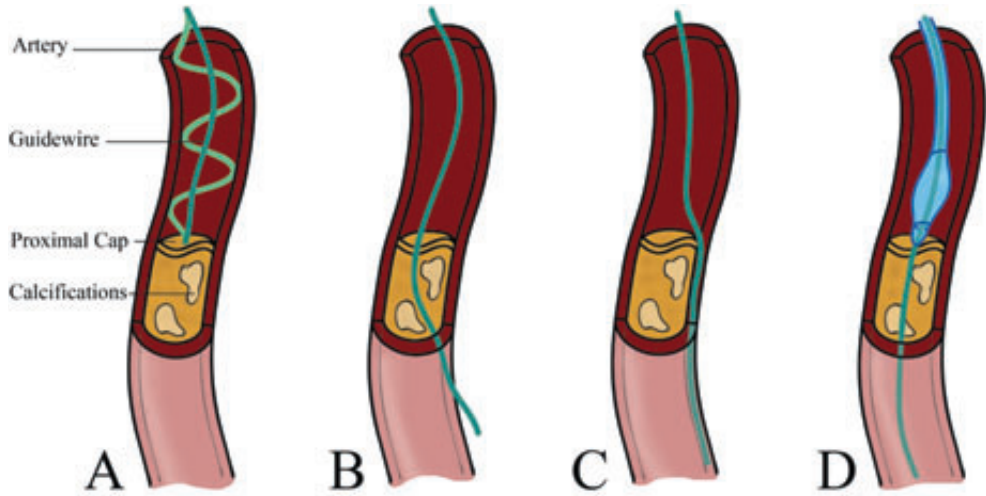
Figure 1.3: Current Failure Modes of PCI of CTOs. A: Guidewire buckling as a result of the high puncture force of the CTO. B: Guidewire deflection during the crossing procedure as a result of calcified regions. C: False lumen creation as the guidewire crosses the CTO via the blood vessel wall. D: Inability to cross the CTO with the balloon catheter.

example of a multifunctional CTO catheter is the *Eagle Eye Catheter* (Philips Medical, Amsterdam, the Netherlands) which combines IntraVascular UltraSound (IVUS) to visualize the blood vessel wall with standard catheter technology; and the *Venture Catheter* (Vascular Solutions, Minneapolis, MI, USA) that is actively steerable in 2 Degrees Of Freedom (DOF). Most of the currently used devices; guidewires, catheters, and dedicated CTO devices, however, are still single-function, passive devices. Even so, advancement of devices and crossing strategies has slowly increased the success rate of PCI in CTOs [1].

Guidewire technology has advanced, resulting in the development of stiffer guidewires more resistant to buckling. Dedicated CTO guidewire designs consist of a stainless steel or nitinol core wire surrounded by an outer coil or polymer cover [9]. Based on the specific design, important guidewire features can be altered. These guidewire features include the tip stiffness, the ability of the guidewire to retain its shape known as its shaping ability, shaft support, torque transmission, slipping ability, the ability to reach far into tortuous arteries known as trackability, and trap resistance. For example, CTO guidewires with stainless steel cores, such as *Whisper* (Abbott Vascular, Abbott Park, IL, USA) and *Pilot* (Abbott Vascular, Abbott Park, IL, USA), provide excellent support and tracking abilities, but are more susceptible to buckling than guidewires with nitinol cores, such as *Crosswire* (Terumo, Tokyo, Japan). Furthermore, in order to decrease the sliding

1

friction between the guidewire and the CTO, low friction coefficient hydrophilic coatings have been added to the guidewires, such as in *Confianza Pro* (Asahi Intecc. Corporation, Nagoya, Japan) and *Fielder* (Asahi Intecc, Nagoya, Japan).

According to the studies by Thind *et al.* [10] and Roy *et al.* [11] a force between 1.5 N and 1.7 N is required to puncture a CTO. Unfortunately, the tip loads of currently available guidewires are in between 0.008–0.26 N, and thus still insufficient to puncture the CTO. It can, therefore, be argued that in order to improve the chance of puncturing the proximal cap of the CTO, sufficient support of the guidewire is a necessity [9]. For this purpose, specialized microcatheters have been developed that are guided over the guidewire to increase the stiffness and thus the buckling resistance. Three examples of currently available microcatheters are *Tornus* (Asahi Intecc, Nagoya, Japan), *Crossboss* (Boston Scientific, Marlborough, MA, USA), and *Corsair* (Asahi Intecc, Nagoya, Japan). Unfortunately, even with these microcatheters, buckling is still observed.

Next to the guidewires and catheters, numerous specialized devices have been developed to treat PCI of CTOs. Many of these devices never made it beyond the clinical trails because they demonstrated high rates of complications or no significantly greater success rates than those achieved by standard catheters/guidewires [1]. Even so, a few devices specifically designed for PCI of CTOs have been approved by the Food and Drug Administration (FDA), such as the *CVX-300 Excimer Laser System* (Spectranetics, Colorado Springs, CO, USA), the *Frontrunner XP* catheter (Cordis, Hialeah, FL, USA; mainly used for peripheral arteries), and the axially vibrating *Crosser catheter* (Bard PV, Tempe, AZ, USA; mainly used for peripheral arteries) [1].

In some situations, mainly when the CTO cannot be crossed via the true lumen due to extensive calcification, the so-called dissection-reentry approach is applied. In this approach, the CTO is bypassed (see Figure 1.3C), crossed in between the intima and adventitia of the blood vessel wall, and subsequently reentered via the blood vessel wall, after which a new lumen is created. Two currently available devices that facility crossing through the blood vessel wall and reentry in the true lumen are the *Outback catheter* (Cordis, Hialeah, FL, USA) and *Stingray LP catheter* (Cordis, Baar, Switzerland), which both use a curved needle for reentry.

1.5. THESIS GOAL

The main goal of this thesis is to present and evaluate innovative device designs developed to improve the technical and procedural success rate of PCI in CTOs. The designs are focused on solving the three major challenges as described above: (1) active steering to navigate and aim the device, (2) puncturing and crossing heavily calcified CTOs without buckling, and (3) successfully reopening of the coronary artery. In order to allow for active steering through the vascular system and CTO, independent from the flow direction or CTO consistency, respectively, a steerable segment will be added to the

1

(support) catheter. Crossing of CTOs, specifically puncturing of the tough proximal cap, will be simplified by increasing the buckling resistance of the crossing tool using dynamic loading methods. Finally, to improve the success rate of the reopening procedure, methods that can remove soft tissues are explored.

Next to these main topics in this thesis, the ability to visualize the CTO using IntraVascular Ultrasound (IVUS) and sense the 3D shape of the catheter with Optical Shape Sensing (OSS) will be explored. Adding an IVUS transducer can aid the interventionist in ensuring correct intraluminal passage and choosing the most suitable entry location, whereas the addition of an Optical Shape Sensing (OSS) fiber allows for 3D reconstruction of the catheter shape. Furthermore, when used in unison, the IVUS and OSS systems allow us to render a 3D volume in front of the device tip, which in turn can aid in choosing the most suitable crossing path.

1.6. THESIS LAYOUT

The thesis can be subdivided into three main parts: (I) Improving Dexterity, (II) High Impact Technologies, and (III) Tissue Removal Technologies. Parts I–III start with a review into the state-of-the-art or biological mechanisms, to get a clear overview of currently available medical devices and inspiration from nature, respectively. Subsequently, the developed instruments are discussed that either allow for active steering, delivering high forces without buckling, or the removal of tissues.

Part I. Improving Dexterity

Chapter 2. Navigating towards Recanalization – a Review.
Crossing CTOs is the most challenging part of the PCI [6]. In this chapter we will review the different strategies that are employed to cross a CTO using dedicated devices, including guidewires, catheters, and specialized crossing tools, such as lasers and vibrating devices.

Chapter 3. A Miniature Multisteerable Device
In order to allow for active control of the crossing path and thus overcome crossing difficulties and navigational challenges, a Ø2 mm 8-DOF multisteerable tip was developed and combined with a forward-looking IVUS transducer and OSS fiber. This configuration allows for 3D reconstruction of the multisteerable tip and occlusion in front of the tip, which can be beneficial to determine the most feasible entry point and ensuring correct intraluminal passage in future.

Chapter 4. 3D-printed Steerable Electrosurgical Grasper
Another field in which an improved steerable instrument is needed is in electrosurgery. Current electrosurgical graspers are rigid and are thus limited in their workspace. To overcome this problem, we introduce the first □5 mm 3D-printed steerable bipolar grasper *Volt*.

Part II. High Impact Technologies

Chapter 5. Buckling Prevention in Nature – a Review

In nature multiple animals are able to penetrate hard substrates using ultrathin mechanisms, such as the ovipositor of the wasp, without buckling. The working principles of these mechanisms are described using buckling theory. Inspiration is drawn from these examples to design a new type of puncture tool that can penetrate the most heavily calcified occlusions.

Chapter 6. Shooting Mechanisms in Nature – a Review

Based on the previous literature review, it became clear that a way to prevent buckling is to increase the impact velocity. In order to increase the impact velocity, a specialized shooting mechanism should be developed. To find inspiration, a literature review was conducted into shooting mechanisms found in fungi, plants, and animals.

Chapter 7. Crossing CTO using a Mechanical Impulse

Drawing inspiration from the identified shooting mechanisms in nature, a rigid high-speed puncture tool *Pulze I* was developed. This puncture tool uses a spring-loaded indenter in combination with an innovative reload mechanism.

Chapter 8. Crossing CTOs using a Mechanical Impulse Catheter

In order to allow for atraumatic navigating through the vasculature, the (rigid) high-speed puncture tool was redesigned into a flexible version *Pulze II*. The mechanical and puncture performance of the flexible hammer was tested on an artificial proximal cap model made out of calcium and gelatin.

Chapter 9. Crossing CTOs using a Newton's Cradle Inspired Catheter

Next to the spring-loaded hammer, two other methods were explored to transfer, and subsequently exert, an impulse onto the CTO. In this chapter, the Newton's cradle-inspired catheter *Cradle* is described. In this catheter the impulse is transferred through a series of balls that are placed inside the lumen of a catheter shaft.

Chapter 10. Crossing CTOs using a Pressure Wave Catheter

Another option that was explored was the use of a hydraulic pressure wave – a longitudinal wave travelling through the fluid with regions of high and low pressure – to transfer the impulse. The device, nicknamed *Wave*, consisted of two plungers inserted into the lumen of a fluid-filled catheter shaft.

Part III. Tissue Removal Technologies

Chapter 11. Applying Force for Recanalization – a Review

Once the CTO is crossed, the coronary should be reopened. There are currently many tools described in the (patented) literature that are specifically designed for this purpose. In this review, these devices are described based on their working principle, specifically if they compress the occlusion against the blood vessel wall, resect plague material from the occlusion, or dissolve the occlusion.

1

Chapter 12. Morcellator for Equine Cushing's disease

Removal of malignant and benign tissues is also an important procedure in other medical fields. In older horses, a tumor can form in the pituitary gland that can cause serious problems, such a lameness and blindness. Unfortunately for horses, the pituitary gland is difficult to reach. Therefore, only oral medication is available that suppresses the symptoms of the disease. Together with an expert veterinarian, a new surgical paradigm with an associated endovascular morcellator was developed that allows for reaching the pituitary gland through the vasculature.

Chapter 13. Miniature Biopsy Needle for Ductoscopy

In this chapter we describe the development of an ultrathin biopsy needle for ductoscopy; a procedure in which the milk ducts of patients are inspected for suspicious lesions using a small fiber-optic endoscope. Currently, no reliable biopsy needle is available for ductoscopy, resulting in the need for a second, more invasive, core of excisional biopsy procedure. The developed biopsy needle allows for taking an intraductal biopsy, bringing early diagnosis of breast cancer one step closer.

Discussion

In this chapter, we discuss our results and present the envisioned design of a dedicated CTO device that combines steering, crossing, and reopening in one multifunctional tool. The required steps for clinical application of the envisioned device are also explained. Naturally, this chapter also discusses the found insights, recommendations, and future research topics.

REFERENCES

[1]   Stone GW, Reifart NJ, Moussa I, Hoye A, Cox DA, Colombo A et al. Percutaneous recanalization of chronically occluded coronary arteries - A consensus document - Part II. Circulation. 2005;112(16): pp. 2530-2537.

[2]   Galassi A, Tomasello S, Reifart N, Werner GS, Sianos G, Bonnier H et al. In-hospital outcomes of percutaneous coronary intervention in patients with chronic total occlusion: insights from the ERCTO (European Registry of Chronic Total Occlusion) registry. EuroIntervention. 2011;7(4): pp. 472-479.

[3]   Stone GW., Reifart NJ, Moussa I, Hoye A, Cox DA, Colombo A, et al. Percutaneous recanalization of chronically occluded coronary arteries. A consensus document - Part I. Circulation. 2005; 112(15): pp. 2364-2372.

[4]   Yalonetsky S, Osherov AB, Strauss BH, Galassi AR, Tomasello S, Khamis H. Chronic Total Occlusions. A guide to recanalization (2nd ed.). Hoboken, NJ: Wiley-Blackwell, 2013.

[5]   Sumitsuji S, Inoue K, Ochiai M, Tsuchikane E, and Ikeno F. Fundamental wire technique and current standard strategy of percutaneous intervention for chronic total occlusion with histopathological insights. JACC: Cardiovascular Interventions. 2011; 4(9): pp. 941-951.

[6]   Kinoshita I, Katoh O, Nariyama J, Otsuji S, Tateyama H, Kobayashi T, et al. Coronary angioplasty of chronic total occlusions with bridging collateral vessels: immediate and

follow-up outcome from a large single-center experience. Journal of the American College of Cardiology. 1995;26(2): pp. 409-415.

[7]   Mack MJ. MInimally invasive and robotic surgery. JAMA. 2001;285(5): pp. 568-572.

[8]   Vitiello V, Lee SL, Cundy TP, and Yang GZ. Emerging robotic platforms for minimally invasive surgery. IEEE reviews in biomedical engineering. 2013;6: pp. 111-126.

[9]   Sianos G, Werner GS, Galassi A, Papafaklis MI, Escaned J, Hildick-Smith D et al. Recanalisation of Chronic Total coronary Occlusions: 2012 consensus document from the EuroCTO club. EuroIntervention. 2012;8(1): pp. 139-145.

[10]   Thind A, Strauss B, Teitelbaum A, Karshafian R, Ladouceur M, Whyne C, et al. A novel method for the measurement of proximal fibrous cap puncture force in chronic total occlusions: the effect of increasing age. EuroIntervention. 2011;6(8): pp. 997-1002.

[11]   Roy T, Liu G, Shaikh N, Dueck AD, and Wright GA. Puncturing plaques: Relating MRI characteristics of peripheral artery lesions to guidewire puncture forces. Journal of Endovascular Therapy. 2016;24(1): pp. 35-46.

PART I

IMPROVING DEXTERITY

Invasive open-heart surgeries are slowly being replaced by minimally invasive endovascular interventions. These new, less invasive, endovascular interventions pose new challenges for the surgeons as compared to open-heart surgery. Whereas in open surgery the surgeons were able to see the operation site with the naked eye and use the full articulating motion of their hands, they must now rely on endoscopic or angiographic visualization in 2D to determine their position in 3D and passive instruments to navigate through the vasculature and CTO. In order to allow for more widespread implementation of complicated endovascular interventions, improvement of current instrumentation is needed. The goal of the upcoming chapters is, therefore, to introduce multiple steerable instruments that provide the surgeon with improved dexterity during endovascular and minimally invasive interventions.

CHAPTER 2

NAVIGATING TOWARDS RECANALIZATION – A REVIEW

AIMÉE SAKES, EVELYN REGAR, JENNY DANKELMAN, AND PAUL BREEDVELD

2

Abstract—Chronic Total Occlusions (CTOs) represent the "last frontier" of percutaneous interventions. The main technical challenges lies in crossing the guidewire into the distal true lumen, which is primarily due to three problems: device buckling during initial puncture, inadequate visualization, and the inability to actively navigate through the CTO. To improve the success rate and to identify future research pathways, this study systematically reviews the state-of-the-art of all existing and invented devices for crossing occlusions. The literature search was executed in the databases of Scopus and Espacenet using medical and instrument-related keyword combinations. The search yielded over 840 patents and 69 articles. After scanning for relevancy, 45 patents and 16 articles were included. The identified crossing devices were subdivided based on the determinant for the crossing path through the occlusion, which is either the device (straight and angled crossing), the environment (least resistance, tissue selective, centerline, and subintimal crossing) or the user (directly steered and sensor enhanced crossing). It was found that each crossing path is characterized by specific advantages and disadvantages. For a future crossing device, a combination of crossing paths is suggested were the interventionist is able to exert high forces on the CTO (as seen in the device approach) and actively steer through the CTO (user: directly steered crossing) aided by intravascular imaging (user: sensor enhanced crossing) or an intrinsically safe device following the centerline or path of least resistance (environment: centerline crossing or least resistance crossing) to reach the distal true lumen.

Keywords— (Chronic Total) Occlusions (CTO), Crossing, Percutaneous Coronary Intervention (PCI), State of the art, Treatment, Recanalization, Review.

2.1. INTRODUCTION

It is often stated that Chronic Total Occlusions (CTOs) represent the "last frontier" of Percutaneous Coronary Interventions (PCIs) [1]. This statement is substantiated by the fact that PCIs in CTOs have considerably lower procedural success rates, in between 55–90%, than those achieved in non-occluded or acutely occluded coronary vessels (>95%), with the higher success rates in the hands of a few dedicated expert operators [1-3]. The main contributor to the lower success rates seen in PCIs of CTOs is the technically challenging procedure, which requires a long learning curve and high technical skill from the interventional cardiologists. Even though recent advances in guidewire, catheter, and crossing device technologies have steadily increased the technical and procedural success rates of PCIs in CTOs over the last five years, CTOs still remain the lesion subtype in which PCI is most likely to fail [1]. Therefore, improvement is still required to reach a widespread 95% success rate of PCIs in CTOs, for even the less experienced operators.

The main technical challenge during PCIs in CTOs, accounting for approximately 80% of procedural failure, lies in guidewire crossing into the true lumen of the distal vessel primarily due to three problems [1]. Firstly, currently available equipment, including guidewires and crossing devices, are often unable to physically cross the tough fibrous cap of the CTO. The small diameter (<0.4 mm) and flexibility of the guidewire (and crossing devices alike) result in limited bending stiffness. Attempting to penetrate the tough proximal cap, therefore, often causes buckling. Since acute lesions are softer and have no fibrous cap, buckling is usually not observed, explaining the higher success rate. Secondly, even if the initial puncture is successful, crossing the CTO remains challenging due to inadequate 3D visualization during the crossing procedure. This inadequate visualization complicates navigating and can, therefore, cause blood vessel wall trauma, false lumen creation, and even discontinuation of the procedure due to uncertainty about the position of the guidewire [3, 1]. Thirdly, the inability to actively navigate across the CTO to, for example, compensate for guidewire deflection by heavily calcified regions or cross highly tortuous vessels, complicates reaching the distal true lumen.

Based on these three main challenges in PCIs of CTOs an international panel of 47 physicians has drafted three main requirements a CTO crossing device must meet to increase the success rate [4]. First of all, the crossing device should be able to move forward even through resistant fibrotic and calcified tissue, either through mechanical means or by using an energy source. Secondly, the crossing device should be able to detect and ensure correct intraluminal passage. Finally, the crossing device should be able to precisely steer through the CTO.

Despite advances in equipment, with crossing devices incorporating at least one of the abovementioned functionalities, CTO recanalization may still be unsuccessful in approximately 25% of cases [1]. As of today, a device incorporating all three of the

2

proposed functionalities is still a work-in-progress. Therefore, it is a necessity to fundamentally explore new ways to safely and effectively cross CTOs and incorporate the three main functionalities that could in future increase the success rate in PCIs of CTOs.

A review of the state-of-the-art in crossing devices could potentially give insight into a future crossing device that incorporates all these functionalities. Even though some reviews exists that describe the current state-of-the-art in crossing devices specifically designed for CTOs, these reviews are incomplete as they mainly focus on providing an overview of currently applied devices; excluding the patented literature [1, 5, 6]. This study explores the entire field, including the patented literature, and systematically reviews the state-of-the-art of all existing and invented crossing devices and methods for crossing total occlusions, including acute occlusions (which are usually softer (thrombotic) than CTOs, which are mainly characterized by heavy calcification), used in clinical practice and designs described in the patented literature. The study ends in a discussion in which we identify future research pathways that could lead to a fundamental improvement in the field.

2.2. LITERATURE SEARCH METHOD

A literature search was executed in the database of Scopus and Espacenet and was limited to the English or Dutch language from the 1950s to the present. The search was broadened to include all kinds of occlusions, including acute and semi-occluded lesions, to get a complete overview of all the devices available for crossing obstructions in the vascular system.

The search terms in the Scopus search engine were subdivided into four categories: (1) occlusion, (2) treatment, (3) medical area, and (4) instrument type. In the occlusion category, the search terms: *occlu*, obstruct*, plaqu*, thromb*, *clot*, obstacle*,* and *barrier** were used. The treatment category included: **canal*, remov*, resect*, dissect*,* and *cut**. In the area category, the following terms were used: *vasc*, cardio*, arter*, vessel*, vein*,* and *cappilar*,* and in the instrumental category: *device*, instrument*, prototype*, guidewire*, catheter*,* and *apparatus**. The categories were connected with the "AND" operator; the search terms either with "AND" or "OR". The "NOT" operator was added to filter out non-relevant articles.

The final literature search in Scopus led to 69 hits. Of these hits, first the titles were scanned for relevancy, after which the abstract was read. If it was concluded that the article fitted the scope of this review as discussed in the previous section, it was included in this review. This led to a total of 16 articles being included in this review.

Subsequently, the Espacenet database was searched for patents relating to crossing devices for occlusions using the following keywords in the title and in the title & abstract, respectively: (*occlu** OR *obstruct** OR *plaqu** OR *thromb** OR *clot*),* and *((vasc** OR *vessel*)* AND *(canal** OR *remov** OR *resect*)).* This led to 845 potentially relevant

patens. By first reading the title of the patents, followed by the summary of the invention, a total of 42 were selected.

2.3. STATE OF THE ART DEVICES

It was found that there are multiple ways or methods to cross an occlusion and reach the true lumen at the distal (or proximal) end of the blood vessel. Which path is followed depends on the chosen crossing device. Three main approaches can be distinguished: the *Device*, *Environment*, and *User* approach (see Figure 2.1). Per approach, the associated devices will be discussed and the intended use, i.e., for acute occlusions or CTOs, and current status, i.e., abandoned, in use, or proposed (amongst others) will be indicated.

2.3.1. Device

In the *Device* approach, the crossing device itself is the most determining factor for the crossing path. The occlusion is crossed in a straight or angled manner, independent of the properties and geometry of the occlusion and blood vessel, as well as the input from the user, called *Straight Crossing* or *Angled Crossing*, respectively.

Straight Crossing
Developed devices that cross the CTO in a straight line use a fluidic (fluid jets) or gaseous medium (lasers) (Figure 2.2). The initial orientation of the tip of these devices determines the crossing direction. It is, therefore, imperative that the tip of the device is perpendicular to the CTO cap and, as best as can be achieved, collinear to the lumen. The crossing speed is controlled by the input power of the laser or fluid jet.
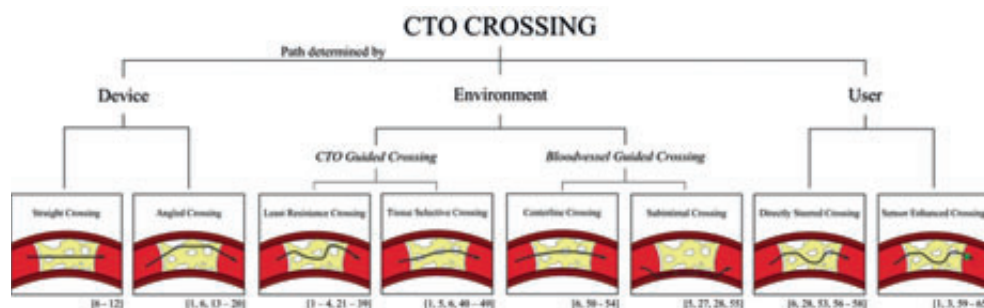
Figure 2.1— CTO Crossing Methods – Overview. Per crossing method the associated references are illustrated in between brackets. Color indications: Red = Blood vessel. Yellow = Plaque material. White = Calcified regions. Green = Sensor.

Fluid Jets (Abandoned, originally in use for acute occlusions): In hydrodynamic thrombectomy, a high-velocity fluid jet is used to fragment and remove occlusive material from the blood vessel wall. For this purpose, high-velocity fluid jets use a fine stream of saline at high pressures (typically between 15–20 kg/cm). Currently, fluid jets used for crossing purposes are abandoned due to safety concerns (note that some still exist for treating purposes). However, Nguyen *et al.* [7] and Delaney *et al.* [8] propose axially directed fluid jets for crossing acute occlusions (Figure 2.2).

2

Lasers (In use for peripheral and coronary CTOs): Medical lasers use a high-energy beam of light to resect or dissolve different tissue types for crossing or debulking purposes. Absorption of the laser energy within the targeted biological tissues creates photochemical and photomechanical reactions that result in conversion of the plaque material in vapor and the development of acoustic shock waves that are able to fragment tissue.

Lasers, such as over-the wire and rapid-exchange excimer laser catheters, are currently in use for CTO crossing in atherectomy. These laser catheters contain a flexible fiber-optic cable made out of as many as 240 high-purity silica fibers arranged around a guidewire lumen, with the distal tip polished and rounded. Examples of laser crossing systems are the *CVX-300 Excimer Laser* (Spectrametrics Inc., Colorado Springs, CO) and the *TURBO elite laser ablation catheter* (FDA approved October, 2006) [6]. Furthermore, in [9-12] different lasers are proposed for crossing acute occlusions and CTOs (see Figure 2.2 for the laser devices proposed by Roth *et al.* [11] and Fischer *et al.* [12])

Unfortunately, heat accumulation is often an issue in lasers, warranting careful advancement through the CTO, slower than 1 mm/second, to increase absorption of the plaque and prevent absorption by the blood vessel wall [6]. To minimize this problem, Pallarito *et al.* [10] and Roth *et al.* [11] suggest using focusing devices (lenses) to narrow the laser beam (see Figure 2.2 for the device proposed by Roth *et al.*). Despite the drawback of heat accumulation, a major advantage of lasers is that buckling is no issue as there are no mechanical forces on the device tip.

Angled Crossing

Many of the current and proposed crossing devices have a rigid tip (L > 2 mm). Since rigid tips do not allow for bending or compression, the tips of these devices cannot adjust to the 3D shape and direction of the CTO. In the flexible device shaft behind the rigid tip, however, bending is possible, which allows for some adjustment to bends in the vascular system when high radial resistance is encountered. The route through the CTO is, therefore, not smooth, but contains multiple acute angles, which from here on out will be referred to as *Angled Crossing*.

Hinged Crossing Device (In use for peripheral and coronary CTOs): *Frontrunner XP* (Ø0.76–1 mm, 2.8 F distal tip, Cordis Corporation, Miami, FL) [1] is an FDA-approved
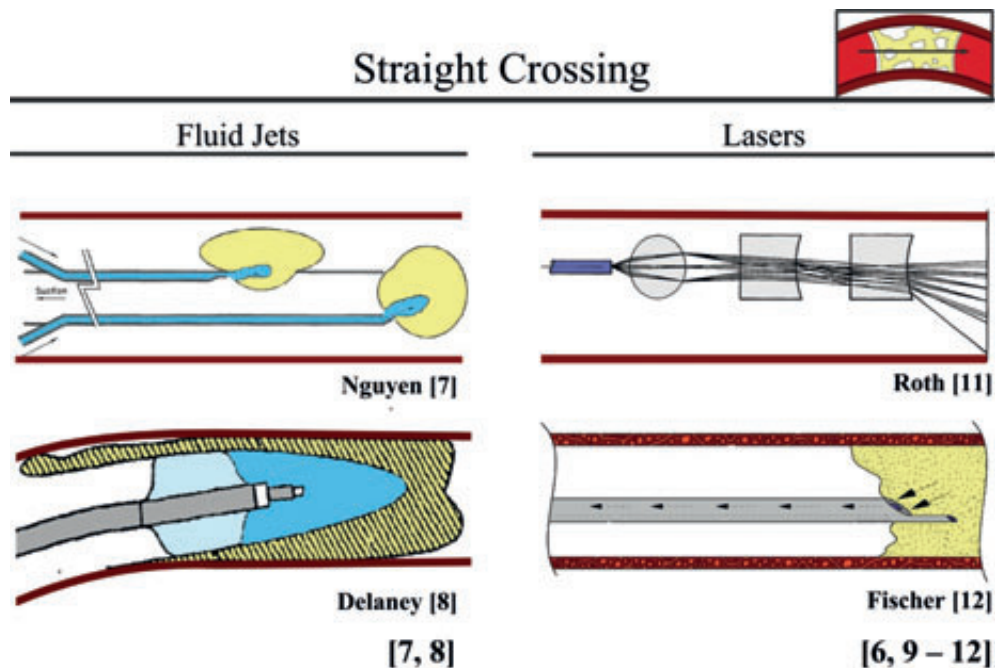
Figure 2.2— **Device: Straight Crossing.** Color indications: Red = Blood vessel wall. Yellow = plaque material. Light blue = balloon. Blue = liquid. Purple = laser.

crossing device specifically designed for crossing heavily calcified CTOs [13]. *Frontrunner XP* uses a hinged bilateral distal tip assembly to cross and subsequently treat the occlusion via the principle of blunt microdissection (see Figure 2.3 for a similar device is described by Maschke *et al.* [14]) [1, 14]. According to Mossop *et al.* [6], procedural success of up to 91% can be achieved in peripheral CTOs.

Axially Rotating Drills (In use for peripheral CTOs and acute occlusions): In atherectomy, axially rotating drills are used to resect and remove plaque from the blood vessel wall. There are three main types of axially rotating drill atherectomy devices: orbital, rotational, and directional. The three main drill types mainly differ in drill bit design.

Current FDA-approved rotating drill atherectomy devices are the *Clot Buster Amplatz Thrombectomy Device catheter* (Ø2.7 mm, *L* = 50 and 120 cm; ATD, Microvena, White Bear Lake, MN; in use for peripheral acute occlusions) (Figure 2.3) [15] and the *Wildcat catheter* (Avinger, Redwood City, CA; in use for peripheral CTOs) [16]. Success rates of 83% and 89% are reported in peripheral total occlusions with *ATD* and *Wildcat catheter*, respectively [16]. *ATD* is actuated by compressed air, rotating a shielded helical cutter at 150 000 rpm [15]. This rotation causes negative pressure in

2

close proximity to the cutter, which sucks the occlusive material towards the drill to macerate it. The *Wildcat catheter*, in comparison, is rotated by hand and driven by a flexible drive shaft. The tip can be altered while inside the body from a passive into an active (more aggressive) configuration. Furthermore, in [17-19] multiple additional rotating drill atherectomy devices are proposed for crossing acute (thrombotic) occlusions and CTOs (see Figure 2.3 for the drill designs proposed by Bashiri *et al.* [18] and Nash *et al.* [19]).

   Drive Belt Mechanism (Proposed for acute occlusions): Thompson *et al.* [20] propose a drive belt mechanism equipped with abrasive devices that shave off and remove small amounts of clot material at a time (Figure 2.3).

2.3.2. Environment

In the *Environment* approach, the direct environment around the device is the determinant for the crossing path. The environment around the device consists of the
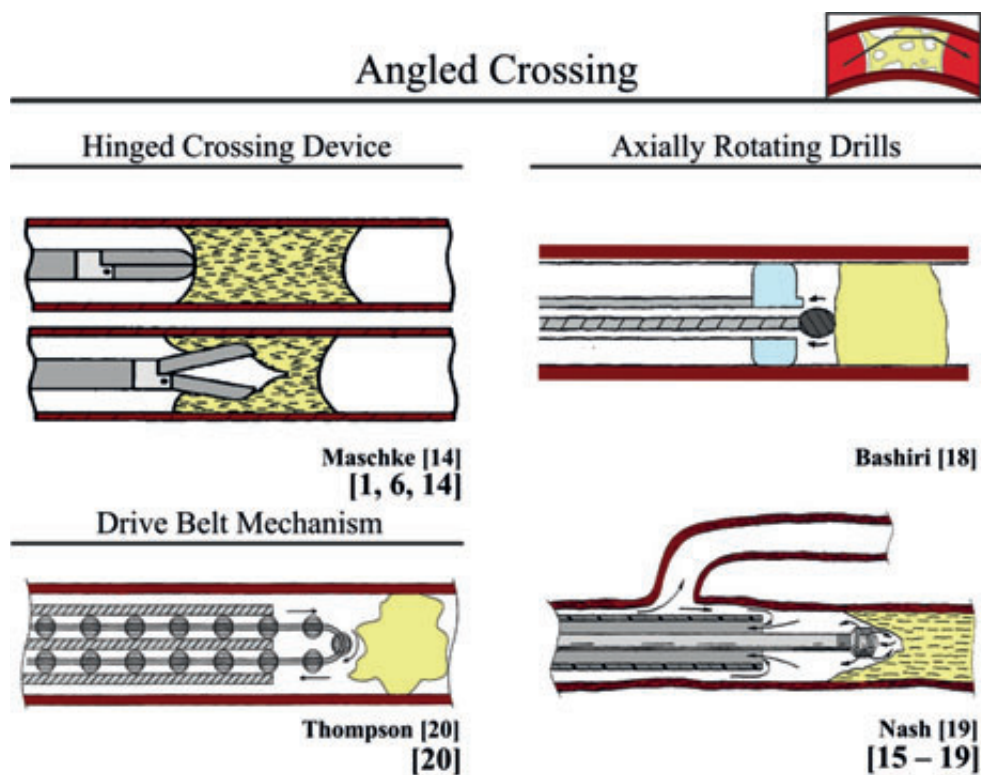
Figure 2.3— Device: Angled Crossing. Color indications: Red = Blood vessel wall. Yellow = plaque material. Light Blue = Balloon.

CTO and the blood vessel (wall). In *CTO guided Crossing*, the difference between biomechanical properties throughout the CTO is the determining factor for the crossing path. In *Blood vessel guided Crossing*, the blood vessel is used as a guide for crossing.

CTO guided Crossing

2

Two different CTO guided crossing paths can be distinguished: *Least Resistance Crossing* and *Tissue Selective Crossing*. In the first approach, less (pressure) resistant tissue types, such as fat, or micro vessels are used to cross the occlusion. This method is, amongst others, used by guidewires; the most common crossing device used in PCI. In the second approach, specific tissue types are targeted, such as calcium, fibrin, or fat, to cross the CTO. Which tissue is targeted depends on the type of crossing device used.

Least Resistance Crossing

Guidewires (In use for coronary CTOs, peripheral CTOs, and acute occlusions): Guidewires are thin (Ø0.22–0.40 mm for coronary application [4]) flexible wires that are inserted into the vascular system to cross occlusions (CTOs and acute occlusions) and guide other endovascular instruments, such as support and balloon catheters, typically during angioplasty. They usually consist of an inner core and outer spring-coil or polymer jacket [3].

As of today, guidewires remain the crossing tool of choice during PCI. Many of the discussed devices can be used in conjunction with a guidewire, but this is not a prerequisite. Over the last five years, the introduction of better guidewire designs (with higher tip loads, i.e., load in grams [g] at which the guidewire start to buckle, amongst others) has drastically improved the success rate of PCIs in CTOs [1, 3]. Dedicated CTO guidewire designs differ based on core design, the presence or absence of a polymer cover, tip design, and the type of coating (Table 2.1) [3].

Cores of contemporary dedicated CTO guidewires differ based on the diameter (with higher tip loads with increasing core diameter), the material used; stainless steel or nitinol, and the presence of core tapering. CTO guidewires with stainless steel cores, such as *Whisper* (Abbott Vascular, Abbott Park, IL, USA) and *Pilot* ((Abbott Vascular, Abbott Park, IL, USA), provide excellent support and tracking abilities (i.e., the ability of the guidewire body to follow the tip around bends). However, they are less flexible and more susceptible to buckling (i.e., have lower tip loads) than guidewires with nitinol cores, such as *Crosswire* (Terumo, Tokyo, Japan) [21, 22].

Another important factor influencing the tip load, support, and trackability of a guidewire is core tapering. Gradual or long tapers (in, for example, *Gaia* (Asahi Intecc. Corp., Nagoya, Japan)) provide less support and lower tip loads, but show greater trackability than short tapers (in, for example, *Confianza* (Asahi Intecc. Corp., Nagoya, Japan)). Tapered core designs are also proposed by [23, 24] (see Figure 2.4 for the design

proposed by Lupton *et al.* [24]).

Placed over the core is either an outer coil or polymer cover [22]. An outer coil (such as in *Persuader* (Medtronic, Minneapolis, MN, USA)) adds flexibility to the distal part of the guidewire and affects the support, tracking, and visibility. Instead of outer coils, some guidewires have a polymer or plastic covering over the tapered wire core (such as in *Whisper* (Asahi Intecc. Corp., Nagoya, Japan)). Polymer covers provide smooth tracking through torturous blood vessels.

Two different tip designs can be distinguished [22]: the core to tip (C2T) design (in which the core of the guidewire is fully extended to the tip (such as in *Runthrough NS* (Terumo Medical Corp., Tokyo, Japan))) and the shaping ribbon (SR) design (in which the core is not fully extended to the tip; instead a small piece of metal bridges the gap between the end of the core and the tip (such as in *PT Graphix Intermediate* (Boston Scientific, Natick, MA, USA))). The C2T design results in a more responsive guidewire, whereas the SR design is characterized by a more atraumatic flexible tip. Additionally, enlarged resilient tip portions (including the Magnum wire (Schneider, Zurich, Switzerland)) [25, 26] (see Figure 2.4 for the design proposed by Abele *et al.* [25]) are proposed to increase the tip load.

In order to decrease the sliding friction, low friction coefficient guidewires containing a hydrophilic (HI), hydrophobic (HO; polymeric), or hybrid (HY) coating (e.g., *Confianza* (Asahi Intecc. Corp., Nagoya, Japan)) are currently available. Hydrophilic coatings attract water and become gelatinous when wet, reducing friction, while hydrophobic coatings repel water, and also reduce friction, but not to the same extent as hydrophilic wires [3]. Available dedicated CTO guidewire types with a hydrophilic polymeric coating on the tip are (amongst others) *Fielder* (Asahi Intecc, Nagoya, Japan) and *Conquest Confianza* (Asahi Intecc, Nagoya, Japan) [2, 27, 28]. Additionally, two patents [25, 29] discuss the use of a hydrophilic coating, and Fearnot *et al.* [30] suggest a guidewire with an antithrombotic coating to decrease friction by dissolving the occlusion in direct contact with the guidewire.

According to Sianos *et al.* [3], the dedicated CTO guidewires should be used in conjunction with a micro catheter in order to prevent flexion and buckling (by improving its columnar strength), and as such improve the chance of a successful crossing procedure. Currently, several different (micro) guiding catheters, such as *Tornus* (Asahi Intecc, Nagoya, Japan), *CrossBoss* (Boston Scientific, Natick, MA, USA), and *Corsair* (Asahi Intecc, Nagoya, Japan) are available that have proven successful in increasing the buckling resistance of dedicated guidewires. Furthermore, Montague *et al.* [31] also proposes to use an introducer sheath (or micro catheter) to improve the columnar strength of the guidewire.

Another challenge in PCI of CTOs is the balloon uncrossable occlusion, in which the guidewire successfully crosses the occlusion, but neither a ballooncatheter nor micro-

catheter can be advanced through the CTO, seen in about 2% of the failure cases [1, 3]. If this is encountered, several strategies can be applied [3]: (1) a second stiff guidewire can be placed proximal to the CTO (preferably in a side-branch), (2) a second balloon can be inflated proximal to the CTO (preferably in a side branch), or (3) the balloon or microcatheter can be exchanged for a *Tornus* (Asahi Intecc, Nagoya, Japan) to enlarge the lumen. Furthermore, to overcome this problem altogether, multiple patents describe combined crossing and treatment tools (see Figure 2.4 for the devices proposed by Samson *et al.* [32] and Gerberding *et al.* [33]) [29, 32-38]. In these designs, a cable-actuated or self-expandable cage-like structure is described that in collapsed state functions as a guidewire and in expanded state as a treatment device, similar to a stent.

Crack Propagation Crossing (Proposed for peripheral CTOs, coronary CTOs, and acute occlusions): In the crack propagation crossing method, proposed by Zakai *et al.* [39] (see Figure 2.4), an elevated pressure between the crossing device and occlusion is used to "crack" or fragment the occlusion at its weakest region. Crack formation and propagation along the occlusion follows the path of least resistance until the distal side is reached and the pressure drops.

Tissue Selective Crossing

Spark Erosion (Proposed for coronary CTOs): In the spark erosion crossing method proposed by Bom *et al.* [40], two electrodes, placed in close proximity to the occlusion, generate sparks to fragment and cross occlusions (Figure 2.5). In this method, the electric conductivity of the tissue types determines the crossing path. As less electrically conductive materials, such as calcium, are not fragmented, whereas those that are electrically conductive, such as collagen and blood, are fragmented, this crossing method is less suitable for highly calcified CTOs.

Mechanical Vibration (In use for peripheral and coronary CTOs): In the mechanical vibration crossing method it is hypothesized that selective penetration depends on the difference in elasticity between the different tissue types. Collagen rich structures, such as the blood vessel wall, are not damaged by vibrational energy as they are elastic and, therefore, move out of the way. In contrast, less elastic atherosclerotic plaque tissue is not able to move out of the way and is thus fragmented.

Mechanical vibration energy is used in vibrational angioplasty. A current FDA-approved vibrational angioplasty device for crossing CTOs is the *Crosser catheter* (originally developed by FlowCardia, Sunnyvale, CA, currently by BARD Peripheral vascular Inc., Tempe, AZ, USA) that consists of a nitinol transmission wire with a blunt tip and a generator [5, 41, 42]. The *Crosser catheter* uses high frequency (21kHz) low-amplitude vibration energy to break through the cap and subsequently the CTO. A success rate of in between 40 and 75% was reported with this device in peripheral CTOs

Table 2.1— Dedicated guidewires frequently used in the treatment of CTOs. Durasteel = high tensile stainless steel, SS = Stainless Steel, N = no, Y = yes, C2T = Core 2 tip, SR = Shaping ribbon, I = Intermediate, HI = Hydrophilic, HO = hydrophobic, and HY = hybrid, hydrophilic shaft, uncoated tip. Tip load is defined as the load in grams [g] at which the guidewire starts to buckle. Table partly adapted from [3].

2

Manufacturer	CTO Guidewire	Diameter [inch/mm]	Core material	Tapering [inch/mm]	Tip design	Polymer cover	Coating	Tip load [g]
Abbott Vascular	Cross-it™ 100, 200, 300, and 400	0.014/0.35	SS	Y [0.01/0.25]	C2T	N	HI	2, 3, 4, and 6
	Whisper™ LS, MS, and ES	0.014 / 0.35	(Durasteel) SS	N	C2T	Y	HI	1
	Pilot™ 50, 150, 200	0.014 / 0.35	(Durasteel) SS	N	C2T	Y	HI	2, 4, and 6
	Progress™ 40, 80 120, 140T, and 200T	0.014 / 0.35	(Durasteel) SS	140T [0.010 / 0.25] 200T [0.009 / 0.23]	C2T	I	HI	4.8, 9.7, 13.9, 12.5, and 13.9
Asahi Intecc Corporation	Intermediate™	0.014 / 0.35	Data unavailable	N	C2T	N	HO	3
	Miraclebros™	0.014 / 0.35	Data unavailable	N	C2T	N	HO	3, 4.5, 6, 9, and 12
	Confianza™, Confianza™ Pro, and Confianza™ Pro "8-20"	0.014 / 0.35	Data unavailable	[0.009 / 0.23] Pro "8-20" [0.008 / 0.20]	C2T	N	HY	9, 12, and 20
	Fielder™, Fielder™ FC, and Fielder™ X-Treme	0.014 / 0.35 X-Treme 0.014 / 0.33	SS	X-Treme [0.009 / 0.23]	C2T	Y	HI	1, 0.8, and 0.8
	Gaia™ 1ˢᵗ, 2ⁿᵈ, and 3ʳᵈ	0.014 / 0.36	SS	1ˢᵗ [0.010 / 0.26] 2ⁿᵈ [0.010 / 0.28] 3ʳᵈ [0.012 / 0.30]	C2T	N	HI	1.7, 3.5, and 4.5
Boston Scientific	Choice™ PT and PT2 LS and MS	0.014 / 0.35	SS	N	C2T	Y	HI	2
	PT Graphix™ Intermediate Graphix P2™ LS and MS	0.014 / 0.35	SS	N	SR	Y	HI	3 and 4
Cordis / Johnson & Johnson	Shinobi™ and Shinobi™ Plus	0.014 / 0.35	Data unavailable	N	C2T	N	HO	2 and 4
Medtronic	Persuader™ 3, 6, and 9	0.014 / 0.35	Data unavailable	9 [0.011 / 0.28]	C2T	N	HI	3, 6, and 9
Terumo	Crosswire™ NT, Hard type 40, and Hard type 80	0.014 / 0.35	Nitinol	N	C2T	N	HI	5.5, 15.6, and 26.7
	Runthrough™ NS Floppy, NS Hypercoat*, and NS intermediate	0.014 / 0.35	Nitinol	N	C2T	N (Y*)	HI	1, 1, and 3.6
	Glidewire™ Gold Neuro	0.011 / 0.27	Nitinol	N	C2T	N	HI	1

[5, 41]. In another currently available vibrational angioplasty device designed by Medical Miracles (UK), a success rate of in between 75 and 77,4% was reported in coronary CTOs [1, 6]. In this device, a conventional coronary angioplasty guidewire is guided through a catheter and vibrated using reciprocal and lateral movements with frequencies between 16 to 100 Hz [1, 6]. Richter *et al.* [43] propose a similar device for crossing, in which a distal attachment mechanism couples a guidewire to the catheter and allows for a vibrating-generating means to add axial vibrating motion to the guidewire tip (see Figure 2.5).

Cavitation (Proposed for peripheral CTOs, coronary CTOs, and acute occlusions): In the cavitation crossing method, small cavitation bubbles are used to fragment specific tissue types. These cavitation bubbles are formed by rapid blood pressure changes, which cause the bubbles to implode, creating shockwaves that are able to fragment tissue. Tissues with high water content (such as fat) or brittle tissues (such as calcium) are fragmented, but vessels and nerves, which have high collagen content, are preserved.

Figure 2.4— Environment CTO: Least Resistance Crossing. Color indications: Red = Blood vessel wall. Yellow = plaque material. Light blue = balloon. Blue = liquid.

Cavitation– Ultrasonic Dissection: In ultrasonic dissection, cavitation bubbles are created using longitudinal vibrations generated by an ultrasonic generator (e.g., a piezoelectric crystal or a magnetic field). Siegel *et al.* describes a series of experiments in peripheral CTOs with an ultrasonic probe system consisting of a piezoelectric transducer, multiple titanium wires to transfer the ultrasonic energy to the tip of the device, and a Ø2.0 mm ball-shaped tip [44]. Similar devices are proposed by Wang *et al.* [45] (for acute occlusions), Nita *et al.* [46] (for all occlusion types), and Carmeli *et al.* (for CTOs) [47] (see Figure 2.5 for the design proposed by Carmeli *et al.* [47]). Siegel *et al.* [44] showed that heavily calcified regions resist recanalization with the ultrasonic probe, making this method less suited for crossing older, more calcified, CTOs. To increase the

effectiveness of ultrasonic dissection in acute occlusions, Evans *et al.* [48] propose the addition of thrombolysis (see Figure 2.5).

Cavitation– Laser: Another method to create cavitation bubbles for tissue fragmentation is a laser, as proposed by Visuri *et al.* [49] (see Figure 2.5). In this technique, small-pulsed burst of laser light are used to create cavitation bubbles that are able to fragment tissues with high water content.

Blood vessel guided Crossing

In *Blood vessel guided Crossing*, the blood vessel wall is used for support during the crossing procedure. A subdivision is made between crossing devices that use the blood
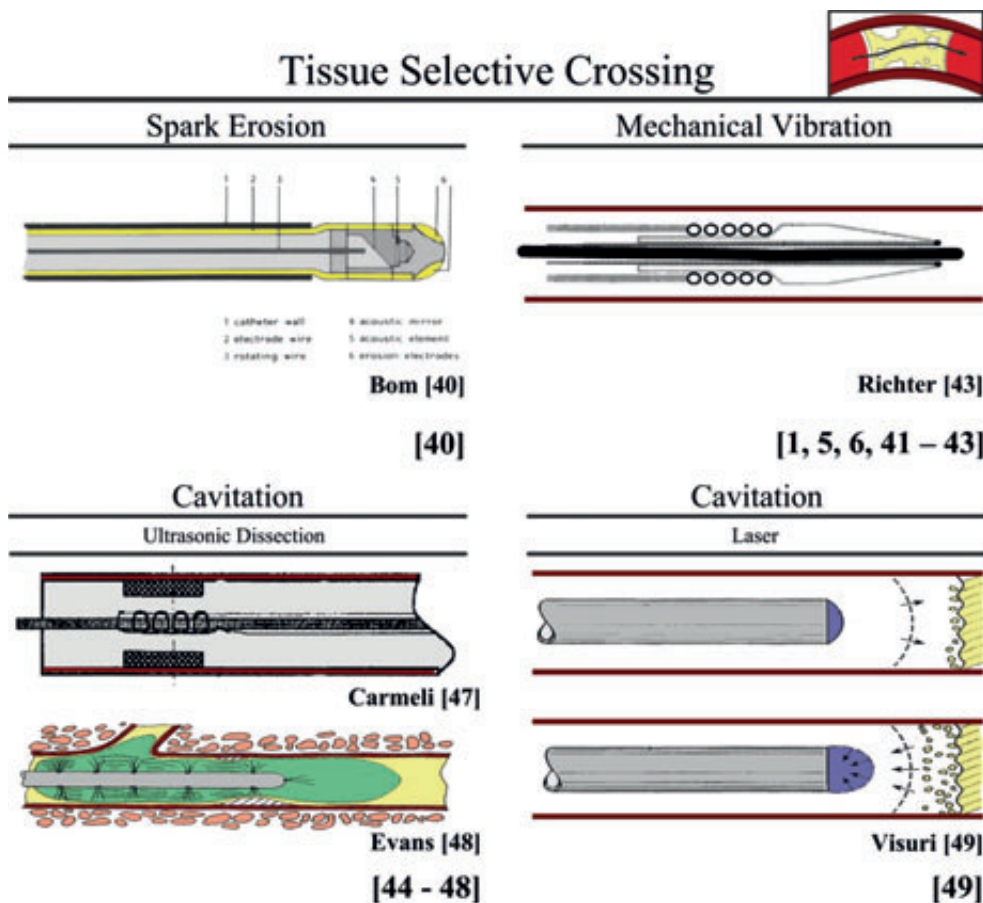
Figure 2.5— Environment CTO: Tissue Selective Crossing. Color indications: Red = Blood vessel wall. Yellow = plaque material. Bright Yellow = electrodes (in upper left schematic illustration). Purple = laser. Green = antithrombotic agent.

vessel wall to cross *via* the centerline of the blood vessel, called *Centerline Crossing,* and crossing devices that cross subintimally, i.e., between the intima and adventitia of the blood vessel wall, and use the support of these layers of the blood vessel wall for crossing, called *Subintimal Crossing*.

Centerline Crossing

2

Centerline following can be achieved with expanding or elastic self-centering mechanisms. In these devices the blood vessel wall is used for supporting and centering the crossing device. Not only does this support prevent blood vessel wall dissection or puncture, it also increases the buckling resistance of the tip of the guidewire or crossing device by increasing the effective diameter of the device. It must be noted, however, that if the crossing device is not translated exactly forward with the self-centering mechanism, true centerline following will be difficult in tortuous and longer occlusions.

Balloons (Undergoing clinical trials and proposed for peripheral CTOs): The centerline crossing *ENABLER-P Balloon Catheter System* (EndoCross Ltd., Yokneam, Israel), described by Buchbinder, is currently undergoing clinical trials for crossing peripheral CTOs [6]. *ENABLER-P* uses a specially designed support balloon that allows the balloon to elongate upon additional cyclical inflation, and as such moves a standard guidewire 3 mm forward without exceeding its inherent diameter. Multiple inflation/deflation cycles advances the guidewire forward through the occlusion. With this device, successful guidewire crossing was achieved in 86,4% of the cases [6]. Furthermore, Roucher *et al.* [50] and Kim *et al.* [51] propose to use a balloon in combination with a central crossing tool for centerline crossing of CTOs (see Figure 2.6).

Expanding Shape Memory Materials (SMM) (Proposed for acute occlusions): Currently no clinically tool is available or undergoing clinical trails using expanding SMMs, such as Shape Memory Alloys (SMAs) and Shape Memory Polymers (SMPs). However, Vardi *et al.* [52], Eckhouse *et al.* [53], and Stinis *et al.* [54] propose a mechanism using (self-) expanding SMAs, such as nitinol, to mimic the shape of the blood vessel wall in combination with a central crossing device (see Figure 2.6 for the designs proposed by Eckhouse *et al.* [53] and Stinis *et al.* [54]). Furthermore, in the designs of Eckhouse *et al.* [53] and Stinis *et al.* [54] the self-centering mechanism is translated forward with the crossing device, in principle allowing for true centerline following (Figure 2.6).

Subintimal Crossing

Due to the stiff proximal and distal cap of the CTO, the guidewire or crossing device will sometimes penetrate the intima and cross the CTO subintimally (between the intima and adventitia of the blood vessel wall). During subintimal crossing, the support of both the intima and adventitia keeps the crossing device collinear to the direction of the blood

2
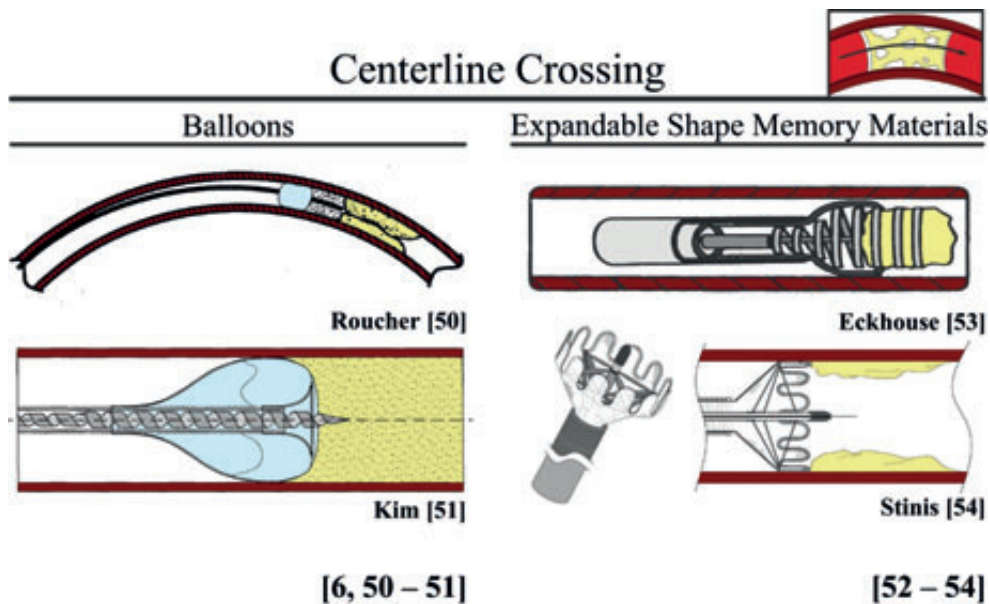
Figure 2.6— Environment Blood Vessel: Centerline Crossing. Color indications: Red = blood vessel wall. Yellow = plaque material. Light blue = balloon.

vessel wall and prevents perforation. This support, however, makes reentry in to the true lumen difficult and is often time consuming [5].

Multiple specialized subintimal crossing and reentry devices are currently in use and being developed to improve reentry to the true lumen, including the *Outback catheter* (Cordis Corporation, Bridgewater, NJ), the *Pioneer catheter* (Medtronic Inc., Santa Rosa, CA), and the *Stingray Re-entry Device* (Boston Scientific, Natick, MA) [5, 27, 28, 55]. These devices use a curved needle to puncture through the intima for reentry into the distal true lumen. This significantly increases the chance of successful reentry and thus the success rate of this crossing method [5].

2.3.3. User

In the *User* approach, all the control of the crossing path is given to the user. In this approach, the user of the crossing device is able to actively steer through the CTO, called *Directly Steered Crossing*. If the user so desires, heavily calcified regions can be circumnavigated. Furthermore, the addition of a tip sensor in *Sensor Enhanced Crossing* can give additional visual information about the position of the crossing device in relation to the direct environment. This information can, subsequently, be used as an extra navigational aid.

2

Directly Steered Crossing

Cable Actuation (In use for peripheral and coronary CTOs): Currently, a number of cable-actuated guidewires (≤ 0.4 mm) are available that can be actively steered through CTOs. The latest Cordis guidewires *Shinobi* and *Wizdom* enable tip deflection in one or two directions with a minimum bending angle of 45 degrees [6]. Furthermore, the *Venture Catheter* (St. Jude Medical, MN) is a support catheter able to deflect all commercially available 0.36 mm guidewires with angles up to 90 degrees [6].

Electroactive Polymer Actuation (Proposed for acute occlusions): Couvillon describes a directly steerable crossing device that uses multiple electroactive polymer actuators to steer the tip of the crossing device [56] (see Figure 2.7). These electroactive polymers act as joints, which enable direct steerability of the crossing device. By increasing the number of electroactive polymers, complex shapes such as three-dimensional s-curves can be achieved.

Segmented Balloons (Proposed for peripheral CTOs, coronary CTOs, and acute occlusions): The device proposed by Petrucci [57] uses a segmented intravascular balloon to steer the crossing device in plane (see Figure 2.7). In plane steering can assure a central position with respect to the CTO, but does not allow for adjusting the tip orientation. A major advantage of this steering technique is, however, that by keeping contact with the blood vessel wall, the buckling resistance is increased.

Directional Stiffness (Proposed for peripheral and coronary CTOs): Melsheimer *et al.* [58] propose a guidewire with a specialized tip geometry for steering (see Figure 2.7). In this approach, the difference in friction (between the tip and occlusion) caused by the orientation of the guidewire in the occlusion is used for steering. By rotating the guidewire, the tip orientation is changed and in this way the direction of motion. A similar approach is suggested by Eckhouse *et al.* [53].

External Magnetic/Electric Field (In use for peripheral and coronary CTOs): Magnetically or electrically enabled crossing tools have coils, magnets, or ferromagnetic materials incorporated inside their tip to enable tip deflection by an external electric or magnetic field outside the patient's body (see Figure 2.7 for a schematic representation of such systems). A currently available fully integrated magnetic navigation system for guidewires and catheters is the *Niobe MNS* (Stereotaxis, St. Louis, MO) with the associated FDA-approved magnetic *PowerAssert radiofrequency guidewire* [6]. Examples of other magnetically enabled guidewires are *Titan* (Stereotaxis, St. Louis, MI) and *Pegasus* (Stereotaxis, St. Louis, MO) [28].

Sensor Enhanced Crossing

The determination of the precise 3D position and orientation of the CTO and crossing device is often difficult to determine with conventional *Computed Tomography (CT)* images. This uncertainty about 3D tip position of the crossing device can lead to blood

2

Directly Steered Crossing

Electroactive Polymer Actuation

Couvillon [56]
[56]

Segmented Balloons

Petrucci [57]
[57]

Directional Stiffness

Melsheimer [58]
[53, 58]

External Magnetic/Electric Field

N S

[6, 28]

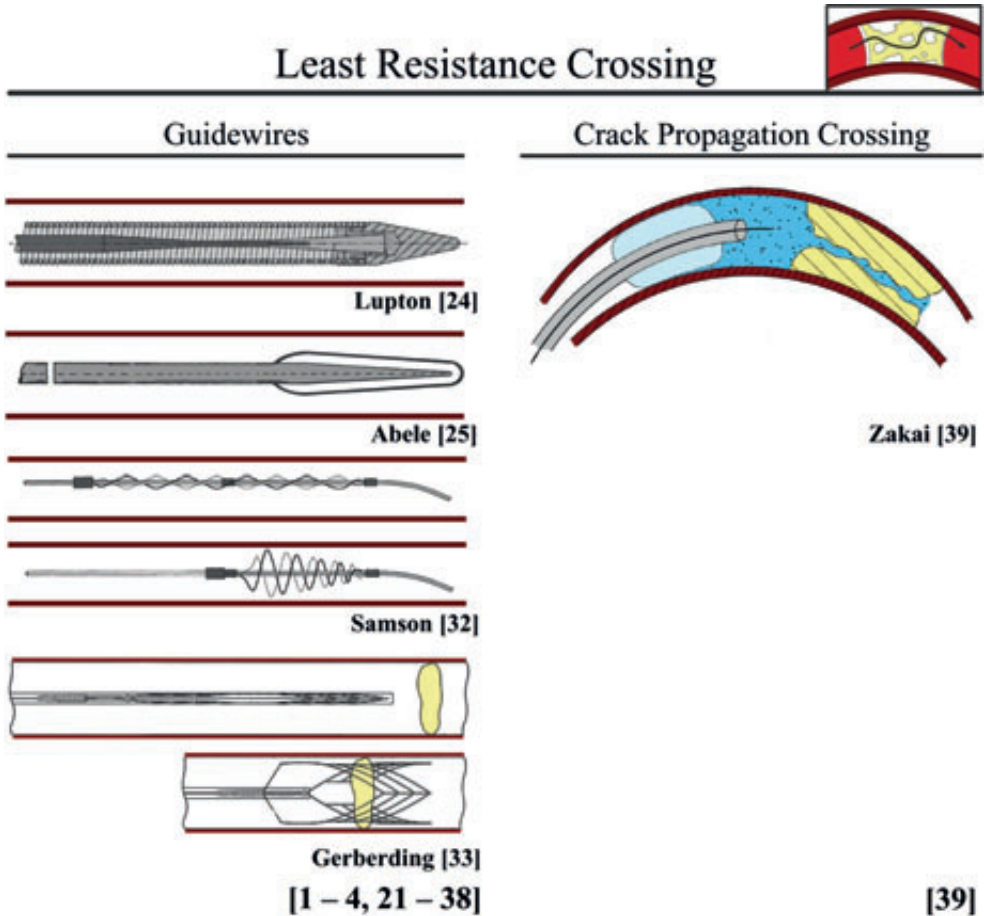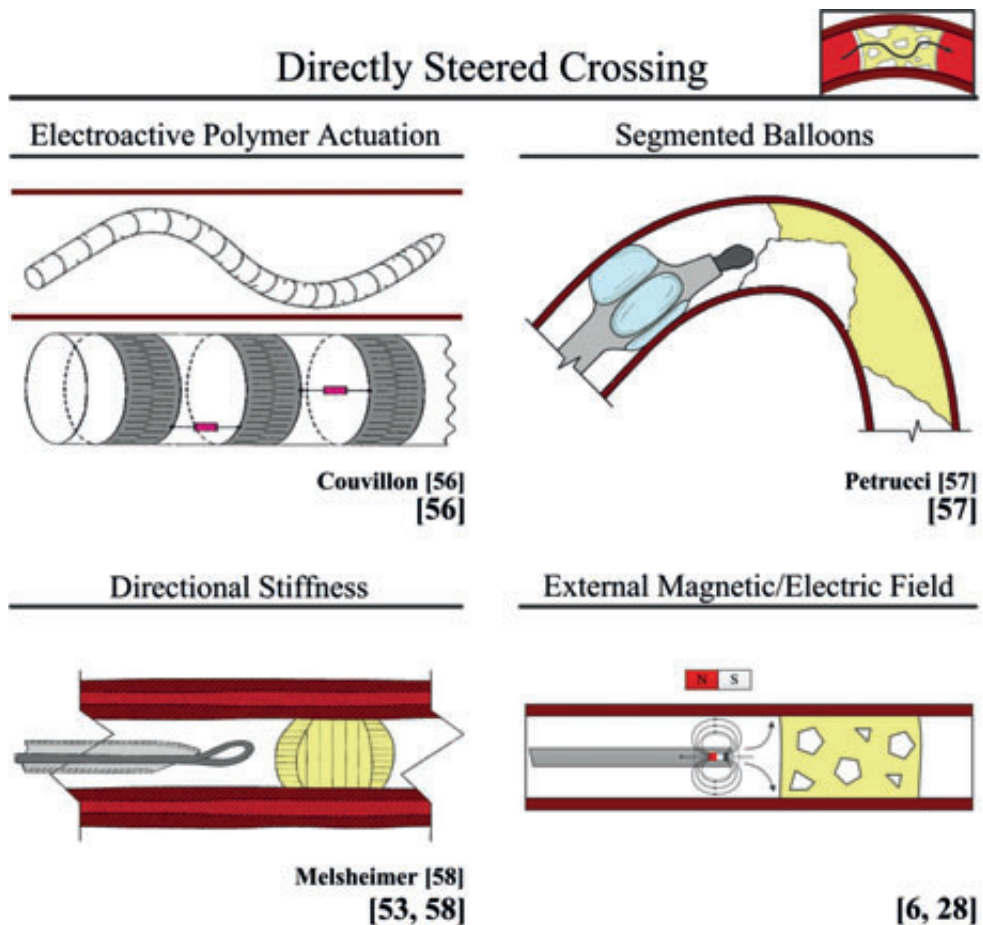**Figure 2.7— User: Directly Steered Crossing.** Color indications: Red = blood vessel wall. Yellow = plaque material. Light blue = balloon. Bright Pink = electroactive actuators.

vessel wall trauma, false lumen creation, and even discontinuation of the procedure. Therefore, there is a need for (intravascular) imaging methods that can give the user additional information about the orientation, position, and tissue types in front of the crossing device.

The latest advance in external cardiac imaging is *Multislice Computed Tomography (MSCT)*. The main fundamental advantage of MSCT in comparison to conventional *CT* is the ability to visualize the CTO in 3D. Although *MSCT* is currently mainly used as a pre-operative imaging technique, the new generation 128-slice *MSCT* scanners are finding their way into the intervention room for real-time 3D imaging of the coronaries [59].

Unfortunately, the resolution level is still relatively low and does not allow for reconstruction of thin intraluminal channels or thin collaterals [3]. Furthermore, one of the major concerns in using *MSCT* is the radiation dose received by the patient [3].

The latest advances in non-iodizing intravascular cardiac imaging techniques (with a higher resolution than *MSCT*) are *Optical Coherence Tomography* (*OCT*) and *IntraVascular UltraSound* (*IVUS*) (see Figure 2.8 for a schematic representation of both systems). In *OCT*, different tissue types are identified based on unique patterns of absorption, reflection, and scatter of near-infrared light [60]. In *IVUS*, the difference in reflectance of ultrasonic sound waves is used to distinguish different tissue types [61].

OCT (or Optical Coherence Reflectometry (*OCR*)) is currently applied as a tissue-selective (imaging) system in two FDA-approved micro-catheters: the *Safe-Cross Radiofrequency Total Occlusion Crossing (TOC) Guidewire System* (Ø0.36 mm, Intraluminal Therapeutics, Carlsbad, CA; in use for coronary CTOs) [1, 60, 62] and the *Ocelot catheter* (Avinger, Redwood City, CA; in use for peripheral CTOs) [63]. In the *TOC,* the *OCR* information is displayed as a waveform and a visible and audible signal warns the interventionist when the device tip approaches the blood vessel wall. A currently available *IVUS* catheter is the *Eagle Eye IVUS Catheter* (Volcano, San Diego, CA; in use peripheral and coronary CTOs) [3]. Furthermore, Webster [61] describes a device that uses *IVUS* for clot identification in combination with a laser for crossing (see Figure 2.8).

Two other imaging techniques for intravascular imaging are proposed in the patented literature using a laser [64] and electrical impedance [65]. In the laser approach, tissue distinction is accomplished by comparing the optical fluorescent characteristics of the excited tissue to that of known healthy and plaque tissue (see Figure 2.8 for a schematic representation of this system) [64]. In the electrical impedance approach, Lafontaine *et al.* [65] suggest using the difference in electrical impedance between the plaque and the blood vessel wall to distinguish between these two tissue types (see Figure 2.8).

2.4. DISCUSSION

2.4.1. Devices in Clinical Practice

Many of the identified devices are specifically designed for crossing total occlusions. Of the discussed devices, however, only a handful is FDA-approved and actually used in clinical practice. Even though quite promising results are achieved with the FDA-approved crossing devices, there is still improvement needed to increase the success rates in the highly calcified CTOs.

2
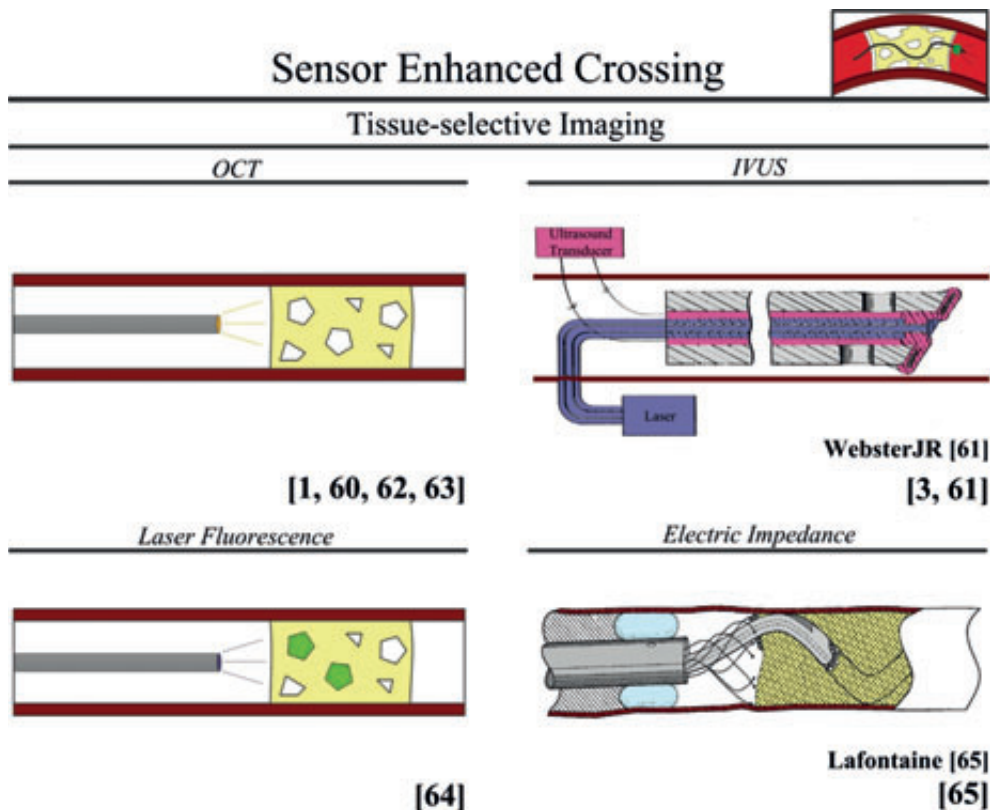
Figure 2.8— User: Sensor Enhanced Crossing. Color indications: Red = Blood vessel wall. Yellow = plaque material. Pink = ultrasound transducer. Light blue = balloon. Orange = Optical Coherence Tomography Imaging. Purple = laser. Bright Green = fluorescence. Abbreviations: OCT = Optical Coherence Tomography. IVUS = Intravascular Ultrasound.

Abandoned Crossing Devices

Even though many different devices have been developed for the treatment of heavily calcified CTOs, most of these devices never progressed beyond the investigational phase because of two main reasons. Firstly, many devices demonstrated excessively high rates of complications, particularly dissection or perforation [1]. Secondly, the success rates of many of abandoned devices was not significantly higher than those achieved by standard crossing devices [1]. Examples of failed CTO devices are axially rotating drill devices and several (excimer) lasers [1].

Abandoned device designs can give important clues to the reasons for the excessive complication rate. First of all, the above-mentioned devices all exhibit an extremely limited ability to adjust to the 3D shape of the blood vessel and CTO. This makes these

instruments potentially more prone to cause trauma, especially in tortuous CTOs. Secondly, lasers (and fluid jets) give limited feedback about the axial depth of the beam, making these devices more difficult to control. Thirdly, many of the axially rotating drill devices are designed with sharp edges to increase the chance of a successful crossing action, which at the same time increases the chance of blood vessel wall trauma.

Aside from directly visible damage to the blood vessel wall, other adverse events such as heat damage can also seriously impair the blood vessel wall and lead to serious complications. Lasers have been known to cause thermal damage to the surrounding tissues, warranting the slow advancement of 1 mm/second to increase absorption within the plaque [6]. Furthermore, we assume that the proposed device relying on spark erosion [40] and high speed rotating drills [15-19] can cause heat damage to the blood vessel wall as well, which may have also have been a potential factor that led to abandonment.

It could be argued that if the benefits outweigh the risks, the device could still be used in clinical practice. Preventive measures could then be taken to minimize the risks of blood vessel wall damage. However, in most cases the devices were not only associated with an increased risk of blood vessel wall damage, but were also not very beneficial when it comes to increasing the success rate of the intervention in comparison to standard crossing devices [1]. Success rates with lasers in coronary CTOs, for example, did not exceed 61% [6].

Current Crossing Devices

In recent years, promising results have been illustrated using crossing devices such as the *Frontrunner XP* and the *Crosser catheter*. Success rates as high as 90% are reported with these new crossing devices. This raises the question if there is still a need for innovative crossing devices. The answer to this question is yes.

The reported high success rates with the new crossing devices are sometimes deceptive. The highest success rates are reported in peripheral CTOs or occlusions younger than 3 months old, and are often in the hands of very experienced operators. For example, the high success rate achieved with *Frontrunner XP* and *Enabler-P* of 91% and 86,4%, respectively, were both achieved in peripheral vessels [6]. Peripheral and younger CTOs are usually less calcified than coronary CTOs and thus easier to cross [1, 2]. This is substantiated by the fact that even though *Frontrunner XP* was originally designed for crossing coronary CTOs, more recently, the device has been increasingly used to facilitate guidewire crossing in peripheral CTOs [13]. Furthermore, it was found that he extent of calcification increases the frequency of complications and decreases the success rate of *Frontrunner XP* [13].

Crossing heavily calcified lesions is, therefore, still the limiting factor for success in most devices. Next to *Frontrunner XP*, the age of the CTO, calcification, and the length of the occlusion, were indicated to negatively affect the success rate in *ATD, Wildcat catheter, Safe-Cross,* and the *vibrational angioplasty device* (Medical Miracles, UK) [6, 16,

2

60, 15]. Calcium is more resistant to compression and resection, and thus requires higher energy input for crossing. Therefore, to improve the success rate the energy delivery on the CTO needs to increase.

Limited directional control is also an issue in most of current crossing device designs. For example, the *vibrational angioplasty device* is considered unsuitable for smaller and tortuous vessels due to limited directional control [6]. Additionally, *Crosser Catheter* has the tendency to move straight inside a vessel, which limits its trackability and increases the chance of entering side-branches and dissection [6]. As coronary CTOs tend to be smaller in diameter and more tortuous than peripheral CTOs, they pose a bigger challenge. Adding the ability to actively navigate through occlusions, such as in steerable guidewires, only solves part of this problem, as visual information is still needed about the relative position of the device in relation to the CTO.

The position of the CTO (in the coronary or peripheral vasculature) is also of influence on the type of crossing device that can be applied in a safe manner. The heart is sensitive to arrhythmogenic effects caused by cavitation, vibration, and heat (for example). Therefore, the use of lasers, mechanical vibration, and cavitation for crossing coronary CTOs are relatively high risk. Since the chance of arrhythmogenic effects is minimal in crossing peripheral CTOs, the treatment options, and the use of a laser (for example), is less risky.

Proposed Crossing Devices

Next to the previously discussed devices, many devices are proposed for crossing CTOs (amongst other occlusion types), but not (yet) seen in clinical practice or trials. Unfortunately, no information is found about the reason that these are not (yet) clinically available. Therefore, assumptions are made based on design considerations.

In general, the medical environment, including the size, shape, and biomechanical properties of the blood vessel and CTO, in which the device needs to function, should be the starting point of the design process. Lack of proper research into the medical environment can lead to device malfunction or procedural failure, which are both assumed to have occurred in several of the proposed designs.

Size restrictions of the device, based on the position of the CTO, will give important clues if certain working principles are feasible or if new issues, such as insufficient force generation, can arise. Additionally, the limitations and abilities of different manufacturing techniques should also be taken into account. Some of the described devices, such as the drive belt mechanism proposed by Thompson *et al.* [20], are most likely impossible to manufacture at the 1 mm diameter scale needed for the coronary application.

The biomechanical properties of the CTO and the blood vessel wall are also important factors to take into account. Since the inability to successfully cross the CTO is the most common failure mode, mainly due to buckling of the guidewire, the buckling resistance of the device should be a major factor to take into account in the design.

However, high buckling resistance should not go hand in hand with an increased risk of blood vessel wall damage, as is the case in lasers and fluid jets. Since buckling and blood vessel wall trauma can both lead to procedural failure, it is important to find middle ground, which is seen in the centerline crossing devices.

Next to individual properties, the difference in biomechanical properties within the CTO itself, as well as the biomechanical difference of the CTO and blood vessel should be taken into account when designing. For example, in the crack propagation crossing method, proposed by Zakai *et al.* [39], it is assumed that the CTO will crack before the blood vessel wall is damaged. However, it is more likely that the pressure needed to cross a heavily calcified CTO is higher than the pressure needed to damage, unnaturally stretch, or even rupture, the blood vessel wall. Additionally, it is assumed that precise steering with the directional stiffness guidewire is difficult since the friction between the different tissue types inside the CTO will differ, resulting in varying deflections of the tip [58].

Finally, non-design related factors that could have halted development of the proposed devices are the required high-risk and high-cost investments to develop, test, legalize, and manufacture a clinical tool. Some of the proposed devices have probably never made it to a testing phase. Which devices this involves is unclear.

2.4.2. Future Crossing Device

Desired Crossing Path

The question remains that if a crossing device was to be developed that is technically able to cross the occlusion, what would then be the best crossing path. All the described crossing paths and associated crossing devices have their advantages and disadvantages. However, the two most important factor that needs to be taken into account when determining the best crossing path is the chance of blood vessel wall damage and buckling resistance of the crossing tool; allowing for crossing heavily calcified regions.

In order to prevent blood vessel wall trauma, it is important to be able to steer clear of the blood vessel wall. Therefore, the crossing device should be able to adapt to the direction and shape of the blood vessel. Since in the *Device* approach (*A*), the environment and user are of minimal influence on the crossing path, this crossing method is not considered feasible for integration in a future crossing device. However, preventing blood vessel wall contact and damage can be achieved in the *Environment* (*B*) and *User* (*C*) defined crossing.

The most obvious choice seems to be to give the user full control of the crossing action (*User* approach). However, the image capability, especially in 3D, of the conventional C-arcs in most clinics, is still limited for a real-time application. Therefore, it is questionable whether the interventionist would have sufficient information at hand to prevent blood vessel wall trauma.

2

Safe intraluminal crossing can be assured by giving the interventionist additional information with a tissue-selective imaging technique (*Sensor Enhanced Crossing*) or by adding a mechanism that ensures the device follows the path of least resistance or centerline through the CTO. Even though both approaches can assure safe crossing, another important factor that should be taken into account is the buckling resistance of the crossing device. In this respect, the *Centerline Crossing* approach is most promising, due to the increase of effective cross-sectional diameter.

Therefore, in order to ensure both safe and successful crossing of the most heavily calcified CTOs, it not only important to steer clear of the blood vessel wall, but also to prevent buckling. This can be assured by combining the user approach, in which the interventionist is able to actively navigate through the CTO and is thus able to circumnavigate heavily calcified regions, with the environment approach, where the blood vessel wall or path of least resistance is followed through the CTO. Furthermore, by adding a tissue-selective imaging technique, as in *Sensor Enhanced Crossing*, the success rate might be improved by giving the user additional information about the consistency and shape of the CTO.

Desired Functionality

According to the experts, if a new device for CTO crossing were to be developed it would be necessary to incorporate three functions: (1) crossing of the harder calcified regions, (2) visualization, and (3) steerability. Some crossing devices were identified that have incorporated one of these functions, such as visualization in the *Ocelot Catheter* (Avinger, Redwood City, CA) [63]. However, not a single device exists that integrates all three functionalities.

In order to achieve all three described functions in a future device it is necessary to look into the possibility of further miniaturization of the device components or to look into shared component use. In the latter approach components are used to achieve multiple functions, such as steering and crossing of heavily calcified regions. An example of a multifunctional device component is a miniature cable. Cables can be used for steering as in the steerable guidewires, visualization as in *OCT* and *IVUS*, actuators as in rotating drills and drive belt mechanisms, and for crossing as in lasers. Cables are thus very versatile, and are available in many different shapes, sizes, and materials. However, miniature cables lack buckling resistance at the required small sizes. It would, therefore, be necessary to look into additional measures to ensure sufficient buckling resistance, such as balloons or expandable structures.

It may also be possible to design a highly effective and safe crossing device without incorporating all three functionalities described by the experts. By focusing on increasing the buckling resistance and preventing blood vessel wall damage, other options, such as an inherent safe device that is able to cross the harder calcified regions and follows the blood vessel wall, may be explored.

2.5. CONCLUSION

In this review, a comprehensive overview is given of current, proposed, and abandoned devices for crossing total occlusions, including CTOs. The identified crossing devices were subdivided based on their crossing paths through the occlusion and subsequently reviewed based on their ability to safely cross heavily calcified CTOs. Insight is given into reasons for abandonment of past crossing devices, needed improvement to current crossing devices, and design considerations for future crossing devices. To improve the success rate for PCI in CTOs in future it is argued that a future crossing device should be able to safely and efficiently cross the hardest CTO lesions using a combined *user* approach, in which the interventionist is able to actively navigate the crossing device, and *environment* approach, to allow for an inherent safe device with improved buckling resistance.

ACKNOWLEDGMENTS

REFERENCES

[1]   Stone GW, Reifart NJ, Moussa I, Hoye A, Cox DA, Colombo A et al. Percutaneous recanalization of chronically occluded coronary arteries - A consensus document - Part II. Circulation. 2005;112(16): pp. 2530-2537.

[2]   Galassi A, Tomasello S, Reifart N, Werner GS, Sianos G, Bonnier H et al. In-hospital outcomes of percutaneous coronary intervention in patients with chronic total occlusion: insights from the ERCTO (European Registry of Chronic Total Occlusion) registry. EuroIntervention. 2011;7(4): pp. 472-479.

[3]   Sianos G, Werner GS, Galassi A, Papafaklis MI, Escaned J, Hildick-Smith D et al. Recanalisation of Chronic Total coronary Occlusions: 2012 consensus document from the EuroCTO club. EuroIntervention. 2012;8(1): pp. 139-145.

[4]   Stone GW, Colombo A, Teirstein PS, Moses JW, Leon MB, Reifart NJ et al. Percutaneous Recanalization of Chronically Occluded Coronary Arteries: Procedural Techniques, Devices, and Results. Catheterization and Cardiovascular Interventions. 2005;66: pp. 217-236.

[5]   Liang GZ, Zhang FX. Novel devices and specialized techniques in recanalization of peripheral artery chronic total occlusions (CTOs) — A literature review. International Journal of Cardiology. 2013;165: pp. 423-429.

[6]   Yalonetsky S, Osherov AB, Strauss BH, Galassi AR, Tomasello S, Khamis H. Chronic Total Occlusions. A guide to recanalization (2nd ed.). Hoboken, NJ: Wiley-Blackwell, 2013.

[7]   Nguyen HD, Mirizzi MS, inventors; Vnus Medical Technologies, Inc., assignee. Methods and Apparatus for Thrombectomy System. World Intellectual Property Organization Patent 2008121481 A1. 2008.

2

[8]   Delaney D, Johansson P, Constantz BR, inventors. Catheter Devices and Methods for their Use in the Treatment of Calcified Vascular Occlusions. United States Patent 20050059955 A1. 2005.

[9]   Bach B, inventor. Method and apparatus for removal of plaque from blood vessels. United States Patent 4765330. 1988.

[10]   Pallarito AL, inventor. Optical Fibre and Laser for Removal of Arterial or Vascular Obstructions. United States Patent 5733277. 1998.

[11]   Roth LA, Herman SJ, Turnquist CR, Sinofsky EL, Wong JY, inventors; C. R. Bard Inc., assignee. Catheter System for Controlled Removal by Radiant Energy of Biological Obstructions. United States Patent 4817601. 1989.

[12]   Fischer FJJ, inventor. Wire Guided Thrombectomy Device. United States Patent 20100063488 A1. 2010.

[13]   Charalambous N, Schafer PJ, Trentmann J, Humme TH, Stohring C, Muller-Hulsbeck S et al. Percutaneous Intraluminal Recanalization of Long, Chronic Superficial Femoral and Popliteal Occlusions Using the Frontrunner XP CTO Device: A Single-Center Experience. Cardiovascular and Interventional Radiology. 2010;33(1): pp. 25-33.

[14]   Maschke M, inventor. Catheter and Medical Apparatus as well as Method for Assisting an Intervention to Remove Plaque. United States Patent 20100241147 A1. 2010 Sep 23.

[15]   Delomez M, Beregi JP, Willoteaux S, Bauchart JJ, d'Othee BJ, Asseman P et al. Mechanical thrombectomy in patients with deep venous thrombosis. Cardiovascular and Interventional Radiology. 2001;24(1): pp. 42-48.

[16]   Pigott JP, Raja ML, Davis T, Connect Trial I. A multicenter experience evaluating chronic total occlusion crossing with the Wildcat catheter (the CONNECT study). Journal of Vascular Surgery. 2012;56(6): pp. 1615-1621.

[17]   Henrie RA, inventor. Catheter for removing occlusive material. United States Patent 4729763. 1988.

[18]   Bashiri M, Cornil A, inventors. Devices and methods for removing occlusions in vessels. United States Patent 20030195536 A1. 2003.

[19]   Nash JE, Fisher WT, DodsonJR CW, inventors; Kensey Nash Corporation, assignee. System for Opening a Lumen in an Occluded Blood Vessel. United States Patent 20080097500 A1. 2008.

[20]   Thompson D, Perkins DH, Johnson J, Silver M, Mauch K, inventors. Obstruction Removal System. World Intellectual Property Organization Patent 2009088783 A2. 2009.

[21]   Bahl VK, Chandra S, Goswami KC, Manchanda SC. Crosswire (TM) for recanalization of total occlusive coronary arteries. Catheterization and Cardiovascular Diagnosis. 1998;45(3): pp. 323-327.

[22]   Erglis A, Narbute I, Sondore D, Grave A, Jegere S. Tools & Techniques: coronary guidewires. Eurointervention. 2010;6: pp. 1-8.

[23]   Ogata W, Katoh O, inventors; Retrovascular, Inc., assignee. Methods and Device for Recanalization of Occluded Body Vessels using a Double-sided Guidewire. United States Patent 20120289983 A1. 2012.

[24]   Lupton HW, Bruzzi M, inventors. Guide Wire for use in Re-canalising a Vascular Occlusion in a Human or Animal Subject. United States Patent 20120197276 A1. 2012.

[25]   Abele JE, Heath KR, Landman MS, Mclaughlin PD, inventors; Boston Scientific Corporation, assignee. Guidewire for Crossing Occlusions in Blood Vessels. United States Patent 5303714. 1994.

[26]   Meier B, Carlier M, Finci L, Nukta E, Urban P, Niederhauser W et al. Magnum Wire for Balloon Recanalization of Chronic Total Coronary Occlusions. The American Journal of Cardiology. 1989;64: pp. 148-154.

[27]   Genereux P, Dangas G. Antegrade, Retrograde, and Combination Strategies for Chronic Total Occlusions. Current Cardiology Reports. 2010;12: pp. 429-439.

[28]   Brilakis ES, Grantham JA, Thompson CA, DeMartini TJ, Prasad A, Sandhu GS et al. The Retrograde Approach to Coronary Artery Chronic Total Occlusions: A Practical Approach. Catheterization and Cardiovascular Interventions. 2012;79(1): pp. 3-19.

[29]   Huffmaster A, inventor. Device for Removing a Blood Clot From a Blood Vessel. World Intellectual Property Organization Patent 2005016156 A1. 2005.

[30]   Fearnot NE, Ragheb AO, Voorhees III WD, inventors; MED Institute, Inc., assignee. Thrombolytic Treated Intravascular Medical Device. United States Patent 5380299. 1995.

[31]   Montague RJ, Blackledge RV, inventors. System, Apparatus and Method for Opening an Occluded Lesion. World Intellectual Property Organization Patent 2009002971 A1. 2008.

[32]   Samson G, Carrison HF, inventors; Target Therapeutics, Inc., assignee. Medical Clot Treatment Device with Distal Filter. United States Patent 20110882493 A1. 2011.

[33]   Gerberding B, Jensen M, Abrams RM, inventors. System and Methods for Capturing and Removing Blood Clots. World Intellectual Property Organization Patent 2012167137 A1. 2012.

[34]   Engelson ET, Samson G, inventors; Target Therapeutics, Inc., assignee. Mechanical Clot Encasing and Removal Wire. United States Patent 6066158. 2000.

[35]   Sakai N, inventor; Wellfind Corporation, Ltd., assignee. Intravascular Thrombus Capturing Instrument. United States Patent 20120016407 A1. 2012.

[36]   Lemelson JH, inventor; Bacchus Vascular, Inc., assignee. Drug units and methods for treating blood clots. United States Patent 5017379 A. 1988.

[37]   Santra S, Mericle RA, Batich CD, Stanley JT, Eskioglu E, inventors; University of Florida Research Foundation, Inc., assignee. Devices and Methods for Disruption and Removal of Luminal Occlusions. United States Patent 20100023038 A1. 2010.

[38]   Tanaka DA, Souza AM, inventors. Vascular Thrombectomy Apparatus and Method of Use. United States Patent 20130289608 A1. 2013 Oct 31.

[39]   Zakai A, Rottenberg D, inventors. Device and Method for Crossing a Vascular Occlusion. World Intellectual Property Organization Patent 2008035349 A1. 2008.

[40]   Bom N, Slager CJ, Egmond FC, Lancee CT, Serruys PW. Intra-Arterial Ultrasonic Imaging for Recanalization by Spark Erosion. Ultrasound in Med & Biol. 1988;14(4): pp. 257-261.

[41]   Khalid MR, Khalid FR, Farooqui FA, Devireddy CM, Robertson GC, Niazi K. A Novel Catheter in Patients With Peripheral Chronic Total Occlusions: A Single Center Experience. Catheterization and Cardiovascular Interventions. 2010;76: pp. 735-739.

[42]   Zander T, Rabellino M, Baldi S, Blasco O, Maynar M. Infrainguinal revascularization using the Crosser (R) vibrational system. Minimally Invasive Therapy & Allied Technologies. 2010;19(3-4): pp. 231-236.

[43]   Richter J, Pansky A, Demer G, inventors; Oscillon LTD, assignee. Device for Recanalization of Vessel Occlusions Using Guide Wire and Method of Use. United States Patent 20110196396 A1. 2011.

[44]   Siegel RJ, Cumberland DC, Myler RK, DonMichael TA. Percutaneous Ultrasonic Angioplasty: Initial Clinical Experience. The Lancet. 1989: pp. 772-774.

[45]   Wang G, Sundaram S, Pant K, Feng J, Storm P, inventors; CFD Research Corporation, assignee. Thrombectomy Microcatheter. United States Patent 20080119780 A1. 2008.

2

2

[46]   Nita H, inventor; Baxter International, Inc., Ultra-sound Catheter for Removing Obstructions from Tubular Anatomical Structures such as Blood Vessels. United States Patent 5405318. 1995.

[47]   Carmeli R, Einav J, Yonat I, inventors; Eyoca Medical, Ltd., assignee. Device and method for opening vascular obstructions. United States Patent 20120302820 A1. 2012.

[48]   Evans M, Dubrul WR, inventors; Bacchus Vascular, Inc., assignee. Thrombolysis Device. United States Patent 6508782 B1. 2003.

[49]   Visuri SR, DaSilva LB, Celliers PM, Alondon R, Maitland IV DJ, Esch VC, inventors; Endo Vasix, Inc., assignee. Photoacoustic Removal of Occlusions from Blood Vessels. United States Patent 20050021013 A1. 2003.

[50]   Roucher JR LR, inventor. Anchoring, Supporting and Centering Catheter System for Treating Chronic Total Occlusions. United States Patent 20040230219 A1. 2004.

[51]   Kim DH, Chin R, inventors. Methods and Apparatus for Treating Vascular Occlusions. World Intellectual Property Organization Patent 2008148041 A1. 2008.

[52]   Vardi G, inventor. Percutaneous Thrombus Extraction Device and Method. World Intellectual Property Organization Patent 2012068452 A1. 2012.

[53]   Eckhouse R, Sudin Y, Eckhouse S, inventors; Rapid Medical, Ltd., assignee. Clot Removal Device with Steerable Element. United States Patent 20130325056 A1. 2013.

[54]   Stinis CT, inventor. Systems, Devices, and Methods for Removing Plaque from a Patient's Vasculature. European Patent 2670318 A1. 2013.

[55]   Azemi T, Fram DB, Hirst JA. Bailout antegrade coronary reentry with the stingray (TM) balloon and guidewire in the setting of an acute myocardial infarction and cardiogenic shock. Catheterization and Cardiovascular Interventions. 2013;82(3): pp. E211-E4.

[56]   Couvillon LAJ, inventor; Boston Scientific Scimed, Inc., assignee. Thrombolysis Catheter. United States Patent 20100191175 A1. 2010.

[57]   Petrucci G, Khanna PK, inventors. Treating Occlusions Within Body Vessels. World Intellectual Property Organization Patent 2013134285 A1. 2013.

[58]   Melsheimer JS, Urbanski J, inventors; Cook, Inc., assignee. Chronic Total Occlusion (CTO) Removal Device. United States Patent 20090093829 A1. 2009.

[59]   Ulzheimer S, Flohr T. Multislice CT: Current Technology and Future Developments. Chapter in: Medical Radiology. Berlin, Germany: Springer, 2009: pp. 3-23.

[60]   Kirvaitis RJ, Parr L, Kelly LM, Reese A, Kamineni R, Heuser RR. Recanalization of chronic total peripheral arterial occlusions using optical coherent reflectometry with guided radiofrequency energy: A single center experience. Catheterization and Cardiovascular Interventions. 2007;69(4): pp. 532-540.

[61]   Webster JR WW, inventor. Catheter for Removing Arteriosclerotic Plaque. World Intellectual Property Organization Patent 8500510. 1985.

[62]   Segev A, Strauss BH. Novel Approaches for the Treatment of Chronic Total Coronary Occlusions. Journal of Interventional Cardiology. 2004;17(6): pp. 411-416.

[63]   Schwindt A, Reimers B, Scheinert D, Selmon M, Pigott JP, George JC et al. Crossing chronic total occlusions with the Ocelot system: the initial European experience. Eurointervention. 2013;9(7): pp. 854-862.

[64]   Macy JR WW, House MD, Murphy-Chutorian DR, inventors. Method and Apparatus for Detecting and Removing Plaque From Arteries by Laser. Canadian Patent 2003535. 1990.

[65]   Lafontaine DM, inventor; Scimed Life Systems, Inc., assignee. Method and Apparatus for Creating Channels Through Vascular Total Occlusions. United States Patent 6416523. 2002.

3

CHAPTER 3

A MINIATURE MULTISTEERABLE DEVICE

AIMÉE SAKES, AWAZ ALI, JOVANA JANJIC, AND PAUL BREEDVELD

3

Abstract— Even though technological advances have increased the application area of Minimally Invasive Surgery (MIS), there are still hurdles to allow for widespread adoption for more complex procedures. The development of steerable instruments, in which the surgeon can alter the tip orientation, has increased the application area of MIS, but they are bulky, which; limits their ability to navigate through narrow environments, and complex, which complicates miniaturization. Furthermore, they do not allow for navigating through complex anatomies. In an effort to improve the dexterity of the MIS instruments, while minimizing the outer dimensions, the previously developed cable-ring mechanism was redesigned, resulting in the thinnest, Ø2 mm (Ø1 mm lumen), 8 Degrees Of Freedom (DOF) multisteerable tip for MIS to date. The multisteerable tip consists of 4 steerable segments of 2-DOF stackable elements allowing for ±90° articulation, as well the construction of complex shapes, actuated by 16 Ø0.2 mm stainless steel cables. In a proof-of-principle experiment, an ultrasound transducer and optical shape sensing fiber were inserted in the lumen and the multisteerable tip was used to perform scanning motions in order to reconstruct a wire frame in 3D. This configuration could in future be used to safely navigate through delicate environments and allow for tissue characterization. Therefore, the multisteerable tip has the potential to increase the application area of MIS in future, as it allows for improved dexterity, the ability to guide several tip tools towards the operation area, and the ability to navigate through tight anatomies.

Keywords— Minimal Invasive Surgyer (MIS), Medical Device Design, Miniature (Multi)Steerable Instruments, Improved Dexterity, Forward-Looking Ultrasound Imaging, Optical Shape Sensing (OSS).

3.1. INTRODUCTION

Minimally Invasive Surgery (MIS) has revolutionized the surgical treatment of many disorders and has multiple advantages over open surgery, including improved survival rates, less scar formation, shorter hospital stays, and lower infection rates [1]. Unfortunately, as of today, the implementation of MIS for more complex procedures has been impeded [2]. For these procedures, the benefits of MIS over open surgery are questionable and often only achieved by expert surgeons in highly specialist hospitals [2]. More widespread implementation of complicated MIS procedures requires improved dexterity and further miniaturization of current, usually rigid, MIS instruments [3-5].

In order to improve the dexterity of current (rigid) minimally invasive instrumentation, a number of (robotic) steerable instruments, such as *Endowrist* (Ø5–8 mm, Intuitive Surgical, Sunnyvale, CA, USA) [6] and *Autonomy Laparo-Angle* (Ø 5 mm, Cambridge Endo, Wrentham, MA, USA) [7], have been developed or are under development [8, 9]. In these instruments, a steerable segment is added to tip section consisting of a pulley mechanism in *Endowrist* or a flexible structure built of a compliant spline in *Autonomy Laparo-Angle*. The addition of the steerable segment increases the Degrees Of Freedom (DOF) of the instrument by two, and allows these instruments to change the orientation of the end-effector (see Figure 3.1). However, even though current steerable instrument designs have been effective in an increasing number of minimally invasive interventions, steerable instruments are generally quite bulky, with a diameter in the Ø5–8 mm range, and complex [10], making them unable to navigate through narrow environments and unsuitable for further miniaturization. Miniature pulley-based instruments such as *Endowrist* are also prone to fatigue due to the small diameter of the pulleys over which the cables are guided [11], which limits the life span of this instrument to approximately 10 procedures. Current steerable instruments are also still not very suitable for highly complex MIS procedures, mainly because of their inability to reach over or behind objects, such as delicate nerves and blood vessels, as these instruments are not able to navigate through complex curves (i.e., curves containing multiple radii and center points, for example S-curves). For this purpose, specialized "multisteerable" instrumentation with enhanced, at least 4 DOF, dexterity is required [3]. In the tips of these multisteerable instruments, multiple steerable segments are stacked on top of each other (see Figure 3.2). A number of multisteerable approaches in the field of surgical instruments and robotics are currently being developed [12-14]. Unfortunately, none of these systems are currently clinically available.

In this study we have developed a novel miniaturized cable-actuated multisteerable tip that allows for navigating through complex curves (≥ 4 DOF). In order to navigate through tight spaces, while minimizing the incision size and trauma to the patient, an instrument diameter of Ø2 mm was set, which is in the smaller spectrum of currently

available rigid minimally invasive instruments [15-17]. The multisteerable tip was not developed for a specific MIS application, but was intended as a first explorative step into improving dexterity, while simultaneously minimizing the outer dimensions. First, we will discuss the design process from a fundamental point of view in which the process of creating a miniature cable-actuated multisteerable instrument will be elaborated. Secondly, we will describe the developed steering unit that was connected to the multisteerable tip to determine the bending stiffness, as well as illustrate its ability to form complex shapes and perform scanning operations. These scanning operations were, subsequently, used in a proof-of-principle experiment in which a forward-looking ultrasound transducer and Optical Shape Sensing (OSS) fiber were guided through the multisteerable instrument for the 3D-reconstruction of a wire-frame positioned in front the tip. Finally, we will discuss our main findings and give recommendations for the development of this tip into a clinical instrument in future.

3
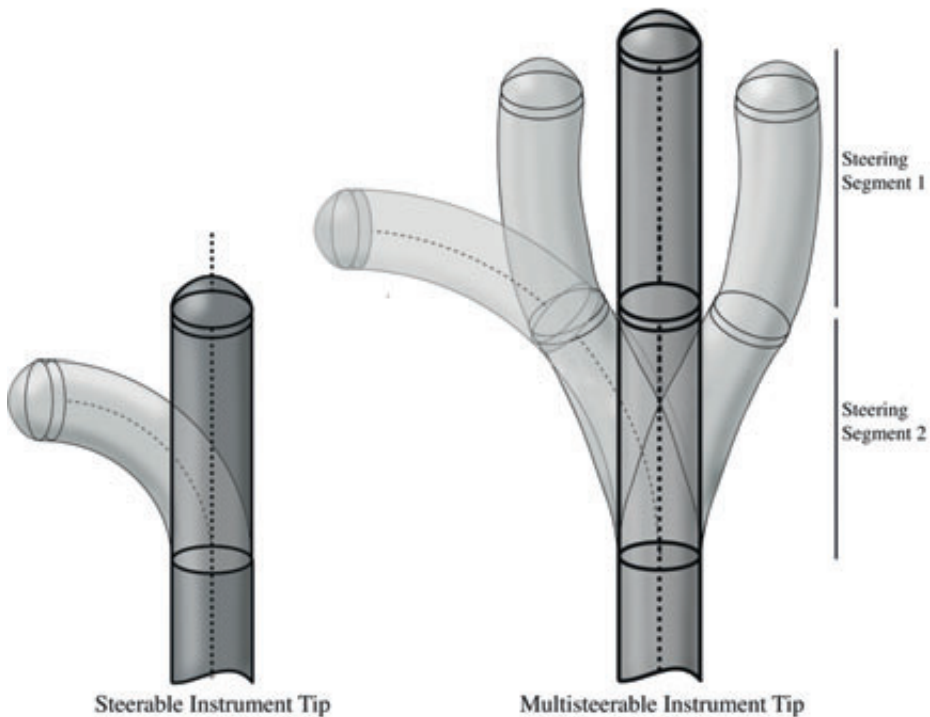
Figure 3.1— Multisteerable Instrument Design and Functionality. Left: Steerable instrument tip. Right: Multisteerable instrument tip. Multisteerable instruments consist of at least two steerable segments stacked on top of each other. Each steering segment can be steered independent from the other(s), allowing the instrument to form complex shapes, such as S-curves, and to reach behind objects.

3.2. DESIGN PROCESS

3.2.1. Design Phase I: Enhancing Dexterity

Cable-Ring Mechanism for Simplicity

In order to find a better alternative for expensive and complex steering mechanisms such as the ones used in *Endowrist* and *Autonomy Laparo-Angle*, at Delft University of Technology a patented steering mechanism has been developed, referred to as the cable-ring mechanism (see Figure 3.2) [18, 19]. The basic cable-ring mechanism consists of two standard coil springs with a ring of cables in between, which are all fixed to the distal tip; allowing for 2-DOF motion. Tip bending is achieved by applying an axial pull load profile on the cables, which locally compresses the compression springs, resulting in tip deflection. The simplicity of the cable-ring mechanism does not come from minimizing the number of parts, but rather from using simple off-the-shelf available parts. Instead of using a complex guidance system to keep the cables in place during actuation, they are now kept in place by the adjoining cables and two concentric compression springs. Furthermore, using only off-the-shelf available parts, such as cables and springs, the cable-ring mechanism can be manufactured at very low costs, making it suitable for miniaturization and disposable use.

3
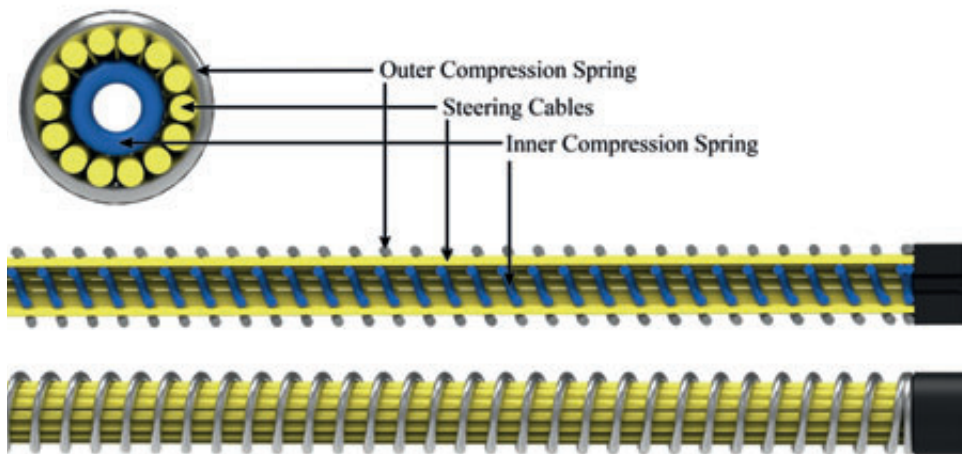
Figure 3.2— Schematic Illustration of the Patented Cable-Ring Mechanism Invented at Delft University of Technology [16]. The cable-ring mechanism consists of an outer compression spring (silver), a ring of steering cables (yellow), and an inner compression spring (blue)

3

Cable-Ring Mechanism for Enhanced Dexterity

The cable-ring mechanism is highly suited for steering multiple, stacked, segments, as an entire ring of cables is used to control 2-DOF tip motion, while in principle only three or four cables are needed. The cable-ring mechanism does have one major downside, however. The stiffness of the tip, in particular the bending and axial stiffness, is relatively low, mainly due to its compliant nature. The spring-based mechanism is under-actuated, allowing the tip to make unwanted flexible sideways motions when bent along a specific angle under the presence of external disturbing forces from the tissue [20]. Furthermore, when encountering axially directed external disturbing forces, the spring-based tip mechanism might axially compress, resulting in a loss of tip functionality.

In an effort to simultaneously minimize the under-actuation problem by decreasing the mechanical number of DOF of the tip structure, while creating high axial stiffness, a new, multisteerable instrument was developed: *Multiflex* (Ø5 mm, see Figure 3.3-3.4). *Multiflex* allows for 10-DOF motion over five rigid steering segments that replace the compliant inner compression spring. The resulting 10-DOF tip (tip length L = 65 mm without distal cap) allows for motions along complex curvatures, such as S-curves, and single radius curves with bending angles up to 225°, enabling the multisteerable tip to navigate through complex anatomic environments. Each of the five steering segments (see Figure 3.3) is actuated using four Ø0.45 mm stainless steel cables (yellow in Figure 3.3) and consists of four incompressible elements: two rounded cylinders (blue in Figure 3.3) that fit in a recess of a slotted cylinder (white in Figure 3.3), forming altogether one pill-like element, and a cylinder containing two spherical recesses and a ring of 20 holes (green in Figure 3.3). The slotted pill-like elements fit inside the spherical recesses of the cylinders and as such form double ball-and-socket type joints. The slots and holes are used for cable alignment and fixation. Alignment is also achieved by neighboring cables, as all cables run through the entire tip section independent on the location where they are fixed, forming a cable-ring structure that continues all the way until the distal cap (see also Figure 3.4). The entire segmented structure is surrounded by five compression springs (grey in Figure 3.3), one for each steering segment, to keep the total of 5 x 4 = 20 steering cables aligned in a cable-ring. To allow for the passage of a tip tool, guidewire, imaging modality such as an ULTRASOUND transducer, or force sensor, the tip contains a lumen of Ø1 mm.

3.2.2. Design Phase II: Minimizing Dimensions

In an effort to further reduce the diameter of *Multiflex*, we developed a new miniaturized multisteerable instrument tip: *Accura* (Ø2 mm, see Figures 3.5-3.6), in which the number of parts is minimized and manufacturability is improved. *Accura* contains four 2-DOF steerable segments, resulting in an 8-DOF multisteerable tip. Each steering element

3
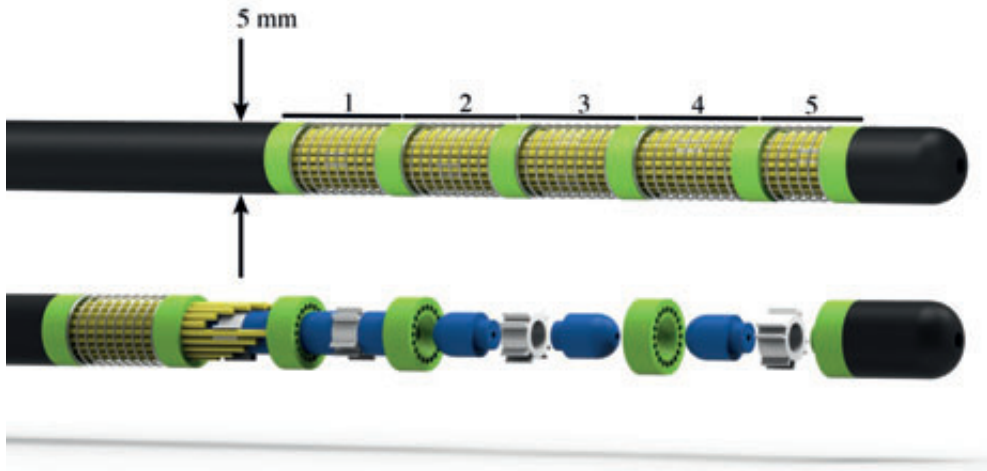
Figure 3.3— Schematic Illustration of the Multisteerable Tip of *Multiflex*. The tip of *Multiflex* has and outer diameter of Ø5 mm and consists of five 2-DOF steerable segments; giving a total of 10 DOF with a total curve angle up to 225°. Each steerable segment consists of two rounded cylinders (blue) that fit into a recess in the slotted cylinder (white); forming one pill-like element, and a ring with holes and two spherical recesses (green) in which the pill-like elements rotate; forming ball-and-socket type joints. The slots in each white element allows for the precise attachment of 4 cables (yellow), resulting in a total of 20 steering cables. The holes in the green elements allow for cable guidance and alignment. A cap (black) is placed on the distal end.

allows for 22.5° deflection, allowing for motions along complex curvatures and single radius curves with a total curve angle of 90°, which is comparable to currently available steerable instruments. Each steerable element (see Figure 3.5) consists of two rings (Ø2 mm, $Ø_{lumen}$ = 1.8 mm, green in Figure 3.5) and two rounded slotted cylinders (Ø2mm, $Ø_{lumen}$ = 1 mm, blue in Figure 3.5). The cables are sequentially guided through the slots of the slotted cylinders and the lumens of the rings. The rings keep the cables positioned in a cable-ring configuration and prevent outwards motion of the cables during bending motion. Every other slotted cylinder is connected to four Ø0.2 mm stainless steel cables (yellow in Figure 3.5), giving a total of 4 x 4 = 16 steering cables. In Figure 3.6, *Accura* is illustrated forming a 90° single-radius curve (*r* = 19 mm), a complex S-curve in one plane, and a complex curve in 3D.

In comparison to *Multiflex*, the segmented structure in *Accura* has been simplified in three ways: 1) the pill-like structure, in the old design consisting out of three elements, is now made out of one single grooved part combining cable alignment with fixation, 2) the

3

Figure 3.4— Multisteerable Tip of *Multiflex*. The match is illustrated for scale purposes.

holes for cable alignment and the spherical recesses are removed, and 3) the outer spring is removed as the relative stiffness of the used stainless steel cables, as compared to their free length, is in this miniaturized design so high that they will stay within the grooves even at the maximum deflection, requiring no need to cover them and limit their outward motion (see for example Figure 3.6). These simplifications allow for easier manufacturability at an extremely small size and a substantially higher aspect ratio between lumen and outer diameter: from 5:1 in *Multiflex* to 2:1 in *Accura*. As a result, *Accura* is to our knowledge world's thinnest multisteerable 8-DOF MIS instrument [9, 13].

3.3. APPLYING THE MULTISTEERABLE TIP

3.3.1. Controlling the Multisteerable Tip

Enhancing the steerability of a multisteerable instrument increases its complexity, especially when multiple DOF need to be controlled simultaneously [3]. In order to explore the possibilities of the *Accura* mechanism, the multisteerable tip was combined with a rigid hollow shaft (Ø2 mm, L = 200 mm) and an experimental steering unit (see Figure 3.7). The steering unit allows for precise and independent control of all the steering segments in the tip using four individual control elements (one for each element)

50
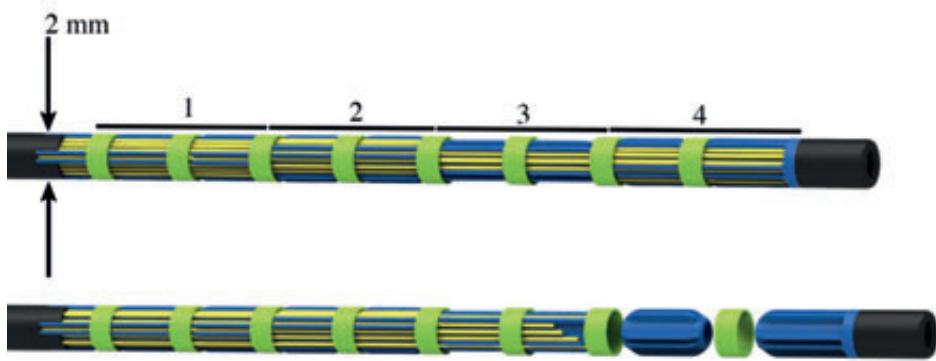
Figure 3.5— Schematic Illustration of the Multisteerable Tip of *Accura*. The tip of *Accura* has and outer diameter of Ø2 mm and consists of four 2-DOF steerable segments; giving a total of 8 DOF, allowing for forming complex shapes and single radius curves with a total curve angle of up to 90°. Each steerable segment consists of two rounded slotted cylinders (blue) and two rings (green) in which the rounded elements rotate; forming ball-and-socket type joints. The slots in the blue element allow for the attachment of four Ø0.2 mm stainless steel cables (yellow) using glue and provide cable guidance.

and can be easily fastened to a standard metric breadboard or optical table. In each of the control elements four steering cables are connected using a dedicated clamping mechanism (red and green in Figure 3.8). Each control element independently controls the sideways and upwards/downwards motion of one segment using two "dials" (green and blue in Figure 3.8). The dials also incorporate a locking mechanism (purple in Figure 3.8) to lock the tip position in place.

3.3.2. Operation Area Visualization

In a joint research project between Delft University of Technology (Delft, the Netherlands) and Erasmus Medical Center (Rotterdam, the Netherlands), *Accura* was used as an experimental facility to investigate the ability to using scanning operations to reconstruct an object in front of the instrument's tip in 3D. The ability to visualize or reconstruct what is in front of the instrument's tip in real time can aid the interventionist to navigate safely through tight anatomical structures or blood filled spaces, as well as allow for the characterization of tissues, which can be useful during biopsy procedures, amongst others. In order to achieve this, a single-element forward-looking ultrasound transducer and an OSS fiber (Ø0.2 mm, 4-cores, developed by Philips Research, In-body Systems, High Tech Campus Eindhoven, the Netherlands) have been integrated in *Accura* and initial tests were performed as described in the study of Janjic *et al.* [21]. Briefly, the forward-looking ultrasound transducer (developed at Erasmus MC, Rotterdam) with a squared aperture (1.4 mm side) was mounted in a forward-looking manner at the tip of

3
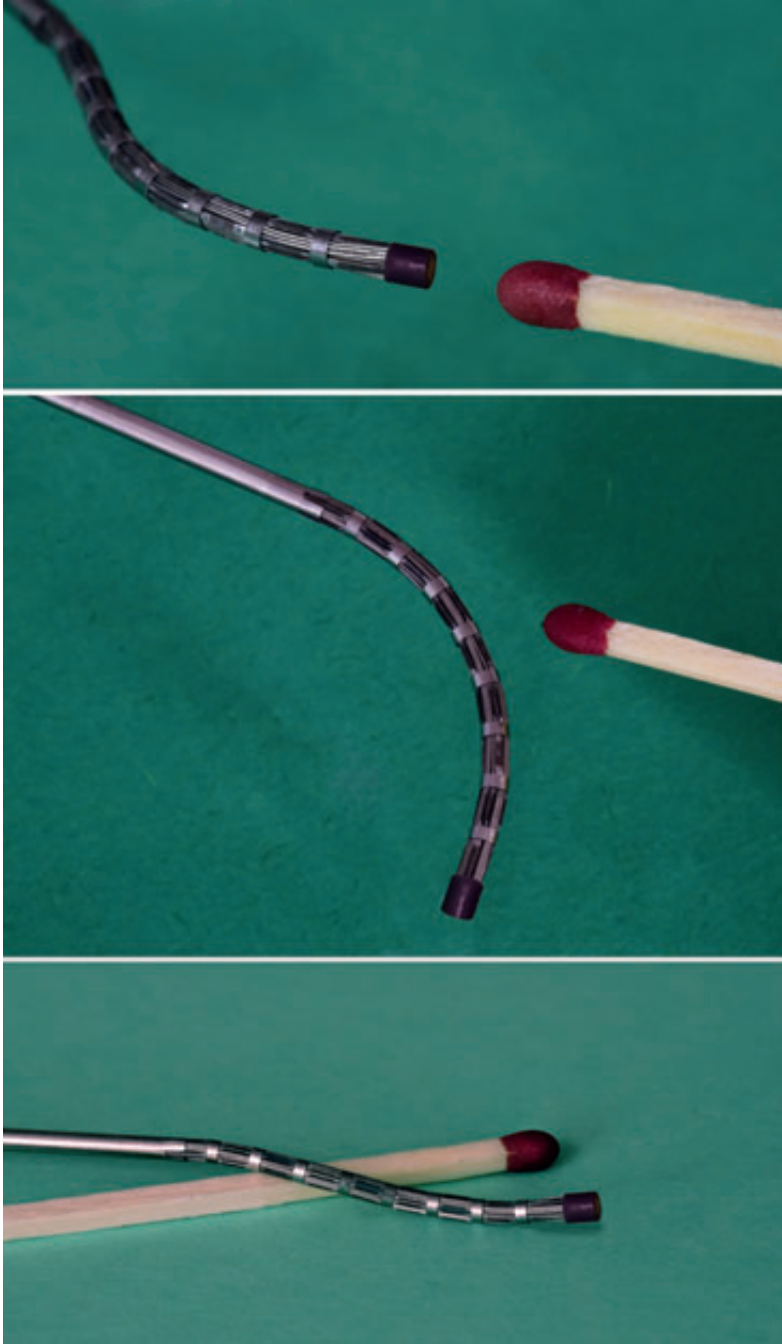
Figure 3.6— Multisteerable Tip of *Accura*. Top: Complex single-plane curve side view. Middle: Single-plane 90° single-radius curve top view. Bottom: Complex 3D-curve side view. The match is illustrated for scale purposes.
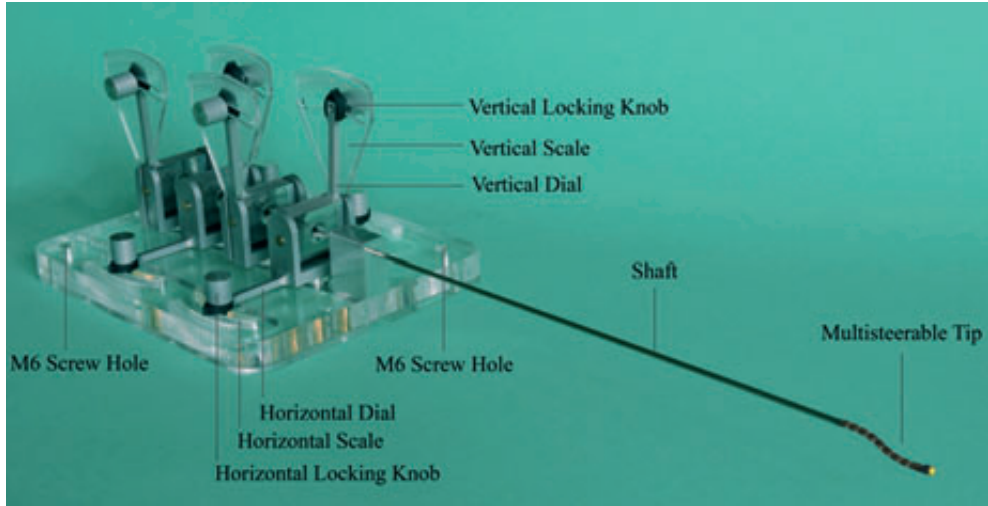
Figure 3.7— Total *Accura* Prototype. The *Accura* steering unit is designed to be easily attachable to a breadboard or optical table using two M6 screws. Each segment is controlled individually using 4 control elements. Each element can be locked individually to fixate the tip at any given shape or allow for a scanning motion. Amplification is minimized to allow for direct and precise control of the tip.

the instrument by means of a round recess in the final tip segment. The coaxial cable (Ø0.16 mm), electrically driving the forward-looking ultrasound transducer, was guided through the lumen of *Accura* together with the OSS fiber protected by a helical hollow strand tube. The 4 inner cores and Fiber Bragg gratings of the OSS fiber enable strain measurements and 3D shape reconstruction based on frequency-domain reflectometry [22, 23].

Preliminary tests with the integrated device were performed to investigate its ability to reconstruct a wire frame (6 parallel tungsten Ø40 μm wires) submerged in demineralized water in 3D space (see Figure 3.9). The estimated average distance between the reconstructed wires was 1.4 mm, which compared to the distance expected from the phantom design leads to a mean relative error of 36%. Even though the wire frame does not closely resemble the clinical situation, it is a first step in determining the feasibility of using a multisteerable tip in combination with forward-looking ultrasound and OSS data for 3D reconstruction of a tissue volume in front of the instrument's tip. By manipulating the control dials, we steered the instrument tip across the wire frame, acquiring both ultrasound and OSS data. The ultrasound data provided information about the distance of the wire to the instrument tip, while the OSS data were used to reconstruct the tip position and direction. The combination of ultrasound data and OSS data enabled us to reconstruct the wires in 3D space (see Figure 3.10).

3
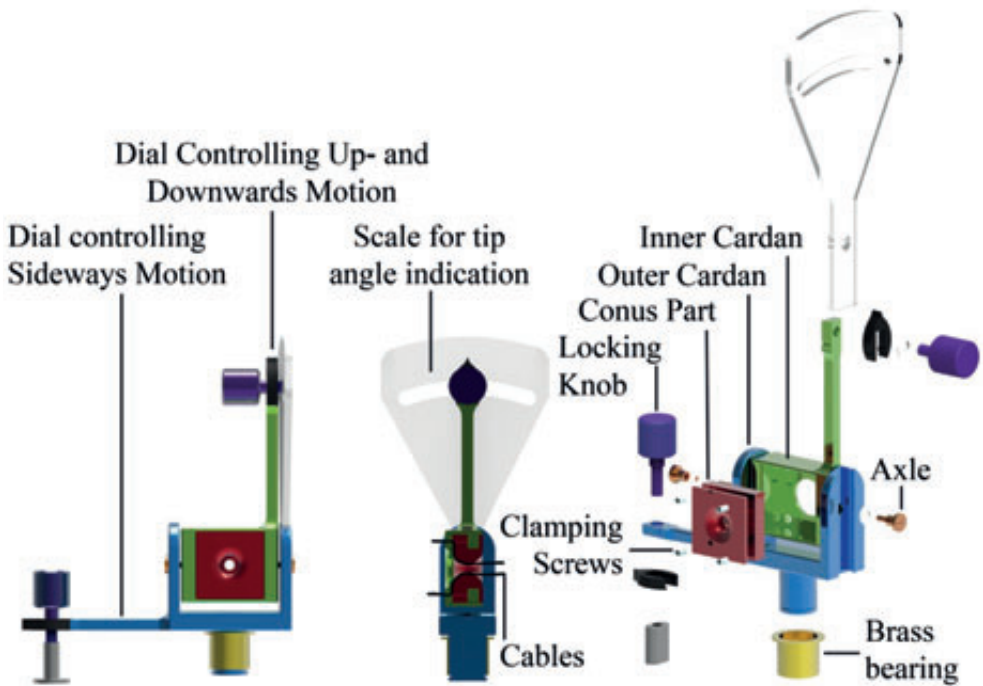
Figure 3.8— Exploded View of the Control Elements of the Handle of Accura. A control element consists of an: outer cardan part (blue; with a dial (black) controlling sideways motion), inner cardan (green; with a dial (black) controlling upwards/downwards motion), conus part (red; that guides the cables), two axles (orange), 4 screws (not indicated), and a scale (transparent). The tip position can be locked in place by tightening the knobs on the dials (purple). The cables are clamped between the inner cardan (green) and conus part (red). To allow for smooth movement of the control elements, a bearing (yellow) is placed over the main axis of the outer cardan part.

3.3.3. Bending Stiffness Determination

While performing medical procedures, high bending stiffness is required to prevent parasitic tip movement by external forces and unwanted tip deflection. In order to determine the bending stiffness range of *Accura*, a proof-of-principle experiment was conducted with the cable tension set to 0 and 0.5 N (see Figure 3.11). A lateral force (*F* [N]) was applied to the tip using a mass of 2, 5, 10, and 15 grams. Subsequently, the lateral deflection (δ [mm]) was measured using a laser interferometer (*OptoNCDT 1402*, Micro-epsilon, maximum resolution 0.6 μm). Each measurement was performed 3 times.

From this data, for each of the two cable pretensions, the overall bending stiffness was calculated. At the 0 N cable pretension, a bending stiffness of approximately $5.0 \cdot 10^{1} \pm 0.6 \cdot 10^{1}$ N/mm was measured. The bending stiffness could be increased to approximately 0.10 ± 0.01 N/mm at a cable tension of 0.5 N (see Table 3.1). Note that these are approximate calculations, as we did not account for internal friction in the tip.

3
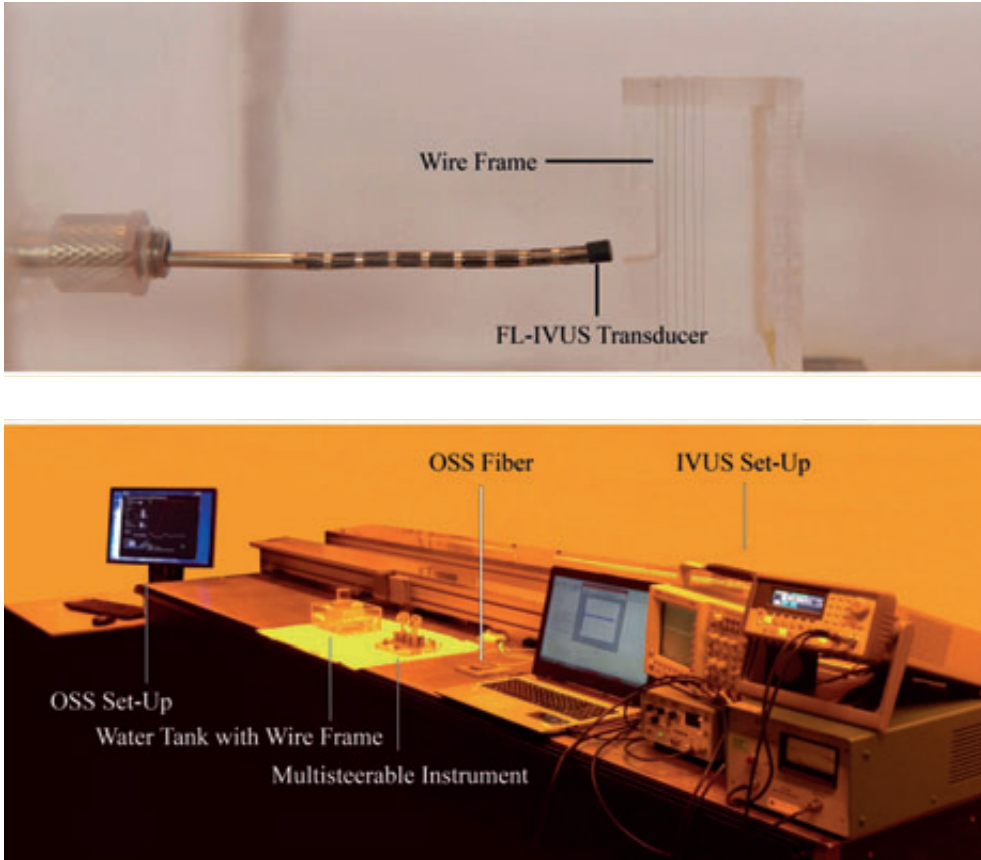
Figure 3.9— Sensor-enhanced Navigating Measurement Set-Up. Top: Multisteerable instrument *Accura* with the mounted forward-looking single-element forward-looking ultrasound transducer and integrated OSS fiber inserted in the water tank with the wire frame. Bottom: The measurement set-up. The set-up consisted of the multisteerable instrument *Accura* with the forward-looking single-element forward-looking ultrasound transducer incorporated at the tip and internal OSS fiber, a water tank (190 x 130 x 50 mm [*l x w x h*]) filled with demineralized water (not illustrated) and the wire frame, the forward-looking ultrasound signal acquisition set-up (consisting of an oscilloscope, a pulse generator, a radiofrequency power amplifier, and an amplification unit), and the OSS system.

3
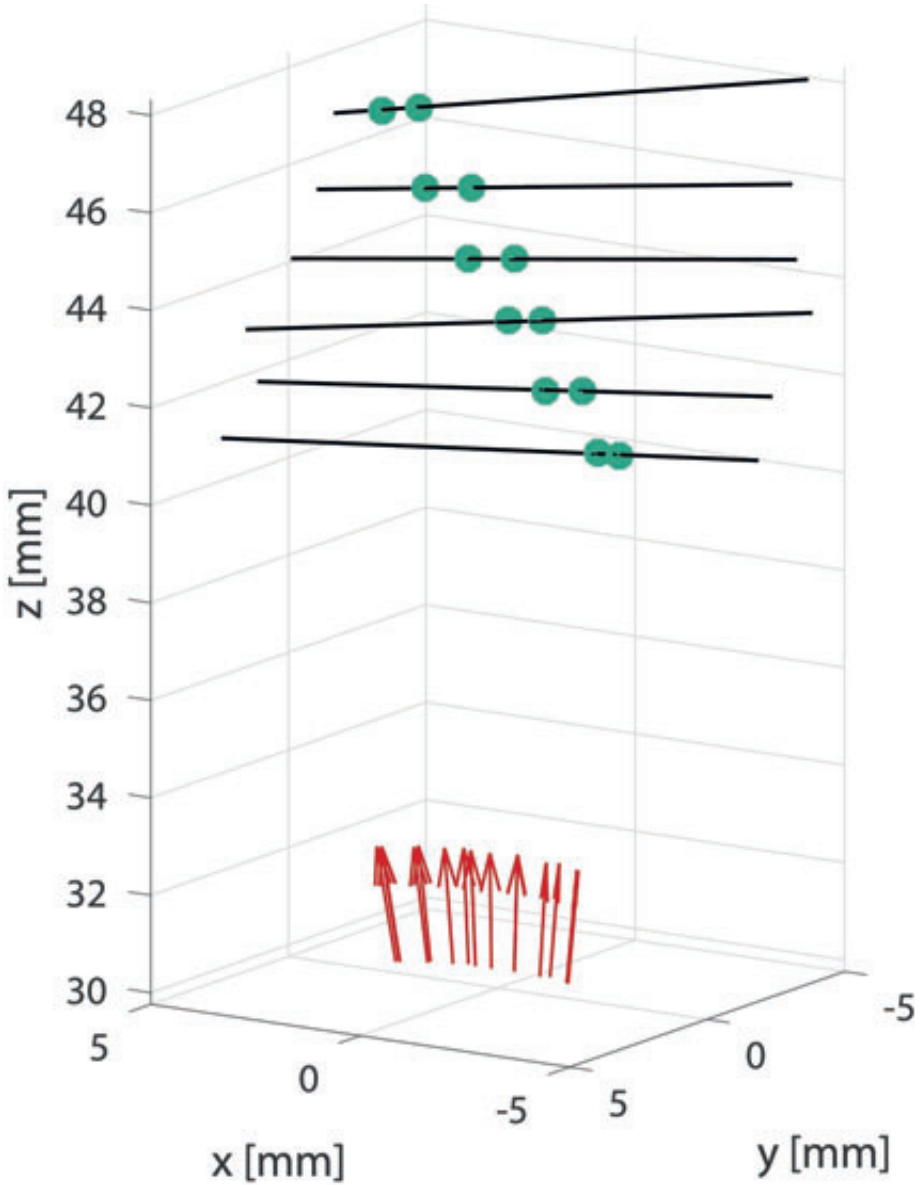
Figure 3.10— Wire Phantom Reconstruction based on the Ultrasound Signal and the OSS Data. The six tungsten wires are reconstructed by fitting lines (black) through the green points, which illustrate the location in 3D space of the wires' ultrasound signal. The red arrows illustrate the scanning pattern of the instrument tip and its direction as obtained from the OSS system.

Table 3.1— Bending Stiffness Experiment Results. The values are indicated as mean ± standard deviation.

Cable Tension [N]	Force F [N]	Deflection δ [mm] (n = 3)	Bending Stiffness [N/mm] (n = 3)
0	0.02	3.3 ± 0.3	$6.0{\cdot}10^{-3} \pm 0.9{\cdot}10^{-3}$
	0.05	15.4 ± 2.6	$3.2{\cdot}10^{-3} \pm 0.5{\cdot}10^{-3}$
	0.10	*	*
	0.15	*	*
	Overall Mean Bending Stiffness: $5.0{\cdot}10^{-3} \pm 0.6{\cdot}10^{-3}$		
0.5	0.02	0.19 ± 0.02	0.11 ± 0.009
	0.05	0.49 ± 0.07	0.10 ± 0.02
	0.10	1.01 ± 0.07	0.10 ± 0.007
	0.15	1.61 ± 0.13	0.09 ± 0.007
	Overall Mean Bending Stiffness: 0.10 ± 0.01		

3

* Unable to measure due to excessive bending of the tip.
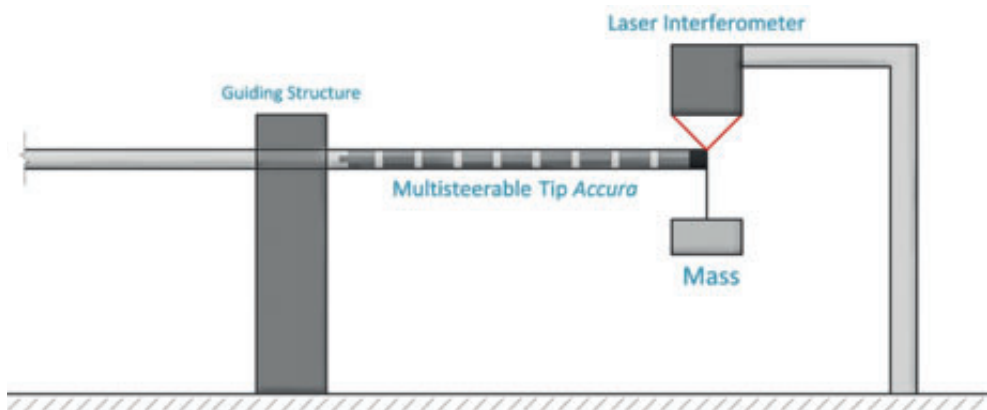
Figure 3.11— Bending Stiffness Measurement Facility. The measurement set up consisted of the multisteerable instrument, a guiding structure to prevent movement of the instrument shaft, a mass connected to the tip to exert a sideways external force on the multisteerable tip, and a laser interferometer (*OptoNCDT 1402*, Micro-epsilon) to measure the tip deflection.

3.4. DISCUSSION

3.4.1. Summary of Main Findings

Further miniaturization of current instruments, as well as improved dexterity, will become a necessity to allow for a more widespread adoption for highly complex MIS procedures. The proposed multisteerable instrument *Accura* increases the dexterity of the surgeon significantly as it allows for 8-DOF tip motion. Furthermore, as the demand of MIS instruments will most likely increase, the manufacturability and reusability are important factors to take into account when designing innovative tools. As the steering elements of *Accura* are relatively simple in design, as they do not contain small holes or intricate structures, they are easy to manufacture and can even be easily molded or 3D-printed in the future.

The bending stiffness of *Accura* was determined to be in between $5.0 \cdot 10$ N/mm and 0.10 N/mm, which is a result of the counterforces delivered by the steering cables during bending and friction between the chain-like steering elements. In a study of Jelinek *et al.* [20], the bending stiffness of two clinically available steerable instruments: (1) *Miflex* (2-DOF, Ø5 mm, Deam Corporation, Amsterdam, the Netherlands) and (2) *Autonomy Laparo-Angle*, was evaluated for different bending angles. The bending stiffness was determined in between 0.56 N/mm in *Laparo-Angle* in a straight configuration and up to 2.94 N/mm in *Miflex* with a bending angle of 60°. As can be seen, *Accura* has a significantly lower bending stiffness than these clinically available instruments. However, this is a rather unfair comparison, as *Accura* is significantly smaller. Unfortunately, no multisteerable instruments are available at Ø2 mm for comparison. Therefore, a rough estimation of the bending stiffness of the commercially available instruments at the Ø2 mm size was made by scaling these values using the difference between the second moment of area ($J = 0.25\pi r$) of the Ø5 mm and Ø2 mm instrument. The second moment of area of a Ø2 mm instrument is approximately 39x smaller than that of a Ø5 mm instrument. Therefore, the bending stiffness of these instruments can be roughly estimated to be within $1.4 \cdot 10$ and $7.5 \cdot 10$ N/mm for a Ø2 mm size. Note that this estimation only takes the effect of the second moment of area on the bending stiffness into account, not the effect of friction or compensating measures such as using larger diameter steering cables. However, using this rough estimation it can be assumed that the bending stiffness of *Accura* is at least equal, if not slightly higher, than that of the downscaled instruments. How this relates to the required bending stiffness for safely and effectively performing several tasks during MIS is unknown and needs further investigation.

3.4.2. Future Perspectives

Increasing Tip Dexterity Accura

Each steering segment of *Accura* allows for approximately 22.5° bending motion, resulting in a total curve angle of 90° with a curve radius of 19 mm of the entire tip segment. The bending radius is relatively high in comparison to that of the 2-DOF commercially available steerable MIS instruments, such as the EndoWrist. In future designs, this bending radius could be decreased by: (1) decreasing the overall length of the slotted cylinders and rings and/or (2) by moving the cables closer to neutral line of the tip. The former is the preferred option, as this would not decrease the bending stiffness of the tip. On the other hand, the latter option will allow for an increase in the maximum bending angle per steering segment, as the bending radius of the cables will decrease. Another option to increase the maximum bending angle per steering segment is to use smaller cables or cables with a lower bending stiffness, as this will increase the maximum allowable bending radius of the cables without causing cable fatigue.

Intuitive Control of the Multisteerable Tip

For the clinical application of *Accura*, redesign of the steering unit is a necessity to allow for intuitive and single-handed control in a clinical setting. During the operation area visualization test, it proved challenging to steer the multisteerable tip, due to the high number of DOF and the design of the handle. This did not enable us to make an intricate scanning pattern, resulting in the relatively high reconstruction error of 36%. In future, improvements to the handle could be made to improve the scanning pattern and as such the image reconstruction.

In a study of Chunman *et al.* [24], a number of control strategies are categorized into three main groups: *parallel single-segment control, serial single-segment control*, and *integrated single-segment control* (see Figure 3.12). In *parallel single-segment control*, each segment has its own controller, and each controller functions independently from the other controller. This type of control strategy was applied in the steering unit of *Accura*. In a *serial single-segment controller*, the motion of each controller depends closely on the motion of the adjacent ones, which is the case in *Multiflex's* handle. Finally, in the *integrated single-segment controller*, also called follow-the-leader controller, only the first (most distal) segment is steered, while the additional segments follow the "leader segment" passively. Even though *integrated single-segment control* may be preferred from an operator's perspective, it does not allow for actively controlling the full range of motion of the multisteerable tip. Therefore, in the future a combination of the *parallel single-segment control* and the *integrated single-segment control strategies* will be looked into, in which the surgeon only needs to steer the most distal segments while the rest of the segments remain in place, similar to the way in which a snake travels through a rocky terrain. This approach will give the surgeon the most freedom in steering the

3

device, while at the same time not making it unnecessarily difficult by the need to control multiple segments simultaneously.

Next to manual control, another option would be to look into robotic control of the multisteerable tip. In this configuration, the cables could be connected to 4 separate robotic controllers, which in turn can be controlled by a master-slave system, similar to the Da-Vinci Robotic System. The advantage of using a robotic system may be enhanced precision, while allowing for the construction of highly complex shapes based on previously obtained CT or MRI data.

Multiple Functionalities in the Multisteerable Tip
As space is often limited, research should also be focused on the integration of multiple functionalities into one instrument. These functionalities should, in the authors' opinion, include: steerability, visualization, and the ability to guide a tip tool towards the
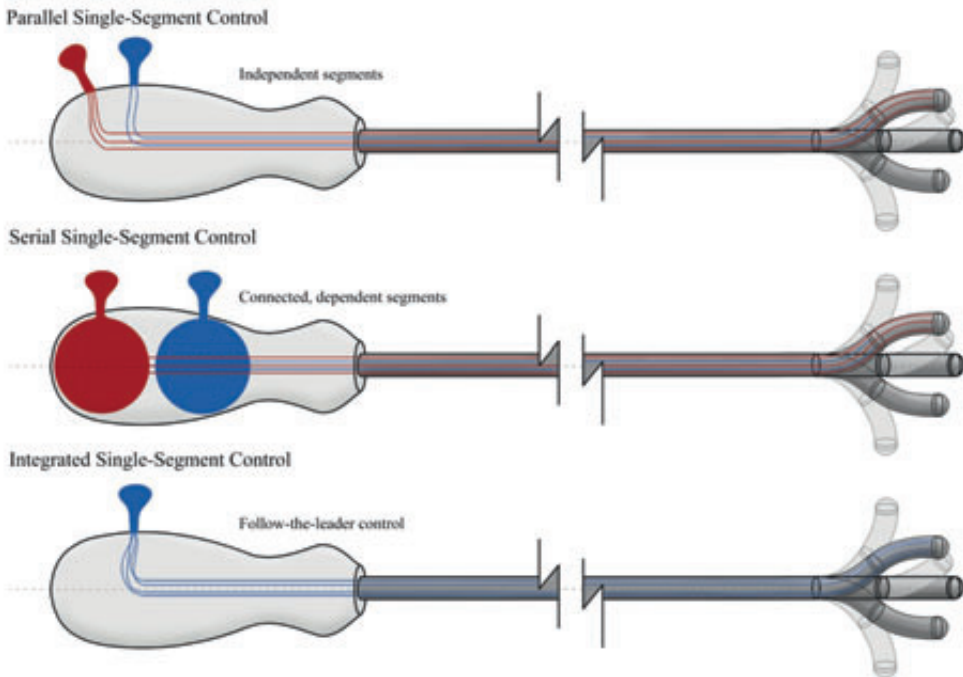
Figure 3.12— Multisteerable Control Strategies. Top: *parallel single-segment control*, in which each segment is controller by a separate controller. This way, each segment can be controlled independently. Middle: *serial single-segment control*, in which each segment is controlled by a separate controller, but the motion of the controller (and thus the tip) is dependent on the position of the adjacent controllers. Bottom: *integrated single-segment control,* in which only the most distal segment is steered, while the other segments follow the "leader segment" passively.

operation site. First steps have been made in *Accura* to integrate multisteerability with a forward-looking ultrasound transducer and OSS fiber to visualize the operation area. The information from the forward-looking ultrasound transducer and OSS fiber can be used for navigational purposes but also for tissue characterization, which can be helpful to distinguish healthy from diseased tissues. Furthermore, since the 3D shape of the instrument's tip and shaft is reconstructed using OSS, the use of X-ray for visualization of difficult-to-reach operation areas or blood-filled spaces may be minimized, as the interventionists can obtain additional information from the combined forward-looking ultrasound and OSS data to image the surroundings and determine their position. Next to visualizing the operation area, the ability to guide a tip tool, such as a scalpel, grasper, or biopsy forceps, through the instrument, or fix one such a tool to the distal tip, will aid the surgeon in reaching the intended goal of the MIS, such as tumor removal or taking a biopsy, without the need for an additional instrument.

3.4.3. Limitations of this Study

The multisteerable *Accura* has not been tested in an *ex-vivo* or *in-vivo* setting. We have only tested *Accura* in demineralized water and visualized a wire frame, which does not closely resemble the intended clinical situation during MIS. In future, we will develop a more representative tissue model for testing purposes. Furthermore, *ex-* and *in-vivo* MIS tasks need to be performed to determine if the bending stiffness of *Accura* is sufficient. Finally, as the forward-looking ultrasound transducer only consisted of a single-element and manually steering *Accura* along the wire frame was challenging, the accuracy of the 3D-reconstruction was relatively low. Currently, the ErasmusMC is working on a multi-element forward-looking ultrasound transducer to increase the accuracy of the 3D-volume reconstruction.

3.5. CONCLUSION

In order to advance further into the field of MIS, miniaturized instruments with enhanced dexterity are a necessity. Currently clinically available rigid and steerable instruments have only a limited amount of DOF and thus do not allow for navigating complex curves, are complex, which complicates miniaturization, and are prone to fatigue. In an effort to improve the surgeon's dexterity, an innovative miniature Ø2 mm 8-DOF multisteerable instrument *Accura* was developed capable of forming single 90° and complex, multi-radii, curves. As of today, *Accura* is to our knowledge the smallest multisteerable 8-DOF MIS instrument. Preliminary test show that the new multisteerable tip allows for constructing complex curves and has a bending stiffness of in between $5 \cdot 10$ and 0.10 N/mm. Further miniaturization and development of the multisteerable tip may allow for a more widespread adoption of MIS for complex procedures in future.

3

REFERENCES

[1]   Fuchs K. Minimally invasive surgery. Endoscopy. 2002; 34(2): pp. 154-159.

[2]   Taylor G, Barrie J, Hood A, Culmer P, Neville A, and Jayne D. Surgical innovations: Addressing the technology gaps in minimally invasive surgery. Trends in Anaesthesia and Critical Care 2013; 3(2): pp. 56-61.

[3]   Vitiello V, Lee SL, Cundy TP, and Yang GZ. Emerging robotic platforms for minimally invasive surgery. IEEE Reviews in Biomedical Engineering. 2013; 6: pp. 111-126.

[4]   Dogangil G, Davies B, and Rodriguez y Baena FR. A review of medical robotics for minimally invasive soft tissue surgery. Proceedings of the Institution of Mechanical Engineers, Part H: Journal of Engineering in Medicine. 2010; 224(5): pp. 653-679.

[5]   Reynoso J, Meyer A, Unnirevi J, and Oleynikov D. Robotics for minimally invasive surgery (MIS) and natural orifice transluminal endoscopic surgery (NOTES). Medical Robotics: Minimally Invasive Surgery. Elsevier Ltd. Publishers, 2013: pp. 210-230.

[6]   IntuitiveSurgical. EndoWrist Instruments. Available from: http://www.intuitivesurgical.com/products/instruments/.

[7]   CambridgeEndo. Autonomy Laparo-Angle Articulating Instrument Technology: Enabling Visualization, Access & Control in Single Port Laparoscopy. Available from: http://www.cambridgeendo.com/technology.

[8]   Catherine J, Rotinat-Libersa C, and Micaelli A. Comparative Review of Endoscopic Devices Articulations Technologies Developed for Minimally Invasive Medical Procedures. Applied Bionics and Biomechanics. 2011; 8(2): pp 151-172.

[9]   Anderson PL, Lathrop RA, and Webster III RJ. Robot-like dexterity without computers and motors: a review of hand-held laparoscopic instruments with wrist-like tip articulation. Expert Review of Medical Devices. 2016; 13(7): pp. 661-672.

[10] Jelínek F, Pessers R, and Breedveld P. DragonFlex smart steerable laparoscopic instrument. Journal of Medical Devices. 2014; 8(1): pp. 015001-1-015001-9.

[11] Jelínek F, Pessers R, Breedveld P. Dragonflex smart steerable laparoscopic instrument. Journal of Medical Devices. 2014; 8: pp. 015001-1-015001-9.

[12] Robinson G, and Davies, JBC. Continuum robots - A state of the art. Proceedings of the 1999 IEEE International Conference on Robotics and Automation held at Detroit, MA, 10-15 May 1999, pp. 2849-2854.

[13] Arkenbout EA, Henselmans PWJ, Jelínek F, and Breedveld P. A state of the art review and categorization of multi-branched instruments for NOTES and SILS. Surgical Endoscopy. 2015; 29(6): pp. 1281-1296.

[14] Scali M, Pusch TP, Breedveld P, and Dodou D. Needle-like instruments for steering through solid organs: A review of the scientific and patent literature. Proceedings of the Institution of Mechanical Engineers, Part H: Journal of Engineering in Medicine. 2017; 231(3), pp. 250-265.

[15]   KLSMartin.   MarCore.   Available   from: http://www.klsmartin.com/fileadmin/Inhalte/Downloads_Prospekte/Chirurgische_Instrumente/ 90-488-16-07_04_15_Cardio_-_marCore.pdf.

[16]   IntuitiveSurgical. EndoWrist/ Single-Site Instrument & Accessoiry Catalog. Available from: http://www.intuitivesurgical.com/assets/docs/1021625- EUrA_Si_System_I&A_Catalog_no_pricing_EU_highres.pdf.

[17]   Ethicon. Laparoscopic Hand Instruments. Available from: http://www.ethicon.com/healthcare- professionals/products/other/lap-hand/laparoscopic-hand-instruments.

[18]   Breedveld P and Scheltes JS, inventors. Instrument for fine-mechanical or surgical applications. United States Patent 20080234545 A1. 2008.

[19]   Breedveld P, Sheltes JS, Blom EM, and Verheij JE. A new, easily miniaturized steerable endoscope. IEEE Engineering in Medicine and Biology Magazine. 2005; 24(6): pp. 40-47.

[20]   Jelínek F, Gerboni G, Henselmans PWJ, Pessers R, and Breedveld P. Attaining high bending stiffness by full actuation in steerable minimally invasive surgical instruments. Minimally Invasive Therapy & Allied Technologies. 2015; 24(2): pp. 77-85.

[21]   Janjic J, Leistikow M, Sakes A, and Soest G3D Imaging with a single-element forward-looking steerable IVUS catheter: initial testing. Proceedings of the IEEE International Ultrasonics Symposium (IUS) held at Tours, France, 18-21 September 2016, pp. 1-4.

[22]   Younge RG, Ramamurthy BS, Tanner N, Schlesinger RL, and Udd E, inventors; Koninklijke Philips Electronics N.V., assignee. Optical fiber shape sensing systems. United States Patent 8050523 B2. 2011.

[23]   Duncan RG, Frogatt ME, Kreger ST, Seeley RJ, Gifford DK, Sang AK, and Wolfe MS. High-accuracy fiber-optic shape sensing. Proceedings of the *SPIE* 6530, Sensor Systems and Networks: Phenomena, Technology, and Applications for NDE and Health Monitoring, San Diego, CA, April 10-12, 2007.

[24]   Fan C, Dodou D, and Breedveld P. Review of manual control methods for handheld maneuverable instruments. Minimally Invasive Therapy & Allied Technologies, 2013; 22(3): pp. 127-135.

3

3

4

CHAPTER 4

3D-PRINTED STEERABLE ELECTROSURGICAL GRASPER

AIMÉE SAKES, KEVIN HOVLAND, GERWIN SMIT, JO GERAEDTS, AND PAUL BREEDVELD

Abstract— In current bipolar electrosurgical instruments, a high frequency electrical sinusoidal wave is passed through the patient's body from an active electrode to the return electrode to cut, coagulate, or desiccate tissues. Even though current bipolar electrosurgical instruments have proven effective in minimizing blood loss, advancement is needed to allow for improved dexterity and adaptability. With current advances in 3D-print processes and its integration in the medical field it has become possible to manufacture patient- and operation-specific instruments. In this study we introduce the first 3D-printed steerable bipolar grasper (□ 5 mm) for use in minimal invasive surgery. The grasper significantly improves dexterity by the addition of two planar joints allowing for ±65° for sideways and ±85° for up- and downwards movement. The joints enable a significantly higher bending stiffness, 4.0 N/mm for joint 1 and 4.4 N/mm for joint 2, than that of currently available steerable instruments. The tip consists of two metallic movable jaws that can be opened and closed with angles up to 170° and allows for grasping and coagulating of tissues; reaching tissue temperatures of over 75 °C for an activation time of ~5 s, respectively. In order to actuate the joint, tip, and electrosurgical system, as well as to tension the steering cables, a ring handle was designed. In summary, the 3D-printed steerable bipolar grasper provides the surgeon with electrosurgical capabilities, improved dexterity, improved stiffness, and the versatility that is needed to provide patient- and operation-specific care.

Keywords— 3D-Printing, Additive Manufacturing, Bipolar Electrosurgery, Medical Device Design, Minimally Invasive Surgery, and Steerable Instruments.

4

4.1. INTRODUCTION

Controlling blood loss is a major challenge in open and minimally invasive surgery (MIS) [1]. Even though the human body has a unique process that stops blood loss after an injury called hemostasis, this process is often too slow or insufficient to stop major bleeding. In order to accelerate the process of hemostasis during MIS, electrosurgery is often used. In electrosurgery, a high frequency (0.3–5 MHz) electrical sinusoidal wave is passed through the patient's body from an active electrode to a return electrode in order to coagulate, cut, or dessicate the target tissue between the electrodes. The effect is determined by the waveform, voltage, and power of the electrosurgical current, as well as the size of electrode tip. The tissue between the electrodes is damaged due to the conversion of the electrical energy of the alternating current into heat. As the water evaporates, tissue fragmentation occurs and the electrode can coagulate or cut straight through the tissue [1].

Even though electrosurgical tools have proven effective in minimizing blood loss, advancement is needed to allow for a higher tool reach and for more adaptable devices that are both patient and operation-specific. Currently, clinically available bipolar electrosurgical tools, such as *Endopath* (Ethicon, Somerville, NJ) [3] and *Aesculap PM438R* (B. Braun Medical B.V., Oss, the Netherlands) [4], are rigid and are thus only able to rotate around, and slide through, the incision point (or trocar). This restricts these instruments to 4 Degrees Of Freedom (DOF) – axial translation/sliding, axial rotation, and radial rotation in two planes (Figure 4.1 Left) – and thus does not allow for reaching around tissues or changing the orientation of the tip of the instrument with respect to the shaft.

In order to improve the reach of the tool it is necessary to increase the DOF of the tip portion by adding a steerable section (or wrist joint; Figure 4.1 Right), such as in the Da Vinci wristed robotic electro-cautery instruments [4]. Furthermore, as each patient and each operation is different, currently available rigid instruments are suboptimal. Even though there are bipolar electrosurgical tools with different tip sections available, there are only a limited amount of options when it comes to shaft size and shape. Easily adaptable, patient-specific, tools are needed to increase the efficiency and ease of MIS procedures, such as in skull base and arthroscopic procedures in which tight spaces need to be navigated. With current advances in 3D printing and its integration with the medical field it has become possible to manufacture patient-specific tools on an on-demand basis. The goal of this study is, therefore, to design and validate a steerable 3D-printed adaptable bipolar grasper for use in electrosurgery to improve upon the workspace of current rigid electrosurgical tools and to allow for an adaptable, patient- and/or operation-specific tool.

4
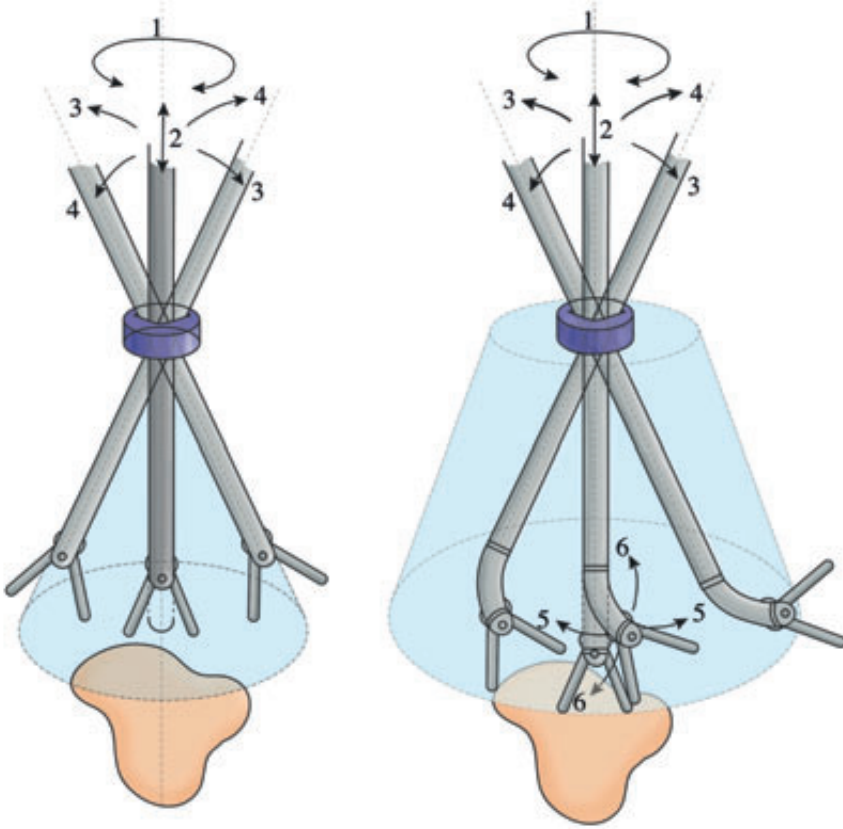
Figure 4.1— Degrees Of Freedom (DOF) and Workspace of Bipolar Electrosurgical Tools. Left: DOF of currently clinical available electrosurgical tools. Right: DOF of the proposed minimally invasive bipolar electrosurgical instrument. Number indications: 1: axial rotation, 2: axial translation or sliding, 3 and 4: radial rotation or pivoting in 2 perpendicular planes, 5: pivoting of the instrument tip, and 6: pivoting of the instrument tip in a perpendicular plane to 5.

4.2. DESIGN REQUIREMENTS

4.2.1. Tip Requirements

At the distal end of the instrument, a grasper should be placed to grip, manipulate, and coagulate tissues. The tip should consist of two movable electrical jaws that are able to grasp tissues in between the jaws, similar to currently available minimally invasive graspers (Figure 4.2). Each jaw should be provided with a profile to improve the grip on slippery tissues (Figure 4.2). The jaws should open to an angle of at least 60° (Figure 4.2), which is comparable to instruments currently used in clinical practice [5, 6]. Furthermore,

the joint that opens and closes the jaws/gripper should be placed in close proximity to the steering joint(s) to increase the control accuracy of the tip. Additionally, the electrical resistivity of the tip material should be lower than $1.8 \cdot 10^{-6}$ Ωm, which is in the range of metals [7], to allow for proper conduction of the electric signal. Finally, the thermal capacity of the tip should be higher than 0.1 J/kgK to prevent the tip from heating up when the current is applied.

4.2.2. Steerability Requirements

As previously discussed, rigid minimally invasive instruments allow for 4 DOF motion around the incision point (the trocar; Figure 4.1 Right). This limited number of DOF greatly restricts the range of motion of the surgeon. To improve the reach of the tool and to allow the surgeon to change the tip orientation (to improve positioning), 2 DOF of bending motion were added to the instrument (Figure 4.1 Right). The bending angle for the steering joint should be equal to or higher than 60° to significantly increase the reach of the tool. Furthermore, the joint should have both a high torsional stiffness to resist twisting/rotation of the joint around the axial axis and a high bending stiffness to resist unwanted bending motion caused by lateral forces. In a study published by Jelinek *et al.* [8], the bending stiffnesses of three steerable instruments – *DragonFlex* (2 DOF, □ 5 mm, 3D-printed, Delft University of Technology, Delft, the Netherlands), *Miflex* (2 DOF, Ø5 mm, Deam Corporation, Amsterdam, the Netherlands), and *Laparo-Angle* (3 DOF, Ø5 mm, CambridgeEndo, Framingham, MA, USA) – were evaluated for different bending

4
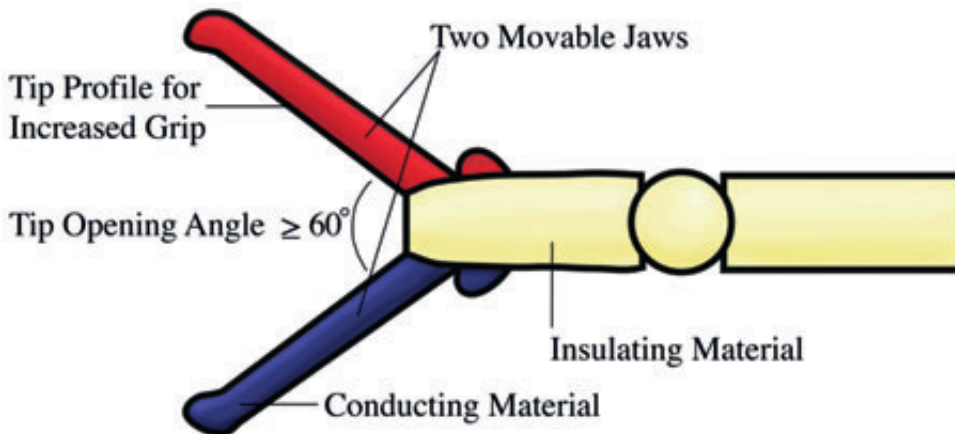
Figure 4.2— Tip Requirements of the Proposed Minimally Invasive Bipolar Electrosurgical Instrument. The tip should contain two movable jaws out of a conducting material with a tip profile to increase grip on the tissue. The movable jaws should open up to at least 60°. An insulating layer separates the two movable jaws.

angles. The bending stiffness ranged from 0.56 N/mm for *Laparo-Angle* in a straight configuration up to 2.94 N/mm for *Miflex* with a bending angle of 60°, with the *Dragonflex* performing most consistently over all bending angles with an overall bending stiffness of around 2 N/mm. Therefore, a bending stiffness of at least 0.56 N/mm is preferred. Unfortunately, no data is available about the torsional stiffness of currently available steerable MIS instruments.

4.2.3. Shaft Requirements

Between the steerable joint and handle of the instrument, a rigid shaft should be placed. The maximum diameter of the shaft is set to 7 mm, which is in the range of conventional laparoscopic instruments [5, 9, 10] and can be used in most procedures. The shape and length of the prototype should be easily adjustable, in order to allow for a patient- and operation-specific tool that can be used to perform MIS in different parts of the body. Similar to the steerable joint, the shaft of the instrument should have high torsional and bending stiffness. Furthermore, the shaft should contain multiple lumens to guide the active and return electrodes from the tip towards the handle. Finally, the shaft should be made out of a material with a high thermal capacity ($\geq$1 J/kgK) and electrical resistivity ($\geq1\cdot10^{12}$ Ωm) – which is similar to common insulators – in order to prevent heating and current leakage from the instrument [7].

4.2.4. Handle Requirements

The instrument should allow for single-handed control. The handle should allow the operator to steer the joint(s), open and close the jaws, and connect the instrument to an electrosurgical unit.

4.2.5. Electrical Circuit Requirements

In general, the frequencies of the waves used in electrosurgery lie between 300 kHz and 5 MHz and the power between 15 and 500 W [1, 11]. Hence, the instrument needs to be able to support these power settings when connected to an electrosurgical unit. For this purpose, the electrodes should be made out of a material with a low electrical resistivity ($\leq1.2\cdot10^{-6}$ Ωm), which is similar to common metals [7]. Furthermore, similar to the shaft, the electrodes should also have a high thermal capacity ($\geq$1 J/kgK) to prevent heating.

4.3. STEERABLE BIPOLAR GRASPER DESIGN

4.3.1. Tip and Joint Design

In Appendix 4.A, we describe the fundamental joint categorization, in which we explain the joint types and ways of guiding the electrical current through or around the joint, the selection process of the joint design, and the joint optimization protocol. In Figure 4.3, the final tip and joint design is illustrated. At the distal tip of the instrument, the two

movable jaws are made out of a metallic, conductive material and form the active and return electrode of the instrument (Figure 4.3). A triangular profile (90° top angle, 1 mm high) is added to the grasping surfaces to increase the grip on the tissue. The tip jaws are insulated from each other (with the exception of the grasping surfaces) by a non-conducting polymeric plate in the middle of the joint to prevent short-circuits (Figure 4.3). The tip jaws are connected to a fixed, non-conducting polymeric axle embedded into the joint. Two non-conducting polymeric outer plates are placed at the outer edge of the joint to provide support to the axle and prevent the tip jaws from sliding sideways (Figure 4.3). The up- and downward movement and the opening and closing of the tip jaws are controlled by two electrode cables that are looped around each of the tip jaws (Figure 4.3). The maximum opening angle of the two movable jaws and curve angle of the joint is 180° (90° in each direction; Figure 4.3). Finally, two steering ribbons actuate the first planar joint that allows for sideways deflection of ± 65°. The steering ribbons are guided through rectangular slots in the connecting element between the two joints and are fixed by injecting an adhesive into the slot (Figure 4.3). Inside the cylindrical planar joint curved slots (r = 2.5 mm; 5.5x electrode cable diameter) are present to guide the electrode steering cables towards the shaft and prevent cable fatigue.

The unique design of both joints, specifically the use of a ribbon to control the joint, has two main advantages. First, the ribbon and cables are placed at the outer edge of the joint, which increases the moment arms and thus reduces the force required to bend the tip, while at the same time increasing the bending stiffness of the joint. For comparison, if a similar cross-sectional area cable was used with a **diameter of** 0.6 mm (2x thicker than the ribbon), the moment arms would have been reduced with approximately 7%. Secondly, due to the minimal thickness of the ribbon it can accommodate small curve radii (0.4 mm in the grasper) without suffering from cable fatigue, allowing for navigating through tight curves.

4.3.2. Shaft and Handle Design

The shaft connects the joint and tip of the instrument with the handle. The shaft has a rectangular shape (□ 5 mm, l = 150 mm). Note that the shaft length, shape (straight versus curved), and size can be easily adapted and, subsequently, 3D-printed, to allow for a patient- and operation-specific grasper. This way, differences in body mass and lengths of patients, for example, can be accounted for. Furthermore, depending on the type of MIS procedure, different shaft shapes, including curved shafts, can come in handy, for example, when navigating through tight spaces. In order to achieve these patient-specific tools, a 3D CAD model of the instrument in combination with patient data obtained from a pre-operative CT or MRI scan could be used.

The electrode cables run through two rounded rectangular lumens in the center of the shaft, while the steering ribbons are guided through rectangular slots near the surface of the shaft (Figure 4.4). At the distal and proximal end of the shaft, two identical

4
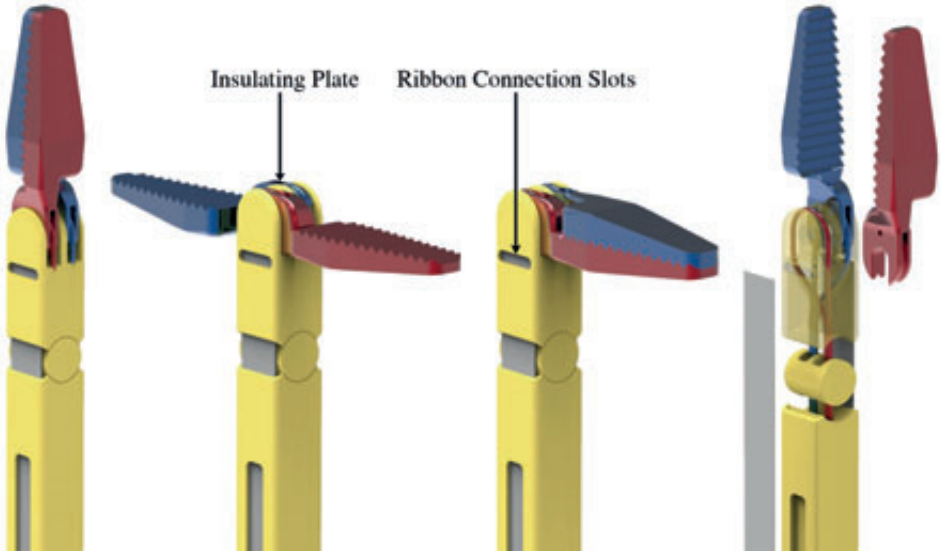
Figure 4.3— Final Tip Design Working Principle. Left: Tip in the closed (0°) configuration with the tip joint in the minimum curve angle (straight: 0°). An insulating plate is present to prevent short-circuiting the instrument. Middle: Tip in the open (180°) configuration with the tip joint in the minimum curve angle (straight: 0°). Right: Tip in the closed (0°) configuration with the tip joint in the maximum curve angle (±90°). The steering ribbon for the more proximal joint is connected to the shaft between the joints using a hook. Color indications: Blue = return electrode, Grey = polymeric steering ribbon, Red = active electrode, Yellow = insulating material.

cylindrical recesses are present in which the two (mirrored) planar joints are contained (Figure 4.4).

The handle allows for single-handed control of the two tip joints, the movable tip jaws, and the electrical circuit. To steer the instrument in 2 DOF and control the tip jaws, the joint structure of the tip is mirrored in the handle (Figure 4.5). A similar approach is seen in the 3D-printed Dragonflex device [12]. The joints are similar to those situated in the tip, with a few exceptions. (1) In order to keep the steering ribbons under tension, two equal tension mechanisms have been added to the connecting element between the two joints (Figure 4.5). The tension mechanisms consist of a rectangular metallic cube with a rectangular lumen through which the steering ribbons are guided and an M2 set screw to fix the steering ribbon in place. (2) The electrode cables are guided through two separate rectangular lumens running from the apex of the second planar joint groove towards and through the ring handle parts, instead of being looped around the joint (Figure 4.5). In this way, by moving, opening, or closing the ring handle parts, the jaws will rotate, open, or close, respectively. Furthermore, in order to keep the electrode cables tensioned, two identical cable-tensioning mechanisms have been added to the ring handle parts, one for

each tip jaw (Figure 4.5). The cable tensioning mechanism consists of a cylindrical tension knob screwed onto a square head M2 full-threaded bolt that is placed within a square recess in the ring handle (Figure 4.5). Inside the M2 screw, a lumen (Ø1 mm) is present through which the electrode cables are guided. To fix the cables to the tensioning mechanisms, a small knot was made at the distal end of the cables and the lumens were filled with an adhesive. By rotating the knob, the screw will translate left or right (depending on the rotation direction) and, as such, will tension or release the electrode cables, respectively. (3) To increase the stability of the joints and prevent the first joint from sliding sideways, two cylindrical protrusions and two outer plates that grip around the protrusions have been respectively added to the joints themselves, the shaft, and the connecting element between the joints (Figure 4.5). (4) Furthermore, stops have been added to the shaft, the connection element between the joints, and the ring handles to prevent damage to the joints and cables due to excessive bending (Figure 4.5). Finally, to connect an electrosurgical unit to the instrument, two fittings have been added to the ring handles (Figure 4.5). In Figure 4.6 the complete final design is illustrated.

4.4. PROTOTYPE DEVELOPMENT

4.4.1. 3D-Printing Process and Material Selection

Material selection is an important aspect of the design process to allow for proper electrical conductivity and heat capacity in both the conductive and insulating parts of the instrument. In Table 4.1 an overview is given of the selected 3D-printable materials and their material properties. At an early stage of the design process more 3D-printable materials were considered. However, another factor that was taken into account was the resolution of the printer, which was often insufficient for our purposes. Therefore, for the polymeric parts (joints, shaft, and handle) we decided to use the *Perfactory 4 Standard* (EnvisionTec GmbH, Gladbeck, Germany) 3D-printer, which allows for high accuracy part manufacturing (with a resolution of 100 µm, 100 µm, and 15-150 µm in the x, y, and z direction, respectively) [13]. The material used for our prototype is R5 Red, a liquid photopolymer that produces robust, accurate, and functional parts with a flexural modulus of 1,190–1,383 MPa and tensile strength of 31–39 Mpa [14]. Unfortunately the thermal capacity and electrical resistivity is untested for this polymer. We, therefore, experimentally determined these variables. To determine the thermal capacity, a heat element (*HM6800*, Minco, Minneapolis, MN) connected to the R5 test rod and a power unit (*ES 030-5*, Delta Elektronika, Zierikzee, the Netherlands; controlled and measured by NI USB-6008, National Instruments, Woerden, the Netherlands) were placed inside an insulated box (220 mm × 200 mm × 120 mm; *l×w×h*). The thermal capacity was measured using 4 thermocouples (NI 9211 in combination with NI USB-9162, National

Instruments, Woerden, the Netherlands); one for the outside temperature, one for the inside temperature, one for the heat element, and one for the R5 test rod. Three
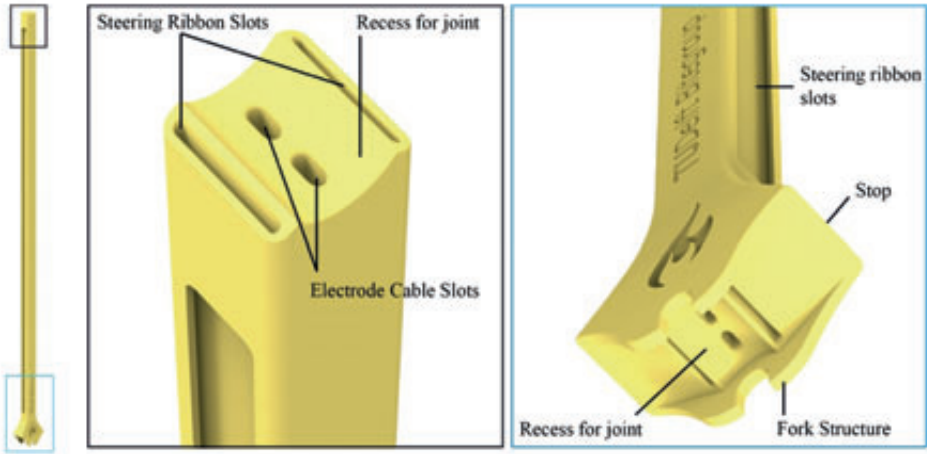
Figure 4.4— Final Shaft Design. Left: Total shaft design. Middle: Distal end of shaft with the rounded rectangular lumens for the electrode cables and steering ribbons and the cylindrical recess for the planar joint. Right: Proximal end of shaft with the rounded rectangular lumens for the electrode cables and steering ribbons, the cylindrical recess for mirrored planar joint, two fork-structures to increase the stability of the joint, and stops to prevent over-bending the joints. Color indications: Yellow = Insulating material.

consecutive tests were performed. Based on these tests, the thermal capacity was estimated as 1182 ± 69 J/kgK ($m = 0.00428$ kg), which is sufficient for our application. The electrical resistivity of the material was determined by connecting an electrometer (*6517A*, Keithley, Beaverton, OR) to the R5 test rod. A value of $\geq 1.67 \cdot 10^{18}$ Ωm was determined ($R \geq 1 \cdot 10^{15}$ Ω, $A = 90 \cdot 10^{-6}$ m^2, and $L = 0.15$ m), which is again sufficient for our application.

For the metal tip jaws, the *SLM 125* (ReaLizer GmbH, Borchen, Germany; using an exposure time of 20 µs, point distance of 10 µm and laser current of 1100 mA) 3D-printer was used as this printer allows for high-precision printing (with a resolution of 20–100 µm in the x, y, and z direction) of the biocompatible titanium alloy Ti6Al4V [15]. Ti6Al4V has a Young's modulus of 113.8 GPa, ultimate tensile strength of 950 Mpa, electrical resistivity of $1.8 \cdot 10^{-6}$ Ωm, and thermal capacity of 560 J/kgK [16], making it highly suitable as a functional part and for guiding electrical currents. However, to be sure that the printing process did not significantly influence the electric resistivity and thermal capacity, two small experiments were conducted. First, the thermal capacity was

measured using the same facility as previously described for the R5 test rod, and was roughly estimated as 732 ± 61 J/kgK. Note that this value may differ per 3D-printer and
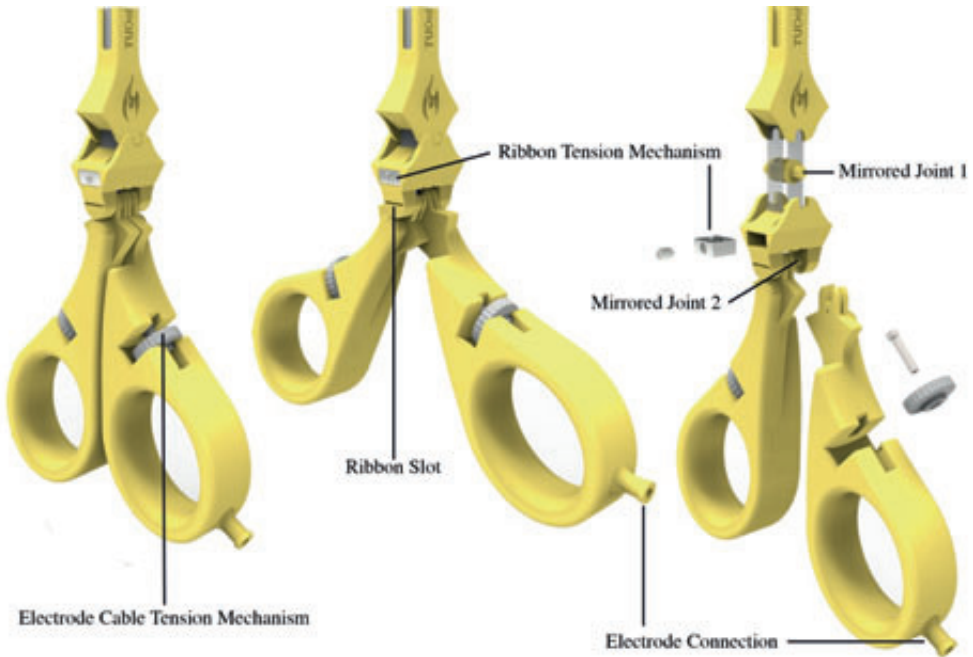
Figure 4.5— Final Handle Design. The handle allows for steering the two joints by mirroring the joint in the handle, opening and closing of the tip jaws, tensioning the steering ribbons and electrode cables, and connecting the electrosurgical unit. Left: Total handle design in the closed configuration. Middle: Handle in the open configuration. Right; Exploded view of the handle. Color indications: Blue = return electrode, Red = active electrode, Yellow = Insulating material.

printer setting. Secondly, the electrical resistivity was measured using an electrometer (2601B, Keithley, Beaverton, OR) and was determined as $7·10^{-6}$ Ωm (with $R = 0.0108$ Ω, $A = 32.2$ mm, and $L = 50$ mm). It can be seen that the printing process (negatively) affects the thermal capacity and electric resistivity of the titanium alloy, which is most likely caused by the porosity of the titanium. Even so, the thermal capacity and electrical resistivity are still suitable for our application.

4.4.2. Cable Selection and Conventional Parts Manufacturing

Next to the 3D-printed parts, some parts were manufactured or ordered, as no suitable 3D-printed alternative was available. This was the case for the steering cables, ribbons, and tension mechanisms, as 3D printing of flexible and axially stiff metals, as well as printing of miniature screw threads, is still very difficult to achieve. For the electrode

4
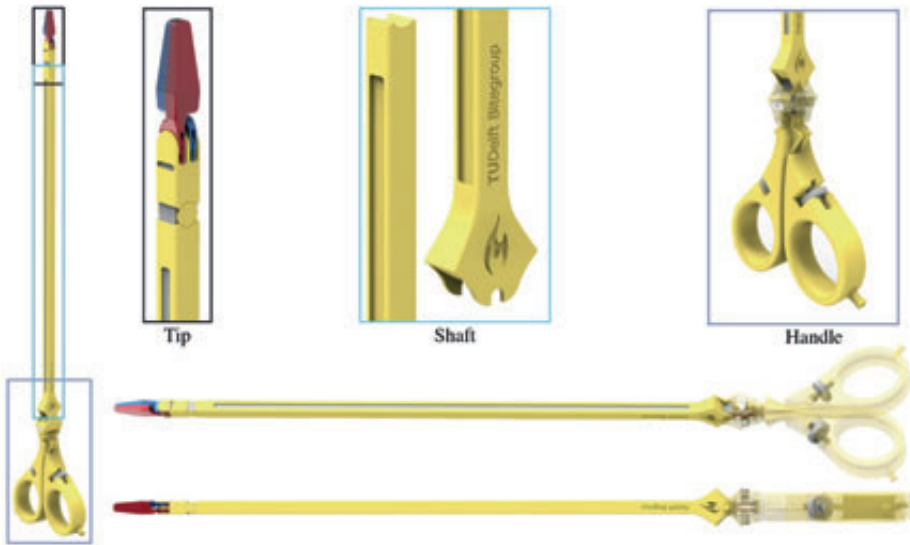
Figure 4.6— Final Design. The final design consists of two movable tip jaws, joint 1 to move the tip up- and downwards with curve angles of ±90°, joint 2 to move the tip sideways (left-right) with curve angles of ±65°, a rectangular 5 mm shaft to guide the steering ribbons and electrode cables towards the handle, the 2 mirrored joints in the handle, 2 ring handle parts to open and close the tip jaws, 2 tension mechanisms to tension the electrode cables (consisting of a tension bolt and ring; situated in the handle) and steering ribbons (consisting of a rectangular box, a tension plate and M2 set screw; situated in the mirrored joint 1), 2 Ø0.45 mm electrode cables, and 2 (4 mm wide; 0.2 mm thick) polymeric steering ribbons.

Table 4.1— Material Properties of the Selected 3D-Printable Materials.

3D-printed Material	3D-Printer	Material Properties			
		Young's Modulus E [GPa]	Ultimate Tensile Strength U [MPa]	Electric resistivity ϱ [Ωm]	Thermal capacity C [J/kgK]
Photopolymer R5	*Perfactory 4 Standard* (EnvisionTec GmbH, Gladbeck, Germany)	1.2–1.4[a]	31–39[a]	≥1.67·10[18] [c]	1182 ± 69 [c]
Ti6Al4V	*SLM 125* (ReaLizer GmbH, Borchen, Germany)	113.8 [b]	950 [b]	7·10[-6] [c]	732 ± 61 [c]

[a] From data in [11]
[b] From data in [13]

[c] Experimentally determined

cables we decided upon using Ø0.45 mm stainless steel AISI 316 6x19 cables (*0229*, Engelmann, Hannover, Germany) [14].These stainless steel cables are biocompatible, axially stiff with a high break load of 148 N [14], and have a low electrical resistivity of $9.4 \cdot 10^{7}$ Ωm (experimentally determined), making them suitable as electrode and steering cables. For the steering ribbon it was decided to use a polymeric ribbon (0.3 mm thick 4 mm wide). As the mechanical properties of the ribbon were unknown, a small experiment was performed in which the ribbon was fixed in a universal testing machine (*Z010*, Zwick, Venlo, the Netherlands). From this small experiment it was determined that the ribbon has a high break load (F_{break}) of 184 ± 16.5 N ($n = 3$), an ultimate tensile strength ($\sigma_{tensile}$) of 153.3 ± 13.75 MPa ($n = 3$), a strain (ε, $n = 1$) of $2.3 \cdot 10^{.}$ (0.02% at 50 N) – 0.37 (37% at F_{break}), and a Young's modulus (E) of approximately 456.4 MPa ($n = 3$), making it highly suitable as a steering cable. If we compare these values with that of a similar thickness stainless steel 1x7 Ø0.3 mm cable, the ribbon has a significantly higher break load [17]. Note that no fatigue tests were performed, as the applied stress during actuation (<10 N) and minimum radius of curvature of cables and ribbon were kept under the fatigue limit (see also Jelinek *et al.* [12] on this topic) and the grasper is intended as a patient-specific, and thus disposable, device in the near future with a limited lifetime.

The steering ribbons and electrode cables were connected to the prototype using Pattex Instant Glue. Finally, the electrode cable and ribbon tensioning systems were manufactured using conventional manufacturing methods out of PolyEther Ether Ketone (PEEK) to prevent short-circuits. In Figure 4.7 an expanded view of the prototype is presented and in Figure 4.8 the final, assembled prototype is displaced in several positions.

4.5. PROOF OF PRINCIPLE EXPERIMENT

In this section we discuss the experiment we performed with the prototype. Two experiments were executed: in the first experiment the movement and strength of the grasper was tested, and in the second experiment the electrical circuit and the accompanying coagulating abilities were verified.

4.5.1. Dependent Variables

Movement and Mechanical Strength
The following dependent variables were tested:

- **Output Angle [°].** The output angle of both joints was measured for different input angles.
- **Bending Stiffness [N/mm].** The bending stiffness of both joints was measured independently.

Electrosurgical Functionalities

The following dependent variables were tested:

- **Instrument Temperature [°C].** During activation of the electrical circuit, the temperature of the instrument was measured at various locations. A maximum instrument temperature of 40 °C was set to prevent unwanted tissue damage.

- **Tissue Temperature [°C].** In this test we evaluated how well the instrument can coagulate or destroy biological tissue. For this purpose, the tissue temperature was measured during activation of the grasper. As previously discussed, a tissue temperature of 65 °C is needed for coagulation and 100 °C for dissection purposes.

4

Figure 4.7— Exploded View of the Final Prototype. The final design consists of the two titanium movable tip jaws, joint 1 to move the tip sideways (left-right) with curve angles of ±65°, joint 2 to move the tip up- and downwards with curve angles of ±90°, a rectangular 5 mm shaft to guide the steering ribbons and electrode cables towards the handle, the 2 mirrored joints in the handle, 2 ring handle parts to open and close the tip jaws, 2 tension mechanisms to tension the electrode cables (consisting of a titanium tension bolt and ring; situated in the handle) and steering ribbons (consisting of a stainless steel rectangular box, a stainless steel tension plate and stainless steel M2 set screw; situated in the mirrored joint 1), 2 Ø0.45 mm electrode cables (biocompatible stainless steel AISI 316 1x7 cables [*LI000017*, Carl Stahl Technocables GmbH, Süssen, Germany]), and 2 (4 mm wide; 0.2 mm thick) polymeric steering ribbons

4
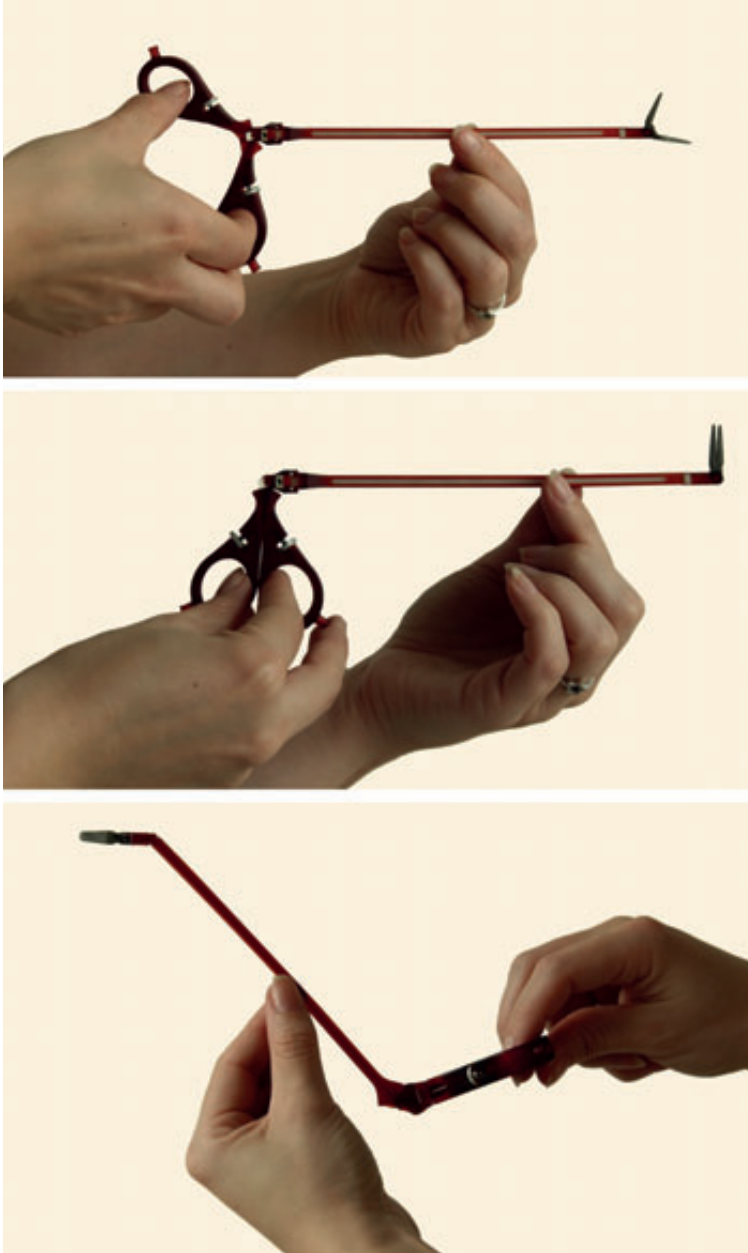
Figure 4.8— Final Prototype. Top: Prototype with open tip jaws. Middle: Prototype with joint 2 in the maximum curve angle of approximately 85°. Bottom: Prototype with joint 1 in the maximum curve angle of 65°.

4.5.2. Independent Variables

The following independent variables were tested:

Movement and Mechanical Strength
- **Input Angle Joint 1 (Ribbon) [°].** Input angles of 0 and 65° were tested for joint 1.
- **Input Angle Joint 2 (Tip) [°].** Input angles of 0 and 90° were tested for joint 2.

Electrosurgical Functionalities
- **Power [W].** The instrument was tested at the 80 W setting of the electrosurgical unit.

4

4.5.3. Experimental Facility

The input and output angle were measured using a protractor and camera placed directly above the prototype (Figure 4.9). The bending stiffness of both joints was evaluated using a universal testing machine (*LS100*, Lloyd Instruments, Bognor Regis, United Kingdom) in which the prototype was horizontally suspended (Figure 4.9). For the electrosurgical functionalities test, the prototype was connected to an electrosurgical unit (*ICC300*, Erbe GmbH, Tübringen, Germany). Subsequently, the instrument and tissue temperature were measured using an infrared camera *A35* (FLIR, Wilsonville, OR, USA). As a tissue phantom, a fresh piece of pig liver was used (Figure 4.9).

4.5.4. Experimental Protocol

The movement and mechanical strength experiments were executed without activating the electrical circuit. The output angles were measured for all input angles (0 and 65° for joint 1 and 0 and 90° for joint 2). Each condition was tested 3 times, resulting in a total of 12 measurements. Finally, the bending stiffnesses of joints 1 and 2 were evaluated individually in the straight configuration. Again, each condition was tested 3 times, resulting in 6 measurements.

The electrical circuit was evaluated by measuring the temperature of the instrument and pig liver by setting the *ICC300* electrosurgical unit to 80 W. A maximum activation time of 5 seconds was chosen. According to a study of Meeuwsen *et al.* [18], the average activation time of an electrosurgical tool is in between 1.4 s and 3.0 s depending on the experience of the surgeon, with a maximum of approximately 15 s. We, therefore, set the maximum activation time of our grasper at 5 s. The instrument and tissue temperatures were measured 3 times.

4.5.5. Data Analysis

From the input and output angle data, the energy losses from handle to tip were calculated. The data from the universal testing machine was processed using Microsoft Excel to determine the bending stiffness of the joint.
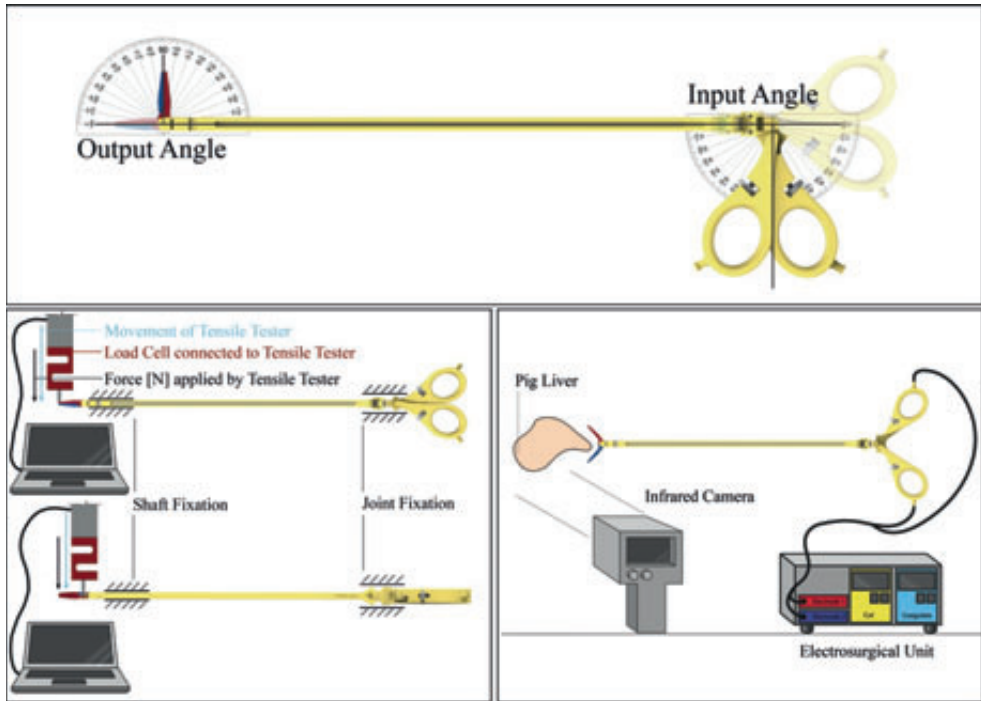
Figure 4.9— Schematic Representation of the Experimental Facility Movement and Mechanical Strength and Electrosurgical Functionalities Tests. Top: Input-output angle measurement facility consisting of the prototype placed above two protractors and a camera to record the joint angles. Bottom Left: Bending stiffness measurement facility consisting of the prototype clamped horizontally in the universal testing machine (*LS100*, Lloyd Instruments, Bognor Regis, United Kingdom). Bottom Right: The experimental facility for the electrosurgical facility test consisted of the prototype connected to an electrosurgical unit (*ICC300*, Erbe GmbH, Werkendam, the Netherlands), an infrared camera (*LS LT*, Optris, Berlin, Germany), and a piece of tofu or pig liver.

For the electrosurgical functionalities experiment, the data from the infrared camera *A35* was read out using Pleora GEV software (Pleora Technologies, Ottawa, Canada) and a program was written to visualize and analyze the tissue temperature over time.

4.6. RESULTS & DISCUSSION

4.6.1. Movement and Mechanical Strength

The proposed bipolar steerable grasper increased the workspace of currently available rigid bipolar graspers. The addition of the joint allows the tip orientation to be controlled, making it possible to reach around structures that would otherwise obstruct the surgery.

4

The instrument can be easily maneuvered and controlled using the ring handles, resulting in a smooth movement of the tip joints. The low steering forces are a result of the design of the joints in which the steering ribbons and cables are placed at the outer edge of the joint to maximize the moment arms. Furthermore, as the ribbon has a very low thickness and is made from braided polymer strands, the bending stiffness is low, again, decreasing the steering forces. The tip of the instrument follows the movement of the handle of the instrument nicely with minimal energy loss; reaching an output angle of 65° for joint 1 and 85° for joint 2 (5.6% energy loss). The minimal energy loss is, again, most likely due to the design of the joints, which minimizes steering forces and thus elongation of the steering ribbons and cables. The grasper does illustrate some hysteresis, mainly due to the friction of the cylindrical joint and ribbons with the shaft. However, we feel that this can be minimized by material choice and adding a (dry) lubricant. When compared to the currently available steerable instruments investigated in the study of Jelìnek *et al.* [8], the bending stiffness was on average 4.0 N/mm (0.7 N/° or $7.9 \cdot 10^{-2}$ Nm/°) for joint 1 (ribbon; $n = 3$; range 3.35 – 4.48;) and 4.4 N/mm (1.5 N/° or $2.9 \cdot 10^{-2}$ Nm/°) for joint 2 (tip; $n = 3$; range 3.43 – 5.14). The bending stiffness of the developed instrument is between 1.4 and 7.8x higher than the currently available tools in the straight configuration, which allows for high precision steering and support during the procedure. The reason for this high bending stiffness is the unique joint design. Both joints allow for only 1 DOF radially rotating motion (planar) and restrict axial rotation and shortening (energy storage). Furthermore, due to the maximized moment arms, the joint diameter could be maximized, thus reducing the influence of residual (radial) forces. Finally, the use of the ribbon maximized the cross-sectional area, while not negatively affecting the moment arms, which resulted in an increase of the bending stiffness.

4.6.2. Electrosurgical Functionalities

The ability to effectively coagulate tissues to stop excessive bleeding during surgery is a necessity for many surgical procedures. In a proof-of-principle experiment, the grasper demonstrated the ability to safely guide an electrical current from the handle to the tip in order to coagulate and destroy tissue in direct contact with the movable jaws (see Figure 4.10), with a maximum measured tissue temperature of 75 °C for an activation time of only 5 seconds. The instrument temperature stayed well below 40 °C due to the large cross-sectional area and low electric resistance of the looped electrode cables, except from the tip, which reached approximately 60 °C. The tip of the grasper increased in temperature due to the increased resistance introduced by the 3D-printing process. An improved printing process can potentially minimize this tip heating effect in the near future. Additionally, an extra isolating layer may be added to the tip jaws.

4.6.3. Current Limitation of 3D-Printing

We have illustrated the ability to 3D-print a steerable electrosurgical grasper for use in MIS. During this process it became apparent that even though we have made huge

4
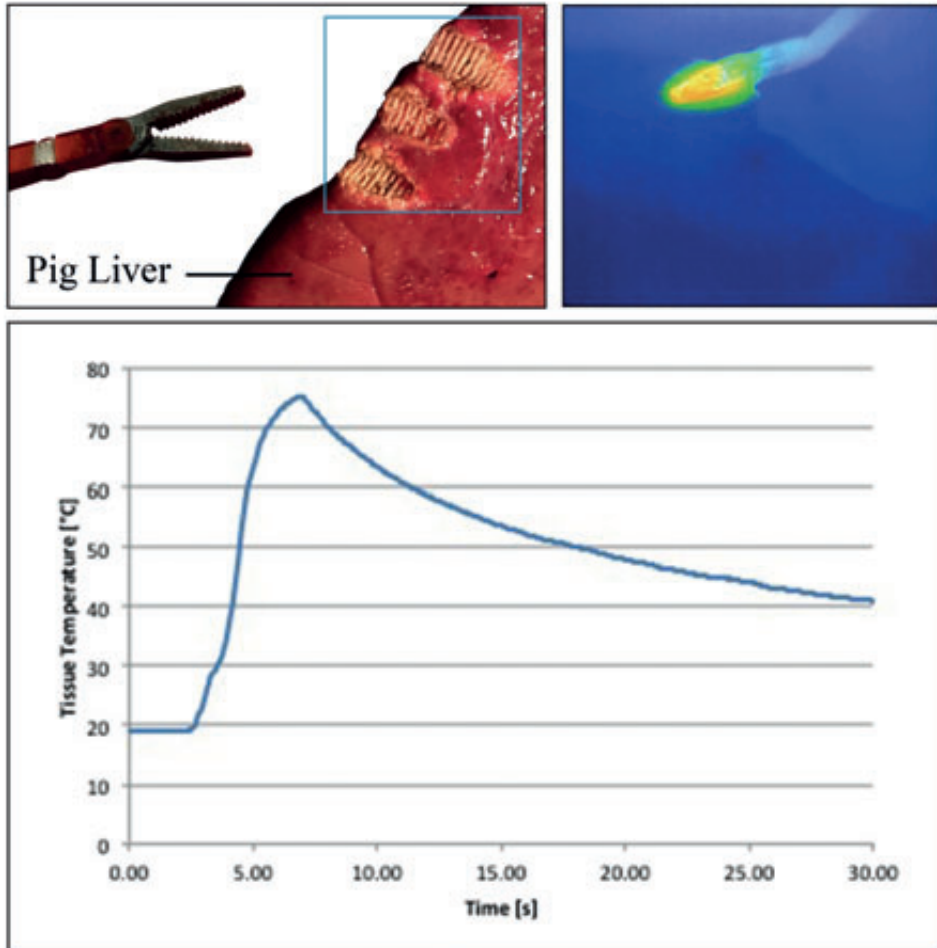
Figure 4.10— Electrosurgical Grasper Coagulating a Piece of Pig Liver. Left: The electrosurgical grasper with pieces of coagulated pig liver (see the cyan rectangle). Middle: Infrared image of the grasper during coagulation. Right: Graph of the tissue temperature over the time. The temperature of the pig liver reached approximately 75°C with an activation time of only 5 seconds, coagulating and dessicating the liver between the tip jaws. The power was set to 80 W.

progress in the last 10 years with 3D-printing technology, there are still some limitations that need to be overcome (see also Appendix 4.A). Mainly with respect to metal 3D-

printing some challenges need to be overcome in order to allow for manufacturing of small functional parts. As of today, no suitable 3D-printing process exists that provides a similar mechanical strength and behavior to off-the-shelf cables and ribbons. Moreover, printing of functional parts or components, such as screw threads is also challenging, especially on a miniature scale. It was also seen that the 3D-printing process can negatively affect the electrical properties of the material, resulting in the higher electric resistivity of the 3D-printed titanium compared to conventionally manufactured titanium ($7 \cdot 10^{-6}$ Ωm versus $1.8 \cdot 10^{-6}$ Ωm, respectively), most likely caused by pores in the material.

Even though 3D printing is still not suitable for large scale manufacturing of MIS instruments, they are rapidly developing. 3D-printers are becoming faster and cheaper, while simultaneously allowing for printing smaller parts at higher resolutions. Together with the versatility of 3D printing, we, therefore, feel that in the near future, many implants and MIS instruments will be manufactured using this technique.

4.6.4. Future Steps and Recommendations

The proposed grasper demonstrated the ability to change the position of the tip relative to the shaft and to coagulate tissues, using only 20 parts. Future developments of this instrument should be focused on exploring different 3D-printed materials and configurations of joint placement, shaft shapes, tip configurations, and handle designs. The location and shape of the connector could be optimized to allow for easy operation and connecting to the electrosurgical unit. Furthermore, in order to manufacture patient-specific tools in the near future, pre-operative data, such as data from a CTO or MRI scan, should be fed into 3D-CAD modeling software to calculate the most optimal shape. This 3D-CAD model could, subsequently, be 3D-printed and assembled prior to the procedure, allowing for patient-specific instruments that will benefit both the patients and surgeons by improving the fit of implants and allowing for safely navigating through tight spaces, amongst others.

4.7. CONCLUSIONS

This study presents the design and validation of the first adaptable and steerable 3D-printed bipolar electrosurgical grasper (□ 5 mm shaft cross-section). The addition of a steering segment significantly increases the reach of the tool, whereas the 3D-printed fabrication protocol means that the design of the instrument is both versatile and adaptable. The instrument provides 2 DOF over two joints with a curve angle of ±65° for sideways (left-right) movement (actuated by 2 polymeric steering ribbons that are 0.3 mm thick and 4 mm wide and ±85° for up- and downwards movement (actuated by two Ø0.45 mm electrode cables). The joints have a significantly higher bending stiffness (by a factor of between 1.4 and 7.8x) than currently available steerable instruments, mainly due to the placement of the cables and ribbons at the outer edge of the instrument and the

joint geometry, which restricts axial rotation and translation. The tip jaws can be opened and closed with angles up to 170° and can be used to coagulate tissues in between the jaws as they are connected to the two electrode cables that both actuate the bending motion and guide electrical current from the handle towards the tip. In the handle the two 1 DOF planar joints are mirrored and the tip jaws are replaced by a ring handle (similar to the handle of a pair of scissors) to control the tip joints and opening and closing of the movable jaws. Furthermore, in the ring handles an electrode cable tension mechanism was integrated to keep the cables and joints under tension and an electrode connector was added to connect an electrosurgical unit to the device. The instrument requires very little steering forces and has demonstrated the ability to coagulate soft tissues, with measured tissue temperatures of 75 °C for an activation time of only 5 seconds. This 3D-printed instrument is the first in its class and opens up future opportunities for patient-specific surgery with a considerably higher reach than the rigid instruments currently available.

ACKNOWLEDGMENTS

REFERENCES

[1]   Taheri A, Mansoori P, Sandoval LF, Feldman SR, Pearce D, and Williford PM. Electrosurgery: part I. Basics and principles. Journal of the American Academy of Dermatology. 2014; 70(4): pp. 591 e1-e14.

[2]   Ethicon. Ethicon Laparoscopic Hand Instruments. Available from: http://www.ethicon.com/healthcare-professionals/products/other/lap-hand/laparoscopic-hand-instruments.

[3]   Bbraun. Aesculap AdTec bipolar: The Blue (R)evolution. Available from: http://www.bbraun.no/documents/Products/AdTec_bipolar_08.10.pdf.

[4]   Intuitive Surgical. EndoWrist Instruments. Available from: https://www.intuitivesurgical.com/products/instruments/.

[5]   Stryker. Stryker Reliability for all Laparoscopic Procedures. Available from: http://www.stryker.com/stellent/groups/public/documents/web_content/126639.pdf.

[6]   Toledo L, Gossot D, Fritsch S, Revillon Y, and Reboulet C. Study of sustained forces and the working space of endoscopic surgery instruments. Annales de chirurgie. 1998; 53(7): pp 587-597.

[7]   Leijendeckers P, Fortuin J, Herwijnen F, and Schwippert G. Polytechnisch zakboek (51st ed.). Amsterdam, the Netherlands: Reed business, 2006.

4

[8]   Jelínek F, Gerboni G, Henselmans PWJ, Pessers R, and Breedveld P. Attaining high bending stiffness by full actuation in steerable minimally invasive surgical instruments. Minimally Invasive Therapy & Allied Technologies. 2015; 24(2): pp 77-85.

[9]   Aesculapusa. Aesculapusa Laparoscopic Instruments Overview. Available from: https://www.aesculapusa.com/assets/base/doc/DOC960-Laparoscopic_Instruments_Overview_Brochure.pdf.

[10]   Stryker. Stryker Laparoscopic Instruments. Available from: http://www.stryker.com/en-us/products/Endoscopy/Laparoscopy/LaparoscopicInstruments/LaparoscopicInstruments/index.htm.

[11]   Alkatout I, Schollmeyer T, Hawaldar NA, Sharma N, and Mettler L. Principles and safety measures of electrosurgery in laparoscopy. Journal of the Society of Laparoendoscopic Surgeons. 2012; 16(1): pp. 130-139.

[12]   Jelínek F, Pessers R, and Breedveld P. DragonFlex smart steerable laparoscopic instrument. Journal of Medical Devices 2014; 8(1), pp. 015001-1-015001-9.

[13]   EnvisionTec. EnvisionTec Perfactory Family P4 Standard. Available from: https://envisiontec.com/3d-printers/perfactory-family/perfactory-4-standard/.

[14]   EnvisionTec. EnvisionTec Perfactory Materials R5. Available from: https://envisiontec.com/3d-printing-materials/perfactory-materials/r5/.

[15]   Realizer. Realizer SLM 125. Available from: http://www.realizer.com/?page_id=2107.

[16]   ASM. ASM Titanium Ti-6Al-4V (Grade 5), Annealed. Available from: http://asm.matweb.com/search/SpecificMaterial.asp?bassnum=MTP641.

[17]   Engelman. Engelman Broschüre Feinseile. Available from: https://engelmann-online.de/wp-content/uploads/2015/09/Broschuere_Feinseile_DE_web.pdf.

[18]   Meeuwsen FC, Guédon ACP, Arkenbout EA, van der Elst M, Dankelman J, and van den Dobbelsteen JJ. The art of electrosurgery: Trainees and experts. Surgical Innovation. 2017; 24(4): pp 373-378.

[19]   Montero PN, Robinson TN, Weaver JS, and Stiegmann GV. Insulation failure in laparoscopic instruments. Surgical Endoscopy. 2010; 24(2): pp 462-465.

[20]   Kodama H. Automatic method for fabricating a three-dimensional plastic model with photo-hardening polymer. Review of Scientific Instruments. 1981; 52: pp 1770-1773.

APPENDIX 4.A: JOINT SELECTION PROCESS

In this section we will discuss the fundamental joint categorization and the selection process of the final joint design based on the printability, joint requirements, and bipolar requirements.

4.A1. Fundamental Joint Categorization

The main challenge of designing a steerable electrosurgical tool is to achieve a reliable and safe way of guiding the current through or around the joint. For this purpose we have made a fundamental categorization of joint types and ways of guiding the electrical current through or around the joint (Figure 4.A1). A first subdivision is based on geometrical properties of the joints (Figure 4.A1). The first group consists of joints made from a single component (*one-piece (compliant) joint*). These joints depend purely on the dimensions of the flexural part enabling the bending and the joint's material properties, such as stiffness or yield strength. Since the joint is formed of a single piece and operates within the range of the material's elastic deformation, it essentially acts as a spring. An example of such a joint is a leaf spring. The second group consists of joints made from more than one component (*multi-piece joint*). These joints rely on either high enough friction between the moving parts in rolling joints, or relatively low friction in sliding joints, to transfer the motion. Many different types of *multi-piece joints* exist (such as rolling or sliding), these will be addressed in a later section.

A second subdivision is based on how the current flows through the joint (Figure 4.A1). The *one-piece* and *multi-piece joint* groups are each divided into three groups: *completely conducting*, *partially conducting*, and *non-conducting* joints. In the *completely conducting* group, the joint itself is made entirely out of conducting material. The joint structure effectively doubles as the electrode. Since the entire joint is conductive, an outer insulating layer is needed to prevent any current from entering the body other than at the tip of the instrument (indicated in green in Figure 4.A1). In the *partially conducting* group, the joint is made from two different materials; a conducting and a non-conducting material. In this group, the electrode is embedded into the joint and is printed in the same cycle as the non-conducting component to create a single part. Finally, in the *non-conducting* group, the joint itself is made entirely from non-conducting material; separate electrodes are needed to guide the electricity through the joint. The key difference between the *partially conducting* and *non-conducting* group is that the electrode in the *partially conducting* group are embedded inside the joint and cannot be removed, whereas the electrodes in the *non-conducting* group are inserted into the joint after manufacturing in an assembly stage.

Within the *non-conducting* group a second distinction can be made between *externally placed electrodes* and *internally placed electrodes*. The *externally placed*
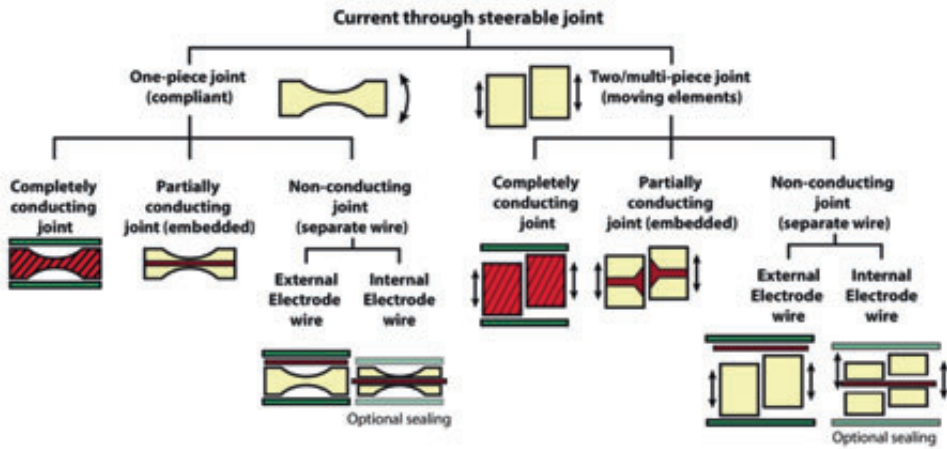
Figure 4.A1— Fundamental Joint Categorization. Color indications: Green = Sealing (insulator), Red = Conductive material, Yellow = Insulating material.

electrodes are guided around the joint, necessitating an insulating layer (indicated in green in Figure 4.A3) to prevent any current from entering the body, whereas the *internally placed electrodes* are guided through the joint itself and thus do not require an insulating layer (indicated in opaque green in Figure 4.A1). It is, however, advisable to use an insulating layer (or sealing) as current leakage (as a result of insulation failure) is thought to be responsible for most injuries caused during electrosurgery [19].

4.A2. Joint Selection Process

4.A2.1. Elimination based on Printability

In Table 4.A1 an overview is given of currently available materials for 3D printing. Although 3D printing of polymers has come a long way since it was first introduced in 1981 (by Hideo Kodama [20]), 3D printing of high-precision structural metal parts has not yet come as far. The main consequence this will have for us is that it is not possible *yet* to print flexible conducting materials. As can be seen from Figure 4.A1, four joint groups rely on flexible (conducting) components. However, only two of those groups rely on flexible conducting components that have been 3D-printed; the *one-piece (compliant) completely conducting joint* group and *one-piece (compliant) partially conducting joint* group. Since we cannot make such components with current technologies, these two groups will be eliminated. Furthermore, for the *multi-piece partially conducting joint* group a multi-material printer is needed. Unfortunately, 3D-printers that can print multiple materials, specifically metallic and polymeric materials, in one cycle, are not readily available. Therefore, the *multi-piece partially conducting joint* group is also

Table 4.A1— Overview of Most Commonly Used Printable Materials. The materials indicated in blue are still under development and not readily available.

Materials:	Metals	Polymers	Ceramics	Hybrids & Others
Flexible		Flexible Photopolymer Resins Rubber		
Rigid	Aluminum (alloys) Cobalt-chromium (alloys) Copper (alloys) Gold (Au) Nickel (alloys) Platinum (PtRu) Silver (Ag) Stainless steel(s) Tantalum (Ta) Tool steels Titanium (alloys) Tungsten (W)	Acrylonitrile Butadiene Styrene (ABS) Chlorinated Polyethylene (CPE) PolyEthylene (PE) PolyAmide (PA) PolyLactic Acid (PLA) PolyPropylene (PP) Photopolymer Resins	Alumina Porcelain Silica	Hybrids: Alumide Photopolymer-ceramic resins Others: Castable Wax Cement (composite) Concrete (composite) Wood

4

eliminated. This leaves us with the *one-piece non-conducting joint, multi-piece completely conducting joint,* and *multi-piece non-conducting joint* groups (Figure 4.A2).

4A2.2. Elimination based on Joint Requirements
Joints can be fundamentally divided into *planar*, *universal*, and *spherical joints*. In Figure 4.A3, schematic representations of these joints for the *one-piece* and *multi-piece* configurations are given. A *planar joint* allows for one rotational DOF; resulting in a two-dimensional circular workspace. An example of such a joint is a leaf spring (*one-piece*) or hinge joint (*multi-piece*). The *universal joint* allows for two rotational DOF; resulting in a three-dimensional spherical workspace. Finally, *spherical joints* allow for three rotational DOF. An example of a *multi-piece spherical joint* is a ball and socket joint.

By looking at the joint requirements and wishes for our instrument, we can eliminate several groups from our joint designs. As previously discussed, the joint should allow for 2 DOF bending motion. For *planar joints* this can only be achieved by placing two joints
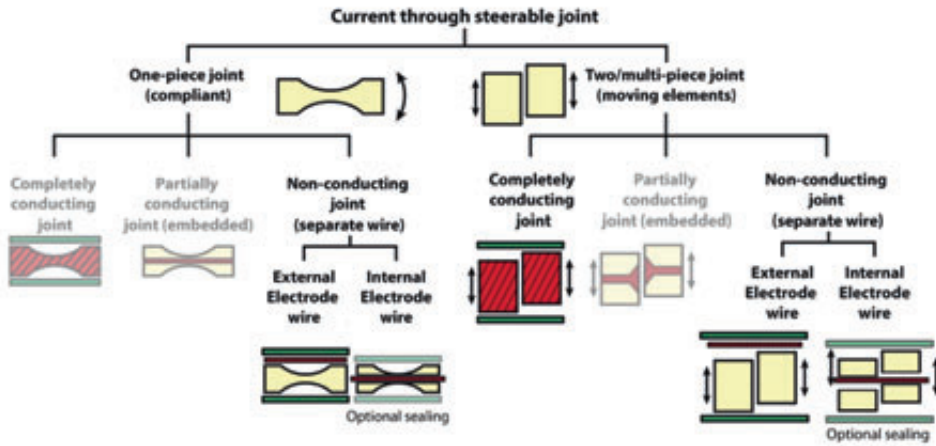
Figure 4.A2— Fundamental Joint Categorization Based on Printability. The *one-piece completely conducting joint*, *one-piece partially conducting joint*, and *multi-piece partially conducting joint* are eliminated as flexible conducting materials are currently not available for 3D-printing and multi-material printing is still limited. Color indications: Green = Sealing (insulator), Red = Conductive material, Yellow = Insulating material.

in sequence. The *universal* and *spherical joint* allow for 2 and 3 DOF motion, respectively.

Another requirement is that the joint should be torsional stiff. This eliminates the *spherical joint*, since this allow for axial rotation and is thus not torsional stiff. Furthermore, when taking a step back to the fundamental joint categorization scheme in Figure 4.A1, it becomes clear that a torsional stiff 2 DOF *non-conducting one-piece joint* is not possible as a single flexible joint with 2 DOF results in a narrow joint design as shown in Figure 4.A3. Even though it is possible to create a semi-stiff *one-piece non-conducting joint* by placing two *planar joints* in sequence, the flexibility (or compliancy) requirement of this joint design (and thus the used material) enables some axial rotation. Furthermore, such a joint requires a continuous force to keep it in a bent state, as it always tries to return to its neutral, straight, state, and, if allowed, the joint may overstretch thus introducing plastic deformation, after which the joint will not return to its straight neutral position. Therefore, this joint group is eliminated. Now only four main groups remain (Figure 4.A4): *multi-piece completely conducting planar joint (2x), multi-piece completely conducting universal joint, multi-piece non-conducting planar joint (2x),* and *multi-piece non-conducting universal joint.*
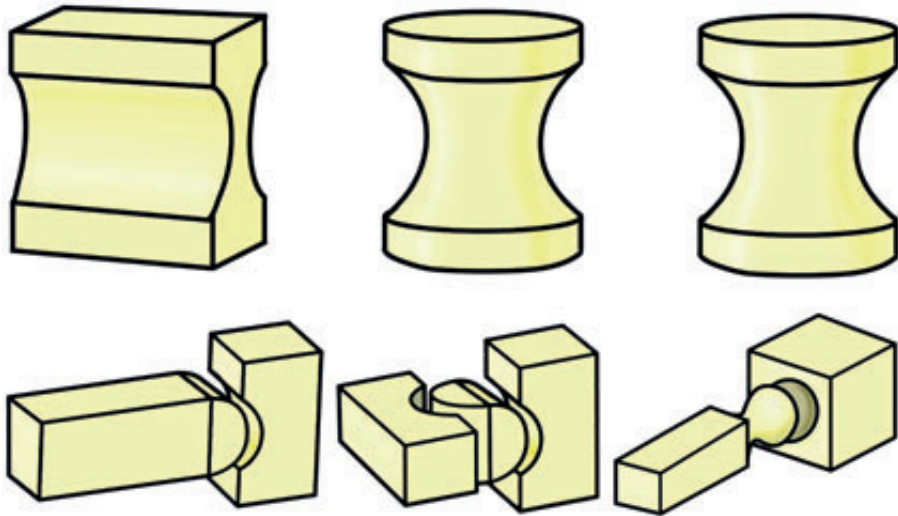
Figure 4.A3— Fundamental Joint Design. Top left: One-piece (compliant) planar joint. Top Middle: One-piece (compliant) universal joint. Top right: One-piece (compliant) spherical joint. Bottom left: Multi-piece planar joint. Bottom Middle: Multi-piece universal joint. Bottom right: Multi-piece spherical joint.

4.A2.3. Elimination based on Bipolar Requirements

In the previous sections we assumed a simple one way current through the joint (monopolar). However, in a bipolar electrosurgical instrument, two separate current paths should be guided through the joint; one active and one return electrode. Therefore, in this section we will create a bipolar representation of the *multi-piece completely conducting universal joint, multi-piece completely conducting planar joint (2x)*, *multi-piece non-conduction universal joint,* and *multi-piece non-conduction planar joint (2x)* (Figure 4.A5). To make the *multi-piece completely conducting universal joint* and *planar joint (2x)* suitable for a bipolar application, it is a necessity to add an insulating layer in the joint to separate the active and return electrode (see Figure 4.A5). As previously discussed, a multi-material 3D-printer that can print metallic and polymeric elements in one cycle is not readily available. Therefore, this category is eliminated. For the bipolar configuration of the *multi-piece non-conduction universal joint and planar joint*, two different configurations need to be taken into account; one with *external electrodes* and one with *internal electrodes* (Figure 4.A5). To make the *multi-piece non-conduction universal joint and planar joint* suitable for bipolar application it is a necessity to add one or more electrode cables to the joint that will make up the active and return electrode,

4
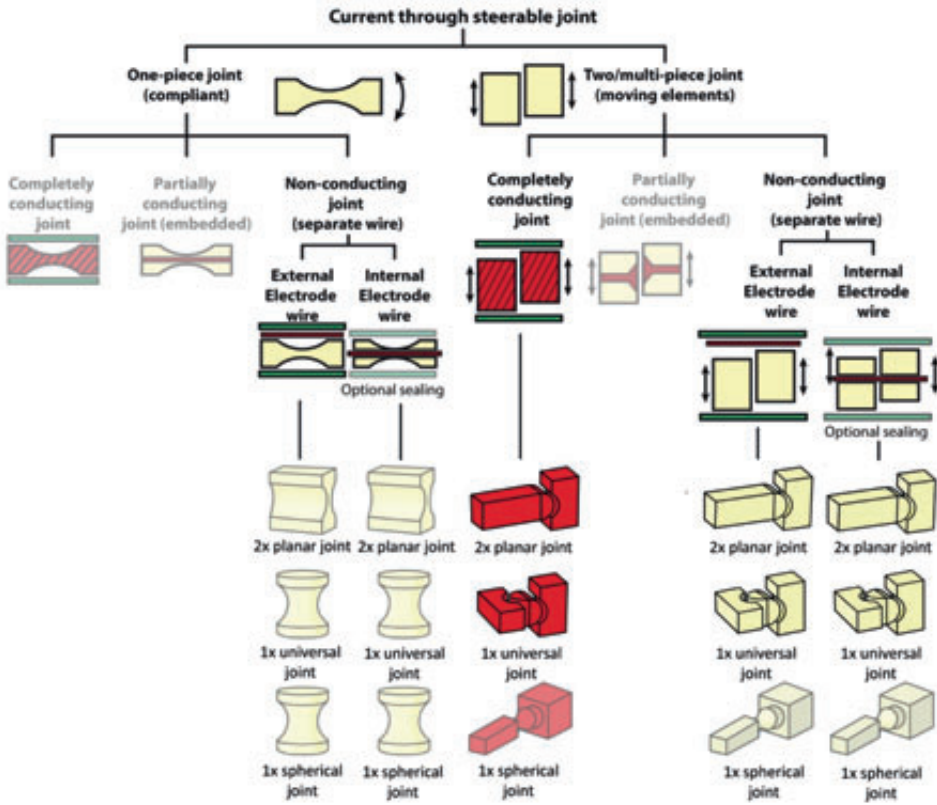
Figure 4.A4— Fundamental Joint Categorization Based on Printability and Design Requirements. Color indications: Green = Sealing (insulator), Red = Conductive material, Yellow = Insulating material.

respectively. For the *external electrode* category, the electrode cables need to be insulated, both from each other and the environment, whereas external insulation is no issue in the *internal electrode* category. Therefore, the *internal electrode* category is preferred.

Based on the discussed pros and cons of the bipolar representation of the given joint categories, only two joint designs remain: *multi-piece non-conduction universal joint* and *multi-piece non-conduction planar joint (2x)*, both with *internal electrodes*. To test the feasibility of these designs, two scaled (2x) prototypes were manufactured using a *Perfactory 4 Standard* (EnvisionTec, Dearborn, MI) 3D printer. From these prototypes it became clear that the *multi-piece non-conduction universal joint* would be too weak and

fragile when printed on a 5 mm scale (Figure 4.A6). We, therefore, decided to eliminate this category. In the next section, the *multi-piece non-conduction planar joint (2x)* with *internal electrode* will be developed further.

4A.2.4. Conceptual Joint Design

In Figure 4.A7, a schematic drawing of the conceptual joint design is given. As can be seen from Figure 4.A7, the design contains a square shaft and two serially placed planar joints. The main benefit of using a square shaft over a circular shaft is that the planar joints can be maximized in size and thus in strength. The first planar joint moves the instrument left and right with a curve angle of 130° (65° in each direction) and consists of a large cylindrical barrel that is confined (on two sides) by a semi-cylindrical recess in the shaft (Figure 4.A7). Two steering cables located at the circumference of the barrel actuate the joint (Figure 4.A7). To prevent cable kinking during bending the barrel contains two hourglass shaped lumina. The second (more distal) planar joint moves the tip upward and downward with a curve angle of 180° (90° in both directions) and consists of a (open) hinge joint in which the tip section contains a semi-cylindrical groove that clicks upon a fixed axle (Figure 4.A7). To steer the joint and to guide electricity to the tip, two Ø0.5 mm cables are used, which are guided through two separate lumens in the center of the first joint and are looped around two separate circular grooves in the tip section (Figure 4.A7). By tensioning the cables, friction between the cables and grooves will keep the cable in place during movement. However, for safety a small hole is present at the apex of the circular grooves through which glue can be applied to fix the cables in place. From here they follow the same path back to the handle of the instrument. By creating a loop at the end of the cables the effective diameter of the cables is doubled, allowing for higher forces that can be exerted on the tip portion. Furthermore, by using a looped cable that bypasses both joints, the chance of electrical interruptions (by loose connections or contacts) and the risk of cable loosening are minimized.

4.A3. Joint Optimization Process

4.A3.1. From Cables to a Ribbon

In most steerable instruments 2 cables are used to control 1 DOF; one for each direction. The required cross-sectional area (or size) of the steering cables is dependent on the required force to bend the joint and the bending stiffness of the cable itself. Instead of 2 cables to control 1 DOF, it is, therefore, also possible to use several smaller cables or even a rectangular ribbon with an equal cross-sectional area. The use of a ribbon to control the joint has two main advantages. First, the wires can be placed very close to the edge of the joint, increasing the moment arm of the cables and thus reducing the required force for bending, as well as increasing the joint size and bending stiffness of the joint (Figure 4.A8). Furthermore, the increase in joint size increases its stability, allows for the incorporation of thicker internal electrode cables, and allows for it to function as a

guidance structure for the cable ribbon during bending motions. The second advantage is the bending radius these wires can accommodate. As a rule of thumb the bending radius of a cable should not be lower than 5x its diameter to prevent cable fatigue. By minimizing the cable thickness, smaller radii can be navigated.

4.A3.2. Tip and Joint Integration

The distance between the tip (with the movable jaws) and the joints should be as small as possible to allow for direct steering and precise tip positioning. In order to minimize the distance between the tip and joints, it was decided to integrate the tip section with the

4
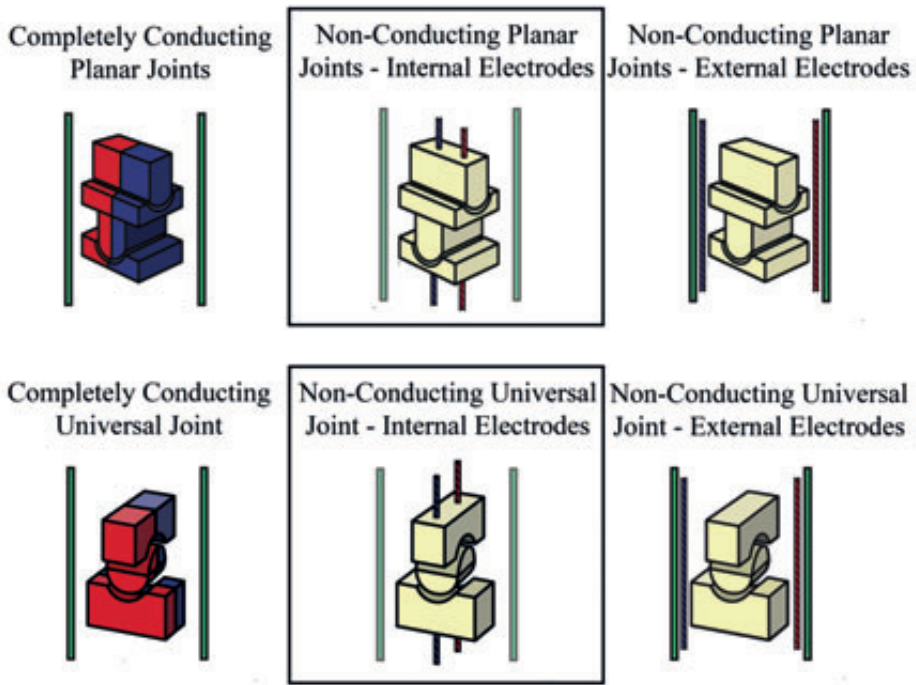
Figure 4.A5— Bipolar Versions of the Joint Designs. Top row from left to right: *multi-piece completely conducting planar joint (2x), multi-piece non-conducting planar joint (2x) with internal electrodes,* and *multi-piece non-conducting planar joint (2x) with external electrodes*. Bottom row from left to right: *multi-piece completely conducting universal joint, multi-piece non-conducting universal joint with internal electrodes*, and *multi-piece non-conducting universal joint with external electrodes*. Due to the inability to print the *multi-piece completely conducting joints* and the preference that the electrode cables are guided through the instrument, the *multi-piece non-conducting joints with internal electrodes* will be developed further (indicated by the black rectangular boxes). Color indications: Blue = return electrode, Green = Sealing (insulator), Red = active electrode, Yellow = Insulating material.
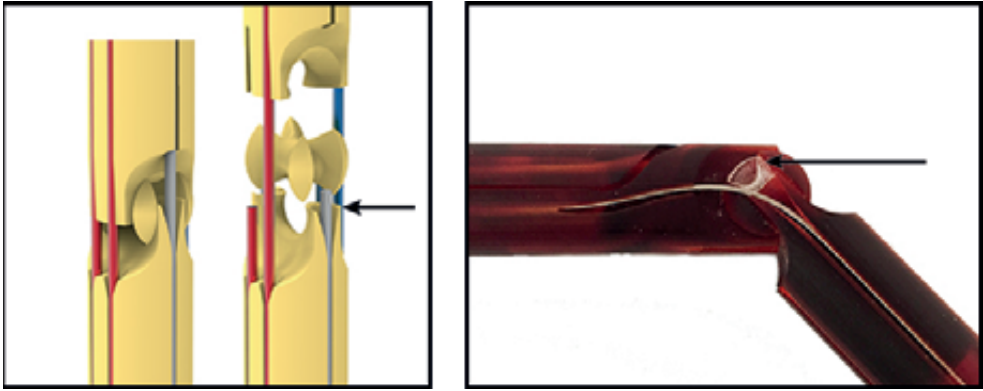
Figure 4.A6— Scaled Prototype Multi-Piece Non-Conduction Universal Joint. Left: Renderings of the *Multi-Piece Non-Conduction Universal Joint* consisting of two "shafts" with rounded cylindrical recesses and a spherical cross. Right: scaled (3x) printed prototype. The arrow indicates the weakest part of the prototype, which, when printed on a 5 mm scale, will be too weak. Therefore, this design was eliminated.
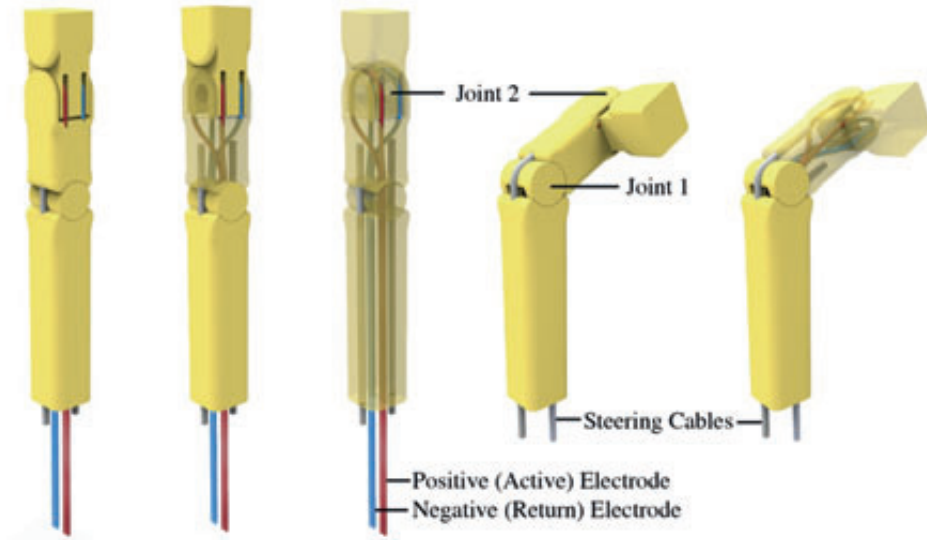
Figure 4.A7— Conceptual One-Piece Non-Conduction Planar Joint Design. Color indications: Blue = return electrode, Green = Sealing (insulator), Grey = polymeric steering cable. Red = active electrode, Yellow = Insulating material.

4
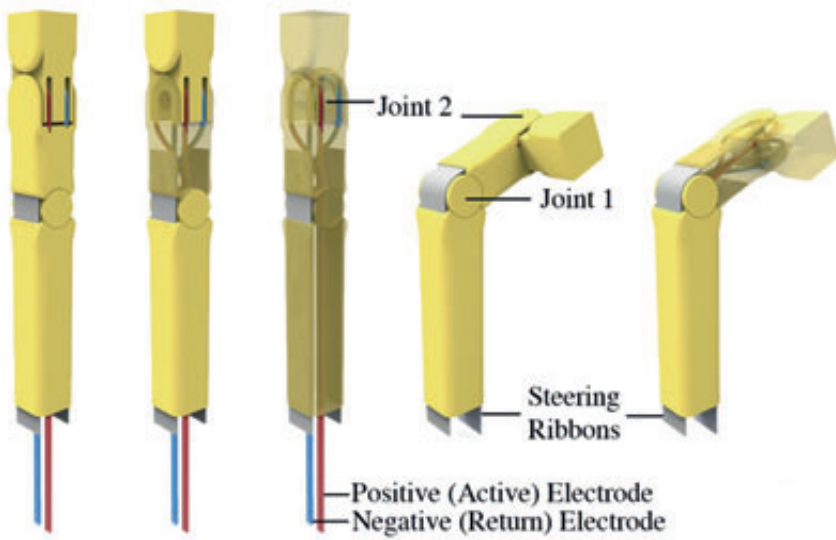
Figure 4.A8— Optimization of the One-Piece Non-Conduction Planar Joint Design; From Cables to a Ribbon. Color indications: Blue = return electrode, Grey = polymeric steering ribbon, Red = active electrode, Yellow = Insulating material.

second planar joint. For this purpose the shaft distally to the second joint was cut through the midline, giving to (basic) separate tip jaws (Figure 4.A9). To each of the jaws one of the electrode cables is connected. As such, the second (distal) planar joint and the connected electrode cables enable the rotation of the entire tip, as well as the opening and closing of the jaws (Figure 4.A9).
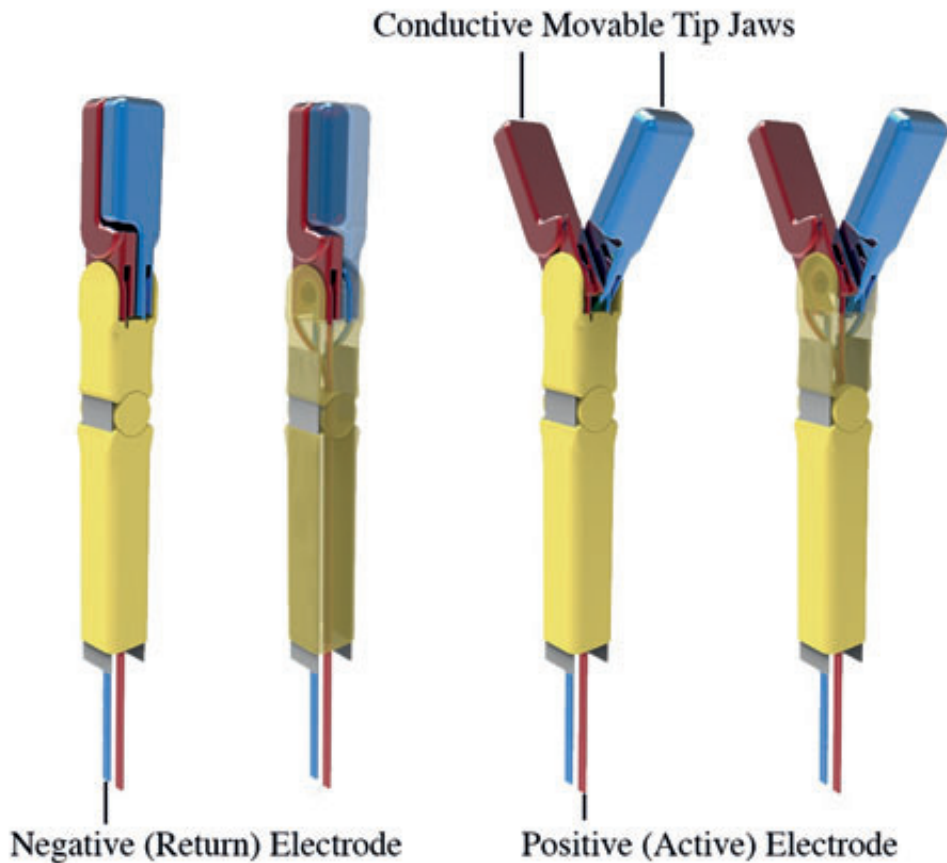
Figure 4.A9— Optimization of the One-Piece Non-Conduction Planar Joint Design: Tip and Joint Integration. Color indications: Blue = return electrode, Grey = polymeric steering ribbon, Red = active electrode, Yellow = Insulating material.

PART II

HIGH IMPACT TECHNOLOGIES

An important step of PCI in CTOs is the crossing procedure. For true lumen crossing the CTO needs to be punctured. Currently, a guidewire is slowly fed through the vasculature and subsequently pushed against the CTO until puncture is achieved. However, as the penetration force of the CTO is often higher than the critical load of the guidewire, buckling is often observed. Buckling is unwanted as it can cause blood vessel wall damage and even procedural failure when the interventionist is unable to cross the CTO. In the upcoming chapters, innovative buckling prevention strategies will be explored and applied to develop several innovative crossing instruments.

<div align="right">

CHAPTER 5   **5**

</div>

BUCKLING PREVENTION IN NATURE – A REVIEW

AIMÉE SAKES, DIMITRA DODOU, AND PAUL BREEDVELD

Published in Bioinspiration & Biomimetics.

Abstract— A typical mechanical failure mode observed in slender percutaneous instruments, such as needles and guidewires, is buckling. Buckling is observed when the axial compressive force that is required to penetrate certain tissue types exceeds the critical load of the instrument and manifests itself by sudden lateral deflection of the instrument. In nature, several organisms are able to penetrate substrates without buckling while using apparatuses with diameters smaller than those of off-the-shelf available percutaneous needles and guidewires. In this study we reviewed the apparatuses and buckling prevention strategies employed by biological organisms to penetrate substrates such as wood and skin. A subdivision is made between buckling prevention strategies that focus on increasing the critical load of the penetration tool and strategies that focus on decreasing the penetration load of the substrate. In total, 28 buckling prevention strategies were identified and categorized. Most organisms appear to be using a combination of buckling prevention strategies simultaneously. Integration and combination of these biological buckling prevention strategies in percutaneous instruments may contribute to increasing the success rate of percutaneous interventions.

5

5.1. INTRODUCTION

5.1.1. Buckling in Percutaneous Interventions

Percutaneous (i.e., "through the skin") interventions are becoming the preferred treatment modality for many disorders, as they are associated with a reduction of trauma, shorter hospital stay, and shorter recovery time. In percutaneous interventions, slender, tubular instruments, such as needles, catheters, and guidewires, often not greater than a few millimeters in diameter, are inserted into the body and are advanced towards the target site.

Typical mechanical failure modes observed in the most slender percutaneous instruments, namely needles and guidewires, are Euler buckling and Brazier buckling [1, 2]. Buckling is a state where an equilibrium configuration becomes unstable under a compressive load and manifests itself by sudden lateral deflection of the instrument. If the deformations of the instrument after buckling are not detrimental for its structural integrity, the instrument will continue to carry the load that made it buckle. However, further increase of the load may cause significant and unpredictable deformations that will eventually lead to a loss of the load-carrying capacity of the instrument.

Buckling in surgical interventions is unwanted for two main reasons. Firstly, the lateral deflection can damage healthy tissue in the direct vicinity of the instrument and cause parasitic movement of the instrument tip, thereby undermining its accurate positioning (a critical function in, for example, percutaneous tissue biopsy, where accuracy of tip positioning in the millimeter scale is needed [3, 4]). Secondly, the loss of structural stability decreases the maximum effective compressive load that the instrument can bear as compared to the unbuckled state. Loss of structural stability can lead to procedural failure if the instrument is no longer able to progress toward the target site or puncture the target tissue. Procedural failure due to buckling is seen in the treatment of Chronic Total Occlusions (CTOs), in which the guidewire is unable to cross the occlusion in about 63% of cases [1] (mostly due to buckling), and in percutaneous needle procedures where buckling leads to obstruction of the lumen of the needle [2].

5.1.2. Aim of this Study

Many organisms are able to penetrate solid substrates using apparatuses with diameters smaller than those of off-the-shelf available percutaneous (hypodermic and biopsy) needles (6–34 Gauge (G) [Ø0.13–5.16 mm]) and guidewires (Ø0.36–0.89 mm), without buckling [5, 6]. It is likely that these organisms employ buckling prevention strategies that differ from those applied in percutaneous instruments. Insight in the buckling prevention strategies found in nature may give important clues about how to minimize the size of current percutaneous instruments while increasing their buckling resistance. The goal of this study is to review the working mechanisms and apparatuses used by biological organisms for buckling prevention during penetration of solid substrates.

First, a brief theoretical framework about buckling is provided, based on which the functional capabilities and limitations of current guidewires and needles are discussed. Next, the morphology and mechanical properties of biological penetration tools and the utilized buckling prevention strategies in nature are reviewed. Finally, the biological penetration tools and associated buckling prevention strategies are discussed in relation to potential future implementation in instruments for percutaneous interventions.

5.2. BUCKLING PREVENTION STRATEGIES

To prevent buckling during substrate penetration, the critical load ($F_{critical}$) of a configuration should be higher than the penetration load ($F_{penetration}$). That is, the buckling ratio of $F_{critical}$ to $F_{penetration}$ should be higher than 1 (Equation 5.1). It follows that there are two ways to increase the buckling ratio: 1) increase the $F_{critical}$ of the penetration tool and 2) decrease the $F_{penetration}$ of the substrate.

$$\frac{F_{critical}}{F_{penetration}} > 1 \tag{5.1}$$

5.2.1. Increase Critical Load ($F_{critical}$)

Increasing the critical load of the penetration tool can be done both under static and under dynamic loading conditions.

Static Loading
Depending on whether the penetration tool is an ideal column (i.e., perfectly straight, homogeneous, and free from initial stress) or a column under initial stress, different static loading buckling theories exist.

Penetration Tools Free From Initial Stress
Euler Buckling. Slender ($\lambda = \frac{Length}{diameter}$ [no units], with $\lambda > 10$), ideal columns under compression are subject to Euler buckling. The critical Euler buckling load ($F_{critical\ Euler}$ [N]) can be calculated as

$$F_{critical\ Euler} = \frac{\pi^2 EI}{(KL)^2}, \tag{5.2}$$

with E being the Young's modulus [N/mm· or GPa], I the second moment of area [mm·], K the effective-length factor that takes into account the end-conditions of the penetration tool (e.g., fixed or pivoted end points) [no unit], and L the unsupported length of the penetration tool [mm] [7].

Needles and guidewires used in percutaneous interventions are subject to Euler buckling. Sarkissian *et al.* [8] experimentally determined the critical Euler load of five different guidewires (Ø0.89 mm; length = 30 cm): U-Nite (Bard Urological, Covington, GA): $F_{critical\ Euler}$ = 0.77 ± 0.29 N (mean ± standard deviation); Sensor (Boston Scientific, Natick, MA): $F_{critical\ Euler}$ = 0.80 ± 0.29 N; Amplatz SuperStiff (Boston Scientific): $F_{critical\ Euler}$ = 1.81 ± 0.91 N; NiCore (Bard Urological): $F_{critical\ Euler}$ = 0.50 ± 0.25 N; and RadiFocus Glidewire (Boston Scientific): $F_{critical\ Euler}$ = 0.60 ± 0.25 N. The tip load of currently available guidewires is also a measure of the critical load and typically ranges from 0.5 to 30 grams (or 0.01–0.30 N, measured with L = 10 mm) [9]. Dunn *et al.* [2] measured the critical load of several epidural needles (17–18 G [Ø1.275–1.496 mm]), after a case report of a broken epidural needle during such an intervention. The buckling load of these needles was determined between 26.69 and 58.18 N.

Brazier Buckling. Slender, ideal, thin-walled columns (shells) under pure bending or combined bending and compressive loading conditions are subject to Brazier buckling. Brazier [10] showed that flattening or ovalization of the cross-section of the column reduces the bending stiffness (*EI*), which in turn causes the column to become unstable and 'jump' to a different configuration (i.e., from straight to flattened and curved) [11]. The critical Brazier buckling load ($F_{critical\ Brazier}$ [N]) can be calculated as

$$F_{critical\ Brazier} = \frac{2\sqrt{2}}{9\sqrt{1-v^2}}\pi t^2\ , \tag{5.3}$$

with *t* being the wall thickness [mm] and *v* Poisson's ratio [no units] [10, 12]. A detailed description of Euler and Brazier buckling is provided in Appendix 5.A.

It must be noted that Brazier buckling is only applicable to shells (i.e., thin-walled structures). As guidewires are solid cylinders, they are not susceptible to Brazier buckling. Needles, on the other hand, are thin-walled (e.g., wall thickness (t) = 0.05 vs. diameter = 5 mm) and can, therefore, be subjected to Brazier buckling (see [2] for an example of a buckled epidural needle).

Local Buckling. If the penetration tool is made out of slender plate elements, local buckling can precede Euler and Brazier buckling. In local buckling, only a section of the penetration tool is buckled, and the axis of the penetration tool is not distorted. When and if local buckling occurs depends on the slenderness *(λ)* of the plate element and the yield stress of the material. Local buckling can be prevented by keeping the slenderness low.

Penetration Tools Under Initial Stress

There are two main types of prestress; precompression and pretension. Penetration tools under initial pretension (by, for example, internal pressure [11]) are characterized by a higher critical load than ideal penetration tools. This becomes apparent by looking at the free-body diagram of penetration tools under initial pretension (Appendix 5.A). The initial

5

pretension counters the buckling load, thereby reducing the tendency of the penetration tool to buckle, as illustrated in Equation 5.4:

$$F_{critical\ penetration\ tools\ under\ initial\ stress} = \left(F_{critical\ ideal} - F_{pretension}\right), \qquad (5.4)$$

with $F_{critical\ ideal}$ being the critical load of an ideal column of similar dimensions to those of the prestressed column [N], and $F_{pretension}$ the force exerted on the penetration tool by the pretension [N].

Dynamic Loading

Increasing the critical load of a penetration tool can also be achieved by subjecting it to dynamic loading. Lock [13] found that if the load duration (*dt*) is sufficiently small (i.e., the step load becomes an impulsive load), a column can sustain higher loads than under static loading. In other words, in dynamic loading conditions, the impulse imparted to the structure rather than the size of the load becomes the most significant load parameter (see Budiansky in [14] for an analytical description).

5.2.2. Decrease Penetration Load ($F_{penetration}$)

Next to increasing the critical load ($F_{critical}$), decreasing the force needed to penetrate the target substrate ($F_{penetration}$) can also prevent buckling (Equation 5.1). A detailed description of methods to decrease the penetration load is given in Appendix 5.B.

Static Loading

In static loading conditions, the penetration load mainly depends on the geometry of the penetration tool. Currently, extensive research is ongoing into needle-tip designs, varying in the number and angularity of the tip facets, and the needle diameter, to achieve low penetration loads [15-21] (see also Van Gerwen *et al.* [22] for a review on needle-tissue interaction forces). In guidewires, tip shape variety is small, as most guidewire tips are conical to prevent vascular damage during the intervention. Nevertheless, Sarkissian *et al.* [8] suggested that the slight difference in the tip's roundness ratio ($\frac{radius_{axial}}{diameter}$) of the Amplatz (0.593; blunt) versus Sensor (0.442; sharp) may be the reason why the penetration load was higher for former ($F_{penetration}$ = 1.45 ± 0.20 N [mean ± standard deviation]) as compared to the latter ($F_{penetration}$ = 1.15 ± 0.15 N). It must be noted that buckling prevention methods relying on tip shape optimization are less effective in tissue types of low cohesiveness, such as brain tissue, where there is limited or no connective tissue to advance the crack created at the tip of the needle or guidewire. To move through such less-cohesive tissue types or substrates, inspiration can be drawn from burrowing methods of worms in sand, such as *Thoracophelia mucronata* that burrows in sand by peristalsis, compacting the sand and minimizing friction [23].

Dynamic loading

Substrate penetration with dynamic (impulse) loading can be described as an inelastic collision (i.e., a collision where all the kinetic energy is transferred into penetration energy) between a moving body (the penetration tool) and an initially non-moving body (the to-be-penetrated substrate/tissue). Environmental damping and the inertia of the target tissue act as a reaction force to the penetration load, thereby preventing movement and deformation of the tissue, which results in a lower penetration load. This effect has been illustrated in multiple studies (e.g., [24, 25]). Furthermore, if the substrate is not allowed to stabilize between two imparted dynamic (impulse) loads, the substrate is subject to vibrational loading. Soft biological tissues, such as skin [26], show time-dependent viscosity, causing the tissue to soften or flow over time when vibrated or agitated, a property also known as thixotropy [27]. This effect can be used to decrease the penetration load, as illustrated by Yang *et al.* [28], in which vibratory actuation (in the kHz range) of a microneedle reduced the penetration load by approximately 70% compared to conventional microneedle insertion using a static axial force.

5.3. BUCKLING PREVENTION STRATEGIES IN NATURE

We propose a categorization of biological buckling prevention strategies based on the two ways to increase the buckling ratio described in Section 2: (1) increase the critical load by utilizing the basic theories of buckling and prevention thereof, that is, Euler buckling, Brazier buckling, local buckling, buckling of penetration tools under initial stress, and dynamic buckling; and (2) decrease the penetration load, under either static loading or dynamic loading conditions (Figure 5.1). For comparison with the biological buckling prevention strategies, quantitative data of morphological and mechanical properties of medical instruments are also presented.

5.3.1. Increase critical load ($F_{critical}$) – Static loading: Euler buckling

According to Euler's formula, the critical load that a slender penetration tool withstands can be increased by increasing E and I or by decreasing K and L (Figure 5.2).

Increase the Young's Modulus of the Penetration Tool

The Young's modulus (E) of the penetration tool is largely determined by the material of the penetrating tool. Most commonly used core materials for guidewires are stainless steel (316L or 304), nitinol, and titanium (Grade 1-4, Ti6Al4V), with E_s of 190–210 GPa, 21–110 GPa (highly non-linear with temperature), and 103–114 GPa, respectively [5, 29-33]. Needles are mostly manufactured out of stainless steel (304, 316L, 420, and 455), with E_s between 190 and 210 GPa [31], or Nitinol [32, 34-36].

The materials which biological penetration apparatuses are made of cannot compete with the E_s of stainless steel, titanium, or nitinol. Sclerotin and keratin are two of the hardest materials found in biological penetration apparatuses.

Insect Cuticles – Sclerotin. The cuticle forms the exoskeleton of insects and is used for protection but also for penetration purposes, as in wasp ovipositors (i.e., egg-laying structure) and mosquito proboscis (i.e., mouthpart). Vincent *et al.* [37] underlined that the E of insect cuticles depends on their components (including chitin, proteins, water, lipids, metal ions such as zinc, manganese, and iron, and calcium carbonate), which may vary in orientation and volume fraction, as well as in the crosslinking degree of the proteins that form the sclerotin. This variety results in a wide range of E_s from 1 kPa to 20 GPa across species (and depending on the measurement direction, as cuticle is anisotropic). For example, high water content leads to soft, compliant cuticles, whereas low water content and high cross-linking degree lead to hard, stiff cuticles.

5
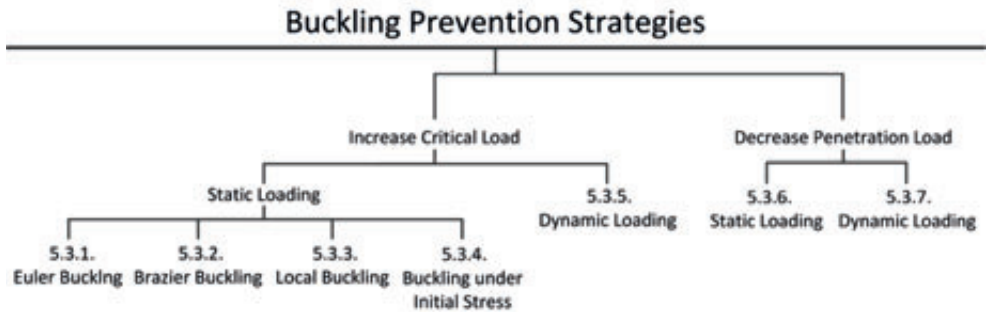
Figure 5.1— Schematic Illustration of the Layout of Section 5.3.
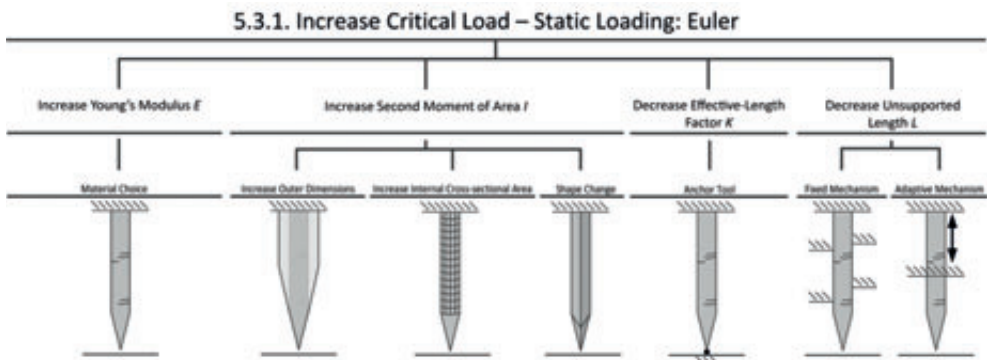
Figure 5.2— Schematic Illustration of Euler-Based Buckling Prevention Strategies. Arrow indication: black = translation of the end support of the penetration tool.

Hymenoptera Ovipositors – Metal Ions. An ovipositor is an organ found across many insect orders, including Hymenoptera (ovipositor diameter ≈ 0.004–0.08 mm, length ≈ 0.5–5.5 mm, λ ≈ 6.25–1375, extracted from figures and data in [38-43]). Ovipositors are used for egg laying and, depending on their morphology and mechanical properties, are able to penetrate soil, plant tissue, bark, wood, and the bodies of (the larvae of) other animals [40]. According to Quicke *et al.* [44], the presence of the metal ions manganese and zinc potentially contributes to the high bending stiffness of the ovipositor in Hymenoptera. Kundanati *et al.* [45] estimated the critical Euler load of the ovipositor of *Apocrypta* to be approximately 6.9 µN, using L = 0.48 mm, r = 9.73 µm, and E = 0.73 GPa. However, it must be noted that the measurements were done with Atomic Force Microscopy (AFM), therefore representing a local E of the ovipositor, without taking into account that the E of the ovipositor may differ from point to point, depending on the local density of the material.

Quills and Spines – Keratin. Some mammals, including porcupines (infraorder Hystricognathi), hedgehogs (subfamily Erinaceinae), echidnas (spiny anteaters), tenrecs, spiny rats, and spiny mice, have developed specialized sharp and stiff hairs for defense [46]. The quills and spines of these animals are composed of α-keratin, a fibrous structural protein [46]. E_s between 3.4 (for 100% relative humidity) and 6.7 GPa (for 0% relative humidity) have been measured for porcupine quills (family Hystricidae) [47].

Woodpecker Beak – Boney Keratin. To uncover insects and grubs from a tree, woodpeckers (family *Picidae*) chisel wood with their beak (Ø ≈ 8 mm, length ≈ 33 mm, λ ≈ 4, deduced from [46]). The beak of the woodpecker consists of an inner core of strong porous bone, a middle foam layer, and a scaled keratin sheath [48, 49]. The bone is the main load bearer and the strongest material of the three, while the keratin scales act as a shock absorber by rubbing against each other, thereby dissipating energy and preventing fracture of the beak during impact [49].

Increase the Second Moment of Area of the Penetration Tool

The second moment of area (I) of the penetration tool can be increased by increasing the internal cross-sectional area, by changing the shape of the penetration tool, or by increasing its outer dimensions. For comparison with the biological buckling prevention strategies, the I of guidewires equals that of a filled circular area, ranging between $8.3 \cdot 10^{-4}$ and $3.2 \cdot 10^{-2}$ mm (Ø0.36–0.89 mm). In some cases the guidewire is supported by a catheter. Catheter support can increase the I up to a factor 10 (common cardiac support catheter Ø2–3 mm) [50], thereby increasing the chance of a successful crossing procedure. Since needles are usually hollow, the I of these instruments depends on the lumen size. For typical needle sizes (6–34 G [Ø0.13–5.16 mm]), the maximum I that can be achieved with current needle design is 16.6 mm^4 (with a minimum of $61.9 \cdot 10^{-6}$ mm), estimated based on off-the-shelf needle diameters and lumens reported in [6].

Increase the Internal Cross-Sectional Area of the Penetration Tool

The internal cross-sectional area of a penetration tool can be increased by incorporating specialized reinforcement structures, such as honeycomb structures, stringers, and bulkheads.

Quills and Spines – Core-rind Structure. The keratin shell of the quills and spines of porcupines, hedgehogs, echidnas, tenrecs, and spiny rats is supported by a low-density cellular core called the "core-rind" structure. Cores of different morphologies have been found across species: isotropic (Porcupine [family Erethizontidae, e.g., species *Erethizon dorsatum:* Ø1.262 mm, length ≈ 40 mm, $\lambda \approx 31.8$] and *Echidnas* [family Tachyglossidae]), isotropic with longitudinal stiffeners (Porcupine [e.g., *Hystrix indica x Hystrix cristata:* $F_{critical\ Euler}$= 25.82 ± 5.34 N, Ø4.81, length = 144 mm, t = 0.213, cross-sectional area = 3.62 mm^2, λ = 29.9 and *Coendou prehensilis: $F_{critical\ Euler}$* = 6.65 ± 1.55 N, Ø1.93 mm, length = 47.19, t = 0.0813, cross-sectional area = 0.47 mm^2, λ = 24.45]), honeycomb-like with longitudinal internal stiffeners (i.e., ridges) and diametric plates (Hedgehog [subfamily Erinaceinae, e.g., species *Erinaceus Europaeus:* $F_{critical\ Euler}$ = 6.54 ± 1.99 N, Ø1.17 mm, length = 20.68 mm, t = 0.05 mm, cross-sectional area = 0.27 mm^2, λ = 16.7–18.7] and *Hemiechinus spinosus* [spiny rat]), or an filled foam core made out of thin closely spaced septa (Tenrec [genus *Setifer*]) (Figure 5.3) [46, 51-53]. Karam *et al.* [51] compared these four core morphologies across 11 species in terms of mechanical efficiency (i.e., the ratio of the critical Euler load of the quill or spine to that of a hollow quill of the same outer dimensions and wall thickness) and found that the most efficient core is the honeycomb-like stiffeners of the hedgehog spine, with a mechanical efficiency of 1.58–1.70 compared to 0.40–0.85 in porcupines with isotropic cores and isotropic cores with longitudinal stiffeners, respectively. According to Vincent *et al.* [53], the honeycomb-like spine structure in *Erinaceus* increases the *I* of the quills and spines by approximately 13% compared to a hollow spine of similar size. Furthermore, in another study by Karam *et al.* [12] it was analytically shown that the critical Euler load of all quills and spines containing a compliant core is greater than the critical Euler load of an unfilled cylinder with equivalent diameter, and that honeycomb-like cores were more effective than foam cores. For more information on buckling prevention related to core morphology see Section 5.3.3.

Hymenoptera Ovipositors – Internal Morphology. The ovipositor of the order Hymenoptera consists of a pair of valves (V1) separated from each other for almost their entire lengths, and a second valve (V2), which is, in some cases, serrated and expanded proximally (Figure 5.4). V1 and V2 are joined together by an interlocking mechanism, called an olistheter (Figure 5.4), which consists of a projected tongue (rhachis) on V2 that fits into a groove (aulax) of both V1 valves [40]. When held together, these structures form the egg canal (Ø ≈ 0.01 mm) [40] (Figure 5.4).
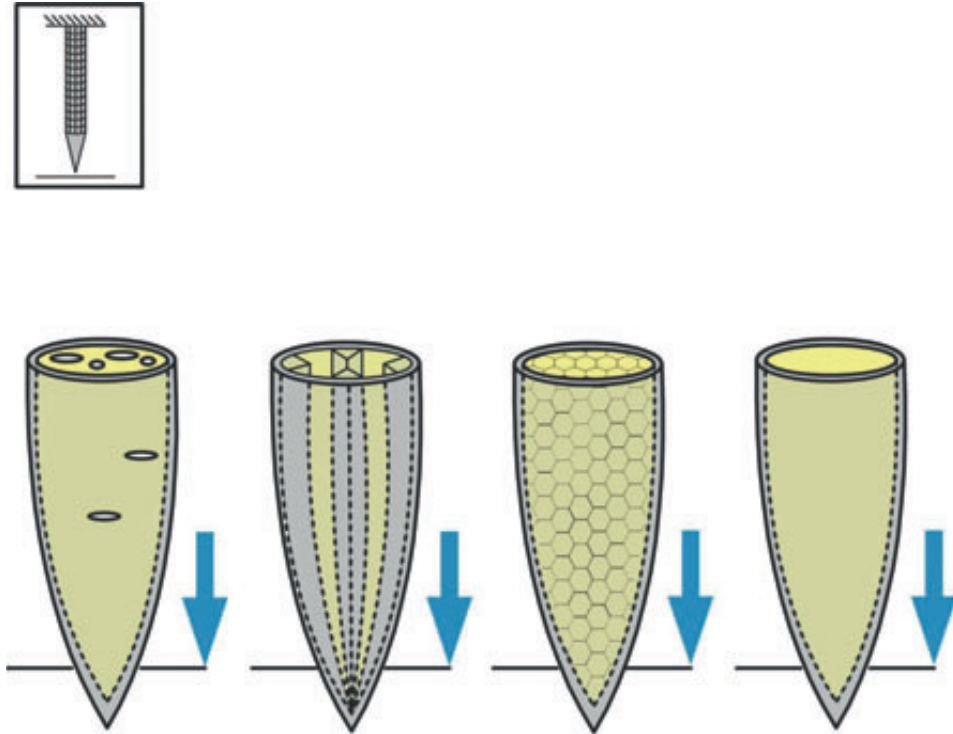
Figure 5.3— Four Types of Core-Rind Structures of Quills and Spines. From left to right: isotropic core, isotropic core with longitudinal stiffeners, honeycomb-like core (with longitudinal stiffeners and diametric plates), and filled foam core. Arrow indication: blue arrow = direction of quill or spine movement. Color indications: grey = penetration tool (quill/spine); yellow = core material or structure.

The cross-section of the ovipositor of Hymenoptera changes over its length, with the olistheter being most pronounced in the distal section of the ovipositor [38]. Furthermore, in several species V2 splits into two separate chambers close to the septum [54]. We suggest that, by retaining the circular cross-section during penetration (i.e., preventing ovalization) and thus keeping the *I* high, this splitting retards the onset of Euler, Brazier, and local buckling.

Shape Change

Placing material away from the neutral line (i.e., a line perpendicular to the chosen horizontal axis, through the centroid of the penetration tool) is more effective in
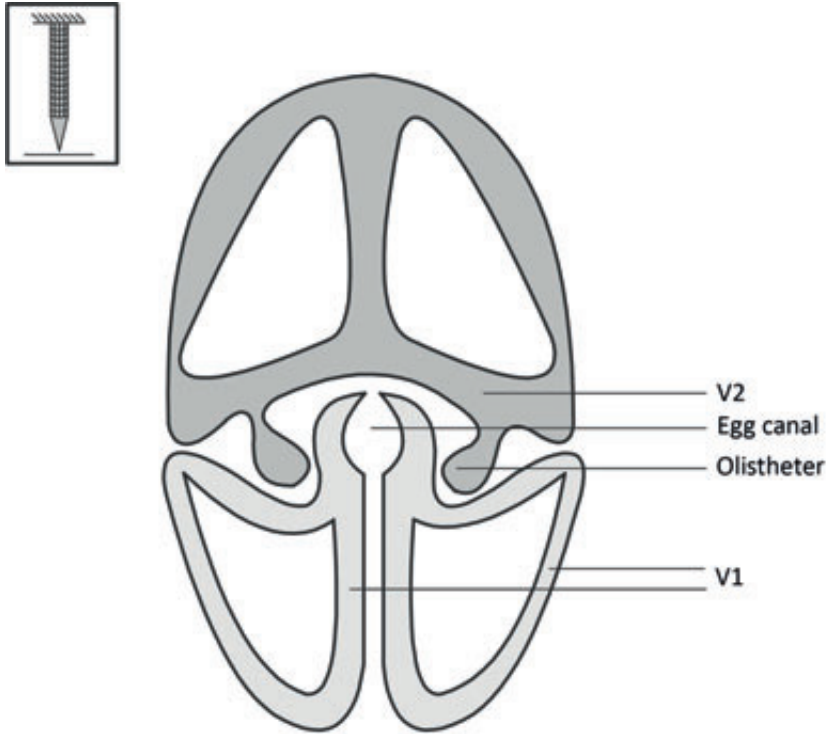
Figure 5.4— Internal Morphology of Hymenoptera (Wasp) Ovipositors (Schematically Illustrated Ovipositor of *Habrobracon Hebetor*, Adapted From [39]). Color indications: light grey = V1; dark grey = V2.

increasing *I* than placing an equal amount of material close to the neutral line. For example, the *I* of a triangular shape is higher than the *I* of a circle with the same cross-sectional area. In medicine, triangular forms are rarely encountered. In nature, on the other hand, triangular struts are found in the form of solid stems of sedges [55]. Furthermore, although the outer shape of the ovipositor in Hymenoptera is in most cases circular or oval, the internal structure of the valves is triangular in some species (see Figure 5.4 and [54]). One may hypothesize that the triangular shape of the valves contributes in increasing the moment area of inertia, thereby preventing buckling.

Increase the Outer Dimensions of the Penetration Tool

Wasp ovipositors used for hard surface penetration have a slightly larger diameter than

those used for softer substrate penetration, leading to a higher I [56]. Similarly, the stingers of wasps, bees, and cicadae are usually tapered, with an increase of the outer dimensions near the proximal end.

Decrease the Effective-Length Factor
One way to reduce the effective-length factor (K) is by anchoring the penetration apparatus to the substrate while allowing axial translation. We found three such biological anchoring methods.

Hymenoptera Ovipositors – Abdomen Anchoring. Amongst others, members of the family Orussidae support the ovipositor during penetration with special ridges, called carinae, which are located at the posterior part of the abdomen. Vilhelmsen *et al.* [39] suggested that bracing the ovipositor with the abdomen is especially important during the early stages of ovipositing, during which minimal lateral support is present. We propose that bracing decreases the K of the ovipositor by preventing tip rotations and lateral translations.

Hymenoptera ovipositors – Barbed Anchoring. The ovipositor of several representatives of the Hymenoptera family has barbs and serrations on their lateral side, which penetrate (by cutting [creating sawdust in *Sirex*, for example] or compressing [displacing] the substrate [illustrated in most parasitic wasps with the thinner ovipositors such as *Orussus*], depending on the exact geometry of the ovipositor and barbs [39]), and subsequently anchor to the substrate. After initial penetration, the hole restricts rotation and lateral movement, thereby decreasing the K-factor to approximately 0.5 (i.e., the K-factor of a penetration tool with two fixed ends). According to Vincent *et al.* [57], it is most likely that when the lateral support is insufficient, the drilling action is aborted, as about 60% of the holes are abandoned after only 3 minutes of drilling (as interpreted by Vincent *et al.* [57] based on data from Spradberry [58]). Additionally, the increase in drilling speed observed with increased hole depth (1.0–1.5 mm/min) suggests that the wasp can exert a greater force on the ovipositor in a deeper hole (as estimated by Vincent *et al.* [57] based on data from Spradbery [58]) most likely resulting from an increase in support (K) and decrease in unsupported length (L).

Mosquito Proboscises – Barbed Anchoring. The proboscis (i.e., tubular mouthpart) of mosquitoes (Ø 11–40 µm, length = 1.5–2 mm, λ = 37.5–182 [59, 60]) is an intricate structure consisting of a protective sheath, called the labium, and the labella located at the tip of the labium (Figure 5.5). The labium envelops the piercing structure, which consists of a cluster of long, thin stylets: the labrum, mandibles, (two, paired) maxilla, and hypopharynx. The labrum and the hypopharnyx form the transport canals of the proboscis. The paired maxillae are thin serrated structures that fulfill the piercing function. The serration or barbs on the maxillae allow the proboscis to anchor to the substrate and as such to decrease the effective-length factor (K), similar to the mechanism seen in the ovipositor of Hymenoptera [59, 60].

Decrease the Unsupported Length

L is the most determining factor for Euler buckling, since by multiplying L by two, $F_{critical\ Euler}$ is reduced by a factor four. Consequently, L should be kept as low possible. Unfortunately, for percutaneous interventions, a large length is often needed in order to reach the operation site, with the length of biopsy needles being as large as 300 mm [61] and guidewire lengths ranging from 500 to 4500 mm [62].

5
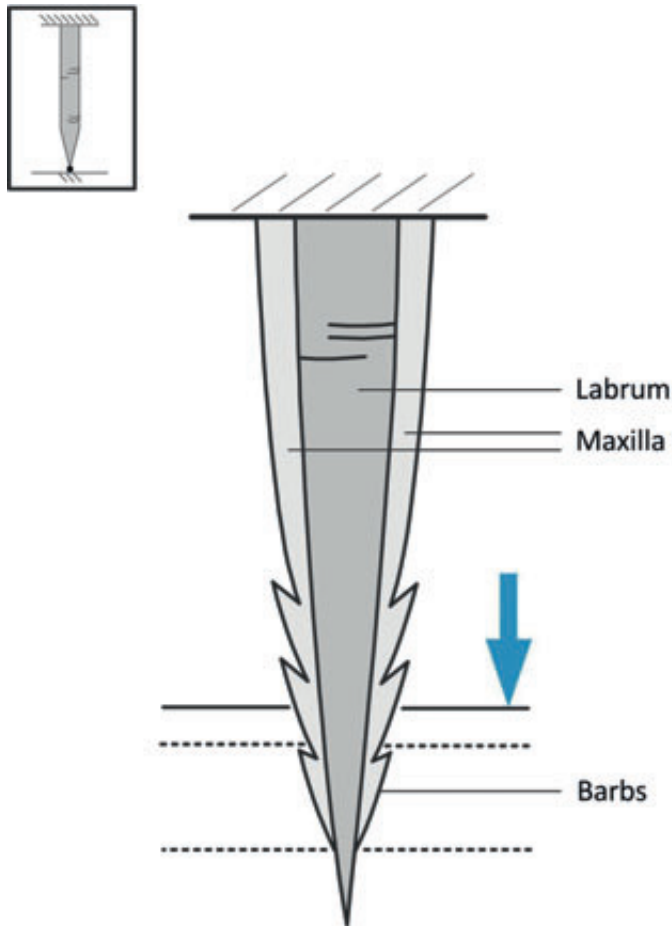
Figure 5.5— Barbed Anchoring of Mosquito Proboscises. Arrow indication: blue arrow = direction of quill or spine movement. Color indications: light grey = maxillae; dark grey = labrum.

Decreasing the unsupported length can be achieved with either a fixed or an adaptive mechanism. In the first case, the organism does not actively adjust the unsupported length during penetration, whereas in the second case, the organism (dynamically) adjusts the unsupported length. It must be noted that decreasing the length L of the penetration tool inside a substrate can lead to a decrease in critical load if excessive friction persists between the penetration tool and surrounding tissue.

Fixed Mechanism

Worms – Setae. Many (polychaete) worms (including roundworms [or nematodes] [63]) possess so-called setae: bristle- or hair-like structures that provide counterforce during substrate penetration (Figure 5.6) [63, 64]. These setae attach to the surface and prevent backsliding during peristaltic motion, as they only allow for movement in one direction, subsequently anchoring the worm in place during penetration. The setae support the worm throughout its body and thus distribute the compressive forces over the entire body (Figure 5.6). By distributing the forces, the unsupported length (L) is minimized, increasing the buckling resistance.

Hymenoptera Ovipositors – Tubercles. In the species *Megarhyssa Nortoni* (family Ichneumonidae), the ovipositor is supported by a longitudinal median groove flanked by a series of tubercles (i.e., round nodules) on the abdominal sterna (Figure 5.7) [39]. According to Vincent *et al.* [57] the tips of these tubercles are highly sclerotized, suggesting that they are very stiff and able to push with considerable force against each other. By preventing deflection, these tubercles decrease the unsupported length (L) of the ovipositor.

Mosquito Proboscises – Lateral Labium Support. To increase the critical load of the fascicle of the proboscis ($F_{critical} \approx 3$ mN [60]; not sufficient to penetrate the skin [60]), the fascicle is laterally supported throughout the penetration process by the labium. Ramasubramanian *et al.* [60] used a mathematical model to assess the effect of the lateral support on the critical load and estimated that the presence of lateral support increases the critical load by a factor of 5.

Adaptive mechanism

Hymenoptera Ovipositors – Hind Leg Support. In many species within the family Aulacidae and in some Ichneumoidea, the ovipositor is held approximately at its midpoint between the hind legs during substrate penetration (Figure 5.8) [39]. This method of holding the ovipositor between the hind legs halves the effective length and thus quadruples the penetration force that the insect can apply without the ovipositor buckling.

Hymenoptera Ovipositors – Reciprocating Penetration. When the ovipositor is lowered to the substrate, the valves thrust into the substrate in an alternating fashion [65]. After one valve has penetrated the substrate, the barbs lock the ovipositor in place by pulling on the substrate, facilitating the penetration of the second valve (Figure 5.9) [57, 66]. The

subsequent alternating movement of the valves drives the ovipositor deeper into the substrate. Since the valves move incrementally forward (traversing a distance of ≤ 0.25 mm per valve movement [39, 40, 54, 67]), the unsupported length inside the substrate is kept low and independent of the insertion depth.

5
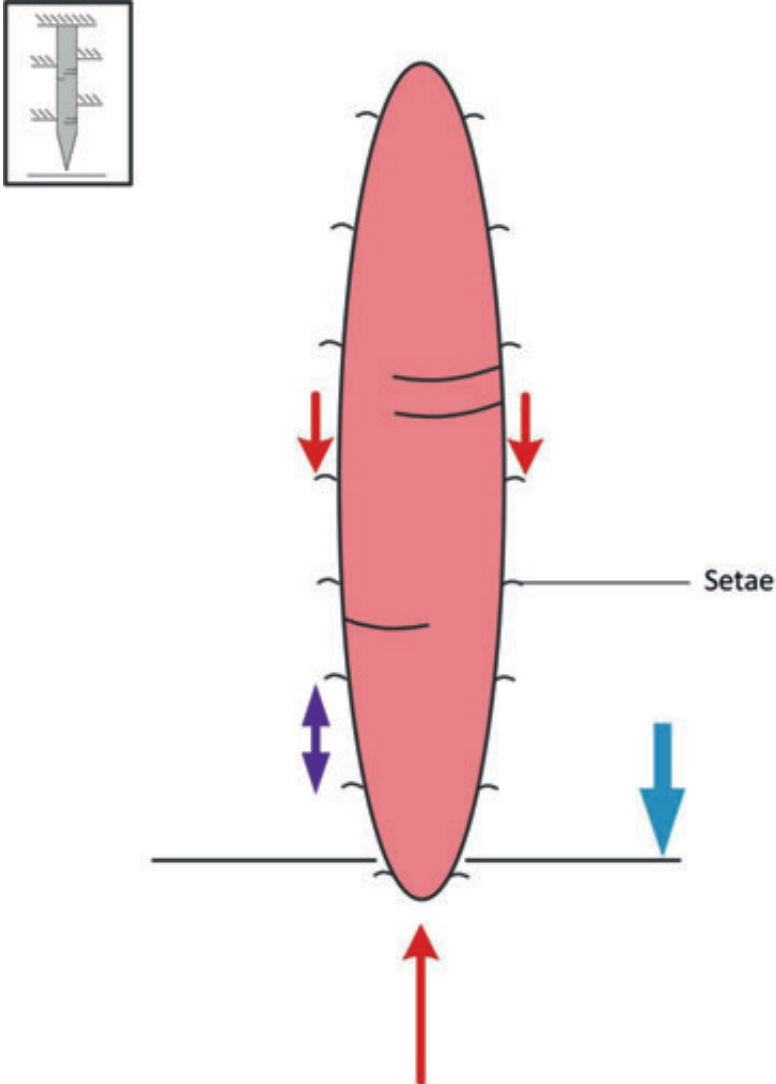
Figure 5.6— Worm Setae. Arrow indications: blue arrow = direction of worm movement through the substrate; purple arrow = unsupported length (L); downward pointing red arrows = penetration load exerted on the substrate by the setae during penetration (note that these forces are present at all indicated setae); upward pointing red arrow = compressive (buckling) load exerted on the worm during substrate penetration. Color indication: pink = muscle.
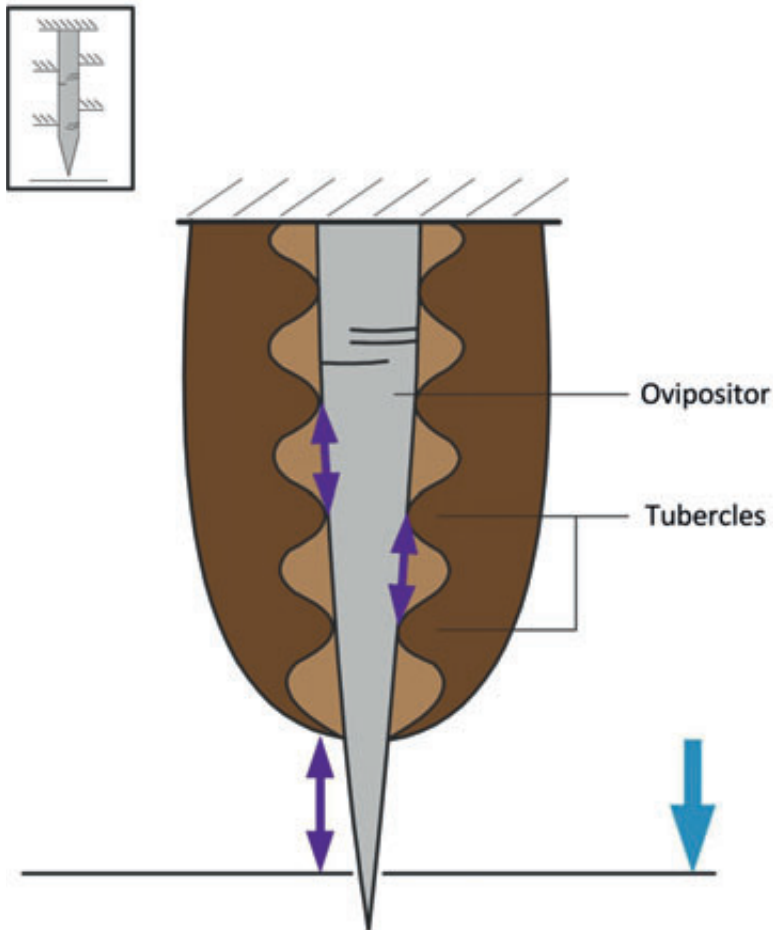
Figure 5.7— Tubercles of Hymenoptera (wasp) Ovipositors (of the species *Megarhyssa Nortoni*). Arrow indications: blue arrow = direction of the ovipositor movement during substrate penetration; purple arrow = unsupported length (*L*). Color indications: brown = hind legs with grooves; grey = ovipositor.

Mosquito Proboscises – Reciprocating Penetration. The penetration of the substrate by the mosquito proboscis occurs via a reciprocal movement of the maxillae (Figure 5.9). Aoyagi *et al*. [68] investigated the mechanism of proboscis penetration in transparent soft slime material (*E* = 0.2 MPa) using high-speed video analysis. They found that the maxillae are advanced into the material in a reciprocating fashion, similar to the mechanism observed in Hymenoptera (Figure 5.10). How this reciprocating movement is performed without an interlocking mechanism of the stylets (such as the olistheter observed in the ovipositor of wasps) remains largely unknown.

5
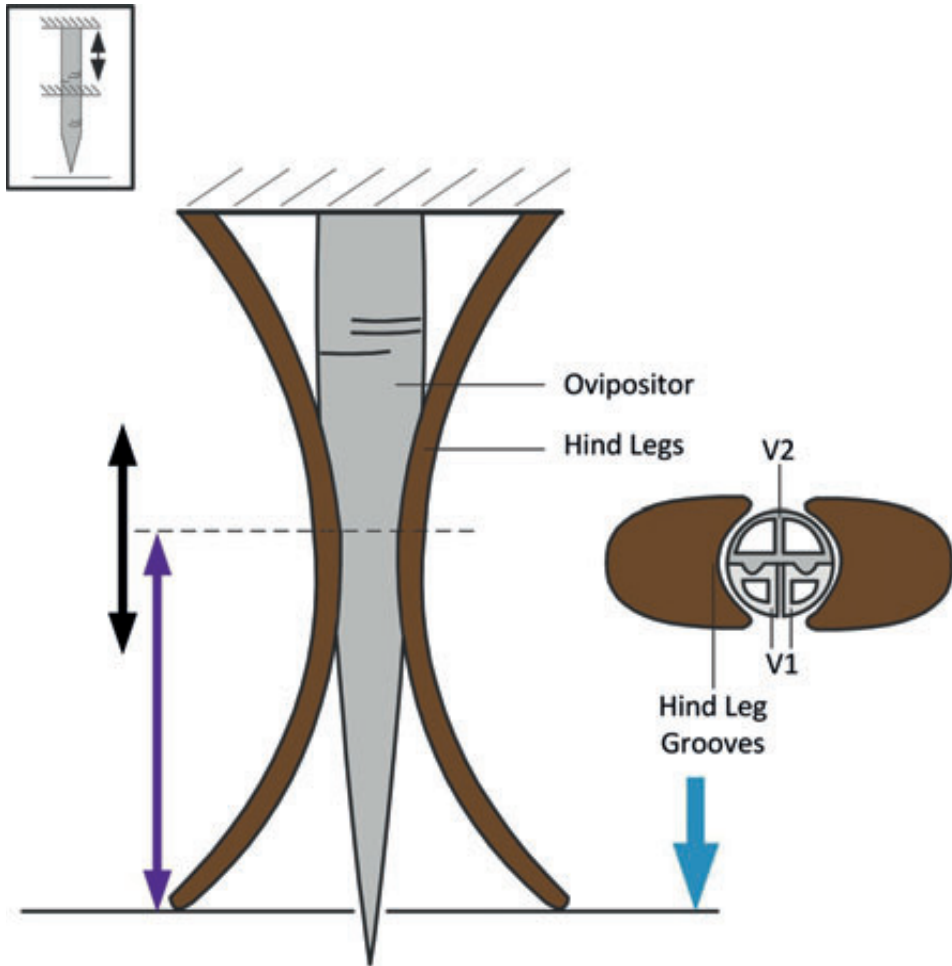
Figure 5.8— Hind Leg Support of Hymenoptera (Wasp) Ovipositors. Arrow indications: blue arrow = direction of ovipositor movement; black arrow = adaptive hind leg support mechanism; purple arrow = unsupported length (*L*). Color indications: brown = hind legs with grooves; light grey = V1; dark grey = V2.

5.3.2. Increase Critical Load ($F_{critical}$) – Static Loading: Brazier Buckling

According to Brazier's formula, the critical load that a slender penetration tool withstands can be increased by increasing *E* and *t* or by decreasing *v* (Figure 5.11).
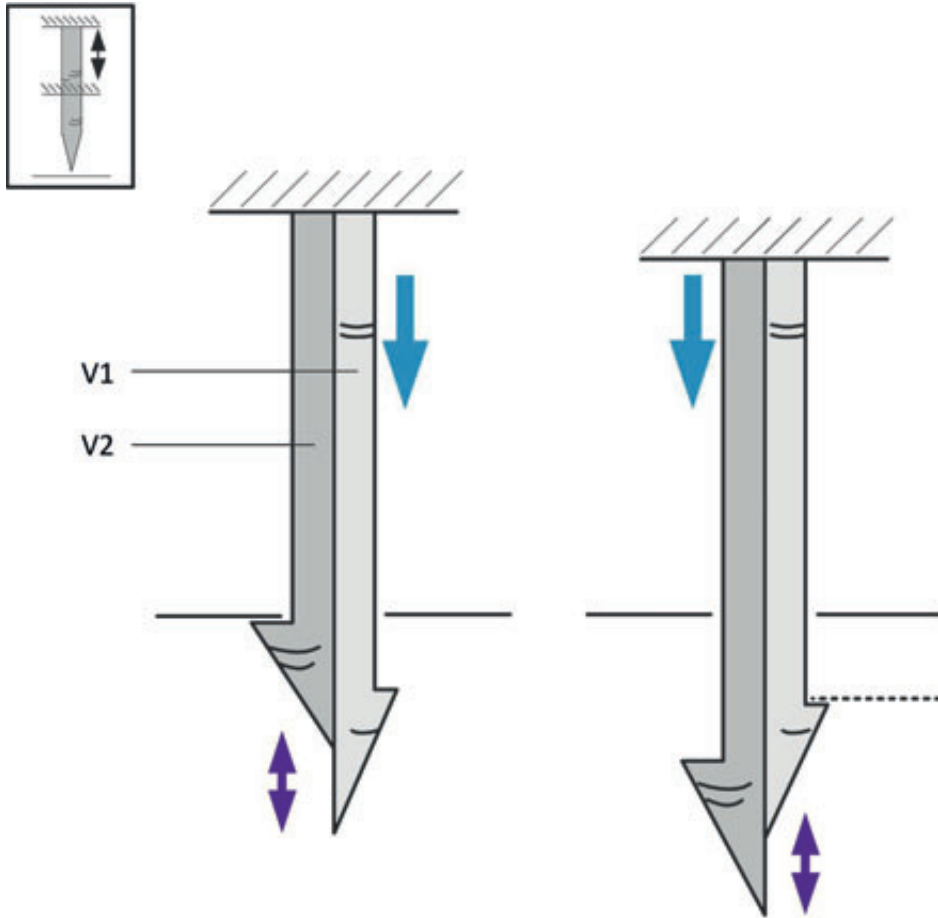
Figure 5.9— Reciprocating Penetration Method of Hymenoptera Ovipositors. Arrow indications: blue arrow = direction of valves V1 and V2 movement; purple arrow = unsupported length (*L*) inside the substrate. Color indications: light grey = V1; dark grey = V2.

Decrease Poisson's Ratio

To prevent Brazier buckling, it is preferred that the material has a low Poisson's ratio. The Poisson's ratios of the most commonly used materials in needles and guidewires are: stainless steel: 0.27–0.31; titanium: 0.29–0.39; and Nitinol: 0.33 [31]. Cho *et al.* [52] modeled porcupine quills with a Poisson's ratio of 0.4 as determined from uniaxial tension experiments. Kundanati *et al.* [45] assumed a Poisson's ratio of 0.37 for an ovipositor of fig wasps (*Apocrypta spp.* and *Ceratosolen fusciceps*). As can be seen, the Poisson's ratios of biological penetration tools are equal to, or even higher than, that of currently used materials in medical instruments.
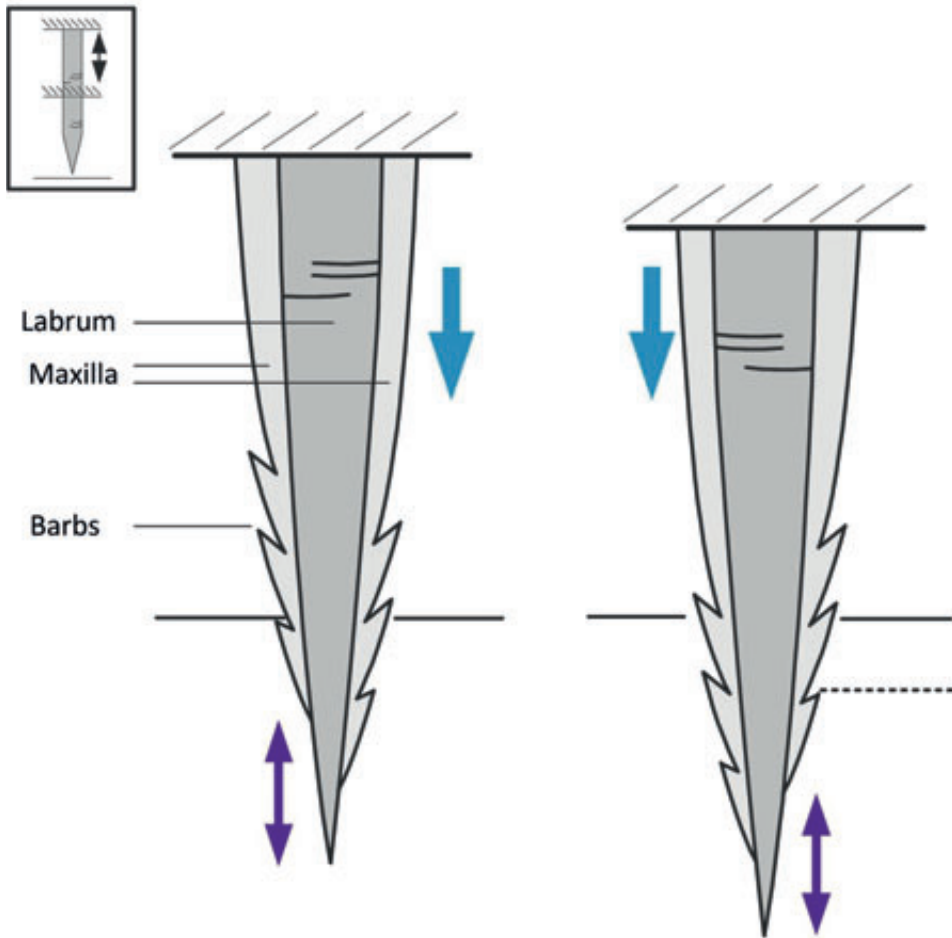
Figure 5.10— Reciprocating Penetration Method of Mosquito Proboscis. Arrow indications: blue arrow = direction of the maxilla movement during substrate penetration; purple arrow = unsupported length inside the substrate (*L*). Color indications: light grey = maxillae; dark grey = labrum.

Increase the Wall Thickness

According to Quicke *et al.* [54], there is a correlation between ovipositor wall thickness and the hardness of the substrate that it penetrates. Ovipositors used for penetrating wood can be recognized by their thick-walled valves (*t* = 0.018–0.042 mm) with small lumens, such as those of *Asperellus* (Labeniae [*t* = 0.025 mm]), *Scambus* (Pimplinae [*t* = 0.018 mm]), *Rhyssa* (Rhyssinae [*t* = 0.042 mm]), and *Megarhyssa* (Rhyssinae [*t* = 0.040 mm]) [54]. For comparison, the wall thickness of needles is usually not smaller than 0.05 mm [6].

120

5.3.2. Increase Critical Load – Static Loading: Brazier
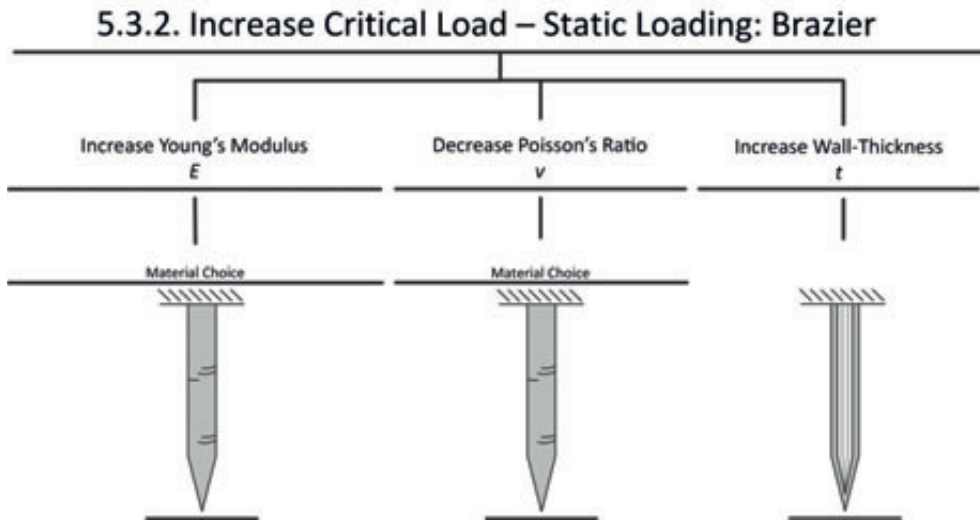
Figure 5.11— Schematic Illustration of Brazier-Based Static Buckling Prevention Strategies.

5.3.3. Increase Critical Load ($F_{critical}$) – Static Loading: Local Buckling

Quills and Spines – Core-rind Structure. Even though the honeycomb-like core morphology in *Erinaceus* has been shown to increase the *I* by 13%, the material is not best placed to increase the *I,* as it would have been more effective to add extra material to the circumference of the spine [53]. Vincent *et al.* [53] suggested that the high buckling resistance in the honeycomb-like core-morphology is likely due to the longitudinal internal stiffeners that prevent the onset of local buckling, as well as due to the diametric plates that prevent Euler, Brazier, and local buckling by retaining the circular cross-section (i.e., preventing ovalization and thus keeping the *I* high during penetration) [53]. This is substantiated by Karam *et al.* [51], who compared four different core morphologies found across 11 species in terms of increasing mechanical efficiency (i.e., the ratio of the critical local bending moment of the quill or spine to that of a hollow quill with the same outer dimensions and wall-thickness) and found values of approximately 3–3.35 for the honeycomb-like cores and 1–1.3 for the isotropic cores, suggesting that the isotropic foam cores and honeycomb-like compliant cores delay the onset of local buckling by providing local support to the quill wall [51, 53].

5.3.4. Increase Critical Load ($F_{critical}$) – Static Loading: Buckling of Penetration Tools Under Initial Stress

Penetration tools under pretension have higher buckling resistance than ideal penetration tools of the same morphology and mechanical properties, due to a reduction in the

resultant force when the penetration tool is under pretension. No clinically available percutaneous instrument was identified that uses pretension to increase the buckling resistance during tissue penetration. However, we found two animals that pretension their penetration tool.

Worms – Pretensioned Penetration. Roundworms or nematodes (e.g., the model species *Caenorhabditis Elegans,* Ø80 μm, length 1 mm, λ = 12.5) are slender worms that are usually between 5 and 100 μm thick and between 0.1 and 2.5 mm long (λ = 1–500) [69]. They have a so-called hydrostatic skeleton, consisting of a fluid-filled chamber surrounded by an elastic non-extendable cuticle and muscles (Figure 5.12), which is used for locomotion (and thus soil penetration) and steering [70, 71]. The liquid is under considerable pressure with respect to the exterior (10–30 kPa) [72]. In nematodes, there are no circular muscles; the contractile parts of their muscle cells are parallel to the axial axis of the worm. By contracting all the muscles at the same time, nematodes are able to substantially increase the hydrostatic pressure inside their body (Figure 5.12). This hydrostatic pressure is a measure of the pressure that can be applied to the substrate, which in turn is a measure of the strength and thus buckling resistance of the worm, as the hydrostatic pressure counters the compressive force during soil penetration, thereby decreasing the resultant force [73]. When the muscles relax, the interior pressure drops and the elastic cuticle restores the original length of the worm.

Hymenoptera Ovipositors – Pretensioned Penetration. As previously discussed, the valves of the ovipositor thrust into the substrate in an alternating fashion [65]. After one valve has penetrated the substrate, the barbs lock the ovipositor in place by pulling on the substrate (Figure 5.13) [57, 66]. The pulling action pretensions the ovipositor, effectively increasing the buckling resistance (Figure 5.12). According to Vincent *et al.* [57], pretensioning the ovipositor of *Sirex noctilio* (Ø0.26 mm, length = 10 mm) increases the critical load by about 20% (from $F_{critical}$ = 0.15 N to approximately 0.18 N).

Cnidarians – Pretensioned Stinging. Cnidarians are an ancient phylum of animals (>500 million years old), including corals, sea anemones, hydrae, and jelly fish. The characteristic cnidarian cell type is the stinging cell, also known as cnidocytes (Ø5–10 μm, length = 3–100 μm, λ = 0.6–20), used for prey capture, defense, and locomotion [74]. All cnidocytes consist of a solid elastic wall and a lid structure with an everted pear- or banana-shaped shaft with a long, highly folded tubule that normally carries three rows of spines used for penetrating purposes [75-77]. The cnidocytes are discharged using osmotic pressure up to 15 MPa in conjunction with the elastically stretched capsular wall (Figure 5.14) [75]. It may be hypothesized that this osmotic pressure increases the critical load of the shaft and tubule by decreasing the resultant compressive force. However, no data is available to substantiate this hypothesis.
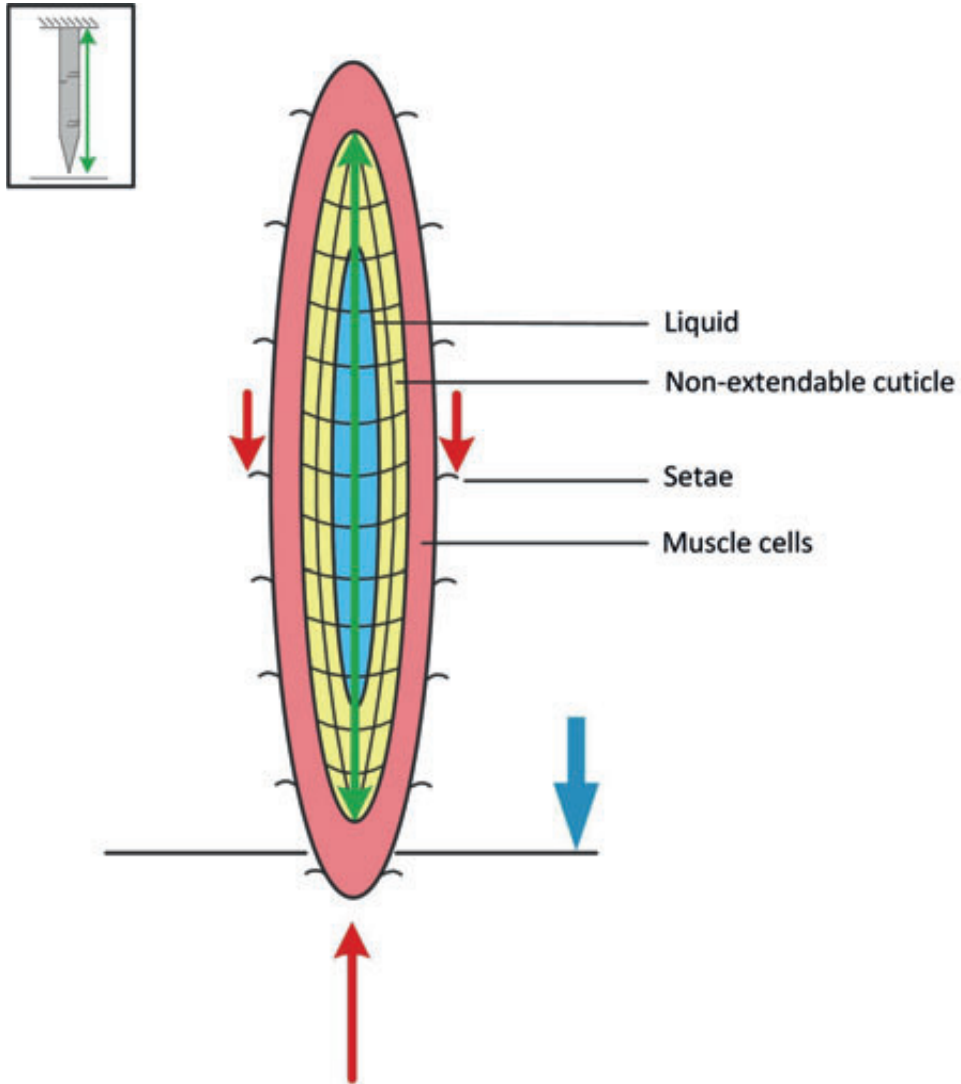
Figure 5.12— Pretensioned Penetration Method of Roundworms And Nematodes. Arrow indications: blue arrow = direction of the nematode movement during substrate penetration; green arrow = generated prestress (or pretension) inside the body of the nematode; downward pointing red arrows = penetration load exerted on the substrate by the setae during penetration (note that these forces are present at all indicated setae); upward pointing red arrow = compressive (buckling) load exerted on the roundworm by the substrate during penetration. Color indications: blue = liquid; yellow = non-extendable cuticle; pink = muscle.

5
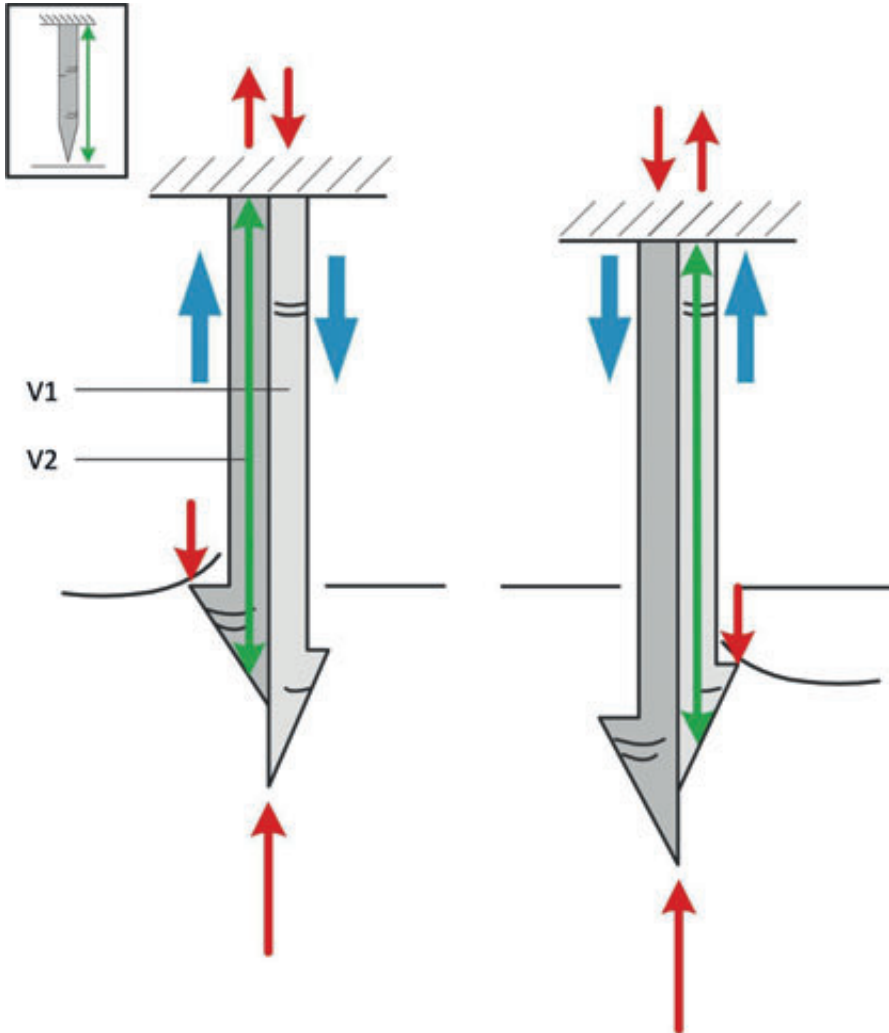
Figure 5.13— Pretensioned Penetration Method of Hymenoptera Ovipositors. Arrow indications: blue arrow = direction of V1 and V2 movement during substrate penetration; green arrow = generated prestress or pretension by the two indicated red arrows in the valve; red arrows on relaxed valve = forces exerted on the valve during substrate penetration. Color indications: light grey = V1; dark grey = V2.

5.3.5. Increase Critical Load ($F_{critical}$) – Dynamic Loading

Next to static loading, the critical load of a penetration apparatus can also be increased by subjecting it to dynamic loading. Two animals, cnidarians and woodpeckers, are identified that exert a dynamic load (impulse) on the substrate.
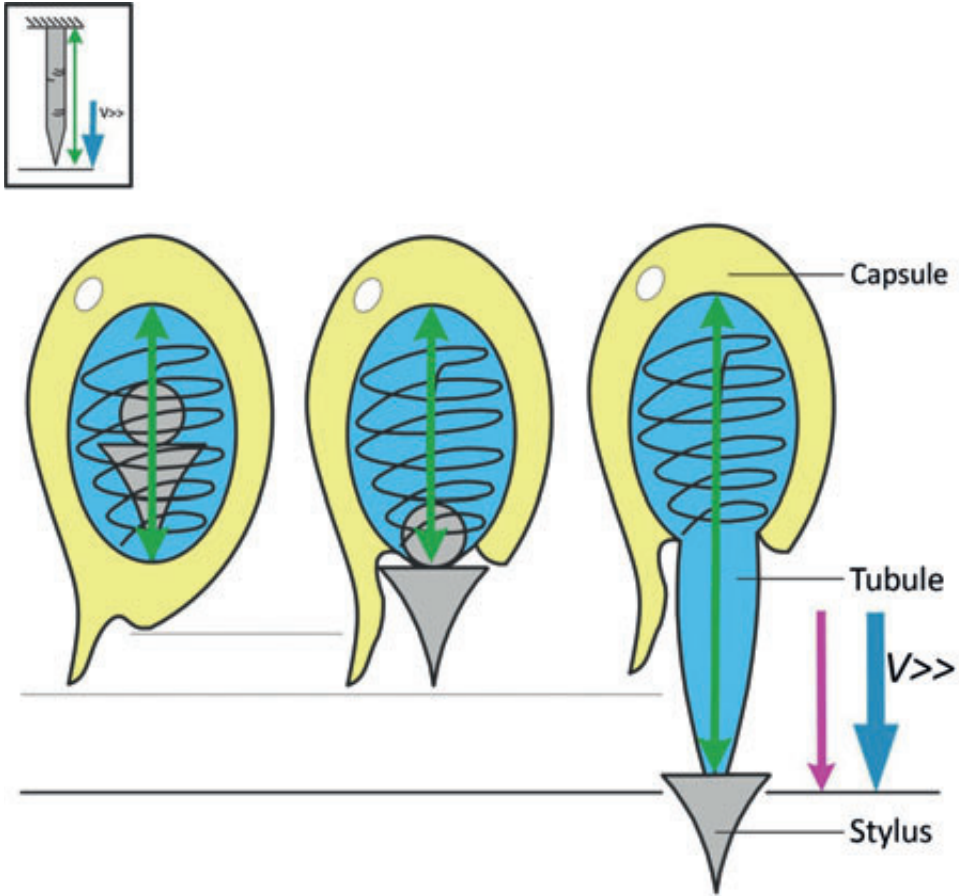
Figure 5.14— Pretensioned and Impulse Stinging By Cnidarians. Arrow indications: blue arrow = direction of stinging cell movement during substrate penetration; pink arrow = exerted impulse on the substrate. Color indications: blue = liquid; grey = stylus of the cnidocyte; yellow = elastic structure of the capsule.

Cnidarians – Impulse Stinging. Cnidocytes are discharged with accelerations of 5,400,000g and an average speed of 18.6 m/s (peak speed of 37.1 m/s; values derived from high-speed images) (Figure 5.14) [75, 78]. The impulse imparted on the cuticle of the prey is estimated to be 37.1 pNs (using a mass of $1\cdot10^{-12}$kg and peak speed of 37.1 m/s) [75, 78]. If the cnidocyte had applied a static force on the cuticle, its critical Euler would have been about $0.48\cdot10^{-3}$ μN (estimated by the authors, neglecting the prestress and assuming $E = 125$ Pa, which is the highest reported E of a cell membrane [79], second moment of area I of a solid cylinder of 10 μm in diameter, $k = 2$, and $L = 100$ μm).

However, according to Nuchter *et al.* [78], a force of 13.2–53.1 µN is delivered on the cuticle of prey, which is substantially higher than the critical load. Furthermore, to penetrate human skin with a tool of similar shape and a diameter as that of a cnidocyte, a force of 0.94–28.3 µN is needed (falling well within the range of the exerted force by the cnidocyte) [18], which would have probably caused buckling of the penetration tool under static loading condition.

Woodpecker – Impulse Chiseling. Woodpeckers are able to chisel wood with speeds of 3–6 m/s [46, 48], resulting in an acceleration of over 1,200g on the tree. Vincent *et al.* [48] mathematically determined that the woodpecker is able to achieve such speeds by using its own natural frequency (Figure 5.15). To achieve this natural frequency, woodpeckers contract powerful muscles connected to the legs and tail during different phases of the chiseling motion. In the swing-back phase the thigh muscles are contracted and the legs are extended, resulting in a backward acceleration, away from the tree. In the swing-forward phase, the force provided by the legs starts to accelerate the body towards the tree. Vincent *et al.* [48] further suggested that the tail feathers provides an additional acceleration force to the body, and that woodpeckers are also able to transform the sinusoidal movement of the body into a saw-tooth-like movement of the beak, resulting in higher speed impact than what would have been possible with a standard oscillating system.

The impulse imparted on the tree is estimated to be 0.81 Ns using a mass of 0.009 kg (data from [64]), an acceleration of the penetration tool of 1,200g, and a time interval of 0.075 s (deduced from [64]). If the woodpecker had applied a static force on the tree, its critical Euler would have been roughly approximated as 1.5 N (estimated by the authors, assuming $E = 6.7$ GPa [keratin], second moment of area I of a solid cylinder of 8 mm in diameter, $k = 2$, and $L = 33$ mm). To penetrate wood with a tool of similar shape and diameter as a woodpecker beak, a force of 250–3150 N is needed (depending on the type of wood) [80], which would have probably caused buckling in the static loading condition.

Mosquito Proboscises – Vibrational Head Movement. According to Ramasubramanian *et al.* [60], mosquitoes use lateral head movements (typically 10–20° from the vertical axis) during the penetration process to prevent proboscis buckling [60]. The lateral head movements range from an initial frequency of 15–17 Hz at the start of the penetration process to about 6 Hz at the end of the penetration process (as a result of increasing stability of the fascicle). In essence, what the lateral head movements do is balance (i.e., follow) the fascicle during penetration, thereby countering divergence instability. The effect of this "follower" load is said to increase the critical load by 20% [60].

5.3.6. Decrease Penetration Load ($F_{penetration}$) – Static Loading

Porcupine Quills – Barbed Penetration. The barbs (length = 100–120 µm, width =
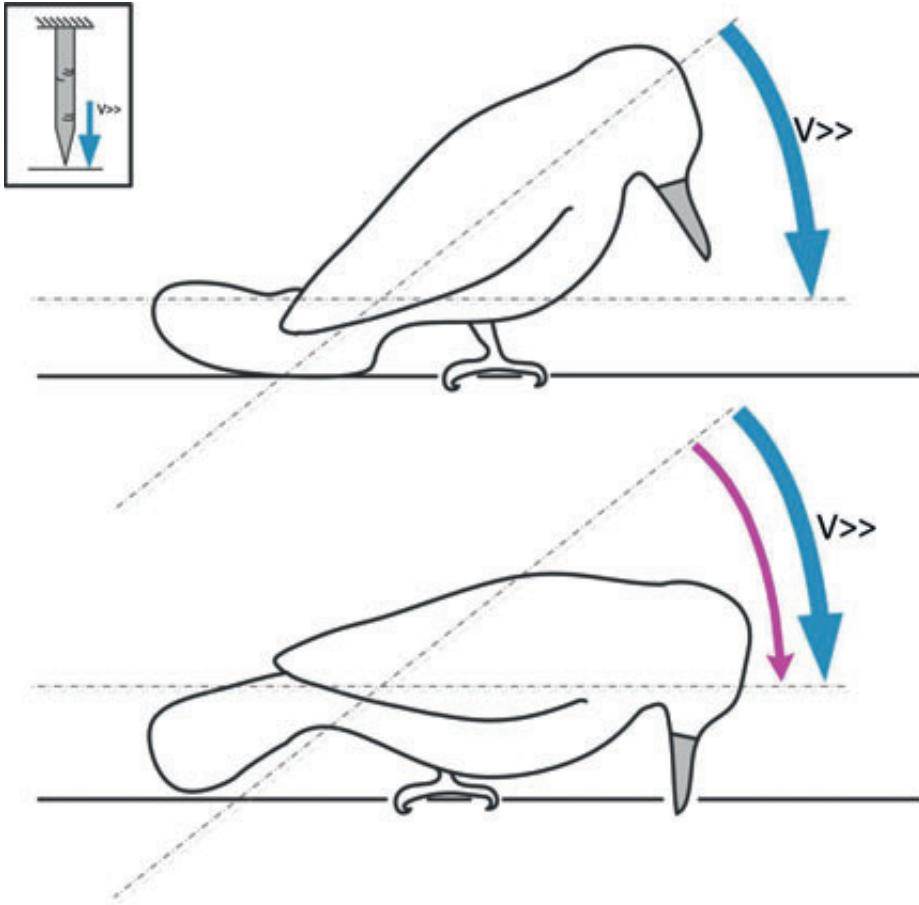
Figure 5.15— Impulse Chiseling by Woodpeckers. Arrow indications: blue arrow = direction of woodpecker movement; pink arrow = exerted impulse on the substrate. Color indications: grey = woodpecker beak.

35–45 µm, and distance between the tip of each barb and the shaft of the quill = 1–5 µm) of porcupine quills have been shown to reduce the force required to penetrate tissue as compared to barbless quills (Figure 5.16). An experiment by Cho *et al.* [52] showed that a quill of the North American porcupine (species *Erethizon dorsatum*) with barbs required 54% lower penetration load ($F_{penetration}$ = 0.33 ± 0.08N [mean ± standard deviation]) in muscle tissue than a barbless quill ($F_{penetration}$ = 0.71 ± 0.09N [mean ± standard deviation]). The reduction in the penetration load is achieved by high stress concentrations along regions of the quill where the cross-sectional diameter grows

rapidly, facilitating tissue cutting. Stress concentration generated by the barbs during penetration is likely to stretch or tear tissue fibers at the interface of the quill. Barbs located near the first geometrical transition zone exhibit the most substantial impact on minimizing the force required for penetration [52].

Mosquito Proboscises – Barbed Penetration. In a study of Kong *et al.* [59], the penetration load of the fascile decreased with the insertion depth after the top skin layer was punctured, and then it leveled out at a low value, or even at a small negative value (i.e., pulling force). Kong *et al.* [59] speculated that the reduction of the insertion force is due to two mechanisms: (1) the tips of the maxillae generate extremely high stresses that are concentrated on the contact points with the skin or tissue, and (2) the continuous cutting of the barbs of the maxillae minimize the frictional force during the penetration process.

Worms – Crack Propagation. Polychaete worms (such as *Nereis virens* and *Cirriformia moore)* burrow through muddy substrates by exerting concentrated dorso-ventral forces (by thickening the body), similar to wedge-driven fracture [23, 81]. To extend the burrow by fracture, the worm needs to apply sufficient stress along the burrow walls that exceeds the fracture toughness of the substrate. The amount of stress that the worm must apply depends on the Young's modulus (E) of the sediment [23]. The exerted forces range from 0.015 ± 0.001 N (mean $\pm$ standard deviation) in gelatin, 0.1 N in muddy sediments with $E = 17$ kPa, and 0.83 N in muddy sediments with $E = 140$ kPa [81]. The advantage of crack propagation burrowing (over conventional penetration methods) is that instead of high longitudinal compressive penetration forces, lateral forces are used to penetrate the substrate by crack propagation. It must be noted that this penetration method is not suitable for non-cohesive substrates, such as sand, as the forces holding the grains together are gravitational rather than adhesive/cohesive and thus do not allow for crack propagation.

5.3.7. Decrease Penetration Load ($F_{penetration}$) – Dynamic Loading

Mosquito Proboscis – Vibrational Penetration. Kong *et al.* [59] observed the penetration mechanism of mosquitoes' proboscis using high-speed videos and measured that in the early stages of penetration, the mosquito used an oscillation frequency of 10–15 Hz to drive the maxillae into the substrate. As penetration proceeded, the frequency was reduced to 6–8 Hz at around half depth and to 3–5 Hz in the last stages of the penetration process [59]. The measured insertion force ranged from 6 to 38 μN, which is approximately three orders of magnitude lower than that of microneedles of a similar size [59]. This reduction in penetration load is most likely the result of time-dependent shear thinning of the human skin caused by vibrational penetration.

5
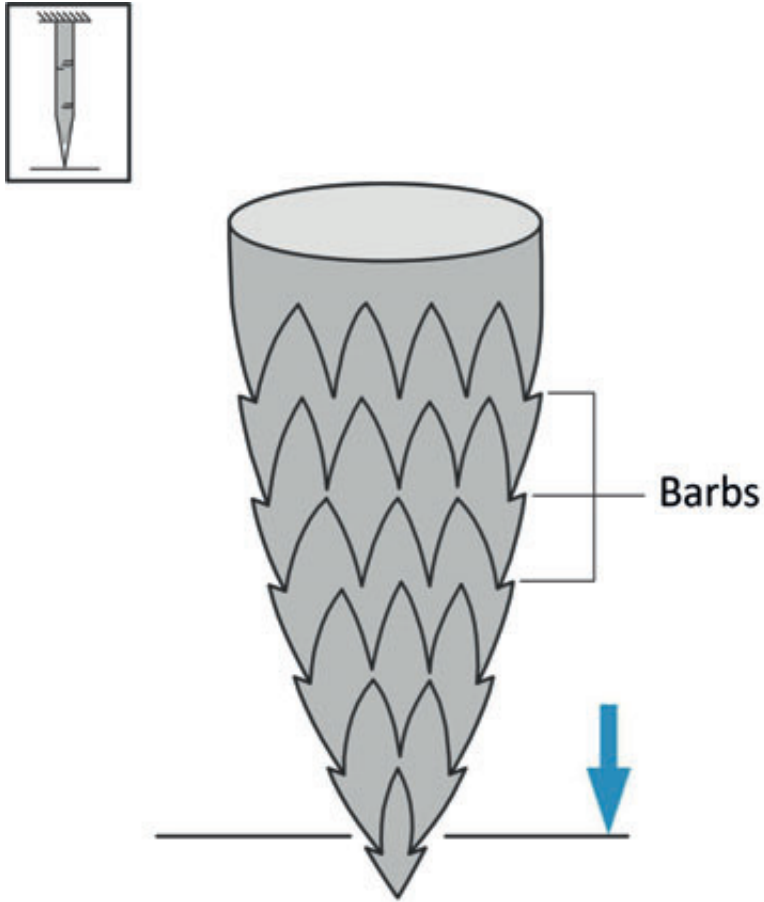
Figure 5.16— Barbed Penetration of Porcupine Quills. Arrow indication: blue arrow = direction of quill movement during substrate penetration. Color indication: grey = quill.

5.4. DISCUSSION

5.4.1. Summary of Main Findings

In total, we identified 28 buckling prevention strategies (Table 6.1). These strategies were subdivided into two groups, depending on whether they increase the critical load of the penetration tool or decrease the penetration load of the substrate. The great majority of the identified buckling prevention strategies increase the critical load of the penetration tool. Of these, most rely on buckling prevention under static loading conditions; only few

Table 6.1— Summary of Buckling Prevention Strategies Found in Nature.

Found in:	Increase $F_{critical}$ [N]								Decrease $F_{penetration}$ [N]	
	Static loading						Dynamic loading	$F_{critical}$ [N]	Static loading	Dynamic loading
	E [GPa]	I [10^3 mm^4]	K []	L [mm]	v []	t [mm]	J [Ns]			
Needles (⌀0.13–5.16 mm)	21–210	0.83–32	2	≤300	0.27–0.33	≥0.05		26.69–58.18*	0.2–6.4 (Human skin)	
Guidewires (⌀0.36–0.89 mm)	21–210	0.0619–16.6	2	500–4500	0.27–0.33			0.25–2.72	1.45±0.13 (CTO)	
Insect ovipositors (⌀0.004–0.08 mm)		–0.5–5.5	2		–0.37	–0.02–0.04		6.9·10^{-18}		
Sclerotin	1·10^{-6}–20									
Internal morphology		>>								
Shape change		>>								
Increase outer dimensions		>>								
Abdomen anchoring			0.5							
Barbed Anchoring			0.5							
Tubercles				<<						
Hind leg support (adaptive)				~50% <<						
Reciprocating penetration				≤0.25						
Increase wall-thickness						>>				
Internal morphology (local)								>>		
Pretension penetration								~20%>>		
Quills and spines (⌀1–5 mm)			2	~20–160	–0.4			~4–30		
Keratin	3.4–6.7									
Core-rind structure (hedgehog)		13% >> than hollow cylinder								
Barbed penetration (porcupine)									54% << than barbless quill	
Core-rind structure (local)								>>		
Woodpeckers (~⌀38 mm)			2	·						
Boney keratin	3.4–6.7									
Impulse chiseling							0.81			

Continuation of Table 6.1— Summary of Buckling Prevention Strategies Found in Nature.

Mosquito proboscies (Ø11–40 μm)		$\sim$ 1.5–2		$3\ 10^3$
Sclerotin	$1\ 10^{-6}$–20			
Barbed anchoring	0.5			
Lateral labium support		<<		5x >>
Reciprocating penetration		<<		
Vibrational head movement				20% >>
Barbed penetration			<<	
Vibrational penetration				10^3 <<
Worms (Ø5–100 μm)	2	$\sim$0.1–2.5		
Setae (fixed)		<<		
Pretension penetration				>>
Crack propagation			<<	>>
Cnidarians (Ø5–10 μm)		$\sim$0.003–0.1		
Pretension stinging				>>
Impulse stinging	$3.7\ 10^{-11}$			

[a] (Ø1.275–1.496 mm)
[b] *Apocrypta* species (Ø19.46 μm).

(stinging of cnidarians and chiseling of woodpeckers) use dynamic (impulse) loading. A relatively small number of buckling prevention strategies rely on decreasing the penetration load of the substrate: the barbed tips of porcupine quills and mosquito proboscises, crack propagation burrowing in worms, and the vibrational penetration in mosquito proboscises.

5.4.2. Buckling Ratio in Biological Penetration Tools Versus Percutaneous Instruments

Critical Load

A direct comparison of the critical loads of the penetration apparatuses found in nature to the critical loads of medical needles and guidewires of similar sizes shows that the critical loads of biological apparatuses are relatively low. For example, the critical loads of hedgehog spines (*Erinaceus europaeus*) and porcupine quills (*Coendou prehensilis* and *Hystrix indicu* x *Hystrix cristata*) are 6.54 ± 1.99 N (mean ± standard deviation) [53], 6.65 ± 1.55 N [53], and 25.82 ± 5.34 N [53], respectively, whereas the critical loads of epidural needles of similar diameter range between 26.69 and 58.18 N [2].

The relatively low critical loads of the penetration apparatuses found in nature are an indication that these animals must employ buckling prevention strategies to penetrate solid substrates such as skin and wood. This is illustrated by Vincent *et al*. [57] and Ramasubramanian *et al*. [60] who found that buckling prevention strategies such as the pretensioning mechanism of the ovipositor and the lateral head movements of the mosquito proboscis increase the critical load by approximately 20% compared to an ovipositor free from initial stress and a proboscis under static loading conditions, respectively.

Penetration Load

Currently, extensive research is ongoing about the optimization of the tip shape of medical needles to decrease the penetration load. In nature, quills of porcupines have been shown to decrease the penetration load into the prey's skin. The estimated penetration load of quills in muscle tissue was determined to be 0.33 ± 0.08 N (mean ± standard deviation), which is approximately 0.26 N lower than the penetration loads measured for hypodermic needles of similar sizes ($F_{penetration}$ = 0.59 ± 0.11N, Ø1.161 ± 0.114 mm [mean ± standard deviation]) [52]. This reduction can be mainly contributed to the barbed tips of these quills (requiring 54% less penetration force than barbless quills), which increase the local stress on the substrate [52]. A similar effect of the barbs and serrations located along the wasp ovipositor on the penetration load may also be hypothesized. Furthermore, by using crack propagation for penetrating a substrate, as used by worms, the (axial compressive) penetration load can be decreased.

Dynamic loading conditions, such as impulsive loading and vibrational loading (making use of thixotropic effects of soft biological tissues) can also be used to decrease

the penetration load [24, 28]. For example, Jelinek *et al.* [24] measured significantly less tissue deformation in chicken liver, a tissue type that is quite similar to human skin and fat, at higher penetration speeds, indicating that a reduction of penetration load by increasing the penetration speed is plausible. It can be hypothesized that dynamic loading of a substrate, such as the high-speed impulse stinging or chiseling used by cnidarians and woodpeckers, respectively, decreases the penetration load by minimizing deformation of the target substrate. Similarly, Yang *et al.* [28] illustrated that vibratory actuation (in the kHz range) of a microneedle reduced the penetration load by approximately 70% compared to conventional microneedle insertion using a static axial force. This effect is illustrated in the vibrational penetration technique of mosquito proboscises that results in a three orders of magnitude smaller penetration force than similar sized microneedles [59].

5.4.3. Combined Buckling Prevention Strategies in Biological Penetration Tools

If we look at the separate values of the (static) parameters of the identified penetration tools in nature, we find that most of these cannot compete with the values seen in percutaneous instruments (with the exception of L and K). For example, the Young's moduli (E) of biological material are much lower than the corresponding Young's moduli of engineering materials commonly used in needles and wires: the highest Young's modulus in biological penetration apparatuses was found for sclerotin with 20 GPa. In comparison, the Young's modulus of 316L stainless steel, typically used in needles and guidewires, is 210 GPa. The Poisson's ratios (v) of biological penetration tools are equal to, or even higher than, those of percutaneous instruments, while a low v is needed for Brazier buckling resistance. Furthermore, the wall thickness (t) of, for example, Hymenoptera ovipositors is almost a factor 3 smaller than the wall thickness of off-the-shelf available needles ($t \geq 0.05$ mm). Even so, these animals are able to penetrate solid substrates, such as wood, with penetration apparatuses smaller in diameter than those seen in percutaneous instruments (the smallest diameter found was 0.004 mm in an insect ovipositor, which is approximately a factor 10 smaller than the smallest off-the-shelf available needles (Ø0.13mm [6])). This is most possibly achieved by combining several strategies (Table 6.1). In the case of the Hymenoptera ovipositor, for example, a multitude of buckling prevention mechanisms are employed (next to the presence of sclerotin and metal ions), including a pronounced olistheter in the distal section of the ovipositor and triangular valves to increase the second moment of area (I), carinae for abdomen anchoring and barbs for substrate anchoring to decrease the effective-length factor (K), tubercles on the abdominal sterna, hind leg support, reciprocating penetration to decrease the unsupported length of the penetration tool (L), and pretension of the valves (reducing the resultant compressive force) to increase the critical load. Note also that some of the described buckling prevention strategies increase Euler, Brazier, and local critical load of the penetration tool simultaneously. For example, in hedgehog spines, the honeycomb-

like core increases the second moment of area (*I*) and simultaneously prevents ovalization (increasing the Brazier and local buckling resistance). Finally, dynamic bucklingprevention strategies can simultaneously increase the critical load and decrease the penetration load. This is, for example, observed in mosquitoes, which use a high-speed reciprocating motion to increase the critical load of the proboscis and to decrease the penetration load of the substrate. It may also be hypothesized that the impulse stinging and chiseling of cnidarians and woodpeckers have a dual functionality.

5.4.4. Transfer of Knowledge From Nature to Percutaneous Instruments

While most of the buckling prevention strategies seen in percutaneous interventions primarily focus on increasing the stiffness of the design by material choice (*E*) and on increasing the second moment of area (*I*) by making the diameter of the instruments larger (cf. the use of a large diameter support catheter over the guidewire), nature offers a wide variety of alternative (and combinable) strategies to prevent buckling without increasing the diameter of the penetration tool. These buckling prevention strategies found in nature can potentially be integrated in future percutaneous instruments. For example, the *I* and local buckling resistance can be increased by an intricate internal structure of the needle or guidewire, such as seen in porcupines and hedgehogs, where instead of a single central lumen in the needle, a multitude of smaller lumens can be used to inject medication or remove tissue masses. Furthermore, preventing lateral deflection during tissue penetration by anchoring the needle or guidewire to the surface can decrease the effective length factor (*K*; increasing the critical load by a factor of about 4), similar to the barbed anchoring strategy of the ovipositor and proboscis to the substrate employed by Hymenoptera and mosquitos, respectively. Additionally, buckling can be prevented by decreasing the unsupported length (*L*) of the percutaneous instruments, as the slenderness of guidewires is often as high as 12,500. In comparison, a maximum slenderness ratio of 1,375 was found for Hymenoptera ovipositors. The *L* can be reduced by distributing the support over the entire instrument, such as seen in worms and Hymenoptera that use setae and tubercles, respectively, or by using a reciprocating motion, similar to that seen in the ovipositor valves (amongst others). Currently, an ovipositor-inspired steerable needle design is under development at Imperial College London, called STING: the Soft-Tissue Intervention and Neurosurgical Guide [82, 83]. By independently reciprocating several interlocking segments, STING is able to access deep brain lesions without buckling.

Next to optimizing the static parameters of the percutaneous instruments in terms of buckling resistance, prestress or dynamic buckling prevention strategies can be used to increase the critical load and decrease the penetration load. For example, an internal lumen in the guidewire or needle could potentially be pressurized using saline, similar to what is seen in the pretension penetration method of nematodes. Furthermore, dynamic buckling prevention strategies such as the use of impulse or vibrational loading of the substrate (a strategy that is currently under investigation) could increase the buckling

resistance of percutaneous instruments by increasing the critical load of the penetration tool while also decreasing the penetration load of the substrate.

One of the challenges in integrating biological buckling prevention strategies in percutaneous tools is the morphological complexity of the penetration apparatuses found in nature, such as the intricate internal structures of porcupine quills and hedgehogs spines and the jigsaw olistheter interconnection of the valves in the wasp ovipositor with a diameter as small as 0.004 mm [38-43]). Such structures are at (or even beyond) the borderline of current microfabrication techniques, which may explain why as of today many of these biological mechanisms have not been applied in the design of medical needles or guidewires.

5.5. CONCLUSION

To improve the success rate of many percutaneous interventions and allow for further miniaturization, it is necessary to prevent buckling during tissue penetration. Current percutaneous instruments, such as needles and guidewires, manifest insufficient buckling resistance. In nature, a variety of buckling-prevention mechanisms and strategies have been found, many of which are not seen in clinical practice. Combining several buckling prevention strategies in one instrument, an approach that is used ubiquitously among biological organisms, may hold the key to improving the buckling resistance of medical needles and guidewires and lead towards further minimization of percutaneous instruments.

ACKNOWLEDGMENTS

REFERENCES

[1]   Stone GW, Reifart NJ, Moussa I, Hoye A, Cox DA, Colombo A, et al. Percutaneous recanalization of chronically occluded coronary arteries - A consensus document - Part II Circulation. 2005: 112(16): pp. 2530-2377.

[2]   Dunn SM, Steinberg RB, O'Sullivan PS, Goolishian WT and Villa EA. A fractured epidural needle: case report and study. Anesthesia & Analgesia. 1992; 75(6): pp. 1050-1052.

[3]   Abolhassani N, Patel R and Moallem M. Needle insertion into soft tissue: A survey. Medical Engineering & Physics. 2006; 29(4): pp. 413-431.

[4]   Abolhassani N, Patel RV and Ayazi F. Minimization of needle deflection in robot-assisted percutaneous therapy. The International Journal of Medical Robotics and Computer Assisted Surgery. 2007; 3(2): pp. 140-148.

[5]   Walker C. Guidewire selection for peripheral vascular interventions. Endovascular Today. 2013;5: pp. 80-83.

[6]   Sigma Aldrich (USA). Syringe needle gauge chart. Available from: http://www.sigmaaldrich.com/chemistry/stockroom-reagents/learning-center/technical-library/needle-gauge-chart.html

[7]   Euler L. Principes généraux de l'état d'équilibre d'un fluide Académie Royale des Sciences et des Belles-Lettres de Berlin, Mémoires. 1757;11: pp. 217-273.

[8]   Sarkissian C, Korman E, Hendlin K and Monga M. Systematic evaluation of hybrid guidewires: shaft stiffness, lubricity, and tip configuration. Urology. 2012;79(3): pp. 513-517.

[9]   Sianos G, Werner GS, Galassi A, Papafaklis MI, Escaned J, Hildick-Smith D, Christiansen EH, et al. Recanalisation of chronic total coronary occlusions: 2012 consensus document from the EuroCTO club. EuroIntervention. 2012;8(1): pp. 139-145.

[10]   Brazier LG. On the flexure of thin cylindrical shells and other "thin" sections. Proceedings of the Royal Society of London. Series A. 1927;116(773): pp. 104-114.

[11]   Calladine CR. Theory of shell structures. New York, NY: Cambridge University Press. 1989.

[12]   Karam GN and Gibson LJ. Elastic buckling of cylindrical shells with elastic cores—I. Analysis International Journal of Solids and Structures. 1995;32(8-9): pp. 1259-1283.

[13]   Lock M. A study of buckling and snapping under dynamic load. El Segundo, CA: Laboratory Operations Aerospace Corporation. Report Number TR-0158 (3240-30)-3; 1967. pp. 1-55.

[14]   Hermann G, Miller JR, Price WJ, Stoker JJ, LaSalle JP, Bolotin VV, et al. Dynamic Stability of Structures. Proceedings of the International Conference on the Dynamic Stability of Structures held at Evanston, IL, 18-20 October 1965.

[15]   Hirsch L, Gibney M, Berube J and Manocchio J. Impact of a modified needle tip geometry on penetration force as well as acceptability, preference, and perceived pain in subjects with diabetes. Journal of Diabetes Science and Technology. 2012;6(2): pp. 328-335.

[16]   Moore J Z, McLaughlin PW and Shih AJ. Novel needle cutting edge geometry for end-cut biopsy. Medical Physics. 2012;39(1): pp. 99-108.

[17]   Han P, Che D, Pallav K and Ehmann K. Models of the cutting edge geometry of medical needles with applications to needle design International Journal of Mechanical Sciences. 2012;65(1): pp. 157-167.

[18]   Shergold OA and Fleck NA. Experimental investigation into the deep penetration of soft solids by sharp and blunt punches, with application to the piercing of skin. Journal of Biomechanical Engineering. 2005;127(5): pp. 838-848.

[19]   Mahvash M and Dupont P E 2010 Mechanics of dynamic needle insertion into a biological material. IEEE Transactions on Biomedical Engineering. 2010;57(4): pp. 934-943.

[20]   Okamura AM, Simone C and O'Leary MD. Force modeling for needle insertion into soft tissue. IEEE Transactions on Biomedical Engineering. 2004;51(10): pp. 1707-1716.

[21]   Okuno D, Togawa T, Saito H and Tsuchiya K. Development of an automatic blood sampling system: control of the puncturing needle by measuring forces. Proceedings of the 20th Annual International Conference of the IEEE Engineering in Medicine and Biology Society held at Hong Kong, China, 29 October - 1 November 1998. pp. 1811-1812.

[22]   van Gerwen DJ, Dankelman J and van den Dobbelsteen JJ. Needle–tissue interaction forces – A survey of experimental data. Medical Engineering & Physics. 2012;34(6): pp. 665-680.

[23]   Dorgan KM. The biomechanics of burrowing and boring. Journal of Experimental Biology. 2015;218: pp. 176-183.

[24]   Jelínek F, Smit G and Breedveld P. Bioinspired spring-loaded biopsy harvester—experimental prototype design and feasibility tests. Journal of Medical Devices ;8(1); pp. 015002-1-001502-6.

5

[25] Heverly M, Dupont P and Triedman J. Trajectory optimization for dynamic needle insertion. Proceedings of the 2005 IEEE International Conference on Robotics and Automation held at Barcelona, Spain, 18-22 April 2005. pp 1646-1651.

[26] Finlay JB. Thixotropy in human skin. Journal of Biomechanics. 1978;11(6-7): pp. 333-342.

[27] Barnes HA. Thixotropy—a review. Journal of Non-Newtonian Fluid Mechanics. 1997;70(1-2): pp. 1-33.

[28] Yang M and Zahn J. Microneedle insertion force reduction using vibratory actuation. Biomedical Microdevices. 2004;6(3): pp. 177-182.

[29] Erglis A, Narbute I, Sondore D, Grave A and Jegere S. Tools & techniques: coronary guidewires. Eurointervention. 2010;6: pp. 1-8.

[30] Schröder J. The mechanical properties of guidewires. Part II: Kinking resistance. Cardiovascular and Interventional Radiology. 1993;16(1): pp. 47-48.

[31] AZoM (UK). Materials information. Available from: http://www.azom.com/materials.aspx

[32] Johnson Matthey Medical Components (USA). Nitinology - Advancing the science of Nitinol. Available from: http://jmmedical.com/nitinol.html

[33] Custom Wire Technologies, Inc. (USA). Guidewire materials. Available from: http://www.medicalguidewiremanufacturer.com/guidewire-materials/

[34] Edlich R F, Thacker J G, McGregor W and Rodeheaver GT. Past, present, and future for surgical needles and needle holders. American Journal of Surgery. 1993;166(5): pp. 522-532.

[35] Larghi A, Fabbri C, Yasuda I, Palazzo L, Tarantino I, Dewitt JM, et al. Tu1639 EUS-guided fine needle tissue acquisition using a nitinol ultra flex 19-gauge needle for transduodenal lesions: a multicenter prospective study. Gastrointestinal Endoscopy. 2015;81(5): pp. AB541.

[36] Connecticut Hypodermics, Inc. (USA). Hypodermic needle materials. Available from: http://connhypo.com/custom-products/hypodermic-needle-materials

[37] Vincent JF and Wegst UG. Design and mechanical properties of insect cuticle. Arthropod Structure & Development. 2004;33(3): pp. 187-199.

[38] Quicke DLJ. Ovipositor mechanics of the braconine wasp genus Zaglyptogastra and the ichneumonid genus Pristomerus. Journal of Natural History. 1991;25(4): pp. 971-977.

[39] Vilhelmsen L, Isidoro N, Romani R, Basibuyuk HH and Quicke DLJ. Host location and oviposition in a basal group of parasitic wasps: the subgenual organ, ovipositor apparatus and associated structures in the Orussidae (Hymenoptera, Insecta). Zoomorphology 2001;121(2): pp. 63-84.

[40] Dweck HKM, Gadallah NS and Darwish E. Structure and sensory equipment of the ovipositor of *Habrobracon hebetor* (Say) (Hymenoptera: Braconidae). Micron. 2008;39(8): pp. 1255-1261.

[41] Ghara M, Kundanati L and Borges RM. Nature's swiss army knives: ovipositor structure mirrors ecology in a multitrophic fig wasp community. Plos One. 2011;6(8): pp. e23642.

[42] Sivinski J, Vulinec K and Aluja M. Ovipositor length in a guild of parasitoids (Hymenoptera: Braconidae) attacking *Anastrepha* spp. fruit flies (Diptera: Tephritidae) in Southern Mexico. Annals of Entomological Society of America. 2001;94(6): pp. 886-895.

[43] Zhen WQ, Huang DW, Xiao JH, Yang DR, Zhu CD and Xiao H. Ovipositor length of three *Apocrypta* species: effect on oviposition behavior and correlation with syconial thickness. Phytoparasitica. 2005;33(2): pp. 113-120.

[44] Quicke DLJ, Wyeth P, Fawke JD, Basibuyuk HH and Vincent JFV. Manganese and zinc in the ovipositors and mandibles of hymenopterous insects. Zoological Journal of the Linnean Society London. 1998;124(4): pp. 387-396.

5

5

[45]   Kundanati L and Gundiah N. Biomechanics of substrate boring by fig wasps. Journal of Experimental Biology. 2014;217(11): pp. 1946-1954.

[46]   Chen PY, McKittrick J and Meyers MA. Biological materials: Functional adaptations and bioinspired designs. Progress in Material Science. 2012;57(8): pp. 1492-1704.

[47]   Fraser RD and Macrae TP. Molecular structure and mechanical properties of keratin. Symposia of the Society of Experimental Biology. 1980;34: pp. 211-246.

[48]   Vincent JFV, Sahinkaya MN and O'Shea W. A woodpecker hammer. Proceedings of the Institution of Mechanical Engineers, Part C: Journal of Mechanical Engineering Science. 2007;221(10): pp. 1141-1147.

[49]   Lee N, Horstemeyer MF, Rhee H, Nabors B, Liao J and Williams LN. Hierarchical multiscale structure–property relationships of the red-bellied woodpecker (*Melanerpes carolinus*) beak. Journal of the Royal Society Interface. 2014;11(96): pp. 1-8.

[50]   Lange RA and Hillis LD. Diagnostic cardiac catheterization. Circulation. 2003;107(17): pp. e111-e113.

[51]   Karam GN and Gibson LJ. Biomimicking of animal quills and plant stems: natural cylindrical shells with foam cores. Material Science and Engineering: C. 1994;2(1-2): pp. 113-132.

[52]   Cho WK, Ankrum JA, Guo D, Chester SA, Yang SY, Kashyap A, et al. Microstructured barbs on the North American porcupine quill enable easy tissue penetration and difficult removal. Proceedings of the National Academy of Sciences. 2012;109(52): pp. 21289-21294.

[53]   Vincent JFV and Owers P. Mechanical design of hedgehogs spines and porcupine quills. Journal of Zoology. 1986;210(1): pp. 55-75.

[54]   Quicke DLJ, Fitton MG, Tunstead JR, Ingram SN and Gaitens PV. Ovipositor structure and relationships within the Hymenoptera, with special reference to the Ichneumonoidea Journal of Natural History. 1994;28(3): pp. 635-682.

[55]   Ennos R. Solid biomechanics. Princeton, NJ: Princeton University Press, 2012.

[56]   Le Ralec J, Rabasse JM and Wajnberg E. Comparative morphology of the ovipositor of some parasitic hymenoptera in relation to characteristics of their hosts. The Canadian Entomologist. 1996;128(3): pp. 413-433.

[57]   Vincent JFV and King MJ. The mechanism of drilling by wood wasp ovipositors. Biomimetics. 1995;3(4): pp. 187-201.

[58]   Spradbery J. Host finding by *Rhyssa persuasoria* (L.), an ichneumonid parasite of siricid woodwasps. Animal Behaviour. 1970;18(part1): pp. 103-114.

[59]   Kong XQ and Wu CW. Mosquito proboscis: An elegant biomicroelectromechanical system. Physical Review E. 2010;82(1): pp. 011910-001915.

[60]   Ramasubramanian MK, Barham OM and Swaminathan V. Mechanics of a mosquito bite with applications to microneedle design. Bioinspiration and Biomimetics. 2008;3(4): pp. 046001-1-046001-10.

[61]   Medax (Italy). Biopsy and special needles. Available from: http://www.medax.org/

[62]   Terumo Interventional Systems (USA). Guidewires. Available from: http://www.terumois.com/products/guidewires/glidewire.html

[63]   Edwards CA and Bohlen PJ. Biology and ecology of earthworms (vol 3). London, UK: Springer Science & Business Media. 1996.

[64]   Gardner S L. Encyclopedia of Biodiversity (2nd ed.) Waltham, MA: Academic Press. pp 420-436. 2013.

[65]   Hermann H. Sting autotomy, a defensive mechanism in certain social Hymenoptera. Insectes Sociaux. 1971;18(2): pp. 111-120.

[66]   Fergusson NDM. A comparative study of the structures of phylogenetic importance of female genitalia of the Cynipoidea (Hymenoptera). Systematic Entomology. 1988;13(1): pp. 13-30.

[67]   Matushkina N and Gorb S. Mechanical properties of the endophytic ovipositor in damselflies (Zygoptera, Odonata) and their oviposition substrates. Zoology. 2007;110(3): pp. 167-175.

[68]   Aoyagi S, Takaoki Y, Takayanagi H, Huang C, Tanaka T, Suzuki M, et al. Equivalent negative stiffness mechanism using three bundled needles inspired by mosquito for achieving easy insertion Proceedings of the International Conference on Intelligent Robots and Systems held at Vilamoura-Algarve, Portugal, 7-12 October 2012. pp 2295-2300.

[69]   Brady NC and Weil RR. Elements of the nature and properties of soils. Upper Saddle River, NJ: Prentice Hall. 2009.

[70]   Niebur E and Erdös P. Theory of the locomotion of nematodes: Dynamics of undulatory progression on a surface. Biophysical Journal. 1991;60(5): pp. 1132-1146.

[71]   Bird A F 1991 *The structure of nematodes* (San Diego, CA: Academic Press) p 316

[72]   Lee D L 1976 *Physiology of nematodes* (London, UK: Macmillian) p 215

[73]   Chapman G. Of the movement of worms. Journal of Experimental Biology. 1950;27: pp. 29-39.

[74]   Cannon Q and Wagner E. Comparison of discharge mechanisms of Cnidarian cnidae and Myxozoan polar capsules. Reviews in Fisheries Science. 2003;11(3): pp. 185-219.

[75]   Özbek S, Balasubramanian PG and Holstein TW. Cnidocyst structure and the biomechanics of discharge. Toxicon. 2009;54: pp. 1038-1045.

[76]   Anderson PAV and Bouchard C. The regulation of cnidocyte discharge. Toxicon. 2009;54: pp. 1046-1053.

[77]   Fautin DG. Structural diversity, systematics, and evolution of cnidae. Toxicon. 2009;54: pp. 1054-1064.

[78]   Nuchter T, Benoit M, Engel U, Özbek S, Holstein TW. Nanosecond-scale kinetics of nematocyst discharge. Current Biology. 2006;16(9): pp**.** R316-R319.

[79]   Kamgoué A, Ohayon J and Tracqui P. Estimation of cell Young's modulus of adherent cells probed by optical and magnetic tweezers: influence of cell thickness and bead immersion. Journal of Biomechanical Engineering. 2007;129(4): pp. 523-530.

[80]   Record S J. The mechanical properties of wood. Salt Lake City, UT: Project Gutenberg. 2004.

[81]   Dorgan KM, Arwade SR and Jumars PA. Burrowing in marine muds by crack propagation: kinematics and forces. Journal of Experimental Biology. 2007;210: pp. 4198-4212.

[82]   Frasson L, Ko S, Turner A, Parittotokkaporn T, Vincent JF and Rodriguez y Baena F. STING: a soft-tissue intervention and neurosurgical guide to access deep brain lesions through curved trajectories. Proceedings of the Institution of Mechanical Engineers, Part H: Journal of Engineering in Medicine. 2010;224(6): pp. 775-788.

[83]   Oldfield MJ, Burrows C, Kerl J, Frasson L, Parittotokkaporn T, Beyrau F, Rodriguez y Baena F. Highly resolved strain imaging during needle insertion: Results with a novel biologically inspired device. Journal of the Mechanical Behaviour of Biomedical Materials. 2014;30: pp. 50-60.

[84]   Timoshenko SP and Gere JM .Theory of elastic stability. Mineola, NY: Dover publications. 1936.

[85]   Zhang Z. Investigation on dynamic pulse buckling and damage behavior of composite laminated beams subject to axial impulse. Halifax, Nova Scotia: National Library of Canada. 2004.

5

[86]   Westbrook JL, Uncles DR, Sitzman BT and Carrie LE. Comparison of the force required for dural puncture with different spinal needles and subsequent leakage of cerebrospinal fluid. Anesthesia & Analgesia. 1994;79(4): pp. 769-772.

[87]   Podder T, Clark D, Sherman J, Fuller D, Messing E, Rubens D, et al. *In vivo* motion and force measurement of surgical needle intervention during prostate brachytherapy. Medical Physics. 2006;33(8): pp. 2915-2922.

5

APPENDIX 5.A: BUCKLING THEORY

In this appendix, several buckling theories are explained.

5.A1. Buckling Prevention Under Static Loading Conditions

5.A1.1. Euler Buckling

Slender, ideal (i.e., perfectly straight, homogeneous, and free from initial stress) penetration tools under compression are subject to Euler buckling (Figure 5.A1). The critical buckling load, $F_{critical\ Euler}$ [N], of these penetration tools can be calculated as in (5.A1) [7].

$$F_{critical\ Euler} = \frac{\pi^2 EI}{(KL)^2} ,$$

(5.A1)

5

with E being the Young's modulus [N/mm' or GPa], I the second moment of area [mm'], K the effective-length factor that takes into account the end-conditions of the penetration tool (e.g., fixed or pivoted end points) [no unit], and L the unsupported length of the penetration tool [mm]. As can be seen from Equation 6.A1, the $F_{critical\ Euler}$ that a penetration tool withstands without buckling can be increased by increasing E and I or by decreasing K and L.

   Young's Modulus (E). E is a measure of the stiffness of an elastic material and is defined as the ratio of the stress ($\sigma\ [\frac{N}{mm^2}] = \frac{F}{A_0}$, with F = force exerted on the material [N] and $A_{_\circ}$ = the cross-sectional area of the material [mm']) to the strain (ε [mm] $= \frac{\Delta L}{L_0}$, with ΔL = the length change of the material [mm] and $L_{_\circ}$ = the original length of the material) in which Hooke's law holds ($E = \frac{\sigma}{\varepsilon} = \frac{F/A_0}{\Delta L/L_0}$). An increase in E can be achieved by changing the material of the penetration tool with a material that has a higher E or by reinforcing the penetration tool.

   Second Moment of Area (I). I is a geometrical property of the penetration tool that represents how the points of the cross-sectional area are distributed with regard to a horizontal axis through the centroid. For example, the I of a circle equals $\frac{\pi}{4}(r_{outer}^4 - r_{inner}^4)$, and that of a triangle equals $\frac{bh^3}{12}$. It can be deduced that by increasing the cross-sectional area, I increases. The cross-sectional area can be increased in two ways: by increasing the outer dimensions or the internal cross-sectional area of the penetration tool. The I can also be increased by changing the shape of the penetration tool, since material placed away from the neutral line (i.e., a line perpendicular to the chosen horizontal axis, through the centroid of the penetration tool) is most effective in

5
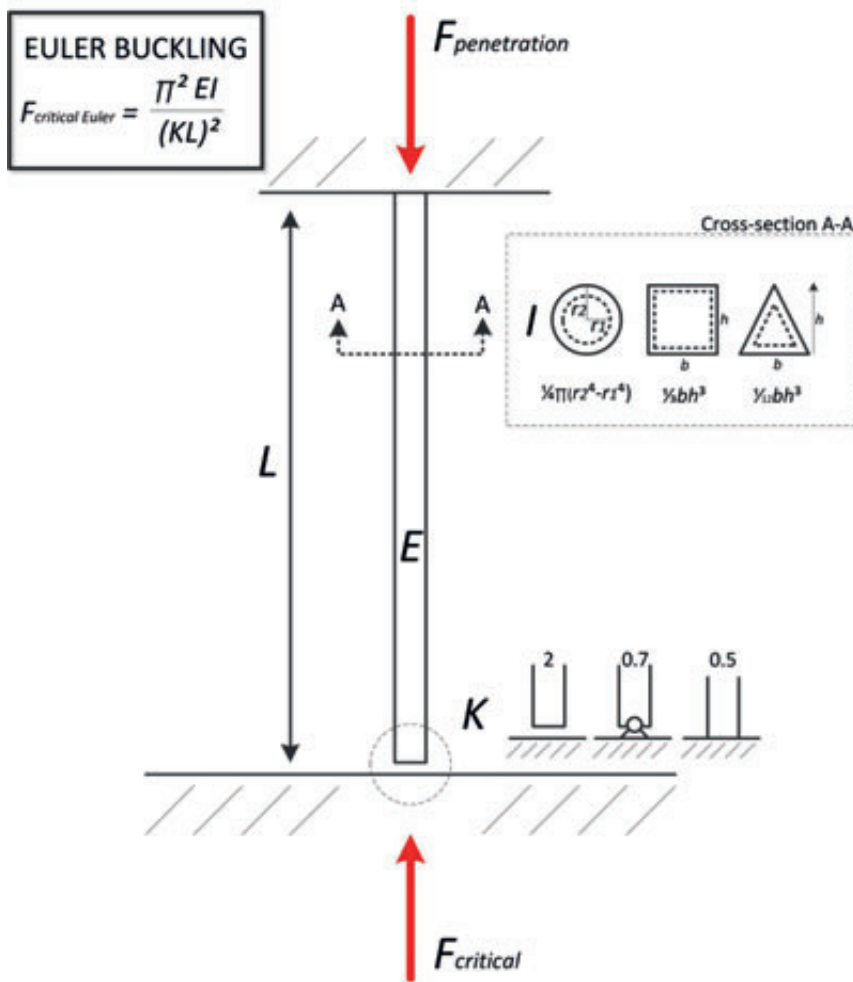
Figure 5.A1— Euler Buckling of an Ideal Penetration Tool Under Compressive Loads, with A = cross-section of the penetration tool, b = base [mm], E = Young's modulus [N/mm²], $F_{critical}$ = critical buckling load [N], $F_{penetration}$ = penetration load [N], h = height [mm], I = second moment of area [mm⁴], K = effective length ratio [no units], L = unsupported length [mm], and r = radius [mm].

increasing I. Therefore, the I of a triangular shape is higher than the I of a circle with the same cross-sectional area.

Effective-Length Factor (K). K is dependent on the end-conditions of the instrument. When one end of the percutaneous instrument is fixed and the other end is free, K equals 2. K can be lowered by pinning both ends ($K = 1$), fixing both ends ($K = 0.5$), or by fixing one end and pinning the other end ($K \approx 0.699$) (Figure 5.A1).

Unsupported Length (*L*). *L* is the most determining factor for buckling, since by multiplying *L* by two, $F_{critical\ Euler}$ is minimized by a factor four. Consequently, *L* should be kept as low possible.

A factor related to *L* and, to some extent, to *I* is the slenderness of the instrument. The slenderness is defined as the unsupported length of the instrument divided by the diameter of the penetration tool (slenderness ratio (λ) = $\frac{L}{\varnothing}$ [no units]) and is an important design parameter, especially in very slender penetration tools ($\lambda > 10$). To prevent buckling, the slenderness of the instrument should be kept as low as possible. In needles the slenderness is often as high as 2,300, whereas in guidewires the slenderness can be as high as 12,500, estimated from [5, 6, 61, 62].

5.A1.2. Brazier Buckling

Brazier buckling deals with buckling of thin-walled penetration tools under pure bending or combined bending and compressive loading (Figure 5.A2). Brazier [10] showed that the longitudinal tension and compression that resist the applied bending moment tend to flatten or ovalize the cross-section, which in turn reduces the bending stiffness (*EI*) (see also [84]. When the maximum *EI* is exceeded, the structure becomes unstable and 'jumps' to a different configuration, which kinks and flattens the structure [11]. The critical moment for Brazier buckling is given by (5.A2) [10, 12], with the critical load given by (5.A3) and (5.A4):

$$M_{critical\ Brazier} = \frac{2\sqrt{2}\,\pi\,Ert^2}{9\,\sqrt{1-v^2}} \, , \qquad\qquad (5.A2)$$

$$F_{critical\ Brazier} = \frac{2\sqrt{2}}{9\,\sqrt{1-v^2}}\pi t^2 E \, , \qquad\qquad (5.A3)$$

$$F_{critical\ Brazier} = c\pi t^2 E \, , \qquad\qquad (5.A4)$$

where *r* is the radius [mm], *t* the wall thickness [mm], *v* Poisson's ratio [no units], and *c* the Poisson factor [no units].

Poisson's Ratio (*v*). *v* is a measure of the Poisson effect, according to which, when a material is compressed in one direction, it tends to expand in the two directions perpendicular to the direction of compression. *v* is the fraction of transverse strain divided by the fraction of axial strain as defined in (5.A5):

$$v = -\frac{\Delta\varepsilon_{trans}}{\Delta\varepsilon_{axial}} \, , \qquad\qquad (5.A5)$$

143

BRAZIER BUCKLING

$$F_{critical\,Brazier} = c\prod t^2 E$$
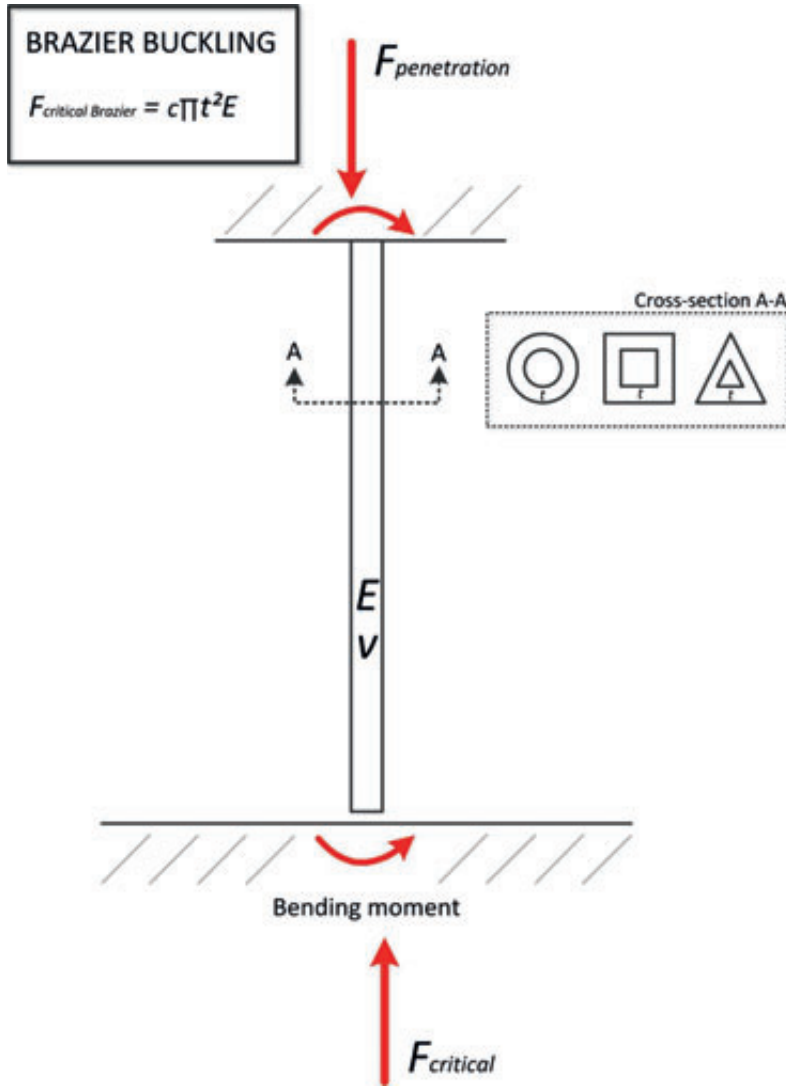
Figure 5.A2— Brazier Buckling of an Ideal Penetration Tool Under Bending, with A = cross-section of the penetration tool, c = Poisson factor [no units], E = Young's modulus [N/mm²], $F_{critical}$ = critical buckling load [N], $F_{penetration}$ = penetration load [N], t = wall thickness [mm], and v = Poisson's ratio [no units].

with ε_{rans} being the transverse strain (negative for stretch and positive for compression) [mm] and ε_{axial} the axial strain [mm] (negative for compression and positive for tension). A smaller Poisson's ratio is preferred, since this gives a higher c value and thus a higher critical load.

144

Wall Thickness (*t*). Brazier buckling is not relevant for solid slender instruments, such as guidewires. It is, however, relevant for needles, as these have a lumen—especially so, since the wall-thickness *t* of these needles can be as small as 0.05 mm [6]. To prevent Brazier buckling, a large *t* is preferred.

Young's Modulus (*E*). For methods of increasing *E*, see previous section.

5.A1.3. Buckling of Penetration Tools Under Initial Stress

There are two basic types of prestress: precompression and pretension. Penetration tools under pretension have an increased critical load in comparison to ideal penetration tools. This becomes apparent by looking at the free body diagram of penetration tools under pretension (Figure 5.A3).

The pretension counters the buckling load, and thus reduces the tendency of the penetration tool to buckle, as illustrated in (5.A6):

$$F_{critical\ columns\ under\ initial\ stress} = \left(F_{critical\ ideal} + F_{pretension} \right), \qquad (5.A6)$$

with $F_{critical\ ideal}$ being the critical load of an identical ideal penetration tool [N] and $F_{pretension}$ the force exerted on the penetration tool by the pretension [N].

5.A2. Buckling prevention under dynamic loading conditions

Increasing the critical load of the penetration tool can be achieved by subjecting it to dynamic loading. In a study by Lock [13], the effect of load duration on the size of the critical dynamic load was investigated for two penetration tools (λ = 2 and 3.5). These authors found that decreasing the load duration led to an increase in the critical load ratio ($\frac{critical\ dynamic\ load}{critical\ static\ load}$). In other words, if the load duration is sufficiently small, the structure can sustain higher (dynamic) loads than in the case of static loading (Figure 5.A4).

Under dynamic loading conditions, the impulse imparted to the structure ($dt \approx 0$) rather than the size of the load becomes the most significant parameter against buckling. An impulse (J [Ns]) is defined as a force ($F_{critical\ Dynamic}$ [N]) multiplied by the load duration of the force (dt [s]), as in (5.A7):

$$J_{critical} = \int_{t_1}^{t_2} F_{critical\ Dynamic} \cdot dt \qquad (5.A7)$$

This effect, where the impulse, rather than the force, is the most determining load parameter for buckling, has been substantiated by an analytical study of Budiansky in [14]. Budiansky computed that loads much in excess of the static buckling loads can be applied to an imperfect structure (i.e., one that is curved, nonhomogeneous, and with initial stress) if the load is removed soon enough (Figure 5.A4). Furthermore, the impulse

buckling response is mainly controlled by the axial components of the end-conditions (K), whereas the rotational constraints have minimal influence [85].
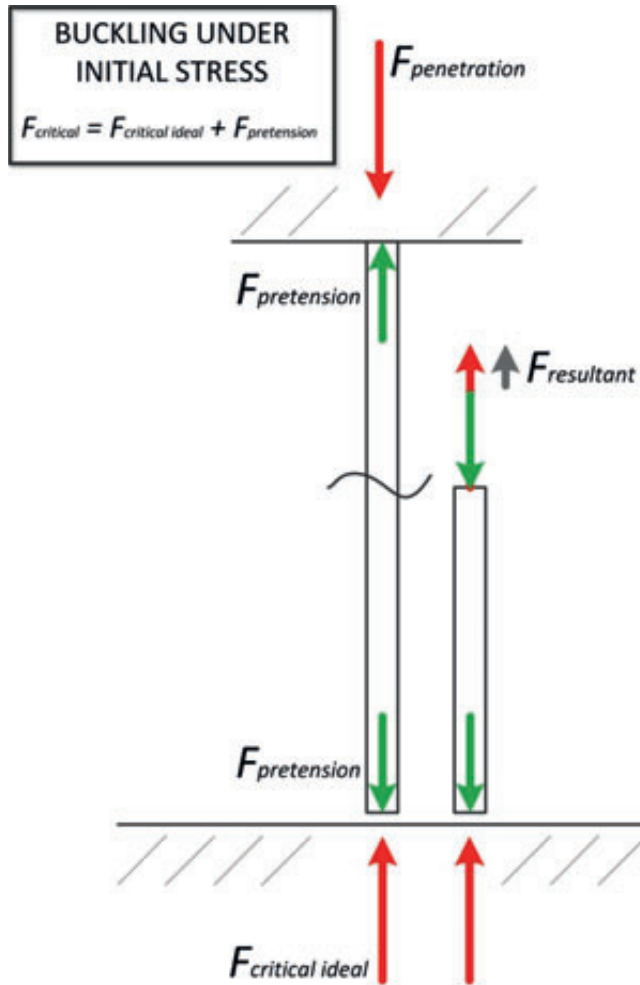
Figure 5.A3— Buckling of Penetration Tools Under Pretension, with $F_{critical\ ideal}$ = critical buckling load [N], $F_{penetration}$ = penetration load [N], $F_{pretension}$ = the force exerted on the penetration load by the pretension [N], and $F_{resultant}$ = the resulting force on the penetration tool [N].
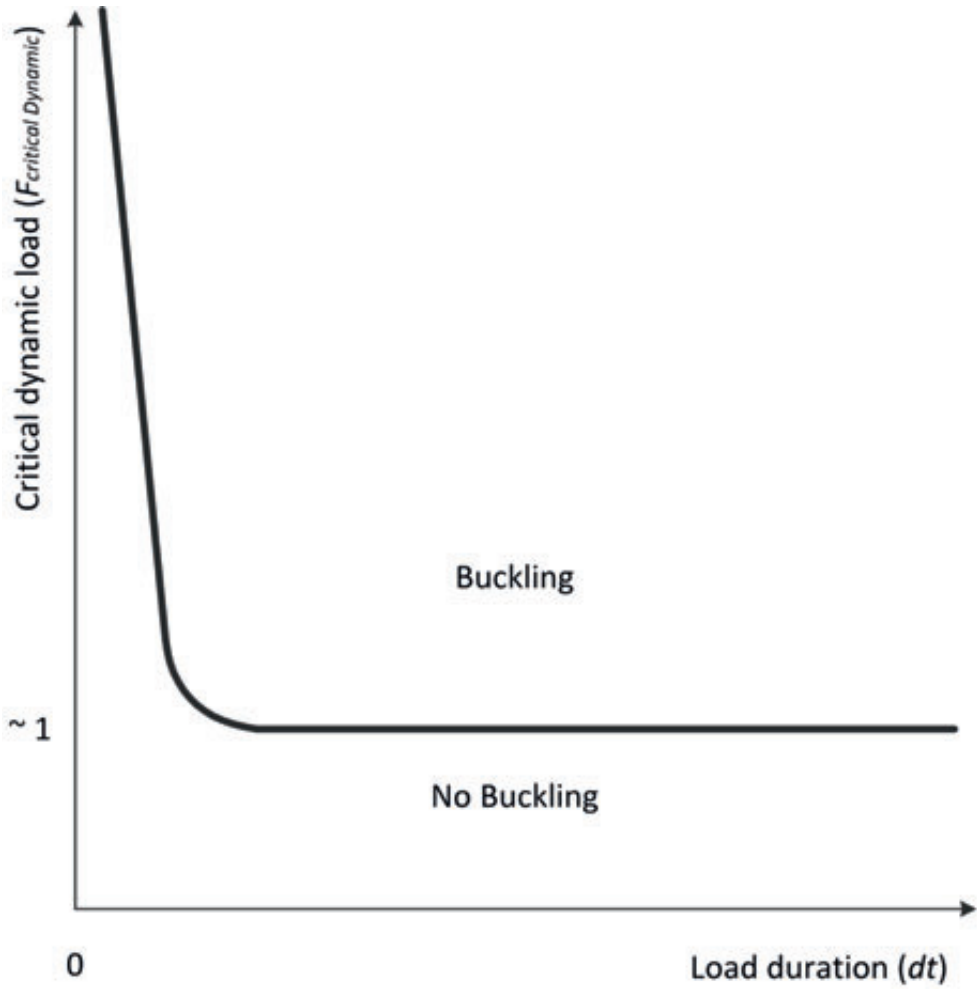
Figure 5.A4— Axial Dynamic Loading of a Penetration Tool.

APPENDIX 5.B: PENETRATION DYNAMICS

5.B1. Penetration Dynamics Under Static Loading Conditions

The penetration load of different tissue types and substrates is dependent on the geometry of the penetration tool (see van Gerwen *et al.* [22] for a review on needle-tissue interaction forces). Currently, a lot of research is ongoing into needle-tip designs to lower the penetration load [15-17].

Needle tips vary in their design, such as the number and angularity of the tip facets, and diameter. The most common needle tip shapes are blunt, beveled, conical, sprotte, diamond (Franseen), and tuohy (Figure 5.B1) [22]. It must be noted, however, that there are many variations of these basic tip designs, often characterized by the presence of numerous facets.

Multiple studies, albeit performed on different materials, have shown dependence of the penetration load on the needle tip shape. For example, the penetration load in silicone (Sil8800) was reported to be approximately 10 N higher for blunt needle tips (Ø1 mm) than for conical tips (Ø1 mm) [18]. In turn, 25 G conical tips (Whitacre, Becton Dickinson) produced higher axial peak loads ($F_{penetration}$ = 0.12 ± 0.02 N [mean ± standard deviation]) than the same size multifaceted bevels (Quincke, Becton Dickinson, $F_{penetration}$ = 0.04 ± 0.01 N) in bovine dura [86]. Furthermore, diamond tips ($F_{penetration}$ ≈ 1.3 N) resulted in almost twice the axial peak load than beveled needles ($F_{penetration}$ ≈ 0.7 N) in porcine heart [19]. Furthermore, Okamura *et al.* [20] showed that an increased number of cutting edges decreased the friction force in silicone. This was further substantiated by Hirsch *et al.* [15], who with preclinical testing demonstrated a significant 23% reduction in penetration load for a 5-facet bevel needle tip as compared to the current 3-facet bevel tips. Finally, Okuno *et al.* [21] showed that for manual insertion of 27 G and 21G beveled needles, the penetration load of human skin increased with needle diameter. The same was illustrated by Podder *et al.* [87] for manual insertion of 18 G and 17 G diamond tip needles.

5.B2. Penetration dynamics under dynamic loading conditions

The main working principle of tissue penetration with dynamic impulse loading can be described as a collision between a moving body (the penetration tool) and an initially non-moving body (the to-be-penetrated tissue). During the contact phase of the two bodies, kinetic energy of the penetration tool is transferred into kinetic energy and other forms of energy, such as heat, deformation energy, and penetration energy. There are two main types of collisions: (1) elastic collision and (2) inelastic collision. In an elastic collision the kinetic energy is conserved, whereas in an inelastic collision (a part of) the kinetic energy is transformed into other energy types. In the case of tissue penetration
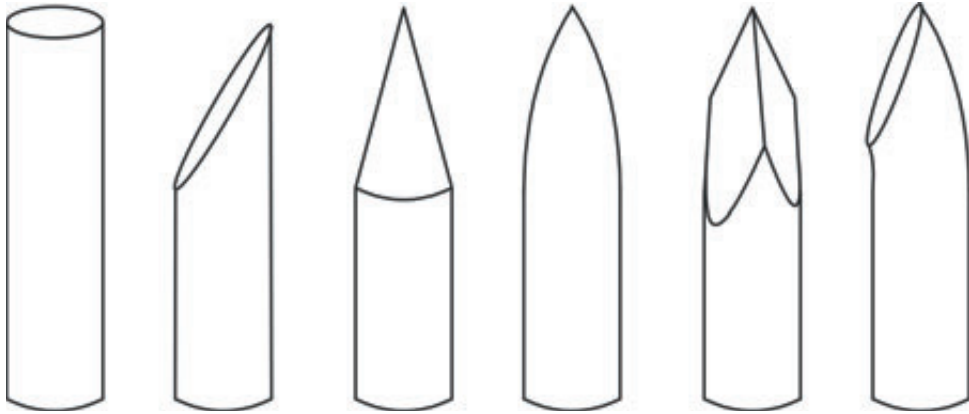
Figure 5.B1— Most Common Needle Tip Geometries. From left to right: blunt, beveled, conical, sprotte, diamond, and tuohy.

5

with a percutaneous instrument, a perfectly inelastic collision is wanted, where all the kinetic energy is transferred into penetration energy and tissue deformation is minimized.

An inelastic collision can be achieved by increasing the insertion speed of the penetration tool. Increasing the speed enables the environmental damping and inertia (i.e., the resistance of the tissue against changes of its state of motion, including changes of its speed and direction) to act as the reaction force to the penetration load (action = – reaction). This reaction force prevents both movement and deformation of the tissue.

By decreasing tissue deformation during the penetration phase, the efficiency ($\eta = \frac{E_{penetration}}{E_{in}} \cdot 100\%$, with E_{in} the energy that goes into cutting and deforming the tissue [J], $E_{penetration}$ the energy that goes into cutting of the tissue [J], and η the efficiency [%]) of the resection procedure can be increased, since less energy is lost into tissue deformation. Furthermore, minimizing energy loss to the environment effectively increases the pressure on the tissue, leading to a decrease in the penetration load. This effect has been illustrated in multiple studies, including Jelinek *et al.* [24] and Heverly *et al.* [25]. Jelinek *et al.* [24] showed that the force needed to penetrate chicken liver decreased from 4 N to approximately 0.3 N when the penetration speed increased from 6 mm/s to 48 mm/s. Heverly *et al.* [25] showed similar results with a 19 G diamond tip needle in porcine heart tissue, where the penetration load asymptotically decreased with increasing penetration speed from approximately 0.7 to 0.45 N.

If the target material is not allowed to stabilize between two imparted dynamic (impulse) loads, the material is subject to vibrational loading conditions. Soft biological tissues often show time-dependent viscosity, causing the tissue to soften or flow over time when vibrated or agitated, also known as thixotropy (or time dependent shear thinning).

This can cause liquid to flow from the surrounding tissue into the operation area, which is unwanted. However, this effect can also be used to decrease the penetration load, which is illustrated by Yang *et al.* [28], where vibratory actuation of a microneedle was shown to reduce the penetration load by approximately 70%.

5

CHAPTER 6

6

SHOOTING MECHANISMS IN NATURE – A REVIEW

AIMÉE SAKES, MARLEEN VAN DER WIEL, PAUL W.J. HENSELMANS, JOHAN L. VAN LEEUWEN, DIMITRA DODOU, AND PAUL BREEDVELD

Published in PLOS ONE.

Abstract—In nature, shooting mechanisms are used for a variety of purposes, including prey capture, defense, and reproduction. This review offers insight into the working principles of shooting mechanisms in fungi, plants, and animals in the light of the specific functional demands that these mechanisms fulfill. We systematically searched the literature using Scopus and Web of Knowledge to retrieve articles about solid projectiles that either are produced in the body of the organism or belong to the body and undergo a ballistic phase. The shooting mechanisms were categorized based on the energy management prior to and during shooting. Shooting mechanisms were identified with projectile masses ranging from $1 \cdot 10^{-9}$ mg in spores of the fungal phyla Ascomycota and Zygomycota to approximately 10,300 mg for the ballistic tongue of the toad *Bufo alvarius*. The energy for shooting is generated through osmosis in fungi, plants, and animals or muscle contraction in animals. Osmosis can be induced by water condensation on the system (in fungi), or water absorption in the system (reaching critical pressures up to 15.4 atmospheres; observed in fungi, plants, and animals), or water evaporation from the system (reaching up to −197 atmospheres; observed in plants and fungi). The generated energy is stored as elastic (potential) energy in cell walls in fungi and plants and in elastic structures in animals, with two exceptions: (1) in the momentum catapult of Basidiomycota the energy is stored in a stalk (hilum) by compression of the spore and droplets and (2) in Sphagnum energy is mainly stored in compressed air. Finally, the stored energy is transformed into kinetic energy of the projectile using a catapult mechanism delivering up to 4,137 J/kg in the osmotic shooting mechanism in cnidarians and 1,269 J/kg in the muscle-powered appendage strike of the mantis shrimp *Odontodactylus scyllarus*. The launch accelerations range from 6.6*g* in the frog *Rana pipiens* to 5,413,000*g* in cnidarians, the launch velocities from 0.1 m/s in the fungal phylum Basidiomycota to 237 m/s in the mulberry *Morus alba*, and the launch distances from a few thousands of a millimeter in Basidiomycota to 60 m in the rainforest tree *Tetraberlinia moreliana*. The mass-specific power outputs range from 0.28 W/kg in the water evaporation mechanism in Basidiomycota to $1.97 \cdot 10^{9}$ W/kg in cnidarians using water absorption as energy source. The magnitude of accelerations involved in shooting is generally scale-dependent with the smaller the systems, discharging the microscale projectiles, generating the highest accelerations. The mass-specific power output is also scale dependent, with smaller mechanisms being able to release the energy for shooting faster than larger mechanisms, whereas the mass-specific work delivered by the shooting mechanism is mostly independent of the scale of the shooting mechanism. Higher mass-specific work-values are observed in osmosis-powered shooting mechanisms ($\leq$ 4,137 J/kg) when compared to muscle-powered mechanisms ($\leq$ 1,269 J/kg). The achieved launch parameters acceleration, velocity, and distance, as well as the associated delivered power output and work, thus depend on the working principle and scale of the shooting mechanism.

Keywords— Bio-inspiration, Catapulting, Ejecting, Elastic Energy Storage, Muscle Contraction, Osmosis, Power Output, Scale Effects, Shooting Mechanisms, Systematic Review, Work, Working Principle.

6

6.1. INTRODUCTION

In nature, shooting mechanisms are used for a variety of purposes including reproduction, prey capture, and defense. Shooting mechanisms evolved multiple times in a diversity of plant and fungal taxa, from the catapulting mechanisms in ferns, the water jet mechanisms in ascomycetes, and the air pressure gun of peat mosses (launching spores with accelerations up to $36,000g$ [1]) (g = magnitude of the gravitational acceleration [9.81 m/s^2]), to the exploding seeds, fruits, and flowers of angiosperms (i.e. flowering plants). Similarly, fast movements occur in disparate animal groups, including stomatopods (marine crustaceans) that use a fast appendage strike to ambush prey, cnidarians that shoot stinging organelles at prey or foe with accelerations reaching $5,413,000g$ [2], and small chameleons that shoot their tongues with accelerations up to $264g$ (in the smallest specimens) to capture elusive prey [3]. Each of these highly effective shooting mechanisms fulfills specific functional demands and has evolved under the influence of natural selection [4]. This has resulted in several unique adaptations that can be linked to a range of successful adaptive radiations (see [5,6] for an example of adaptive radiation in lungless salamanders, family Plethodontidae).

    Insight into the working principles of biological shooting mechanisms can provide important clues about how to design dedicated artificial shooting mechanisms, that could be used, for example, for puncturing biological tissues with high accuracy (needed in biopsies) and high-speed pick-and-place applications. Over the past few decades, the morphology and working principles of shooting mechanisms found in plants [7,8] and fungi [9,10] have been reviewed, but a comprehensive review on shooting mechanisms in animals and a comparative analysis of shooting mechanisms across kingdoms are still missing. Here we intend to fill this gap by providing a comparative overview of shooting mechanisms found in these taxa. We focus on the energy management prior to and during shooting, as a key element that enables the extreme performance of biological shooting mechanisms. Specifically, the identified shooting mechanisms are classified depending on how the energy is generated, stored, and transformed into kinetic energy of the projectile. As shooting mechanisms are found from micro- to macroscale, scaling effects will also be addressed. For this purpose, we will discuss the launch acceleration, velocity, distance, and direction, as well as the power and work delivered by the shooting mechanism per unit mass.

6.2. LITERATURE SEARCH METHOD

6.2.1. Search Strategy and Eligibility Criteria

We conducted two separate search queries: one for shooting mechanisms in plants and fungi, and one for animals, since the terminology used for plants and fungi differs from that in animal studies. The literature searches were performed in Scopus and the Web of

Science Core Collection (last update: 05 May 2016). The full search queries and search strategies are provided in Appendix 6.A.

We only considered articles in the English language and focused the literature search on solid projectiles. Only shooting mechanisms in which the projectile is produced in the body (e.g. a spore or seed) or is part of the body (e.g. chameleon tongue) and undergoes a ballistic trajectory were included. We excluded the following systems: (1) Shooting mechanisms in which foreign objects are used as projectiles (occurring often in throwing actions). (2) Liquid and gas projectiles, such as the Archer fish that shoots down prey from overhanging foliage with a fast, forceful water shot [12] and the Bombardier beetle that uses a liquid venom for defense [13]. (3) Jumping and throwing actions, sometimes referred to as shooting (e.g. the catapult mechanisms used by froghopper to jump with accelerations of up to 408g [14]). (4) Mechanisms in which shooting is directly triggered by the environment, such as spore and seed launch by means of raindrop impact [15] and buzz-pollination in flowers, in which pollen are ejected by means of bumble bee vibrations [16,17]. (5) Single-cellular or subcellular shooting mechanisms. (6) Relatively slow (tongues in some frogs [18]) and fast (tentacle strike in squid [19]) extensions by muscular hydrostats that are not truly ballistic.

6.2.2. Study Selection

The plants and fungi search yielded 290 and 233 articles in the Scopus and Web of Science databases, respectively, with 172 duplicates between the databases, resulting in 351 unique articles. The titles and abstracts of these articles were screened for relevance by two of the authors. The full text of a paper was assessed if both authors did not reject a title or abstract based on the eligibility criteria. Disagreements were resolved by discussion and consensus, which led to a selection of 48 articles. In addition, 20 articles were retrieved from the reference lists of these papers, resulting in 68 articles included in the review. For the full search strategy and study selection in plants and fungi see Appendix 6.A

The animal search queries yielded 408 and 186 articles in the Scopus and Web of Science databases, respectively, with 143 duplicates between the two databases, resulting in 451 unique articles. Following the same protocol as described for the plants and fungi, a total of 51 articles were selected. Fourteen additional articles were retrieved from the reference lists, resulting in 65 articles included in this review. The full search strategy and study selection in animals is given in Appendix 6.A.

6.3. CATEGORIZATION

We based our categorization of the examined biological shooting mechanisms on the employed energy management, which typically involves (1) energy generation, (2) energy storage, and (3) energy transformation.

6.3.1. Energy Generation

In all the identified shooting mechanisms in plants and fungi, energy for shooting is generated through osmosis (i.e. the diffusion of water through a semi-permeable membrane triggered by a change in concentration of osmolytes, that is, ions, sugars, and alcohols, in two neighboring solutions). To achieve osmosis, the osmolytes are actively transported through the cell membrane against a concentration gradient. This is accomplished by either transmembrane protein pumps (ATPases), which power the active transport by splitting adenosine triphosphate (ATP), or coupled transport pumps that use potential energy by exploitation of an electrochemical gradient. Depending on the direction of the water exchange, three osmosis-controlled mechanisms of energy generation can be distinguished: (1) water condensation on the outer surface of the shooting mechanism, (2) water absorption into the cells of the shooting mechanism, and (3) water evaporation from the cells of the shooting mechanism. Plants use only water absorption and water evaporation, whereas in fungi all three osmosis-controlled mechanisms occur. Some animals also use an osmosis-controlled water absorption mechanism, but the energy for shooting is most often generated by the contraction of muscle fibers located in the proximity to or even in the projectile. To achieve contraction, muscle fibers contain myofibrils, which have serially arranged contractile units, called sarcomeres (see [18] for the sliding-filament theory). The sarcomeres contain a lattice of actin and myosin filaments, which are able to slide along each other. When an impulse arrives at the neuromuscular junction, neurotransmitters (such as acetylcholine) are released, which in turn causes an action potential of the sarcolemma and ultimately the release of calcium ions (Ca^+) from the sarcoplasmic reticulum. The Ca^+ binds to Troponin C (a regulatory protein) on the actin filament, which then exposes the binding location for the myosin heads of the myosin filaments (with adenosine diphosphate (ADP) and inorganic phosphate bound to its nucleotide binding pocket). Hence, cross-bridges can be formed between the actin and myosin filament. Cross-bridges can make a mechanical power stroke at the expense of one ATP-bond per cycle. The release of ADP and inorganic phosphates from the myosin enables the myosin filaments to pull the actin filaments inwards, shortening the muscles. Finally, the binding of ATP to the myosin head allows it to break the cross-bridges with the actin filament.

6.3.2. Energy Storage

The generated energy is stored in a medium as elastic energy (a form of potential energy) until it reaches a critical level or is released by a triggering mechanism. In plants and fungi, the energy for shooting is generally stored as elastic energy using pressure changes inside the cell that deform the cell wall. The absorption of water into the cell pushes the expandable plasma membrane against the rigid cell wall (also known as turgor pressure), resulting in a turgid cell, whereas the evaporation of water causes a negative pressure

6

(with respect to ambient) inside the cell that pulls the plasma membrane from the cell wall, resulting in a plasmolyzed cell [8]. In two of the identified mechanisms, energy is not primarily stored in the cell wall: (1) in the momentum catapult of Basidiomycota, energy is stored in a stalk by an increase and shift in the center of mass of the spore [19] and (2) in *Sphagnum*, energy is mainly stored in pressurized air contained within a spherical capsule [1]. In animals, the energy for shooting is stored as elastic energy in collagen or other fibrous structures such as resilin. Storing energy in elastic structures can be advantageous over direct use of energy for muscle contraction, because elastic tissue structures can recoil much faster than muscles can shorten [20,21]. In other words, while contracting muscle tissues have a peak mass-specific power output of 373 W/kg in amphibians at 25 °C [22] and 1,121 W/kg in quail flight muscle [23,24], elastic tissues can reach power outputs of, for example, 470,000 W/kg in mantis shrimps [25]. Furthermore, the mechanical properties of elastic tissues are less temperature-sensitive than muscle contraction, allowing the animals to use their launch mechanisms over a wide temperature range [26-28].

6.3.3. Energy Release & Transformation

The stored energy is released and transformed to kinetic energy of the projectile. In plants, the elastic energy is released by the fracture of molecular bonds or cavitation inside the cytoplasm of the cells. Similar release mechanisms occur in fungi. An exception is found in the fungi genus *Sphaerobolus*, where the stored elastic energy is released by the eversion of a membrane [10]. In animals, the stored elastic energy for shooting is either released by eversion of the projectile itself in cnidarians [29], relaxation of collagen fibers in the ballistic tongues in chameleons [30] and lungless salamanders [31], or release of a latch in stomatopods [25]. Unfortunately, not all release mechanisms in animals are known or sufficiently understood, such as those of frogs that use a rapid jaw movement to project their tongue [16]. Finally, the stored energy is transferred to the projectile, which gains kinetic energy, using a specific catapult mechanism.

6.4. FUNGI

Figure 6.1 illustrates the shooting mechanisms identified in fungi, allocated based on the energy management criteria discussed above. At the end of the section, an overview of all retrieved and calculated launch parameters and the associated measurement methods is provided (see Table 6.1).

6.4.1. Osmosis: Water condensation

Elastic Energy Storage in Sterigma – Fracture Release Mechanism: Momentum Catapult

In Basidiomycota, a phylum of fungi including many edible mushrooms, most spores are
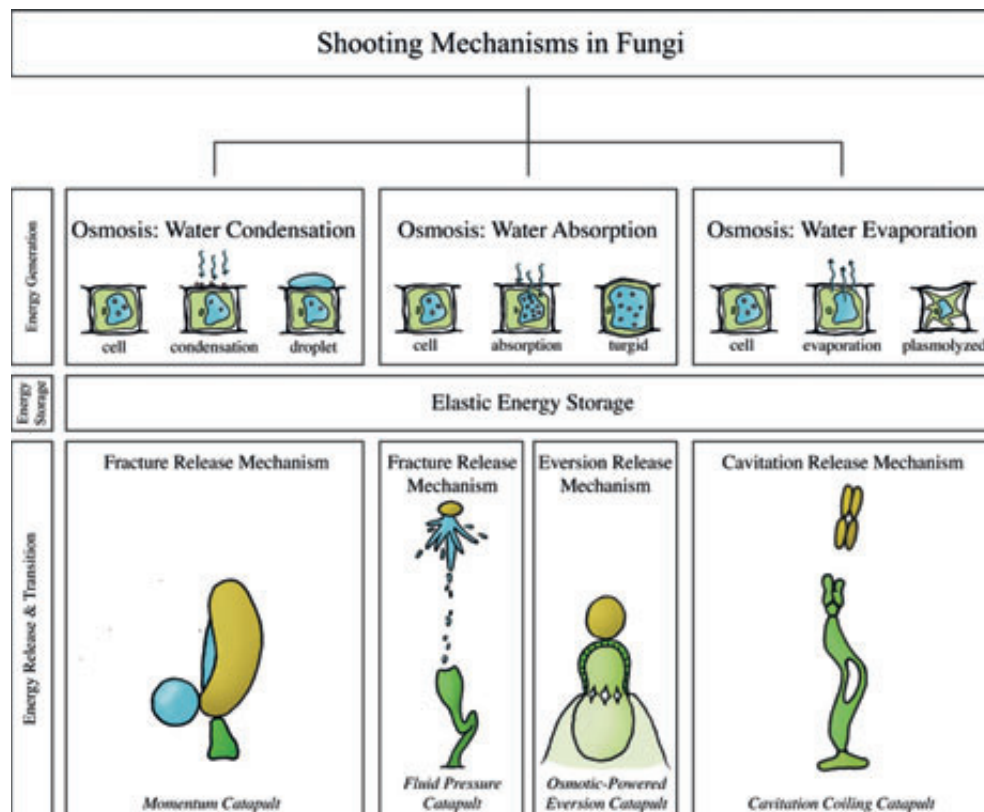
Figure 6.1— The Structural Categorization of the Identified Shooting Mechanisms in Fungi, Allocated Based on the Energy Management Criteria Discussed Above. Momentum catapult: observed in the phylum Basidiomycota, schematic illustration of *Auricularia auricular*. **Fluid pressure catapult**: observed in the phylum Ascomycota and the genera *Pilobolus* and *Basidiobolus* of the phylum Zygomycota, schematic illustration of *Pilobolus kleinii*. **Osmotic-powered eversion catapult**: observed in the genus *Sphaerobolus*. **Cavitation coiling catapult**: observed in genera and species of the phylum Ascomycota and Basidiomycota, schematic illustration of *Zygophalia jamaicensis*.

actively dispersed by a momentum catapult: a shooting mechanism characterized by the coalescence of two water droplets (the so-called Buller's drop and adaxial drop [32]) on the spore surface that generate the energy needed to discharge the spore(s) by momentum transfer [19,33-37]. The sporogenous cell of the concerning species typically consists of cup-shaped reproductive units called basidiospores or ballistospores (mass without the droplets $8.4 \cdot 10^{-7}$ milligram [mg] and with droplets $1.5 \cdot 10^{-6}$ mg in *Itersonilia perplexans* [35]), connected to a stalk (sterigma) by the hilum (Figure 6.2A). Noblin *et al.* [19] describe the shooting mechanism of Basidiomycota as a four-stage process: (1) The nearly

spherical Buller's drop and the hemispherical adaxial drop grow due to the secretion of osmolytes onto the spore surface, lowering the center of mass of the spore (Figure 6.2A–B). (2) Buller's drop and the adaxial drop reach a critical size, contact each other, and begin to coalesce, generating a compression force on the stalk and a counterforce on the spore (Figure 6.2B–C). (3) The two drops continue to coalesce, leading to momentum transfer from the merged drop to the spore (total momentum of drop and spore of approximately $2.4 \cdot 10^{-12}$ kilogram meter per second [kg·m/s] [35]), with the stalk now under a tension force (Figure 6.2C). (4) The hilum breaks under the tension created by the momentum transfer and the braking of the drop at the spore's tip [38], releasing the spore (Figure 6.2D). The variation in the size of the spores and Buller's drops produces a range of launch accelerations from 3,302 to 25,484g [35,38-40], launch velocities from 0.1 to 1.8 m/s [34,38,40], and launch distances from a few thousand of a millimeter [mm] in the smallest spores to a few millimeters in the larger spores [32,34,35,38,40]. Given their small size and mass, spores operate in a low Reynolds number (i.e. a dimensionless quantity that quantifies the relative effect of inertial and viscous drag forces) regime, where friction drag is relatively high. The spores are, therefore, strongly decelerated after release from the sterigma and reach relatively small release distances in spite of the high accelerations. The larger the spore, the least it is affected by drag. It is hypothesized that the species with the shorter ranges (<0.1 mm) propel their spores from fertile tissues, whereas species that discharge their spores over larger distances (≥0.5 mm) liberate them directly into the airstream, thereby (slightly) increasing their probability of escaping the laminar boundary layer [40].

6

6.4.2. Osmosis: Water absorption

Elastic Energy Storage in Cell Wall – Fracture Release Mechanism: Fluid Pressure Catapult

The fluid pressure catapults, or squirt gun mechanisms, are most common in the largest fungal phylum Ascomycota [10,41-51], including lichenized species (i.e. composite organisms that arise from algae or cyanobacteria and live among the filaments of a fungus in a symbiotic relationship), but have also evolved among the Zygomycota [41].

The defining feature of Ascomycota is their asci: fluid-filled sacs, from which spores (ascospores) are ejected (Figure 6.3A–D). Osmolytes inside the ascus lead to inflow of water through the ascus membrane, which increases turgor pressure inside the ascus and causes expansion and stretching of the ascus wall (Figure 6.3C). After reaching a critical pressure of 0.31–1.54 megapascal [MPa] relative to ambient (in between 3 and 15.4 atmospheres [atm]) [41,43,44,47], the spores are discharged together with the liquid content of the ascus through a pore, slit, or operculum (Figure 6.3C), located at the tip of the ascus. The highest launch acceleration and velocity are reported for *Gibberella zeae* and are 870,000g and 34.5 m/s, respectively [43,50]. The spore and fluid projection is powered by the release of elastic energy from the contracting wall of the ascus. The liquid
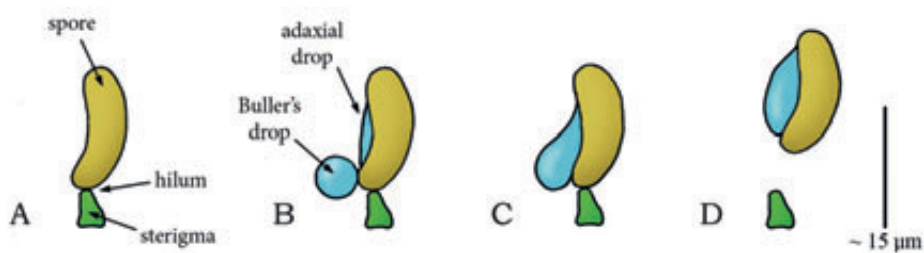
Figure 6.2— Momentum Catapult Mechanism in the Phylum Basdiomycota (Species *Auricularia auricular*). (A) The sporogenous cell of Basdiomycota before discharge with the spore attached to the sterigma at the hilum. (B) By secreting osmolytes, Buller's drop and the adaxial drop grow on the surface of the spore. (C) When Buller's drop reaches a critical size, the two drops coalesce, generating a compression force on the sterigma. (D) A rapid shift of the joint center of mass of the spore and the coalesced drops puts tension on the hilum. When a critical tensile stress is reached, the hilum breaks and the spore (together with the coalesced drops) is discharged. Drawings based on schematic drawings in [34]. Scale bar 15 micrometer [μm].

6

in the container is nearly incompressible and can, therefore, store only a negligible amount of elastic energy. Launch distances of approximately 0.3 m have been reported for *Ascobolus immersus* [41] and the "spitting" fungus *Glomerobolus gelineus* [52], which is high-enough to reach the turbulent boundary layer, enabling dispersal by wind. It has been shown that, in order to maximize launch distance, energy losses during ejection and drag are minimized by the shape of the operculum [48] and spores [45], respectively. Furthermore, by synchronizing the ejection of thousands of spores, ascomycetes create a favorable flow of air that carries spores through the laminar boundary layer, around intervening obstacles, and towards the turbulent boundary layer, negating the range constraints imposed by (viscous friction) drag, thereby generating 20 times greater launch distances than that of individually discharged spores [46]. Finally, a rotational movement of the spores at 1,200 rotations per minute (comparable to the rotational movement of a bullet after leaving the coiled riffling of a barrel of a gun or cannon [51]) is observed after discharge [51], which can potentially decrease the effect of the wind on the trajectory of the spores. Large launch distances tend to increase the average dispersal distance by wind, which enables the species to reach far-away habitats.

The fluid pressure catapult is also observed in the genera *Pilobolus* (class: Mucoromycotina, order: Mucorales, family: Pilobolaceae) and *Basidiobolus* (class: Zygomycetes, order: Entomophthorales, family: Basidiobolaceae; recently questions have been raised about the placement of Basidiobolaceae within the Entomophthorales) within the Zygomycota (a phylum of fungi consisting of approximately 1,050 species that are characterized by spherical spores (length = 0.03–0.07 mm [53]) developed for sexual reproduction [41]). *Pilobolus* grows on herbivore dung and is commonly known as the

squirt-gun or hat thrower fungus. *Pilobolus* grows spore-producing structures (sporangiophores) that consist of a stalk (sterigma) and a balloon-like vesicle (Figure 6.4A–B). In the common species *Pilobolus kleinii*, a package filled with spores (sporangium; containing between 30.000–90.000 spores [10]) is formed at the tip of the vesicle (Figure 6.4B). Due to (osmotic) absorption of water, the balloon-like vesicle swells, and the hydrostatic pressure in it increases. When a critical pressure of about 0.55MPa relative to ambient (about 5.5 atm) [10,41] is reached, the spore package breaks free from the vesicle (in 0.01–0.03 ms [53]) and is propelled by a jet of cell sap with a peak acceleration up to 21,407g and a peak launch velocity of 16 m/s (mean: 9 m/s), resulting in a launch distance of 2.5 m for launch angles of 70–90° to the horizontal (estimated from figures in [54]) (Figure 6.4 C–D) [10,41,50,55]. Again, the spore and fluid projection is powered by the release of elastic energy from the contracting wall of the vesicle, which is converted into kinetic energy of the ejected spores and some deformation of the stalk of the sporangiophore. The launch distance is larger than in the Ascomycota because the spore package remains intact, resulting in an overall larger mass

6
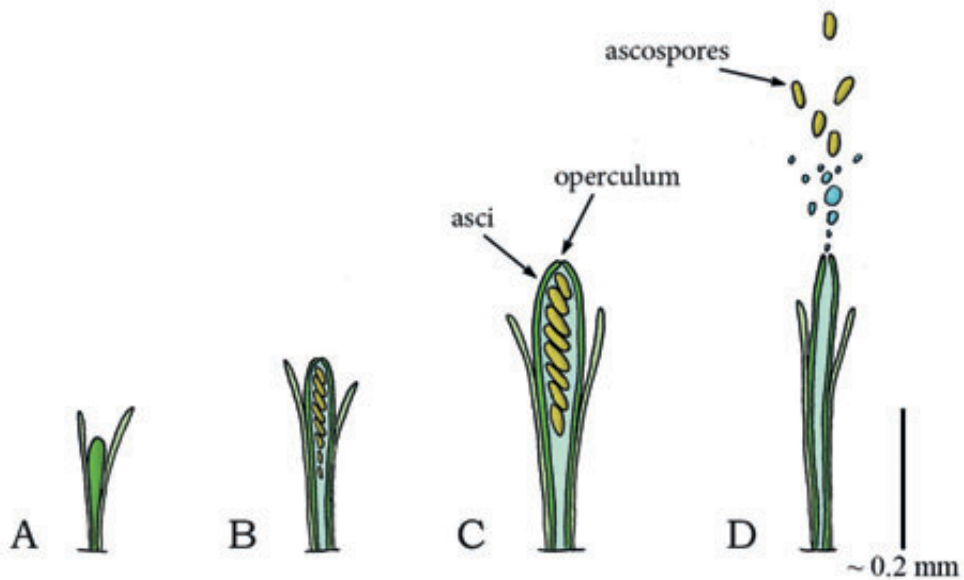
Figure 6.3— Fluid Pressure Catapult Mechanism in the Phylum Ascomycota (Species *Ascobolus immersus*). (A) Early stage of ascus development in Ascomycota. (B) Developed ascus containing the ascospores. (C) Osmotic water absorption increases turgor pressure and drives the expansion of the ascus. (D) When a critical pressure is reached (range: 0.30–1.54 MPa), the operculum breaks open, allowing contraction of the expanded wall, which drives the discharge of the ascospores together with the cell sap from the ascus. Drawings based on schematic drawings in [50]. Scale bar 0.2 mm (200 μm).
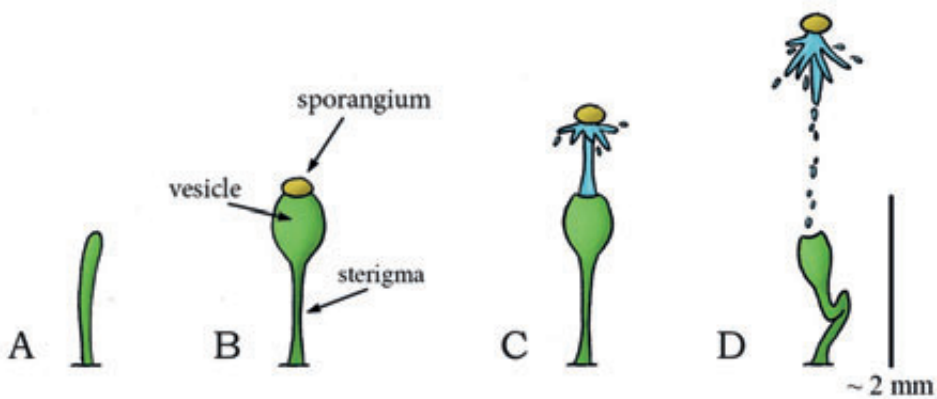
Figure 6.4— Fluid Pressure Catapult Mechanism in the Zygomycete *Pilobolus kleinii*. (A) Early stage of sporangiophore growth in *P. kleinii*. (B) Sporangiophore development showing the sterigma (stalk), balloon-like vesicle, and the sporangium at the tip. (C) When a critical pressure (of about 0.55 MPa relative to ambient) is reached, the sporangium breaks free from the sporangiophore and is propelled forward by a cell sap jet that is powered by the contracting vesicle wall. (D) Collapse of the sporangiophore after discharge of the sporangium. Drawings based on high-speed video images in [54]. Scale bar 2 mm.

of the projectile and thus a lower influence of viscous drag (see Equation 7.1), as the decelerating drag force is (approximately) proportional to the square of the spore radius (*r*), while spore inertia is proportional to its mass and thus to *r* for a spherical object[40].

$$F_{drag} = {}^{1}/_{2}\, \rho A v^{2} C_{d},$$ (7.1)

with ρ = density of the fluid [kg·m], *A* = cross-sectional area (πr^2 for spherical objects) [m], *v* = velocity of the projectile [m/s], and C_d = drag coefficient (i.e. a dimensionless quantity that quantifies the drag of an object in a fluid environment).

Basidiobolus is a genus of microscopic fungi that inhabit the guts of small animals and is known to cause rare infections in the host species, including humans [41]. The spore-producing structure of *Basidiobolus ranarum,* for example*,* is similar to that of *Pilobolus*, with the major difference that *B. ranarum* discharges a single spore (called conidium). The wall of the spore-bearing structure ruptures around its circumference with an estimated internal pressure of 0.01–0.72 MPa relative to ambient, and the spore is discharged with a peak launch acceleration of 152,905*g* and a peak launch velocity of 9 m/s (mean: 4 m/s), resulting in a peak launch distance of 0.02 m (with an theoretical

maximum of 0.05 m using Stokes drag) [41]. The difference in launch distance between *Pilolobus* and *Basidiobolus* is a physical consequence of the difference of size and thus effect of the viscous drag on the spores (see also Equation 7.1). This is substantiated in a study of Fischer *et al.* [56], in which the Reynolds number for the launch of *Pilobolus* and *Basidiobolus* were calculated as 167 and 10, respectively, indicating a higher effect of viscous drag in *Basidiobolus*.

Elastic Energy Storage in Cell Wall – Eversion Release Mechanism: Osmotic-Powered Eversion Catapult

Another type of active spore dispersal in the phylum Basidiomycota can be found in the genus *Sphaerobolus* (class: Agaricomycetes, order: Gaestrales, family: Geastraceae). *Sphaerobolus* is known as the cannonball fungus or artillery fungus, and is usually found on dung, decaying wood, or vegetative litter [57]. The generic name is deducted from the Greek words sphear, meaning sphere, and obulus, meaning throw, as the fungus discharges a spore-filled round package called gleba (diameter [Ø] of 1 mm). Discharging is led by the osmotic-powered eversion of a membrane that surrounds the package [10], similar to the kids toy "jumping poppers". The immature base of *Sphaerobolus* is a closed sphere (Figure 6.5A). At maturity, this sphere splits radially from its apex, forming a toothed (star-shaped) cup that envelops the spore-filled package (Figure 6.5B) [10]. The cup consists of a firm outer case and an elastic inner membrane (peridium). By solubilization of glycogen and subsequent absorption of water, the turgor pressure within the radially oriented cells of the elastic inner membrane increases [10,58]. As the inner membrane has a concave form, the exposed ends of the radially orientated cells are more compressed than their bases, resulting in strain within the cell walls. The sudden eversion of the membrane relieves the strain and discharges the spore package (approximately vertically) with an estimated peak launch velocity of 10 m/s, reaching up to 6 m from its base (Figure 6.5C–D) [9,59]. The large launch distance (partly) compensates for a low efficacy of wind dispersal, as the gleba is most likely too heavy to be swept away over large distances by the wind.
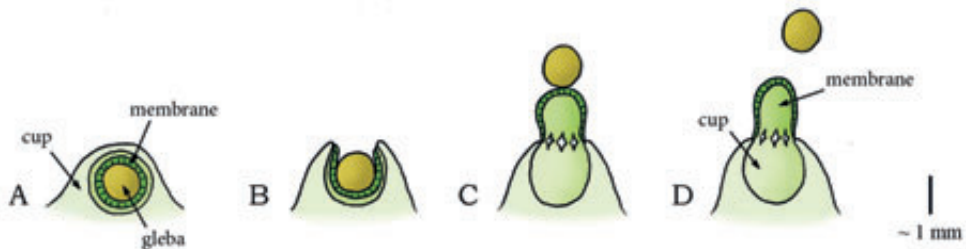
Figure 6.5— Osmotic-Powered Eversion Catapult Mechanism in the Genus *Sphaerobolus*. (A) Immature fruiting body of *Sphaerobolus*. (B) The developed fruiting body with the exposed gleba (Ø1 mm, contains

the spores) that is supported by an elastic membrane within a firm outer case of the cup. (C–D) When a critical pressure is reached inside the cells of the elastic membrane, the membrane everts rapidly, discharging the gleba from the cup. Scale bar 1 mm.

6.4.3. Osmosis: Water evaporation

Elastic Energy Storage in Cell Wall – Cavitation Release Mechanism: Cavitation Coiling Catapult

Cavitation-based spore discharge is observed in fungi imperfecti (i.e. fungi that do not fit into the commonly established taxonomic classifications). The fungi imperfecti represent asexually reproducing genera in the phyla Ascomycota and Basidiomycota. Cavitation-based spore discharge was first observed in *Deightoniella torulosa* (incertae sedis, phylum: Ascomycota, class: Dothideomycetes, order: Capnodiales, family: Mycosphaerellaceae), a pathogen causing banana fruit-spot [60]. This fungus grows its spores on stalks called conidiophores. When dehydration causes the cell membranes to shrink, the cell walls start caving inwards, which increases the tension within these walls and slowly deforms the structure. Continuous negative pressure that exceeds the tensile strength of the cytoplasm causes the cytoplasm to fracture, resulting in the appearance of a gas bubble (or cavitation bubble) that releases the wall tension and causes the walls to rapidly return to their original shape (similar to a coiling motion), catapulting the spores out of the conidiophore [60].

6
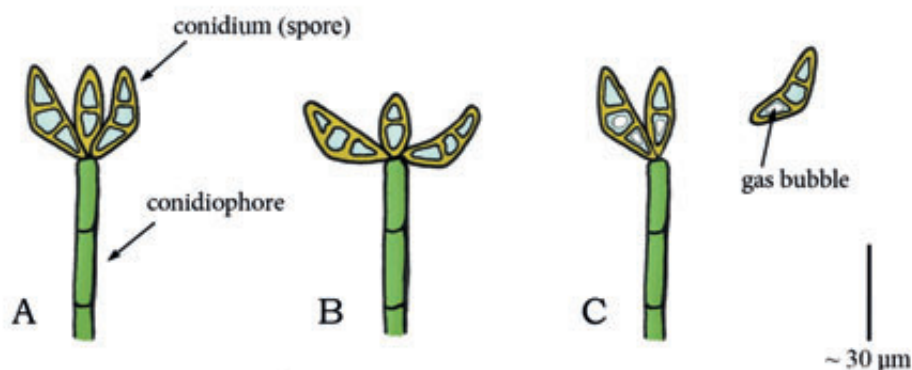
Figure 6.6— Cavitation Catapult Mechanism in *Curvularia*. (A) Conidiophore in *Curvularia* with a cluster of boat-shaped conidia (spores) at its apex. (B) Outward movement of the conidia caused by drying. (C) When a critical negative pressure (relative to ambient) is reached, the sudden appearance of a gas bubble in the conidia releases the stored elastic energy and causes a rapid return movement of the conidia to their original shape, which disrupts the connection with the conidiophore and launches the conidia. Drawings based on schematic drawings in [61]. Scale bar 30 µm.

Species of the genus *Curvularia* (phylum: Ascomycota, class: Euascomycetes, order: Pleosporales, family: Pleosporaceae) are pathogens of plants and soil that are found in tropical regions. In at least two species, *C. lunata* and *C. geniculate,* spore discharge is also triggered by cavitation. In these species, the young conidiophore bears a cluster of boat-shaped (asexual) spores (conidia) at its apex (Figure 6.6A) [61]. During drying, the spores slowly move either inwards, outwards, or to the side, with respect to the attachment to the conidiophore (Figure 6.6B). When a critical negative pressure is reached in a spore, cavitation bubbles appear, resulting in a rapid return movement of the spore to their original shape which disrupts the connection with the conidiophore and launches the spore (Figure 6.6C) [61].

A cavitation coiling catapult mechanism is also observed in the species *Zygophiala jamaicensis* (phylum: Ascomycota, class: Dothideomycetes, order: Microthyriales, family: Schizothyriaceae). This pathogen grows on banana leafs and consists of a conidiophore with two sporogenous cells and conidia at the apex of the conidiophore (Figure 6.7A). Drying of the conidiophore causes it to deform into an S-shape (Figure 6.7B) [61]. At the sudden appearance of a gas bubble, the conidiophore springs back to its former shape, discharging the conidia from the sporogenous cells (Figure 6.7C, D) [61].

Meredith *et al.* [61] suggested that the cavitation coiling catapult mechanism also holds for *Memnoniella subsimplex* (phylum: Ascomycota, class: Sordariomycetes, order: Hypocreales, family: Stachybotriaceae), a common invader of decaying banana leafs. This fungus consists of erect, straight conidiophores [61]. The (asexual) spores are formed in a chain-like fashion, with each chain containing as many as 25 spores (Figure 6.8A). Drying causes the conidiophore to twist about its longitudinal axis and rapidly rotate through nearly 360° (Figure 6.8B). Although the twisting motion of the conidiophore greatly assists the detachment of loosely connected spores [61], Meredith [61] speculates instead that the energy for discharge is related to the appearance of gas bubbles in the conidia (Figure 6.8C). A similar twisting motion and appearance of gas bubbles is observed in *Corynespora cassiicola* (phylum: Ascomycota, class: Dothideomycetes, order: Pleosporales, family: Corynesporascaceae) and in *Alternaria tenuis* (phylum: Ascomycota, class: Dothideomycetes, order: Pleosporales, family: Pleosporaceae), both containing conidia, borne singly or in chains of 2–6 at the apex of the conidiophore [61].

Unfortunately little is known about the launch acceleration, velocity, and distance of cavitation-based spore discharge in fungi imperfecti. Furthermore, the working principles of the cavitation-based spore discharge in many fungal species, such as those in *M. subsimplex* [58], are still to be determined.
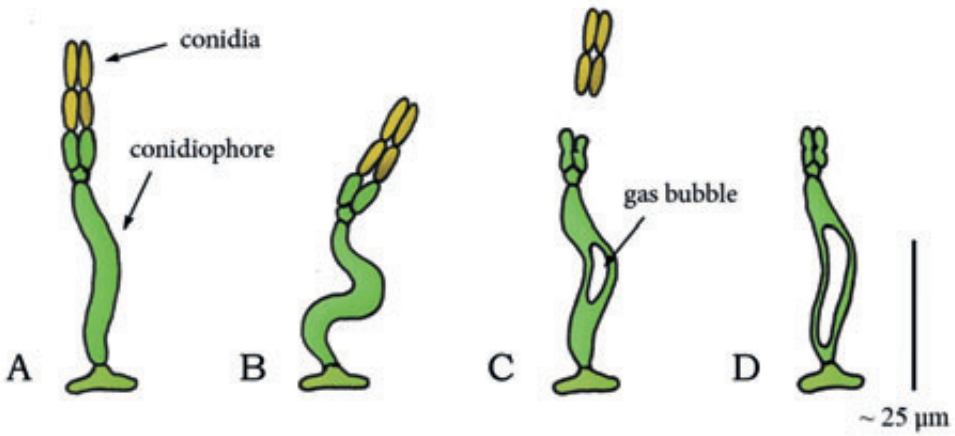
Figure 6.7— Cavitation Catapult Mechanism in *Zygophalia jamaicensis*. (A) Conidiophore of *Z. jamaicensis* with two divergent conidia at its apex. (B) S-shaped compression of the conidiophore by drying. (C) When a critical negative pressure (compared to ambient) is reached, the sudden appearance of the gas bubble in the conidiophore releases the stored elastic energy in the cell walls and discharges the conidia from the sporogenous cells. (D) Conidiophore after discharge. Drawings based on schematic drawings in [61]. Scale bar 25 μm.

6
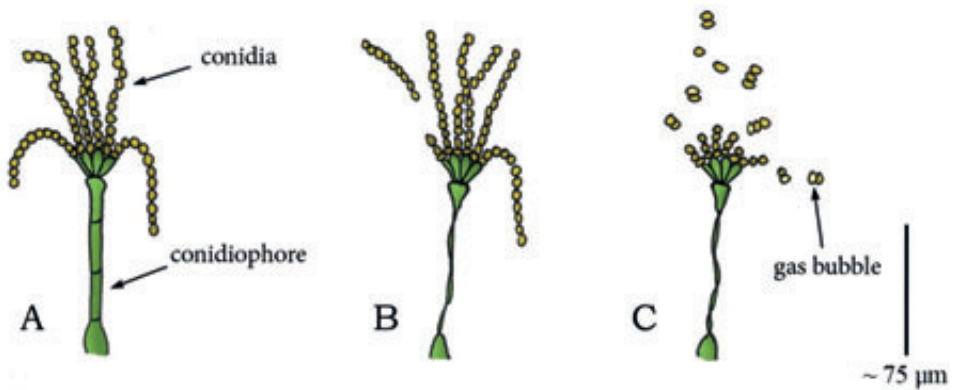
Figure 6.8— Cavitation Catapult Mechanism in *Memnoniella subsimplex*. (A) Conidiophore of *M. subsimplex* with conidia in a chain-like fashion at its apex. (B) Twisting of the conidiophore during drying discharges loosely connected conidia. (C) In [61] it is suggested that a critical "negative" pressure (compared to ambient) causes the sudden appearance of gas bubbles in the conidia that releases the tension in the cell walls of the conidia, resulting in a rapid return motion, and the subsequent discharge of the conidia. Drawings based on schematic drawings in [61]. Scale bar 75 μm.

6

Table 6.1— Summary of Launch Parameters of the Identified Shooting Mechanisms in Fungi. For the projectile mass, launch velocity, launch acceleration, launch distance, and launch angle, the measurement technique is coded as following: Standard = measured using a high-speed video camera. Bold = calculated by referred authors using measured launch parameters. *Italics* = manual measurement of the parameter (e.g. from photograph stills, without the use of a high-speed video camera). Standard* = estimated by us from data/figure in indicated reference(s); for the power output per unit mass the launch acceleration [m/s²] is multiplied with the launch velocity [m/s] and for the work per unit mass the power output [W/kg] is integrated over the launch duration [s]. The launch parameters are indicated as mean (± standard deviation), peak (indicated with "peak" behind the value), or a range (minimum value–maximum value). Per launch parameter, the peak value identified in this review is indicated by a blue-lined box (with the exception of the launch angle).

Fungi	Projectile mass [mg]	Launch acceleration [g]	Launch velocity [m/s]	Launch distance [m]	Launch angle [°]	Power output [W/kg]	Launch duration [ms]	Work [J/kg]
Elastic Energy Storage - Fracture Release Mechanism								
Momentum Catapult								
Basidiomycota [32]								
Osmosis: Water Condensation								
Aleurodiscus gigasporus [34]	*0.017*	-	*0.53*	0.0018 peak	-	-*	-	-
Auricularia auricula [38,40]	0.37·10⁻⁶	3,302–12,000	1.23 (0.87–1.62)	45·10⁻⁵ ± 2·10⁻⁵	-	2.8·10⁻¹–1.45·10⁻¹*	0.01	0.28–1.45*
Itersonilia perplexans [35,38]	*1.5·10⁻⁵*	~25,484	0.67ᶜ	1·10⁻³	75*	1.64·10⁻¹*	<0.01*	<1.64*
Hyphodontia latitans [34]	0.6·10⁻⁹	-	1.05	4·10⁻⁴ peak	-	-*	-	-
Gymnosporangium juniper – virginianae [40]	0.003	-	1.11 (0.66–1.35)	13·10⁻⁴ ± 6·10⁻⁵	-	-	-	-
Osmosis: Water Absorption								
Elastic Energy Storage - Fracture Release Mechanism								
Fluid Pressure Catapult [56]	1·10⁻⁵–2·10⁻³							
Ascomycota								
Ascobolus immersus [10,41,56]	0.001	183,486 peak	14ᵈ (5–18)	0.3 peak	-	3.24·10² peak*	<0.06*	<1,944*
Calbarella zeae [10,43,50]	0.2·10⁻⁶	870,000	34.5	2.8·10⁻³–8.5·10⁻³	-	2.94·10⁴*	-	-
Neurospora tetrasperma [45]	-	-	1.24 (1.80 peak*)	-	60*	-	-	-
Podospora anserina [41]	-	152,905 peak	21ᵈ (10–25)	0.2 peak	-	3.74·10² peak*	<0.096*	<3,390*
Sclerotinia sclerotiorum [46]	-	-	8.4	0.01	90*	-	-	-
Glomerobolus gelineus [52]	-	-	-	0.33 peak	-	-	-	-

Continuation of Table 6.1—Summary of Launch Parameters of the Identified Shooting Mechanisms in Fungi.

Zygomycota							
Pilobolus							
Pilobolus kleinii [8,10,41,50,53-55]	21,407 peak	9^d (2-16)	2.5 peak	70-90*	$3.36 \cdot 10^6$ peak*	0.01-0.03	112.2 peak*
Basidiobolus							
Basidiobolus ranarum [41,56]	152,905 peak	4^d (2-9)	0.02 peak	-	$1.35 \cdot 10^7$ peak*	< 0.024*	< 324*
Elastic Energy Storage - Eversion Release Mechanism							
Osmotic-powered Eversion Catapult							
Basidiomycota							
Sphaerobolus [9,10,59]	-	10 peak	6 peak	90*	.:	-	-
Osmosis: Water Evaporation							
Elastic Energy Storage – Cavitation Release Mechanism							
Cavitation Coiling Catapult							
Ascomycota							
Deightoniella torulosa [60]	-	-	-	-	-	-	-
Zygophiala jamaicensis [61]	-	-	-	-	-	-	-
Curvularia							
Curvularia lunata [61]	-	-	-	-	-	-	-
Curvularia geniculate [61]	-	-	-	-	-	-	-
Mvenmoniella subsimplex [61]	-	-	-	-	-	-	-
Corynespora cassiicola [61]	-	-	-	-	-	-	-
Alternaria tenuis [61]	-	-	-	-	-	-	-
Basidiomycota							

ª Additional information *Aleurodiscus gigasporus* and *Hyphodontia latitans*:

- *A. gigasporus*: available surface tension energy $2.9 \cdot 10^{-11}$ J, energy to break connection $1.6 \cdot 10^{-14}$ J, proportion of total energy consumed in fracture 0.1%, kinetic energy of launch $2.7 \cdot 10^{-12}$ J (9.3%).

- *H. latitans*: available surface tension energy $2.6 \cdot 10^{-14}$ J, energy to break connection $1.6 \cdot 10^{-14}$ J, proportion of total energy consumed in fracture 61.5%, kinetic energy of launch $3.4 \cdot 10^{-16}$ J (3.4%).

6

6

[b] spore mass $8.4 \cdot 10^{-13}$ kg [35]

[c] Total momentum of drop and spore of approximately $2.4 \cdot 10^{-12}$ kg·m/s [35]

[d] Median value [41]

[e] The power required for gleba discharge is approximately 0.1 W [59]

6.5. PLANTS

Figure 6.9 illustrates the shooting mechanisms identified in plants, allocated based on the energy management criteria discussed above. An overview of all retrieved launch parameters and the associated measurement methods is provided in Table 7.2.
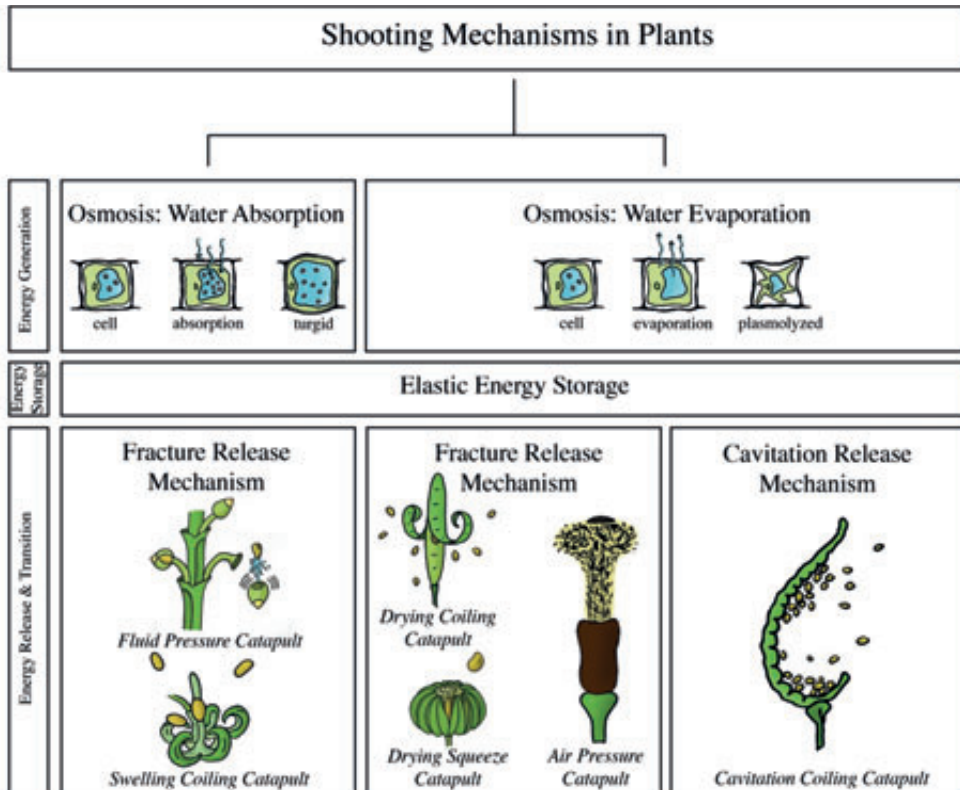
Figure 6.9— The Structural Categorization of the Identified Shooting Mechanisms in Plants, Allocated Based on the Energy Management Criteria Discussed Above. Fluid pressure catapult: observed in the genus *Arceuthobium*. **Swelling coiling catapult**: observed in the genus *Impatiens*, *Cornus canadensis*, and *Morus alba*, schematic illustration of *Impatiens capensis*, **Drying coiling catapult**: observed in the genus *Cardamine* and the family Fabaceae, schematic illustration of *Cardamine parviflora*. **Drying squeeze catapult**: observed in the family Euphorbiaceae, the Rutaceae family, the genus *Illicium*, the species *Oxalis acetosella*, and the *Viola* family, schematic illustration of *Hura crepitans*. **Air pressure catapult**: observed in the genus *Sphagnum*. **Cavitation coiling catapult**: observed in the family Polypdiaceae and genus *Selaginella*, schematic illustration of *Polypodium aureum*. In contrast to the situation in fungi, no shooting mechanisms were identified in the water condensation category.

For some of the described species that ballistically disperse their seeds or pollen, a description of the working principle of the shooting mechanism was not found in our literature search, for example, for *Phlox drummondii* (phylum: Tracheophyta, class: Magnoliopsida, order: Ericales, family: Polemoniaceae) [62]. These species will not be discussed, as placement is uncertain.

6.5.1. Osmosis: Water absorption

Elastic Energy Storage in Cell Wall – Fracture Release Mechanism: Fluid Pressure Catapult

Arceuthobium (phylum: Tracheophyta, class: Magnoliopsida, order: Santalales, family: Santalaceae (sandalwoods)), commonly known as dwarf mistletoes, is a genus of plants that parasitizes members of Pinaceae and Cupressaceae in Africa, Asia, Europe, Central America, and North America. The ripe fruit of dwarf mistletoes consists of broadly fusiform-spheric seeds attached on short stems (pedicels; Figure 6.10A) [63,64]. An abscission zone, representing the weakest region of the fruit, develops between the stems and the base of the fruit [65]. Inside the fruit, a layer of viscin tissue surrounds each seed (mass of 2–3 mg [65,66]). During swelling of the fruit, the viscin tissue expands and starts to exert a hydrostatic force on the seeds and a tensile stress in the cell walls. After a critical pressure is reached, the cell walls of the pedicel break at the abscission zone, discharging the seeds (in approximately $4.4 \cdot 10^{-4}$ s [65]) and liquid cell content with a deducted initial launch acceleration of 4,791g and launch velocity of 13.7 m/s (terminal velocity 7.5 m/s) in *A. vaginatum* [65]. Hinds *et al.* [67] measured the initial mean velocity of the seeds of four dwarf mistletoe species *A. cyanocarpum* (seed mass 0.9 mg), *A. douglasii, A. cryptopodum* (seed mass 2.3 mg), and *A. americanum* (seed mass 2.0 mg) as 21.3, 22.3, 25.4, and 26.1 m/s, respectively (mean of the four species together 24 m/s). The highest measured launch distance is 14.6 m in *A. cryptopodum* [68] (Figure 6.10B–C). The data by Hawksworth *et al.* [65] and Hinds *et al.* [67] is used by Robinson *et al.* [66] to compute a computer model to determine the epidemiology of dwarf mistletoes.

Elastic Energy Storage in Cell Wall – Fracture Release Mechanism: Swelling Coiling Catapult

The genus *Impatiens* (phylum: Tracheophyta, class: Magnoliopsida, order: Ericales, family: Balsaminaceae), also known as jewelweed and touch-me-not, contains about 850 to 1,000 species of flowering plants found across the Northern Hemisphere and the tropics. In this genus, reproductive units are launched (without fluidic discharge) by a coiling motion of the plant cells. *I. capensis* and *I. glandulifera* grow capsules that consist of five valves around a central stalk (the columella) (Figure 6.11A). The valves contain a bilayer structure [69]: an inner cell-layer that shortens and an outer cell-layer that

6
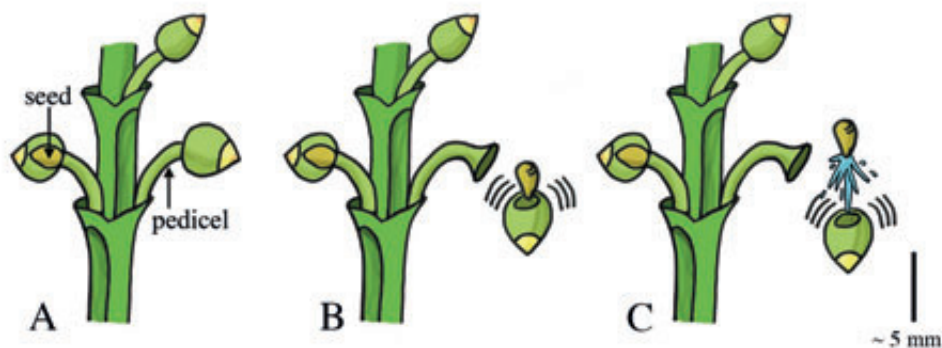
Figure 6.10— Fluid Pressure Catapult Mechanism in *Arceuthobium*. (A) The ripe fruits of *Arceuthobium* that contains the fusiform-spheric seeds and are attached to short stems (pedicels). (B–C) When a critical pressure is reached, the fruit breaks free from the pedicel and discharges the seed together with the liquid cell content. Scale bar 5 mm. Drawings based on schematic drawings in [65].

6

expands by water absorption. Specifically, as the deformation of the adjacent valves is obstructed by their connection to the columella, the inflow of water in the valves tensions the inner cell-layer and compresses the outer cell-layer (Figure 6.11B–C), which in turn results in storage of elastic energy of up to 124 J/kg in the valves of *I. patiens* [69]. Release of tension, as a result of dehiscence of the valves from the columella, creates an inward curvature in the valves, shortening the formerly expanded tension-bearing layer and expanding the formerly compressed layer (Figure 6.11B–D). When the cracks between the valves reach a critical length, rapid (complete) dehiscence allow the valves to rapidly (3 ms) coil towards their relaxed coiled shape, which transforms the stored elastic energy of 8,870 micro-Joule [µJ] into kinetic energy of 0.2–89 µJ of the seeds in *I. capensis* [69] (mean mass 10.7 mg)—an efficiency of approximately 0.5% (the remaining 95% of the energy is used for crack propagation and is dissipated). This results in a peak launch velocity of 4.1 m/s (mean: 1.24 m/s) and a peak seed launch distance of approximately 1.75 m with a mean launch angle of 17.4° to the horizontal in *I. capensis* [69]. In *I. glandulifera*, the stored elastic energy is transformed into 0.4 mJ kinetic energy of the seeds (an efficiency of approximately 44%) [70], resulting in a peak launch velocity of 12.4 m/s (mean: 6.2 m/s), a peak launch distance of 10 m (mean: 3 m), and a mean launch angle of 47.8° to the horizontal [71].

The species *Cornus canadensis* (phylum: Tracheophyta, class: Magnoliopsida, order: Cornales, family: Cornaceae (dogwoods)), commonly known as bunchberry dogwood, is an herbaceous subshrub with white flowers and red fruits. *C. canadensis* has a slightly
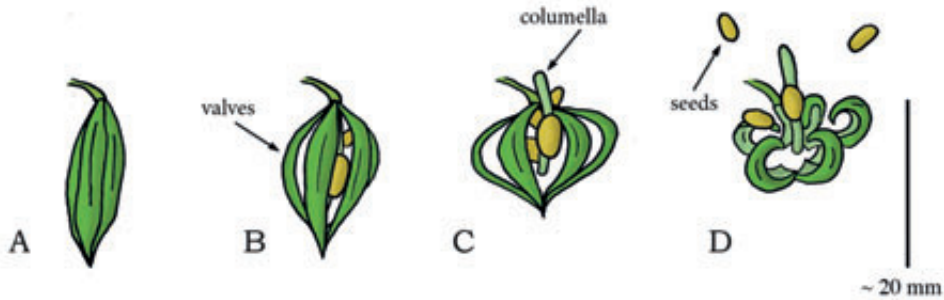
Figure 6.11— Swelling Coiling Catapult Mechanism in *Impatiens capensis.* (A) The seedpod consisting of five interconnected valves. Elastic energy is stored in the seedpod by the absorption of water in the valves. When a critical pressure is reached, dehiscence of the valves from the columella and subsequent coiling discharges the seeds (A–D). (A) Shows the situation at *t* = 0 ms. Duration from (A) to (D) lasts about 3 to 4 ms. Drawings based on schematic drawings in [69]. Scale bar 20 mm.

6

different coiling catapult mechanism for dispersing pollen than that of *Impatiens*. The flower bud of *C. canadensis* contains four interconnected petals and four stamens (Figure 6.12A–B). During flower development, the filaments of the stamens grow faster than the petals. Since the upper ends of the filaments are held in place by the petals, the filaments bend (thereby storing elastic energy) and emerge from between the petals (Figure 6.12A–B). By fracture of the petal connection, the petals rapidly (~ 0.3 ms [72]) separate and flip backwards, allowing the filaments to unfold and accelerate vertically (similar to the way a baseball is accelerated by the sequential deployment of a pitcher's shoulder, elbow, and wrist [33] and a miniature medieval trebuchet [73]) (Figure 6.12C). When the peak vertical velocity is reached (~0.5 ms after petal opening [72]), the filaments start accelerating horizontally and separate from each other, releasing the pollen (mass 0.024 mg [72]) with a mean launch acceleration of 2,446*g* and a peak vertical component of the launch velocity of 7.5 m/s [72,73] (Figure 6.12D). The pollen grains are launched to a height of about 0.027 m with a launch angle of 70–90° to the horizontal (estimated from a figure in [73]) [73].

Another example of a coiling catapult that aids in pollen dispersal is found in the flower buds of *Morus alba* (phylum: Tracheophyta, class: Magnoliopsida, order: Rosales, family: Moraceae (mulberries)), commonly known as the white mulberry tree. *M. alba*, native to northern China, reaches 10 to 20 m in height. The tree has tear-shaped leafs and white fruits and is widely cultivated to feed commercially grown silkworms. The flower bud of this tree contains four stamens. Each stamen consists of a filament with an anther (that contains the pollen) attached at its apex. The anther, in turn, is constrained in movement by the pistillode (i.e. the female ovule-bearing part of the flower bud) and fine threads (Figure 6.13A–B). By water absorption, turgor pressure in the filaments increases
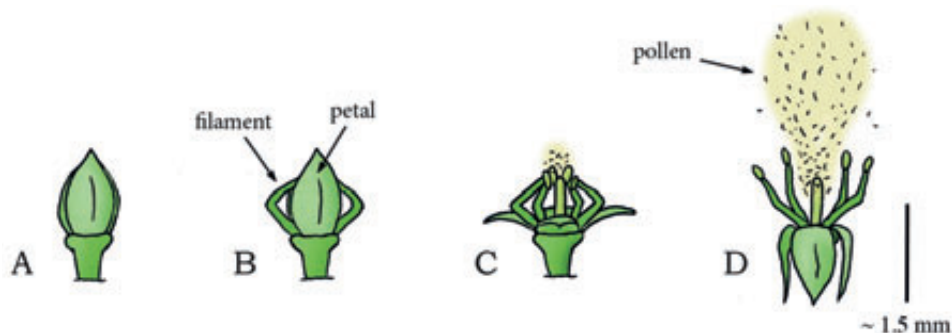
Figure 6.12— Swelling Coiling Catapult Mechanism in *Cornus canadensis*. (A) Immature flower bud of *C. canadensis*. (B) Mature flower bud with filaments emerging from between the petals as the former have grown faster than the latter. (C–D) When a critical pressure is reached, dehiscence of the connection that hold the petals together allow the petals and filaments to unfold rapidly, releasing the stored elastic energy and discharging the pollen into the air. Drawings based on high-speed video images in [73]. Scale bar 1.5 mm.

6

and the filaments bend, storing elastic energy [74]. A drop in relative humidity of the environment leads to slight drying of the anther, which in turn causes the pollen-laden anther to pull away from the base of the filament, tearing the fine threads by which the anther was closed and held in place (Figure 6.13A–B). When the anther subsequently slides off the pistillode, the stored elastic energy in the filament is released, catapulting the anther in an approximately circular path with a peak angular launch acceleration of 5,000,000 radian per second squared [rad/s] while releasing the pollen with an estimated peak linear launch acceleration of 2,500*g* and a peak launch velocity of 237 m/s (mean: 170 m/s) [74] (Figure 6.13C–D).

6.5.2. Osmosis: Water evaporation

Elastic Energy Storage in Cell Wall – Fracture Release Mechanism: Drying Coiling Catapult

In the mustard family Brassicaceae (phylum: Tracheophyta, class: Magnoliopsida, order: Brassicales) a wide variety of seed dispersal methods are found, including the drying coiling catapult in the genus *Cardamine,* commonly known as bittercress. *Cardamine* is a large genus of over 150 flowering plant species growing in diverse habitats all over the world. In this genus, reproductive units are catapulted by a coiling motion of the plant cells (without fluidic discharge) [75]. The fruit of *C. parviflora*, a winter annual that grows up to 35 mm tall, consists of two valves, with the seeds being adhered on the thin internal wall (called the replum) separating the valves (Figure 6.14A–B). During dehiscence, the valves coil outwards in approximately 4.7 ms [75], exposing and launching the seeds
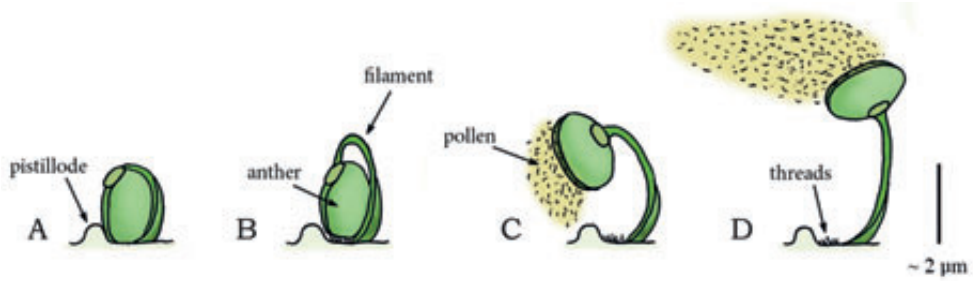
Figure 6.13— Swelling Coiling Catapult Mechanism in the Mulberry *Morus alba*. (A) One of the four filaments with attached anther in the flower bud of *M. alba*. (B) The pressurized filament grows and bends, storing elastic energy as deformation is obstructed by the fine thread connections and the pistillode. (C) Slight drying of the anther tears the thread connections. (D) The anther is catapulted in an approximately circular arch driven by the stored elastic energy of the filament while releasing the pollen. Drawings are based on schematic drawings in [74]. Scale bar 2 μm.

6

(mass of 0.15 mg [75]) with a peak launch velocity of 12 m/s (mean: 6.3 m/s) and a mean launch angle of 52.2° to the horizontal, resulting in a peak launch distance of about 2 m (mean: 0.94 m) (Figure 6.14C–D) [75]. The coiling of the valves in *C. parviflora* is presumably driven by a bi-layered cell-structure that stores an energy amount of approximately 89 J/kg, with energy transfer efficiency to the seeds of 21.3% [75] (cf. the bi-layered cell-structure hypothesized for *I. capsensis* in [69] and presented above). However, disagreement exists about whether drying or swelling is the driving force in the explosive seed dispersal in *Cardamine*. Based on high-speed video analysis and mechanical energy storage measurements (calculated from the integral of the force-length relationship in the valves as measured with a force transducer), Hayashi *et al.* [75] suggest that the valve curling is driven by the absorption of water. Based on electron microscopic images of the cell structure, Vaughn *et al.* [76], on the other hand, argue that the tension built in *Cardamine* is generated upon drying and explicitly refute the model proposed by Hayashi *et al.* [75]. Because Vaughn *et al.* [76] provide more compelling evidence based on the cell structure found in the valves, we classified this mechanism into the water evaporation category. More research is warranted to precisely determine the working principle of the shooting mechanism in *Cardamine*.

Similar drying coiling catapult mechanisms as observed in *Cardamine* are found in the Fabaceae (phylum: Tracheophyta, class: Magnoliopsida, order: Fabales), commonly known as the legume, pea, or bean family. Fabaceae is the third largest land plant family of economically important flowering plants, including trees, shrubs, and herbaceous
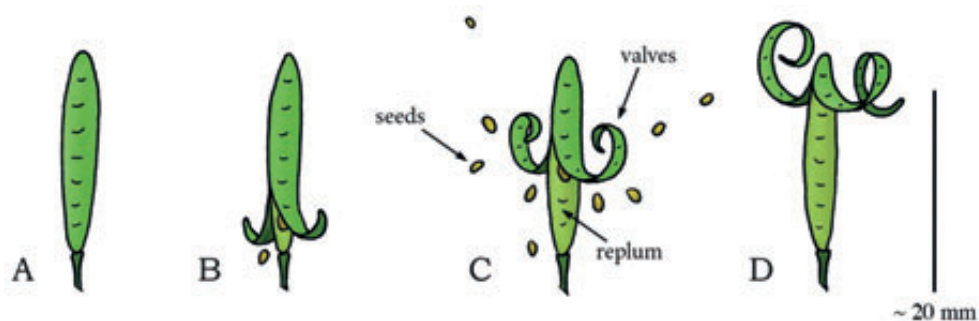
Figure 6.14— Drying Coiling Catapult Mechanism in *Cardamine parviflora* (Brassicales). (A) Immature untriggered seedpod. (B) Early stage of dehiscence of the seedpod with two valves starting to coil outwards. (C) When a critical pressure is reached, the valves coil rapidly outwards, discharging the seeds. (D) The seedpod after discharge. Drawings based on schematic drawings in [75]. Scale bar 20 mm.

6

plants. An example of a drying coiling catapult is found in the legume species *Cytisus multiflorus*, commonly known as the white Spanish broom. The fruit of *C. multiflorus* is a hairy legume pod (resembling a pea pod up to 3 cm in length), which contains four to six seeds. Desiccation of the pod creates tension in different cell layers at different angles. After a critical tension is reached, explosive dehiscence of the pod discharges the seeds at launch distances of up to 4 m [77]. The legume *Tetraberlinia moreliana* uses a slight variant of the drying coiling catapult mechanism. The mature seedpods (containing on average two seeds; mean seed mass 2.53 g) of this rainforest tree are woody structures resembling the shape of a dragonfly wing (Figure 6.15A) [78]. The seedpod consists of two valves enveloping the seeds. Drying of the pods causes tension between the valves, as they would deform into a helical shape without constraints (representing a minimum in the elastic energy content). When a critical pressure is reached, the valves break apart and rapidly coil into a helical shape, discharging the seeds with a peak launch velocity of 70 m/s (mean: 37 m/s), and a peak launch distance of 60 m with a mean launch angle of 17.3° to the horizontal (Figure 6.15B–C) [78]. According to Van der Burgt *et al.* [78] the seeds were not significantly influenced by the wind or aerodynamic lift force during the free flight phase of their experiment and are most likely not dispersed by animals. The measured dispersal distance is thus a direct derivative of the ballistic dispersal process (and the encountered viscous drag). However, based on the shape of the valves, we hypothesize that aerodynamics force may play a significant role and wind dispersal is a real possibility. Finally, the legume *Bauhinia purpurea* also ballistically disperses its seeds [79], but its mechanism was not found in literature.
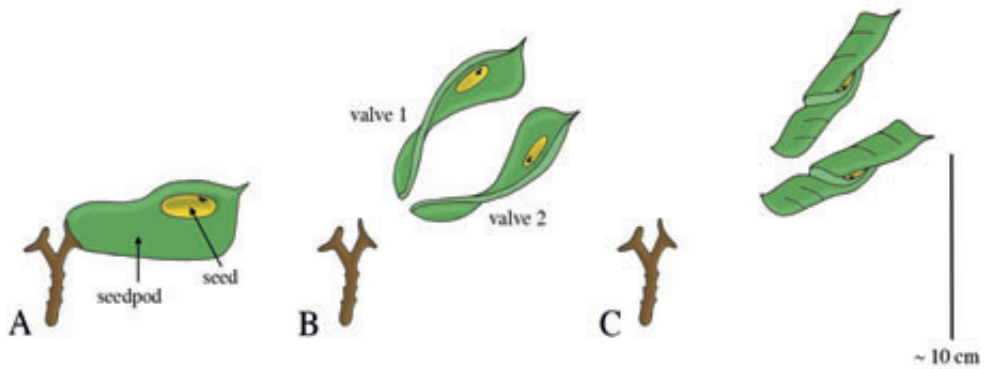
Figure 6.15— Drying Coiling Catapult Mechanism in *Tetraberlinia moreliana.* (A) A fruiting pedicel with one mature seedpod, consisting of two valves (right) and one exploded seedpod (left). Drying of the valves causes tension in the connection between the valves and stalk of the fruiting pedicel, as the preferred dry shape of the valves is helical. (B) Dehiscence of the valves discharges the seeds. (C) Fully dried valve with seed. Drawings based on schematic drawings in [78]. Scale bar 10 cm.

6

Hildebrand [80] was the first to describe the structure of the fruits of Acanthaceae (phylum: Tracheophyta, class: Magnoliopsida, order: Lamiales) that enables them to ballistically disperse their seeds. The seed capsules of the Acanthaceae subfamily Acanthoideae can either be discharged using water absorption or water evaporation, but in both cases the mechanism for discharge is similar [81]. Witztum *et al.* [81] describe the working mechanism of *Ruellia simplex* (synonym *Ruellia brittoniana*), also known as Britton's wild petunia. In this species, the seed capsule consists of two interconnected slender valves enveloping 16–20 seeds (mean seed mass 1.78 mg). A valve consists of three main layers; an inner "resistant" cell-layer (when it dries it only shrinks very minimally), a middle "inert" layer, and an outer "active" cell-layer that shrinks considerably by water evaporation [81] (similar to a bimetal [81]). As the deformation of the adjacent valves is obstructed by their connection, the water evaporation from the valves tensions the active layer. Drying of the capsule thus results in the storage of elastic energy in the valves. Dehiscence of the connection holding the two valves together releases the elastic potential energy stored in the valves and transfers it into kinetic energy of both the valves and seeds. In *Ruellia simplex*, dehiscence is due to moisture absorption of the capsule beak (after the capsule has dried), which weakens the pectic "glue" that holds the valves together, whereas in other species dehiscence is due to the high stress in the bonding layer. The seeds of *R. simplex* are thrown for distances of up to 3 m with a launch angle of 40° [81]. It is suggested by Witztum *et al.* [81] that the mechanical design is optimized to increase the launch distance of the seeds by an optimal cross-sectional

area division of the tissue types in the active and resistance layers, the presence of the "inert" layer, and the use of "jaculators" that optimize the launch angle of the seeds. Another Acanthaceae species that actively disperses it seeds is *Acanthus mollis* [81].

In Geraniaceae (phylum: Tracheophyta, class: Magnoliopsida, order: Geraniales), a family of flowering plants including the genus *Geranium*, multiple ballistic shooting mechanisms for seed dispersal are observed [62]. Stamp *et al.* [62] investigated three species of wild geranium (*G. carolinianum*, *G. maeulatum*, and *G. molle*) in terms of seed dispersal distance and seed morphology. Mean seed dispersal distances of 3.29 m, 3.02 m, and 1.79 m have been observed in *G. carolinianum, G. maeulatum,* and *G. molle*, respectively. Evangelista *et al.* [82] describes the working mechanism of another geranium species: *Erodium cicutarium*, commonly known as common stork's-bill and pinweed. The fruit of this species consists of five interconnected valves (pericarps), containing seeds (mean mass of 5 mg) with so-called awns (i.e. hair- or bristle-like appendages of the seed) (Figure 6.16A) [82]. The preferred dried shape of the cellular structure of the awn is helical, inducing tension in the joined structure of the valves upon drying of the awns. When a critical tension is reached, the joined structure fractures, which releases and subsequently discharges the awns at a mean launch angle of 40° to the horizontal with a peak launch velocity of 10 m/s (mean: 4 m/s), resulting in a peak launch distance of 0.75 m (mean: 0.51 m) (Figure 6.16B–D) [82].

6
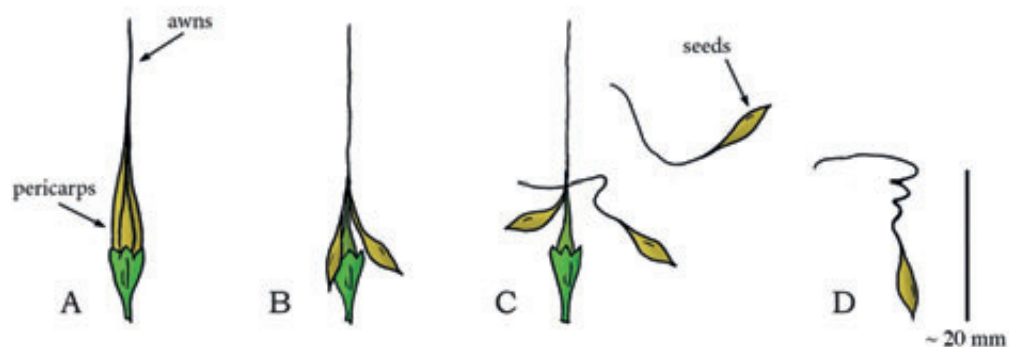
Figure 6.16— Drying Coiling Catapult Mechanism in the Geranium *Erodium cicutarium.* (A) Fruit consisting of five interconnected pericarps with long awns. (B) Dehydration of the awns creates tension in the awns, as the preferred dry shape of the awns is helical, resulting in dehiscence. (C) When a critical stress is reached, complete dehiscence of the connection between the awns discharges the seeds. (D) A discharged dry seed with awn. Drawings based on a photograph in [82]. Scale bar 20 mm.

Elastic Energy Storage in Cell Wall – Fracture Release Mechanism: Drying Squeeze Catapult

Within the spurge family of Euphorbiaceae (phylum: Tracheophyta, class: Magnoliopsida, order: Malpighiales), several species, including *Hura crepitans* and *Mercurialis annua*, are known for their active seed dispersal mechanism. *H. crepitans*, native to tropical regions of North and South America, including the Amazon, is an evergreen spurge tree, which contains long dark spines and a smooth bark. *H. crepitans* is also known as monkeys' dinner bell and monkeys' pistol because of the loud sound made by the fruit capsule during dehiscence, signaling the monkeys that it is time to eat. The fruit of this species is a pumpkin-shaped capsule, consisting of several compartments (carpels) arranged around a central axis (Figure 6.17A–B) [79]. A slightly different geometry of the fruit capsule is observed in the spurge *M. annua*, a small annual herb native to Europe, North Africa, and the Middle East. The fruit of *M. annua* resembles two interconnected spheres, each containing one seed (mass 0.6–3.6 mg), with a suture line running across each of the spheres [83]. *H. crepitans* and *M. annua* both catapult their reproductive units by a "squeeze" force generated by water evaporation in the plant cells. Dehydration-induced tension in the different layers of cells of the fruit wall causes the carpels to separate from the central axis and split into two halves that eject the seeds (mean mass 1,020 mg in *H. crepitans*). In *H. crepitans*, a peak launch velocity of 70 m/s (mean: 43 m/s), a peak launch distance of 45 m (mean: 30 m), and mean launch angle of 34.2° to the horizontal was found [79,84] (Figure 6.17C–D). For *M. annua*, a peak launch distance of 1.3 m (mean: 0.41 m) is reported [83]. The energy storage mechanism and the specific cell structure responsible for the shooting action of both species have not yet been unraveled fully.

6
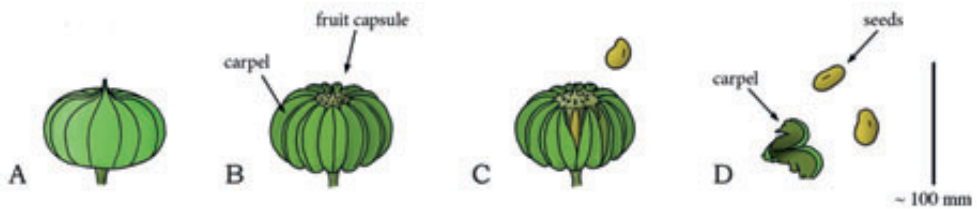
Figure 6.17— Drying Fracture Catapult Mechanism in the *Hura crepitans*. (A) The immature fruit of *H. crepitans*. (B) The full-grown fruit, consisting of several carpels embracing the seeds. (C) When a critical pressure is reached, the carpels split open from the central axis, discharging the seeds. (D) A separated carpel and launched seeds. Drawings based on schematic drawings in [79]. Scale bar 100 mm.

Multiple species of the Rutaceae family (phylum: Tracheophyta, class: Magnoliopsida, order: Sapindales), for example *Metrodorea nigra* [85], the genus *Illicium* (phylum: Tracheophyta, class: Magnoliopsida, order: Austrobaileyales, family: Schisandraceae), for example *Illicium floridanum* (mean seed mass 45 mg) [86], and *Oxalis acetosella* (phylum: Tracheophyta, class: Magnoliopsida, order: Oxalidales, family: Oxalidaceae (woodsorrels)) (mean seed mass 0.9 mg) [87] also use a drying squeeze catapult for discharging their seeds. Similar to *H. crepitans*, the fruits of these families and genera generally consist of multiple interconnected carpels that are radially arranged from a central stalk. During development, the fruits show small splits along the line of separation between the carpels or on the carpel surface. Dehydration of the carpels creates tension along the weakest regions (i.e. the connections between the carpels or along a so-called suture line running along the circumference of the carpels themselves), which eventually causes dehiscence, splitting the carpels into two halves or the carpels from the central stalk. The seeds are subsequently discharged with a launch angle of 40–60° to the horizontal, resulting in a peak launch distance of 5.8 m (mean: 2.5 m) in *I. floridanum* [86]. Furthermore, a peak launch distance of 2 m was found in *O. acetosella* [87].

6

Ballisitic seed dispersal occurs also in *Viola* (phylum: Tracheophyta, class: Magnoliopsida, order: Malpighiales, family: Violaceae), a genus of flowering plants, which share a remarkably similar floral structure [62,88]. Two example species with active seed dispersal are *V. eriocarpa* and *V. striata* [62]. Their shooting mechanism was suggested to be similar to a marble being squeezed by the fingers [88]. A peak launch distance of 5.4 m was found in *V. eriocarpa* [88].

Elastic Energy Storage in Air and Cell Wall – Fracture Release Mechanism: Air Pressure Catapult

In *Sphagnum* (phylum: Bryophyta, class: Sphagnopsida, order: Sphagnales, family: Sphagnaceae), a genus of approximately 120 species of mosses, generally known as peat moss, reproductive units are catapulted by an air jet. The spores of *Sphagnum* are developed within spherical capsules grown on short stalks [89]. The spherical capsule comprises two parts: an upper spore-filled chamber and a bottom air-filled chamber (Figure 6.18A). The capsule wall consists of four to five layers of cells, delimited by a circular line along the operculum rim, which circumscribes the lid of the capsule [89] (Figure 6.18A). The mature capsule is much darker than the stalk; it absorbs light relatively well, which promotes heating and drying of the capsule on sunny days. The mature drying capsule contracts radially, transforming the capsule shape from spherical to cylindrical [33,90,91] (Figure 6.18B). Both the circumference and volume of the capsule reduce, raising the air pressure in the bottom air-filled chamber until a critical pressure (estimated between 0.2 and 0.5 MPa [1,33,90]) is reached. Fast release of the lid triggers

explosive spore discharge by the internal air pressure, at a peak acceleration of 36,697g [1] and a peak launch velocity of 30 m/s (mean: 18 m/s) [90] that propels the spores (20,000 to 240,000 spores per capsule) with an estimated launch angle 80–90° (as measured from a figure in [89]) as high as 0.20 m above the moss (Figure 6.18C–D) [89,90,92]. As we discussed in the section on ascomycetes, the collective discharge of many spores is required to minimize the effect of viscous drag, enabling spores to travel larger distances [1]. In this shooting mechanism, the energy is stored primarily in the compressed air, as well as in the cell wall. The explosive mechanism is no longer observed when the air chamber in the spore capsule is punctured, as this reduces the pressure in the chamber to the ambient value. Nevertheless, the spores can be released slowly from punctured capsules because the lid (partly) separates from the capsule at large radial contractions of the capsule [91]. We note an important difference here compared to shooting mechanisms that rely on the compressive liquid-filled containers discussed above: since a liquid is nearly incompressible (bulk modulus is about $2 \cdot 10^9$ Pascal [Pa = N/m] for water; for air 10^5 Pa), only a small amount of energy can be stored in the liquid, whereas in *Spagnum* the main energy storage used for shooting is in the compressed air.

6

Elastic Energy Storage in Cell Wall – Cavitation Release Mechanism: Cavitation Coiling Catapult

Cavitation-based spore discharge, similar to that of fungi imperfecti, is also observed in the family Polypodiaceae (phylum: Tracheophyta (Pteridophyta), class: Polypodiopsida/
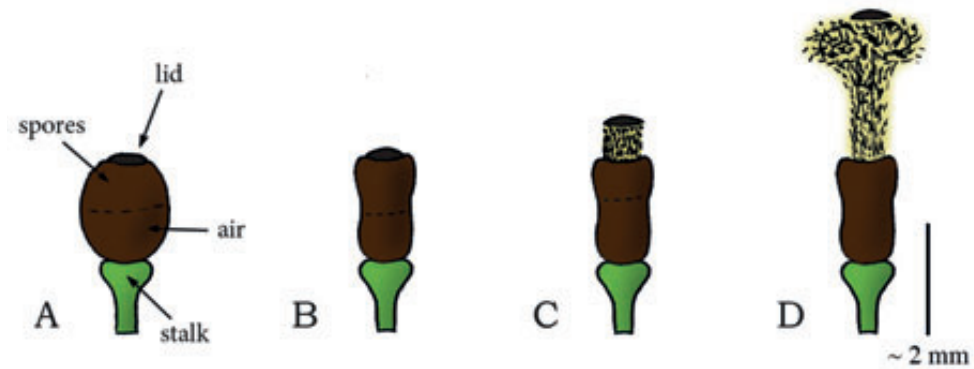
Figure 6.18— Air Pressure Catapult Mechanism in the Genus *Sphagnum*. (A) The mature spherical spore capsule of *Sphagnum* filled with spores and air (equal portions). (B) Deformation of the capsule into cylindrical shape due to drying, which raises the air pressure in the capsule. (C–D) When a critical

pressure is reached, sudden fraction of the capsule lid explosively discharges the spores from the capsule. Drawings based on schematic drawings in [1]. Scale bar 2 mm.

Pteridopsida, order: Polypodiales), also known as common or polypod ferns (e.g. the species *Adiantum peruvianum* [93] and *Polypodium aureum* [94]) [8,37,94,95]. Most species in the family Polypdiaceae are epiphytes (i.e. plants that grow harmlessly on another plant and derive water and nutrients directly from the air, rain, and decaying material in their surroundings). The spore-bearing structure of common ferns consists of a stalk and an annulus of twelve or thirteen cells forming a circular crest that encloses the spores (Figures 6.19 and 6.20A). Evaporation of water from the cells' cytoplasm brings the radial walls closer together and makes the lateral walls collapse internally (Figures 6.19A–C and 6.20A–C), causing the annulus to open at the stomium (Figure 6.20A) and expose the spores (Figure 6.20B) [93]. When the water tension reaches a critical negative value of -9 to -20 MPa relative to ambient [8,93], the cytoplasm fractures and cavitation occurs within adjacent cells (Figure 6.19D and Figure 6.20C), leading to a quick release of the stored elastic energy of the cell walls as the annulus snaps back to its original shape (~0.01 ms [94]). This rapid motion catapults the spores with a peak launch acceleration of approximately 100,000g and a peak launch velocity of 10 m/s in *Polypodium aureum* (Figure 6.20D) [94,95]. From data in [93], we estimated a peak spore launch distance of 0.057 m in *A. peruvianum*.

A similar pollen dispersal mechanism as those in common ferns is observed in representatives of the genus *Selaginella* (phylum: Tracheophyta (Lycopodiophyta), class: Lycopodiopsida, order: Selaginellales, family: Selaginellaceae), such as in *Selaginella martensii,* a spikemoss that is native to Mexico and Central America and in which both microspores and megaspores are actively dispersed [96]. *S. martensii* has ascending stems with spore-bearing structures, or sporangia, born on the top surface of a modified leaf or sporophyll and clustered together into cones, also known as strobili, approximately between a few centimeters and 30 cm above the soil surface [96]. Active dispersal of the microspores is due to cavitation-induced drying of the valves of the microsporangium. Due to drying, the two valves separate along the dehiscence line and bend away from each other up to an angle of 150° [96]. When the water tension reaches a critical negative pressure, cavitation occurs within the valves, leading to a quick release of the stored elastic energy as the valves snap back to their original shape and catapult the microspores with a peak launch velocity of 0.6 m/s, resulting in a peak launch distance of 6 cm [96]. Presumably, the compressed air between the valves results into a jet that helps to disperse the microspores. Additionally, Schneller *et al.* [96] noticed that thousands of microspores are discharged simultaneously, allowing for a greater dispersal distance and the crossing of the boundary layer by negating the range constraints imposed by viscous drag just as in ascomycetes and *Sphagnum*. The dispersal mechanism of megaspores of *S. martensii* is slightly different and consists of two main steps. First, the lower boat-like part of the spore-bearing structure (comprising two valves) constricts upon drying, pressing the

6

two upper spores together until they are discharged, similar to the drying squeeze catapult (see above). Next, the bases of the lower boat-like part of the spore-bearing

6

Table 6.2— Summary of Launch Parameters of the Identified Shooting Mechanisms in Plants. For the projectile mass, launch velocity, launch acceleration, launch distance, and launch angle, the measurement technique is coded as following: Standard = measured using a high-speed video camera. Bold = calculated by referred authors using measured launch parameters. *Italics* = manual measurement of the parameter (e.g. from photograph stills, without the use of a high-speed video camera). <u>Underlined</u> = calculated by referred authors using a mathematical model of the shooting mechanism. Standard* = estimated by us from data/figure in indicated reference(s); for the power output per unit mass the launch acceleration $[m/s^2]$ is multiplied with the launch velocity $[m/s]$ and for the work per unit mass the power output $[W/kg]$ is integrated over the launch duration $[s]$. Bold* = calculated by us using the mean of the parameter ± 3 standard deviations. The launch parameters are indicated as mean (± standard deviation), peak (indicated with "peak" behind the value), or a range (minimum value–maximum value). Per launch parameter, the peak value identified in this review is indicated by a blue-lined box (with the exception of the launch angle).

Plants	Projectile mass [mg]	Launch acceleration [g]	Launch velocity [m/s]	Launch distance [m]	Launch angle [°]	Power output [W/kg]	Launch duration [ms]	Work [J/kg]
Osmosis: Water Absorption								
Elastic Energy Storage - **Fracture Release Mechanism**								
Fluid Pressure Catapult								
Arceuthobium [53,65-68]								
Arceuthobium americanum [67]	2.0	·	26.1 ± 0.2	·	·	·	0.1-0.2*	·
Arceuthobium cyanocarpum [67]	0.9	·	21.3 ± 0.3	·	·	·	·	·
Arceuthobium cryptopodum [67,68]	2.3	·	25.4 ± 0.3	14.6 peak	·	·	·	·
Arceuthobium douglasii [67]	·	·	22.3 ± 0.4	·	·	·	·	·
Arceuthobium vaginatum [65]	·	~ 4,791	~ 13.7	4.6	·	·	~ 0.44	·
Swelling Coiling Catapult								
Impatiens								
Impatiens capensis [69]	10.7 ± 0.4 (7.7-19.7)	·	1.24 ± 0.14 (4.1 peak)	1.75 peak	17.4 ± 5.2	·	4.2 ± 0.4	-*
Impatiens glandulifera [70,71]	20.7 (8.8-30.3)	·	6.19 (2.57-12.4)	0-10	47.8 (37.1-79.7)	·	·	·

6

6

Continuation of Table 6.2— Summary of Launch Parameters of the Identified Shooting Mechanisms in Plants.

Cornus canadensis [72,73]	0.024	2,446 ± 612	3.1 ± 0.5	0.025 (0.022-0.027)	70-90*	7.3·10⁴* (1.9·10⁵ peak*)	0.5	36.5 (95 peak)*
Morus alba [74]	-	2,500 peak^b	170-237^b	-	0-180*	2.6·10⁵ (5.81·10⁶ peak*)	≤0.025	≤6.5 (≤145.3 peak*)
Osmosis: Water Evaporation								
Elastic Energy Storage – Fracture Release Mechanism								
Drying Ceiling Catapult								
Brassicaceae								
Cardamine								
Cardamine parviflora [75,76]	0.15 ± 0.09	-	6.29 ± 2.73	0.94 ± 0.46	52.2 ± 23.9	1.9·10⁴* (2.64·10⁵ peak*)^c	4.7 ± 1.3	89.3 ± 40.5
Fabaceae								
Cytisus	-	-	-	4 peak	-	-	-	-
Tetraberlinia moreliana [78]	2,530	-	37.1	60 peak	17.3 ± 11	-	-	-
Acanthaceae								
Ruellia simplex [81]	1.78	-	-	2-3	40	-	-	-
Geraniaceae								
Geranium [62]								
Geranium carolinianum	3.5 ± 0.3	-	-	3.29 ± 0.7	45.5 ± 3.1	-	-	-
Geranium maculatum	6 ± 0.9	-	-	3.62 ± 0.76	47.3 ± 10.0	-	-	-
Geranium molle	1.1 ± 0.1	-	-	1.79 ± 0.43	61.2 ± 2.1	-	-	-
Erodium								
Erodium cicutarium [82]	5 ± 1	-	4 ± 2^d	0.51 ± 0.08	40 ± 30	-	-	≤*
Drying Squeeze Catapult								
Euphorbiaceae								
Hura crepitans [8,79,84]	1,020 (700-1,430)	-	43 (14-70)	30 (45 peak)	34.2 (20-48)	-	0.01-0.035*	-
Mercurialis annua [83]	0.7-3.6	-	-	0.41 ± 0.31 (1.3 peak)	-	-	-	-

Continuation of Table 6.2— Summary of Launch Parameters of the Identified Shooting Mechanisms in Plants.

Taxon / Mechanism							
Rutaceae							
Metrodorea nigra [85]	·	·	·	·	·	·	+
Illicium							
Illicium floridanum [86]	45 ± 4 (50 peak)	2.5 ± 1.4 (5.8 peak)		40-60	·	·	+
Oxalis acetosella [87]	0.9 (0.3–1.5)	2 peak		·	·	·	+
Viola [62,88]							
Viola blanda		1 (0.1–3.8)		·	·	·	+
Viola curculliata		1.5 (0.1–2.1)		·	·	·	+
Viola eriocarpa	6 ± 0.9	1.2 (0.2–5.4)		67.5 ± 14.5	·	·	+
Viola papilionacea		2.1 (0.05–4.8)		·	·	·	+
Viola pedata		1.4 (0.25–5.1)		·	·	·	+
Viola rostrata		1.2 (0.1–4.2)		·	·	·	+
Viola striata	1.1 ± 0.2	1.5 (0.4–3)		·	·	·	+
Air Pressure Catapult							
Sphagnum [1,33,89,90]	·(36,697 peak)	16 (30 peak)	0.15 (0.1–0.2)	80-90*	$\cdot(1.08 \cdot 10^7\ \text{peak*})$	0.01	·(108 peak*)[1]
Elastic Energy Storage - Cavitation Release Mechanism							
Cavitation Ceiling Catapult							
Polypodiaceae (common ferns) [94,95]							
Polypodium aureum [94,95]	~100,000	10	0.01–0.02	·	$9.81 \cdot 10^4$*	≤ 0.01	≤ 98.1*
Adiantum peruvianum [93]	6,320 at 3.1 m/s	2.4 ± 1 (5.0 peak)	0.057 peak*	·	$1.48 \cdot 10^5$ ($3.09 \cdot 10^5$ peak)*	0.01*	1.48 (3.09 peak)*
Selaginella							
Selaginella martensii [96]	·(0.6)‡	0.01–0.05	·		< 1		·

6

[a] Stored elastic energy: 8.87 J (efficiency of 0.5%) [69]

[b] Average angular velocity: 69,800 rad/s and peak angular acceleration: $5 \cdot 10^6$ rad/s^2 [74]

[c] Mean estimated stored energy: 0.482 ± 0.219 J ($21.3 \pm 10.3\%$ efficiency) [75]

[d] Initial angular velocity: 200 ± 100 rad/s [82]

[e] Estimated released elastic energy: $2.72 \cdot 10^{-3}$ J [82]

[f] Energy stored in the compressed air: 0.27 mJ [1]

[g] Indicated values for microspore discharge. Macrospore (mass 0.0014 mg) discharge via drying squeeze catapult with a mean launch velocity of 4.5 m/s and a mean launch distance of 0.21 m (peak 0.65 m) [96]. The estimated impulse of one macrospore is 6.3 pN·s [96].

structure clash together and eject the second spore pair (mean mass $1.4 \cdot 10^{-3}$ mg). The spores are ejected with a peak launch velocity of 4.5 m/s, resulting in a peak launch distance of 0.65 m (mean: 0.21 m) [96]. The estimated impulse of one megaspore is 6.3 picoNewton second [pN·s] [96].

6
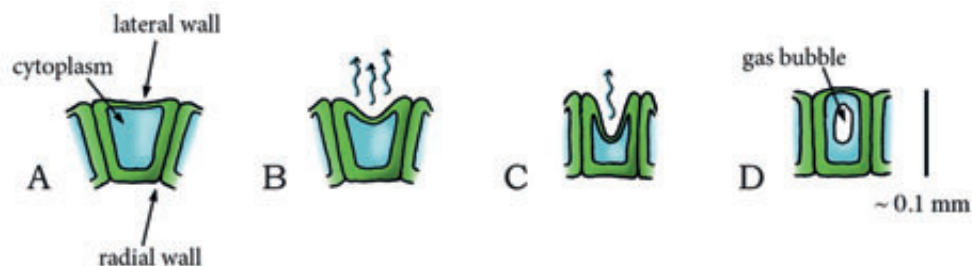
Figure 6.19— Cavitation in Plant Cells. A regular plant cell consisting of a cell wall and cytoplasm. (B) Evaporation of water from the cell causes the radial walls to come closer together and the lateral wall to cave inwards. (C) The lateral wall is caved inwards completely. (D) When a critical pressure is reached, the cytoplasm fractures and a gas (cavitation) bubble appears, causing the walls to rapidly snap back to their original form. Drawings based on figures in [95]. Scale bar 0.1 mm (100 μm).
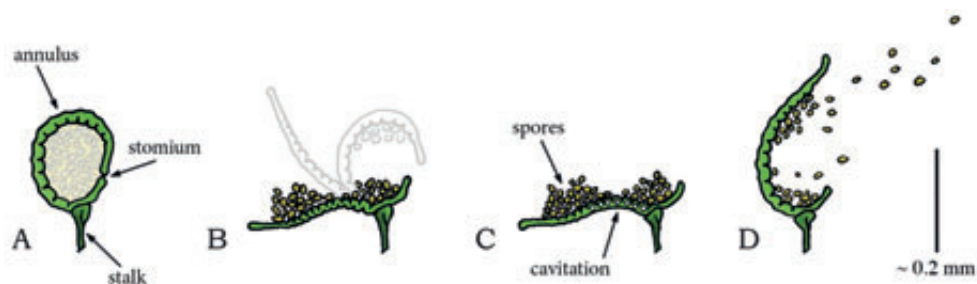
Figure 6.20— Cavitation Catapult Mechanism in the Family Polypodiaceae or Common Ferns. (A) The mature sporangium in common ferns consisting of a stalk and an annulus enclosing the spores. (B) Dehydration of the annulus cells causes the radial cell walls to come closer together and the lateral walls to collapse internally, straightening the annulus. (C) When a critical pressure (between -9 and -20 MPa relative to ambient) is reached, cavitation occurs in the cells of the annulus. (D) Discharge of the spores by quick release of the elastic energy stored in the cell walls as the annulus snaps back to its original shape. Drawings based on high-speed images in [94]. Scale bar 0.2 mm (200 μm).

6.6. ANIMALS

Figure 6.21 illustrates the shooting mechanisms identified in animals, allocated based on the energy management criteria discussed above. In contrast to the plants and fungi, where shooting mechanisms are primarily used for increasing reproductive success, in the animal kingdom, shooting mechanisms have also evolved for prey capture, locomotion, and anti-predator defense. An overview of all retrieved launch parameters and the associated measurement methods of the identified shooting mechanisms in animals is provided in Table 6.3.

6.6.1. Osmosis: Water Absorption

Elastic Energy Storage in Cell Wall – Eversion Release Mechanism: Osmotic-Powered Eversion Catapult

The eversion catapult is a mechanism referring to the discharge process of the cnidocyte: a specialized explosive stinging cell used for prey capture, anti-predator defense, and locomotion (Figure 6.22A) [29,97-103]. The cnidocyte is the distinguishing feature of Cnidaria, an ancient phylum of aquatic animals (>500 million years old) that includes jellyfish, sea anemones, and corals [104]. Three main types of cnidocytes are identified: (1) spirocysts, which are used to immobilize prey as they surround and adhere to prey; (2) ptychocysts, which are used by sea anemones to construct the tube in which they live; and (3) nematocysts, the most diverse group of cnidocytes, of which at least some are associated with penetration and the injection of venom [29,103,105]. Each cnidocyte contains an organelle called cnida. The cnida comprises a bulb-shaped capsule with a multi-layered [106,107] collagenous wall and a lid (operculum) that closes the capsule [100,108]. Attached to the capsule is an inverted shaft with a highly folded 3–100-μm long hollow tubule (mass of 2.3 ng; accelerated mass approximately 1 ng [2]) containing a thorn-like stylus of varying morphology between species [106-110]. Within the cnida, regulation of osmolytes leads to water absorption, which increases the osmotic pressure up to 15 MPa [102,108]. This water absorption subsequently expands the volume of the cell and stretches the elastic collagenous capsule wall [2,29,101]. When the sensory receptor (cnidocil) of the cell is triggered by either physical or chemical stimuli (e.g. vibrations or light changes) [97,98,100,101], the operculum opens, and the shaft with the tubule everts [2,97,101,104,106-109] and is discharged from the cell with a peak launch acceleration of 5,413,000g and a peak launch velocity of 37.1 m/s (mean: 18.6 m/s) [2,29] (Figure 6.22B–C). Next, the shaft and stylus punch a hole into the prey's cuticle or skin of 100–600 μm in depth in jellyfish [101], with an acceleration force of 13.2–53.1 μN, kinetic energy of 0.17–0.7 μJ, and a theoretical penetration pressure of nearly 8 GPa, which is in the range of bullets [2,29] (Figure 6.22B–D). The high penetration pressure is partly due to the small surface of the stylus. Based on the acceleration and velocity data, we estimated a peak mass-specific power output of shooting mechanism of 1.97·10^9

W/kg, which is about $1.75 \cdot 10^6$ times the maximum mass-specific power output of muscles [23,24], indicating the use of an elastic enhancement mechanism for the shooting action. Finally, the tubule completely everts under the built pressure and releases toxic substances into the prey or foe.
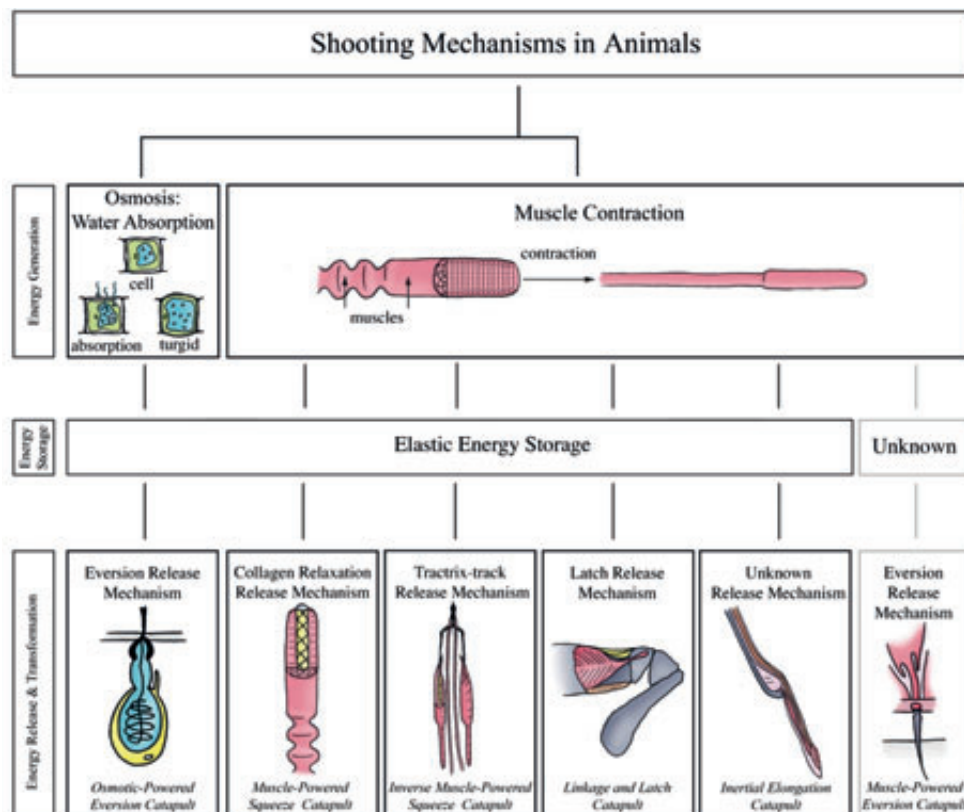
Figure 6.21— The Structural Categorization of the Identified Shooting Mechanisms in Animals, Allocated Based on the Energy Management Criteria Discussed Above. Osmotic-powered eversion catapult: observed in the phylum Cnidaria. **Muscle-powered squeeze catapult**: observed in the family Chamaeleonidae, schematic illustration of *Chameleo calyptratus*. **Linkage and latch catapult**: observed in the order Stomatopoda, schematic illustration of *Odontodactylus scyllarus*. **Inertial elongation catapult**: observed in the families Bufonidae, Microhylidae, Dendrobatidae, Megophryidae, Leptodactylidae, and Ranidae within the order Anura, schematic illustration of *Bufo marinus*. **Muscle-powered eversion catapult**: observed in the families Ariophantidae, Bradybaenidae, Dyakiidae, Helicidae, Helminthoglyptidae, Hygromiidae, Parmacellidae, Urocyclidae, and Vitrinidae, within the clade Stylommatophora.
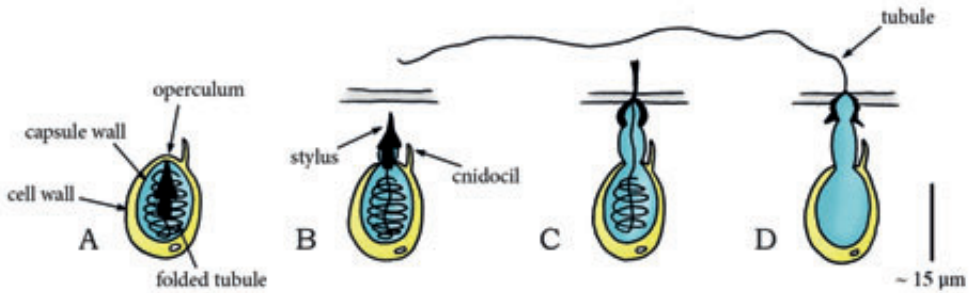
Figure 6.22— Osmotic-Powered Eversion Catapult Mechanism in the Phylum Cnidaria. (A) The cnidocyte, consisting of a cell wall, capsule wall, folded tubule, and enclosed operculum. (B–C) After triggering the cnidocil, the operculum opens, and the shaft with stylus is discharged into the prey's cuticle. (D) The cnidocyte with a totally everted tubule. Drawings based on schematic drawings and high-speed video images in [29]. Scale bar 15 µm.

6

6.6.2. Muscle Contraction

Elastic Energy Storage in Collagen Fibers – Collagen Relaxation Release Mechanism: Muscle-Powered Squeeze Catapult

The use of a prehensile tongue for capturing prey is a typical feature of the three main iguanian lizard families Iguanidae, Agamidae, and Chamaeleonidae (phylum: Chordata, class: Reptilia, order Squamata) [111]. Although all iguanian lizards use their tongue to capture prey, there are differences in the mechanism and the maximum protrusion and projection distances of the tongue. Three mechanisms of tongue protrusion are observed: (1) the tongue may undergo hydrostatic elongation, (2) the tongue may be drawn anteriorly out of the mouth by the M. genioglossus (i.e. a strong tongue muscle running from the tongue to the anterior part of the lower jaw, the chin), and (3) contraction of the M. verticalis (i.e. an intrinsic tongue muscle found at the borders of the anterior part of the tongue) surrounding a stiff bone called the entoglossal process may cause the tongue to slide forward [112]. As only the third mechanism of tongue protrusion can contain a ballistic phase, we will only discuss this mechanism. It must be noted, however, that the different mechanisms of tongue projection in iguanian lizards are not mutually exclusive and may be combined to create a variety of tongue movements.

Chamaeleonidae (phylum: Chordata, class: Reptilia, order: Squamata, suborder: Iguania), a family of old-world lizards known as chameleons, are a distinctive and highly specialized clade of over 200 described species that are found in warm habitats such as rain forest, savannas, and deserts, with various species occurring in Africa, Madagascar, Southern Europe, and Southern Asia. They are known (amongst others) for their ballistic

tongue, which they use for ambushing and catching prey. For this purpose, they use a muscle-powered squeeze catapult that consists of a slender cylindrical tongue bone, the entoglossal process, surrounded by thin nested sheaths with helically wound collagen fibers (in clock-wise and anti-clockwise directions) [30] and a peripheral tubular accelerator muscle with spiral-shaped muscle fibers that are oriented perpendicular to the longitudinal direction [113] (Figure 6.23A). The accelerator muscle is activated approximately 200–300 ms prior to discharge in *Chameleo jacksonii* [114]. Contraction of the muscle fibers in the accelerator muscle leads to an inwardly directed normal force on the sheaths and a longitudinal pressure gradient in the muscle due to volume conservation [30]. Radial contraction of the accelerator muscle and its concomitant elongation (due to volume conservation) stretches and tensions the collagen fibers in the sheaths between the muscle and bone, primarily by the elongation of the sheaths [26,30] (Figure 6.23B). The stretched collagen fibers store elastic energy and exert inwardly directed normal stresses on the underlying bone. At a certain elongation of the accelerator muscle and sheaths, the most anterior collagen fibers in the collagen sheaths slide over the tip of the tongue bone, which starts the tongue projection. The force exerted by the stretched sheaths on the tongue tip results in a longitudinal (axial) reaction force of the bone on the tongue pad, which accelerates the pad forward [113]. This leads to a sliding motion of the sheaths and a sequential push off from the tongue tip of the entire sheaths (cf. 'sliding spring theory' [113]). The motion of the sheaths over the tongue tip reduces their diameter locally, allowing the helically arranged collagen fibers to shorten and thus release the stored elastic energy [30,113,115]. This elastic energy is directly converted into kinetic energy of the tongue pad. Frictional losses are thought to be very low due to the smooth inner and outer surfaces of the innermost sheath and the tongue bone, respectively, and the presence of a lubricant. Recently, the elastic mechanism has been modeled by Moulton *et al.* [116]. The tongue is projected forward up to 200% of the snout-vent (or body) length until it contacts the prey, such as a locust [30,115,117] (Figure 6.23C–D). The actual projection distance depends on initial prey distance and species. A highly viscous mucus on the tip of the tongue [118] and shape-adaptable concavity of the anterior pad [117] prevent the prey from escaping at this point. Finally, the tongue is retracted by the retractor muscles (Figure 6.23A) [119]. The launch acceleration, velocity, and power output depends on species, with the higher values measured (using high-speed video cameras or Doppler radar [120]) in the smaller species [3,121]. The maximum reported acceleration is 264*g*, observed in *Rhampholeon spinosus* [3], and the maximum reported peak launch velocity is 6 m/s, observed in *Chameleo melleri* [30]. Most mass-specific power output values for tongue projection in chameleons exceed 3,000 W/kg [3,30], with a maximum of 14,040 W/kg in *R. spinosus* [3], indicating that an elastic-recoil mechanism is used to enhance power output during the projection phase. This elastic mechanism allows chameleons to perform consistently in a large temperature range [26,27].

6
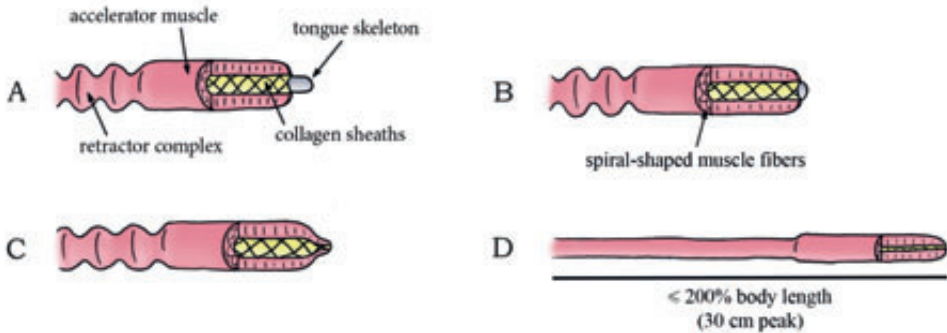
Figure 6.23— The Muscle-Powered Squeeze Catapult Mechanism in the Family Chameleonidae or Chameleons (Species *Chameleo pardalis*). (A) The chameleon tongue consisting of the tongue skeleton (entoglossal process), accelerator and retractor muscles, and nested collagen sheaths. (B) Activation of spiral-shaped muscle fibers in the accelerator muscle leads to radial contraction and elongation of the muscle and stretches the helically wound collagen fibers in the sheaths. (C–D) The accelerator muscle and sheaths slide off the tip of the bone, releasing the stored elastic energy, and forcing the tongue forward. Drawings based on schematic drawings in [30]. Scale bar indicates a length of up to 200% body length (peak distance of 30 cm in *Chameleo calyptratus* [30]).

Plethodontidae (phylum: Chordata, class: Amphibia, order: Urodela), known as lungless salamanders, form the largest family of salamanders, with over 380 species described. Most plethodontid species are located in damp regions on the Western Hemisphere, with species found in British Columbia, Brazil, Southern Europe, and South Korea. Since Plethodontidae lack lungs, they rely on respiration through their skin and tissues lining their mouths. Ballistic tongues have evolved in at least three different clades of the lungless salamanders [31]. Their ballistic tongues are used to catch elusive prey such as flies [122]. The description given below is typical for the situation in the genera *Hydromantes* and *Bolitoglossa*. They use a muscle-powered squeeze catapult mechanism which might be considered as the inverse version of the mechanism employed by chameleons [123]. In the lungless salamanders, the tongue skeleton is made of seven flexible, interlinked cartilages, forming a fork with two posteriorly pointing teeth [117,124,125]. Each tooth (the 'epibranchial cartilages') of the fork is surrounded by a connective tissue sheath and the protractor muscle (the M. subcualis rectus, the function of which corresponds to that of the accelerator muscle in the chameleon), which in turn is connected to the body of the salamander [123,126] (Figure 6.24A). The protractor muscles are activated approximately 123 ms prior to launch in *Hydromantis imperialis* [123]. Their contraction presumably stretches the collagen fibers in the sheaths between each of the

6

protractor muscles and the tongue skeleton, loading the sheaths with elastic energy. The protractor muscles and sheaths drive the posterior ends of the skeleton forward (Figure 6.24B) [123,126]. The tongue skeleton is guided through a tractrix-shaped track in the mouth formed by the lateral wall of the cavity of the retractor muscles [125]. At a critical pressure (delivered by the protractor muscles), the tongue skeleton folds towards the midline as it slides forward through the tractrix-shaped track, forming a thin elongated lingual skeleton that is shot towards prey [122,124,126] with a peak launch distance of 80% of the body length in *Hydromantes* [117,122-124,127] (Figure 6.24C). A peak launch acceleration of 458*g* and a peak launch velocity of 7.0 m/s have been observed in *Bolitoglossa dofleini* [31]. The majority of the mass-specific peak-power output values for tongue projection in lungless salamanders exceed 2,000 W/kg, with a measured maximum of 18,129 W/kg in *B. dofleini* [31,128], indicating that an elastic-recoil mechanism is used to enhance power output [128]. Furthermore, tongue projection performance is maintained over a large temperature range (2–24°C), corroborating the presence of a catapult mechanism [128]. After the sticky tongue pad has contacted the prey, with a force between 0.026–0.44 gram depending on the distance to the target [126], it is rapidly retracted and the mouth is opened further to make room for the tongue and prey [122,124,128]. Finally, the mouth closes, enwrapping the prey. Thus, in the

6
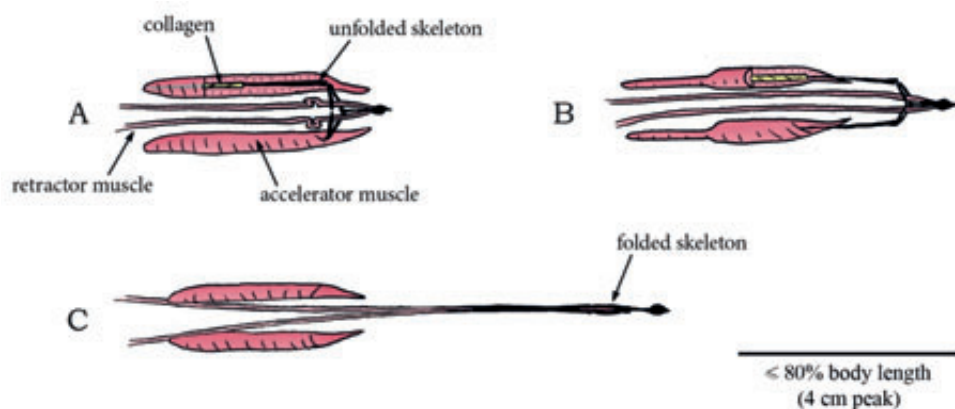
Figure 6.24— The Muscle-Powered Squeeze Catapult Mechanism in the Family Plethodontidae or Lungless Salamanders (Species *Hydromantes supramontis*). (A) The tongue with the unfolded tongue skeleton, two accelerator (or protractor) muscles, collagen fibers in the sheaths between the accelerator muscles, and retractor muscle. (B) Contraction of the accelerator muscle loads the sheaths with elastic energy and forces the two posterior ends of the skeleton forward. (C) Folding of the tongue skeleton to the midline during discharge. Drawings based on schematic drawings in [127]. Scale bar indicates a length of up to 80% of the body length (peak launch distance 4 cm in *Hydromantes genei* [31]).

lungless salamanders, the tongue skeleton is accelerated off the muscles and projected towards the prey, whereas in chameleons the soft parts of the tongue are accelerated off the entoglossal process. The catapult mechanism that evolved in both these disparate clades is nevertheless very similar. The different tongue architectures are presumably the result of different initial conditions of the evolutionary process that yielded these highly effective prey capture devices.

Elastic Energy Storage in Saddle-Shaped Structure – Latch Release Mechanism: Linkage and Latch Catapult
Stomatopoda (phylum: Arthropoda, class: Malacostraca), commonly known as mantis shrimps, is an order of marine crustaceans consisting of over 450 species. Mantis shrimps come in a variety of sizes, from a few centimeters up to 40 centimeters, and colors, from brown to several vivid colors in the peacock mantis shrimp (*Odontodactylus scyllarus*). They can be found in shallow, tropical and subtropical marine habitats. These solitary crustaceans spend most of their time hiding in rock formations or burrows, from where they either ambush prey by sitting and waiting for prey to chance upon them, or hunt, chase, and kill prey using a fast appendage strike, which produces forces of up to 1,500 N depending on appendage size [129,130]. The appendage consists of a saddle-shaped elastic structure located between the base (or merus) and the flexing part (or propodus) of the appendage (Figure 6.25A). This saddle-shaped spring is compressed and latched by the simultaneous contraction of the extensor and flexor muscles (Figure 6.25B) [131]. When the flexor muscle relaxes, the latch is released, allowing the appendage to rotate outwards (Figure 6.25C–D) [129-133] with a maximum reported peak launch acceleration of 10,601g and a peak launch velocity of 23 m/s observed in *O. scyllarus* [25,131]. Based on this data, a mean power output of 470,000 W/kg is conservatively calculated in *O. scyllarus* [25]. Furthermore, *O. scyllarus* and some other species of mantis shrimps are so fast that they are able to create cavitation bubbles that can aid to stun prey by generating shockwaves, bright light flashes, and rapidly heat the water, when they implode [25,130].

Elastic Energy Storage – Unknown Release Mechanism: Inertial Elongation Catapult
Early studies of the feeding system in anurans (frogs of the phylum Chordata, class: Amphibia) identified three basic mechanisms of tongue protraction: hydrostatic elongation, mechanical pulling, and inertial elongation [134,135]. As only the third mechanism contains a ballistic phase, only this mechanism will be discussed. The inertial elongation catapult is probably the most prevalent mechanism of tongue protraction among anurans (frogs of the phylum: Chordata, class: Amphibia) [134] and is characterized by tongue lengthening under inertial and muscular loading using a rapid jaw depression [16,134-136]. It has evolved at least seven times independently in the

6
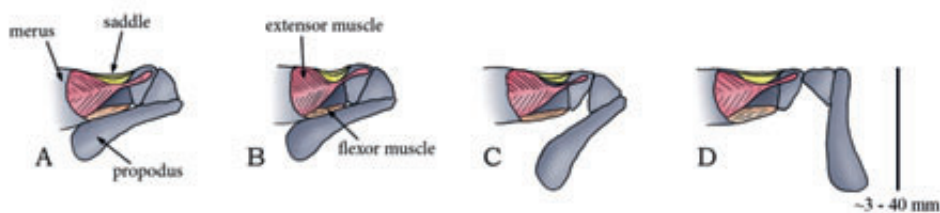
Figure 6.25— Linkage and Latch Catapult Mechanism in the Phylum Stomatopoda (Species *Odontodactylus scyllarus*). (A) The appendage of the mantis shrimp consisting of a saddle-shaped elastic structure located between the merus and the propodus. (B) Compression of the saddle and latching of the propodus by the simultaneous contraction of the extensor and flexor muscles. (C–D) Release of the latch by relaxation of the flexor muscle, allowing outward movement of the propodus. Drawings based on schematic drawings in [133]. Scale bar indicates the length of the propodus, which is in between 3 and 40 mm.

families Bufonidae (of which *Bufo* is the most widespread genus) [16], Hylidae (including the genera *Pachymedusa* and *Phyllomedusa*) [16,137], Microhylidae (including the genus *Dyscophus*) [138], Dendrobatidae, Megophryidae, Leptodactylidae, and Ranidae (including the genus *Rana*) [135,136,139,140]. The tongues of most frogs and toads in these families are attached anteriorly at the front of the jaw and have a resting length of approximately the size of the jaw [117] (Figure 6.26A). During tongue protrusion, the tongue initially shortens by contraction of the protractor muscle, moving the tongue up- and forward (Figure 6.26B). Subsequently, a rapid jaw depression elongates and moves the tongue downwards under inertia to catch elusive prey [16,136,138,139,141] (Figure 6.26C–D). The maximum reported tongue acceleration is 31.6g and the maximum reported peak tongue velocity is 2.9 m/s, both observed in *Bufo marinus* [136]. After the prey is caught, the retractor muscle retracts the tongue, while the mouth is opened further to accommodate the prey (Figure 6.26B) [139].

There are several indications that elastic recoil is used in the rapid jaw depression. Firstly, the jaw depressor muscles are active prior to the onset of jaw depression, pointing towards an energy-storing phase [142]. Secondly, the ballistic tongue protrusion is not influenced by temperature changes (tested between 10 and 35°C), yet pronounced differences are visible for tongue retraction and mouth closing [139,143]. Thirdly, the power of ballistic mouth opening reaches a peak of 9,600 W/kg [142] and 1,783 W/kg (885 W/kg for tongue protrusion) [139] in *B. alvarius* and *Rana pipiens*, respectively, exceeding what amphibian muscles can directly produce [22] by more than 10 times in the case of *B. alvarius* and by almost 5 times in *R. pipiens*.
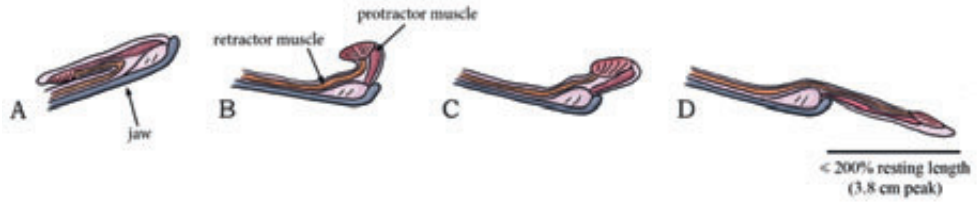
Figure 6.26— Inertial Elongation Catapult Mechanism in the Order Anura (Species *Bufo marinus*). (A) The jaw and tongue of frogs and toads using the inertial elongation catapult in rest position. (B) Contraction of the protractor muscle moves the tongue up- and forward. (C–D) Rapid jaw depression accelerates and elongates the tongue using the tongue's own inertia. Drawings based on schematic drawings in [16]. Scale bar indicates a length of up to 200% of the resting length (peak launch distance 3.8 cm in *Rana pipiens* [139]).

6

Unknown – Eversion Release Mechanism: Muscle-Powered Eversion Catapult
In many terrestrial snails and slugs, a relatively strange mating process can be observed in which both mating partners try to shoot a calcareous (love) dart out of the genital pore into the skin of "unlucky" mating partner [144]. Dart shooting is present in at least 9 families; the Ariophantidae, Bradybaenidae, Dyakiidae, Helicidae (including the genus *Cornu*), Helminthoglyptidae, Hygromiidae, Parmacellidae, Urocyclidae, and Vitrinidae, within the clade Stylommatophora (phylum: Mollusca, class: Gastropoda), which comprises 60 families of snails and slugs. The darts consist of a corona of pleated blades that connect the dart to the body of the snail, a concave connection of the corona to the main shaft of the dart, called the flare, and a shaft with multiple vanes [145] covered in mucus that reconfigures the female reproductive system and allows for more sperm to fertilize the eggs; increasing the dart shooter's paternity [144,146,147]. Darts exhibit large diversity, with some species having simple cone-shape darts and others having curved or contorted darts [146]. Surrounding the darts is the so-called dart sac. Dillaman [145] and Koene *et al.* [147] described the dart sac as a muscular organ with layers of connective tissue surrounding mainly the posterior end of the dart (near the corona). Unfortunately, the description of the shooting action is limited to a claim that the dart is externalized by the eversion of the dart sac (Figure 6.27A–D) [144,146]. Based on dart sac morphology, one may assume that the dart sac muscles with connective tissue drive the eversion upon activation. However, additional research is warranted to determine the working principle of this dart shooting mechanism, as well as the associated launch parameters.

Table 6.3. Summary of Launch Parameters of the Identified Shooting Mechanisms in Animals. Abbreviations: BL = body length, SL = skull length, SD = strike distance, RL = resting length, ML = mandible length, BM = body mass, PV = (time to) peak velocity, PA = (time to) peak acceleration. For the projectile mass, launch velocity, launch acceleration, launch distance, and power output, the measurement technique is indicated as: Standard = measured using a HSV camera. **Bold** = calculated by referred authors using measured launch parameters. *Italics* = manual measurement of the parameter (e.g. from photograph stills, without the use of a high-speed video camera). Standard* = estimated by us from data/figure in indicated reference(s); for the power output per unit mass the launch acceleration [m/s²] is multiplied with the launch velocity [m/s] and for the work per unit mass the power output [W/kg] is integrated over the launch duration [s]. On some occasions the time to peak acceleration or time to peak velocity is used to calculate the work per unit mass delivered by the shooting mechanism, this is indicated with PA and PV, respectively. **Bold*** = calculated by us using the mean parameter ± 3 standard deviations. The launch parameters are indicated as mean (± standard deviation), peak (indicated with "peak" behind the value), or a range (minimum value–maximum value). Per launch parameter, the peak value identified in this review is indicated by a blue-lined box.

Animals	Projectile mass [g]	Launch acceleration [g]	Launch velocity [m/s]	Launch distance [m]	Power output [W/kg]	Launch duration [ms]	Work [J/kg]
Elastic Energy Storage - Eversion Release Mechanism							
Osmotic-powered Eversion Catapult							
Osmosis: Water Absorption							
Cnidaria (cnidarians) [2,29,102,103,105]	1·10⁻⁹ –2.3·10⁻⁹	5.41·10⁶ peak	18.6 (37.1 peak)	0.0006 peak	1.97·10⁹ peak*	0.0021*	4,137*
Muscle Contraction							
Elastic Energy Storage - Geometrical Release Mechanism							
Muscle-Powered Squeeze Catapult							
Iguania (iguanian lizards)							
Chamaeleonidae (chameleons) [117]				200% BL peak			
Bradypodion melanocephalum [3]	·	93.8–112.1	3.9–4.3	0.079–0.083	4,920–5,840	19.3–23.3	95–135.5*
Bradypodion occidentale [3]	·	57.2–57.6	3.9–4.2	0.094–0.12	2,880–3,160	25.3–28	72.9–88.5*
Bradypodion pumilum [3]	·	60–82.9	3.7–3.9	0.084–0.12	3,020–4,140	26.7–34.7	80.6–143.7*
Bradypodion sp. "emerald" [3]	·	53.8–96.2	3.7–4.6	0.11–0.15	2,600–5,720	29–34	75.4–194.5*
Bradypodion thamnobates [3]	·	50–92.5	2.9–4.3	0.10–0.14	1,802–4,680	20–38.7	36–181.1*
Brookesia superciliaris [3]	·	137.6–142.7	4.4–5	0.07–0.09	7,920–9,080	17.5–19.7	140.2–170.9*
Calumma p. parsonii [3]	·	42.5 peak	4.9 peak	0.2 peak	2,080 peak	39 peak	112.3 peak*
Chamaeleo calyptratus [3,8,26,30,115]	·	41 (52.4 peak)	3.9 (5.0 peak)	0.13 (0.07–0.32)	1,092 (3,490 peak)	13–48	14.2–167*
Chamaeleo jacksonii [112]	·	17 peak	3.7* (6.5 peak*)	0.097 ± 0.002	608.7 peak*	27.8 ± 2	21.7 peak*
Chamaeleo melleri [30,34]	4	38.1 ± 2.5 (40.8 peak)	6 peak	-	1,584 ± 176 (3,000 peak)	~20	31 (60 peak)*
Chamaeleo pardalis [8,30]	·	34.7 ± 3.4	5 peak	-	1,170 ± 176 (3,000 peak)	~20	23.4 (60 peak)*

6

6

Continuation of Table 6.3. Summary of Launch Parameters of the Identified Shooting Mechanisms in Animals.

Species							
Furcifer lateralis [3]	-	74 peak	4.1 peak	0.11 peak	4,080 peak	32.3 peak	131.8 peak*
Furcifer oustaleti [3]	-	29.2–46.3	3.6–4.8	0.18–0.27	1,410–2,980	47.3–54.6	66.7–162.7*
Kinyongia fischeri [3]	-	59.1–67.4	4.5–4.8	0.177–0.179	3,020–4,420	37–41.3	141.3–182.6*
Kinyongia tenuis [3]	-	116.2 peak	4.9 peak	0.1 peak	7,820 peak	12.9 peak	96.2 peak*
Rhampholeon acuminatus [3]	-	119.3–132.5	4.8–5.2	0.082–0.097	7,720–8,840	22.7–23.3	175.2–206*
Rhampholeon spinosus [3]	-	180.4–264	5.1–5.3	0.11–0.12	12,100–14,040	18.3–22.7	221.4–318.7*
Rieppeleon brevicaudatus [3]	-	111.1–165.1	3.6–5.4	0.037–0.1	5,120–11,620	9.7–18.7	49.7–217.3*
Trioceros cristatus [3]	-	77.8 peak	4.7 peak	0.17 peak	5,220 peak	36.7 peak	191.6 peak*
Trioceros hoehnelii [3]	-	76.6–77.2	4–4.3	0.11–0.2	3,480–4,500	31–48.3	107.9–217.4*
Trioceros jacksonii xantholophus [3]	-	65.3 peak	4.4 peak	0.16 peak	4,140 peak	34 peak	140.8 peak*
Trioceros johnstoni [3]	-	62 peak	4.6 peak	0.19 peak	4,060 peak	47.7 peak	190.8 peak*
Trioceros montium [3]	-	68.3–71.5	4.2–4.5	0.16–0.18	3,920–4,560	33.3–39.3	130.5–179.2*
Plethodontidae (lungless salamanders) [117]	~1			89% BL peak			28.8*
Bolitoglossa dofleini [31]	0.79	177 ± 11.1 (458 peak)	3.8 ± 0.1 (7 peak)	0.02 (0.03 peak)	4,109 ± 424 (18,129 peak)	7 ± 0.4 (4 ± 0.3 PA)	(16.5–44.1*) (6.4 ± 0.5 PA)
Eurycea guttolineata [31,128]	1.29	80.7 ± 6.5 (105.6 peak)	2.3 ± 0.2 (3.2 peak)	0.009 (0.02 peak)	1,778 ± 229 (2,467 peak)	7 ± 0.4 (4 ± 0.3 PA)	12.4* (6.3–20.2*) (4.1 ± 0.3 PA)
Eurycea wilderae [31]	-	140.4 ± 10.6 (203.1 peak)	2.5 ± 0.1 (3.2 peak)	0.009 (0.02 peak)	2,818 ± 322 (5,921 peak)	7 ± 0.4 (4 ± 0.3 PA)	19.7* (10.7–48.6*) (4.1 ± 0.3 PA)
Hydromantes genei [31]	-	102.9 ± 5.9 (119.7 peak)	4.6± 0.1 (4.9 peak)	0.03 (0.04 peak)	1,860 ± 330 (4,305 peak)	13 ± 1 (6 ± 1 PA)	24.2* (8.7–45.6*) (6.5 ± 0.9 PA)
Hydromantes imperialis [31]	1.04	82.6 ± 11 (93.6 peak)	4.0 ± 0.0 (4.2 peak)	0.03 (0.04 peak)	2,495 ± 428 (2,923 peak)	13 ± 1 (6 ± 1 PA)	32.4* (12.1–46.8*) (6.5 ± 0.9 PA)
Hydromantes platycephalus [31]	-	42.1 ± 6.6 (100.3 peak)	2.7 ± 0.2 (3.7 peak)	0.03 (0.04 peak)	908 ± 186 (2,443 peak)	13 ± 1 (6 ± 1 PA)	11.8* (3.5–39.1*) (6.5 ± 0.9 PA)
Hydromantes supramontis [31,127]	-	-	-	0.6 (80% BL)	-	-	-
Elastic Energy Storage – Latch Release Mechanism							
Linkage and Latch Catapults							
Stomatopoda (mantis shrimps)	-	925–10,601*	5.7–23*	-	$5.19 \cdot 10^4$–$4.7 \cdot 10^6$**		
Alachosquilla vicina [131]	-	925 ± 331*	5.7 ± 0.91*	-	$5.19 \cdot 10^5$** ($1.61 \cdot 10^6$ peak*)	3.26± 0.41 (1.1 ± 0.02 PV)	169.2* (722.9 peak*) (57.09*(186.8 peak*) PV)
Elastic Energy Storage – Unknown Release Mechanism							
Odontodactylus scyllarus [25,131]	-	6,626–10,600	14–23*	0.08 peak SD	$4.7 \cdot 10^6$‡	2.7 PA	1,269 peak* PA
Inertial Elongation Catapult							

Continuation of Table 6.3. Summary of Launch Parameters of the Identified Shooting Mechanisms in Animals.

Anura (toads and frogs)							
Bufonidae [16]							
Bufo alvarius [142]	10.3 ± 0.89	-	-	-	-	-	-
Mouth opening value:	-	20.2-80.4	0.7-1.0	200% BL	-	2	5.4-19.2[b]
Bufo marinus [16,136,141]	0.75 ± 0.05	25.5-31.6	2.9 peak	0.039 ± 0.002 (0.023-0.059)	896.6 peak*	31 ± 1 (25-42)	37.2*
Mouth opening value:	-	-	-	-	-	-	-
Hylidae [16,137]							
Pachymedusa dacnicolor [137]	-	-	1.7-2.9*	0.012 ± 0.001	-	7 ± 0.6	-
Mouth opening value:	-	-	-	-	-	50 ± 4.4	-
Microhylidae [138]							
Dyscophus guineti [16,138,141]	0.81 ± 0.1	4.9-14.7	1.2 ± 0.07 (2.2 peak)	0.0011 ± 1 10⁻⁴	168.6-316.8*	16.6 ± 0.9 (6.4±1.2 PV)	2.3-6.1 (0.5-3.2 PV)*
Mouth opening value:	-	-	1.3 ± 0.05	-	-	1.7 ± 0.9 PV	-
Dendrobatidae							
Megophryidae							
Leptodactylidae							
Ranidae							
Rana pipiens [139]	0.9 ± 0.05	6.6-45.8	0.6-3.2	0.009-0.038	25-885	17-92	0.4-81.4*
Mouth opening value:	-	3.2-10.1	0.1-0.8	-	115-1,763	9-24	0.6-6.3[c]

Unknown approach - Eversion Release Mechanism

Muscle-Powered Eversion Catapult

Stylommatophora (snails and slugs) [144-147]							
Ariophantidae	-	-	-	-	-	-	-
Bradybaenidae	-	-	-	-	-	-	-
Dyakidae	-	-	-	-	-	-	-
Helicidae	-	-	-	-	-	-	-
Helminthoglyptidae	-	-	-	-	-	-	-
Hygromiidae	-	-	-	-	-	-	-
Parmacellidae	-	-	-	-	-	-	-
Urocyclidae	-	-	-	-	-	-	-
Vitrinidae	-	-	-	-	-	-	-

[a] The angular accelerations [rad/s^2] and angular speed [rad/s] of the mantis shrimp appendage strike are measured in *Alachosquilla vicina* and *Odontodactylus scyllarus* as:

- *A. vicina* [131]: $2.58 \cdot 10^6 \pm 1.04 \cdot 10^6$ rad/s^2 and $1.61 \cdot 10^3 \pm 0.34 \cdot 10^6$ rad/s
- *O. scyllarus* [25,131]: unknown and 670–990 rad/s peak

[b] Total work 4.3 mJ [142]

[c] Our own calculations show different numbers: 1–42.8 J/kg. Maximum kinetic energy of ballistic opening 0.029–0.28 ml [139]

6

199
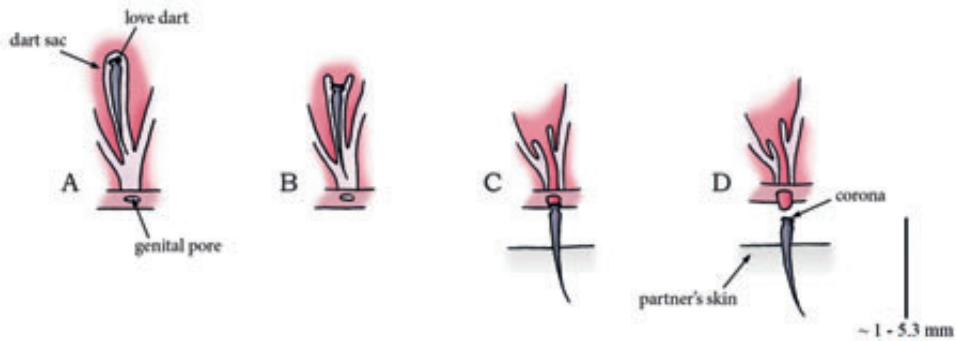
Figure 6.27— Muscle-Powered Eversion Catapult Mechanism in the Clade Stylommatophora (Species *Cornu aspersum*). (A) The dart organ morphology, consisting of a fully developed love dart and a muscular dart sac. (B) Eversion of the dart sac, forcing the love dart to be externalized through the genital pore. (C–D) Piercing and release (at the corona) of the love dart into the mating partner. Drawings based on schematic drawings in [145]. Scale bare indicates the length of the love dart, which is in between 1–5.3 mm in length (longest dart found in *Chilostoma cingulatum* [146]).

6.7. DISCUSSION

6.7.1. Energy Generation, Storage, and Transformation

This systematic review provides an overview of the working principles of shooting mechanisms found in nature with a focus on the energy management prior to and during the shooting action. In fungi, energy for shooting is generated via osmosis in the form of either water condensation on the system, water absorption into the system, or water evaporation from the system. In plants, energy for shooting is also generated via osmosis, in the form water absorption into the system or water evaporation from the system; the water condensation mechanism is not observed. In animals, the energy for shooting is mostly produced by muscles, with the exception of the phylum Cnidaria, in which energy is generated via osmosis (water absorption specifically).

In all identified shooting mechanisms in plants and fungi, the generated energy is gradually stored as elastic energy using specialized wall structures, often comprising several cell layers, with two exceptions: the momentum catapult and the air pressure catapult. In the former, the energy for shooting is stored in the sterigma by a shift in the center of mass, whereas in the latter, energy is primarily stored in the compressed air trapped inside the containers (apart from energy stored in stored in the cell walls). In animals, the generated energy is gradually stored in elastic structures such as collagen or resilin. The use of elastic structures is advantageous when high launch accelerations and velocities are desired, as elastic structures can recoil much faster than muscles can shorten [20,21], which leads to a higher power output during the launch of the projectile. Furthermore, the power release of these elastic structures is less temperature-sensitive

6

than that of the muscles (because the work production by the muscles is much less temperature dependent than the power output), allowing the animals to perform over a wide temperature range [26-28]. However, albeit "slow", the non-elastically enhanced hydrostatic and directly muscle-powered tongue protrusion mechanisms found in anurans [16] and iguanian lizards [112] allow for a better control of the direction of motion of the tongue during protrusion, which is very hard (if not impossible) in elastically enhanced shooting mechanisms.

The trigger for the release of the energy needed to discharge the projectile differs greatly between shooting mechanisms. Fracture of the cell walls and the development of gas bubble(s) within the structure surrounding the projectile are common triggers in plants and fungi. Another trigger found in fungi is the eversion of the structure (e.g. membrane) surrounding the projectile. Eversion as a release mechanism is also encountered in animals, in the phylum Cnidaria and the clade Stylommatophora (snails and slugs), specifically. In order to trigger the eversion of the structure or projectile, a generally small "energy bump" needs to be overcome which prevents an uncontrolled release. This energy can possibly be delivered by a slight outwards movement of the cup or cnida, which straightens the membrane or shaft in *Sphaerobolus* and Cnidaria, respectively. In the family Chameleonidae (chameleons), elastic relaxation of the collagen sheaths as they slide off the tongue bone is used as trigger in tongue shooting, whereas in Plethodontidae (lungless salamanders) the elastic energy is released when the forked lingual skeleton folds medially by the tractrix-shaped muscle track; allowing the collagen sheaths to propel the tongue bone out of the mouth and relax. Unfortunately, the release mechanism in the inertial elongation catapult in anurans (frogs and toads) has not been fully unraveled yet. It may be questioned whether reloadability of the shooting mechanism compromises launch velocity and acceleration.

In non-reloadable shooting mechanisms such as those in fungi and plants (which release energy by fracture, cavitation, or eversion), mechanical stresses can be increased upon failure of the cells. In reloadable systems such as most mechanisms in animals (except for the osmotic-powered and muscle-powered eversion catapult), mechanical stresses should be kept below the threshold of permanent tissue damage, so that complete reloading of the shooting mechanism is possible. In other words, the performance of shooting mechanisms in animals that are used for prey capture might be constrained by the reusability requirement.

Directly after the release trigger, the projectiles are discharged. A variety of catapult mechanisms, such as the coiling catapults, squeeze catapults, and muscle-powered eversion catapults, are identified that transform the (stored elastic) energy into kinetic energy of the projectile. For the small untethered projectiles, such as spores, seeds, and pollen, present in fungi and plants, the adhesion and surface tension that binds them together and to their support must be overcome during this phase [33], which in turn may result in the need for high launch velocities and accelerations to reach sufficient launch

6

distances. Projectiles have been identified ranging from $10^{\cdot}$ mg (spore mass) in Ascomycota and Zygomycota to approximately 10,300 mg (tongue mass) in *B. alvarius*. Tables 8.1, 8.2, and 8.3 show that the highest accelerations are found in the launch of microscale projectiles, with peak accelerations of up to 5,413,000g in cnidarians (projectile mass of approximately $1 \cdot 10^{-6}$–$2.3 \cdot 10^{-6}$ mg) [2] and 870,000g in *G. zeae* (projectile mass of approximately $0.2 \cdot 10^{-6}$ mg) [21]. For larger projectiles, such as the tongue in lungless salamanders (tongue mass of approximately 1,000 mg), peak accelerations reach "only" 458g in *B. dofleini* [31]. Why is this the case? According to Newton's second law (force = mass times acceleration), a smaller projectile mass can be given an equal acceleration with a lower force. However, mass increases with length cubed, whereas force tends to increase with cross-sectional area and thus length squared. On a small scale, drag forces become more dominant; consequently, micrometer-scale projectiles are decelerated in their free flight almost instantaneously after discharge. In other words, for the same initial launch velocity and acceleration, larger projectiles travel farther than smaller ones if the effect of external flow (e.g. wind) is not taken into account [34].

Depending on the main function of the shooting mechanism, e.g. food capture or seed dispersal, different characteristics of the shooting mechanism are of importance, such as the launch velocity, launch acceleration, dispersal distance, spread, and accuracy. In plants and fungi, the dispersal distance and spread are the most important parameters. The effectiveness of the shooting mechanisms in terms of improving survival of the spore or seed can be mainly deducted from the dispersal patterns [69]. Seed or spore dispersal over even a short distance from the plant (beyond the canopy) or fungus can already increase the probability of seed or spore survival. However, high dispersal distances and spread tend to increase the survival rate and reproductive success [77,86,94]. Furthermore, by projecting spores into an airstream (wind), fungi or mosses can increase the probability of encountering susceptible hosts or environments [10]. To negate the negative effects of viscous drag on the launch distance, plants and fungi often synchronize the discharge of thousands of (often small) pollen, seeds, and spores, such as in ascomycetes [46], *Sphagnum* [1], and *S. martensii* [96], or optimize the shape of the projectile [45]. In animals, on the other hand, high launch acceleration, launch velocity, and accuracy are needed, as the shooting mechanisms are critical for territory and self-defense, prey capture, substrate attachment, and locomotion. For example, in chameleons and lungless salamanders, the tongue is critical for catching elusive prey, and in cnidarians the cnidocysts are important for self-defense and locomotion (amongst others) [97]. A trade-off seems to be present between the launch velocity (and acceleration) and accuracy, with faster shooting mechanisms being less accurate. For example, in anurans the inertial elongation catapult mechanism has an accuracy of approximately 33%, whereas the non-elastically enhanced and much slower hydrostatic mechanism has an

accuracy of over 99% [16]. This difference in accuracy can be mainly led back to the lack of feedback control (i.e. the inability to adjust the trajectory during the shooting action) of the inertial elongation catapult and muscle-powered squeeze catapult.

6.7.2. Power output, Work, and Scale Effects

The scale of the shooting mechanisms, in particular the mass of the projectile, has been shown to affect the launch acceleration and velocity of the projectile. If we look into the power output per unit mass, it becomes clear that the highest values are found in the shooting mechanisms with projectiles that have a size at microscale. For example, the shooting mechanisms identified in *C. canadensis* and *C. parviflora*, with projectile masses of 0.024 mg and 0.15 mg, respectively, have an power output that is more than 46 times higher than that of *C. melleri* and *B.dofleini*, with a tongue mass of 4,000 mg and 1,000 mg, respectively (see Tables 8.2 and 8.3). Furthermore, Anderson [3] found that smaller chameleons, such as *R. spinosus* (12,100–14,040 W/kg), outperform larger species, such as *Furcifer oustaleti* (1,410–2,980 W/kg) in terms of power output per unit mass. The highest identified power output found is in cnidarians ($1.97 \cdot 10^9$ W/kg), which shoot their stinging cells with a mass of in between 1–2.3 ng.

We also investigated the work per unit mass (J/kg; calculated by integrating the power output per unit mass over the launch duration) delivered by the shooting mechanisms (see Tables 8.1–8.3). It appears that the work per unit mass is largely independent of the scale of the mechanism. For example, similar work per unit mass values have been calculated in the microscale shooting mechanism of the fungus *P. kleinii* (sporangiophore length 2 mm; 201.5 J/kg) and the tongue shooting mechanism of the much larger chameleon *Trioceros cristatus* (with a body length of 25–28 cm; 191.8 J/kg). If we look into the difference between osmotic-powered (0.3–4,137 J/kg) and muscle-powered mechanisms (0.4–1,269 J/kg), higher values of work per unit mass are observed in the mechanisms using osmosis as energy source. The scale-dependent power output and scale independent work per unit mass per shooting mechanism substantiate that the smaller shooting mechanisms are able to release the energy for shooting faster than the larger mechanisms. However, additional research is necessary to determine the work per unit mass more precisely per shooting mechanism, as our calculations give an approximate value based on the launch duration and power output value.

6.7.3. Limitations of This Study

A systematic approach was undertaken to maximize the chance of identifying relevant shooting mechanisms in nature. However, chances still remain that relevant shooting mechanisms have been overlooked by, for example, missing relevant keywords, by only including literature that was published in the English language, and by not searching in grey literature. Moreover, the lack of a full description of the biomechanical structure and activity of the complete elastic enhancement system in some of the shooting mechanisms

6

have led to uncertain placement of these mechanisms in the classification schemes. Finally, for many of the described shooting mechanisms, one or more of the launch parameters, such as those of the cavitation coiling catapult of fungi imperfecti, and information about the exact working principle, such as that of *Viola*, were not found.

6.7.4. Implications for Future Research & Applications

Future studies could be focused on supplementing the current knowledge of the working principles, including a full description of the cell structure and morphology of the shooting mechanism, and launch parameters of many of the described shooting mechanisms that are currently missing, such as the shooting mechanism in love dart shooting snails. Furthermore, some of the launch parameters can be determined with greater accuracy by using modern technology such as high-speed cameras. Additionally, shooting mechanisms that involve a liquid projectile, such as used in archerfish [11], and elastically enhanced movements, such as the Venus Flytrap [8], could be investigated in more detail based on energy management during the rapid movements. Insight into these mechanisms may point towards still unidentified working principles of shooting in nature.

The described shooting mechanisms can be used in a biomimetic approach to develop faster and smaller artificial shooting mechanisms. Opportunities can be found in applications requiring accurate cutting, separation, or connection of (e.g. soft, slippery, or elastic) materials, high forces or accelerations, as well as slender structures that suffer from buckling (a typical failure mode in percutaneous tools, such as guidewires, catheters, and needles, and slender industrial tools, such as nails and needles) [148,149].

6.8. CONCLUSIONS

In this paper a structured overview of biological projectile shooting mechanisms is provided. The reviewed shooting mechanisms are described based on how energy is managed prior to and during the shooting action, that is, how the energy is generated, stored, and transformed to kinetic energy of the projectile. Two main energy sources are identified: osmosis (in plants, fungi, and animals) and muscle contraction (in animals). The generated energy is gradually stored in an elastic structure, and transformed into kinetic energy of the projectile using a variety of release, trigger, and catapult mechanisms. The launch parameters were found to be mainly dependent on the size of the projectile, with smaller projectiles being launched at higher accelerations and velocities. The highest identified launch acceleration is $5.41 \cdot 10^6 g$, observed in cnidarians, and the highest velocity is 237 m/s, observed in the mulberry *M. alba*. These high accelerations are a necessity to partly negate the effects of viscous drag on small reproductive units in fungi and plants. Furthermore, in smaller shooting mechanisms discharging projectiles on microscale, higher mass-specific power outputs (up to $1.97 \cdot 10^9$ W/kg in cnidarians) are observed, meaning that the smaller mechanisms are able to

release the stored elastic energy faster than larger ones. This becomes especially apparent when comparing the mass-specific power output (ranging from 0.28–4,137 J/kg) with the mass-specific work, which is mostly scale-independent, with similar values in the microscale shooting mechanism of *P. kleinii* (201.5 J/kg) and the tongue shooting mechanism of the much larger chameleon *Trioceros cristatus* (191.8 J/kg). However, osmotic-powered shooting mechanisms seem to be able to store more energy per kilogram (≤ 4,137 J/kg) than muscle-powered mechanisms (≤ 1,269 J/kg). The given insights into the working principles improves the understanding of how nature is able to exhibit extreme launch parameters, can aid in unraveling the working principles of other, less researched, shooting mechanisms, and can potentially be used as inspiration for the design of faster artificial shooting mechanisms.

REFERENCES

[1]   Van Leeuwen JL. Launched at 36,000g. Science. 2010; 329(5990): pp. 395-396.

[2]   Nüchter T, Benoit M, Engel U, Özbek S, and Holstein TW. Nanosecond-scale kinetics of nematocyst discharge. Curr Biology. 2006;16(9): pp. R316-R318.

[3]   Anderson CV. Off like a shot: Scaling of ballistic tongue projection reveals extremely high performance in small chameleons. Nature: Scientific Reports. 2016;6: pp. 1-9.

[4]   Alexander RM. Optima for animals. Princeton, NJ: Princeton University Press, 1996.

[5]   Wake DB and Deban SM. Terrestrial feeding in salamanders. Chapter in: Feeding: form, function and evolution in tetrapod vertebrates. San Diego, CA: Academic Press, 2000: pp 95-116.

[6]   Lombard RE and Wake DD. Tongue evolution in the lungless salamanders, family Plethodontidae: IV. Phylogeny of plethodontid salamanders and the evolution of feeding dynamics. Systematic Biology. 1986;35(4): pp. 532-551.

[7]   Ridley HN. Dispersal of plants throughout the world. Kent, United Kingdom: L.Reeve and Company, 1930.

[8]   Forterre Y. Slow, fast and furious: Understanding the physics of plant movements. Journal of Experimental Botany. 2013;64(15): pp. 4745-4760.

[9]   Ingold CT. Fungal spores. Their liberation and dispersal. Oxford, United Kingdom: Oxford University Press, 1971.

[10]   Money N and Fischer MF. Biomechanics of spore release in phytopathogens. Chapter in: Plant relationships. Berlin, Germany: Springer Berlin Heidelberg, 2009: pp. 115-133.

[11]   Elshoud G and Koomen PA. Biomechanical analysis of spitting in archer fishes (Pisces, Perciformes, Toxidae). Zoomorphology. 1985;105(4): pp. 240-252.

[12]   Dean J, Aneshansley DJ, Edgerton HE, and Eisner T. Defensive spray of the bombardier beetle: A biological pulse jet. Science. 1990;248(4960): pp. 1219-1221.

[13]   Burrows M. Biomechanics: Froghopper insects leap to new heights. Nature. 2003;424(6948): pp. 509-509.

[14]   Hassett MO, Fischer MWF, Sugawara ZT, Stolze-Rybczynski J, and Money NP. Splash and grab: Biomechanics of peridiole ejection and function of the funicular cord in bird's nest fungi. Fungal Biology. 2013;117(10): pp. 708-714.

6

[15]   De Luca PA, Cox DA, and Vallejo-Marín M. Comparison of pollination and defensive buzzes in bumblebees indicates species-specific and context-dependent vibrations. Naturwissenschaften. 2014;101(4): pp. 331-338.

[16]   Nishikawa KC. Neuromuscular control of prey capture in frogs. Philosophical Transactions of the Royal Society B: Biological Sciences. 1999;354(1385): pp. 941-954.

[17]   Kier W and van Leeuwen JL. kinematic analysis of tentacle extension in the squid *Loligo pealei*. Journal of Experimental Biology. 1997;200(1): pp. 41-53.

[18]   Huxley H. The mechanism of muscular contraction. Science. 1969;164(3886): pp. 1356-1365.

[19]   Noblin X, Yang S, and Dumais J. Surface tension propulsion of fungal spores. Journal of Experimental Biology. 2009;212(17): pp. 2835-2843.

[20]   Higham TE and Irschick DJ. Springs, steroids, and slingshots: The roles of enhancers and constraints in animal movement. Journal of Comparative Physiology B: Biochemical, Systemic, and Environmental Physiology. 2013;183(5): pp. 583-595.

[21]   Alexander RM. Tendon elasticity and muscle function. Comparative Biochemistry and Physiology Part A: Molecular & Integrative Physiology. 2002;133(4): pp. 1001-1011.

[22]   Lutz GJ and Rome LC. Built for jumping: The design of the frog muscular system. Science. 1994;263(5145): pp. 370-372.

[23]   Askew GN and Marsh RL. Muscle designed for maximum short-term power output: Quail flight muscle. Journal of Experimental Biology. 2002;205(15): pp. 2153-2160.

[24]   Askew GN and Marsh RL. The mechanical power output of the pectoralis muscle of blue-breasted quail (*Coturnix chinensis*): The in vivo length cycle and its implications for muscle performance. Journal of Experimental Biology. 2001;204(21): pp. 3587-3600.

[25]   Patek SN, Korff WL, and Caldwell RL. Biomechanics: Deadly strike mechanism of a mantis shrimp. Nature. 2004;428(6985): pp. 819-820.

[26]   Anderson CV and Deban SM. Ballistic tongue projection in chameleons maintains high performance at low temperature. Proceedings of the National Academy of Sciences of the United States of America. 2010;107(12): pp. 5495-5499.

[27]   Anderson CV and Deban SM. Thermal effects on motor control and in vitro muscle dynamics of the ballistic tongue apparatus in chameleons. Journal of Experimental Biology. 2012;215(24): pp. 4345-4357.

[28]   Deban SM and Richardson JC. Cold-blooded snipers: Thermal independence of ballistic tongue projection in the salamander *Hydromantes platycephalus*. Journal of Experimental Zoology Part A. 2011;315 A(10): pp. 618-630.

[29]   Özbek S, Balasubramanian PG, and Holstein TW. Cnidocyst structure and the biomechanics of discharge. Toxicon. 2009;54(8): pp. 1038-1045.

[30]   De Groot JH and van Leeuwen JL. Evidence for an elastic projection mechanism in the chameleon tongue. Proceedings of the Royal Society B: Biological Sciences. 2004;271(1540): pp. 761-770.

[31]   Deban SM, O'Reilly JC, Dicke U, and van Leeuwen JL. Extremely high-power tongue projection in plethodontid salamanders. Journal of Experimental Biology. 2007;210(4): pp. 655-667.

[32]   Buller A. Researches on fungi. Volume I. London, United Kingdrom: Longmans, Green and Company, 1909.

[33]   Martone PT, Boller M, Burgert I, Dumais J, Edwards J, Mach K, et al. Mechanics without muscle: Biomechanical inspiration from the plant world. Integrative and Comperative Biology. 2010;50(5): pp. 888-907.

6

[34]   Fischer MWF, Stolze-Rybczynski JL, Cui Y, and Money NP. How far and how fast can mushroom spores fly? Physical limits on ballistospore size and discharge distance in the Basidiomycota. Fungal Biology. 2010;114(11-12): pp. 669-675.

[35]   Turner JCR and Webster J. Mass and momentum transfer on the small scale: How do mushrooms shed their spores? Chemical Engineering Science. 1991;46(4): pp. 1145-1149.

[36]   Money NP. More *g*'s than the space shuttle: Ballistospore discharge. Mycologia. 1998;90(4): pp. 547-558.

[37]   Vogel S. Comparative biomechanics: Life's physical world (2nd ed.). Princeton, NJ: Princeton University Press, 2013.

[38]   Pringle A, Patek SN, Fischer M, Stolze J, and Money NP. The captured launch of a ballistospore. Mycologia. 2005;97(4): pp. 866-871.

[39]   Pennisi E. Society for integrative and comparative biology meeting. Water launches spores like a rocket. Science. 2006;311(5759): pp. 331.

[40]   Stolze-Rybczynski JL, Cui YL, Stevens MHH, Davis DJ, Fischer MWF, and Money NP. Adaptation of the spore discharge mechanism in the Basidiomycota. Plos One. 2009;4(1): pp. 1-6.

[41]   Yafetto L, Carroll L, Cui Y, Davis DJ, Fischer MWF, Henterly AC, et al. The fastest flights in nature: High-speed spore discharge mechanisms among fungi. Plos One. 2008; 3(9): pp. 1-5.

[42]   Wolf FA. Mechanism of apothecial opening and ascospore expulsion by the cup-fungus *Urnula-craterium*. Mycologia. 1958;50(6): pp. 837-843.

[43]   Trail F, Gaffoor I, and Vogel S. Ejection mechanics and trajectory of the ascospores of *Gibberella zeae* (anamorph *Fuarium graminearum*). Fungal Genetics and Biology. 2005;42(6): pp. 528-533.

[44]   Trail F and Seminara A. The mechanism of ascus firing - merging biophysical and mycological viewpoints. Fungal Biol Reviews. 2014;28(2-3): pp. 70-76.

[45]   Roper M, Pepper RE, Brenner MP, and Pringle A. Explosively launched spores of ascomycete fungi have drag-minimizing shapes. Proceedings of the National Academy of Sciences of the United States of America. 2008;105(52): pp. 20583-20588.

[46]   Roper M, Seminara A, Bandi MM, Cobb A, Dillard HR, and Pringle, A. Dispersal of fungal spores on a cooperatively generated wind. Proceedings of the National Academy of Sciences of the United States of America. 2010;107(41): pp. 17474-17479.

[47]   Fischer M, Cox J, Davis DJ, Wagner A, Taylor R, Huerta AJ, et al. New information on the mechanism of forcible ascospore discharge from *Ascobolus immersus*. Fungal Genetics and Biology. 2004;41(7): pp. 698-707.

[48]   Fritz JA, Seminara A, Roper M, Pringle A, and Brenner MP. A natural o-ring optimizes the dispersal of fungal spores. Journal of the Royal Society Interface. 2013;10(85): pp. 1-8.

[49]   Heald FD and Walton RC. The expulsion of ascospores from the perithecia of the chestnut blight fungus, *Endothia parasitica* (Murr.) and. American Journal of Botany. 1914;1(10): pp. 499-521.

[50]   Trail F. Fungal cannons: Explosive spore discharge in the Ascomycota. Fems Microbiol Letters. 2007;276(1): pp. 12-18.

[51]   Olivier APS, Swart CW, Pohl CH, van Wyk PWJ, Swart HC, Coetsee E, et al. The "firing cannons" of *Dipodascopsis uninucleata* var. Uninucleata. Canadian Journal of Microbiology. 2013;59(6): pp. 413-416.

[52]   Kohlmeyer J and Volkmann-Kohlmeyer B. Fungi on *Juncus roemerianus* .6. *Glomerobolus* gen nov, the first ballistic member of Agonomycetales. Mycologia. 1996;88(2): pp. 328-337.

6

[53] Skotheim JM and Mahadevan L. Physical limits and design principles for plant and fungal movements. Science. 2005;308(5726): pp. 1308-1310.

[54] Page RM. Sporangium discharge in *Pilobolus*: A photographic study. Science. 1964;146(3646): pp. 925-927.

[55] Buller A. Researches on fungi. Volume VI. London, United Kingdom: Longmans, Green and Company, 1934.

[56] Fischer MWF, Stolze-Rybczynski JL, Davis DJ, Cui YL, and Money NP. Solving the aerodynamics of fungal flight: How air viscosity slows spore motion. Fungal Biology. 2010;114(11-12): pp. 943-948.

[57] Grossman RF. Attack of the artillery fungus on vinyl siding. Journal of Vinyl & Additive Technologies. 2005;11(2): pp. 63-64.

[58] Engel H and Schneider J. Die umwandlung von glykogen in zucker in den fruchtkörpern von *Sphaerobolus stellatus* (thode) pers., vor ihrem abschluss. Berichte der Deutsche Botanischen Gesselshaft. 1963;75: pp. 397-400.

[59] Buller A. Researches on fungi. Volume V. Hyphal fusions and protoplasmic streaming in the higher fungi, together with an account of the production and liberation of spores in *Sporobolomyces*, *Tilletia*, and *Sphaerobolus*. London, United Kingdom: Longmans, Green and Company; 1933.

[60] Meredith DS. Spore discharge in *Deightoniella torulosa* (syd.) Ellis. Annals of Botany. 1961;25(3): pp. 271-278.

[61] Meredith DS. Violent spore release in some fungi imperfecti. Annals of Botany. 1963;27(1): pp. 39-47.

[62] Stamp NE and Lucas JR. Ecological correlates of explosive seed dispersal. Oecologia. 1983;59(2-3): pp. 272-278.

[63] Debruyn RAJ, Paetkau M, Ross KA, Godfrey DV, and Friedman CR. Thermogenesis-triggered seed dispersal in dwarf mistletoe. Nature Communications. 2015;6(6262): pp. 1-5.

[64] Friedman CMR, Ross BN, and Martens GD. Antibodies raised against tobacco aquaporins of the pip2 class label viscin tissue of the explosive dwarf mistletoe fruit. Plant Biology. 2010;12(1): pp. 229-233.

[65] Hawksworth FG. Ballistics of dwarf mistletoe seeds. Science. 1959;130(3374): pp. 504.

[66] Robinson DCE and Geils BW. Modelling dwarf mistletoe at three scales: Life history, ballistics and contagion. Ecological Modeling. 2006;199(1): pp. 23-38.

[67] Hinds T and Hawksworth F. Seed dispersal velocity in four dwarfmistletoes. Science. 1965;148(3669): pp. 517-519.

[68] Hinds TE and Hawksworth FG, McGinnies WJ. Seed discharge in Arceuthobium: A photographic study. Science. 1963;140(3572): pp. 1236-1238.

[69] Hayashi M, Feilich KL, and Ellerby DJ. The mechanics of explosive seed dispersal in orange jewelweed (*Impatiens capensis*). Journal of Experimental Botany. 2009;60(7): pp. 2045-2053.

[70] Deegan RD. Finessing the fracture energy barrier in ballistic seed dispersal. Proceedings of the National Academy of Sciences of the United States of America. 2012;109(14): pp. 5166-5169.

[71] Chapman DS and Gray A. Complex interactions between the wind and ballistic seed dispersal in *Impatiens glandulifera* (Royle). Journal of Ecology. 2012;100(4): pp. 874-883.

[72] Whitaker DL, Webster LA, and Edwards J. The biomechanics of *Cornus canadensis* stamens are ideal for catapulting pollen vertically. Functional Ecology. 2007;21(2): pp. 219-225.

[73] Edwards J, Whitaker D, Klionsky S, and Laskowski MJ. Botany: A record-breaking pollen catapult. Nature. 2005;435(7039): pp. 164.

6

[74]   Taylor PE, Card G, House J, Dickinson MH, and Flagan RC. High-speed pollen release in the white mulberry tree, *Morus alba* L. Sexual Plant Reproduction. 2006;19(1): pp. 19-24.

[75]   Hayashi M, Gerry SP, and Ellerby DJ. The seed dispersal catapult of *Cardamine parviflora* (Brassicaceae) is efficient but unreliable. American Journal of Botany. 2010;97(10): pp. 1595-1601.

[76]   Vaughn KC, Bowling AJ, and Ruel KJ. The mechanism for explosive seed dispersal in *Cardamine hirsuta* (Brassicaceae). American Journal of Botany. 2011;98(8): pp. 1276-1285.

[77]   Moreno Marcos G, Gomez Gutierrez JM, and Fernandez Santos B. Primary dispersal of *Cytisus multiflorus* seeds. Pirineos. 1992;140: pp. 75-88.

[78]   Van der Burgt XM. Explosive seed dispersal of the rainforest tree *Tetraberlinia moreliana* (Leguminosae - Caesalpinioideae) in Gabon. Journal of Tropical Ecology. 1997;13(1): pp. 145-151.

[79]   Swaine M and Beer T. Explosive seed dispersal in *Hura crepitans* L.(Euphorbiaceae). New Phytologist. 1977;78(3): pp. 695-708.

[80]   Hildebrand F. Die verbreitungsmittel der pflanzen. Leipzig, Germany: Engelmann, 1873.

[81]   Witztum A and Schulgasser K. The mechanics of seed expulsion in Acanthacaea. Journal of Theoretical Biology. 1995;176(4): pp. 531-542.

[82]   Evangelista D, Hotton S, and Dumais J. The mechanics of explosive dispersal and self-burial in the seeds of the filaree, *Erodium cicutarium* (Geraniaceae). Journal of Experimental Biology. 2011;214(4): pp. 521-529.

[83]   Lisci M and Pacini E. Fruit and seed structural characteristics and seed dispersal in *Mercurialis annua* L. (Euphorbiaceae). Acta Societatis Botanicorum Poloniae. 1997;66(3-4): pp. 379-386.

[84]   Vogel S. Living in a physical world II. The bio-ballistics of small projectiles. Journal of Biosciences. 2005;30(2): pp. 167-175.

[85]   De Souza LA, Da Rosa SM, and Moscheta IS. Anatomy of the developing fruit of *Metrodorea nigra* A. St.-Hil. (Rutaceae). Brazilian Archives of Biology and Technology. 2008;51(6): pp. 1171-1179.

[86]   Roberts ML and Haynes RR. Ballistic seed dispersal in *Illicium* (*Illiciaceae*). Plant Systematics and Evolution. 1983;143(3): pp. 227-232.

[87]   Berg H. Differential seed dispersal in *Oxalis acetosella*, a cleistogamous perennial herb. Acta Oecologica. 2000;21(2): pp. 109-118.

[88]   Beattie AJ and Lyons N. Seed dispersal in viola (Violaceae): Adaptations and strategies. American Journal of Botany. 1975: 62(7): pp. 714-722.

[89]   Sundberg S. Size matters for violent discharge height and settling speed of *Sphagnum* spores: Important attributes for dispersal potential. Annals of Botany. 2010;105(2): pp. 291-300.

[90]   Whitaker DL and Edwards J. *Sphagnum* moss disperses spores with vortex rings. Science. 2010;329(5990): pp. 406.

[91]   Duckett JG, Pressel S, P'ng KMY, and Renzaglia KS. Exploding a myth: The capsule dehiscence mechanism and the function of pseudostomata in *Sphagnum*. New Phytologist. 2009;183(4): pp. 1053-1063.

[92]   Ingold C. Spore liberation (1st ed.). Oxford, United Kingdom: Clarendon Press, 1965.

[93]   Poppinga S, Haushahn T, Warnke M, Masselter T, and Speck T. Sporangium exposure and spore release in the peruvian maidenhair fern (*Adiantum peruvianum*, Pteridaceae). Plos One. 2015;10(10): pp. 1-20.

[94]   Noblin X, Rojas NO, Westbrook J, Llorens C, Argentina M, and Dumais, J. The fern sporangium: A unique catapult. Science. 2012;335(6074): pp. 1322.

6

[95] King AL. The spore discharge mechanism of common ferns. Proceedings of the National Academy of Sciences of the United States of America. 1944;30(7): pp. 155-161.

[96] Schneller J, Gerber H, and Zuppiger A. Speed and force of spore ejection in *Selaginella martensii*. Botanica Helvetica. 2008;118(1): pp. 13-20.

[97] Morabito R, Marino A, Lauf PK, Adragna NC, and La Spada G. Sea water acidification affects osmotic swelling, regulatory volume decrease and discharge in nematocytes of the jellyfish *Pelagia noctiluca*. Cellular Physiology and Biochemistry. 2013;32(7): pp. 77-85.

[98] Plachetzki DC, Fong CR, and Oakley TH. Cnidocyte discharge is regulated by light and opsin-mediated phototransduction. BMC Biology. 2012;10(17): pp. 1-9.

[99] Tardent P and Holstein T. Morphology and morphodynamics of the stenotele nematocyst of *Hydra attenuata* Pall. (Hydrozoa, Cnidaria). Cell and Tissue Research. 1982;224(2): pp. 269-290.

[100] Oppegard SC, Anderson PA, Eddington DT. Puncture mechanics of cnidarian cnidocysts: A natural actuator. Journal of Biological Engineering. 2009;3(17): pp. 1-11.

[101] Kitatani R, Yamada M, Kamio M, and Nagai H. Length is associated with pain: Jellyfish with painful sting have longer nematocyst tubules than harmless jellyfish. Plos One. 2015;10(8): pp. 1-13.

[102] Anderson PAV and Bouchard C. The regulation of cnidocyte discharge. Toxicon. 2009;54(8): pp. 1046-1053.

[103] Fautin DG. Structural diversity, systematics, and evolution of cnidae. Toxicon. 2009;54(8): pp. 1054-1064.

[104] Brinkman DL, Aziz A, Loukas A, Potriquet J, Seymour J, and Mulvenna J. Venom proteome of the box jellyfish *Chironex fleckeri*. Plos One. 2012;7(12): pp. 1-9.

[105] Cannon Q and Wagner E. Comparison of discharge mechanisms of Cnidarian cnidae and Myxozoan polar capsules. Reviews in Fishery Science. 2003;11(3): pp. 185-219.

[106] Godknecht A and Tardent P. Discharge and mode of action of the tentacular nematocysts of *Anemonia sulcata* (Anthozoa: Cnidaria). Marine Biology. 1988;100(1): pp. 83-92.

[107] Mariscal RN and McLean RB. The form and function of cnidarian spirocysts - 2. Ultrastructure of the capsule tip and wall and mechanism of discharge. Cell and Tissue Research. 1976;169(3): pp. 313-321.

[108] Garcia-Arredondo A, Rojas A, Iglesias-Prieto R, Zepeda-Rodriguez A, and Palma-Tirado L. Structure of nematocysts isolated from the fire corals *Millepora alcicornis* and *Millepora complanata* (Cnidaria: Hydrozoa). Journal of Venomous Animals and Toxins Including Tropical Diseases. 2012;18(1): pp. 109-115.

[109] Colin SP and Costello JH. Functional characteristics of nematocysts found on the scyphomedusa *Cyanea capillata*. Journal of Experimental Marine Biology and Ecology. 2007;351(1-2): pp. 114-120.

[110] Carré D, Carré C, and Mills CE. Novel cnidocysts of Narcomedusae and a Medusivorous ctenophore, and confirmation of kleptocnidism. Tissue and Cell. 1989;21(5): pp. 723-734.

[111] Ott M, Ostheim J, and Sherbrooke WC. Prey snapping and visual distance estimation in texas horned lizards, *Phrynosoma cornutum*. Journal of Experimental Biology. 2004;207(17): pp. 3067-3072.

[112] Meyers JJ and Nishikawa KC. Comparative study of tongue protrusion in three iguanian lizards, *Sceloporus undulatus*, *Pseudotrapelus sinaitus* and *Chamaeleo jacksonii*. Journal of Experimental Biology. 2000;203(18): pp. 2833-2849.

6

[113]   Van Leeuwen JL. Why the chameleon has spiral–shaped muscle fibres in its tongue. Philos. T. Philosophical Transactions of the Royal Society of London B: Biological Sciences. 1997;352(1353): pp. 573-589.

[114]   Wainwright PC and Bennett AF. The mechanism of tongue projection in chameleons: I. Electromyographic tests of functional hypotheses.Journal of Experimental Biology. 1992;168(1): pp. 1-21.

[115]   Müller UK and Kranenbarg S. Power at the tip of the tongue. Science. 2004;304(5668): pp. 217-219.

[116]   Moulton DE, Lessinnes T, O'Keeffe S, Dorfmann L, and Goriely A. The elastic secrets of the chameleon tongue. Proceedings of the Royal Society A. 2016;472(2188): pp. 20160030.

[117]   Crumly CR. Insectivorous vertebrates. Chapter in: Encyclopedia of insects (2nd ed.). Academic press, 2009. pp. 514-516.

[118]   Brau F, Lanterbecq D, Zghikh L-N, Bels V, and Damman P. Dynamics of the prey prehension by chameleons through viscous adhesion: A multidisciplinary approach. Nature Physics. 2016;12(10): pp. 931-935.

[119]   Herrel A, Meyers JJ, Aerts P, and Nishikawa KC. Functional implications of supercontracting muscle in the chameleon tongue retractors. Journal of Experimental Biology. 2001;204(21): pp. 3621-3627.

[120]   Singh A, Hafner N, Lubecke V, and Butler M. A data efficient method for characterization of chameleon tongue motion using doppler radar. Proceedings of the 34th IEEE Annual International Conference Engineering in Medicine and Biology Society held at San Diego, CA, 28 August - 1 September 2012.

[121]   Herrel A, Redding CL, Meyers JJ, and Nishikawa KC. The scaling of tongue projection in the veiled chameleon, *Chamaeleo calyptratus*. Zoology. 2014;117(4): pp. 227-236.

[122]   Deban SM and Marks SB. Metamorphosis and evolution of feeding behaviour in salamanders of the family Plethodontidae. Zoological Journal of the Linnean Society. 2002;134(4): pp. 375-400.

[123]   Deban SM and Dicke U. Activation patterns of the tongue-projector muscle during feeding in the imperial cave salamander *Hydromantes imperialis*. Journal of Experimental Biology. 2004;207(12): pp. 2071-2081.

[124]   Deban SM and Dicke U. Motor control of tongue movement during prey capture in plethodontid salamanders. Journal of Experimental Biology. 1999;202(24): pp. 3699-3714.

[125]   Lombard RE and Wake DB. Tongue evolution in the lungless salamanders, family Plethodontidae I. Introduction, theory and a general model of dynamics. Journal of Morphology. 1976;148(3): pp. 265-286.

[126]   Thexton AJ, Wake DB, and Wake MH. Tongue function in the salamander *Bolitoglossa occidentalis*. Archives of Oral Biology. 1977;22(6): pp. 361-366.

[127]   Deban SM and Wake DB, Roth G. Salamander with a ballistic tongue. Nature. 1997; 389: 27-28.

[128]   Anderson CV, Larghi NP, and Deban SM. Thermal effects on the performance, motor control and muscle dynamics of ballistic feeding in the salamander *Eurycea guttolineata*. Journal of Experimental Biology. 2014;217(17): pp. 3146-3158.

[129]   Claverie T, Chan E, and Patek SN. Modularity and scaling in fast movements: Power amplification in mantis shrimp. Evolution. 2011;65(2): pp. 443-461.

[130]   Patek SN and Caldwell RL. Extreme impact and cavitation forces of a biological hammer: Strike forces of the peacock mantis shrimp *Odontodactylus scyllarus*. Journal of Experimental Biology. 2005;208(19): pp. 3655-3664.

6

[131]   De Vries MS, Murphy EAK, and Patek SN. Strike mechanics of an ambush predator: The spearing mantis shrimp. Journal of Experimental Biology. 2012;215(24): pp. 4374-4384.

[132]   Patek SN, Rosario MV, and Taylor JRA. Comparative spring mechanics in mantis shrimp. Journal of Experimental Biology. 2013;216: pp. 1317-1329.

[133]   Patek SN, Nowroozi BN, Baio JE, Caldwell RL, and Summers AP. Linkage mechanics and power amplification of the mantis shrimp's strike. Journal of Experimental Biology. 2007;210(20): pp. 3677-3688.

[134]   Meyers JJ, O'Reilly JC, Monroy JA, and Nishikawa KC. Mechanism of tongue protraction in microhylid frogs. Journal of Experimental Biology. 2004;207(1): pp. 21-31.

[135]   Deban SM, O'Reilly JC, and Nishikawa KC. The evolution of the motor control of feeding in amphibians. American Zoologist. 2001;41(6): pp. 1280-1298.

[136]   Nishikawa KC and Gans C. Mechanisms of tongue protraction and narial closure in the marine toad *Bufo marinus*. Journal of Experimental Zoology. 1996;199(11): pp. 2511-2529.

[137]   Gray LA and Nishikawa KC. Feeding kinematics of phyllomedusine tree frogs. Journal of Experimental Biology. 1995;198(2): pp. 457-463.

[138]   Monroy JA and Nishikawa KC. Prey location, biomechanical constraints, and motor program choice during prey capture in the tomato frog, *Dyscophus guineti*. Journal of Comparative Physiology A: Neuroethology, Sensory, Neural, and Behavioral Physiology. 2009;195(9): pp. 843-852.

[139]   Sandusky PE and Deban SM. Temperature effects on the biomechanics of prey capture in the frog *Rana pipiens*. Journal of Experimental Zoology Part A: Ecological Genetics and Physiology. 2012;317(10): pp. 595-607.

[140]   Wolff JB, Lee MJ, and Anderson CW. Contribution of the submentalis muscle to feeding mechanics in the leopard frog, *Rana pipiens*. Journal of Experimental Zoology Part A: Comparative Experimental Biology. 2004;301(8): pp. 666-673.

[141]   Peters SE and Nishikawa KC. Comparison of isometric contractile properties of the tongue muscles in three species of frogs, *Litoria caerulea, Dyscophus guinetti,* and *Bufo marinus*. Journal of Morphology. 1999;242(2): pp. 107-124.

[142]   Lappin AK, Monroy JA, Pilarski JQ, Zepnewski ED, Pierotti DJ, and Nishikawa KC. Storage and recovery of elastic potential energy powers ballistic prey capture in toads.Journal of Experimental Biology. 2006;209(13): pp. 2535-2553.

[143]   Deban SM and Lappin AK. Thermal effects on the dynamics and motor control of ballistic prey capture in toads: Maintaining high performance at low temperature. Journal of Experimental Biology. 2011;214(8): pp. 1333-1346.

[144]   Chase R. The function of dart shooting in helicid snails. American Malacological Bulletin. 2007;23(1-2): pp. 183-189.

[145]   Dillaman R. Dart formation in *Helix aspersa* (Mollusca, Gastropoda). Zoomorphology. 1981;97(3): pp. 247-261.

[146]   Koene JM and Schulenburg H. Shooting darts: Co-evolution and counter-adaptation in hermaphroditic snails. BMC Evolutionary Biology. 2005; 5(25): pp. 1-13.

[147]   Koene JM and Liew TS, Montagne-Wajer K, Schilthuizen M. A syringe-like love dart injects male accessory gland products in a tropical hermaphrodite. Plos One. 2013;8(7): pp. 1-4.

[148]   Lock M. A study of buckling and snapping under dynamic load. El Segundo, CA: Laboratory Operations Aerospace Corporation. Report Number TR-0158 (3240-30)-3; 1967. pp. 1-55.

[149]   Sakes A, Dodou D, and Breedveld P. Buckling prevention strategies in nature as inspiration for improving percutaneous instruments: A review. Bioinspiration & Biomimetics. 2016;11(2): pp. 021001-1-021001-26.

6

APPENDIX 6.A: FULL SEARCH QUERIES

6.A1. Plants and Fungi Search Queries

For the plants and fungi, the following search query was conducted in Scopus: TITLE-ABS-KEY ((projectile$ OR pollen OR seed$ OR *spore* OR perid* OR gleba) W/10 (shooting OR expulsion OR firing OR eject* OR catapult* OR launch* OR propel*)) OR TITLE-ABS-KEY ((explosive OR violent OR forceful) W/2 (discharge OR dispersal)) AND TITLE-ABS-KEY (organism$ OR species OR plant* OR flower* OR tree* OR vine* OR fung* OR *moss* OR grass* OR weed* OR herb*) AND NOT TITLE-ABS-KEY (military OR forens* OR germinat* OR propellant OR machine*) AND NOT TITLE-ABS-KEY ((launch*) W/3 (project OR program OR experiment* OR initiative$)).

In the Web of Science Core Collection the following search query was used: (TS= ((projectile$ OR "pollen" OR seed$ OR *spore* OR perid* OR "gleba") NEAR/10 ("shooting" OR "expulsion" OR "firing" OR eject* OR catapult* OR launch* OR propel*)) OR TS= (("explosive" OR "violent" OR "forceful") NEAR/2 ("discharge" OR "dispersal"))) AND TS= (organism$ OR "species" OR plant* OR flower* OR tree* OR vine* OR fung* OR *moss* OR grass* OR weed* OR herb*) NOT TS= ("military" OR forens* OR germinat* OR "propellant" OR machine*) NOT TS= (launch* NEAR/3 ("project" OR "program" OR experiment* OR initiative$)).

6.A2. Animals Search Queries

For the animals category, the following search query was executed in the database of Scopus: TITLE-ABS-KEY ((projectile$ OR *dart$ OR arrow$ OR cnid* OR tongue$ OR appendage$) W/10 (shooting OR firing OR striking OR strike OR projecting OR projection OR protract* OR catapult* OR launch* OR eject* OR propel*)) OR TITLE-ABS-KEY ((cnid*) W/10 (discharg*)) AND TITLE-ABS-KEY (organism$ OR species OR fauna OR zoo* OR animal* OR nonhuman OR creature$ OR genus) AND NOT TITLE-ABS-KEY (military OR forens* OR germinat* OR propellant OR machine* OR plasma OR ioniz* OR archaeology OR euthanasia OR an$esthesia OR thalam*) AND NOT TITLE-ABS-KEY ((launch*) W/3 (project OR program OR experiment* OR initiative$)) AND NOT TITLE-ABS-KEY ((tongue$ OR tal$) W/2 (flick*)).

In the Web of Science Core Collection, the following search query was used: (TS= ((projectile$ OR *dart$ OR arrow$ OR cnid* OR tongue$ OR appendage$) NEAR/10 ("shooting" OR "firing" OR "striking" OR "strike" OR "projecting" OR "projection" OR protract* OR catapult* OR launch* OR eject* OR propel*)) OR TS= ((cnid*) NEAR/10 (discharg*))) AND TS= (organism$ OR "species" OR "fauna" OR zoo* OR animal* OR "nonhuman" OR creature$ OR "genus") NOT TS= ("military" OR forens* OR germinat*

OR "propellant" OR "machinery" OR "plasma" OR ioniz* OR archaeolog* OR "euthanasia" OR an$esthesia OR thalam*) NOT TS= (launch* NEAR/3 ("project" OR "program" OR experiment* OR initiative$)) NOT TS= ((tongue$ OR tail$) NEAR/2 flick*).

6.A3. Search Strategies

In Figures 6.A1 and 6.A2 the search strategies followed for identifying the shooting mechanisms in plants, fungi, and animals are illustrated.

6

Plants and Fungi Search Strategy

Records identified in the
Scopus database
(n = 290)

Records identified in the
Web of Knowledge
database Core collection
(n = 233)

Duplicates removed
(n = 172)

Title and abstract of records screened
(n = 322)

Records excluded based on
eligibility criteria
(n = 269)

Inaccessible records
(n = 12)

Full-text records assessed for eligibility
(n = 70)

Full-text records excluded
based on eligibility criteria
(n = 22)

Records eligible for inclusion
(n = 48)

Additional records retrieved
from reference lists of the
included literature
(n = 20)

Records included in review
(n = 68)

Figure 6.A1— Plants and Fungi Search Strategy.

6

Animals Search Strategy

Records identified in the Scopus database (n = 408)

Records identified in the Web of Knowledge database Core collection (n = 186)

Duplicates removed (n = 143)

Title and abstract of records screened (n = 451)

Records excluded based on eligibility criteria (n = 379)

Inaccessible records (n = 8)

Full-text records assessed for eligibility (n = 64)

Full-text records excluded based on eligibility criteria (n = 13)

Records eligible for inclusion (n = 51)

Additional records retrieved from reference lists of the included literature (n = 14)

Records included in review (n = 65)

Figure 6.A2— Plants and Fungi Search Strategy.

CHAPTER 7

CROSSING CTOS USING A MECHANICAL IMPULSE

7

AIMÉE SAKES, MARLEEN VAN DER WIEL, DIMITRA DODOU, AND PAUL BREEDVELD

Published in Cardiovascular Engineering and Technology.

Abstract—In this study we investigated whether exerting an impulse on a Chronic Total Occlusion (CTO) improves the success rate of CTO crossing as compared to the currently used method of statically pushing the guidewire against the CTO. A prototype (Ø2mm) was developed that generates translational momentum using a spring-loaded indenter and converts it to an impulse during impact. Mechanical performance was evaluated by measuring the peak force and momentum for different spring compressions and strike distances in air and blood-mimicking fluid. Puncture performance, in terms of number of punctures, number of strikes to puncture, and energy transfer from the indenter to the CTO, was assessed for six tip shapes (stamp, wedge, spherical, pointed, hollow spherical, and ringed) on three CTO models with different weight percentages of gelatin and calcium. As a control, a Ø0.4 mm rigid rod was tested. A maximum indenter momentum of 1.3 mNs (velocity of 3.4 m/s), a peak force of 19.2 N (vs. 1.5 N reported in literature and 2.7 N for the control), and CTO displacement of 1.4 mm (vs. 2.7 mm for the control) were measured. The spherical and ringed tips were most effective, with on average 2.3 strikes to puncture the most calcified CTO model. The prototype generated sufficient peak forces to puncture highly calcified CTO models, which are considered most difficult to cross during PCI. Furthermore, CTO displacement was minimized, resulting in a more effective procedure. In future, a smaller, faster, and flexible clinical prototype will be developed.

7

7.1. INTRODUCTION

During Percutaneous Coronary Interventions (PCI), a small guidewire (Ø0.36 mm) is gradually driven through the vasculature from an incision point in the groin or wrist towards an occlusion in the coronaries. Once arrived at the occlusion, a static (axial) load is applied on the guidewire by the interventional cardiologist from outside the body to puncture and cross the occlusion, after which the occlusion is reopened using a balloon catheter. Coronary Chronic Total Occlusions (CTOs), defined as heavily calcified, complete coronary occlusions of over 3 months old, represent the most challenging lesion type to be crossed during PCI, requiring a high skill level of the interventional cardiologists [1]. The development and use of several dedicated guidewires, such as the *Confianza Pro* (Asahi Intecc, Nagoya, Japan) and the *Progress 200T* (Abbott Vascular, Abbott Park, IL), dedicated crossing and support catheters, such as the *Tornus* (Asahi Intecc, Nagoya, Japan) and the *Crossboss* (Boston Scientific, Natick, MA), crossing tools, such as the *Frontrunner XP* (Ø0.76–1 mm; Cordis Corporation, Miami, FL), the *Crosser Catheter* (Ø0.6–1.5 mm; BARD Peripheral Vascular Inc., Tempe, AZ), and the *Truepath* (Ø0.43 mm; Boston Scientific, Natich, MA), and crossing strategies (see Sakes *et al.* [2] for a comprehensive overview) have contributed to a steady increase in the technical success rate of PCI in CTOs (i.e., the ability to cross the CTO and to successfully reopen the artery), as well as in the overall procedural success rate of these interventions (i.e., the proportion of procedures with no nosocomial major adverse cardiac events) [3]. However, the overall procedural success rate is still undesirably low. Whereas experienced operators can achieve success rates of up to 90%, success rates of experienced operators not specialized in CTO PCI are lower than 55% [4]. The success rate is further depended on the characteristics of the CTO, of which age, increasing occlusion length, tortuosity, and cap ambiguity are historical predictors for technical and procedural failure, and to a lesser extent the used crossing technique (i.e., antegrade, retrograde, or a combined technique) [3, 5].

Failing to cross heavily calcified CTOs intraluminally (i.e., crossing through the original coronary lumen and CTO body) with a guidewire accounts for approximately two-third of PCI failures and is mainly the result of guidewire buckling [6]. Guidewire buckling occurs because the required puncture force of the CTO often exceeds the maximum load that the guidewire tip can sustain. Furthermore, the static load applied on the CTO may lead to displacement of the CTO up to 4 mm (estimated based on [7]). Such a large displacement not only leads to energy dissipation, thereby reducing the maximum force that can be delivered on the CTO, but also increases the chance of blood vessel wall damage due to stretching.

Guidewire buckling can be prevented by increasing the critical load of the guidewire, by decreasing the penetration load of the CTO, or by bypassing the CTO using so-called

dissection re-entry techniques. In the latter case, the CTO is crossed *via* the much softer blood vessel wall. Because this method damages the blood vessel wall and re-entry is often challenging [8], we will focus on intraluminal crossing methods instead. Most clinically applied methods of preventing guidewire buckling aim to increase the critical load of the guidewire. This can be achieved by encompassing the guidewire with a support catheter or by employing a second device as support, such as a balloon catheter (balloon anchoring technique) or a guidewire (wire anchoring technique) [5]. Despite these measures, crossing difficulties (mainly due to guidewire buckling) are still observed [5].

To increase the buckling resistance of the guidewire and prevent the energy dissipation associated with CTO displacement, a possible solution could be to use a dynamic loading method, in which a moving guidewire or dedicated CTO device would collide with a stationary CTO, converting translational momentum of the guidewire to an impulse exerted on the CTO. Here momentum is defined as mass (m [kg]) x velocity (v [m/s]) of the guidewire ($p = mv$ [kgm/s]), and impulse is defined as the integral of the impact peak force (F_{peak} [N]) over the time interval dt [s] during which it acts (J [Ns] = $\int F_{peak}\, dt$). Due to the (high) velocity of the guidewire, the damping of the blood vessel wall and the inertia of the CTO act as a "counterforce" to the impulse, and as such restrict the displacement of the CTO and the associated energy dissipation (Figure 7.1). Furthermore, the critical buckling load of the crossing guidewire under dynamic impulse loading condition increases with decreasing load duration [9].

The goal of this study was to explore the use of dynamic impulse loading for puncturing heavily calcified coronary CTOs. For this purpose, a prototype puncture tool able to deliver an impulse onto a CTO was designed and experimentally tested.

7.2. DESIGN

7.2.1. Tip Design

To define the prototype diameter required for atraumatic navigation through the vascular system, the diameters of the arteries that potentially need to be crossed during PCI from the incision point to the lesion site were analyzed based on angiographic and ultrasound data in [10-16]. Coronary CTOs are found in the Right Coronary Artery (RCA), Left Anterior Descending (LAD), Left Circumflex (LCx), and Left Main Trunk (LMT) [5]. In order to reach the coronary CTO, two main approaches can be taken [17]: (1) the radial approach, in which the CTO is reached via the radial artery in the wrist, and (2) the femoral approach, in which the CTO is reached via the common femoral artery. The smallest artery that needs to be crossed to reach the CTO is the RCA, which has a minimum diameter of 2.2 mm [12]. Accordingly, the maximum prototype diameter was set to 2 mm.
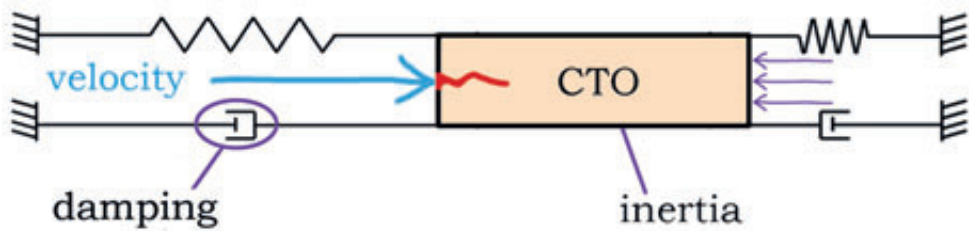
Figure 7.1— Impulse Crossing Method. The guidewire or crossing tool (blue arrow) collides with the CTO (orange), converting translational momentum to an impulse during impact, which in turn punctures the CTO (red jagged line). Due to the high velocity of the crossing tool, the inertia of the CTO and the damping of the blood vessel wall deliver the majority of the reaction force (purple arrows) and thus minimize CTO displacement and energy dissipation to the blood vessel wall (indicated by the spring and damper combination).

The prototype tip consists of three components: (1) an actuation component that transfers the translational momentum through the instrument shaft towards the tip, (2) an indenter that applies an impulse onto the CTO, and (3) a reload mechanism that reloads and releases the actuation component.

Actuation Component
The actuation component consists of a compression spring located at the distal tip of the instrument. Translational momentum is generated by compressing the spring with a load mechanism and a position block (Figure 7.2). By varying the spring compression distance, the momentum (p) of the indenter can be adjusted.

Indenter
The indenter receives the momentum generated by the compression spring and subsequently applies an impulse onto the CTO. The indenter consists of two parts: the indenter tip and the indenter stop.

Indenter Tip
To explore the potential of dynamic impulse for puncturing a CTO and to allow for testing multiple tip shapes, the indenter tip was designed to be interchangeable. For the tip shapes, inspiration was drawn from commonly used indenter shapes in the field of rock fracturing and needle interventions. In total, six tip shapes were chosen (Figure 7.3): two blunt solid shapes (a right-angled *stamp* indenter and a *spherical* indenter with the tip radius equal to the indenter radius), two sharp solid shapes (a *wedge* indenter and a *pointed* indenter, both with an edge radius of 0.2 mm), and two hollow shapes (a *hollow spherical* indenter and a *ringed* indenter). The hollow-shaped indenters allow for guiding

another system through the shaft and tip, such as a guidewire or balloon catheter, in a future (hollow) prototype, which could be advantageous for clinical use. The *ringed* indenter was designed with a maximized inner passage diameter: the indenter diameter minus four times the edge radius. The *hollow spherical* indenter was designed with a spherical tip and a Ø0.4 mm lumen, through which the thinnest (coronary) guidewires can pass.

Indenter Stop.

In order to make sure that the indenter has a controllable reach, a stop mechanism was integrated into the design. The stop mechanism is connected to the indenter by means of a rod (Ø1 mm) and is positioned proximal to the position block (Figure 7.2). During spring loading, the indenter stop, and thus the indenter, is pulled backwards (i.e., towards the handle of the instrument) until maximum spring compression is reached. Subsequently, the indenter stop is released and accelerated forward by the spring force until it reaches the position block.

Reload Mechanism

To allow for multiple impacts onto the CTO, a reload mechanism was implemented in the prototype. To reload the device, we used a compliant lock mechanism consisting of a gripper with two flexible barbed plates (Figure 7.2, yellow) and an inner movable core (Figure 7.2, blue). By translating the gripper forward into the hollow section of the indenter stop, the plates of the gripper deform inwards and passively lock into place. Subsequently, the core is pushed forward into the hollow section to actively lock the grip. We opted for a mechanism that works without control feedback, since most of the haptic feedback will be lost during operation.

Prototype Tip Design

A functional prototype was manufactured based on the final tip design (see Figures 7.4 and 7.5). We decided to design a rigid prototype in which the shaft is scalable to different lengths and allows for future redesign into a flexible prototype. The outer shaft of the prototype tip is subdivided into three parts to improve manufacturability and consists of two standardized Ø2.0 x 0.1 mm (Ø x wall thickness) stainless steel (*SS*) capillary tubes (C and E in Figure 7.4) that fit around both ends of the position block (containing a Ø1.2 mm central lumen; D in Figure 7.4; *SS*). The compression spring (B in Figure 7.5; *C00170003016,* Associated Spring SPEC, Evasham, UK; $\emptyset_{outer}$ = 1.7 mm, $\emptyset_{wire}$ = 0.32 mm, *L* = 16 mm; *K* = 1.3 N/mm; $L_{max\ compression}$ = 3.5 mm) is placed distally to the position block within the capillary tube. The indenter consists of two interconnected (screwable) parts: (1) the indenter tip (A in Figure 7.4; Ø1.8 mm; *L* = 6 mm; *SS*) with variable tip shapes, and (2) a Ø1.0 mm rod connected to the indenter stop (F in Figure 7.4; Ø1.8 mm;
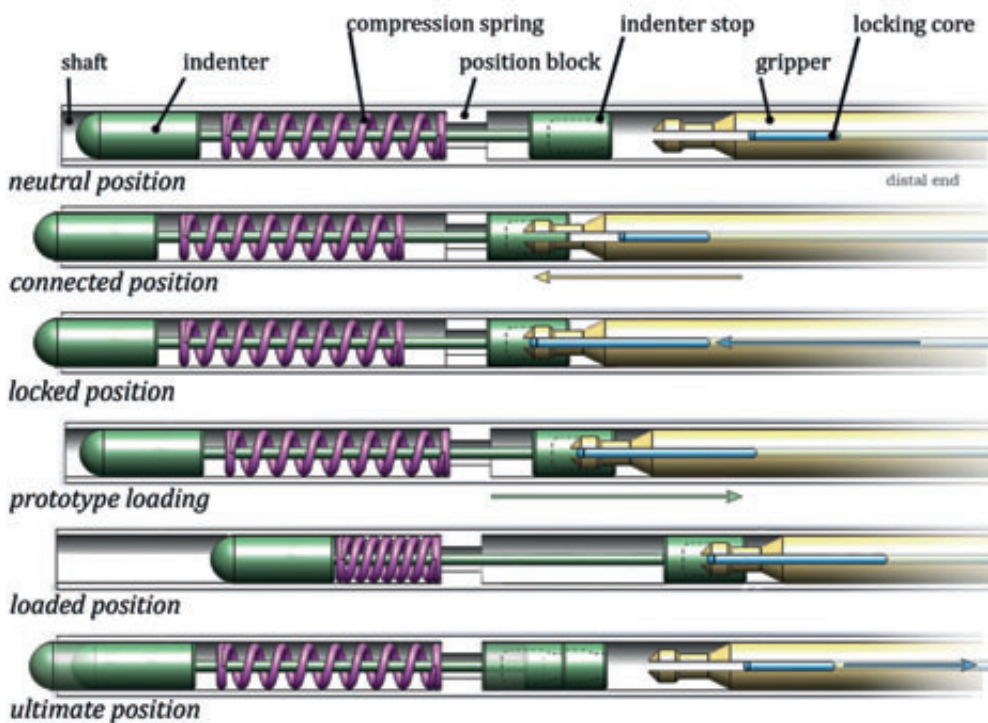
Figure 7.2— Tip Design. The tip consists of five main parts: an outer shaft (grey), an indenter (green) with indenter stop, a compression spring (purple), a position block (white), and a reload mechanism (gripper: yellow and locking core: blue). Row indications: (1) Neutral position, showing the spring (purple) in rest (free length). (2) Connected position, showing the gripper inserted into the indenter stop. (3) Locked position, showing the gripper locked into place into the indenter stop by moving the locking core forward. (4) Spring compression by pulling the load mechanism backwards. (5) Loaded position, showing the spring being compressed by translating the load mechanism with the indenter stop backwards. (6) Ultimate position, showing the indenter being released and accelerated forward by the compression spring until the indenter stop reaches the position block.

SS). The tip of the gripper (Ø1.8 mm; Ø0.5 mm inner lumen; *SS;* G1 in Figure 7.5) fits within the hollow section (containing of a narrowed opening and a 45° slanted surface) of the indenter stop (distal end of F in Figure 7.4), whereas the other (proximal) end of the gripper is connected to a square sliding bearing (G2 in Figure 7.4; brass) that is designed to fit in the handle. The compliant movement of the gripper, necessary to allow the gripper move through the narrowed opening of the hollow part, is possible by the axial slit (w = 0.35 mm). The locking core (I1 in Figure 7.4; Ø0.5 mm; tempered steel) runs through the gripper towards the handle where it is connected to a square sliding bearing (G2 in Figure 7.4).
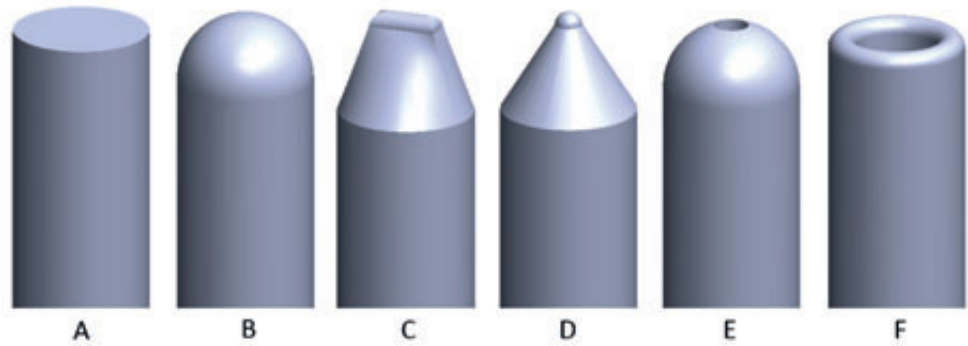
Figure 7.3— Indenter Tip Shapes. From left to right: (A) stamp indenter, (B) spherical indenter, (C) wedge indenter, (D) pointed indenter, (E), hollow spherical indenter with guidewire passage, and (F) ringed indenter.

7.2.2. Handle Design

The handle (Figures 7.5 and 7.6) mechanically controls the gripper and core at precise distances and allows for locking the mechanism in the "loaded" position. The main enveloping box (26 mm x 41 mm x 25 mm [l x w x h]) consists of a bottom (L in Figures 7.5 and 7.6) and a top part (K in Figures 7.5 and 7.6), both made of aluminum, and functions as the handle of the device, allowing for loading, locking, and surmounting of the prototype in an experimental setup (Figure 7.6). An axial slot was carved in the bottom of the square sliding bearing (connected to the gripper; G2 in Figure 7.5), which, together with a screw in the enveloping box, limits the motion range of the gripper. The gripper is controlled by the square sliding bearing (G2 in Figure 7.5) that is connected to a handgrip (H in Figure 7.5; brass) by means of a M6 screw thread. The core is connected to a second handgrip (I2 in Figure 7.5; *SS*) that is guided through the brass handgrip connected to the gripper. Finally, a support part (J in Figures 7.5 and 7.6; brass) is connected to the proximal end of the box and guided around the capillary tube to prevent buckling and bending of this structure.

An overview of the steps to load, trigger, and release the indenter is given in Figure 7.7. (0) Before loading the spring, the control input core (I2 in Figure 7.5) is pulled approximately 10 mm out of the handgrip. (1) The handgrip is pushed into the handle until the gripper is positioned inside the hollow insert of the indenter (connected position in Figure 7.2). (2) The handgrip of the core (I2 in Figures 7.5 and 7.6) is pushed into the handle to lock the gripper in place (locked position in Figure 7.2). (3) Both the handgrip and control input core are pulled out of the handle until the connection between the handgrip and the square sliding bearing becomes visible (G2 and H in Figure 7.5; loaded

Figure 7.4— Prototype Tip Design and Control Interface. Letter indications: (A) Indenter, (B) Compression spring, (C) Capillary tube front, (D) Position block, (E) Capillary tube back, (F) Indenter stop, (G1) Gripper reload mechanism, (G2) Square sliding bearing connected to the gripper, (H) Handgrip gripper, (I1) Core reload mechanism, and (I2) Handgrip core. The match is shown for scale purposes.

position in Figure 7.2). (4) At this stage, the gripper and indenter can be locked in the "loaded" position (or the spring compression distance can be altered) by twisting the handgrip (H in Figures 7.5 and 7.6). (5) To release the spring, the core handgrip (I2 in Figures 7.4 and 7.5) is pulled out of the handle, releasing the gripper and allowing the indenter to accelerate (towards the ultimate position in Figure 7.2).

7.3. MATERIALS AND METHODS

7.3.1. Experiment 1: Mechanical Performance of the Prototype

In Experiment 1, the indenter momentum and the impact peak force were measured as a function of the strike distance, the spring compression distance, and the medium through which the indenter was launched.

Measurement Variables

    Dependent Variables

1. **The indenter momentum (p)** generated by the compression spring. p was calculated by multiplying the indenter mass (m) with the indenter velocity (v).
2. **The impact peak force (F_{peak})** delivered by the indenter.
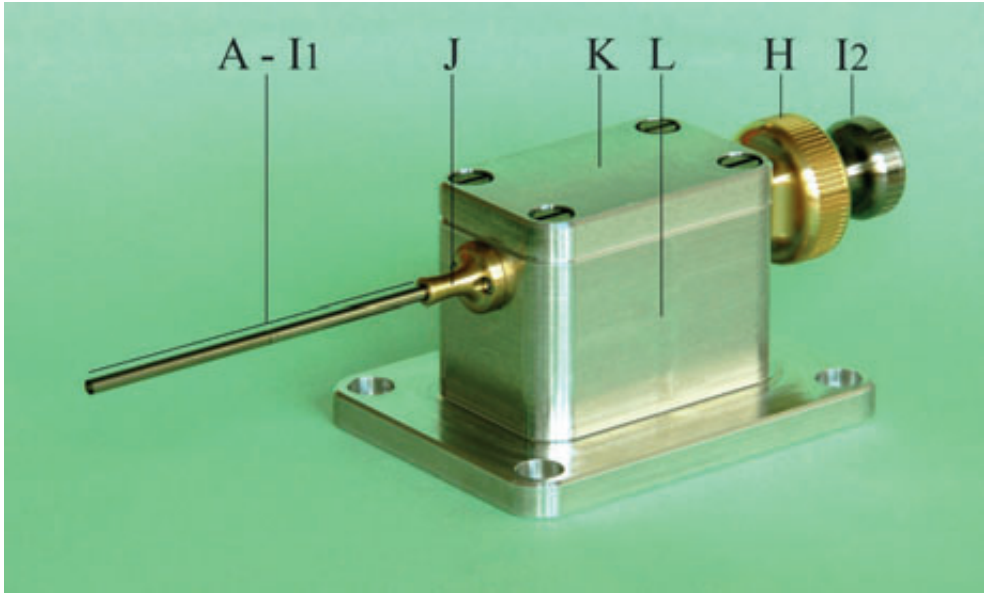
Figure 7.5— Final Design. Letter indications: (A) Indenter, (B) Compression spring, (C) Capillary tube front, (D) Position block, (E) Capillary tube back, (F) Indenter stop, (G1) Gripper reload mechanism connected to (G2) Square sliding bearing, (H) Handgrip gripper connected to G2 (and thus the gripper G1) by means of a screw thread, (I1) Core reload mechanism connected to (I2) Handgrip core, (J) Support capillary tube, (K) Lid, and (L) Enveloping box. In the bottom of part L, a slot is present through which a screw is inserted (not indicated) and connected to G2 to limit the reach of the gripper (G1; Figure 7.4). G1, G2, and H are inserted in the rectangular cutout of the enveloping box L.

Independent Variables

1. **Strike distance**. To evaluate the effect of the distance between the prototype tip and the CTO (e.g., due to incorrect positioning) on the indenter momentum and impact peak force, two strike distances (i.e., the distance from the indenter in neutral position [see Figure 7.2] to the object onto which the impulse is delivered) were tested: 1 mm and 3 mm. The former was selected as the minimum distance between the indenter and the target object, as this allowed the indenter to bounce back after the collision. By bouncing back, static loading of the CTO was prevented. The 3 mm distance was just under the maximum indenter reach (designed at 4 mm).

2. **Spring compression distance**. To evaluate the effect of the actuation force on the indenter momentum, three spring compression distances were tested: 3.5 mm (corresponding to the maximum compression distance of the spring), 2.8 mm, and 2.0 mm. The 2.8 mm and 2.0 mm spring compression distances were realized by twisting (and thus unscrewing) the brass handgrip H (Figures 7.4 and

7

7.5) 360 and 720, respectively. The 2.0 mm spring compression distance corresponded to the minimum distance required for the indenter to reach an object at 3 mm distance.

3. **Surrounding medium**. The mechanical performance was evaluated in air and in Blood-Mimicking Fluid (BMF), with the latter approximating the clinical environment more closely than air. The BMF was made of 25% weight percentage (wt%) glycerine and 75 wt% clear water, a mixture widely used to simulate blood (sometimes with added element such as nylon particles and sodium iodide to improve the optical properties for Doppler flow and particle image velocimetry measurements) [18-21]. In Cheng *et al.* [21], an exponential formula was presented to calculate the viscosity of a glycerol-water mixture. The formula was numerically derived based on experimental data from earlier studies and was used to develop and validate a correlation model that estimates the viscosity of glycerol-water mixtures. The formula applies for all glycerol concentration (0 and 100 wt%) and temperatures between 0 and 100 °C. According to this formula, the viscosity of blood (2.5–2.8 mPas at 36–40 °C) at an ambient temperature of 18°C can be approximated with a mixture of 25 wt% glycerine and 75 wt% clear water.

7
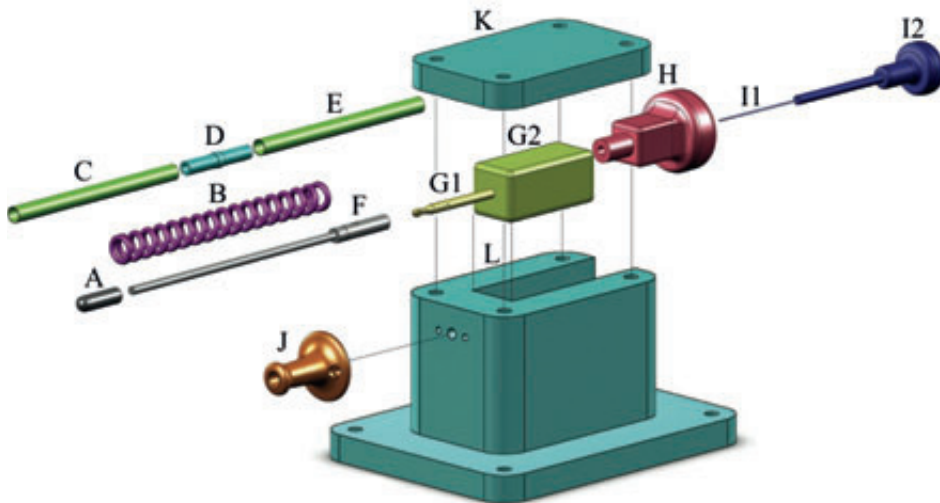
Figure 7.6— The Complete Assembled Prototype. Letter indications: for (A–I2) see Figure 7.4, (J) Support capillary tube, (K) Lid, and (L) Enveloping box. Part G (not indicated, see Figure 7.4) is placed inside part L. In the bottom of part L a screw is inserted (not indicated) to limit the reach of the gripper (G1; Figure 7.4).
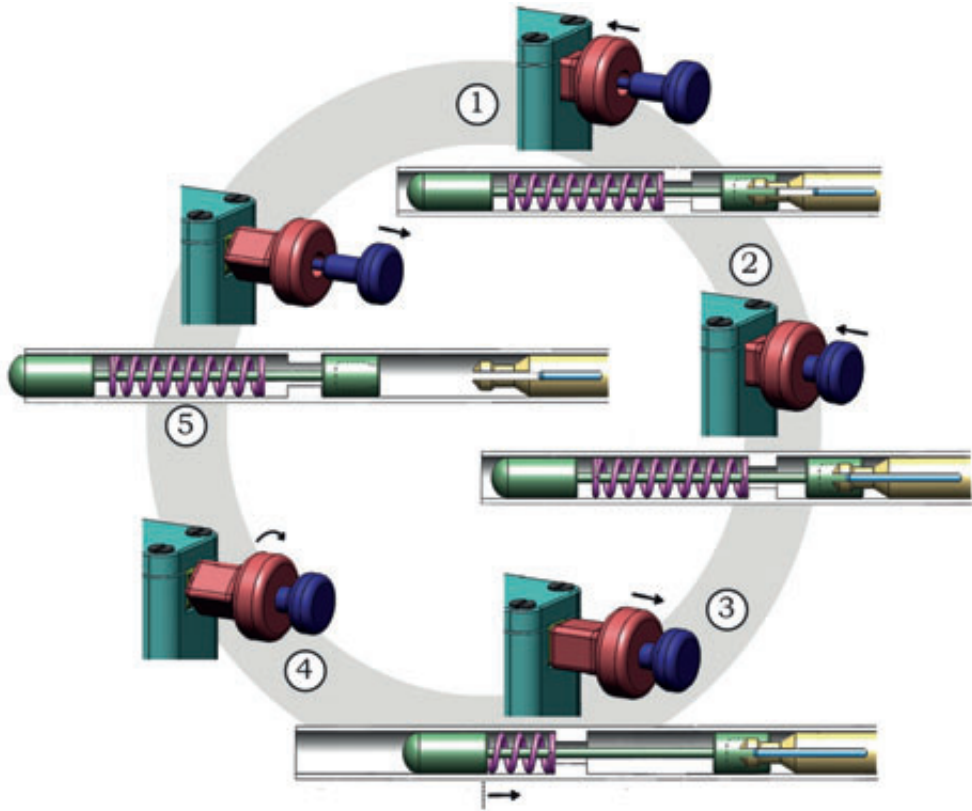
Figure 7.7— Working Principle of the Handle. (0) The gripper is decoupled from the system (neutral position). (1) The control input gripper (red: H), and thus the gripper (yellow: G1), is translated forward to couple the gripper (yellow: G1) with the indenter (A). (2) The gripper (yellow: G1) is locked in place by translating the control input core (blue: I2), and thus the core (I1), forward. (3) The control input gripper (red: H), and with it the control input core (blue: I2), is pulled backwards to load the prototype (loaded position). (4) If desired, the prototype can be locked in the loaded position by rotating the control input gripper (red: H). (5) The prototype is released by pulling the locking core (blue: I2) further backwards.

Measurement Setup

The prototype was suspended vertically, with its tip pointing downwards, in a construction of Thorlabs optomechanics (Thorlabs, Inc., Newton, NJ), consisting of a solid aluminum breadboard (*MB3030/M*), a construction rail (*XE25L375/M*), and a single-axis translation stage (*PT1/M*) (Figure 7.8). The prototype was fastened on the translation stage using an intermediate plate construction. The indenter strike was received by a small

aluminum table (for the measurements in air) or bucket (in which the prototype tip was immersed for the measurements in BMF) fastened on top of a miniature load cell (*LSB200, FSH00103*, FUTEK Advanced Sensor Technology, Inc., Irvine, CA; see Figure 7.8). The effect of gravity in this experiment was considered negligible, since the estimated gravity force is three orders of magnitude smaller than the maximum spring force.

For the determination of the indenter momentum, the indenter velocity was measured from High Speed Videos (HSVs) made with a *Photron Fastcam APX-RS* (Photron, Inc., San Diego, CA) at a frame rate of 10 kHz, and the indenter mass was measured with a high precision balance (*Mettler PJ360 DeltaRange*, Mettler-Toledo International Inc., Columbus, OH).

The impact peak force was measured with the miniature load cell, connected to an analogue signal conditioner (*CPJ RAIL*, SCAIME, Annemasse, France) and a data acquisition system with a sampling rate set to 50 kHz (*NI USB-6211*, National Instruments Corporation, Austin, TX). This system was controlled through LabVIEW 2014 (National Instruments Corporation, Austin, TX). For each of the impact peak force measurements, 1 s of data before and 1 s after the indenter strike were sampled.

Measurement Protocol

The impact peak force was measured for all 12 conditions defined by the three independent variables: 2 strike distances x 3 spring compression distances x 2 surrounding media. The indenter velocity was measured only in air, thus for 6 conditions (2 strike distances x 3 spring compression distances), as it was not possible to video capture the motion in BMF. Each condition was tested five times.

Data Analysis

Per measurement, the indenter velocity was determined by dividing the travelled distance of the indenter tip (from neutral position to impact) with the elapsed time (0.1 ms per image) using the associated software package Photron FASTCAM Viewer v3.5.3. Subsequently, the indenter moment per measurement was determined by multiplying the indenter velocity with the indenter mass. Finally, per condition, the mean indenter velocity and mean indenter momentum with their associating standard deviations were determined across the five repetitions.

The data from the miniature load cell was processed with MATLAB 2013b (The Mathworks, Inc., Natick, MA) to identify the impact peak force (highest value measured) for each measurement and the mean impact peak force (i.e., the mean of the five impact peak forces measured) per condition. Furthermore, to determine the effect of the surrounding medium on the impact peak force, the ratio between the mean peak force in BMF was compared to that in air (F_{peak} BMF/F_{peak} Air [-]) for each condition.
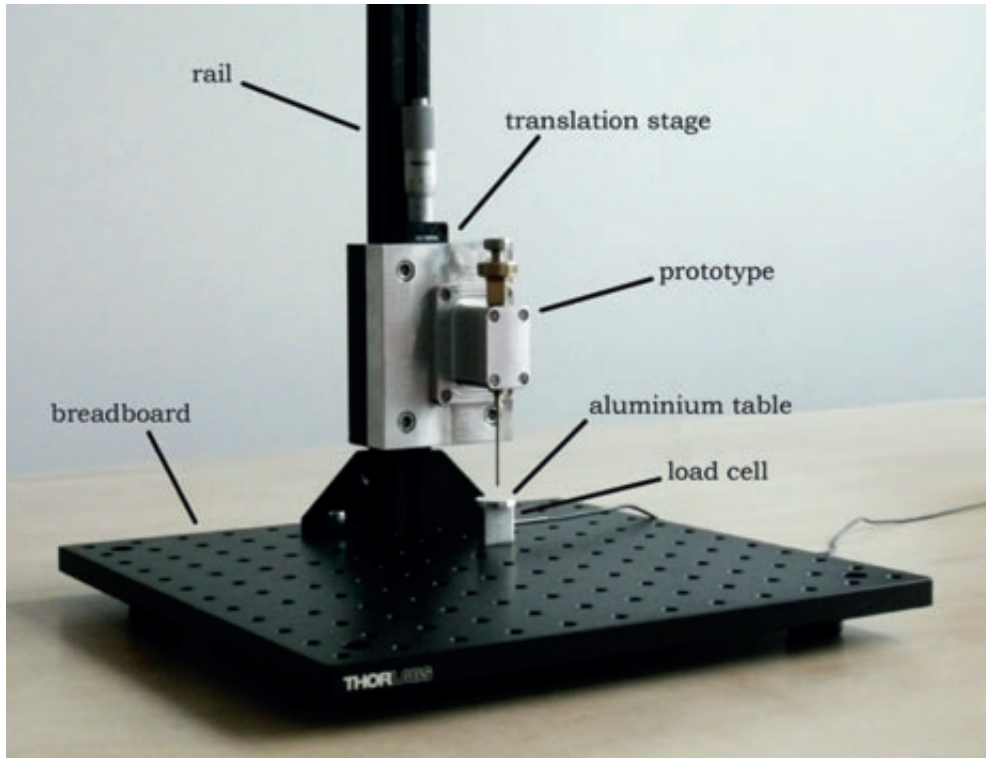
Figure 7.8— Measurement Setup for Experiment 1. The measurement setup consisted of a breadboard, (25 mm construction) rail**,** and a single-axis translation stage to which the prototype was connected. The prototype tip was pointing downwards onto a miniature load cell, on top of which a small aluminum table or bucket was fastened to receive the impact peak force in air and blood mimicking fluid, respectively. For the velocity measurement, an HSV-camera was placed next to the breadboard.

7.3.2. Experiment 2: Puncture Performance of the Prototype

In Experiment 2, the puncture performance of the prototype was evaluated on a CTO model by measuring the number of punctures, the puncture success rate, the number of indenter strikes necessary to achieve a puncture, and the distribution of energy dissipation between the indenter and the CTO model, as a function of the indenter tip shape and the hardness of the CTO model.

Measurement Variables

   Dependent Variables

A CTO is a heterogeneous mix of materials, including intracellular and extracellular

lipids, smooth muscle cells, a collagen-rich extracellular matrix, cholesterol, dense collagen, and calcium [1, 17]. Collagen forms the major structural component of the extracellular matrix of the CTO. CTOs can be soft, hard, or contain both hard and soft regions [1]. Soft CTOs are usually younger than hard CTOs and mainly consist of fat-laden cells and loose fibrous tissue, whereas hard CTOs are characterized by dense fibrous tissue and contain calcified regions [1]. This age-related increase in calcium and collagen content of CTOs substantiates the difficulty of crossing older occlusions.

The calcification process is similar to bone development and generally consists of two main mechanisms [17]. 1) High phosphate levels in the CTO cause smooth muscle cells to differentiate into osteoblasts, eventually resulting in the formation of HydroxyApatite (HA; a calcium phosphate usually denoted as $Ca_{10}(OH)_2(PO_4)_6$)) crystals and thus calcified regions [21]. 2) Cytokines (i.e., proteins that can signal other cells) signalize osteoblast and osteoblast-like cells to the CTO from circulating stem cells, smooth muscle cells, or pericytes (i.e., contractile cells that wrap around the endothelium of the blood vessel wall), which will eventually develop into HA crystals and thus calcification [21].

Along the length of the CTO, three regions can be distinguished, with distinct material properties: (1) the proximal cap, (2) the main body (core), and (3) the distal cap of the CTO [17]. The proximal cap is a thickened fibrous structure at the proximal end (i.e., the first side encountered by the blood flow) of the CTO. It is the hardest part of the lesion and contains particularly densely-packed collagen and calcified tissue. The distal cap is also a thickened structure but somewhat thinner and softer than the proximal cap. The core between the two caps is softer and consists mostly of organized thrombus and lipids [1].

In order to evaluate the performance of the prototype to cross a CTO, we decided to focus on puncturing the proximal cap of heavily calcified CTOs, as this is the hardest, most difficult part to penetrate during PCI. Puncture performance was evaluated in terms of efficiency and efficacy. Specifically, the following three measures were defined:

1. **Number of punctures**. This measure was used as an indication of the efficacy of the puncture (binary classification: puncture vs. no puncture). In our experiment, puncture is defined as complete breakage of the proximal cap. The maximum number of strikes allowed per trial was set to 10.
2. **Number of strikes for puncture**. This measure was used as an indication of the efficiency of the puncture (scale classification).
3. **Energy transfer from the indenter to the CTO model**. The main working principle of the impact method is the collision between a moving body (the indenter) and an initially non-moving body (the CTO). During impact, kinetic energy of the indenter can be transferred into kinetic energy of the CTO or dissipated into heat, deformation, or fracture. There are two main types of

collisions that can occur: (1) an elastic collision and (2) an inelastic collision. An elastic collision is featured by conservation of kinetic energy, whereas in the case of an inelastic collision kinetic energy dissipates into other forms of energy. For our application, the elastic collision is drawn as the *"worst case scenario"*, as both the indenter momentum and kinetic energy are conserved and transferred to the CTO, leading to CTO displacement. The *"ideal scenario"*, on the other hand, is a perfect inelastic collision, where the two colliding bodies stick together after collision, and the maximum amount of kinetic energy is absorbed by the CTO, potentially resulting in CTO puncture. Whether the occurring collision is elastic or inelastic depends on the characteristics of the CTO and its environment, such as the CTO mass, damping coefficient, and spring constant, as well as on the velocity and mass of the indenter. To determine the type of collision, the following two variables were measured:

Indenter bounce velocity. To estimate the amount of energy absorbed by the environment and the CTO combined and to compare this energy absorption in the cases of puncture versus no puncture, the average velocity of the indenter after bouncing away from the proximal cap was measured.

CTO displacement. To determine the type of collision (i.e., elastic or inelastic) and estimate the amount of energy absorbed by the environment and CTO separately, the CTO displacement was measured.

All measurements in Experiment 2 were conducted with the maximized impact condition as identified from Experiment 1 (i.e., strike distance of 1 mm and spring compression distance of 3.5 mm). A pilot study we conducted indicated that testing with lower impact forces would only provide trivial evidence of a lower efficacy and efficiency than the maximized condition.

Independent Variables

The puncture performance of the prototype was evaluated as a function of the following two variables:

1. **Indenter tip shape**. The tip shape that is the most efficient and effective in puncturing a CTO depends on the material properties of the CTO. Fracture of brittle materials leads to material pulverization and chip formation and is usually conducted with blunt tip shapes. Fracture of ductile materials, on the other hand, associates with material tearing and is commonly achieved by using sharp tip shapes, such as needles. Due to the uncertainty of the material properties of the CTO and its environment, the previously described tip shapes were tested: *stamp*, *spherical*, *wedge*, *pointed*, *hollow spherical with guidewire passage*, and *ringed.*

2. **Proximal cap hardness**. The development of a representative CTO animal

model has been proven difficult mainly due to the lack of spontaneous atherosclerosis in animals [1]. Recently, Suzuki *et al.* [22] succeeded in developing an animal model (pig and rabbit) that was histologically similar to human CTOs by implanting hydroxyapatite-coated bio-absorbable polymer sponges in the coronaries. Even though the use of animal models is preferred for device evaluation, these are expensive and do not allow for consecutive tests and evaluation under constant test conditions. Therefore, it was decided to build an artificial CTO model to determine the feasibility of technology. The proximal cap model was made from calcium sulfate ($CaSO_4$; *SHERAALPIN Hartgips hellblau*, SHERA Werkstoff-Technologie GmbH & Co. KG) and a gelatin mixture (*sheet gelatin*, Dr. Oetker, Bielefeld, Germany). These materials were selected to mimic the high calcium and collagen concentrations found in the proximal caps of heavily calcified CTOs. Calcium sulfate is a mineral that can be found in the human body and has similar mechanical properties as organic HA crystals. Specifically, the compressive strength of $CaSO_4$ is 44 MPa (after 1 hour) and that of (carbonated) HA formed at body temperature approximately 30–70 MPa [23]. Higher compressive strengths are found in calcium-deficient HA ($Ca_9HOH(PO_4)_6$ (approximately 170 MPa) and sintered HA (up to 500 MPa) [23]. However, the HA crystals found in CTOs are most often referred to as carbonated HA; it is unclear whether calcium-deficient HA is present in CTOs and whether sintered HA is formed in a different way than natural HA (as it is manufactured using significantly higher temperatures than body temperature). Therefore, the lower compressive strength values found for carbonated HA seem more likely to represent naturally found HA in CTOs.

To mimic the densely-packed collagen and overall heterogeneous morphology of the CTO at the proximal cap, the calcium sulfate was mixed with gelatin, which is the product of structural and chemical degradation of collagen.

Transluminal calcium ≥50% (as assessed by Multi-Detector Computed Tomography (MDCT)) is a strong predictor for PCI failure. In a study of Cho *et al.* [24], the calcium burden of CTOs was determined using MDCT. In this study a mean calcium percentage (determined as the percentage of calcium cross-sectional area divided by vessel area) of 53.9 ± 20.3% was found in the PCI-failure cases. As we focus on crossing the most calcified CTOs, proximal caps with three degrees of hardness were tested (called henceforth *ductile*, *reference*, and *brittle*) with a calcium percentage over 50%. The *ductile* model was created with 50 wt% calcium powder and 50 wt% gelatin mixture in a Ø10 mm circular slice and represented the mean calcium percentage in CTOs in the PCI-failure group in [24]. The *reference* model was created with 75 wt%

calcium powder and 25 wt% liquid gelatin mixture. Whereas reported average concentrations of calcium content within calcified CTOs are generally lower than 75% [24], CTO caps are heterogeneous and thus local calcium concentrations as high as 75% are expected. Next to the reference model, a *brittle* model (77 wt% calcium powder and 23 wt% clear water) was also prepared to represent the most heavily calcified CTOs that can be encountered.

Proximal caps are on average 0.5 mm thick [25]. Due to molding difficulties to produce homogeneous 0.5 mm models, a model thickness of 1 mm was set.

Unlike acute occlusions, CTOs are strongly connected to the blood vessel wall, which in turn is connected to cardiac muscle tissue of the heart. In order to simulate the environment of the CTO while allowing for consecutive measurement of the prototype under stable test conditions, it was chosen to simulate the environment of the CTO using a mixture of 25 wt% gelatin and 75 wt% water. When set, this mixture has an estimated Young's modulus between 100 kPa and 130 kPa, resembling the Young's modulus of cardiac muscle tissue [26]. Furthermore, to emulate the strong blood vessel wall connection, a Ø10 mm notch with approximately 7 mm depth was created in the center of the gelatin mixture (Ø50 mm, 26 mL; Figure 7.9) in which the proximal cap model was placed. This notch also allowed for simultaneous stretching and compressing of the gelatin, similar to the clinical situation. For a complete overview of the steps followed to manufacture the CTO models, see Appendix 7.A.

Measurement Setup
For Experiment 2, the prototype was suspended in the same way as described in Experiment 1 (see Figure 7.10). The sole difference was that, instead of load cell, a CTO model was placed directly under the prototype (Figure 7.9).

Measurement Protocol
The number of punctures and the number of strikes were measured for all 18 conditions defined by the two independent variables (6 indenter tip shapes x 3 degrees of model hardness). Additionally, to evaluate the overall effectiveness of the impact method as a function of the CTO model hardness, the results from all six tip shapes were grouped together per CTO model, resulting in a data analysis of 3 groups within the 18 performed trials. Each of the *ductile*, *reference*, and *brittle* models were prepared in a single batch to limit the variability in the CTO models, and all measurements were conducted within 4 hours, to limit the effect of CTO model hardening over time. Three measurements were conducted per condition.

The measurements of the energy transfer from the indenter to the CTO model were conducted with the spherical tip shape. One energy transfer measurement was conducted for the *ductile* and *reference* models and two for the *brittle* model.
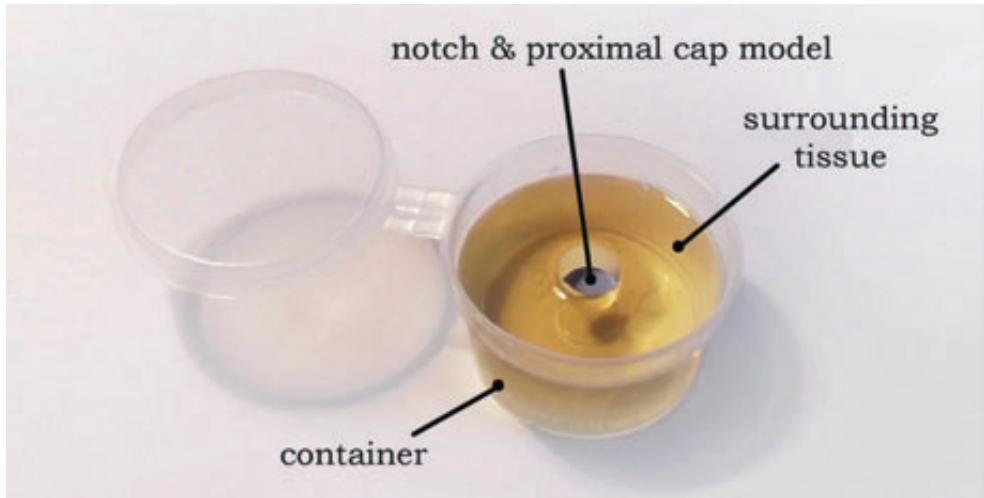
Figure 7.9— The CTO Model. The CTO model consisted of a small container (Ø 50 mm, 26 mL) filled with gelatin representing the surrounding cardiac tissue (environment model), in which a Ø1 mm, 1 mm thick slice of stiffened plaster cast mixed with gelatin/water was placed.

7
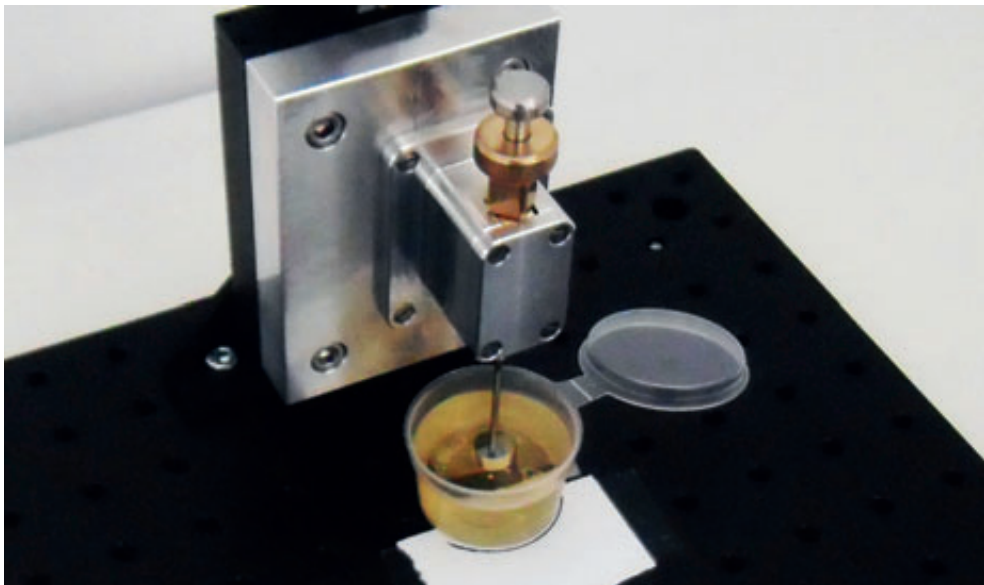
Figure 7.10— Measurement Setup for Experiment 2. The measurement setup consisted of the same Thorlabs facility as in Experiment 1 (see Figure 7.8), with the only difference that instead of the load cell, the CTO model (see Figure 7.9) was placed directly under the prototype tip.

Data Analysis

Per indenter tip shape and CTO model, the number of strikes to achieve puncture and the number of punctures were counted. Furthermore, per CTO model (tip shapes grouped together), the number of punctures, the success rate (defined as the percentage of punctures across the 18 conditions), as well as the minimum, maximum, and mean number of strikes across the 18 conditions to achieve puncture were determined.

To estimate energy transfer from the indenter to the CTO, the indenter momentum and kinetic energy ($E_{kinetic} = \frac{1}{2}mv^2$, with m = mass of the indenter [kg] and v = the velocity of the indenter [m/s]) 0.1 ms before and 0.1 ms after impact was calculated using the indenter velocity derived from the HSV images using the method previously described. Furthermore, the maximum displacement of the CTO model per measurement was manually derived from the captured HSV images, and the energy absorbed by the (gelatine) environment was calculated as $U = \frac{1}{2}VE\varepsilon^2$, with V = volume of the gelatine (26 mL), E = Young's modulus of the gelatine (115 kPa), and ε = strain of the gelatine during impact (approximated as the displacement of the proximal cap model divided by the original location).

7.3.3. Control Experiment

In order to compare the performance of the newly developed device with that of currently used guidewires and to assess the validity of the used CTO model, a separate control experiment was performed. In this experiment, a rigid Ø0.4 mm stainless steel rod was used to model the flexible guidewire tip. The rigid rod model was driven into the ductile and reference CTO model (equal to the previously described models) by a linear stage. The force required to puncture the CTO model as well as the resulting displacement of the model were measured. The velocity of the insertion ranged between 0.1, 0.5, 5, 50, 500, and 1000 mm/s, to simulate low velocity and high velocity insertion. Currently used insertion velocities of the guidewire are not described in literature. Therefore, a wide velocity range was tested, with the higher insertion velocities chosen to determine the effect of high-speed insertion.

7.4. RESULTS

7.4.1. Experiment 1: Mechanical Performance of the Prototype

Indenter Momentum

In Figure 7.11, a typical HSV image sequence of an indenter strike is illustrated. The calculated momenta for each of the six tested conditions (2 strike distances x 3 spring compression distances) are illustrated in Table 7.1. The mean velocity generated with maximized actuation force was 3.4 m/s, which translates to a mean indenter momentum

Figure 7.11— Example of an HSV Image Sequence of an Indenter Strike with an Object Distance of 3 mm and a Spring Compression Distance of 3.5 mm. An average indenter velocity of 3.0 m/s can be derived.

Table 7.1— Velocity (mean ± standard deviation, $n = 5$) and Mean Indenter Momentum ($p = mv$) for the Six Conditions.

Strike Distance / Spring Compression Distance	Indenter Velocity [v; m/s]	Indenter Momentum [p; mNs]
1 mm / 3.5 mm	3.4 ± 0.11	1.33 ± 0.04
3 mm / 3.5 mm	3.0 ± 0.16	1.17 ± 0.06
1 mm / 2.8 mm	2.2 ± 0.07	0.86 ± 0.03
3 mm / 2.8 mm	1.3 ± 0.20	0.51 ± 0.08
1 mm / 2.0 mm	1.0 ± 0.05	0.39 ± 0.02
3 mm / 2.0 mm[a]	-	-

[a] For this condition, the velocity of the indenter could not be determined with accuracy due to the minimal travelled distance of the indenter out of the outer shaft.

of 1.33 mNs (for $m = 0.39$ grams). Decreasing the compression spring distance and increasing the strike distance was associated with a decrease in indenter velocity. In the condition of minimal spring compression distance (2 mm), the indenter did not reach the ultimate position (3 mm).

Impact Peak Force

Impact Peak Force in Air

Figure 7.12 shows the impact peak force measurements in air. The data were approximately normal (based on a one-sample Kolmogorov-Smirnov test). The impact peak forces (mean ± standard deviation, $n = 5$) are presented in Table 7.2. The maximum mean impact peak force was approximately 19.2 N, generated with maximized actuation

force and independent of the strike distance. The impact peak force decreased with decreasing spring compression distance.

Impact Peak Force in BMF

Figure 7.13 shows the impact peak force measurements in BMF. Data were approximately normal. The impact peak force in BMF was approximately a factor 0.49 to 0.11 lower than that of the impact peak force in air (Table 7.2). The strike distance was of greater influence on the impact peak forces in BMF than in air, which is illustrated by a lower impact peak force in BMF in comparison to air and F_{peak} BMF/F_{peak} Air ratio for a strike distance of 3 mm.

7

Figure 7.12— Impact Peak Force of the Indenter in Air. Each color (*n* = 5 strikes) represents a different strike distance x spring compression distance combination. For each indenter strike, represented by one line, time 0 corresponds to the maximum impact peak force.

7.4.2. Experiment 2: Puncture Performance of the Prototype

Number of Punctures, Success Rate, and Number of Strikes

Table 7.3 shows the puncture performance for the different indenter tip shapes (see also Figure 7.14 for a typical result of multiple impact strikes on the three CTO models with the spherical indenter). For the *ductile* model, the indenter left an imprint of plastic material deformation, but did not manage to penetrate the model within 10 strikes. The measurements on the *reference* model did not show convincing results to indicate which tip shapes were the most effective and efficient. However, the *wedge* tip shape was the only tip shape able to puncture the model during all three tests (6 strikes on average). Finally, for the *brittle* model the most efficient and effective tip shapes were the *spherical* (2.7 strikes on average), the *spherical with guidewire passage* (2.7 strikes on average), and the *ringed* (2 strikes on average) tip shape. The *pointed* tip shape was generally less effective and efficient to puncture the *brittle* model, as compared to all other tip shapes. Specifically, the only case in which the *brittle* model was not punctured occurred with the pointed tip shape. Moreover, in its two successful cases, this indenter needed 8 strikes to puncture the model, which is much higher than the average of 2.5 strikes required with the other five tip shapes (*n* = 15).

Table 7.4 shows the number of punctures, success rate, and the number of strikes for puncture, for the *ductile*, *reference*, and *brittle* models. It can be seen that the number of punctures (efficacy) and the success rate increased, and number of strikes for puncture (efficiency) decreased with increasing model hardness.

Energy Transfer from the Indenter to the CTO Model

The average velocity of the (spherical) indenter after bouncing from the proximal cap model was approximately 0.5 m/s in the cases in which the proximal cap model was not punctured (Table 7.5). No differences were observed in the bouncing velocities for the different proximal cap models. A slightly higher bounce velocity of 0.8 m/s was observed when the brittle proximal cap model was punctured (Table 7.5).

The maximum displacement of the proximal cap models in case no puncture occurred was between 0.8 and 0.9 mm (Figure 7.15 and Table 7.5). A larger displacement was observed for the punctured *brittle* model in comparison to the models in which no puncture was achieved, with a maximum of 1.4 mm (Table 7.5). Based on this data, the energy loss of the indenter is estimated to be between 2.34 and 2.11 J (~95–98% energy loss, see Table 8.5). Most of this energy was absorbed by the proximal cap of the CTO model (about 95–99%), whereas the remaining 1–5% was absorbed by the gelatin.
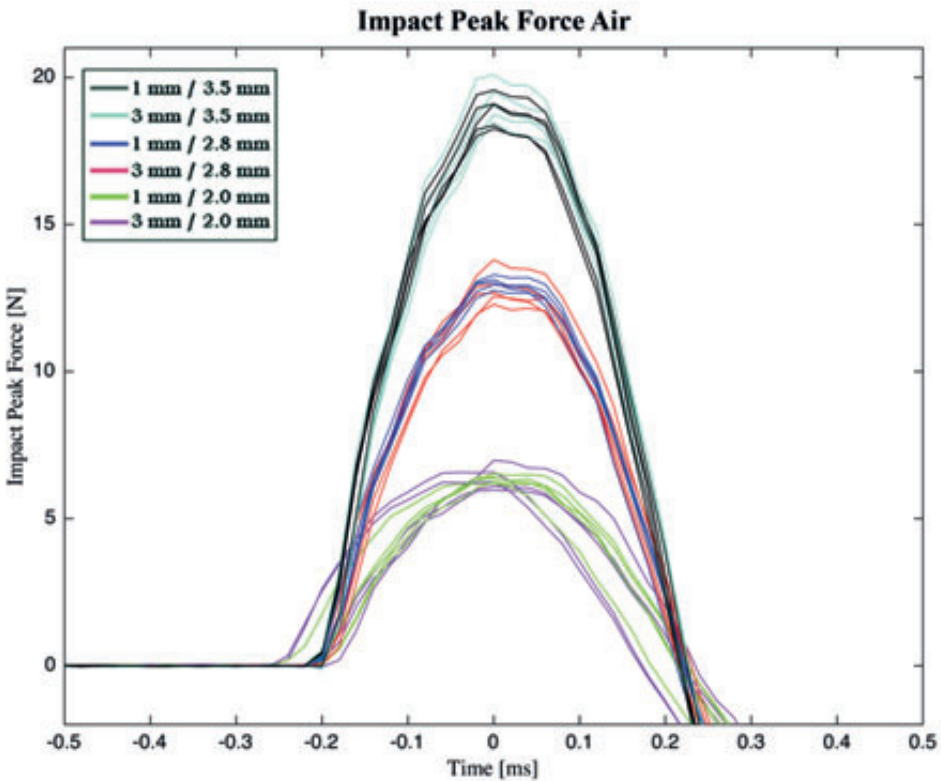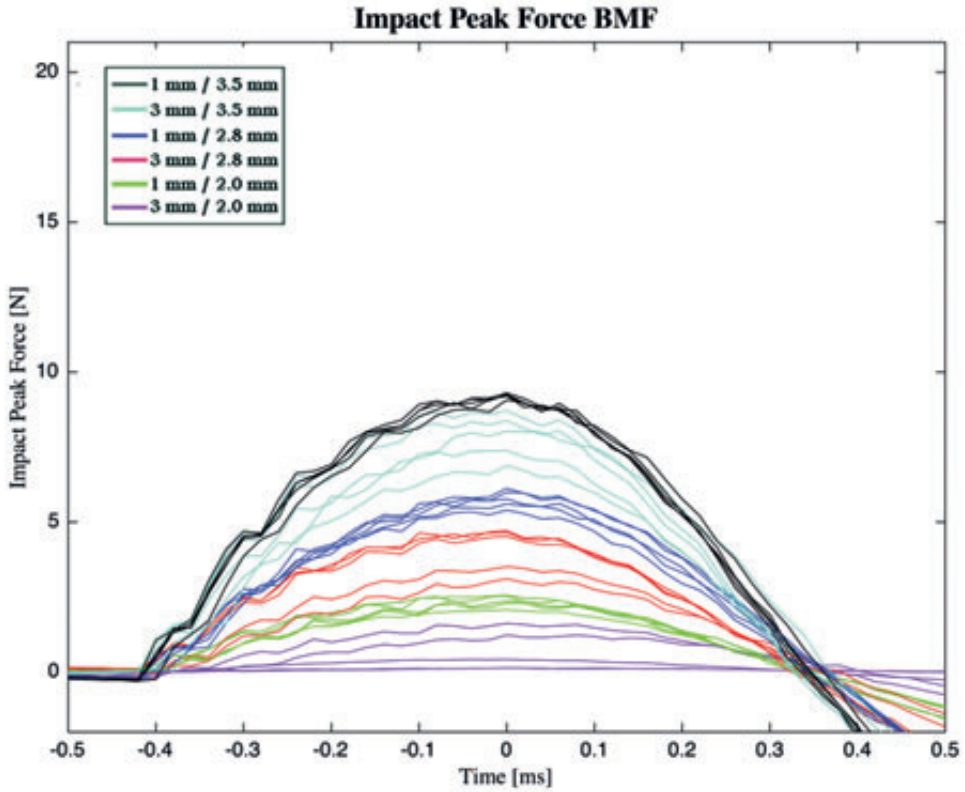
Figure 7.13— Impact Peak Force of the Indenter in BMF. Each color (*n* = 5 strikes) represents a different strike distance x spring compression distance combination. For each indenter strike, represented by one line, time 0 corresponds to the maximum impact peak force.

Table 7.2— Impact Peak Force F_{peak} (Mean ± Standard Deviation, *n* = 5) in Air and in Blood Mimicking Fluid (BMF) for the Six Conditions, and Ratio of the Impact Peak Force in BMF and Air (F_{peak} BMF / F_{peak} Air).

Strike Distance / Spring Compression Distance	F_{peak} Air [N]	F_{peak} BMF [N]	F_{peak} BMF / F_{peak} Air [-]
1 mm / 3.5 mm	18.9 ± 0.55	9.2 ± 0.08	0.49
3 mm / 3.5 mm	19.2 ± 0.65	7.9 ± 0.75	0.41
1 mm / 2.8 mm	13.0 ± 0.20	5.8 ± 0.29	0.45
3 mm / 2.8 mm	12.9 ± 0.58	4.1 ± 0.74	0.32
1 mm / 2.0 mm	6.4 ± 0.13	2.4 ± 0.20	0.38
3 mm / 2.0 mm	6.4 ± 0.41	0.7 ± 0.68	0.11

Table 7.3— Number of Strikes to Puncture the Proximal Cap Models, using Indenters with Different Tip Shapes. The tip shapes are presented in the top row. The CTO model type and test number (*n* = 3) are given in the left two columns.

Type of model	#	*Stamp*	*Spherical*	*Wedge*	*Pointed*	*Spherical GW*[a]	*Ringed*
Ductile model	I	No puncture	No puncture	No puncture	No puncture	No puncture	No puncture
	II	No puncture	No puncture	No puncture	No puncture	No puncture	No puncture
	III	No puncture	No puncture	No puncture	No puncture	No puncture	No puncture
Reference model	I	9	4	6	No puncture	No puncture	5
	II	No puncture	5	7	7	9	10
	III	6	No puncture	5	No puncture	10	9
Brittle model	I	2	3	3	8	3	2
	II	3	3	3	8	2	2
	III	5	2	3	No puncture	3	2

Note. The maximum number of strikes was set to 10 and # indicates the test number (I, II, or III)

[a] Spherical indenter with guidewire passage

Figure 7.14— Typical Proximal Cap Models after Striking the Indenter Multiple Times Onto Them. The illustrated proximal cap models were struck with the spherical indenter tip shape, on (A) the *ductile* model (10 strikes on all of the models), (B) the *reference* model (from left to right: 4, 5, and 10 strikes), and (C) the *brittle* model (from left to right: 3, 3, and 2 strikes).

Table 7.4— Number of Punctures (All Tip Shapes Combined) for the Three CTO Models.

Type of Model	Number of Punctures	Success Rate	Mean Number of Strikes (range)
Ductile Model	0 / 18	0 %	-
Reference Model	13 / 18	72 %	7.3 (4–8)
Brittle Model	17 / 18	94 %	3.4 (2–8)

241
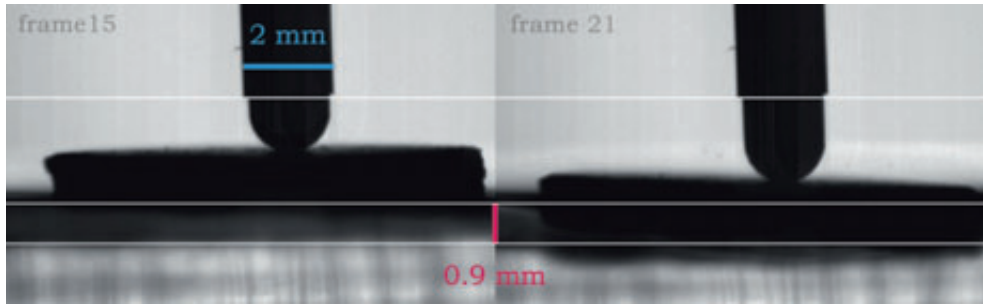
Figure 7.15— A Visualization of yhe Analysis of HSV Images to Derive the Maximum CTO Displacement of a Non-Punctured Brittle Model using the Spherical Indenter.

Table 7.5— Energy Transfer From the Indenter to the CTO Model.

Type of Model	Initial Velo-city Inden-ter [m/s]	Initial Momentum [mkgm/s]	Initial Kinetic Energy [mJ]	Bounce Velocity Indenter [m/s]	Bounce Momentum [mkgm/s]	Bounce Kinetic Energy [mJ]	Loss Kinetic Energy Indenter [mJ]	CTO displacement [mm]	Energy Absorption Gelatin [mJ]	Energy Absorption CTO [mJ]
Ductile Model (no Puncture)	3.3	1.29	2.16	0.5	0.20	0.05	2.11 (97.74%)	0.8	0.020 (1%)	2.09 (99.0%)
Reference Model (no Puncture)	3.5	1.37	2.39	0.5	0.20	0.05	2.34 (97.96%)	0.8	0.020 (0.9%)	2.32 (99.1%)
Brittle Model (no Puncture)	3.3	1.29	2.16	0.5	0.20	0.05	2.11 (97.74%)	0.9	0.025 (1.2%)	2.09 (98.8%)
Brittle Model (Punctured)	3.5	1.37	2.39	0.8	0.31	0.12	2.26 (94.78%)	1.4	0.060 (5.4%)	2.20 (94.6%)

7.4.3. Control Experiment

The mean force to penetrate through the CTO model was 0.24 ± 0.09 N for the ductile model and 2.7 ± 1.1 N for the reference model. No significant differences were found in

penetration force for the different insertion velocities for each CTO model as determined by two separate ANOVAs. The displacement of the CTO model ranged between 1 and 2.7 mm, with the lowest value measured for the highest penetration velocity.

7.5. DISCUSSION

7.5.1. Summary of Main Findings

Mechanical Performance

     Indenter Momentum

The theoretical maximum velocity of the indenter (frictional effects neglected) was calculated as 6.6 m/s at the moment the indenter protrudes from the prototype, using Equations. (7.1–7.4):

$$F = K \cdot x, \tag{7.1}$$

$$a = \frac{F}{m}, \tag{7.2}$$

$$v = v_0 + a \cdot t \text{ , and} \tag{7.3}$$

$$s = s_0 + v \cdot t, \tag{7.4}$$

with a = acceleration [m/s^2] of the spring and thus the indenter, F = actuation force of the spring [N] of 4.55 N, K = spring constant [N/mm] of 1.3 *N/mm*, m = mass of the indenter [grams] of 0.39 grams, x = maximum spring compression distance [mm] of 3.5 mm, s = distance travelled [mm], s_0 = distance travelled at time t [mm], t = time step [s], v = velocity of the indenter [m/s] at $t_1 = t_0 + t$, and v_0 = velocity of the indenter [m/s] at time t_0.

     From the indenter mass and theoretical maximum velocity of the indenter, a theoretical maximum indenter momentum of 2.34 mNs can be deduced. The actual (measured) indenter momentum of 1.40 mNs (with an associated velocity of 3.6 m/s) is approximately 40% lower than the theoretical value. It can thus be concluded that friction between the indenter, compression spring, and outer shaft plays an important role within the mechanism. Potentially, a higher efficiency may be realizable by reducing frictional effects. This could, for example, be achieved by a different material choice for the moving parts (the indenter and spring) and the surrounding catheter tube, or by lubricating the moving parts.

Impact Peak Force.

In Thind *et al.* [7], the puncture force of 2, 6, 12, and 15 weeks old rabbit femoral CTOs was measured using a probe similar in profile to a Ø0.36 mm guidewire. These authors found that the puncture force is significantly lower in CTOs younger than 6 weeks of age (0.61 N and 0.78 N in CTOs of 2 and 6 weeks old, respectively) than in those older than 12 weeks (1.21 N and 1.52 N in CTOs of 12 and 15 weeks old, respectively). These values are in line with Roy *et al.* [27], in which puncture forces of excised peripheral CTOs between 0.3 and 1.7 N for soft (containing loose fibrous tissue, fat, thrombus, or micro-blood vessels) and hard (containing collagen and speckled calcium) CTOs, respectively, were measured.

In the control experiment, it was also found that the less calcified CTO models required significantly lower penetration forces. For the brittle model slightly higher penetration forces were found compared to the animal model in Thind *et al.*[7], which could have been caused by the larger diameter of the rigid rod we used (Ø0.4 mm vs. Ø0.36 mm), the thickness of the proximal cap (1 mm), and the consistency of the model. Nonetheless, the 0.2–2.7 N penetration force found in the artificial CTO model is comparable to the values found in the animal model of Thind *et al.* [7] and Roy *et al.* [27].

The maximum tip load (i.e., the load in grams that a guidewire can withstand before buckling) of dedicated coronary CTO guidewires ranges between 0.8 and 26.7 grams, which is equal to 0.008 and 0.26 N [5]. If we compare the maximum tip load of dedicated guidewires (i.e., ~0.26 N) [5], with the required penetration force of the reference CTO model (2.7 N), it becomes clear that buckling is likely when using dedicated coronary CTO guidewires. It can, therefore, be argued that a dedicated CTO guidewire is unable to penetrate the reference model.

In the prototype experiments, maximum mean impact peak forces of 19.2 N and 9.2 N were measured in air and BMF, respectively, which in theory is sufficient to puncture the CTO. Moreover, even though impact peak forces were 50 to 90% lower in the BMF than in air, they were still above the values in Thind *et al.* [7]. It must be noted, however, that since no experiments have been performed on real CTOs, there is still uncertainty about the required impact peak force to puncture real in-vivo CTOs.

Puncture Performance

Number of Punctures & Number of Strikes.

The highest puncture performance and efficiency was observed for the brittle CTO models. The effectiveness of the impact method to puncture the more ductile CTO models was limited, which can be explained by the fact that ductile materials absorb energy from the impact loads by deformation (elastic and plastic). This finding is

consistent with the fact that the impulse method is more widely used to fracture hard and brittle materials, rather than tough and/or elastic materials.

Puncture performance of the prototype was assessed using the six indenter tip shapes on the three proximal cap models. For the *ductile* models, it was expected to see improved puncture performance in terms of number of punctures and number of strikes for puncture with the sharp indenter tip shapes. Even though no puncture was achieved, the sharpest tools (pointed and wedge indenter) did leave a clearly visible imprint. For the *brittle* models, the ringed tip shape was the most effective, whereas the pointed indenter tip shape showed the least effective results. For the non-pointed indenter tip shapes tested, no distinction could be made regarding their efficiency or effectiveness on fracturing models; all performed similarly well in fracturing the brittle material models and were able to puncture reference models, with more ductile characteristics. Furthermore, the "open" shapes (*hollow spherical* and *ringed*) performed comparably to the "closed" shapes (*stamp, spherical*, and *wedge*), while being advantageous for future clinical prototypes in which a guidewire may need to be guided through the crossing instrument. Due to the uncertainty of the material characteristics of real CTOs, it is difficult to provide a recommendation about which tip shape is the most suitable for CTO crossing. Nonetheless, it can be suggested that the pointed indenter tip shape may be the least appropriate for fracturing CTOs, as these are usually heavily calcified and thus brittle.

During puncture some minor chips of the CTO proximal cap model were formed, which are potentially harmful as they can lead to stroke in the smaller blood vessels of the brain, for example. In order to minimize this risk, the device should only be used to penetrate the proximal cap of the CTO; crossing of the CTO body should be executed using a dedicated guidewire. Furthermore, it is recommended that the device is used in combination with a proximal emboli filter or active aspiration.

Energy Transfer from the Indenter to the CTO Model

The observed maximum displacements of the CTO models (1.4 mm) were lower than the displacements of over 4 mm reported for guidewires statically pushed against a CTO until puncture is achieved (derived from [7]). Furthermore, in the control experiment, the average displacement of proximal cap models induced by an almost static (0.1 mm/s) guidewire force was 2.1 mm ($n = 4$). It may, therefore, be argued that the impulse method shows merit to minimize stretch of the blood vessel wall during PCI of CTOs. However, other negative effects due to the impulse should be investigated, such as the risk of blood vessel wall damage as a result of a direct hit or damage due to device failure, in which, for example, the indenter or spring disconnect from the device.

In our experiments, the amount of kinetic energy lost during the indenter strike was large (kinetic energy before and after collision were determined at 2.2 mJ and 0.1 mJ, respectively), indicating that the collisions with the CTO models were highly inelastic,

albeit not purely inelastic, since up to 5.4% of the energy dissipated in the environment. To limit the displacement of the CTO and associated energy dissipation, the velocity of the indenter should be increased, allowing the inertia and damping of the CTO and its environment to provide a higher counterforce to the applied impulse than in the current design. This could be achieved by diminishing the effect of dry and viscous friction between the moving parts, by increasing the actuation force, and by minimizing the indenter mass. Furthermore, in a future experiment, the energy dissipation to the environment should be estimated by measuring the energy absorbed by the CTO proximal cap model on a fixed surface.

The higher bounce velocity of the indenter and CTO model displacement observed in the cases of successful CTO model puncture compared to the cases when no puncture was achieved can be explained by two possible phenomena. First, it is likely that in the cases of successful puncture, tilting of the two parts of the proximal cap model after fracturing has led to a more concentrated distribution of the impact force on the gelatin, leading to a larger displacement as compared to the cases of no puncture. Second, in the case of puncture less energy is likely to be lost in the proximal cap model, compared to a non-puncture case.

7.5.2. Design recommendations

The most important redesign step of the prototype concerns the transformation of the rigid design into a flexible clinical instrument. In order to allow for navigating towards the lesion site, a flexible shaft will need to be placed between the tip section and the handle. The flexible shaft should be axially incompressible or force neutral (such as a Bowden cable) to prevent axial compression and movement during activation of the tip section. Furthermore, the inner locking core needs to be replaced by a flexible cable that runs from the distal tip of the device, through the flexible shaft, towards the handle. To actuate the gripper, a flexible axially stiff tube or cables should also run through the shaft of the device. Additionally, the rigid tip parts such as the outer shaft, gripper, position block, and indenter, need to be redesigned to allow for bending motion. For this purpose, the outer shaft can be replaced by a flexible shaft similar to a catheter, a flexible cable can replace the connection between the indenter tip and stop, and the position block and the gripper can contain joints to allow for bending motions while restricting axial compression or extension. Moreover, compression of the spring during actuation may straighten the previously bend catheter shaft, potentially resulting in undesired pressure on, and thus damage of, the arterial wall. The addition of steering cables can possibly prevent or counteract this effect by retaining the bend shape of the catheter during loading and unloading. Another important issue that needs to be addressed is that of the loss of the indenter caused by failure of the connection with the indenter stop. By adding a second stop at the distal end of the catheter, the risk of indenter loss may be minimized. Finally, to allow for hand-held operation of the prototype, the enveloping box needs to be

redesigned. The handle can, in theory, be 3D-printed in any arbitrary shape to meet the needs and preferences of the operator, as long as it contains an insert for the loading, locking, and trigger mechanism.

The prototype has proven effective in puncturing the CTO models. However, it is recommended that the indenter velocity is increased to further decrease the CTO displacement and increase the puncture effectiveness. For this purpose, the effect of the BMF viscosity should be minimized by, for example, adding a sealing that prevents blood from entering the prototype. Furthermore, stiffer spring designs should be investigated, and the effect of friction within the device tip should be minimized by, for example, using low friction coefficient material combinations. Finally, different types of output characteristics need to be investigated, including different vibrating motions, to determine the most optimal output characteristic for achieving puncture of the different CTO models.

To allow for atraumatic navigating through the vasculature and account for diameter differences between patients, the prototype should be further miniaturized. Current clinically available dedicated CTO devices have a diameter of in between Ø0.43 and Ø1.5 mm, so miniaturization to at least the Ø1.5 mm is preferred. Miniaturization of the prototype is relatively easy to achieve due to the small number of parts (14) and low complexity of the prototype. The main challenge lies in the miniaturization of the gripper and its counterpart, the indenter stop.

7.5.3. *Limitations of this Study*

The development of an accurate and reproducible coronary CTO model is a complex undertaking and, up to today, has not produced a representative replica of a CTO. This is mainly because simulating calcification and the inflammatory component is difficult. In order to evaluate the device performance, it was chosen to use an artificial CTO model. This CTO model allowed us to test the device under controlled conditions, which is not possible using an animal CTO model. However, image analysis of the CTO models to further characterize them is needed. This will determine how well the artificial CTO models mimic real CTOs. In future research it is recommended that the device is tested in an animal CTO model, such as the one described by Thind *et al.* [7], to further determine its effectiveness.

7.6. CONCLUSION

The low success rates of endovascular revascularization of CTOs can be mainly attributed to the inability to cross the proximal caps of heavily calcified CTOs. In an effort to pursue improved crossing ability, we investigated a new crossing method in which an impulse is applied onto the CTO. Using an impulse to penetrate the proximal cap of heavily calcified CTOs is proven to be advantageous as it increases the buckling resistance of the

tool, minimizes movement of the CTO, and can potentially decrease the penetration load. A proof-of-principle prototype was developed that uses a spring-loaded indenter with interchangeable tip shapes and a compliant reload mechanism. The prototype was evaluated in terms of its mechanical performance and puncture effectiveness on CTO models made of gelatin and calcium. From this experiment it became clear that the proposed impulse prototype outperforms currently available dedicated CTO guidewires when it came to puncture performance. A maximum mean indenter velocity of 3.6 m/s, translating to an indenter momentum of 1.33 mNs, and a maximum mean impact peak force of 9.2 N were measured in BMF. This impact peak force is well over what can be delivered by dedicated CTO guidewires, as well as the 1.52 N puncture force previously measured in rabbit femoral CTOs of 15 weeks of age, and should thus be sufficient to penetrate real CTOs [7]. Furthermore, the displacement of the CTO model was significantly less with the proposed prototype than in a control experiment with a rigid rod and in the animal CTO model of Thind *et al.* [7]. In contrast to current CTO devices and guidewires, the prototype was most effective and efficient on the *brittle* CTO models using the *spherical, hollow spherical with guidewire passage,* and *ringed* tip shape. Future developments will be focused on developing a smaller (Ø1 mm), faster, and flexible clinical prototype that allows for penetrating both soft and hard CTOs with minimal tissue deformation and energy dissipation. This prototype will be guided over a guidewire through the vasculature towards the occlusion in one of the coronaries where it can aid in penetrating the proximal caps of the most heavily calcified CTOs.

7

ACKNOWLEDGMENTS

REFERENCES

[1]   Stone GW., Reifart NJ, Moussa I, Hoye A, Cox DA, Colombo A, et al. Percutaneous recanalization of chronically occluded coronary arteries. A consensus document - Part I. Circulation. 2005; 112(15): pp. 2364-2372.

[2]   Sakes A., Regar E, Dankelman J, and Breedveld P. Crossing total occlusions: navigating towards recanalization. Cardiovascular Engineering and Technology. 2016;7(2): pp. 103-117.

[3]   Stone GW, Reifart NJ, Moussa I, Hoye A, Cox DA, Colombo A, et al. Percutaneous recanalization of chronically occluded coronary arteries - A consensus document - Part II. Circulation. 2005;112(16): pp. 2530-2537.

[4]   Galassi A, Tomasello S, Reifart N, Werner GS, Sianos G, Bonnier H, et al. In-hospital outcomes of percutaneous coronary interventions in patients with chronic total occlusion:

insights from the ERCTO (European Registry of Chronic Total Occlusion) registry. Eurointervention. 2011; 7(4): pp. 472-479.

[5]   Sianos G, Werner GS, Galassi A, Papafaklis MI, Escaned J, Hildick-Smith D, et al. Recanalisation of chronic total coronary occlusions: 2012 consensus document from the EuroCTO Club. EuroIntervention. 2012;8(1): pp. 139-145.

[6]   Kinoshita I, Katoh O, Nariyama J, Otsuji S, Tateyama H, Kobayashi T, et al. Coronary angioplasty of chronic total occlusions with bridging collateral vessels: immediate and follow-up outcome from a large single-center experience. Journal of the American College of Cardiology. 1995;26(2): pp. 409-415.

[7]   Thind A, Strauss B, Teitelbaum A, Karshafian R, Ladouceur M, Whyne C, et al. A novel method for the measurement of proximal fibrous cap puncture force in chronic total occlusions: the effect of increasing age. EuroIntervention. 2011;6(8): pp. 997-1002.

[8]   Stone GW, Colombo A, Teirstein PS, Moses JW, Leon MB, Reifart NJ, et al. Percutaneous recanalization of chronically occluded coronary arteries: Procedural techniques, devices, and results. Catheterization and Cardiovascular Interventions. 2005;66(2): pp. 217-236.

[9]   Lock M. A study of buckling and snapping under dynamic load. El Segundo, CA: Laboratory Operations Aerospace Corporation. Report Number TR-0158 (3240-30)-3; 1967. pp. 1-55.

[10]   Boutouyrie P, Bussy C, Lacolley P, Girerd X, Laloux B, and Laurent S. Association between local pulse pressure, mean blood pressure, and large-artery remodeling. Circulation. 1999;100(13): pp. 1387-1393.

[11]   Dodge J, Brown BG, Bolson EL, and Dodge HT. Lumen diameter of normal human coronary arteries. Influence of age, sex, anatomic variation, and left ventricular hypertrophy or dilation. Circulation. 1992;86(1): pp. 232-246.

[12]   Kahraman H, Ozaydin M, Varol E, Aslan SM, Dogan A, Altinbas A, et al. The Diameters of the aorta and its major branches in patients with isolated coronary artery ectasia. Texas Heart Institute Journal. 2006;33(4): pp. 463-468.

[13]   Kotowycz MA and Džavík V. Radial artery patency after transradial catheterization. Circulation: Cardiovascular Interventions. 2012;5(1): pp. 127-133.

[14]   Saito S, Ikei H, Hosokawa G, and Tanaka S. Influence of the ratio between radial artery inner diameter and sheath outer diameter on radial artery flow after transradial coronary intervention. Catheterization and Cardiovascular Interventions. 1999;46(2): pp. 173-178.

[15]   Sandgren T, Sonesson B, Ahlgren ÅR, and Länne T. The diameter of the common femoral artery in healthy human: influence of sex, age, and body size. Journal of Vascular Surgery. 1999;29(3): pp. 503-510.

[16]   Yoo BS, Yoon J, Ko JY, Kim JY, Lee SH, Hwang SO, et al. Anatomical consideration of the radial artery for transradial coronary procedures: arterial diameter, branching anomaly and vessel tortuosity. International Journal of Cardiology. 2005;101(3): pp. 421-427.

[17]   Yalonetsky S, Osherov AB, Strauss BH, Galassi AR, Tomasello S, and Khamis H. Chronic Total Occlusions. A guide to recanalization (2nd ed.). Hoboken, NJ: Wiley-Blackwell, 2013.

[18]   Ramnarine KV, Nassiri DK, Hoskins PR, and Lubbers J. Validation of a new blood-mimicking fluid for use in doppler flow test objects. Ultrasound in Medicine & Biology. 1998;24(3): pp. 451-459.

[19]   Samavat H, and Evans J. An ideal blood mimicking fluid for doppler ultrasound phantoms. Journal of medical physics/Association of Medical Physicists of India. 2006;31(4): pp. 275-278.

[20]   Yousif MY, Holdsworth DW, and Poepping TL. A blood-mimicking fluid for particle image velocimetry with silicone vascular models. Experiments in Fluids. 2011;50(3): pp. 769-774.

7

[21] Cheng NS. Formula for the viscosity of a glycerol-water mixture. Industrial & Engineering Chemistry Research. 2008;47(9): pp. 3285-3288.

[22] Suzuki Y, Oyane A, Ikeno F, Lyons JK, and Yeung AC. Development of animal model for calcified chronic total occlusion. Catheterization and Cardiovascular Interventions. 2009;74(3): pp. 468-475.

[23] Martin R and Brown P. Mechanical properties of hydroxyapatite formed at physiological temperature. Journal of Material Science: Materials in Medicine. 1995;6(3): pp. 138-143.

[24] Cho JR, Kim YJ, Ahn CM, Moon JY, Kim JS, Kim HS, et al. Quantification of regional calcium burden in chronic total occlusion by 64-slice multi-detector computed tomography and procedural outcomes of percutaneous coronary intervention. International Journal of Cardiology. 2009;145(1): pp. 9-14.

[25] Barrett S, Sutcliffe M, Howarth S, Li ZY, and Gillard J. Experimental measurement of the mechanical properties of carotid atherothrombotic plaque fibrous cap. Journal of Biomechanics. 2009;42(11): pp. 1650-1655.

[26] Houwink R and De Decker HK. Elasticity, plasticity and structure of matter. Cambridge, UK: Cambridge University Press, 1971.

[27] Roy T, Liu G, Shaikh N, Dueck AD, and Wright GA. Puncturing plaques: Relating MRI characteristics of peripheral artery lesions to guidewire puncture forces. Journal of Endovascular Therapy. 2016;24(1): pp. 35-46.

7

APPENDIX 7.A: CTO MODEL PREPARATION

In this appendix, the procedure that was followed to prepare the environment models (representing the surrounding cardiac tissue) and proximal cap models is described.

7.A1. Environment Models

The following steps were followed to prepare the environment models:

1. Weigh a specific amount (depending on the quantity you need) of gelatin (*Sheet gelatin*, Dr. Oetker, Bielefeld, Germany).
2. Put the gelatin sheets in a bath of cold fresh water (~ 15 °C), and leave to soak for 5 minutes.
3. Take the gelatin sheets from the bath and wring them meticulously before putting them in a plastic container.
4. Weigh the new (soaked) mass of the gelatin sheets, and add an amount of cold clear water to create the 25 wt% of gelatin.
5. Put the gelatin-filled container in a bath of warm water (~ 50 °C) and stir gently until the content is completely liquid.
6. Take the container out of the bath and leave it to rest for approximately 15 minutes, during which all bubbles will float to the surface and can be removed from the mixture.
7. Pour the gelatin mixture in a small container that is placed in the mold illustrated in Figure 7.A1.
8. Close the mold with the lid to create a notch within the gelatin volume.
9. Leave the gelatin-filled containers for approximately 1 hour in a refrigerator (~ 2 °C), before gently removing the lid of the mold from the gelatin (see Figure 7.A2).
10. Close the lid of container and leave the gelatin mixture to harden in the refrigerator for another 24 hours.

Note: To ensure constant tissue stiffness, the tissue model is to be used directly from the refrigerator (< 1 hour).

7.A2. Proximal Cap Models

The following steps were followed to create the proximal cap models:

1. Prepare the gelatin mixture as described in step 1–6 from the previous procedure (surrounding tissue model).
2. Weigh a specific amount (depending on the quantity you need) of calcium sulfate powder (*SHERAALPIN Hartgips hellblau*, SHERA Werkstoff-Technologie GmbH & Co. KG).
3. Put the powder in a small plastic cup and add a correct amount of gelatin mixture into the cup.
    -   For the *ductile* proximal cap model: 50 wt% calcium sulfate powder and 50 wt% gelatin mixture;
    -   For the *reference* proximal cap model: 75 wt% calcium sulfate powder and 25 wt% gelatin mixture;
    -   For the *brittle* proximal cap model: 77 wt% calcium sulfate powder and 23

wt% clear water.

4. Stir the mixture gently, while holding the cup in a bath of warm water (~ 50 °C), until a homogeneous mixture has formed.

5. Pour the mixture onto the cap-model mold, and close with force to get a 1 mm thick slice of proximal cap models (see Figure 7.A3).

6. Leave the filled cap-model mold for 20 minutes in a refrigerator (~ 2 °C) to stiffen.

7. Remove the cap-model mold from the refrigerator and open it to take out the formed slice of (at this moment still flexible) material.

8. Press the small circles from the material with the help of a thin-walled tube, as shown in Figure 7.A3.

9. Pack the models into cling film, and leave them for another 24 hours in the refrigerator.

Note: To ensure constant material stiffness, the model is to be used directly from the refrigerator (< 1 hour).

Figure 7.A1— The Mold for Creating the Environment Models. The mold consists of laser-cut disks in between which 10 circular containers can be placed. The lid of the mold, in which several rods are placed, creates the notches.
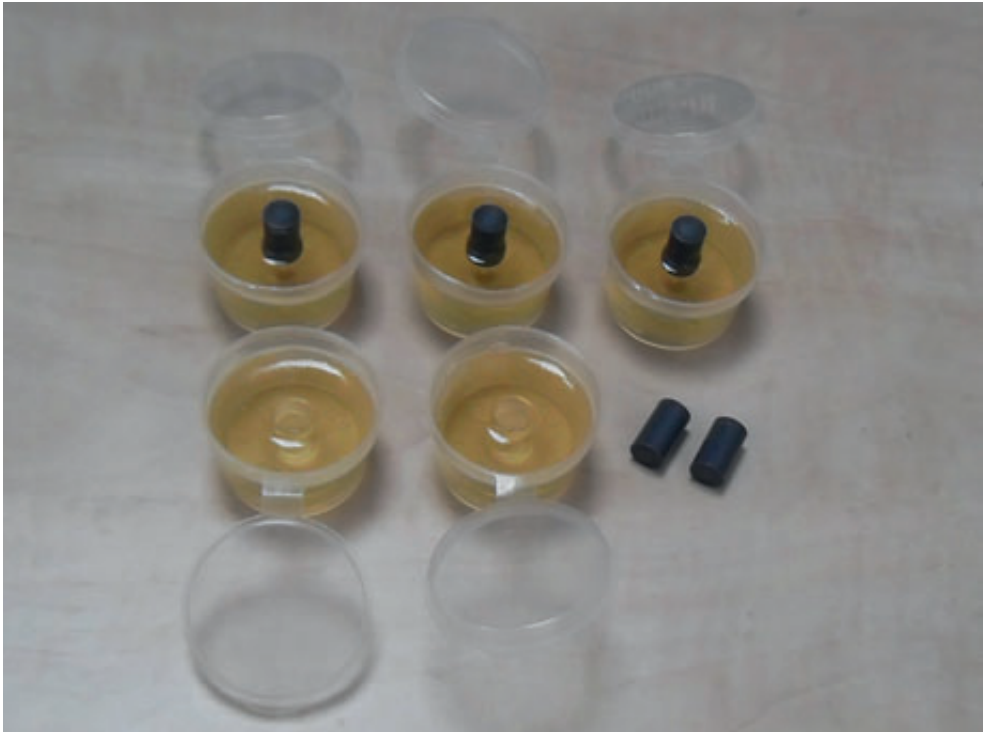
Figure 7.A2— Environment Models with Notches in the Center.
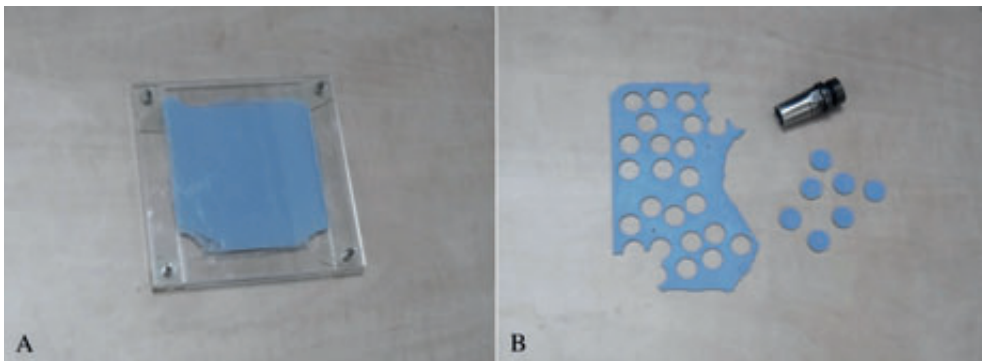
Figure 7A.3— The Proximal Cap Models. Left: Mold for the proximal cap models, to create the desired 1 mm material thickness, filled with the gelatin/plaster cast mixture. Right: the complete molded slice of material (left), thin-walled tube to press the circles (top right), and final proximal cap models (lower right)

7

CHAPTER 8

CROSSING CTOS USING A MECHANICAL IMPULSE CATHETER

8

AIMÉE SAKES AND PAUL BREEDVELD

Abstract—Percutaneous Coronary Interventions (PCI) of Chronic Total Occlusions (CTOs) are considered technically challenging, resulting in a relatively low success rate of in between 55–95%. The main reason for PCI failure is the inability to puncture the tough proximal cap of the CTO due to buckling of the guidewire. In order to improve the endovascular treatment of CTOs, a new flexible crossing prototype has been developed that enables effective crossing of CTOs without buckling. Buckling is prevented by an increase of the critical load of the crossing tool by using a dynamic loading method, in which a high-speed indenter collides with an initially non-moving CTO. The flexible prototype consists of a spring-loaded indenter, which is actuated using a core wire that runs from the tip of the device through an extension spring in the shaft towards the handle. In the handle the tip is manually actuated using a compliant (re)load mechanism, allowing for loading, locking, and (re)loading of the prototype while inserted in the vasculature. The mechanical performance, in terms of the output impulse (and accompanying impulse peak force) and indenter momentum, of the prototype was evaluated in a straight and looped (360°) configuration using a load cell and high-speed camera, respectively. Furthermore, the puncture performance was evaluated on an artificial proximal cap CTO model constructed out of a mixture of gelatin and hydroxyapatite. An average indenter velocity of 0.95 ± 0.15 m/s and input peak force of 0.32 ± 0.08 N in the straight configuration and 0.27 ± 0.10 N in the looped configuration were measured. The prototype illustrated the ability to puncture highly calcified proximal cap CTO models, within 3.15 strikes. Further development of this crossing prototype may in time increase the chance of a successful crossing procedure of heavily calcified CTOs.

Keywords— Buckling Prevention, Catheter Technology, Chronic Total Occlusions (CTOs), Impulse, Percutaneous Coronary Interventions (PCIs), Medical Device Design.

8

8.1. INTRODUCTION

8.1.1. The Last Frontier in Endovascular Interventions

During the last centuries, endovascular interventions have dramatically changed the field of vascular and heart surgery [1]. Advances in the endovascular interventional techniques and devices have dramatically decreased the mortality rate of many heart diseases, including Ischemic Heart Disease [2]. Even so, advances are still needed in the endovascular treatment of the so-called Chronic Total Occlusions (CTOs), considered one of the last frontiers in cardiovascular interventions. A CTO is defined as a heavily calcified total occlusion of over three months old. As of today crossing CTOs is one of the most technically challenging procedures that interventionists face, resulting in a relatively low procedural success rate of 55–90% depending on the characteristics of the CTO and experience of the operator, amongst others. In comparison, in acute lesions a success rate of over 95% can be reached for even the less experienced interventionist [3-5].

8.1.2. Static Loading of the CTO: Current Challenges

In the endovascular treatment, or the Percutaneous Coronary Intervention (PCI), of CTOs, a thin flexible guidewire (Ø0.36–0.89 mm [6]) is inserted in the vasculature at the upper thigh (femoral artery) or the wrist (radial artery) and subsequently guided towards the lesion site, were the procedure is performed under Compute Tomography (CT) guidance. The most common failure mode of PCI in CTOs is the inability to successfully cross a guidewire through the occlusion into the original lumen of the distal vessel, accounting for approximately 60% of the failure cases [5,7]. The inability to cross the CTO with a guidewire can be mainly attributed to guidewire buckling. Crossing CTOs is challenging, as the puncture force required to penetrate the CTO is often larger than the maximum axial load that the guidewire can support without buckling, also known as the critical load.

8.1.3. Dynamic Loading of the CTO: Future Pathways

In order to prevent buckling of slender structures such as guidewires, a number of static or dynamic buckling prevention strategies can be applied [8,9]. Currently, only static buckling prevention methods are being used in clinical practice, in which the critical load of the guidewire is increased by increasing the Young's modulus E [GPa] of the guidewire or by using dedicated support or balloon catheters that increase the second moment of area I [mm⁻] and decrease the unsupported length L [mm] (Figure 8.1B–C) [4]. Examples are the development of stiffer guidewires with nitinol cores, such as *Crosswire* (Terumo, Tokyo, Japan), and the development of specialized support catheters, such as *Tornus* (Asahi Intecc, Nagoya, Japan), *CrossBoss* (Boston Scientific, Natick, MA, USA), and *Corsair* (Asahi Intecc, Nagoya, Japan). Even though these developments have
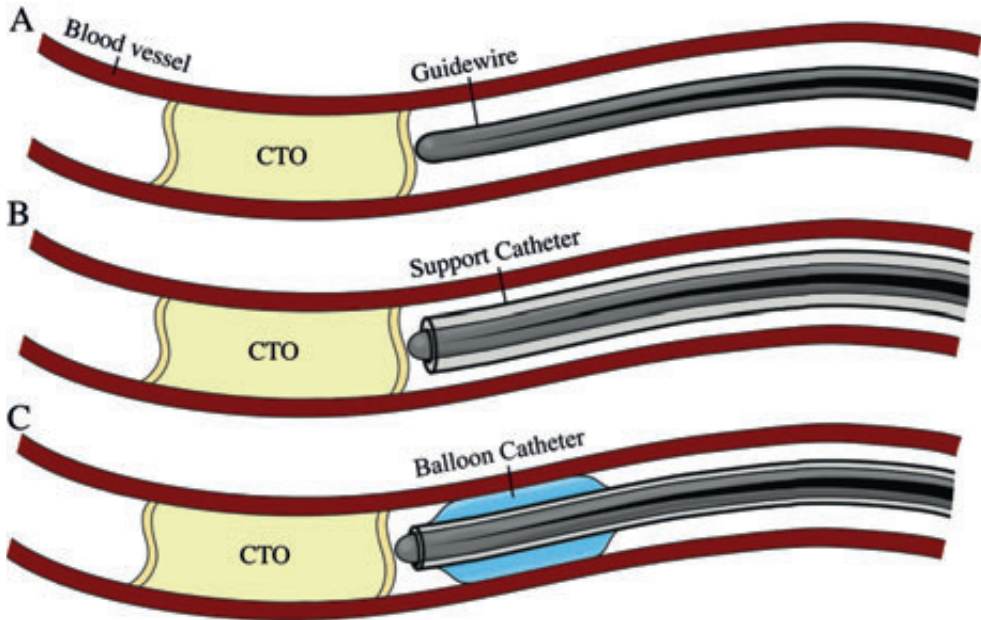
8

Figure 8.1— Static Buckling Prevention Strategies in use. A) Guidewire inserted into an occluded artery with tapered core (black). B) Guidewire surrounded by a support catheter to improve the buckling resistance by increasing the second moment of area *I*. C) Guidewire supported by a balloon catheter to improve the buckling resistance by increasing the second moment of area *I* and decreasing the unsupported length *L*.

8

significantly decreased the technical difficulty of the PCI of CTO, guidewire buckling is still observed in clinical practice. Furthermore, as a relatively low *E* is needed to safely guide the guidewire through the arteries and the *I* cannot be increased much further due to size restriction of the arteries, the use of these variables is relatively limited.

In this study, we propose a dynamic loading method to prevent buckling. In dynamic loading methods, a moving body, in our case a guidewire, collides with an initially non-moving body, the CTO, during which the bodies will undergo a short period of energy transfer (Figure 8.2). The translational momentum *p* [kgm/s] of the guidewire, defined as the product of mass *m* [kg] times velocity *v* [m/s], will be converted into an impulse *J* [Ns], defined as the integral of the force *F* [N] over the time interval *dt* [s] for which it acts, and transferred to the CTO (see Equation 8.1).

$$p = m\Delta v = J = \int F \, dt \tag{8.1}$$

The advantage of using dynamic loading to prevent buckling is that the critical load of the guidewire can be adjusted independently of its geometrical properties [10]. The
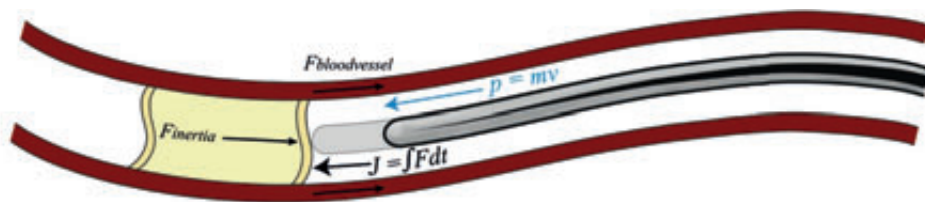
Figure 8.2— Dynamic Buckling Prevention Strategy. The guidewire with mass *m* [kg] is moving with a velocity *v* [m/s] through the blood vessel, giving it momentum *p* [kgm/s]. During the collision the momentum *p* is transferred into an impulse *J* [Ns]. The inertia of the CTO, as well as the damping and spring properties of the arterial wall, provide the reaction forces to the incoming impulse *J*, and thus prevent movement of the CTO.

critical load when applying an impulse *J* onto the guidewire increases with a decrease in the time interval *dt.* In other words, the impulse *J* itself, rather than the applied force *F* or the Euler buckling parameters, becomes the most important parameter in determining the critical load [10]. Furthermore, multiple studies [11,12] have shown that applying an impulse on human tissues can decrease the penetration load and tissue deformation during penetration.

8.1.4. Goal of this Study

The goal of this study was to design and test a prototype "*Pulze* catheter" capable of applying an impulse onto a CTO for crossing purposes. In a previous study a rigid flexible prototype was designed and tested on several CTO models [13]. In this study, the rigid prototype will be developed further into a flexible prototype. First we will describe the design process, from the parameterization to the conceptual design of the prototype. Next, we will describe an experimental set up in which we will determine the mechanical and puncture performance of the prototype. Finally, we will discuss the results and propose recommendations for future steps.

8.2. PULZE CATHETER DEVELOPMENT

8.2.1. Dimensions

The *Pulze* catheter should be flexible and able to safely travel from the incision point through the vasculature towards the occlusion site in one of the coronaries of the heart (Figure 8.3). Based on an analysis of the vascular routes (see Sakes *et al.* [14]), including curve angles, curve diameters, and artery diameters that need to be travelled, a maximum instrument diameter of 2 mm was set (Figure 8.3) [13]. Furthermore, the prototype should at least be able to pass curves with curve angles of 90° and curve diameters of 50 mm, which results in a maximum allowable rigid length of the tip of 6.5 mm (Figure 8.3) [13].
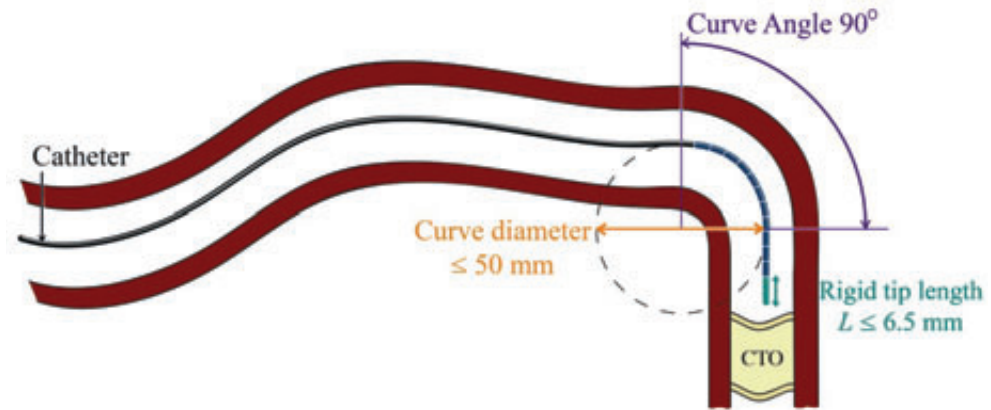
Figure 8.3— Parameterization of the required flexibility of the prototype tip. The maximum rigid length (*L*) of the prototype is deducted from the required curve angle, curve diameter, and artery diameter of the intersections passed through from incision to lesion site.

Finally, the prototype should be able to reach the occlusion site from the incision point. Depending on the incision point and lesion site, the required length will differ. For this first prototype, it was decided to set the length to 400 mm, which allows for traveling towards the coronaries of the heart via the internal jugular or subclavian vein.

8.2.2. Momentum

In the proposed *Pulze* catheter, momentum is generated using spring energy. In order to generate the maximum amount of momentum, high spring stiffness is needed. During the collision of the device's tip with the CTO, the momentum will be converted into an impulse, which in turn will be transferred to the CTO. In an ideal scenario, the maximum amount of kinetic energy is absorbed by the CTO and transferred into fracture formation. The amount of transferred kinetic energy, however, mainly depends on the biomechanical behavior of the CTO and its environment. A simplified model was drafted consisting of a massive block representing the CTO, and a spring-damper system representing the tissue around the CTO (Figure 8.4), with the inertial force of the CTO being equal to the product of its inertial mass *m* [kg] and the acceleration *a* [m/s], the damping force of the environment equal to the product of the damping coefficient *c* [Ns/m] and the velocity *v* [m/s] of the CTO, and the spring force in the device tip to the product of the spring constant *k* [N/m] and the compression distance *x* [m]. The inertia of the CTO, as well as the damping and spring-properties of the environment, resist displacement and changes in velocity and acceleration of the CTO and can, therefore, create a counterforce to the impulse applied by the device tip during the collision (Figure 8.4). This counterforce minimizes CTO displacement and thus allows for the CTO itself to
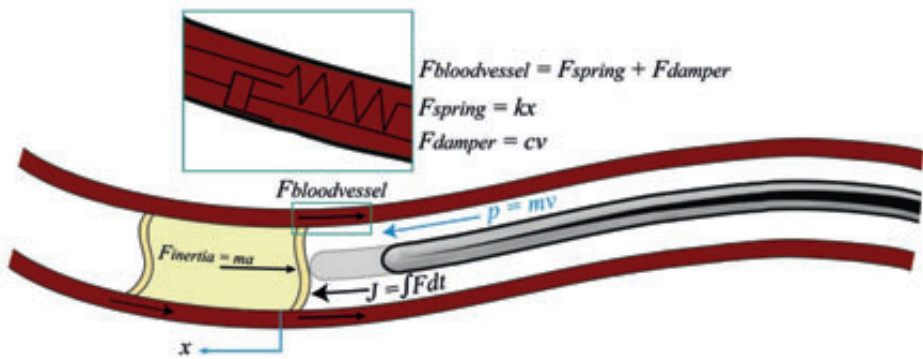
Figure 8.4— Simplified CTO Collision model. The CTO and its environment can be modeled as a rigid block supported by a spring-damper system. For explanation see text. Blue = movement of the guidewire and CTO, Dark grey = guidewire, Light grey = support catheter, Red = arterial wall, and Yellow = CTO.

absorb the kinetic energy that is provided by the device tip. Increasing the impact velocity will increase the damping in the vessel wall; reducing the displacement of the CTO within the artery even more. Therefore, it is important to strive towards high indenter velocity.

8.2.3. Design

Tip & Shaft Design

Pulze's tip (Figure 8.5) consists of a two-piece end-effector, called the indenter (m = 0.074 g), consisting of (1) an interchangeable filleted cylindrical tip that delivers the impulse onto the CTO, screwed onto (2) a second cylindrical part that is connected to a Ø0.5 mm stainless steel core wire (1x19, L = 400 mm, mass of 1.9 grams) used to load the tip. The indenter is actuated by two nested compression springs ($D_{outer\ spring}$ = Ø2 mm, $D_{inner\ spring}$ = Ø1 mm, length L = 10 mm, spring constant both springs combined k = 1.9 N/mm) to maximize the acquired spring energy. The compression springs are abutted by the indenter distally and a "stop" proximally that also connects the tip of the prototype to the shaft.

The shaft (D_{outer} = Ø2 mm, D_{inner} = Ø1.4 mm, L = 385 mm; Specialty Silicone Fabricators, Tustin, CA) is made out of silicone (SSF-METN-719, 55 durometer), which is a biocompatible material in use for commercially available catheters [16]. Inside the silicone shaft, a custom made closed Bowden cable (D_{outer} = Ø1 mm, d = 0.2 mm; Advanex Europe, Southwell, UK) was placed to compensate for the axial compressive forces on the shaft during spring actuation in the tip. The outer shaft and the Bowden cable are fixed inside the stop in the tip.
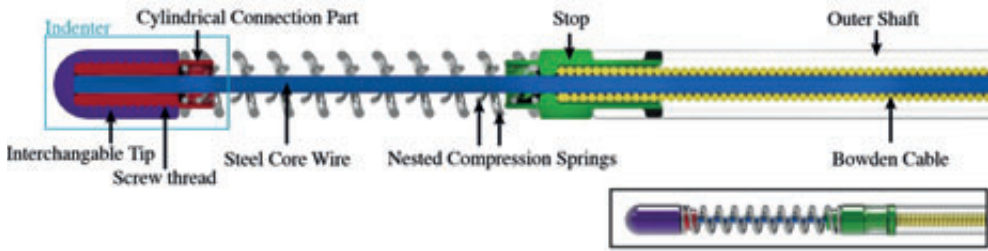
Figure 8.5— Cross-section of *Pulze's* tip and shaft design. The tip consists of a two-piece indenter with an interchangeable tip (purple) and a connection part (red) to connect the indenter to the steel core wire (blue). The tip is loaded by a Ø0.5 mm stainless steel core wire (blue) that compresses the nested compression springs (grey). The stop (green) abuts the springs and envelops the Bowden cable (yellow) that compensates for the forces applied on the outer shaft (transparent) by the compression spring.

Handle Design

The handle mechanically controls the indenter and allows for locking the mechanism in the "loaded" position (Figure 8.6). The outer handle piece (black) was made out of aluminum and can be easily exchanged and altered to the surgeon's preference. The outer handle piece contains an aluminum cylinder (grey, Ø18 mm, L = 80 mm) that envelops the (re)load mechanism. The aluminum cylinder, in turn, contains a brass bearing (red, Ø12 mm, L = 50 mm), which allows for smooth motion of the aluminum load element (green, m = 6.26 g) during actuation. The stainless steel core wire is guided through the bearing and is connected to the aluminum load element using a M2 set screw. To prevent rotation of the load element during actuation, the M2 set screw is guided through a slot in the aluminum cylinder and outer handle piece. The steel core wire is controlled by a loading handle (brown) that is connected to the aluminum load element by means of a compliant gripper (stainless steel; pink). This compliant gripper consists of two flexible barbed plates connected to the loading handle by means of an M4 screw thread and an inner movable core (light blue) connected to a trigger (blue). By translating the loading handle with gripper forward into the load element, the plates of the gripper deform inwards and lock into place. Subsequently, the trigger core is pushed forward into the loading handle to actively lock the grip. The mechanism is subsequently loaded by pulling both the loading handle with trigger backwards. By twisting the loading handle, the tip can be locked in the "loaded" position. Finally, by moving the trigger backwards and out of the loading handle, the gripper plates move inwards and release the aluminum load element, which in turn accelerates forward. In order to compensate for the friction in the handle mechanism, the aluminum cylinder contains a compression spring (Ø10.67 mm, spring constant k = 8.56 N/mm) that pushes the load element forward during unloading. Between the brass bearing and the load element, a dual-disk
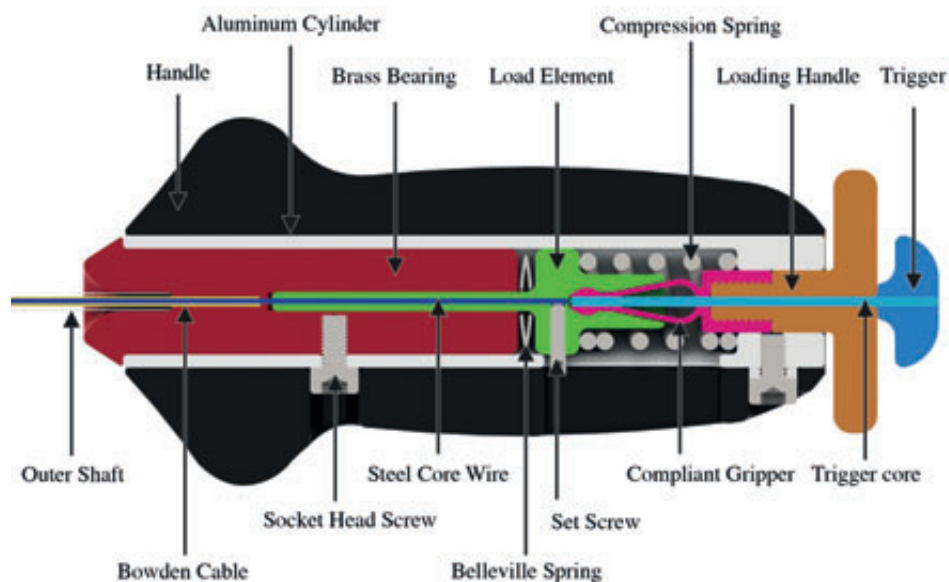
Figure 8.6— Cross-section of *Pulze's* handle. For explanation see text.

Belleville spring (Amatec, Alphen a/d Rijn, the Netherlands) is placed to dampen the load element at the end of its unload cycle. An overview of the different steps to load, trigger, and release the indenter is given in Figure 8.7. Figures 8.8 and 8.9 show the final, assembled, prototype.

8.3. PROOF OF PRINCIPLE EXPERIMENT

8.3.1. Experiment Goal

The goal of the proof-of-principle experiment was to determine the mechanical and puncture performance of the developed *Pulze* catheter. For this purpose, a proof-of-principle experiment was performed.

8.3.2. Experimental Variables

Dependent Variables
The mechanical performance of the *Pulze* catheter was evaluated using the following two variables:

1.   **The impact peak force (F_{peak})** delivered by the indenter.
2.   **The indenter velocity (v)** generated by the compression springs.

263

In order to evaluate the ability of the prototype to cross a CTO, we decided to focus on puncturing the proximal cap of heavily calcified CTOs, as the cap represents the hardest, most difficult part to penetrate during PCI. The following dependent variables were measured:

1. **Number of punctures** ($n_{punctures}$). This measure was used to estimate the efficacy of the prototype in achieving puncture of a CTO model (binary classification: puncture versus no puncture). In our experiment, puncture was defined as complete fracture line that ran through the CTO model.

2. **Number of strikes for puncture** ($n_{strikes}$). This measure was used to estimate the efficiency of the prototype in achieving puncture.

All measurements were conducted for the maximum compression distance of $x = 4$ mm.

8
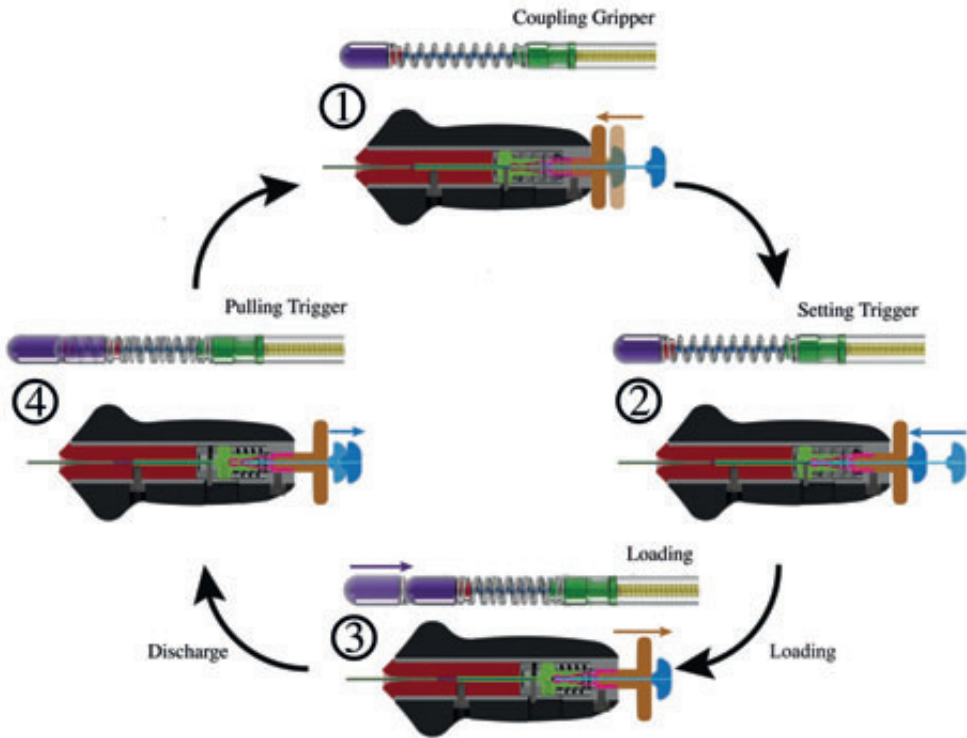
Figure 8.7— Working principle of *Pulze's* handle. (1) The gripper is decoupled from the system (neutral position). The handrip (light brown), and thus the compliant gripper (purple), is translated forward to couple the gripper with the load element (green). (2) The gripper is locked in place by translating the trigger (blue) forward. (3) The loading handle with the trigger is pulled backwards to load the prototype. (4) The tip is released by pulling the control input core (blue) further backwards until the ultimate position is reached.

Figure 8.8— Assembled *Pulze* catheter tip with match for scale reference.

8
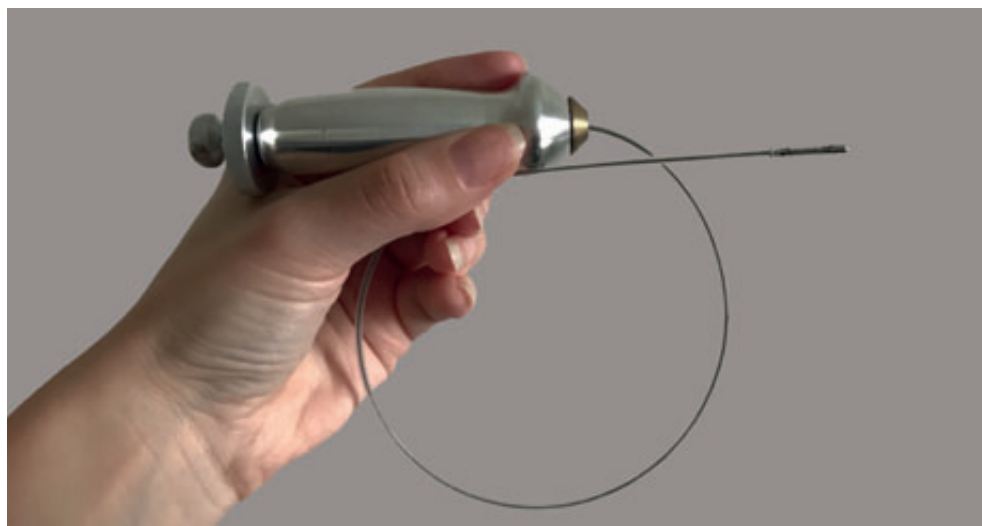
Figure 8.9— Assembled *Pulze* catheter.

Independent variables

In order to reach the CTO, it is necessary to cross several intersections and curves in the vascular system. In order to determine the effect of curvature on F_{peak}, different curvatures have been tested. The most prevalent location of a CTO within the coronary arteries is the Right Coronary Artery (RCA) [17]. For the peripheral arteries, the Superficial Femoral Artery (SFA) is the most common location for a CTO to occur [18]. In order to approach these two locations, four endovascular routes can be taken, as analyzed in Sakes *et al.* [14]. Based on this analysis two curvatures were selected: 0 (straight) and 360° (looped 1x). In combination with the curve angle, a curve diameter of 50 mm was selected, which is the minimum diameter encountered in endovascular approaches [13].

8.3.3. Experimental Facility

Mechanical Testing Facility

For testing the performance of *Pulze* catheter, a breadboard (*MB3030/M*, Thorlabs, Newton, NJ, USA) was used (Figure 8.10). The prototype was fastened on a single-axis translational stage using a V-mount clamp. In order to test the effect of the curve angle and radius on F_{peak}, guidance structures were used to confine the shaft. The delivered F_{peak} was measured using a miniature S-beam load cell (*LSB210, QSH00519*, FUTEK Advanced Sensor Technology, Inc., Irvine, CA, USA). An analogue signal conditioner (*CPJ RAIL*, SCAIME, Annemasse, France), and a data acquisition system with a sampling rate set to 10 kHz (*NI USB-6211*, National Instruments Corporation, Austin, TX) were connected to the load cell for data acquisition. The load cell was controlled through *LabVIEW 2014* (National Instruments Corporation, Austin, TX).

For the determination of *v*, a high-speed camera *Photron Fastcam APX-RS* (Photron USA, Inc., Tokyo, Japan) was placed adjacent to the prototype and set to a frame rate of 10 kHz. The mass of the indenter and the stainless steel core wire was measured with a high precision balance (*Mettler PJ360 DeltaRange*, Mettler-Toledo International Inc., Columbus, OH).

CTO Proximal Cap Model

CTOs are a heterogeneous mix of materials, including lipids, smooth muscle cells, (dense) collagen, cholesterol, and calcium [5,19]. Collagen forms the major structural component of the CTO. Older CTOs are usually characterized by dense collagen and increasing calcification, resulting in a higher chance of PCI-failure. A CTO can be subdivided into three main regions: (1) a heavily calcified proximal cap, (2) a softer core, and (3) a distal cap. As the proximal cap of the CTO represents the most distinct physical barrier for crossing, it was chosen to build an artificial CTO proximal cap model (see Figure 8.11). In order to mimic the calcium content of the proximal cap, calcium sulfate (CaS) was used. Gelatin was used to mimic the collagen content. In a study of Cho *et al.* [20], the mean calcium percentage of CTOs was found to be 53.9 ± 20.3% (mean ± standard deviation)
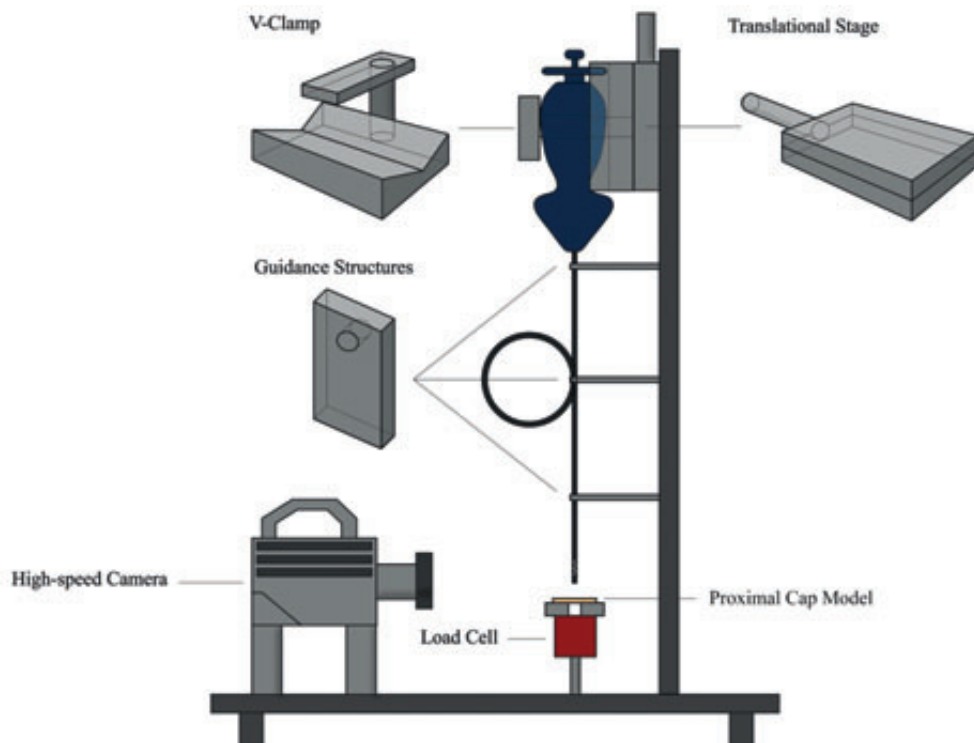
Figure 8.10— Measurement Facility.

8

Figure 8.11— Artificial Proximal Cap Models.

for failed PCI cases. It was, therefore, chosen to manufacture a proximal cap model with 55 wt% CaS powder and 45 wt% liquid gelatin mixture consisting of 25wt% gelatin powder and 75wt% clear water. The proximal cap models were prepared in a Ø5-mm circular slice of approximately 0.5 mm thick; equal to the mean CTO proximal cap thickness [21]. The proximal cap was placed on top of a metal disk with a Ø4 mm hole.

8.3.4. Experimental Protocol

In order to characterize the prototype, first the generated impact peak force was measured without the proximal cap model for the two curvatures. Each measurement was repeated ten times. Subsequently, the indenter velocity was measured four times using the high-speed camera. Finally, the number of punctures and the number of strikes were measured for the proximal cap model. The maximum number of strikes to achieve puncture was set to ten. Again, each measurement was repeated three times with three different proximal cap models. In order to limit the variability within the proximal cap models, all measurements were conducted within two hours after model preparation.

8.3.5. Data Analysis

Per measurement, the data from the S-beam load cell was processed with *MATLAB 2015b* (The Mathworks, Inc., Natick, MA) to calculate F_{peak} exerted on the load cell by integrating the force over the time. Subsequently, the mean F_{peak} with the associating standard deviations were calculated over the ten repetitions. Two two-tailed t-tests were conducted to determine if the curvature had a significant ($p > 0.05$) influence on the exerted impulse and impact peak force. The mean indenter velocity was calculated across the four repetitions using the associated software package Photron FASTCAM Viewer v3.5.3. The number of punctures $n_{punctures}$ and number strikes $n_{strikes}$ upon puncture were determined across three repetitions by eye. From this observation the number of punctures, as well as the minimum, maximum, and mean number of strikes to achieve puncture were determined.

8.4. RESULTS & DISCUSSION

8.4.1. Mechanical Performance

Figure 8.12 shows a typical HSV image sequence of the indenter. The average velocity of the indenter was calculated as 0.95 ± 0.15 m/s ($n = 4$). Figure 8.13 illustrates the measurements of the force over the time. A mean impact peak force of 0.32 ± 0.08 N was measured in the straight configuration. A slightly lower value of 0.27 ± 0.10 N was found for the looped configuration. The measured F_{peak} was not significantly influenced by the curve angle and radius combination, as determined by the two-tailed t-test ($p = 0.23$).

Figure 8.12— Example of a HSV image sequence of the indenter of *Pulze*. Based on the image sequences, an average indenter velocity of 0.95 ± 0.15 m/s was derived. The time between frames is 1 ms.

8.4.2. Puncture Performance

Typical punctures of the different proximal cap models are illustrated in Figure 8.14. The prototype was able to puncture all three models within 4 strikes, with an average of 3 strikes needed for puncture ($n = 3$), in the straight configuration. In the looped configuration, a slightly higher number of strikes of at average 3.3 were required for puncture ($n = 3$). As can be seen, the CTO model type did not significantly influence the number of punctures and number of strikes.

8.4.3. Limitations of this Study

The main limitation of this study is the use of an artificial CTO model constructed out of a mixture of gelatin and calcium to validate the puncture performance of the prototype. In this model we did not account for elasticity of the CTO environment. Therefore, the results only give a first indication about the use of an impulse to puncture through highly calcified CTOs. Unfortunately, currently no easily obtainable CTO (animal) models are

available for extensive prototype evaluation. The development of an accurate and reproducible coronary CTO model is challenging mainly due to two reasons: (1) mimicking CTO pathology, especially the calcification is difficult and (2) inducing the inflammatory response that starts the development of a CTO has been challenging. Recently, Suzuki *et al.* [22] developed a highly calcified pig model by inserting a bio-absorbable polymer sponge coated in hydroxyapatite in one of the coronaries of the peripheral vessels, which may pave the way to improved device testing in the future.

8
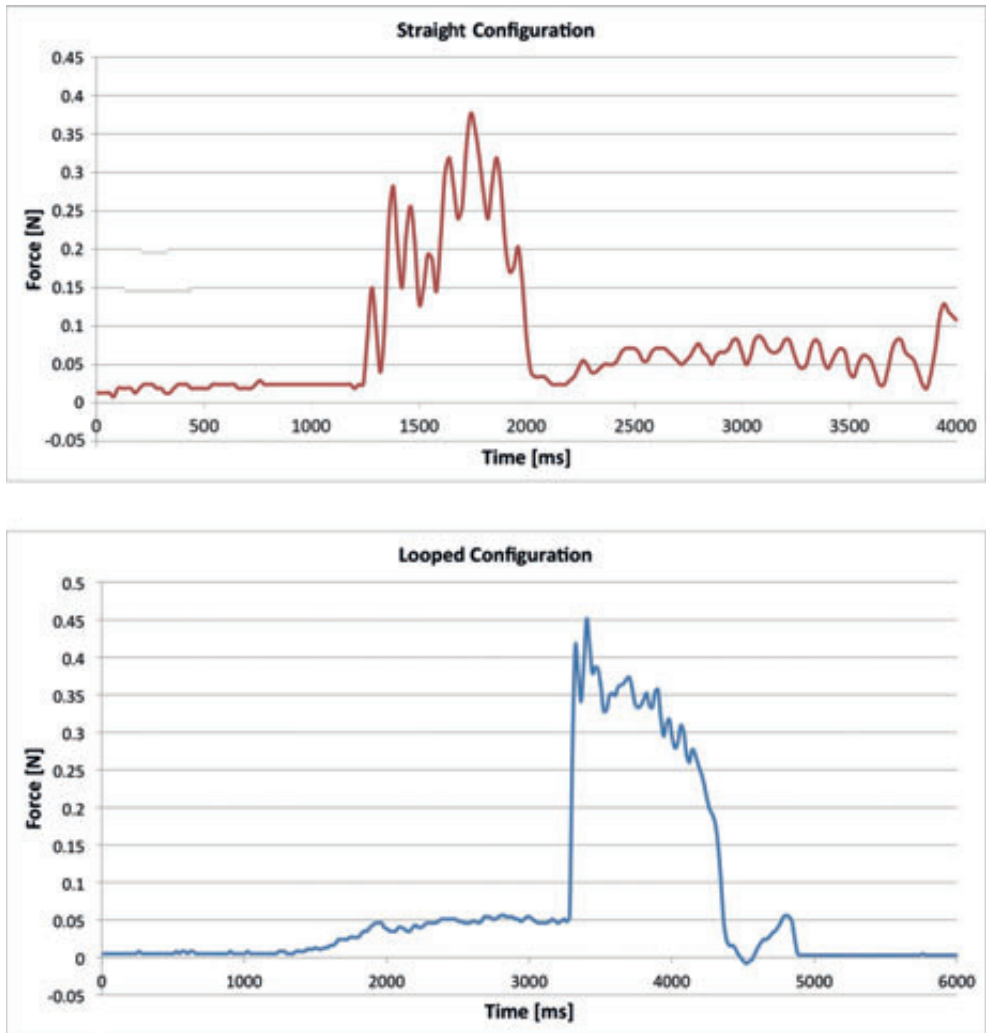
Figure 8.13— Example measurement of the force over the time in the straight (left) and looped configuration (right).

Figure 8.14— Typical punctures of the proximal model.

8.4.4. Implications for Future Research

For future research it is a necessity to test the prototype on an animal model, such as the one developed by Suzuki *et al.* [22], or on real CTO tissue, as this will give a decisive answer to the question of whether or not the device is able to penetrate CTOs. Furthermore, in order to integrate the device in the PCI procedure it is also a necessity to add a lumen to the device to allow for the device to be guided over a guidewire during the insertion procedure. In order to fulfill this requirement, the Ø0.5 mm core wire should be replaced by a hollow tube with an inner lumen of 0.4 mm connected to a spherical indenter. Furthermore, as compared to dedicated coronary CTO devices, such as *Crosser* (Ø1.3–1.6 mm, Bard Peripheral Vascular, Tempe, AZ, USA), as well as support-catheters, such as *Tornus* (Ø1mm, Asahi Intecc, Nagoya, Japan), the proposed prototype is still on the large size. Therefore, in a future clinical prototype, the possibility of minimizing the outer dimensions should be researched. Additionally, the effect of multiple consecutive strikes or vibrating output on the puncture effectiveness of CTOs could be researched. Finally, to increase device safety, the addition of a steering segment can be researched. A steerable segment minimizes the chance of blood vessel wall damage as it allows for proper aiming of the device tip during the procedure. Additionally, adding a steering segment simplifies the navigational phase or insertion process during PCI.

8.5. CONCLUSIONS

In this study we designed and tested a new prototype, called the *Pulze* catheter that uses an impulse to penetrate the CTO. By using an impulse during the crossing procedure higher forces can be delivered onto the CTO without the risk of device buckling. The *Pulze* catheter was able to puncture the CTO proximal cap models with an average of 3.3

number of strikes for penetration in a looped configuration. In future, the prototype will be developed further into a clinical prototype and tested on an animal model similar to the one described by Suzuki *et al.* [22] to validate the effectiveness on real CTOs. We feel that with continued developed that the proposed *Pulze* catheter can enable effective crossing of highly calcified CTOs without buckling and while following a tortuous path.

ACKNOWLEDGEMENTS

REFERENCES

[1]   Schanzer A, Steppacher R, Eslami M, Arous E, Messina L, et al. Vascular surgery training trends from 2001-2007: A substantial increase in total procedure volume is driven by escalating endovascular procedure volume and stable open procedure volume. Journal of Vascular Surgery. 2009; 49(5): pp. 1339-1344.

[2]   Goldman LEE and Cook EF. The decline in ischemic heart disease mortality ratesan analysis of the comparative effects of medical interventions and changes in lifestyle. Annals of Internal Medicine. 1984; 101(6): pp. 825-836.

[3]   Stone GW., Reifart NJ, Moussa I, Hoye A, Cox DA, Colombo A, et al. Percutaneous recanalization of chronically occluded coronary arteries. A consensus document - Part I. Circulation. 2005; 112(15): pp. 2364-2372.

[4]   Sianos G, Werner GS, Galassi A, Papafaklis MI, Escaned J, Hildick-Smith D et al. Recanalisation of Chronic Total coronary Occlusions: 2012 consensus document from the EuroCTO club. EuroIntervention. 2012;8(1): pp. 139-145.

[5]   Stone GW, Reifart NJ, Moussa I, Hoye A, Cox DA, Colombo A et al. Percutaneous recanalization of chronically occluded coronary arteries - A consensus document - Part II. Circulation. 2005;112(16): pp. 2530-2537.

[6]   Walker C. Guidewire selection for peripheral vascular interventions. Endovascular Today. 2013; 5: pp. 80-83.

[7]   Kinoshita I, Katoh O, Nariyama J, Otsuji S, Tateyama H, Kobayashi T, et al. Coronary angioplasty of chronic total occlusions with bridging collateral vessels: immediate and follow-up outcome from a large single-center experience. Journal of the American College of Cardiology. 1995;26(2): pp. 409-415.

[8]   Euler L. Principes généraux de l'état d'équilibre d'un fluide Académie Royale des Sciences et des Belles-Lettres de Berlin, Mémoires. 1757;11: pp. 217-273.

[9]   Sakes A, Dodou D, and Breedveld P. Buckling prevention strategies in nature as inspiration for improving percutaneous instruments: a review. Bioinspiration & Biomimetics. 2016; 11(2): pp. 021001.

[10]   Lock M. A study of buckling and snapping under dynamic load. El Segundo, CA: Laboratory Operations Aerospace Corporation. Report Number TR-0158 (3240-30)-3; 1967. pp. 1-55.

8

[11]   Heverly M, Dupont P and Triedman J. Trajectory optimization for dynamic needle insertion. Proceedings of the 2005 IEEE International Conference on Robotics and Automation held at Barcelona, Spain, 18-22 April 2005. pp 1646-1651.

[12]   Jelínek F, Smit G and Breedveld P. Bioinspired spring-loaded biopsy harvester—experimental prototype design and feasibility tests. Journal of Medical Devices ;8(1); pp. 015002-1-001502-6.

[13]   Sakes A, van der Wiel M, Dodou D, and Breedveld P. Endovascular Crossing of Chronic Total Occlusions Using an Impulse: An Explorative Design Study. Cardiovascular Engineering and Technology. 2017; 8(2): pp. 145-163.

[14]   Sakes A, Nicolaï T, Karapanagiotis J, Breedveld P, and Spronck JW. Crossing total occlusions using a hydraulic pressure wave: A feasibility study. Plos One. Under Review.

[15]   Thind A, Strauss B, Teitelbaum A, Karshafian R, Ladouceur M, Whyne C, et al. A novel method for the measurement of proximal fibrous cap puncture force in chronic total occlusions: the effect of increasing age. EuroIntervention. 2011;6(8): pp. 997-1002.

[16]   Stenqvist O, Curelau I, Linder LE, Gustavsson B. Stiffness of central venous catheters. Acta Anaesth Scand 1983; 27(2); 153-157.

[17]   Stone GW, Colombo A, Teirstein PS, Moses JW, Leon MB, Reifart NJ et al. Percutaneous Recanalization of Chronically Occluded Coronary Arteries: Procedural Techniques, Devices, and Results. Catheterization and Cardiovascular Interventions. 2005;66: pp. 217-236.

[18]   Nadal LL, Cynamon J, Lipsitz EC, and Bolia A. Subintimal angioplasty for chronic arterial occlusions. Techniques in vascular and interventional radiology. 2004; 7(1): pp. 16-22.

[19]   Yalonetsky S, Osherov AB, Strauss BH, Galassi AR, Tomasello S, Khamis H. Chronic Total Occlusions. A guide to recanalization (2nd ed.). Hoboken, NJ: Wiley-Blackwell, 2013.

[20]   Cho JR, Kim YJ, Ahn CM, Moon JY, Kim JS, Kim HS, et al. Quantification of regional calcium burden in chronic total occlusion by 64-slice multi-detector computed tomography and procedural outcomes of percutaneous coronary intervention. International Journal of Cardiology. 2009;145(1): pp. 9-14.

[21]   Barrett S, Sutcliffe M, Howarth S, Li ZY, and Gillard J. Experimental measurement of the mechanical properties of carotid atherothrombotic plaque fibrous cap. Journal of Biomechanics. 2009;42(11): pp. 1650-1655.

[22]   Suzuki Y, Oyane A, Ikeno F, Lyons JK, and Yeung AC. Development of animal model for calcified chronic total occlusion. Catheterization and Cardiovascular Interventions. 2009;74(3): pp. 468-475.

8

8

CHAPTER 9

CROSSING CTOS USING A NEWTON'S CRADLE CATHETER

AIMÉE SAKES AND PAUL BREEDVELD

9

Abstract—A major challenge encountered during minimal invasive surgery is transferring high forces through small and flexible instruments, such as needles and catheters, due to their low buckling resistance. In this study we have determined the feasibility of using a Newton's Cradle-inspired catheter (patented) to transfer high force impulses. Exerting a high-force impulse on the tissue increases the critical buckling load and as such can prevent buckling. The system consisted of an input plunger onto which the impulse is given, a (flexible) shaft filled with Ø2 mm stainless steel balls, and an output plunger to transfer the impulse to the target tissue. In the proof-of-principle experiment, the effect of clearance (0.1, 0.2, and 0.3 mm), length (100, 200, and 300 mm), shaft type (rigid vs. flexible), curve angle (0, 45, 90, 135, and 180°), and curve radius (20, 40, 60, and 100 mm) on the efficiency was determined. The catheter was able to deliver forces of 6 N without buckling. The average impulse efficiency of the system was 35%, which can be further increased by optimizing the design. As such, this technology is promising for high force delivery in miniature medical devices during minimal invasive surgery in future.

Keywords— Buckling, Catheter, Feasibility, Force, Guidewires, Impulse, Medical Device Design, Momentum, Minimal Invasive Surgery, Newton's Cradle.

9

9.1. INTRODUCTION

In order to demonstrate the conservation of momentum and energy (see Equation 9.1), Sir Isaac Newton developed the *Newton's Cradle*. *Newton's Cradle* consists of a series of identical metal balls suspended in a metal frame by two wires in a v-formation (Figure 9.1). If one ball is pulled away from the other balls and is subsequently released, it will gain momentum p (the product of its mass m [kg] times its velocity v [m/s]), which will subsequently be converted into an impulse J (the integral of the force F [N] over the time dt [s] for which it acts) when it strikes the second ball (see Equation 9.1). This second ball will acquire, and subsequently transfer, the impulse to the third ball, and so on; producing a pressure wave that propagates through the intermediate balls. When the pressure wave reaches the most distal ball, this ball is able to gain momentum and will, subsequently reverse the direction of motion of the pressure wave. Assuming entirely elastic behavior, momentum loss is zero, allowing for a successive oscillating motion of the two outer balls.

$$dp = m \cdot dv = \int_{t_1}^{t_2} \sum F \cdot dt \qquad (9.1)$$

with:
dp = change in momentum p [kgm/s]
m = mass [kg]
dv = change in velocity v [m/s]
F = force [N]
dt = time interval for which the force F acts [s]

9

A *Newton's Cradle* inspired mechanism, such as illustrated in Figure 9.2, can be interesting for medical applications in which high forces need to be transferred by flexible or ultrathin devices, such as guidewires, catheters, or needles, which are susceptible to buckling. Buckling is characterized by a sudden sideways deflection of the slender device subjected to high compressive loads, which is unwanted as it can cause damage to the surrounding tissues and decreases the force that can be applied by the tip, e.g., when puncturing a coronary occlusion in the heart using a guidewire. Exerting an impulse on the tissue can allow for applying high forces on tissues as it prevents buckling in two main ways. (1) The use of an impulse increases the maximum compressive load, also known as the critical load, the device can withstand before buckling [1]. (2) Using an impulse to penetrate tissues can decrease the penetration load by minimizing energy losses to the environment. This effect can be mainly attributed to the inertia of the target tissue that acts as a counterforce to the incoming impulse, and thus decreases energy loss by tissue movement and deformation [2, 3] (see also Sakes *et al.* [4] on this topic).
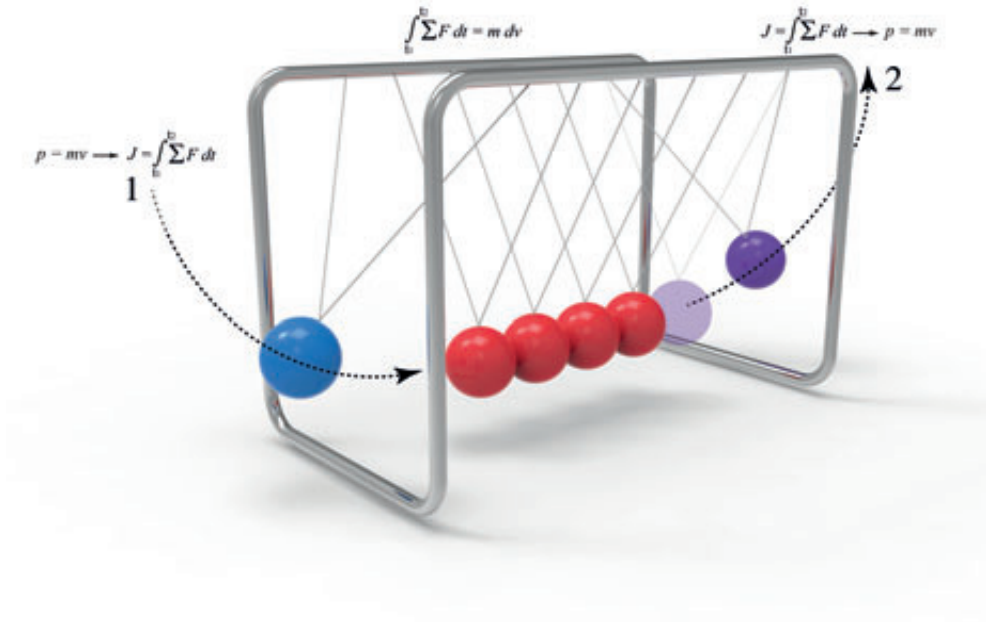
Figure 9.1— *Newton's Cradle.* Color indications: blue = input ball, purple = output ball, and red = intermediate balls.

9
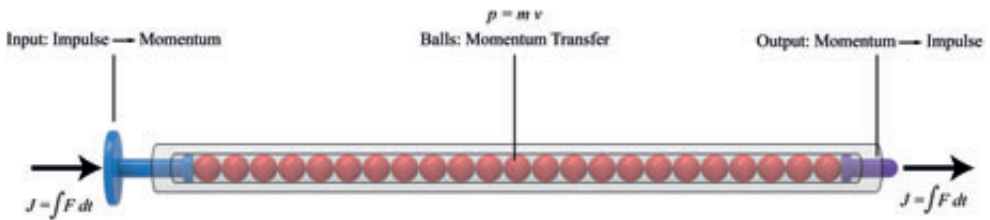
Figure 9.2— Schematic Representation of the *Newton's Cradle's* Inspired Mechanism. Color indications: blue = input plunger, purple = output plunger, red = balls.

Furthermore, as tissue deformation is decreased, a more precise cut or placement of the device can be achieved [2]. In this study we will, therefore, investigate the feasibility of using a *Newton's Cradle* inspired mechanism for low-friction transfer of high-force impulses through slender shafts. For more information on the theory of *Newton's Cradle* we would like to refer to the studies of Kinoshita *et al.* [5], Ceanga *et al.* [6], and Donahue *et al.* [7].

278

9.2. MATERIALS AND METHODS

9.2.1. Experimental Goal

The goal of our experiment was to explore the possibility of using a *Newton's Cradle* inspired mechanism, and thus a series of balls, to transfer an impulse through a long, slender, shaft. In order to achieve this goal, the quality of the impulse transfer in terms of efficiency, as well as the ability of the *Cradle* prototype to exert high peak forces without buckling, needed to be determined. For comparison, a Ø2 mm stainless steel needle (wall thickness 0.2 mm, L = 300 mm) can withstand approximately 2.6 N before buckling and a similar size catheter only 0.003 N [8]. Additionally, the experimental variables that potentially influence this impulse transfer, such as the length of the prototype and the effect of curves, need to be researched.

9.2.2. Cradle Prototype

The *Cradle* prototype consisted of a Ø2.5 mm shaft filled with Ø2 mm stainless steel balls (Figures 9.3 and 9.4). The balls were contained within a shaft with two polymer caps at either side to prevent the balls from falling out. At the proximal end, a Ø1.5 mm input plunger was placed that transferred the input impulse to the balls. At the distal end, a second Ø1.5 mm output plunger was placed that transferred propagating pressure wave of the balls into an output impulse onto the target. In order to ensure contact between the balls, a compression spring was placed distal to the output plunger. Exchanging the balls and shaft could be easily achieved by a screw cap at the distal end of the shaft.

9.2.3. Experimental Variables

9

Dependent Variables
In order to determine the quality of the impulse transfer, the following dependent variables were measured at a fixed input impulse:
1. **The output impulse (J_o)** delivered by the output plunger.
2. **The output peak force ($F_{peak\ out}$)** delivered by the output plunger.

Independent variables
The effect of the specific configuration of the *Cradle* prototype on the impulse transfer was researched by sequentially altering the following independent variables:
1. **Clearance (c).** The inner diameter of the shaft was varied to determine the influence of the clearance between the balls and shaft. The clearance will most likely have an effect on the impulse and peak force efficiency due to two main effects: (1) friction between the balls and the shaft and (2) misalignment of the balls. The clearance between the balls and the shaft was set to 0.1, 0.2, and 0.3 mm.
2. **Shaft type.** In order to determine the effect of the shaft material on the efficiency

of the device, two different shafts were tested: a rigid stainless steel shaft and a double-braided axially and radially stiff cardiac catheter (*Mach 1^tm* 8F, Boston Scientific, Marlborough, MA, USA).

3. **Length (*L*).** During each collision, energy will be lost, mainly due to friction between the balls and the shaft. The number of balls, and thus contact points, will thus likely have an effect on the impulse and peak force efficiency. The effect of the number of balls on the energy loss was determined by setting the length of the shaft to 100, 200, and 300 mm, resulting in a total of 50, 100, and 150 Ø2 mm balls in the shaft, respectively.

4. **Curve angle (*α*).** In endovascular interventions, it is a necessity to cross several intersections and curves in the body. In order to determine the effect of these curves on energy loss, it was decided to subject the prototype to single-constant radius curves (*r* = 40 mm) with four different curve angles: 45, 90, 135, and 180° and to compare the impulse and peak force efficiency to that in the straight configuration.

3. **Curve radius (*r*).** The effect of the curve radius was researched by subjecting the prototype to single-constant radius curves with a curve angle $\alpha = 90°$ and four different curve radii: 20, 40, 60, and 100 mm.

The **input impulse (*J_i*)** and the associated **input peak force (*F_{peak\ in}*)** delivered onto the input plunger were set at 0.4 Ns and 5 N, respectively, and were measured throughout the experiments.

9
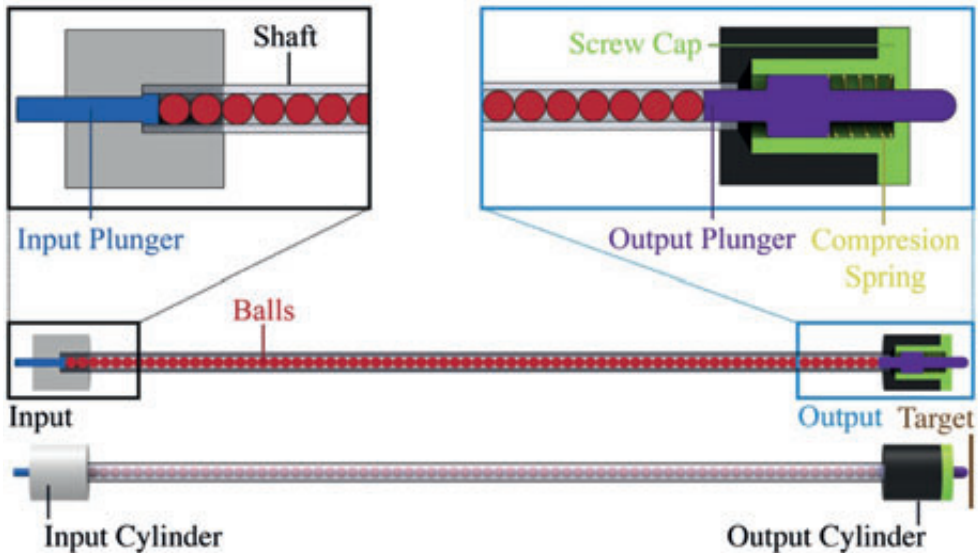
Figure 9.3— Schematic Illustration of the *Cradle* Prototype for Testing Purposes.

9.2.4. Experimental Facility

For determining the feasibility of the *Cradle* prototype, an experimental facility was built (Figure 9.5). The input impulse was delivered by a solenoid actuator connected to a construction rail and was set to approximately 0.4 Ns using a voltage of 5.5 V (Power unit *ES 030-5*, Delta Elektronika, Zierikzee, the Netherlands) and an actuation time to 100 ms. The delivered input and output impulses were measured using two miniature S-beam load cells (*LSB200 FSH00102* and *LSB200 FSH00104*; FUTEK Advanced Sensor Technology, Inc., Irvine, CA, USA) located at the in- and output, respectively. The input load cell was directly connected to the solenoid using an M3 screw thread and a pin to deliver the impulse onto the input plunger. For data acquisition, an analogue signal conditioner (*CPJ RAIL*, SCAIME, Annemasse, France), and a data acquisition system with a sampling rate set to 10 kHz (*NI USB-6211*, National Instruments Corporation, Austin, TX) were connected to the load cells. The load cells were controlled through *LabVIEW 2016* (National Instruments Corporation, Austin, TX). The *Cradle* prototype was connected to an input and output mechanism at the proximal and distal end, respectively (see Figure 9.5).

9
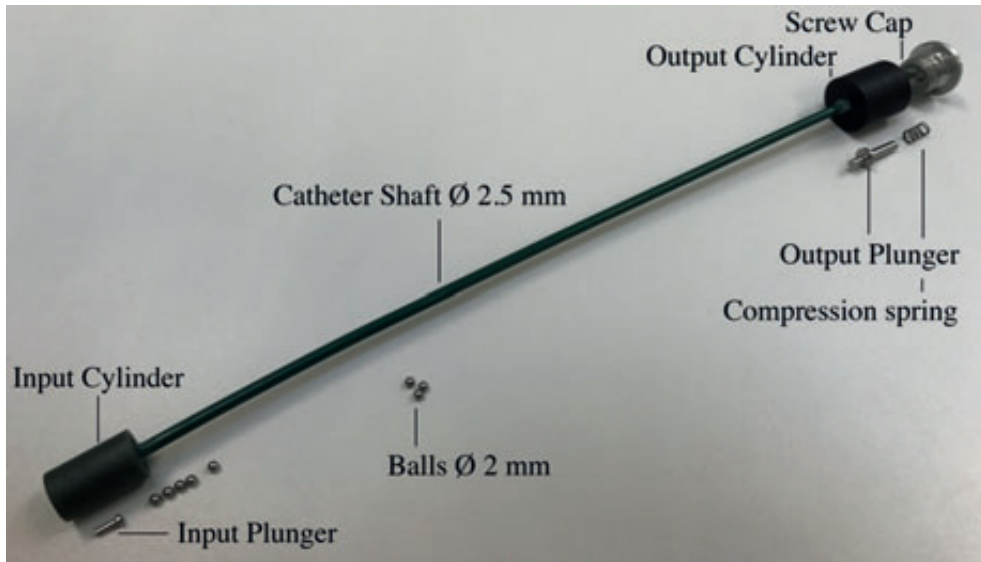
Figure 9.4— The *Cradle* Prototype for Testing Purposes. The prototype consisted of the stainless steel input plunger onto which the input impulse was given, the Ø2.5 mm shaft containing the Ø2 mm stainless steel balls to transfer the impulse, and a stainless steel output plunger in combination with a compression spring to exert the impulse onto the target. In order to confine the plungers and balls in the axial direction, two polymeric cylinders were placed at the in- and output. Furthermore, a screw cap was added to the output cylinder to allow for easy filling of the catheter with the stainless steel balls.
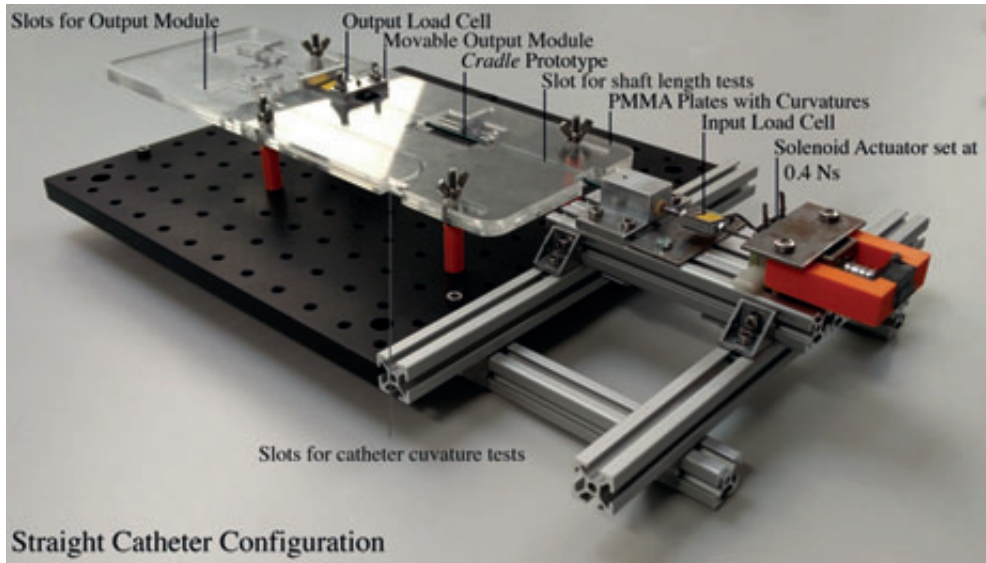
Figure 9.5— Experimental Facility. For explanation see text.

In order to test the effect of the curve angle and radius on the impulse and peak force efficiency and to confine the prototype's shaft, three stacked transparent laser cut 3 mm thick PMMA plates were used: (1) a solid bottom plate, (2) a middle plate containing the curvatures (see Figure 9.6), and (3) a solid top plate, in between which the prototype was placed. These plates were connected to a breadboard (*MB3030/M*, Thorlabs, Newton, NJ, USA) using four aluminums rods and M6 socket head screws. Since the solenoid and the input module were placed on two parallel construction rails, they could be easily translated left or right to accommodate the different laser cut curves in the PMMA plates.

9.2.5. Experimental Protocol

From the dependent variables, two efficiencies were calculated: (1) the impulse efficiency and (2) peak force efficiency. The efficiency values were used to determine the effect of the different independent variables on the impulse transfer. First, the effect of the clearance between the balls and the shaft on the impulse and peak force efficiency of the *Cradle* prototype was determined using the rigid stainless steel shaft of 200 mm in length. From these tests, the clearance with the smallest energy losses was determined. Subsequently, the effect of shaft type was determined using the stainless steel shaft and catheter of 200 mm in length in the straight configuration and with a clearance of 0.3 mm. Thirdly, the effect of shaft length on the efficiency was determined using the flexible
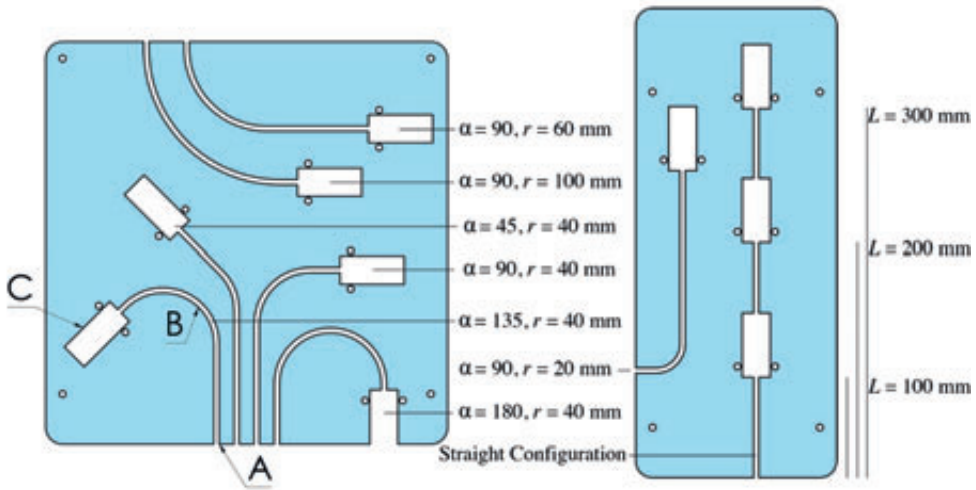
Figure 9.6— Schematic Representation of the Curvatures to which the *Cradle* Prototype was Subjected. The curvatures were laser cut in a 3 mm thick PMMA plate. Letter indications: A= slot for catheter, B= curvature to which the catheter is subjected, C= insert for the output module containing the output load cell.

catheter shaft in the straight configuration. Fourthly, the effect of the curve angle on the efficiency was determined for the 200 mm long flexible catheter shaft with a 40 mm curve radius. Finally, the effect of the curve radius on the efficiency, was tested for the 200 mm long flexible catheter with a 90° curve angle. Each condition was tested 50 times.

9.2.6. Data analysis

Per measurement, the data from the S-beam load cell was processed with *MATLAB 2015b* (The Mathworks, Inc., Natick, MA) to calculate the impact peak force and the impulses J_i and J_o [Ns] by integrating the force F [N] over the time dt [s] for which it acted. Subsequently, the mean output peak force and mean output impulse with the associating standard deviations were calculated per condition. The efficiency of the system [%] was determined in two ways: (1) dividing the output impulse by the input impulse and multiplying this value by 100 and (2) by dividing the output peak force by the input peak force and multiplying this value by 100, for the different clearances, lengths, curve angles, and curve radii. One-way ANOVAs were conducted to determine whether the clearance, length, curve angle, and curve radius had a significant influence on the efficiency. A T-test was performed to determine the effect of the shaft type.

9.3. RESULTS

9.3.1. General Findings

Figure 9.7 illustrates an overview of the obtained data from the load cells. The highest peak force measured during the experiment was 6 N in the straight configuration. As can be seen from Figure 9.7, the load cells have a block shape with a slight peak at the start. It was also observed that the input peak force was not constant (see Table 9.1) for all the tests even though the solenoid was calibrated and powered using the 5.5 V setting. Furthermore, the input impulse duration was also slightly different per configuration; a longer impulse duration of approximately 70 ms was found for the straight catheter configuration, while an impulse duration of approximately 30 ms was found for the rigid stainless steel tube (see Figure 9.7). Furthermore, it was noticed that the catheter slightly shifted during actuation.

9.3.2. Effect of Clearance on the Efficiency

Table 9.1 illustrates an overview of the effect of the clearance and input momentum on the efficiency. As can be seen from Table 9.1, the peak force efficiency ranged from 32 to 57% and the impulse efficiency from 30 to 57%. The peak force and impulse efficiency were negatively, and statistically significantly, affected by the clearance as determined by two one-way ANOVAs (F (2, 237) = 1796, p = 6.6·10^{-144} & F (2, 237) = 2067, p = 10·10^{-161}, respectively). A clearance of 0.2 mm resulted in the highest efficiency.
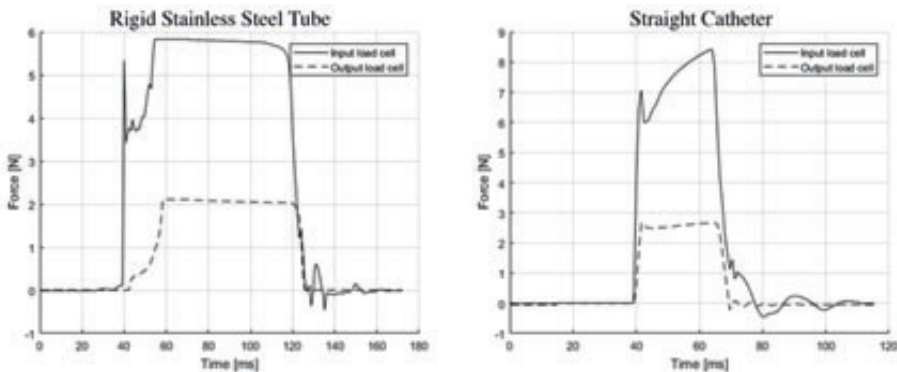
9

Figure 9.7— Two Examples of Force versus Time Graphs of the Input and Output Load Cell for the Straight Configuration Rigid Stainless Steel Tube (Left) and Catheter (Right).

9.3.3. Effect of Shaft Type and Length on the Efficiency

The shaft type significantly influenced the peak force and impulse efficiency of the system as determined by two t-tests (t (198) = 17.1, p = 5.5·10^{-41} & t (198) = 18.2, p =2.8·10^{-44}, respectively). A slightly higher efficiency was found for the catheter in the straight configuration. The impulse efficiency was 30.1 ± 2.1% for the rigid stainless steel tube and 34.2 ± 0.8% for the catheter (see Table 9.2). The length of the catheter negatively, and statistically significantly, affected the peak force and impulse efficiency as determined by the one way ANOVAs (F (2, 237) = 22020, p = 6.9·10^{-270} & F (2, 237) = 33933, p = 4.8·10^{-294}).

9.3.4. Effect of Curvature on the Efficiency

The curve angle negatively affected the peak force and impulse efficiency of the system (see Table 9.3) as determined by two one-way ANOVAs (F (4, 395) = 106.6, p = 1.2·10^{-32} & F(4, 395) = 214.8, p = 7.6·10^{-72}). The impulse efficiency was approximately 7.1% lower in the highly curved situation (α = 135° and r = 40 mm). The curve radius also statistically significantly affected the efficiencies, with the lowest impulse and peak force efficiency found for the smallest radius of 20 mm (F (3, 316) = 299.2, p = 5.8·10^{-92} & F (3, 316) = 380.8, p = 1.5·10^{-104}).

9.4. DISCUSSION

9.4.1. Summary of Main Findings

In this study, we have determined the feasibility of using a series of balls to transfer an impulse through a flexible shaft. The catheter was able to deliver high forces up to 6 N without buckling. In the current set-up we could not increase the input impulse due to the capacity of the load cells, but we feel that higher values can be achieved in future. The impulse efficiency ranged in between 17.3 and 60.0%, with an average of 35%. The length had the greatest influence on the efficiency, while the curve angle and radii had only a minimal influence of in between 5–7%, which is beneficial for clinical situations where tortuous paths need to be followed towards the operation area. A slightly higher efficiency was found for the catheter shaft in the straight configuration than for the stainless steel tube, which is most likely due to a decrease in the friction coefficient between the balls and shaft. A clearance of 0.2 mm between the balls and the shaft resulted in the highest efficiency. However, the optimal clearance is yet to be determined and will most likely lie somewhere in the 0.1 and 0.3 mm range.

During the experiments it was observed that the input peak force was not constant throughout the tests even though the solenoid actuator was powered at an equal setting. This difference in input peak force is most likely caused by the difference in contact stiffness during impact in the different configurations, which in turn might be caused by

9

the clearance, flexibility of the catheter shaft, or the curve. Also, due to the difference in contact stiffness the duration of the impulse changed for the different configurations, resulting in an increase of approximately 40 ms for the more flexible configuration in which the catheter was used in comparison to that of the rigid configuration. It must also be noted that the difference in magnitude and duration of the impulse may have affected the efficiency of the system.

Table 9.1— The Effect of the Clearance and Input Impulse of the Shaft on the Efficiency. The effect of the clearance was tested using the rigid stainless steel shaft. The length of the capillary tube was set to 200 mm.

Clearance [mm]	Mean Input Peak Force [N]	Mean Input Impulse [Ns]	Mean Output Peak Force [N]	Mean Output Impulse [mNs]	Mean Peak Force Efficiency [%]	Mean Impulse Efficiency [%]
0.1	9.9 ± 0.5	$2.4 \cdot 10^{-1} \pm 14.0 \cdot 10^{-3}$	3.7 ± 0.3	$8.8 \cdot 10^{-2} \pm 8.2 \cdot 10^{-3}$	36.9 ± 1.6	37.3 ± 2.0
0.2	4.0 ± 0.3	$1.5 \cdot 10^{-1} \pm 9.6 \cdot 10^{-3}$	2.3 ± 0.1	$8.6 \cdot 10^{-2} \pm 5.6 \cdot 10^{-3}$	57.1 ± 3.9	56.9 ± 3.6
0.3	7.5 ± 0.1	$1.7 \cdot 10^{-1} \pm 5.8 \cdot 10^{-3}$	2.4 ± 0.2	$5.4 \cdot 10^{-2} \pm 3.9 \cdot 10^{-3}$	32.0 ± 2.4	30.1 ± 2.1

Table 9.2— The Effect of the Shaft Type (Rigid Stainless Steel Tube versus Flexible Catheter) and Length on the Efficiency. The effect of the shaft types was tested in the straight configuration and a clearance of 0.3 mm between the balls and the shaft.

Shaft Type:	Length [mm]	Mean Input Peak Force [N]	Mean Input Impulse [Ns]	Mean Output Peak Force [N]	Mean Output Impulse [mNs]	Mean Peak Force Efficiency [%]	Mean Impulse Efficiency [%]
Rigid	200	7.5 ± 0.1	$1.7 \cdot 10^{-1} \pm 5.8 \cdot 10^{-3}$	2.4 ± 0.2	$5.4 \cdot 10^{-1} \pm 3.9 \cdot 10^{-3}$	32.0 ± 2.4	30.1 ± 2.1
Catheter	100	5.6 ± 0.1	$5.5 \cdot 10^{-1} \pm 16.3 \cdot 10^{-3}$	3.3 ± 0.08	$3.1 \cdot 10^{-1} \pm 9.9 \cdot 10^{-3}$	58.6 ± 1.0	60.0 ± 1.0
	200	4.9 ± 0.1	$4.9 \cdot 10^{-1} \pm 6.7 \cdot 10^{-3}$	1.8 ± 0.04	$1.7 \cdot 10^{-1} \pm 3.6 \cdot 10^{-3}$	36.6 ± 1.2	34.2 ± 0.8
	300	6.9 ± 0.2	$6.0 \cdot 10^{-1} \pm 16.1 \cdot 10^{-3}$	1.5 ± 0.06	$1.0 \cdot 10^{-1} \pm 7.1 \cdot 10^{-3}$	22.0 ± 1.1	17.3 ± 1.0

Table 9.3— The Effect of the Curvature of the Shaft on the Efficiency. The effect of the curvature was tested using the flexible catheter shaft with a clearance of 0.3 mm between the balls and shaft.

Shaft Type:	Curve Angle [°]	Curve Radius [mm]	Mean Input Peak Force [N]	Mean Input Impulse [Ns]	Mean Output Peak Force [N]	Mean Output Impulse [Ns]	Mean Peak Force Efficiency [%]	Mean Impulse Efficiency [%]
Flexible Catheter	0°	∞	4.9 ± 0.1	$4.9 \cdot 10^{-1} \pm 6.7 \cdot 10^{-3}$	1.8 ± 0.04	$1.7 \cdot 10^{-2} \pm 3.6 \cdot 10^{-3}$	36.6 ± 1.2	34.2 ± 0.8
	45°	40	6.2 ± 0.1	$5.9 \cdot 10^{-1} \pm 9.6 \cdot 10^{-3}$	2.2 ± 0.04	$2.0 \cdot 10^{-1} \pm 3.7 \cdot 10^{-3}$	35.0 ± 0.9	34.0 ± 0.6
		20	3.1 ± 0.08	$3.3 \cdot 10^{-1} \pm 6.9 \cdot 10^{-3}$	1.0 ± 0.05	$9.5 \cdot 10^{-2} \pm 5.0 \cdot 10^{-3}$	32.9 ± 1.2	29.1 ± 1.3
		40	4.6 ± 0.07	$4.6 \cdot 10^{-1} \pm 6.2 \cdot 10^{-3}$	1.7 ± 0.05	$1.5 \cdot 10^{-1} \pm 3.9 \cdot 10^{-3}$	36.1 ± 2.5	32.5 ± 1.8
	90°	60	3.6 ± 0.2	$3.7 \cdot 10^{-1} \pm 14.5 \cdot 10^{-3}$	1.4 ± 0.04	$1.3 \cdot 10^{-1} \pm 3.8 \cdot 10^{-3}$	38.4 ± 1.6	35.0 ± 1.3
		100	4.4 ± 0.1	$4.5 \cdot 10^{-1} \pm 10.9 \cdot 10^{-3}$	1.7 ± 0.06	$1.6 \cdot 10^{-1} \pm 5.5 \cdot 10^{-3}$	37.8 ± 1.3	34.5 ± 1.3
	135°	40	5.6 ± 0.1	$5.4 \cdot 10^{-1} \pm 8.3 \cdot 10^{-3}$	1.8 ± 0.1	$1.5 \cdot 10^{-1} \pm 7.4 \cdot 10^{-3}$	32.3 ± 2.3	27.9 ± 1.6
	180°	40	4.9 ± 0.1	$4.9 \cdot 10^{-1} \pm 10.9 \cdot 10^{-3}$	1.6 ± 0.1	$1.4 \cdot 10^{-1} \pm 13.4 \cdot 10^{-3}$	31.9 ± 2.9	29.0 ± 2.7

9

In this study we have determined both the impulse and peak force efficiency of the *Cradle* prototype. The impulse efficiency is the most determining factor in determining the overall efficiency, and thus energy loss, of the system. The peak force efficiency, on the other hand, is an important factor to determine the feasibility in a clinical setting. It is not a good measure for the determine the energy losses of the *Cradle* prototype, as the exerted output peak force is dependent on the (bio)mechanical properties of the target, with high values found for rigid targets. In our experiments, we were able to transfer high forces through flexible shafts and curves, with a maximum measured force of 6 N. Higher forces are achievable, but could not be tested due to the capacity of the load cells.

9.4.2. Limitations of this Study

In this study we have not determined the feasibility of using this system in a clinical situation. An application that would benefit from a flexible tool that can deliver high forces without buckling is the endovascular treatment of Chronic Total Occlusions (CTOs). A CTO is a heavily calcified complete occlusion of an artery that is difficult to cross due to the required high penetration forces. As a result, buckling often occurs (see also Sakes *et al.* [9] on this topic). Furthermore, as there is a clear trend towards even
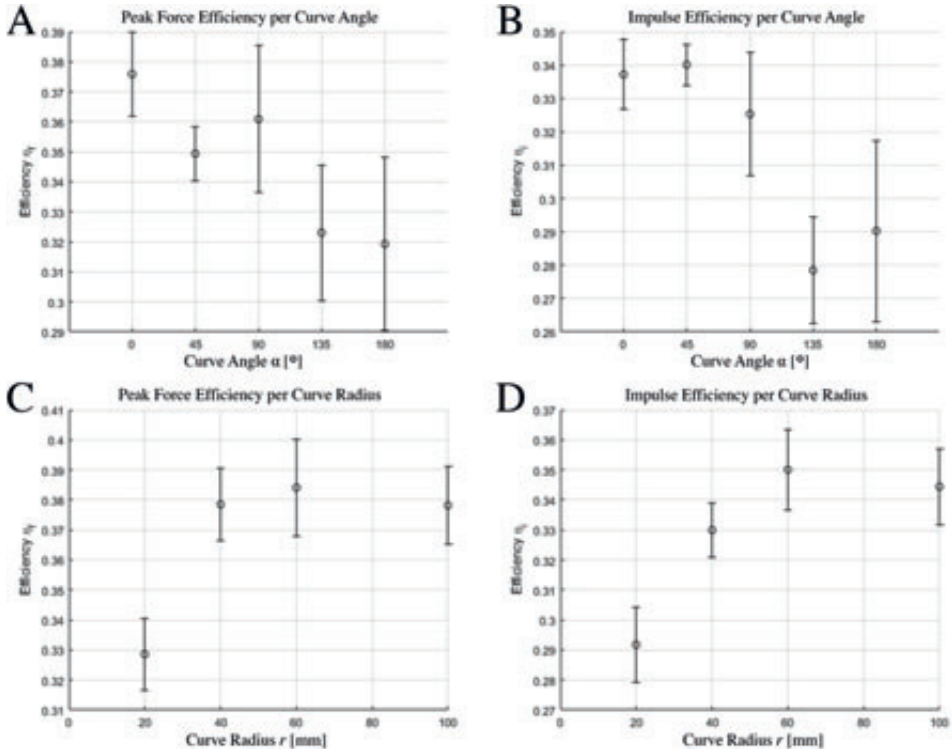
Figure 9.8— Impulse and Peak Force Efficiency of the Catheter in the Curved Configuration. (A) Peak force efficiency of the catheter in different curve angles (r = 25 mm). (B) Impulse efficiency of the catheter in different curve angles (r = 25 mm). (C) Peak force efficiency of the catheter in different curve radii (α = 90°). (D) Impulse efficiency of the catheter in different curve angles (α = 90°).

smaller, needle-like, instruments, buckling will become a more important failure mode that needs to be taken into account in the near future. In order to prevent buckling and as such increase the success rate of the endovascular treatment of CTOs, as well as percutaneous needle procedures, a *Cradle*-inspired catheter could be beneficial.

9.4.3. Recommendations

With optimization of the current design and facility, a higher efficiency could be obtained in future. For this purpose, research should be conducted to determine the most optimal clearance and material combination of the balls and shaft. Furthermore, it is also of importance to determine the optimal pretension, and thus contact stiffness, between the balls to minimize energy loss. In the current prototype, a relatively weak spring was used

with a spring constant of 0.97 N/mm. In future, the effect of compression springs of different spring constants on the efficiency could be researched.

In order to integrate the catheter in a laparoscopic or endovascular procedure in the near future it is a necessity to allow for single-handed control and adjusting of the output peak force, as well as ensure the safety of the device. The safety of the device could be improved by incorporating the catheter shaft with the output plunger. This will minimize the chance of loss of the indenter or the balls. Additionally, the ability to actively steer the tip during the procedure should be researched, as this can increase the effectiveness of the procedure and decrease the chance of unwanted tissue damage. Finally, in order to navigate through narrow tortuous pathways and decrease the invasiveness of the procedure, it is a necessity to further reduce the outer diameter of this catheter. Due to the simplicity of the design, further diameter reduction should be possible towards a sub-millimeter scale. However, it must be noted that both the impulse and peak force efficiency will most likely decrease when miniaturizing the outer diameter, as the number of balls, and thus contact points will increase. The same also goes for increasing the length, which increases the required number of balls. Therefore, other ball-shapes should be researched, such as cylinder-types, to minimize the number of contact points.

9.5. CONCLUSIONS

This study has illustrated that it is feasible to transfer high-force impulses through a series of balls confined within a rigid shaft or flexible catheter. This technique could be beneficial for medical instruments that suffer from buckling, such as guidewires and needles, especially since there is a trend for further miniaturization. More research is needed to allow for high efficiency impulse transfer in even smaller and longer devices. In the future we will continue this investigation and will develop this tool into a handheld clinical prototype.

ACKNOWLEDGMENTS

REFERENCES

[1]   Lock M. A study of buckling and snapping under dynamic load. El Segundo, CA: Laboratory Operations Aerospace Corporation. Report Number TR-0158 (3240-30)-3; 1967. pp. 1-55.

[2]   Jelínek F, Smit G, Breedveld P. Bioinspired Spring-Loaded Biopsy Harvester—Experimental Prototype Design and Feasibility Tests. Journal of Medical Devices. 2014; 8(1): pp. 015002-1-015002-6.

[3]   Heverly M, Dupont P and Triedman J. Trajectory optimization for dynamic needle insertion. Proceedings of the 2005 IEEE International Conference on Robotics and Automation held at Barcelona, Spain, 18-22 April 2005. pp 1646-1651.

[4]   Sakes A, Dodou D, and Breedveld P. Buckling prevention strategies in nature as inspiration for improving percutaneous instruments: a review. Bioinspiration & Biomimetics. 2016; 11(2): pp. 021001.

[5]   Kinoshita T, Wenger T, and Weiss DS. A quantum Newton's cradle. Nature 2006; 440(7086): pp. 900-903.

[6]   Ceanga V and Hurmuzlu Y. A new look at an old problem: Newton's cradle. Journal of Applied Mechanics. 2011; 68(4): pp. 575-583.

[7]   Donahue CM, Hrenya CM, Zelinskaya A, and Nakagawa K. Newton's cradle undone: Experiments and collision models for the normal collision of three solid spheres. Physics of Fluids 2008; 20(11): pp. 113301.

[8]   Stenqvist O, Curelau I, Linder LE, Gustavsson B. Stiffness of central venous catheters. Acta Anaesth Scand 1983; 27(2); 153-157.

[9]   Sakes A, Regar E, Dankelman J, Breedveld P. Crossing total occlusions: Navigating towards recanalization. Cardiovasc Eng Techn 2016; 7(2):103-117.

9

CHAPTER 10

CROSSING CTOS USING A HYDRAULIC PRESSURE WAVE CATHETER

AIMÉE SAKES, TJIBBE NICOLAI, JORDAN KARAPANAGIOTIS, PAUL BREEDVELD, AND JO W. SPRONCK

10

Submitted.

Abstract— Crossing highly calcified occlusions is technically challenging mainly due to guidewire buckling. In an effort to prevent buckling, a catheter that uses a dynamic impulse load is proposed. The proposed *Wave* catheter consists of an input plunger to generate an impulse at the handle, a hydraulic pressure wave confined within a Ø2 mm catheter to transfer the impulse towards the tip, and an output plunger to transfer the impulse to the occlusion. To determine the feasibility of this catheter, an experiment was performed in which the input and output impulses were recorded as a function of the catheter type, curvature, and plunger travel distance. Additionally, the system was tested on artificial CTO models to determine the clinical validity. The catheter has illustrated the ability to safely transfer high-force impulses of up to 43N (1.5 N required) with only minimum catheter type and no curvature dependency, allowing for delivering high-force impulses through tortuous vasculature and under any angle. Furthermore, the catheter was able to penetrate the artificial CTO models within 1 strike.

Keywords— Catheter Technology, Chronic Total Occlusions (CTOs), Hydraulic Pressure Wave, Percutaneous Coronary Interventions (PCIs), Medical Device Design.

10

10.1. INTRODUCTION

With continued development of smaller and more advanced instruments, such as advanced catheters and stiffer and more responsive guidewires, invasive open heart surgeries are slowly being replaced by minimally invasive "nonsurgical" cardiovascular interventions [1-3]. One of the last frontiers of cardiovascular interventions is the Percutaneous Coronary Intervention (PCI) of Chronic Total Occlusion (CTO), defined as heavily calcified total occlusions of an artery of at least three months old. CTOs are characterized as the most technically challenging lesions interventionist face, evidenced by a significant lower success rate in between 50–90% in comparison to acute lesions where success rates of over 95% are achieved [4]. The main failure mode in the percutaneous treatment of CTOs is the inability to cross the occlusion, accounting for approximately 60% of the failure cases [5], mainly due to guidewire buckling (Figure 10.1). Guidewire buckling occurs if the force needed to puncture the CTO, which is usually around 1.5 N [6], exceeds the critical buckling load ($F_{critical}$) of the guidewire, which is around 0.008–0.26 N depending on the type of guidewire and the unsupported tip length [7]. Buckling is unwanted as the bifurcations can damage the blood vessel wall and it lowers the force the guidewire or catheter can deliver onto the target tissue area, which can eventually result in procedural failure and transfer to the much more invasive Coronary Artery Bypass Grafting (CABG) open heart surgery if the occlusion cannot be crossed.

Buckling of slender, flexible, cylindrical instruments, such as catheters and guidewires, can be prevented by decreasing their slenderness λ – defined as the length L [mm] divided by the diameter $\varnothing$ [mm] of the instrument –, by increasing the Young's Modulus E [GPa] of their material, or by increasing the second moment of area I [mm·] by changing the shape of the instrument [8,9]. However, as the anatomy of the vasculature restricts the instrument diameter, a certain flexibility is required to travel safely through the vasculature, and a certain length is required to reach the occlusion site, these variables cannot be altered significantly. Therefore, in order to improve the buckling resistance of the endovascular instruments and improve the procedural success rates of PCIs of CTOs, we propose to use a mechanical impulse J [Ns], defined as the integral of a force F [N] over the time interval dt [s] for which it acts, during the crossing procedure. Using an impulse to dynamically load the guidewire and CTO can prevent buckling in two main ways: (1) the critical load of the guidewire increases with a decrease in the time interval [10] and (2) dynamic loading of the CTO can lower the required penetration load, as illustrated in the studies of Heverly and Jelínek *et al.* [11,12], as the environmental damping and the inertia of the target tissue can act as a reaction force to the impulse force.

10

In order to apply an impulse J onto the CTO, translational momentum p, defined as the product of mass m [kg] and velocity v [m/s], should be generated inside the guidewire or crossing tool. Translational momentum can be generated using many different methods, either locally in the distal tip of the crossing tool or proximally in the handle. In this study, we propose to use a hydraulic pressure wave to transfer translational momentum through the catheter (Figure 10.2). A hydraulic pressure wave is characterized as a longitudinal wave with regions of increased density, known as compressions, and regions of reduced density, known as rarefactions, through a fluid (Appendix 10.A). In order to initiate a hydraulic pressure wave, a sudden chance in velocity of the fluid is needed. In our proposed tool, an input impulse J_{input} [Ns] is applied on an input plunger proximally inserted into the lumen of a flexible tube or catheter. The applied input impulse is subsequently converted into translational momentum p of the fluid in the form of a hydraulic pressure wave. Finally, the translational momentum p of the fluid is converted into an output impulse J_{output} [Ns] during the distal impact on the CTO.

Even though several shockwave catheters are described in the patent literature in which the translational momentum or shockwave is created inside the distal catheter tip using a shockwave generator, specifically an electric arc [13-15], there are three main advantages of generating the translational momentum proximally. (1) The tip remains flexible, whereas the tip of distally generated momentum catheters incorporate a generator with connector, making the tip rigid and less suited for motion through curved vasculature. (2) The complexity of the catheters in which the pressure wave is generated distally is relatively high in comparison to the complexity of our proposed proximally generated momentum catheter. (3) The output characteristic of the proposed proximally generated momentum catheter can be easily altered by changing the input characteristic, whereas the output characteristic in distally generated momentum catheters is limited mainly due to the size restrictions of the generator.

The goal of this study was to determine the feasibility of a hydraulic pressure wave to transport translational momentum p through a catheter that in turn can be transformed into an output impulse J_{output} that can be used to puncture and cross CTOs. In order to answer this question, a proof-of-principle experiment has been carried out. In this experiment, the effect of the magnitude of the input impulse, the elastic behavior of the catheter, and the curvature of the catheter, on the efficiency of the system was determined by dividing the output peak force through the input peak force. We hypothesized that the efficiency of the system is negatively influenced by the elasticity of the catheter, but remains unchanged by curvatures of the catheter shaft. Additionally, the effectiveness of the catheter in puncturing artificial CTO models was tested. Finally, based on the proof-of-principle experiment outcomes, a conceptual design of a hydraulic pressure wave catheter is proposed.

10

Figure 10.1— Buckling of the Guidewire During the Endovascular Treatment of CTOs. The guidewire is pushed from outside the body against the CTO (yellow) using a penetration force ($F_{penetration}$). The CTO exerts an opposite compressive force onto the guidewire until puncture is achieved at approximately 1.5 N according to Thind *et al*. [6]. If the compressive force exerted by the CTO exceeds the critical buckling load ($F_{critical}$) of in between 0.008–0.26 N depending on the guidewire, buckling of the guidewire tip, indicated by the dark grey line, will occur.
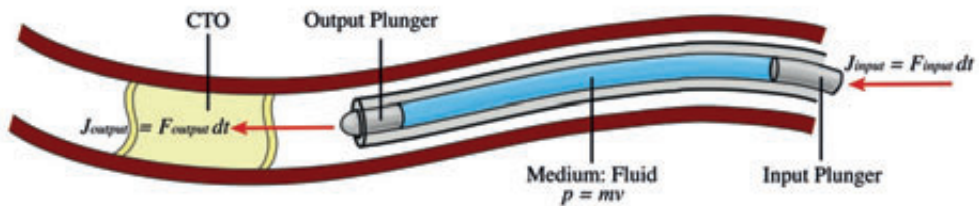

Figure 10.2— Hydraulic Pressure Wave Concept for Crossing CTOs. In this concept, a dynamic input impulse J_{input} [Ns] is exerted on the input plunger of the device. J_{input} is converted into translational momentum p [kgm/s] of the plungers and fluid (blue). Finally, p is converted into an output impulse J_{output} [Ns] during the collision of the CTO with the output plunger. In the clinical situation, the plunger may be in direct contact with the CTO and a preload may be applied.

10

10.2. RESULTS

10.2.1. Peak Force Efficiency

In this study we have tested the peak force efficiency of our proposed hydraulic pressure wave catheter using a Ø2 mm 1 m long clinically available catheter. At the proximal and distal end of the catheter a plunger was placed to transfer the impulse to the fluid. The catheter was fixed to the experimental facility at the in- and output. The input impulse was given by a mass-spring system. In order to measure the in- and output peak force, two load cells were placed at the in- and output, respectively. Figure 10.3 shows an example of the input and output force characteristics of the catheter as a result of an input impulse. From this figure we could deduct the acceleration of the input mass (1 in Figure 10.3), the input peak force (2 in Figure 10.3), the velocity of the pressure wave (3 in

Figure 10.3), the output peak force and impulse (4 in Figure 10.3), and the reflections of the pressure wave. The peak force efficiency η was calculated by dividing the output peak force over the input peak force and multiplying this value by 100%. In Table 10.1 an overview of the experimental results is illustrated. As can be seen from Table 10.1, the peak force efficiency was negatively, and statistically significantly, affected by the magnitude of the input impulse as determined by a one-way ANOVA ($F(2, 48) = 11.36$, $p = 9.2 \cdot 10^{-5}$). In other words, the higher the input impulse the lower the peak force efficiency. The mean peak force efficiency was 71.0 ± 11.2% (mean ± standard deviation) for an input impulse of 0.025 Ns, 67.6 ± 7.6% for an input impulse 0.0375 Ns and 56.0 ± 9.7% for an input impulse of 0.05 Ns.

In order to investigate the effect of traveling through multiple curves in the vasculature to reach the CTO on the efficiency of the catheter, the catheter was evaluated in two configurations: (1) straight 0° configuration and (2) curved 1080° (3x360°) configuration with a curve radius r of 25 mm. The mean peak force efficiency of the hydraulic pressure wave catheter was not affected by the catheter curvature in terms of mean peak force efficiency, as determined by a two-tailed t-test ($t(32) = 2.0$, $p = 0.3$), allowing for very efficient energy transfer through tortuous environments. The measured peak force efficiency was 56.0 ± 9.7% for the straight 0° configuration, and 58.7 ± 5.1% for the curved 1080° (3x360°) configuration.
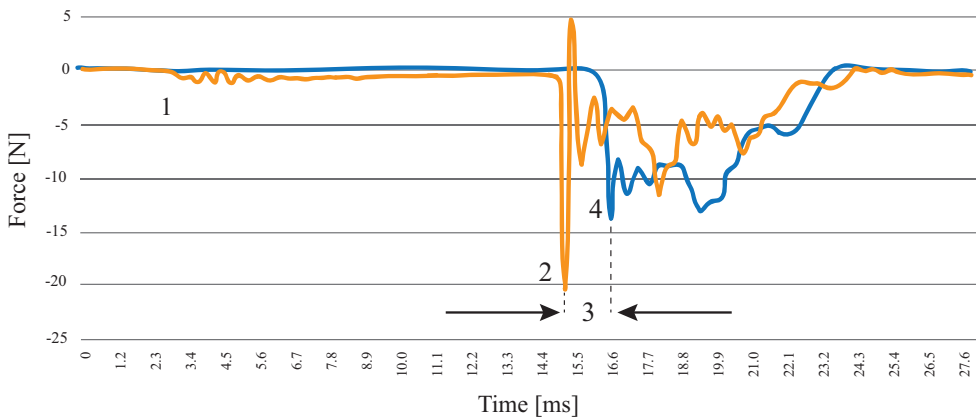
10

Figure 10.3— Measured Input (Orange) and Output (Blue) Force Characteristics of the Impulse. Observations: (1) Release and acceleration of input mass, (2) Input peak force and oscillations of the input load cell, (3) Wave interval: time it takes for the hydraulic pressure wave to reach the output of the catheter, and (4) Output peak force and oscillations of the load cell.

In order to test the effect of the elasticity of the catheter shaft, two catheter types were tested in the straight configuration: (1) the elastic single-braided *Mach1 6F CLS4* guide catheter (Boston Scientific, Marlborough, MA) and (2) the stiffer double-braided *Impulse 6F AL3* angiographic catheter (Boston Scientific, Marlborough, MA). From the experiments it was determined that the efficiency of the catheter was influenced by the elasticity of the catheter shaft ($t(32) = 2.0$, $p = 1.7 \cdot 10^{-}$). The peak force efficiency was approximately 13% lower ($\eta = 56.0 \pm 9.7\%$) for the more elastic single-braided catheter as compared to the stiffer double-braided catheter ($\eta = 69.4 \pm 4.9\%$).

The effect of the distance between the CTO and the output plunger, defined as the plunger travel distance *d,* on the peak force efficiency and output peak force was investigated, as in the clinical situation it might be challenging to establish direct contact with the CTO. Three plunger travel distances *d* were compared: (1) $d = 0$ mm, in which the output plunger was in direct contact with the load cell, (2) $d = 2$ mm, and (3) $d = 4$ mm. It was determined that the peak force efficiency was significantly influenced by the output plunger travel distance *d* as determined by a one-way ANOVA ($F(2, 48) = 285.6$, $p = 2.2 \cdot 10^{-27}$). The mean peak force efficiency was positively correlated with an increased travel distance and ranged from $56.0 \pm 9.7\%$ for $d = 0$ mm, $199.7 \pm 26.1\%$ for $d = 2$ mm, and $213.0 \pm 16.6\%$ for $d = 4$ mm, resulting in a maximum output peak force of 43 N for $d = 4$ mm. Looking at a typical measurement of the in-contact situation in which the plunger is in direct contact with the output load cell, and the no-contact situation in which the plunger travels either 2 or 4 mm until impact, it becomes clear that the output characteristic for both situations is significantly different (Figure 10.4). In the no-contact situation a more concentrated force-time characteristic was found, whereas a much broader force-time characteristic was found for the in-contact situation.

10.2.2. Velocity

10

The velocity of the hydraulic pressure wave *v* was measured by dividing the length of the catheter ($L = 1$ m) through the elapsed time between the input and output peak force. Table 10.2 illustrates an overview of the experimental results with respect to the velocity of the hydraulic pressure wave. As can be seen from Table 10.2, the velocity of the hydraulic pressure wave was in between 330 and 820 m/s, with a mean of 569 m/s. The mean velocity of the hydraulic pressure wave was not significantly influenced by the input impulse, as determined by a one-way ANOVA ($F(2, 48) = 0.4$, $p = 0.7$). A mean wave velocity of 556.8 ± 134.0 m/s was found for an input impulse of 0.025Ns, 585.7 ± 87.3 m/s for an input impulse of 0.0375Ns, and 580 ± 70.0 m/s for an input impulse of 0.05Ns. The effect of the catheter type (singe or double braided) on the mean velocity of the hydraulic pressure wave was not statistically significant either ($t(32) = 2.0$, $p = 0.9$).

Table 10.1— Overview of Experimental Results per Independent Variable. The values are indicated as mean ± standard deviation ($n = 17$).

Independent Variable	Independent Variable Value	Input Peak Force [N]	Output Peak Force [N]	Mean Peak Force Efficiency η [%]
Input Impulse	**0.025 Ns**	8.3 ± 0.8	5.8 ± 0.5	71.0 ± 11.2
	0.0375 Ns	13.0 ± 1.1	8.7 ± 0.6	67.6 ± 7.6
	0.05 Ns	19.7 ± 1.9	11.0 ± 1.5	56.0 ± 9.7
Catheter Curvature at $J_{input} = 0.05$ Ns	**0°**	19.7 ± 1.9	11.0 ± 1.5	56.0 ± 9.7
	1080° (3x360° = 3 loops) ($r = 25$ mm)	18.4 ± 1.8	10.7 ± 0.7	58.7 ± 5.1
Catheter Type at $J_{input} = 0.05$ Ns	**Single-braided**	19.7 ± 1.9	11.0 ± 1.5	56.0 ± 9.7
	Double-braided	18.4 ± 1.8	10.7 ± 0.7	69.4 ± 4.9
Plunger Travel Distance (d) at $J_{input} = 0.05$ Ns	**0 mm**	19.7 ± 1.9	11.0 ± 1.5	56.0 ± 9.7
	2 mm	18.8 ± 1.6	37.3 ± 14.2	199.7 ± 26.1
	4 mm	19.0 ± 1.7	40.5 ± 1.5	213.0 ± 16.6

Table 10.2— Measured Wave Velocities Versus the Input Impulses and Catheter Types. The values are indicated as mean ± standard deviation ($n = 17$).

Independent Variable	Independent Variable Value	Velocity of the Hydraulic Pressure Wave [m/s]
Input Impulse	**0.025 Ns**	556.8 ± 134.0
	0.0375 Ns	585.7 ± 87.3
	0.05 Ns	580.0 ± 70.0
Catheter Type*	**Single-braided**	580.0 ± 70.0
	Double-braided	554.0 ± 73.6

* Using an input impulse of 0.05 Ns

10

10.2.3. Clinical Validation

The double-braided catheter was tested on artificial CTO models as described in the methods section. The CTO models consisted of a cap model representing the proximal cap, a core model representing the CTO body, and an environment model representing the clinical environment of the CTO. The entire model was submerged in Blood-Mimicking Fluid (BMF). In order to resemble the clinical situation more closely, the catheter was free to translate at the distal end and was not confined along the shaft. The hydraulic wave catheter was able to puncture all the artificial CTO models within 1 strike ($n = 5$).
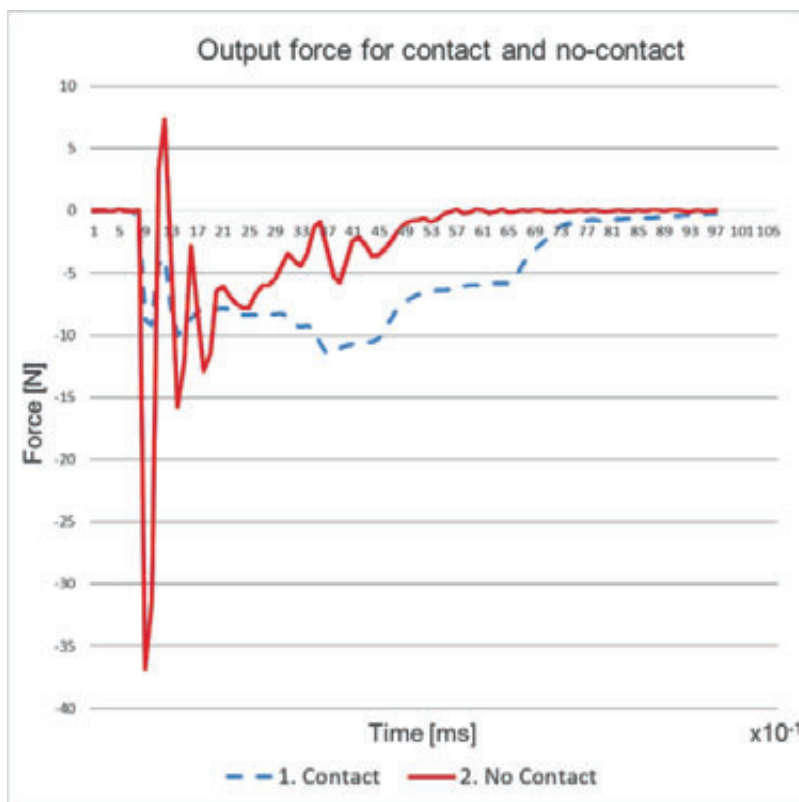
Figure 10.4— Typical Output Force-Time Characteristics of an In-Contact (d = 0 Mm; Dotted Blue Line) and No-Contact Situation (d = 2.0 Mm; Red Line). As can be seen from the figure, a higher output peak force is achieved in the no-contact situation when compared to the in-contact situation. Furthermore, the force-time characteristic of the in-contact situation is much broader than that of the no-contact situation.

10.3. DISCUSSION

10.3.1. Summary of Main Findings

Efficiency Measurements

The feasibility experiment has illustrated the feasibility of using a hydraulic pressure wave to transfer an impulse through a flexible shaft with high efficiency. Our hydraulic pressure wave catheter was capable of transferring high output peak forces of up to 43 N through flexible catheter shafts (Ø2 mm) without buckling. The curvature of the catheter shaft did not significantly influence the efficiency of the system, which is beneficial since several tight curves need to be crossed in order to reach the CTO.

The magnitude of the input peak force negatively affected the efficiency of the system. In other words, a higher magnitude pressure wave dissipated more over time than a lower magnitude pressure wave. This finding is in line with the results from a simulation on the effect of pipe wall friction on pressure loss (see Appendix 10.A).

The flexibility of the catheter was found to significantly influence the efficiency, which is mainly due to the overall, radial and axial, expansion of the catheter shaft, absorbing a part of the impulse energy. However, even though the flexibility of the catheter negatively influenced the efficiency, the difference in efficiency was relatively low; approximately 13%. This is beneficial for the clinical application of the device as different catheters are often used for different procedures. A minimal dependency on the catheter elasticity allows the surgeon to pick the most suitable catheter for the procedure.

Changing the output plunger travel distance resulted in the ability to actively change the output characteristic. High output peak forces up to 43 N acting for a short ~0.3 ms time interval were generated when the plunger was not in direct contact with the sensor, whereas lower output peak forces up to 14 N over a longer time interval of ~0.4 ms were achieved with direct contact. The different force-time characteristic between these two situations is mainly caused by the rapid acceleration of the output plunger, and thus higher terminal velocity and momentum, which results in high, but short-lived, peak forces. Even though the overall efficiency decreased with increasing output plunger travel distance, mainly due to energy losses between the plunger and cylinder, the ability to achieve high peak forces is beneficial when puncturing heavily calcified CTOs. It must be noted, however, that in the clinical situation, the blood in front of the CTO will significantly damp the plunger. Furthermore, due to the flexible environment of the CTO and the flexibility of the CTO itself, the peak force will be significantly less in the clinical situation.

10

Velocity Measurements

The mean pressure wave velocity was found to be approximately 570 m/s, which is slightly higher as expected from the calculated values in Appendix 10.A. The experimental results illustrate no significant difference between the mean velocities of the hydraulic pressure waves for the different input impulses and catheter types. One possible explanation is that the difference in elasticity of the chosen catheters was too small to cause a significant difference in the wave velocity. For more information on this topic, we would like to refer to Appendix 10.A.

Clinical Feasibility

The hydraulic pressure wave was highly effective in puncturing the artificial CTO models. All the CTO models were punctured within 1 strike, while the catheter tip was free to translate, similar to what will be encountered in a clinical situation. This result clearly

illustrates that the *Wave* catheter has great potential for puncturing CTO during PCIs in the near future.

10.3.2. Limitations of this Study

In the current measurement facility, the lack of a fluid seal between the plunger and the cylinder caused minor fluid leakage during operation; decreasing the efficiency, and required filling the catheter after each test. Furthermore, on some occasions this also caused air to become entrapped in the system, which decreased the efficiency due to the compressibility of the air bubbles.

10.3.3. Recommendations for Future Research

Increase of Efficiency & Safety

Even though our hydraulic pressure wave catheter has illustrated the ability to transfer impulses through tortuous shafts with high efficiency, we feel that a further increase in efficiency is possible by redesign. Energy loss can be mainly contributed to the expansion of the catheter wall (Appendix 10.A). Therefore, the use of an even stiffer catheter shaft in which the overall, radial and axial, expansion is minimized could be researched. Furthermore, during the experiments it was found that small air bubbles in the system would significantly reduce the efficiency. In order to prevent entrapped air bubbles in the catheter, in future an alternative way of filling and sealing the catheter should be researched. Finally, in the current design, the cylinders contain a so-called series junction at the cylinder-catheter interface caused by the different inner diameters of both parts, which partly reflects the pressure wave; decreasing the efficiency of the system (Appendix 10.A). In order to prevent this effect, as well as potentially reduce the friction between the output plunger and the cylinder, a different tip geometry can be looked into in which the output plunger is incorporated in the catheter shaft (Figure 10.5). Finally, it is imperative to test the catheter in an *ex-* or *in-vivo* situation to determine its effectiveness and safety in a clinical situation that closely resembles that of PCIs of CTOs.

10

Effectiveness on CTO Models

In order to get a conclusive answer on the feasibility of the hydraulic pressure wave catheter for increasing the success rate of PCI in CTOs, it is a necessity to test the catheter on animal CTO models. In theory, the system can deliver output forces high enough to puncture the caps of CTOs, as Thind *et al.* [6] measured a maximum force of 1.5 N to penetrate a rabbit CTO and forces up to 43 N were measured for our device. However, in a clinical situation the viscosity of the blood and flexibility of the environment will damp the output, resulting in significantly lower peak forces. Our catheter has illustrated the ability to puncture the CTO model submerged in Blood-Mimicking-Fluid (BMF) within 1 strike. The catheter was allowed to translate, to more closely resemble the clinical

situation and the CTO model. Even though the CTO model is artificial, it still illustrates the effectiveness of the catheter striking a flexible model.

The effect of the output characteristic on the effectiveness and efficiency to puncture CTOs should be researched. In the current experiment, single strikes, with different force-time characteristics, were used to test the performance. In the near future, research could be conducted to optimize this force-time characteristic for puncturing CTOs. Furthermore, it is also possible to exert multiple executive strikes by guiding multiple pressure waves through the catheter. Additionally, research could be conducted into different tip shapes to determine the most effective and efficient shape to puncture CTOs (see also Sakes *et al.* [15] on this topic).

Miniaturization Outer Dimension

For a future clinical prototype the possibility of miniaturization should be looked into. Current dedicated coronary CTOs devices, such as guidewire and catheters, have a diameter in between Ø0.35–1.1 mm [17,18]. Due to the simplicity of our design, miniaturization to a Ø1 mm size should be possible. For the catheter shaft, a regular double-braided Ø1 mm (3F) could be used, while the output plunger should be minimized towards a sub-millimeter scale. The main issue in miniaturization is achieving a proper fluid seal and filling of the catheter without air bubble entrapment. Therefore, redesign of the plungers, in which they are incorporated in the catheter shaft, may be a necessity.

Integration in Clinical Practice

Based on the findings in the proof-of-principle experiment and future clinical application, a conceptual design, named *Wave* catheter (Figure 10.5), containing a Ø1 mm 3F double-braided radially stiff catheter shaft (L = 1 m) connected to a handle was designed. To allow for ergonomic handling and single-handed control the mechanisms are encompassed by a 3D-printed handle piece, which can be adjusted to the surgeon's preference. The handle contains an adjustable input impulse mechanism to set the preferred output peak force using a translating knob and a pistol-grip trigger mechanism to deliver the input impulse. An additional motor can be connected to the handle piece to allow for high-frequency pulsating inputs.

In the envisioned PCI "wave" procedure, the *Wave* catheter will be guided over a standard guidewire (Figure 10.6) towards the operation area. Once arrived at the CTO, the *Wave* catheter will be activated to puncture the proximal cap of the CTO. In order to prevent fragments from entering the blood stream we recommend to use an emboli filter proximal to the CTO at this stage. After angiographic confirmation that the proximal cap is fractured, a high stiffness guidewire is guided through the catheter and subsequently used to cross the CTO body. Finally, the *Wave* catheter is removed from the vasculature

and a balloon catheter can be slid over the guidewire towards the CTO to reopen the coronary artery.

Expansion of Application Areas

The simplicity and versatility of the *Wave* catheter makes it highly suitable for other medical applications as well, for example, to fragment, penetrate, or drill through other types of brittle materials or tissues, such as gall-, kidney-, bladder-, and liver-stones, bone, and (calcified) tumors.
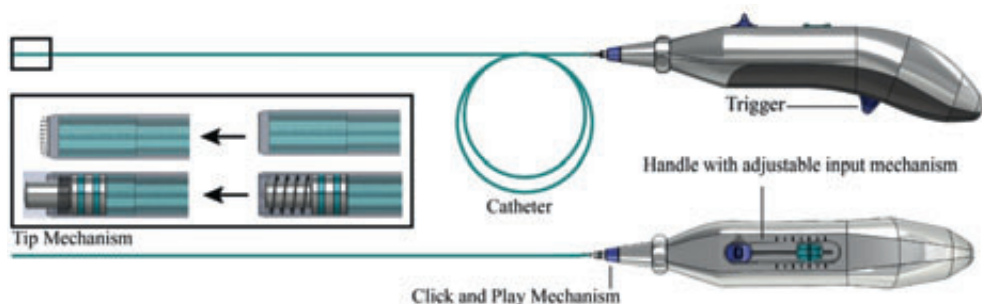

Figure 10.5— Conceptual Catheter Design. The *Wave* catheter consists of handle that allows for actively adjusting the input impulse and characteristic, as well as triggering the mechanism. A click-and-play mechanism is used to connect a pre-filled catheter shaft to the handle. The catheter tip shape can be altered based on the application; from blunt to sharp. Furthermore, the effect of an integrated or free-moving piston will be researched.
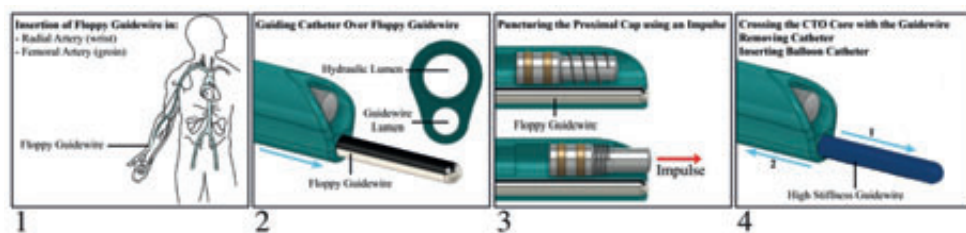

Figure 10.6— Envisioned PCI Procedure with the *Wave* catheter. (1) A floppy guidewire is inserted into the vasculature via the radial artery (wrist) or femoral artery (groin) and guided towards the CTO. (2) Once arrived at the CTO, the hydraulic pressure wave catheter is guided over the floppy guidewire. (3) The *Wave* catheter punctures the proximal cap of the CTO. (4) Once, the proximal cap is punctured, the floppy guidewire is retracted and a high stiffness guidewires is guided towards the CTO. Subsequently, the high stiffness guidewire is used to cross the CTO. Finally, the *Wave* catheter is removed and a balloon-stent catheter is guided over the guidewire to reopen the artery.

10.4. CONCLUSIONS

The proposed system has proven to transfer high-force impulses up to 43 N (1.5 N required) through a highly curved shaft with high efficiency, allowing for high force delivery onto the CTO, independent from the shaft shape and under any tip angle. Different catheter types only minimally affected the efficiency, with a decrease of approximately 13% for a more flexible shaft, allowing the surgeon to choose the most suitable catheter type for the application. In future the catheter will be further developed into a smaller, Ø1 mm, handheld device that allows for single-handed control and easy adjusting of the output peak force. The hydraulic pressure wave catheter may pave the way towards a more widespread adoption of PCIs of CTOs for even the less experienced interventionists by allowing for easy puncture of the most heavily calcified CTOs in the most distal and difficult to reach areas.

10.5. METHODS

10.5.1. Mechanical Feasibility

Experimental Goal
The main goal of the experiment was twofold: (1) evaluate the performance of the hydraulic pressure wave catheter in terms of delivered peak force and (2) determine the feasibility of using the hydraulic pressure wave catheter for crossing CTOs. For this purpose, an experimental facility was developed.

Research Variables
   Dependent Variables
1. **Output peak force (F_{output}).** In order to determine the feasibility of using a hydraulic pressure wave to puncture a CTO, the output peak force F_{output} was measured. In order to puncture a CTO, the output peak force should be at least 1.5 N according to a study of Thind *et al.* [6].
2. **Pressure wave velocity (v).** The velocity of the hydraulic pressure wave was calculated to test two assumptions: (1) decreased catheter elasticity increases the velocity (Korteweg *et al.* [19]) and (2) the magnitude of the pressure wave, or in other words, the input impulse, does not affect the velocity (Marey *et al.* [20]). In order to determine the velocity of the hydraulic pressure wave, the time between the input (F_{input}) and output peak force F_{output} was measured.

   Independent Variables
1. **Input peak force (F_{input}).** Together with F_{output}, the input peak force F_{input} was measured and altered to determine the peak force efficiency η of the *Wave* catheter.

10

Three input peak forces were set: 8 N, 13 N, and 20 N. The associated input impulses were approximately 0.025, 0.0375, and 0.050 Ns, respectively. The time interval of the input impulse was approximately 0.3 ms.

2. **Catheter curvature [diameter and angle].** In order to reach the CTO in the Right Coronary Artery (RCA) [21] or Superficial Femoral Artery (SFA) [22], it is necessary to cross several intersections and curves in the vascular system. In order to determine the effect of curvature on energy losses, and in turn the output peak force, different curvatures have been tested.

   The geometry, in terms of radius, angle, and diameter, of endovascular routes to reach the RCA or SFA has been analyzed in Appendix 10.B. All curves were modeled as circles. The curve radii of these stylized single-radius curves ranged between 20 mm in the aortic arch and 100 mm in the Common Femoral Artery (CFA). Based on this analysis, a curve radius of 25 mm was selected, which is close to the minimum radius encountered in the endovascular approaches. When adding the encountered curves and their curve angles from incision point to occlusion site, the accumulated curve angle may be as high as 1080°. Therefore, it was chosen to loop the catheter 3 times; 3x360° or 1080°, in order to simulate an extremely tortuous environment.

3. **Catheter type.** Catheters come in different shapes, sizes (most commonly between Ø0.6–3.0 mm), constructions, and materials. Depending on the type of intervention, the stage of the intervention, and the interventionist's preference, different catheters are used; from very stiff ones that provide support during the procedure, to floppy ones allowing for atraumatic navigating through the vasculature. The support catheters usually consist of several braided structures encased in a polymer, whereas the floppy catheters are usually made out of a single polymer [23]. During PCI of CTOs, floppy catheters are not used; instead support catheters are used to provide additional strength to the guidewire. In order to determine the effect of catheter morphology, and thus stiffness, on its ability to transfer and confine the hydraulic pressure wave through the catheter, we used two different 6F (Ø2 mm, L = 1 m) cardiac support catheters of varying stiffness: the more elastic single-braided *Mach1 6F CLS4* guide catheter (Boston Scientific, Marlborough, MA) and the stiffer double-braided *Impulse 6F AL3* angiographic catheter (Boston Scientific, Marlborough, MA).

4. **Output plunger travel distance (d).** This parameter describes the travel distance of the output plunger before it hits the CTO. The main reason this parameter was included was to test the difference in efficiency and impact peak force between an "in-contact" situation (d= 0 mm) and a "no-contact" situation (d = 2 mm or d = 4 mm) as in the clinical situation it might be challenging to determine whether the device is in direct contact with the CTO.

10

Experimental Facility

The experimental facility is illustrated in Figures 10.7 and 10.8. The input impulse was generated by a compression spring (Ø8.63 mm, spring constant k = 0.37 N/mm) vertically suspended in a construction rail using 2 L-shaped brackets. The input impulse was altered by manually varying the spring compression distance from 10, 15, to 25 mm, and validating these settings using an input load cell (*LSB210, QSH00519*, FUTEK Advanced Sensor Technology Inc., Irvine, CA) connected to the load mechanism, resulting in an input peak force of 8, 13, and 20 N. For data acquisition and analysis, an analogue signal conditioner (*CPJ RAIL*, SCAIME, Annemasse, France) and a data acquisition system (*NI USB-6211*, National Instruments Corporation, Austin, TX) with a sampling rate set to 50 kHz were connected to the input load cell. The input load cell was controlled through *LabVIEW 2014* (National Instruments Corporation, Austin, TX).

The input impulse was delivered upon a stainless steel input plunger (Ø2 mm shaft, Ø5 mm cap), placed within an input cylinder. This input plunger converts and transfers the generated impulse of the mass-spring system into translational momentum of a column of saline fluid of 9g salt/L inside the catheter. The tight fit between the input plunger and the input cylinder strongly reduced fluid leakage. The input cylinder was connected to the aluminum connection block, which was vertically suspended in the 25 mm connection rail.

In order to confine the fluid, the two 6F cardiac catheters were used as previously discussed. Each catheter was attached to the input cylinder using an epoxy resin and guided along a breadboard (*MB3090/M*, Thorlabs Inc., Newton, NJ; Figs. 7 and 8). It was chosen not to confine the catheter entirely along its length to closely resemble the clinical situations in which the catheter is also able to move inside the vasculature.

The output of the catheter consisted of an output plunger with cylinder (identical to the input plunger with cylinder) fitted in an aluminum connection block connected to a second connection rail (identical to the input). The output peak force was measured using an output load cell (*LSB200, FSH00103*, FUTEK Advanced Sensor Technology Inc., Irvine, CA), connected to an analogue signal conditioner (*CPJ RAIL*, SCAIME, Annemasse, France) and a data acquisition system (*NI USB-6211*, National Instruments Corporation, Austin, TX) with a sampling rate set to 50 kHz, and controlled through *LabVIEW 2014* (National Instruments Corporation, Austin, TX). The output load cell was placed into direct contact with, or slightly above to test the effect of the plunger travel distance d, the output plunger using a right-angle bracket connected to the connection rail.

Experimental Protocol

At the start of the experiment, a validation test was executed in order to verify that the catheter shaft itself did not transfer the impulse. Subsequently, the catheter was filled with

saline by removing both plungers and injecting saline into the lumen using a syringe until the catheter was fully filled and saline started to spill from the distal end.

The output peak force was measured for all measurements defined by the four independent variables (3 input peak forces, 2 curvatures, 2 catheter types, and 3 output plunger travel distances). The output peak force was derived from the load cell data. The effect of the input impulse and the associated peak force value on the peak force efficiency was measured in the straight configuration for the *Impulse 6F AL3* angiographic catheter (Boston Scientific, Marlborough, MA) with the output plunger in direct contact with the output load cell. The effect of the curvature was measured for an input peak force of 20 N, the output plunger in direct contact with the output load cell, and the *Impulse 6F AL3* angiographic catheter. The effect of the catheter types was measured using an input peak force of 20 N with both catheters in the straight configuration with the output plunger in direct contact with the output load cell. Finally, the effect of the output plunger travel distance was measured for the *Impulse 6F AL3* angiographic catheter in the straight configuration with an input peak force of 20 N. The velocity of the
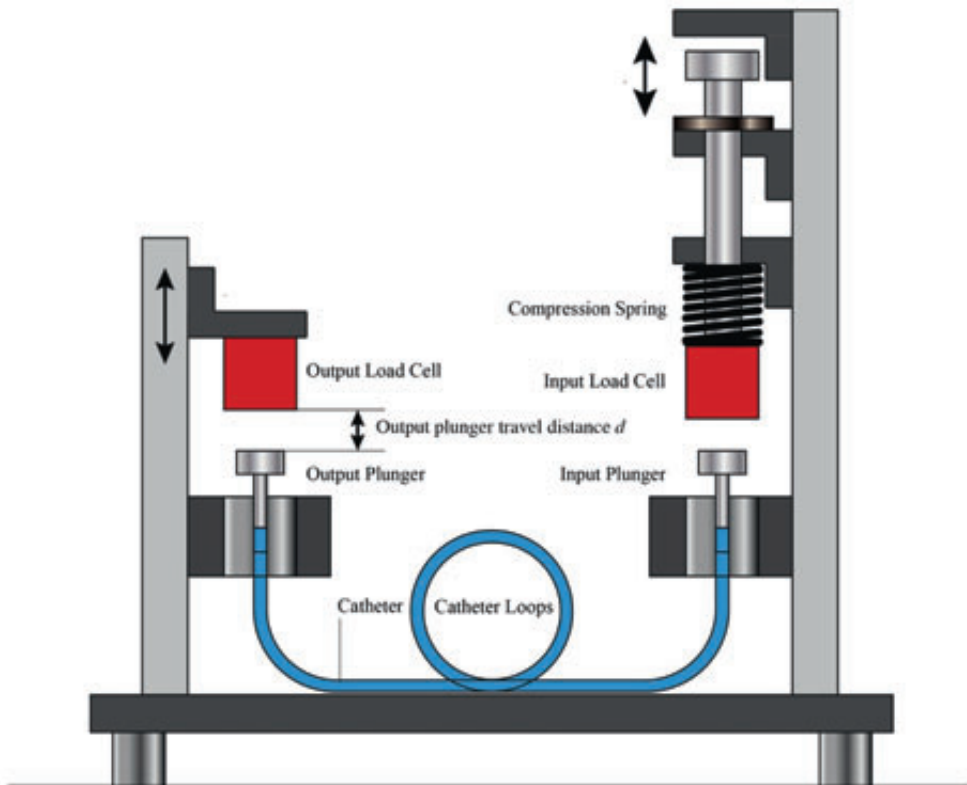
Figure 10.7— Schematic Representation of the Measurement Facility and the Research Variables. For explanation see text.
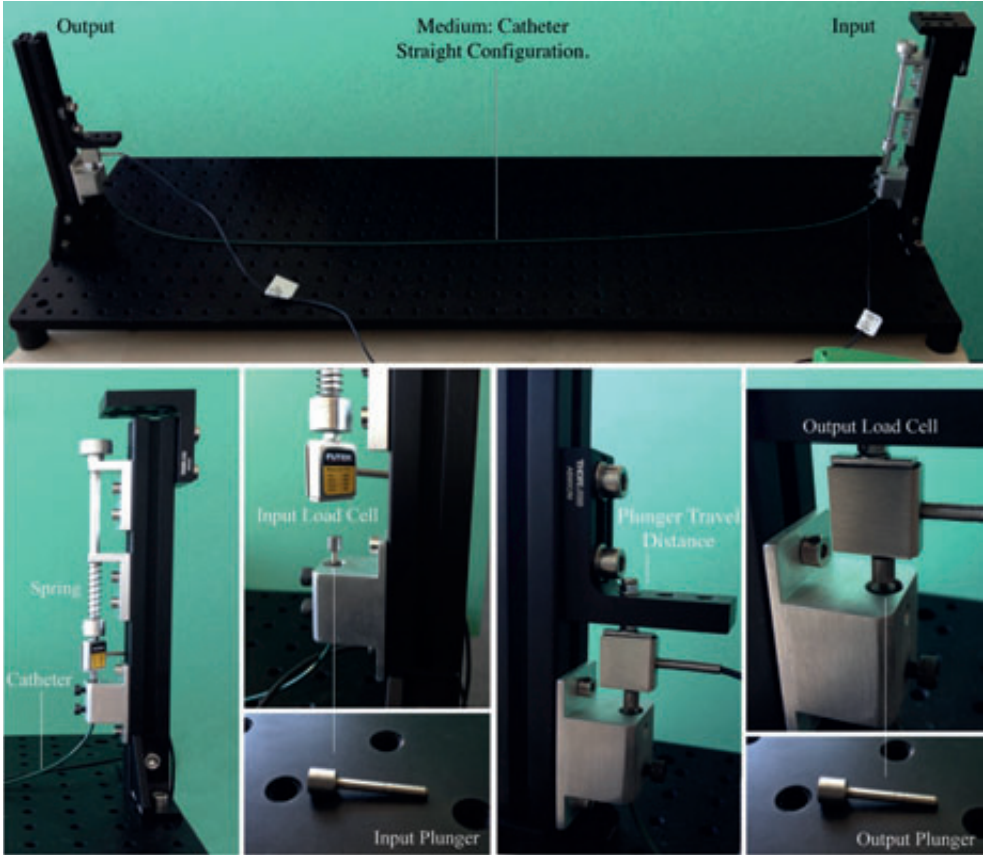
Figure 10.8— Final Measurement Facility. For explanation see text.

pressure wave was measured for the 3 input impulses, 2 curvatures, and 2 catheter types, similarly as described for the output impulse.

A Power analysis was conducted to calculate the required minimum number of repetitions to detect an effect of the independent variables on the efficiency of the system. The required number of repetitions was calculated using G*Power software [24] to be a minimum of 15 repetitions using a significance level p of 0.05 and an effect size of 0.4. We decided to test each condition 17 times to minimize the effect of outliers; resulting in a total of 612 tests.

Data Analysis

Per test, the data from the load cells were processed with *MATLAB 2015b* (The Mathworks, Inc., Natick, MA) to identify the input peak force and output peak force for each measurement. Per condition, the mean input peak force and mean output peak force, with their accompanying standard deviations, were determined across the 17 repetitions. Furthermore, per condition the peak force efficiency η was calculated. The velocity of the pressure wave was derived using the time interval between peak 2 and peak 3 (Figure 10.3). The distance over which the pressure wave travelled was known since the two catheters used were cut to a length of 1 m; allowing us to calculate the velocity from the plotted data.

10.5.2. Clinical Validity

In order to evaluate the clinical validity of the hydraulic pressure wave catheter, an artificial CTO model was built. In this model, calcium sulfate (CaS) was used to mimic the calcium content of the CTO and gelatin, the product of degradation of collagen, to mimic the collagen content of the CTO. The model consisted of a proximal cap, representing the hardest, most calcified region, placed on top of a core model, surrounded by an environmental model (Figure 10.9). The proximal cap model consisted of 55 wt% CaS powder and 45 wt% liquid gelatin mixture, which represented the mean value of the failed PCI of CTO procedures in a study of Cho *et al.* [25]. The models had a diameter of Ø5 mm and were approximately 0.5 mm of thick; equal to the mean CTO proximal cap thickness [26]. The core of the CTO was mimicked using a mixture of 35 wt% CaS and 65 wt% gelatin, representing the overall average percentage of calcium in CTOs found in the study of Cho *et al.* [25]. The core model had a diameter of Ø5 mm and length of 20 mm, which equals the cut-off value above which PCI of CTOs becomes progressively difficult [18]. The environment model consisted of 25 wt% gelatin and 75 wt% water,
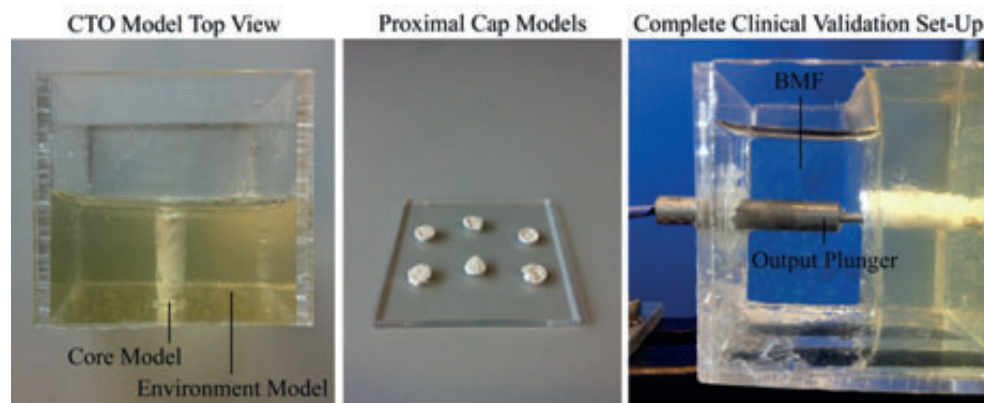
10

CTO Model Top View | Proximal Cap Models | Complete Clinical Validation Set-Up
BMF
Output Plunger
Core Model
Environment Model

Figure 10.9— Clinical Validity Experimental Facility. The experimental facility consisted of a rectangular box in which the CTO model was submerged in Blood-Mimicking Fluid (BMF). The CTO model consisted of a proximal cap model (Ø5 mm, 0.5 mm thick), core model (Ø5 mm, 20 mm long), and environment model.

which results in an estimated Young's modulus between 100 kPa and 130 kPa, resembling the Young's modulus of cardiac muscle tissue [27]. Finally, the model was submerged into Blood Mimicking Fluid (BMF) to mimic the viscosity of the blood in the coronary arteries, which is in between 2.8 and 3.8 mPas. The BMF was made out of 30 wt% glycerine and 70 wt% clear water of 20°C, resulting in a viscosity of approximately 3.0 mPas [28].

Each model was tested 5 times. The input peak force was set to 36 N and the indenter was placed in direct contact with the plunger. The number of punctures was evaluated by eye. In order to resemble the clinical situation more closely the catheter was allowed to translate freely.

In order to determine the required force to penetrate the CTO model, a small control experiment was performed. In this control experiment, a static force of approximately 1.2 ± 0.4 N (*n* = 8) was needed to puncture the cap with a Ø2 mm stainless steel rod. This value is similar to the value found in the study of Thind *et al.* [6].

ACKNOWLEDGEMENTS

10

REFERENCES

[1]   Iribarne A, Easterwood R, Chan EY, Yang J, Soni L, et al. The golden age of minimally invasive cardiothoracic surgery: current and future perspectives. Future cardiology. 2011; 7(3): pp. 333-346.

[2]   Stone GW., Reifart NJ, Moussa I, Hoye A, Cox DA, Colombo A, et al. Percutaneous recanalization of chronically occluded coronary arteries. A consensus document - Part I. Circulation. 2005; 112(15): pp. 2364-2372.

[3]   Stone GW, Reifart NJ, Moussa I, Hoye A, Cox DA, Colombo A et al. Percutaneous recanalization of chronically occluded coronary arteries - A consensus document - Part II. Circulation. 2005;112(16): pp. 2530-2537.

[4]   Galassi A, Tomasello S, Reifart N, Werner GS, Sianos G, Bonnier H et al. In-hospital outcomes of percutaneous coronary intervention in patients with chronic total occlusion: insights from

the ERCTO (European Registry of Chronic Total Occlusion) registry. EuroIntervention. 2011;7(4): pp. 472-479.

[5]   Kinoshita I, Katoh O, Nariyama J, Otsuji S, Tateyama H, Kobayashi T, et al. Coronary angioplasty of chronic total occlusions with bridging collateral vessels: immediate and follow-up outcome from a large single-center experience. Journal of the American College of Cardiology. 1995;26(2): pp. 409-415.

[6]   Thind A, Strauss B, Teitelbaum A, Karshafian R, Ladouceur M, Whyne C, et al. A novel method for the measurement of proximal fibrous cap puncture force in chronic total occlusions: the effect of increasing age. EuroIntervention. 2011;6(8): pp. 997-1002.

[7]   Sakes A, Regar E, Dankelman J, and Breedveld P. Crossing Total Occlusions: Navigating Towards Recanalization. Cardiovascular Engineering and Technology. 2016; 7(2): pp. 103-117.

[8]   Euler L. Principes généraux de l'état d'équilibre d'un fluide Académie Royale des Sciences et des Belles-Lettres de Berlin, Mémoires. 1757;11: pp. 217-273.

[9]   Sakes A, Dodou D, and Breedveld P. Buckling prevention strategies in nature as inspiration for improving percutaneous instruments: a review. Bioinspiration & Biomimetics. 2016; 11(2): pp. 021001.

[10]   Lock M. A study of buckling and snapping under dynamic load. El Segundo, CA: Laboratory Operations Aerospace Corporation. Report Number TR-0158 (3240-30)-3; 1967. pp. 1-55.

[11]   Heverly M, Dupont P and Triedman J. Trajectory optimization for dynamic needle insertion. Proceedings of the 2005 IEEE International Conference on Robotics and Automation held at Barcelona, Spain, 18-22 April 2005. pp 1646-1651.

[12]   Jelínek F, Smit G and Breedveld P. Bioinspired spring-loaded biopsy harvester—experimental prototype design and feasibility tests. Journal of Medical Devices ;8(1); pp. 015002-1-001502-6.

[13]   Adams JM, Hawkins D, and Alferness CA, inventors; Hawkins D, Alferness CA, and Adams JM, assignees. Shockwave balloon catheter system. United States Patent 2011/0166570 A1. 2011.

[14]   Hawkins D and Adams JM, inventors. Drug delivery shockwave balloon catheter system. United States Patent 2010/0114065 A1. 2010.

[15]   Hawkins D and Adams JM, inventors. Shockwave valvuloplasty catheter system. United States Patent 2015/0238209 A1. 2015.

[16]   Sakes A, van der Wiel M, Dodou D, and Breedveld P. Endovascular Crossing of Chronic Total Occlusions Using an Impulse: An Explorative Design Study. Cardiovascular Engineering and Technology. 2017; 8(2): pp. 145-163.

[17]   Walker C. Guidewire selection for peripheral vascular interventions. Endovascular Today. 2013; 5: pp. 80-83.

[18]   Sianos G, Werner GS, Galassi A, Papafaklis MI, Escaned J, Hildick-Smith D et al. Recanalisation of Chronic Total coronary Occlusions: 2012 consensus document from the EuroCTO club. EuroIntervention. 2012;8(1): pp. 139-145.

[19]   Korteweg D. Ueber die Fortpflanzungsgeschwindigkeit des Schalles in elastischen Röhren. Annalen der Physik. 1878; 241(12): pp. 525-542.

[20]   Marey M. Mouvement des Ondes Liquides pour Servir a la Théorie du Pouls. Travaux du Laboratoire de M. Marey. 1875.

[21]   Stone GW, Colombo A, Teirstein PS, Moses JW, Leon MB, Reifart NJ et al. Percutaneous Recanalization of Chronically Occluded Coronary Arteries: Procedural Techniques, Devices, and Results. Catheterization and Cardiovascular Interventions. 2005;66: pp. 217-236.

10

[22]   Nadal LL, Cynamon J, Lipsitz EC, and Bolia A. Subintimal angioplasty for chronic arterial occlusions. Techniques in vascular and interventional radiology. 2004; 7(1): pp. 16-22.

[23]   Stenqvist O, Curelau I, Linder LE, Gustavsson B. Stiffness of central venous catheters. Acta Anaesth Scand 1983; 27(2); 153-157.

[24]   Faul F, Erdfelder E, Buchner A, and Lang AG. Statistical power analyses using G* Power 3.1: Tests for correlation and regression analyses. Behavior research methods. 2009; 41(4): pp. 1149-1160.

[25]   Cho JR, Kim YJ, Ahn CM, Moon JY, Kim JS, Kim HS, et al. Quantification of regional calcium burden in chronic total occlusion by 64-slice multi-detector computed tomography and procedural outcomes of percutaneous coronary intervention. International Journal of Cardiology. 2009;145(1): pp. 9-14.

[26]   Barrett S, Sutcliffe M, Howarth S, Li ZY, and Gillard J. Experimental measurement of the mechanical properties of carotid atherothrombotic plaque fibrous cap. Journal of Biomechanics. 2009;42(11): pp. 1650-1655.

[27]   Houwink R and De Decker HK. Elasticity, plasticity and structure of matter. Cambridge, UK: Cambridge University Press, 1971.

[28]   Cheng NS. Formula for the viscosity of a glycerol-water mixture. Industrial & Engineering Chemistry Research. 2008;47(9): pp. 3285-3288.

10

APPENDIX 10.A: THE HYDRAULIC PRESSURE WAVE

10.A1. What is a Hydraulic Pressure Wave?

In order to understand the mechanics of a periodic longitudinal pressure wave, we consider a long tube filled with a fluid and two plungers at each end, as in Figure 10.A1. If we push the input plunger in, we compress the fluid near plunger; increasing the pressure in this region. This region then pushes against the neighboring region of fluid, and so on, resulting in a wave pulse that moves along the tube until it reaches the output plunger. The output plunger is accelerated by the wave and can exert an impulse on the environment.

Now we suppose we move the input plunger back and forth along a line parallel to the main axis of the tube with simple harmonic motion. This motion forms regions in the fluid where the pressure and density are greater or less than the equilibrium values. We call a region of increased density a "compression" and a region of reduced density a "rarefaction". The compressions and rarefactions move towards the output plunger with constant velocity *v*.

For a mathematical description of the wave, a so-called wave function is required that describes the position of a fluid particle in the medium at any time (see Equation 10.A1). The displacement of such a particle *y* is a function of the position *x* and the point in time *t*.

$$y(x,t) = A\cos\left[\omega\left(\frac{x}{v} - t\right)\right] = A\cos 2\pi f\left(\frac{x}{v} - t\right) \qquad (10.A1)$$
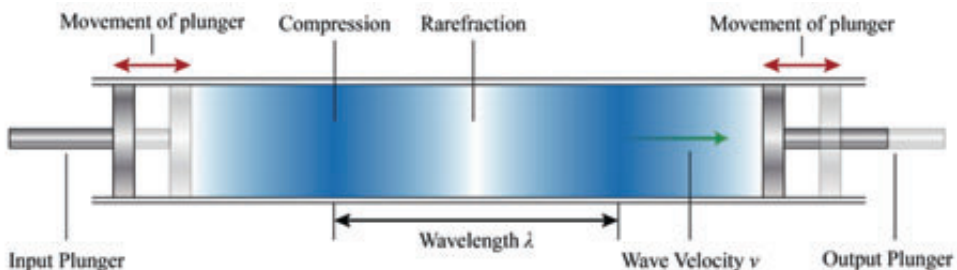
10

Figure 10.A1— A Longitudinal Hydraulic Pressure Wave travelling to the Right. First, we move the input plunger to the right, which compresses the fluid near the plunger. The compressed region subsequently pushes against the neighboring region, and so on, resulting in a pressure wave that travels from the input to the output plunger. Once arrived at the distal end, the pressure wave pushes against the output plunger, which subsequently starts to accelerate. Note also that if we pull the input plunger back also rarefactions (low pressure regions) can be generated.

313

with A = the amplitude [m], ω = the angular frequency ($2\pi f$) [rad/s], x = is the position along this axis [m], v = the wave velocity, t = the point in time [s], and f = frequency [Hz].

10.A.2. Transfer of the hydraulic pressure wave

Velocity of the Hydraulic Pressure Wave

On what properties of the medium does the velocity depend? A pressure wave causes compressions and rarefaction in the fluid, so the velocity is related to how easy or difficult it is to compress the fluid. This value is represented by the bulk modulus K [N/m] of the fluid. On the other hand, inertia, which is related to mass and thus its density ρ [kg/m], resists the return to the equilibrium state. Thus the velocity of the unconfined pressure wave can be described as:

$$v = \sqrt{\frac{K}{\rho}} \tag{10.A2}$$

The velocity of a hydraulic pressure wave confined in an elastic pipe is different, usually much lower, from that in unconfined water. This difference was first described by Frizell and can be deducted from Equation 10.A3, in which the velocity of the hydraulic pressure wave (v [m/s]) in a thin-walled cylindrical pipe is calculated [2]. From Equation 11.A3 it can be seen that the wave velocity v can be increased by increasing ρ and K of the fluid or E and e of the shaft. When the Young's modulus E of the shaft becomes large, which is the case in a perfectly rigid shaft, the wave velocity would approach that of an unconfined pressure wave. Furthermore, it can be seen that within this linearized model the amplitude (or magnitude) of the pressure wave does not affect the wave velocity (see also Marey *et al.* [4] on this topic).

$$v = \sqrt{\frac{1}{\rho(\frac{1}{K}+\frac{D}{Ee})}} \tag{10.A3}$$

with ρ = density of fluid [kg/m], K = bulk modulus of fluid [Pa], D = diameter of pipe [m], E = Young's modulus of the shaft [Pa], e = wall thickness of the shaft [m].

The effect of pipe wall elasticity on the wave velocity can be explained by fluid-structure interaction, in which the propagating pressure wave interacts with the elastic and deformable catheter shaft. In general, three interaction mechanisms can be distinguished: shear stresses between the fluid and shaft, the axial compression of the shaft by radial deformation during pressure surges (called Poisson coupling), and

movement of shaft generated by an imbalance of forces in curves. Shear stresses between the fluid and shaft are dependent on the dynamic viscosity and velocity of the fluid at the boundary. At the boundary, the velocity of the fluid particles is almost zero, also known as the no-slip condition, so the most determining factors are the dynamic viscosity of the fluid, which is approximately 1.0 mPas at 20 °C. Axial compression of the shaft is caused by radial extension of the catheter shaft that results from the passing pressure wave. Increased elasticity increases the radial extension and thus decreases wave velocity as it partly absorbs the volume displaces by the pressure wave. Movement of the catheter shaft also decreases the amplitude of the wave as it partly takes the momentum of the pressure wave.

With Equations 10.A1 and 10.A3 we can make a prediction on the wave velocity of the hydraulically actuated catheter using a density ρ of 999 kg/m (water), a bulk modulus K of 2.19·10^9 Pa, diameter D of 2 mm, and wall thickness e of 0.2 mm. The effect of the Young's modulus E on the wave velocity v is plotted in Figure 10.A2. The plotted line approaches a horizontal asymptote, which represents the wave velocity through a perfectly rigid shaft. As the Young's moduli of the single- and double-braided catheter are unknown, an estimation is made based on the volume ratio and Young's moduli of the PolyTetraFluoroEthylene (PTFE or Teflon; $E = 0.4$ GPa and $V = 98\%$) liner and stainless steel braiding ($E = 180$ Gpa and $V = 2\%$) 6. Using Equation 10.A1, a wave velocity of 580 m/s is estimated.

Energy Losses of the Hydraulic Pressure Wave
In the proposed system a pressure wave travels from the handle to the tip. Between the input and the output the pressure wave can decrease in pressure, and thus energy, as the result of:

1. Friction between the fluid and the surface of the wall, also known as friction coupling;
2. Pressure loss due to elasticity of the shaft walls;
3. Partial reflection losses in bends, valves and tees, also known as junction coupling, and
4. Mechanical friction losses in junction couplings.

In conventional pipe flow, friction between the fluid and catheter shaft surface can be mainly attributed to the surface roughness of the inner surface (see Figure 10.A3). This can be explained by the no-slip boundary condition that states that the velocity at the fluid–solid boundary is equal to that of the solid boundary. At the fluid-solid boundary, the adhesive forces between the fluidic and solid particles are larger than the cohesive

10

forces within the fluid, which brings the fluid velocity to zero at the boundary. This effect is amplified by an increase of surface roughness on a molecular level. Especially in the case of a small diameter tube, the boundary layer is relatively large.

Unfortunately, the effects of friction on propagating pressure waves are not that well described. Therefore, the effect of pressure loss due to friction between the fluid and the surface of the wall was simulated using COMSOL. When this friction effect was turned off the pressure wave did not dissipate over time and traveled back and forth along the pipe. This demonstrates no other pressure loss effects are included in the model and the wave is perfectly reflected. The loss in pressure over time showed a logarithmic decay when friction was included using the Churchill friction model [7] (see Figure 10.A4). The exponential decay illustrates that the friction effect depends on the magnitude of the pressure wave. A higher magnitude pressure wave dissipates faster due to surface roughness than a lower magnitude pressure wave.

Energy losses can also be caused by partial deflection and friction in abrupt bends, valves, and tees, as well as by catheter wall elasticity. As there is little information available on energy losses due to these effects, it was decided to perform the feasibility experiment. The feasibility experiment is described in detail in the main manuscript.
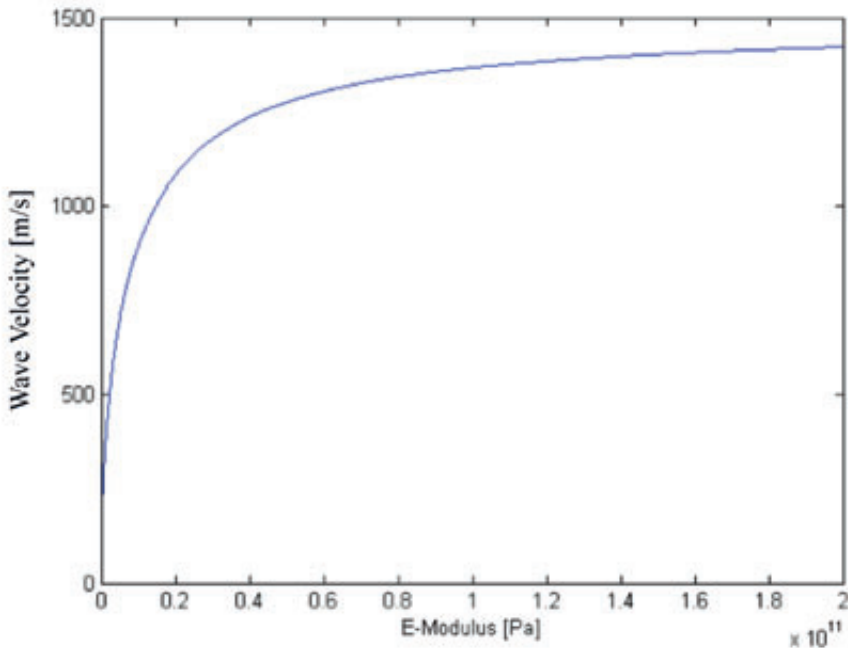
10

Figure 10.A2— Wave Velocity versus the Young's Modulus of the Shaft. The graph illustrates that a slight change in the Young's modulus of the shaft has a large effect on the velocity as the slope of the graph is high in the 0 – 20 GPa range.
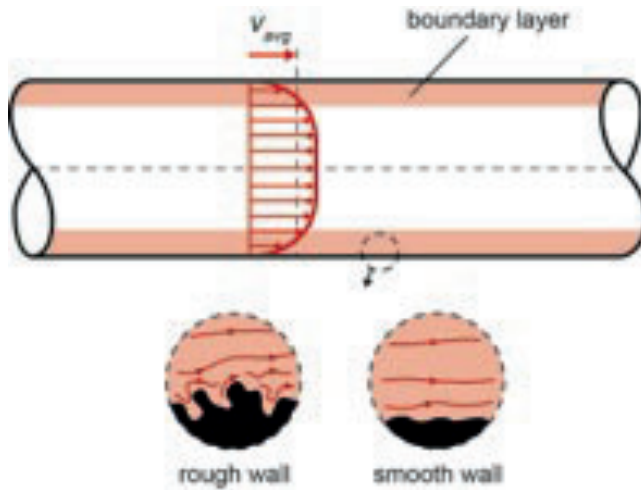
Figure 10.A3— Pressure Loss Effect due to Surface Roughness. No-slip behavior at the boundary layer results in a decreased average velocity (v_{avg}) and pressure losses.
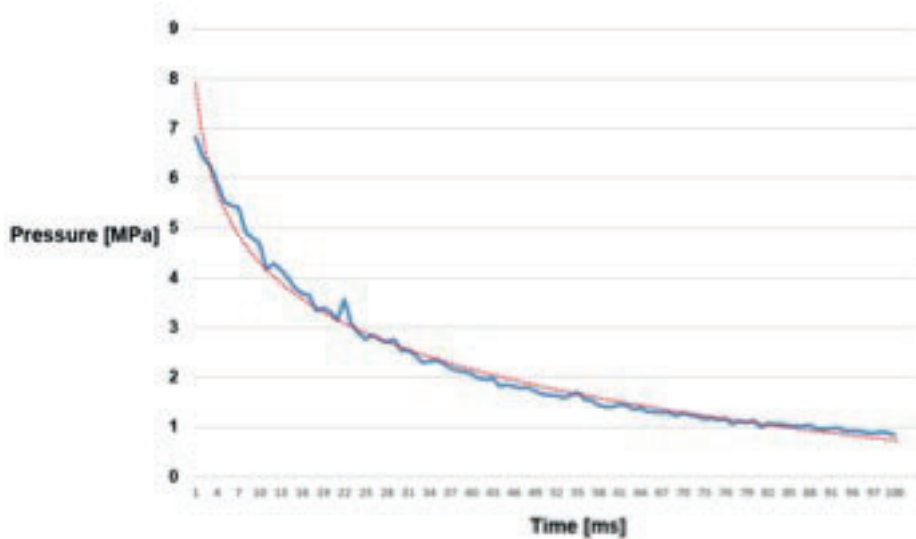

Figure 10.A4— COMSOL Simulation showing the Pressure Drop over Time in an Elastic Pipe as a Result of Surface Roughness (Blue Line). A logarithmic trend line provides an approximation of the simulation (red line). Formula of the trendline: $y = -1.552*\ln(x)+7.8797$.

10.A3. Wave Reflection and Transmission

Reflection coefficient

When a pressure wave approaches a boundary, such as a dead end in the system, the wave is reflected. The reflection coefficient describes the ratio between the incident wave (the pressure wave before reflection) and the reflected wave (see Equation 10.A4). In case of a dead end, the reflected pressure wave has the same sign and same magnitude as that of the incident wave ($r = 1$) [3]. In the hydraulic system of the proposed concept, a moving piston is present, which represents an active dead end. Therefore, the reflected pressure wave has the same sign as the incident wave but a significantly decreased magnitude. In the ideal situation, the reflected pressure wave would be zero. The movement and properties of the piston, the friction of the seal and the contact of the piston with a material determine the magnitude of the reflected wave in case of the proposed concept.

$$r = \frac{wave_{reflected}}{wave_{incident}} \tag{10.A4}$$

Series junction

In a junction, a pressure wave can get reflected and/or transmitted. A series junction represents the transition of two pipes with different diameters, wall thicknesses, and/or friction factors. When a pressure wave approaches a series junction, the pressure wave is partly reflected back into the same pipe and partly transmitted further down the pipe. For a series junction a specific reflection coefficient (*r;* see Equation 10.A5) and transmission coefficient (*s;* see Equation 10.A6) exists.

$$r = \frac{wave_{reflected}}{wave_{incident}} = \frac{\frac{A_1}{v_1} - \frac{A_2}{v_2}}{\frac{A_1}{v_1} + \frac{A_2}{v_2}} \tag{10.A5}$$

$$s = \frac{wave_{transmitted}}{wave_{incident}} = \frac{\frac{2A_1}{v_1}}{\frac{A_1}{v_1} + \frac{A_2}{v_2}} \tag{10.A6}$$

Where A = cross-sectional area of pipe 1 or 2 [mm] and v = wave velocity of pipe 1 and 2 [m/s].

10.A4. References

[1]   Frizell J. Pressures resulting from changes of velocity of water in pipes. Proceedings of the American Society of Civil Engineers. 1898; 23(6): pp. 414-421.

[2]   Korteweg D. Ueber die Fortpflanzungsgeschwindigkeit des Schalles in elastischen Röhren. Annalen der Physik. 1878; 241(12): pp. 525-542.

[3]   Chaudhry MH. Applied hydraulic transients (3rd ed.). New York, NJ: Springer, 1979.

[4]   Marey M. Mouvement des Ondes Liquides pour Servir a la Théorie du Pouls. Travaux du Laboratoire de M. Marey. 1875.

[5]   Tijsseling A. Fluid-structure interaction in liquid-filled pipe systems: a review. Journal of Fluids and Structures. 1996; 10(2): pp. 109-146.

[6]   The Engineering Toolbox. Modulus of elasticity or Young's modulus - and tensile modulus for common materials. Available from: http://www.engineeringtoolbox.com/young-modulus-d_417.html.

[7]   Churchill WS. Friction-factor equations spans all fluid-flow regimes. Chemical Engineering. 1977; 7: pp. 91-92.

10

APPENDIX 10.B: ARTERY MODELING

This appendix provides a detailed description of the travel path through the human vascular system to reach the occlusion site. This information, together with geometrical details of the vascular system and calculations, was used to define the geometrical design requirements of the prototype.

10.B1. Endovascular Routes

The most prevalent location of a coronary CTO is the Right Coronary Artery (RCA) [8]. For the peripheral arteries, the Superficial Femoral Artery (SFA) is the most common location [9]. To approach the RCA and SFA, several endovascular routes can be taken. Two common approaches for each of the occlusion locations were selected for this analysis:

1.   RCA–Transfemoral approach
2.   RCA–Radial approach
3.   SFA–Ipsilateral antegrade approach
4.   SFA–Contralateral retrograde approach

Per approach, the vascular route is specified in detail in Table 10.B1 and illustrated in Figure 10.B1. In the case of a transfemoral approach, the vascular system is entered at the groin into the Common Femoral Artery (CFA). From here, the path travels upwards, towards the heart. For the radial approach, the vascular system is entered at the wrist into the Radial Artery (RA). In this approach, the path travels upwards through the arm and shoulder towards the heart. For both the ipsilateral antegrade and contralateral retrograde approaches, the vascular system is entered at the groin, either on the ipsilateral or the contralateral side of the body.

10.B.2. Artery Diameters, Curve Radii, and Bifurcation Angles

The geometry of the four described endovascular routes was analyzed in more detail. This analysis included the determination of the average artery diameters, curve radii of the arteries, and the artery bifurcation angles. The artery diameters of all arteries that are passed in one of the four approaches have been obtained from literature (see Table 10.B2). It can be seen that the diameters differ slightly between sources. Therefore, an average diameter (defined as the mean of the smallest and largest number given in Table 10.B2) was calculated. The curve radii and bifurcation angles have been estimated based on illustrations and data in [8-19], and are given in Tables 10.B3 and 10.B4, respectively.

10

The presented artery diameters, curve radii, and bifurcation angles that are encountered in the analyzed endovascular approaches have been used to model the routes in simplified nodes. These nodes represent the curves and bifurcations that need to be passed by the guidewire or crossing tool to reach the RCA or SFA. The annotations of the nodes, as well as the simplified illustrations of the nodes, are given in Figure 10.B2.

Table 10.B1— The detailed Arterial Paths of the Four Selected Endovascular Approaches.

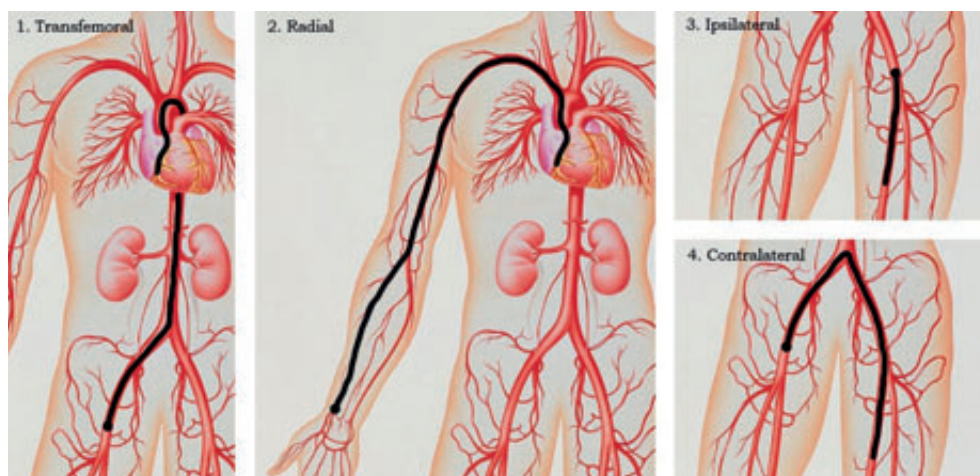| RCA–Transfemoral	RCA–Radial	SFA–Ipsilateral	SFA–Contralateral
Common femoral artery	Radial artery	Common femoral artery	Common femoral artery
External iliac artery	Brachial artery	Superficial femoral artery	External iliac artery
Common iliac artery	Axillary artery		Common iliac artery
Descending aorta	Subclavian artery		Common iliac artery
Aortic arch	Brachiocephalic artery		External iliac artery
Ascending aorta	Aortic arch		Common femoral artery
Right coronary artery	Ascending aorta		Superficial femoral artery
	Right coronary artery		

Figure 10.B1— The Arterial Routes of the Four Selected Endovascular Paths in the Body. (1) Right Coronary Artery (RCA)–Transfemoral approach, (2) RCA–Radial approach, (3) Superficial Femoral Artery (SFA)–Ipsilateral antegrade approach, and (4) SFA–Contralateral retrograde approach. Figures adapted from [11].

10

10.B3. Endovascular Instrument Flexibility

Based on the previously described analysis, a guideline for the maximum stiff part length (*L*) of the prototype to pass through the curves and bifurcations was derived (Figure 10.B3). To do that, the bifurcation was translated into a curvature with the help of Equations 10.B1–B3.

$$Y = D_{large} - \tfrac{1}{2}D_{small}\, , \qquad\qquad\qquad\text{(10.B1)}$$

$$X = \frac{cos\alpha \cdot Y}{1-cos\alpha}\, \text{, and} \qquad\qquad\qquad\text{(10.B2)}$$

$$R_{curve} = X + Y\, , \qquad\qquad\qquad\text{(10.B3)}$$

with α = bifurcation angle [°], D_{large} = diameter of the largest artery [m], D_{small} = diameter of the smallest artery [m], and R_{curve} = curve radius [m]. Equations 10.B4–B6 were subsequently used to derive the maximum stiff part length:

$$P = R_{curve} - R_{art} + \O_{instr}, \qquad\qquad\qquad\text{(10.B4)}$$

$$Q = R_{curve} + R_{art}\, \text{, and} \qquad\qquad\qquad\text{(10.B5)}$$

$$L = \sqrt{Q^2 - P^2}, \qquad\qquad\qquad\text{(10.B6)}$$

10

with *L* = rigid part length [m], R_{art} = radius of the smallest artery [m], and $\O_{instr}$ = instrument diameter [m]. For the calculations, an instrument diameter of 2 mm was used.

In Table 10.B5 the results of the calculations are presented. It can be seen that the bifurcation from the radial artery to the brachial artery and the curve in the RCA itself are the most restrictive nodes for reaching a lesion in the RCA, allowing for a maximum stiff part length (*L*) of only 6.9 mm. Reaching a CTO in the SFA is much less restrictive, with a minimum required stiff part length of 8.7 mm. Taking the estimated maximum stiff part lengths into account, and accounting for variability in artery diameter, curve radii, and bifurcation angles, the maximum stiff part length was set at 6.5 mm.

Table 10.B2— Diameters [mm] of the encountered arteries in the in the 4 previously described coronary and peripheral interventional approaches.

	Diameters from Avolio [10]	Diameters from Kahraman *et al.* [14]	Diameters from [12,13,15-19]	Mean Artery Diameter
Common iliac artery	10.4	9.1–10.4		**10.0**
External iliac artery	5.4–5.8	8.0		**6.4**
Common femoral artery			7.5 (*f*) [17] 10.4 (*m*) [17]	**8.9**
Superficial femoral artery	4.8			**4.8**
Aortic arch	21.4–22.4			**21.9**
Ascending aorta	29.0	32.6		**30.8**
Brachiocephalic artery	12.4			**12.4**
Subclavian artery	8.0			**8.0**
Axillary artery	6.2–7.2			**6.7**
Brachial artery	4.8–5.6			**5.2**
Radial artery	3.2		2.3 [12] 2.8 (*f*) [15,16] 3.1 (*m*) [15,16] 2.4 (*f*) [19] 2.7 (*m*) [19]	**2.8**
Descending aorta	19.0–20.0 (*t*) 11.4–17.4 (*a*)	28.9		**19.3**
Right coronary artery		2.2 (*d*) 2.9 (*p*)	1.9 (*d*) [13] 4.0 (*p*) [13]	**2.8**

Note. f = female, *m* = male, *d* = distal, *p* = proximal, *a* = abdominal, and *t* = thoracic

Table 10.B3— Estimated curve radii [mm] of the encountered blood vessels in the 4 previously described coronary and peripheral interventional approaches.

Approach	Artery	Curve radius [mm]
RCA–Transfemoral **SFA–Ipsilateral** **SFA–Contralateral**	Common femoral artery → External iliac artery → Common iliac artery	100
RCA–Transfemoral	Brachial artery → Axillary artery → Subclavian artery	60
RCA–Transfemoral **RCA–Radial**	Aortic arch	20
RCA–Transfemoral **RCA–Radial**	Right coronary artery	29

Note. RCA: Right Coronary Artery. SFA: Superficial Femoral Artery

10

Table 10.B4— Estimated curve angles [°] of the encountered nodes in the 4 previously described coronary and peripheral interventional approaches.

Approach	Node	Bifurcation Angle [°]
RCA–Radial	Radial artery to the Brachial artery	150
RCA–Radial	Brachiocephalic artery to the Aortic arch	90
RCA–Transfemoral **RCA–Radial**	Aortic arch to the Right coronary artery	90
SFA–Contralateral	Common iliac artery to contralateral Common iliac artery	90

Note. RCA: Right Coronary Artery. SFA: Superficial Femoral Artery
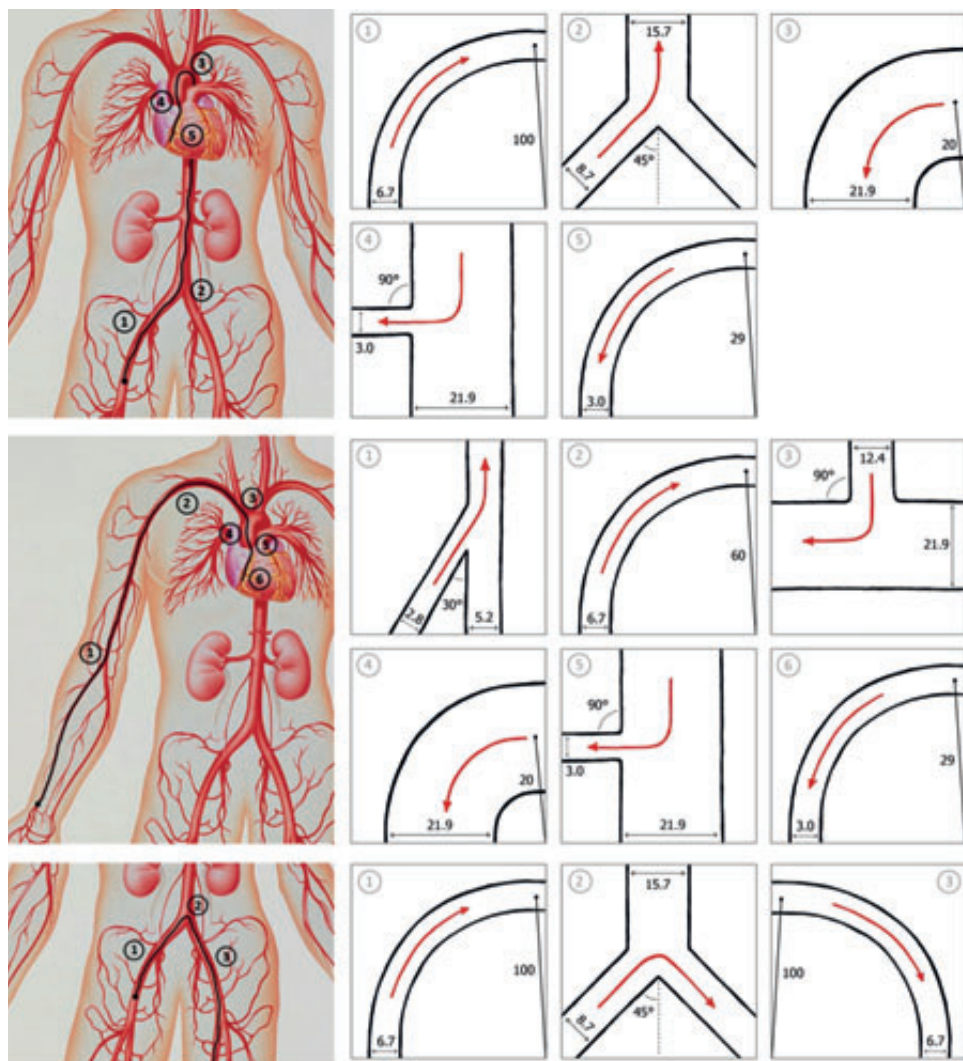
10

Figure 10.B2— Analysis of the vascular routes and corresponding nodes. Top row: The nodes for Right Coronary Artery (RCA)–Transfemoral approach: (1) Common femoral artery, external Illiac artery, and common iliac artery, (2) Common iliac artery to the descending aorta, (3) Aortic arch and ascending aorta, (4) Ascending aorta to right coronary artery, and (5) Right coronary artery. Middle row: the nodes for the RCA–Radial approach: (1) Radial artery to brachial artery, (2) Axillary artery and subclavian artery, (3) Subclavian artery to the brachiocephalic artery, (4) Aortic arch and ascending aorta, (5) Ascending aorta to right coronary artery, (6) Right coronary artery. Bottom row: the nodes for the Superficial Femoral Artery (SFA)–Contralateral retrograde approach: (1) Common femoral artery, external Illiac artery, and common iliac artery, (2) Common iliac artery to contralateral common iliac artery, (3) Common iliac artery, external iliac artery, and common femoral artery. The SFA–Ipsilateral antegrade approach to the SFA may be described as part of the contralateral retrograde approach. Figures adapted from [11].
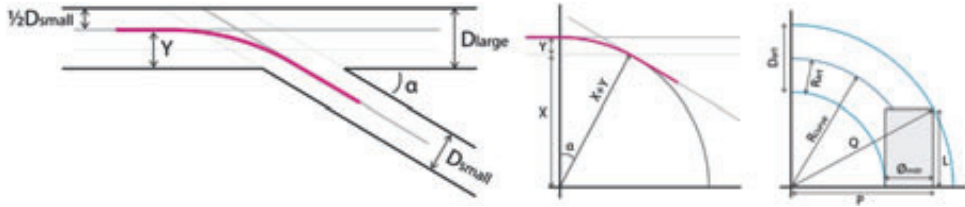
10

Figure 10.B3— Simplified drawings showing the formula derivation for calculating the maximum stiff part length of an endovascular instrument to travel through set curvatures and bifurcations. Top: Input variables of Equations. 11.B1–B3. Bottom Left: Derivation of Equations. 11.B1–B3. Bottom Right: Inputs and derivation of Equations. 11.B4–B6.

Table 10.B5. Calculation results for the maximum rigid part length [mm] of the instrument tip for all of the modeled nodes illustrated in Figure B2.

RCA – Transfemoral		RCA – Radial		SFA – Ipsilateral		SFA – Contralateral	
Node	**Length**	**Node**	**Length**	**Node**	**Length**	**Node**	**Length**
1	29.8	1	6.9			1	29.8
2	36.7	2	23.9			2	8.7
3	28.9	3	18.6			3	29.8
4	7.0	4	28.9				
5	6.9	5	7.0				
		6	6.9				

10

Note. RCA: Right Coronary Artery. SFA: Superficial Femoral Artery. The most restrictive nodes are indicated in blue

10.B4. References

[1]   Frizell J. Pressures resulting from changes of velocity of water in pipes. Proceedings of the American Society of Civil Engineers. 1898; 23(6): pp. 414-421.

[2]   Korteweg D. Ueber die Fortpflanzungsgeschwindigkeit des Schalles in elastischen Röhren. Annalen der Physik. 1878; 241(12): pp. 525-542.

[3]   Chaudhry MH. Applied hydraulic transients (3rd ed.). New York, NJ: Springer, 1979.

[4]   Marey M. Mouvement des Ondes Liquides pour Servir a la Théorie du Pouls. Travaux du Laboratoire de M. Marey. 1875.

[5]   Tijsseling AS. Fluid-structure interaction in liquid-filled pipe systems: a review. Journal of Fluids and Structures. 1996; 10(2): pp. 109-146.

[6]   The Engineering Toolbox. Modulus of Elasticity or Young's Modulus - and Tensile Modulus for common Materials. Available from: http://www.engineeringtoolbox.com/young-modulus-d_417.html.

[7]   Churchill WS. Friction-factor equations spans all fluid-flow regimes. Chemical Engineering. 1977; 7: pp. 91-92.

[8]   Stone GW, Colombo A, Teirstein PS, Moses JW, Leon MB, Reifart NJ et al. Percutaneous Recanalization of Chronically Occluded Coronary Arteries: Procedural Techniques, Devices, and Results. Catheterization and Cardiovascular Interventions. 2005;66: pp. 217-236.

[9]   Nadal LL, Cynamon J, Lipsitz EC, and Bolia A. Subintimal angioplasty for chronic arterial occlusions. Techniques in vascular and interventional radiology. 2004; 7(1): pp. 16-22.

[10]   Avolio A. Multi-branched model of the human arterial system. Medical and Biological Engineering and Computing. 1980; 18(6): pp. 709-718.

[11]   Bavosi J. Artwork of the Human Arterial System. Available from: http://fineartamerica.com/featured/artwork-of-human-arterial-system-john-bavosi.html.

[12]   Boutouyrie P, Bussy C, Lacolley P, Girerd X, Laloux B, and Laurent S. Association between local pulse pressure, mean blood pressure, and large-artery remodeling. Circulation. 1999;100(13): pp. 1387-1393.

[13]   Dodge J, Brown BG, Bolson EL, and Dodge HT. Lumen diameter of normal human coronary arteries. Influence of age, sex, anatomic variation, and left ventricular hypertrophy or dilation. Circulation. 1992;86(1): pp. 232-246.

[14]   Kahraman H, Ozaydin M, Varol E, Aslan SM, Dogan A, Altinbas A, et al. The Diameters of the aorta and its major branches in patients with isolated coronary artery ectasia. Texas Heart Institute Journal. 2006;33(4): pp. 463-468.

[15]   Kotowycz MA and Džavík V. Radial artery patency after transradial catheterization. Circulation: Cardiovascular Interventions. 2012;5(1): pp. 127-133.

[16]   Saito S, Ikei H, Hosokawa G, and Tanaka S. Influence of the ratio between radial artery inner diameter and sheath outer diameter on radial artery flow after transradial coronary intervention. Catheterization and Cardiovascular Interventions. 1999;46(2): pp. 173-178.

[17]   Sandgren T, Sonesson B, Ahlgren ÅR, and Länne T. The diameter of the common femoral artery in healthy human: influence of sex, age, and body size. Journal of Vascular Surgery. 1999;29(3): pp. 503-510.

[18]   Sianos G, Werner GS, Galassi A, Papafaklis MI, Escaned J, Hildick-Smith D et al. Recanalisation of Chronic Total coronary Occlusions: 2012 consensus document from the EuroCTO club. EuroIntervention. 2012;8(1): pp. 139-145.

[19]   Yoo BS, Yoon J, Ko JY, Kim JY, Lee SH, Hwang SO, et al. Anatomical consideration of the radial artery for transradial coronary procedures: arterial diameter, branching anomaly and vessel tortuosity. International Journal of Cardiology. 2005;101(3): pp. 421-427.

10

PART III

TISSUE REMOVAL TECHNOLOGIES

The final step in the PCI procedure is reopening the coronary artery. In the majority of the cases a balloon catheter with premounted stent is used for this purpose. In the case of CTOs, however, it is often challenging to feed the balloon catheter through the occlusions and, once in place, to compress the clot material against the blood vessel wall due to the severe calcification. Therefore, alternative strategies to remove soft tissues are explored in the upcoming chapters.

CHAPTER 11

APPLYING FORCE FOR RECANALIZATION – A REVIEW

AIMÉE SAKES, EVELYN REGAR, JENNY DANKELMAN, AND PAUL BREEDVELD

Published in IEEE Reviews in Biomedical Engineering.

11

Abstract— This aim of this review was to analyze and review the state of the art devices for the endovascular treatment of chronic and acute total occlusions in the different vascular beds (coronary, peripheral, carotid, and intracranial arteries) based on the forces exerted on the occlusion during treatment. The literature search was executed in the databases of Scopus and Espacenet. Overall, 120 patents and 49 articles have been reviewed and categorized. The identified treatment tools were divided into three treatment modalities: Compression, Resection, and Conversion. A further subdivision was made based on the force direction, i.e. axial, radial, tangential, or energy conversion process (dissolving or state change). The working principles of the identified treatment tools relate strongly to the (biomechanical) properties of the occlusion and environment. In order to increase procedural success, especially in chronic occlusions, the applied force should be increased by applying buckling prevention methods, the penetration force decreased by smart tip design or dynamic loading, and the energy dissipation to the environment minimized. Insight in the working principles of the treatment tools and their effect on the environment can in future aid designers to overcome current challenges and develop new, innovative treatment tools.

11

11.1. INTRODUCTION

In percutaneous interventions, commonly known as angioplasty, stenotic or narrowed arteries are reopened using endovascular devices, such as guidewires and (balloon) catheters. Percutaneous interventions are being performed in various vascular beds, most commonly the coronary arteries of the heart (Percutaneous Coronary Interventions [PCI]), followed by the peripheral arteries of the legs (Percutaneous Transluminal Angioplasty [PTA]), the carotid arteries in the neck (PTA), and recently also the intracranial arteries in the head (Percutaneous Intracranial Angioplasty [PIA]). The degree of arterial narrowing is variable ranging from mild lumen narrowing to complete, total vessel occlusion. When it comes to total vessel occlusion two major pathomechanisms should be principally differentiated. First, the *acute* total occlusion, caused by intravascular *thrombosis*, which leads to the clinical syndrome of infarction. Acute infarction is a life-threatening situation and thus requires urgent treatment with the goal of reopening the artery as quickly as possible. Second, the *chronic* total occlusion (CTO), caused by intravascular *calcification* which leads to the clinical syndrome of exercise-induced, or silent ischemia, is a clinically stable situation and is being treated in an elective setting [1].

Reopening CTOs is considered the "last frontier" in percutaneous interventions, substantiated by the fact that they represent the most technically challenging lesion subset that interventionists face [2-5]. Most data are available for PCI, with procedural success rates for CTO treatment that are in between 45% and 5% lower than those achieved in non-chronically occluded lesions [2-4]. Even though the technical and procedural success rate of PCI in CTOs has gradually increased over the last five years with improvements in equipment and operating techniques, CTOs remain the lesion subset for which PCI is most likely to fail [2]. The most common failure mode in PCIs of CTOs remains the inability to successfully cross the guidewire across the occlusion into the distal true lumen, accounting for approximately 80% of the failure cases [2]. Heavy calcification complicates initial penetration, as the guidewire is often not able to apply sufficient force to penetrate and cross the tough fibrous (proximal or distal) cap of the CTO due to buckling. In contrast, in acute (thrombotic) total occlusions no calcification is present, resulting in a significantly lower force to cross the lesion, and thus in fewer difficulties during the crossing procedure. Furthermore, even if initial puncture and the subsequent crossing procedure is successful, the final step in the procedure; the actual reopening of a heavily calcified CTO, is often complicated as heavily calcified regions resist compression and resection, resulting in the inability to cross or dilate the lesion, observed in 2% to 9% of the failure cases [2].

The aim of this study is to analyze and review the patented and current state of the art treatment tools for the endovascular recanalization of chronic and acute total occlusions in the different vascular beds based on the forces exerted on the occlusion

11

during treatment. By describing the underlying working principles of the treatment tools and relating these principles to the clinical environment in which they are used, potential solutions to currently encountered challenges, such as the previously described crossing and treatment difficulties in CTOs, and new creative ideas for recanalizing total occlusions can emerge. Even though some reviews exist that give an overview of the current treatment tools used during PCIs of CTOs (e.g., [2, 6, 7]), never before have these treatment tools been fundamentally discussed from a force-delivery point-of view. Furthermore, by looking deeper into the treatment tools designed specifically for chronic and acute lesions in the different vascular beds, a much broader picture is sketched of the entire field of treatment tools. This "cross-fertilization" can be used, for example, by designers for the development of new, innovative treatment tools, and by clinicians to expand their knowledge on the used treatment tools in other vascular beds and occlusions types, than their area of expertise.

11.2. LITERATURE SEARCH METHOD

The literature search was executed in the database of Scopus and Espacenet and included journal articles and patents in the English or Dutch language from the time period from the 1950s to the present. The search was broadened to include devices designed for all total occlusion types to get a complete overview of all endovascular treatment devices. Rigid shafted instruments were excluded.

The search terms in the Scopus web engine were subdivided into four categories: (1) occlusion, (2) treatment, (3) medical, and (4) instrument. In the occlusion category, the search terms: *occlu*, obstruct*, plaqu*, thromb*, *clot*, obstacle*,* and *barrier** were used. The treatment category included: *canal*, remov*, resect*, dissect*,* and *cut**. In the area category, the following terms were used: *Vasc*, cardio*, arter*, vessel*, vein*,* and *cappilar*,* and in the instrumental category: *device*, instrument*, prototype*, guidewire*, catheter*,* and *apparatus**. The categories were connected with the "AND" operator, the search terms either with "AND" or "OR". The literature search in Scopus led to 416 hits. Of these hits, first the titles were scanned for relevancy, after which the abstract was read. This led to the inclusion of 49 articles.

The Espacenet database was searched using the following keywords in the title and in the title & abstract, respectively: (Occlu* OR obstruct* OR plaqu* OR thromb* OR clot*) and ([Vasc* OR vessel*] AND [canal* OR remov* OR resect*]). This led to 845 potentially relevant patens. By first reading the title of the patents, followed by the summary of the invention, a total of 120 patents were included in this review.

11.3. METHODOLOGY

11.3.1. Device Categorization

On a fundamental level, the treatment tools for recanalizing chronic and acute occlusions can be subdivided into three distinct treatment modalities: *Compression*, *Resection*, and *Conversion* (Figure 11.1). In the *Compression* treatment modality, commonly known as angioplasty, the occlusive material is compressed against the blood vessel wall with a device that exerts a radial force in the direction of the blood vessel wall. In the *Resection* treatment modality, also known as atherectomy in peripheral and coronary arteries, the occlusive material is resected from the blood vessel wall using an *Axial* (in the direction of the blood vessel), *Radial* (from the center of the blood vessel in the direction of the blood vessel wall), *Tangential* (in the direction of the circumference of the blood vessel wall) or a combination of these forces, called *Hybrid*. Finally, in the *Conversion* treatment modality, the occlusive material is converted into a liquid or gaseous state by breaking the cross-links (from hereon out called *Dissolving* [commonly known as thrombolysis]) or by using light or electric energy (from hereon out called *State Change*).

11.3.2. Device Definitions

Per treatment modality, the associated devices are discussed. Per device, the current status, intended location, and occlusion type are indicated in between brackets. For the
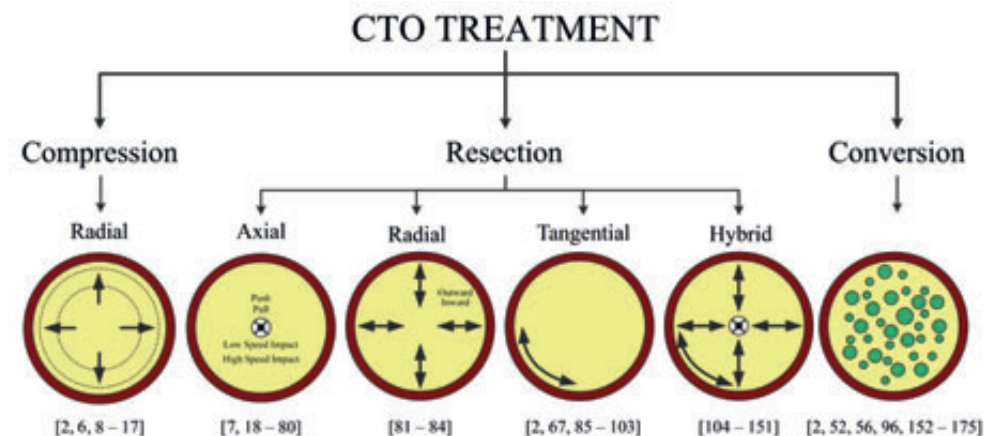

Figure 11.1— Subdivision of the different treatment tools. The arrows indicate the forces on the environment during treatment. Color indications: Red = Blood vessel wall. Yellow = Plaque material. Green = Conversion agent.

device status, a subdivision is made between devices currently used in clinical practice (indicated as: in use for), devices currently under development (indicated as: under development for), devices that are currently abandoned (indicated as: abandoned, originally in use for), and devices that are proposed in the patented literature and are not (yet) seen in clinical practice (indicated as: proposed for). The intended location is subdivided in peripheral occlusions (i.e., occlusions in peripheral blood vessels, such as the legs), coronary occlusions (i.e., occlusions in the coronaries of the heart), carotid occlusions (i.e., occlusions in the carotid artery located in the neck), and intracranial occlusions (i.e., occlusions in the blood vessels in the brain). If the intended location is not indicated, the location data will be omitted from the device definition. Finally, a subdivision is made between two major groups of occlusion types: chronic occlusions and acute occlusions.

It must be noted that most treatment tools require a previous successful crossing procedure before treatment can commence. In these device the previously placed guidewire serves as guide during the recanalization procedure. However, this dependence on a successful crossing procedure can be especially difficult in chronic total occlusions, in which the inability to cross the occlusion is the most common failure mode.

11.4. STATE OF THE ART DEVICES

11.4.1. Compression

Based on the emerging evidence of positive clinical effects, such as improved survival rates, of revascularization of chronic total occlusions through angioplasty (in which the occlusive plaque material is crossed using a guidewire and subsequently compressed against the blood vessel wall), Stone *et al.* [2] conclude that angioplasty should be considered the preferred initial treatment modality in patients for which high procedural success rates are anticipated (Figure 11.2). A subdivision is made between compression by balloon, compression by stent, and compression by instrument.

Compression by balloon
Balloon angioplasty (In use for peripheral, coronary, and carotid chronic and acute occlusions): Balloon angioplasty is widely used for compression of chronic and acute occlusions. A balloon catheter is guided over a guidewire towards the distal end of the occlusion, after which it is inflated to a fixed size using water pressure 75 to 500 times normal blood pressure (6–20 atmospheres) to compress the occlusion against the blood vessel wall. A relatively common (>2%) complication during angioplasty is myocardial infarction [2]. Myocardial infarction is caused by thrombus formation during the

procedure in acute total occlusions and by occlusion of the side branches or collaterals in chronic total occlusions [2].

To prevent thrombus from entering the blood stream, most proposed designs combine the angioplasty balloon with a proximal occlusive balloon (Alaswad *et al.* [8]) or aspiration (Kokate *et al.* [9] [Figure 11.2]). Furthermore, Qureshi *et al.* and Wholey *et al.* [10, 11] propose a specialized balloon design that integrates an embolic filter, and Loerelius *et al.* [12] a balloon containing hot liquid that thermally acts on the blood vessel wall to prevent plaque debris from entering the blood stream (see Figure 11.2 for the designs of Qureshi *et al.* [10] and Wholey *et al.* [11]). Finally, Nahoom [13] proposes a hybrid compression and resection balloon that uses an adhering coating to attach the plaque to the device during compression.

Another limiting factor in crossing total occlusions, especially chronic occlusions, is obtaining sufficient buckling resistance of the guidewire and balloon catheter to cross the occlusion. For this purpose, the balloon anchoring technique can be used in which a (second) balloon catheter is placed close to the occlusion or in a side-branch to provide additional support to the guidewire and balloon catheter during the crossing procedure. In a case study of Grancini *et al.* [14], a novel application of this technique, called the Balloon Anchoring Intraluminal Tracking (BAIT) technique, is described in which the balloon catheter was place immediately upstream from the occlusion.
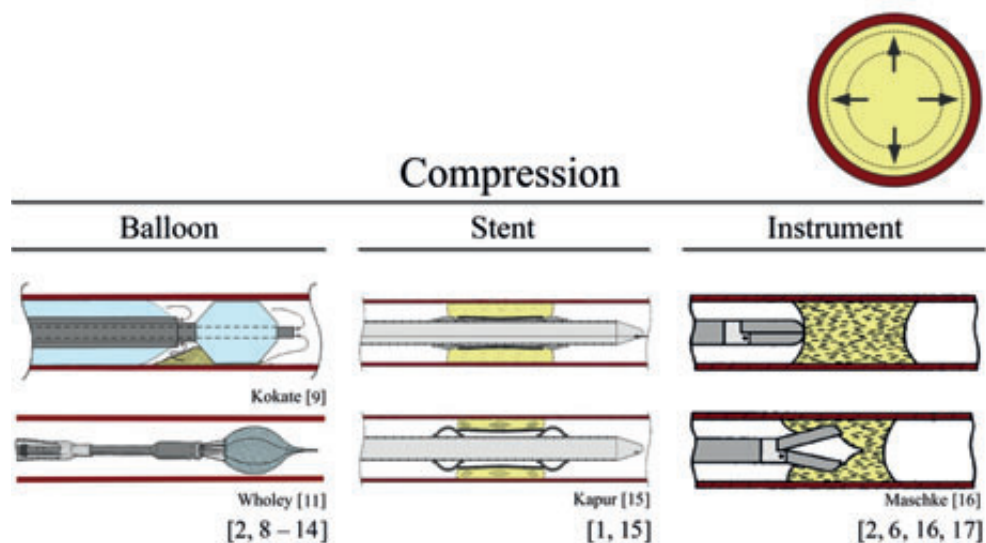

Figure 11.2— Compression – Treatment tools that compress the clot material against the blood vessel wall. Color indications in schematic pictures: Light Blue = balloon. Dark Red = Blood vessel wall. Bright Red = hot liquid. Yellow = plaque material.

Compression by stent

   Stent angioplasty (In use for peripheral, coronary, and carotid chronic and acute occlusions): In most cases balloon angioplasty is followed by the placement of a permanent stent (i.e., an expandable wire mesh or laser-cut tube) to prevent recoil of the blood vessel wall, called stent angioplasty. Coronary stents have been shown to reduce the rates of acute closure and late restenosis compared to balloon angioplasty alone [1]. Extensive literature is available on stent design and placement. Stents can be mainly subdivided into self-expandable (i.e., in which they expand by using shape memory alloys) or balloon-expandable (i.e., in which they are guided and expanded using a balloon catheter) versions. In the patented literature, Kapur *et al.* [15] (Figure 11.2) describe a retrievable expandable stent in combination with electrodes to improve the effectiveness of the compression action of the occlusive material.

Compression by instrument

   Blunt micro dissection (Frontrunner XP) (In use for peripheral chronic occlusions): An entirely different approach to compress the occlusive material against the blood vessel wall is proposed in *Frontrunner XP* (Cordis Corporation, Miami, FL; in use for peripheral chronic occlusions) (see Figure 11.2 for a similar device design suggested by Maschke *et al.* [16]) [2, 16]. *Frontrunner XP* uses a hinged grasper-like treatment tool for crossing and compressing the occlusion against the blood vessel wall. The device is first advanced through the CTO in the closed grasper configuration, after which it is pulled back in the open grasper configuration for compression and disruption. In a small prospective study by Mossop *et al.* procedural success was achieved in 91% of resistant peripheral CTOs, with no complication related to the device itself [6, 17].

11.4.2. Resection

In the *Resection* treatment modality the occlusive material is removed from the blood vessel wall using an *Axial*, *Radial*, *Tangential* or a combination of these forces, hereon out called *Hybrid*.

Resection – Axial

In this section, devices that use an axial force in the direction of the blood vessel are discussed. A further subdivision is made between devices using a low speed (normal operating procedure of guidewire crossing, ±0.1 mm/s) or high-speed axial treatment force.

   Low-Speed Impact Force

In mechanical thrombectomy, so-called retrievers are used for acute ischemic stroke treatment (intracranial acute occlusions). These retrievers use expandable structures, often made out of superelastic materials such as nitinol, to disrupt and remove the acute

11

occlusions. If the retrievers are deployed proximal to the lesion, the retrievers provide an axial push force (*(1) Push*) for resection, whereas a pull force (*(2) Pull*) is applied when the retriever is deployed distally to the occlusion. However, if the retrievers are deployed inside (central to) the lesion, the retriever applies a radial force in the direction of the blood vessel wall during resection and an axial pull force during removal. In this section the proximally and distally deployed retrievers will be discussed, in the *Resection – Hybrid* Section the central retrievers will be discussed.

(1) Push

Proximal Mechanical Retrievers (In use for intracranial acute occlusions): A currently FDA-approved proximal mechanical retriever for the treatment of ischemic stroke is *Penumbra* (Penumbra Inc., Alameda, CA). *Penumbra* uses a separator at the tip of the instrument combined with aspiration to disrupt and remove the occlusive clot using an axial push force [18-21]. Geunther *et al.* [22] propose a different designed proximal mechanical retriever in combination with a distal balloon and [23, 24] a proximal expandable cylindrical tube cutter in combination with a distal balloon for axial clot resection and removal, respectively (Figure 11.3).

(2) Pull

An axial pull force can theoretically be applied proximal and distal to the occlusion. In a proximally applied pull force high grip is needed on the occlusion. No devices were found using this method. In a distally applied pull force, a previous crossing action is needed, after which a larger diameter device can apply the push force. This technique is utilized by distal mechanical retrievers, which will be discussed in the upcoming sections.

Distal Mechanical Coil Retrievers (In use for intracranial acute occlusions): Coil retrievers are made out of one or more non-interconnecting coiled wires for clot engaging and removing. They arrive and cross the clot in the linear formation, after which they (self-) expand for clot engaging and removal using an axial pull force. A currently FDA approved coil retriever is *Merci Retriever* (Concentric Medical, Mountain View, CA), which consists of a flexible nitinol wire with attached filaments that, once deployed, will form a corkscrew-shaped cage structure that entraps the clot [25, 26]. Furthermore, multiple distal mechanical coil retriever designs are proposed in [27-34] (see Figure 11.4 for an example by Gobin *et al.* [29]). The retrievers proposed by Engelson *et al.* [32], Maitland *et al.* [33], and Sakai *et al.* [34] have dual-functionality, since in collapsed state they function as a guidewire and in the expanded state as the coil retriever, and thus allow for crossing, treating, and removing in one tool.

A variant of a coil retriever is a snare retriever, where one or multiple adjustable diameter loops are used for axial clot resection and removal. A currently available snare
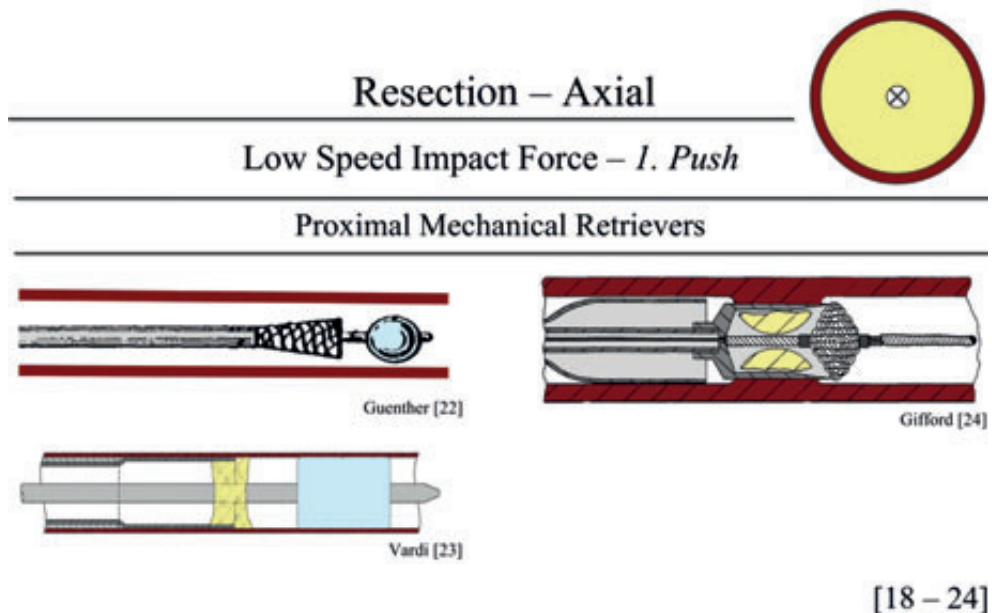
11

Figure 11.3— Resection – Axial – Low-speed Impact Force – Push: treatment tools that resect the clot material from the blood vessel wall using a low-speed axial impact push force. Color indications in schematic pictures: Light Blue = balloon. Dark red = blood vessel wall. Yellow = plaque material.

retriever is *Amplatz Gooseneck* (Initially developed by Microvena, White Bear Lake, MN, currently available with Covidien ev3, Irvine, CA) [35, 36]. Furthermore, Goto *et al.* [37] and Asakura *et al.* [38] describe the *Clot-retrieving wire* (Terumo, Tokyo, Japan) that uses three nitinol loops that self-expand into a tulip-like shape for clot engaging, resecting, and removing using an axial pull force (Figure 11.4). Finally, Kucharczyk *et al.* [39] propose a totally different design coil retriever in which a soft micro-coil mesh is used for clot resection (Figure 11.4).

11

     Distal Mechanical Stent Retrievers (Proposed for intracranial acute occlusions): In contrast to coil retrievers, stent retrievers use cage-like *interconnected* structures for clot capturing and removing. Most stent retrievers are designed for central clot resection. However, some designs are proposed that use a distal stent retriever (using an axial pull force for resection) for improving clot engagement and preventing atherosclerotic debris from entering the blood stream. The propositions include the use of a distal stent retriever of various designs [40-48] (see Figure 11.4 for an example by Tanaka *et al.* [40]) and the combination of a distal stent retriever with a second device, such as a second stent retriever [49, 50] (Figure 11.4), and a proximal balloon [51].

Distal Mechanical Brush Retrievers (In use for intracranial acute occlusions): In distal mechanical brush retrievers, a central wire is equipped with radially oriented filaments. An example of such a device is the CE marked *Phenox CRC* (Phenox, Bochum, Germany), which consists of a flexible nitinol/platinum alloy core wire with attached (brush like) radially orientated polyamide microfilaments [52, 53]. A similar device is proposed by Hannes *et al.* [54] (Figure 11.4) with the addition of an expandable stent retriever to entrap and remove the clot.

Distal Mechanical Balloon Retrievers (Proposed for intracranial acute occlusions): Distal mechanical balloon retrievers, proposed by Nakhjavan *et al.* [55] and Agrawal *et al.* [56], use a sharp-edged balloon to resect and remove clot material from the blood vessel wall using an axial pull force. In the device proposed by Nakhjavan *et al.* [55] one proximal sharp-edged bucket-shaped balloon is combined with a distal conical balloon for clot resection and distal occlusion, respectively (Figure 11.4). Agrawal *et al.* [56] describe a simpler device with one sharp-edged cylindrical balloon around a hollow inner aspiration catheter and a distal cylindrical balloon for clot resection and removal, respectively (Figure 11.4).

High-Speed Impact Force

Resection tools that use a high-speed axial impact force are assumed to use the inertia of the occlusion as the reaction force during resection. If the treatment tool is able to use the inertia of the occlusion as the reaction force for resection, the forces on the blood vessel wall will be minimized, preventing blood vessel wall trauma. In theory, a high-speed push or pull force can be exerted on the occlusion. However, no devices were found that use a high-speed impact pull force. Therefore, in this section only devices that exert a high-speed impact push force on the occlusion are discussed (see also Figure 11.5).

Axial Vibration (In use for peripheral and coronary chronic occlusions): In axial vibration, an axially translating or vibrating motion is used to mechanically disrupt the occlusion by (axially directed) mechanical impact forces, commonly known as vibrational angioplasty. Adjusting the frequency and amplitude of the translations allows for the adaptation to, as well as the ability to cross and disrupt, different tissue types. An example of a currently available CE marked device that uses axial vibration for disruption is the *Vibrational Angioplasty Device* (Medical Miracles, UK; in use for peripheral and coronary chronic occlusions) [7].

The *Vibrational Angioplasty Device* is a handheld motorized device that generates axial movements in a standard dedicated guidewire of 16 to 100 Hz. Summarized results of difficult to treat coronary CTOs, show a success rate of 75% with this device [7]. Additionally, multiple axially vibration devices and actuation methods are proposed for disruption of chronic total occlusions (location undefined). Carmeli *et al.* [57] propose to
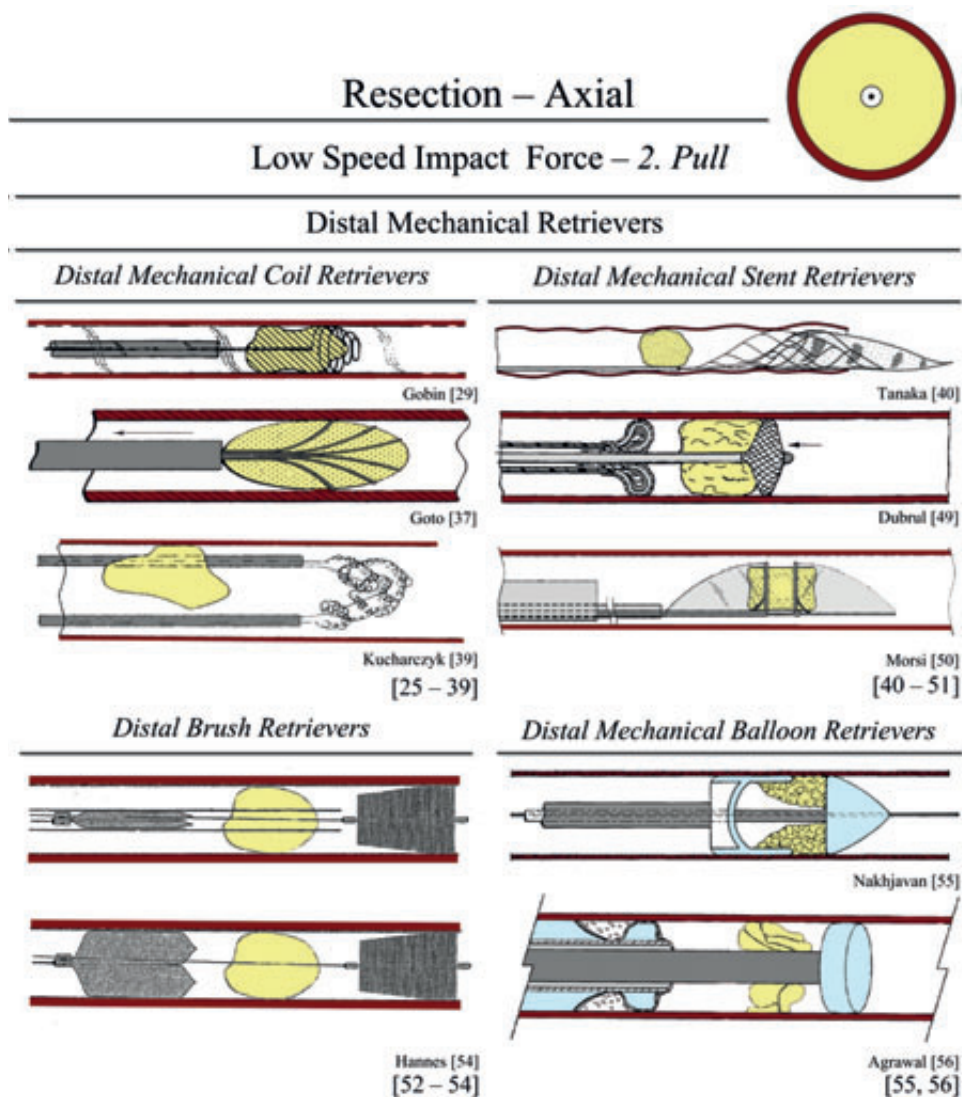
11

Resection – Axial

Low Speed Impact Force – *2. Pull*

Distal Mechanical Retrievers

Distal Mechanical Coil Retrievers

Gobin [29]

Goto [37]

Kucharczyk [39]

[25 – 39]

Distal Mechanical Stent Retrievers

Tanaka [40]

Dubrul [49]

Morsi [50]

[40 – 51]

Distal Brush Retrievers

Hannes [54]

[52 – 54]

Distal Mechanical Balloon Retrievers

Nakhjavan [55]

Agrawal [56]

[55, 56]

11

Figure 11.4— Resection – Axial – Low-speed Impact Force – Pull: treatment tools that resect the clot material from the blood vessel wall using a low-speed axial impact pull force. Color indications in schematic pictures: Light Blue = balloon. Dark red = blood vessel wall. Yellow = plaque material.

use transducers or a magnetic field, Pansky *et al.* [58] hydraulic pressure chambers, and Pansky *et al.* [59] spring-elements (Figure 11.5). Furthermore, both patents by Pansky *et al.* [58, 59] provide a means of adjusting the amplitude or frequency of the oscillations to match the hardness and morphology of the targeted tissue.

Ultrasonic Dissection (In use for peripheral chronic and acute occlusions): In ultrasonic dissection, high-speed (axially) oscillating sound waves in the ultrasonic range cause the formation of cavitation bubbles, which in turn cause shockwaves that are able to disrupt different tissue types [60-64] (see Figure 11.5 for two examples by Rubenchik *et al.* [61]; proposed for coronary acute occlusions, and Wang *et al.* [62]; proposed for acute occlusions). Ultrasonic devices have been shown to have tissue selectivity, with collagen rich structures such as blood vessel walls able to resist fragmentation [63]. However, Siegel *et al.* [64] have shown that heavily calcified occlusions resist recanalization with ultrasound.

In order to fragment highly calcified occlusions, ultrasonic probes are combined with axially oscillating members to achieve both mechanical and ultrasonic disruption in the clinically available *Crosser catheter* (FlowCardia, Sunnyvale, CA; in use for peripheral chronic occlusions) [65, 66] the currently abandoned *UltraSound-driven Oscillating probe Aspirating Thrombectomy* (*US-OAT*, Storz GmbH, Tuttlingen, Germany; originally used for peripheral acute occlusions) device [67], as well as with antithrombotic agents in *the EndoWave System* (EKOS Corporation, Bothell, WA; for peripheral acute occlusions) which is currently under development [68]. In a study of Galassi *et al.* [69], a success rate of 84.8% is described using *Crosser catheter* for recanalizing coronary chronic occlusions, with no periprocedural myocardial infarction, perforation or 30 day major adverse cardiac events. For *EndoWave*, a success rate of 85–95% was reported in peripheral acute occlusions by Owens *et al.* [68].

Axial Fluid Jets (In use for peripheral acute occlusions): Many identified treatment devices use fluids, such as saline and antithrombotic fluids, for resection purposes. In this section, only the devices that use a focused high-speed axial fluid jet, commonly known as rheolytic thrombectomy, are discussed. A currently available fluid jet is *AngioJet* (Initially developed by Possis Medical, Minneapolis, MN, currently available with Boston Scientific, Marlborough, MA; in use for peripheral acute occlusions), which uses a constrained axial fluid jet located at the circumference of the device in combination with venturi for resection [70, 71]. Similar devices are described in [72-75] (see Figure 11.5 for examples by Drasler *et al.* [73] and Bonnette *et al.* [75]; both proposed for acute occlusions). Patents [76-80] describe fluid jets with axially directed unconstrained jets (see Figure 11.5 for the designs of Nerarcher *et al.* [77]; proposed for acute occlusions, and Delaney *et al.* [80]; proposed for peripheral and coronary chronic occlusions). Finally, one paper mentions several abandoned devices, including *Oasis* (Boston Scientific, Natick, MA; abandoned, originally in use for peripheral acute occlusions), *Hydrolyzer* (Cordis Endovascular, Warren, NJ; abandoned, originally in use for acute occlusions), and *NeuroJet* (Possis Medical, Minneapolis, MN; abandoned, originally in use for intracranial acute occlusions) [53].
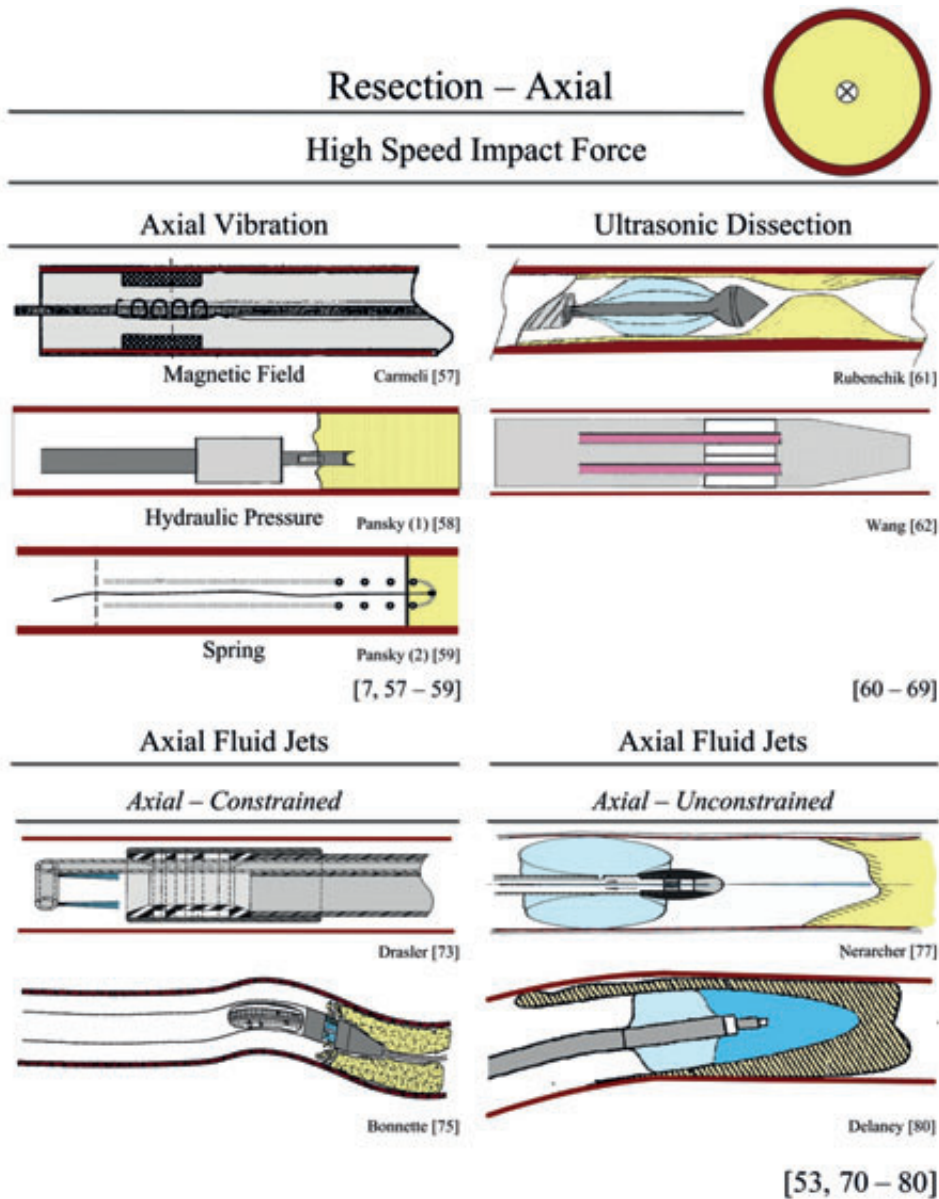
11

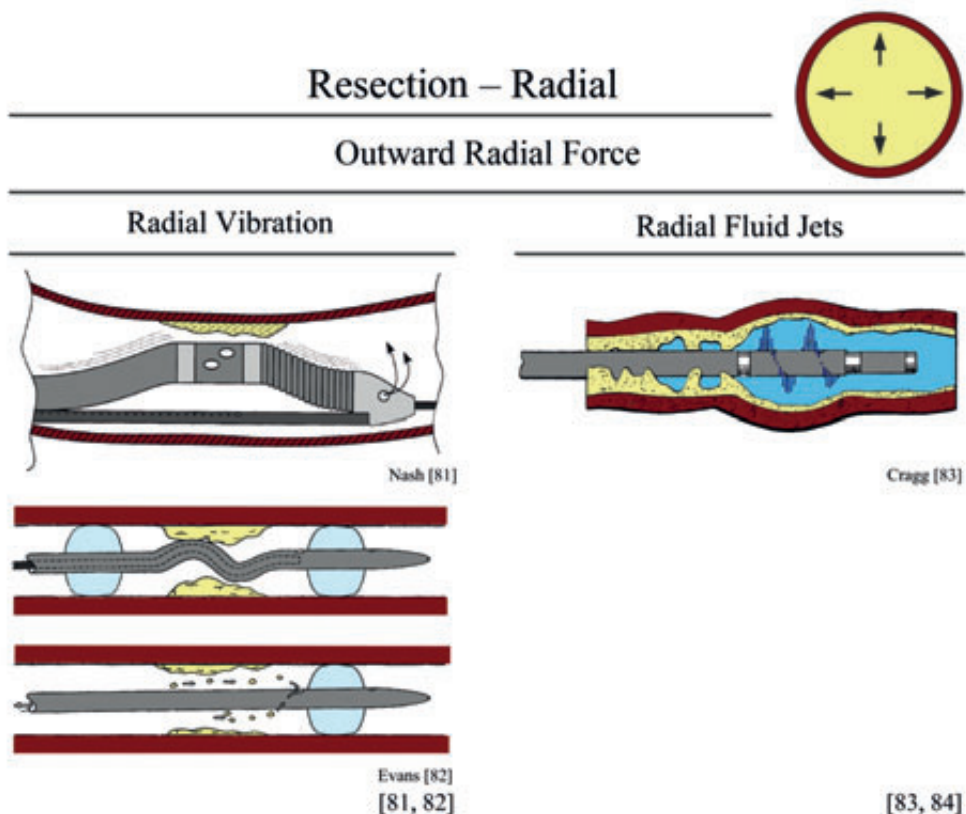**Figure 11.5— Resection – Axial – High-speed Impact Force: treatment tools that resect the clot material from the blood vessel wall using a high-speed axial impact push force.** Color indications in schematic pictures: Light Blue = balloon. Blue = Fluid. Dark red = blood vessel wall. Yellow = plaque material. Pink = ultrasonic transducer.

Resection – Radial

In theory, in the *Radial* approach the resection device can use a radially directed force from the center of the lumen towards the blood vessel wall (outward radial force), or vice versa (inward radial force), to resect the occlusion from the blood vessel wall. Unfortunately, the latter force direction is not possible in the endovascular environment without adding another force vector. Therefore, only devices using an outward radial force will be discussed.

Outward Radial Force

Radial Vibration (Proposed for acute occlusions): In radial vibration, a radially vibrating or translating motion is used to mechanically disrupt the occlusion by (radially directed) mechanical impact forces. Just as in axial vibrating tools, the radial vibrating tools can adapt and disrupt different tissue types based on the frequency and amplitude of the translations

Two patents propose radially vibrating motion for disruption; Nash *et al.* [81] and Evans *et al.* [82]. The former device, proposed by Nash *et al.* [81], uses a wire-guided monorail catheter with a working head that is able to separate and move away from the guidewire to exert radial forces on the occlusion for disruption (Figure 11.6). In the latter device, proposed by Evans *et al.* [82], the radial vibration or translation is achieved by inserting a non-linear portion in the tip of the device (Figure 11.6).

Radial Fluid Jets (Proposed for peripheral and coronary acute occlusions): In radial fluid jets, a narrow radially directed fluid beam is used for disruption. Both Cragg *et al.* [83] (Figure 11.6) and Saito *et al.* [84] propose such a device containing multiple radially directed antithrombotic fluid jets to effectively reestablish the blood flow.

Resection – Tangential

Devices that exert tangential forces on the occlusion during resection use an axially rotating motion of the resection tool. In this review only one type of endovascular occlusion treatment device was identified using tangential resection forces: atherectomy rotating drills.

Atherectomy Rotating Drills (In use for peripheral and coronary chronic and acute occlusions): Atherectomy rotating drills use axially rotating specialized drill bits to resect and remove occlusive material from the blood vessel wall using a tangential force (see also Figure 11.7). The drills mainly differ on drill bit design, which can be broadly subdivided into burrs and helically grooved drill bits, and actuation method (will not be discussed further).

An elliptic burr is used in the clinically available *Rotablator* (Initially developed by Heart Technology Incorporated, Bellvue, WA, currently available with Boston Scientific, Marlborough, MA; in use for coronary chronic occlusions) [85]. As of today, *Rotablator*

11

remains an important treatment tool for more complex coronary chronic occlusions, with minimal changes to its design for the last 25 years. Similar elliptic bur designs are proposed by Dance *et al.* [86] (in which a fluid vortex is created by the rapid rotation of the burr that draws in and macerates the occlusive material) proposed for acute occlusions) and Bashiri *et al.* [87] (proposed for acute occlusions) (see Figure 11.7 for the device proposed by Dance *et al.* [86] and Bashiri *et al.* [87]). A currently abandoned elliptic burr rotating drill device is the *Kensey or Trac Wright Catheter* (Theratek International Corporation, Miami Lakes, FL; abandoned, originally in use for peripheral chronic and acute occlusions) [2, 67, 88].

11

Figure 11.6— Resection – Radial – Outward Radial Force: treatment tools that resect the clot material from the blood vessel wall using an outward radial force. Color indications in schematic pictures: Light Blue = balloon. Blue = fluid. Dark Red = blood vessel wall. Yellow = plaque material.

A helically grooved drill bit is used in the currently clinically available *Wildcat catheter* (Avinger, Redwood City, CA; in use for peripheral chronic occlusions) [89], as well as proposed in [90-93] (see Figure 11.7 for an example by Shiber *et al.* [90]; proposed for chronic and acute occlusions). *Wildcat catheter* is able to change from a passive bit configuration, in which the helical drill bit is mostly shielded, to a more aggressive bit configuration, in which the helical drill bit is more exposed, when more resistance is encountered [89]. Successful peripheral CTO crossing and recanalization with *Wildcat catheter* was reported in 89% of the patients [89]. A currently abandoned helical grooved drill is the *ROtational Angioplasty Catheter System* (*ROTACS,* Oscor, FL; abandoned, originally in use for peripheral chronic occlusions) [2].

To prevent blood vessel wall damage some devices use a shielded drill head, such as in the clinically available devices *Rotarex* (Straub Medical, Wang, Switzerland; in use for peripheral acute occlusions for over 20 years) [94, 95] and *the Silverhawk Plaque Excision System* (Rockhawk, Covidien (ev3), Irvine, CA; in use for peripheral acute occlusions) [96]. *Rotarex* is a highly effective and efficient treatment tool for peripheral acute and chronic occlusions with reported success rates of over 95% [94]. Shielded drill heads are also proposed by Nash *et al.* [97] (proposed for chronic and acute occlusions) and used by the currently abandoned *Rotating spiral Aspiration Thrombectomy (RAT) device* (Angiomed AG, Karlsruhe, Germany; originally in use for acute occlusions) [67]. Furthermore, to achieve faster resection speeds but prevent trauma, Henrie *et al.* [98] propose to combine an inner axially rotating drill with antithrombotic agents. Another method to prevent vessel wall trauma is proposed by Petrucci *et al.* [99] (proposed for chronic and acute occlusions) and Kim *et al.* [100] (proposed for chronic and acute occlusions), in which an expandable balloon with a central drill head allows for central crossing and treating of the occlusion (Figure 11.7). Furthermore, in the design proposed by Petrucci *et al.* [99], the balloon also allows for steering the drill head on plane. Additionally, two devices proposed by Arat *et al.* [101] (proposed for acute occlusions) and To *et al.* [102] (proposed for acute occlusions) also provide a means for steering the drill head using a cable or special spring mechanism, respectively (Figure 11.7). Finally, Maschke *et al.* [103] (proposed for coronary acute occlusions) propose to integrate an imaging sensor into the tip of the proposed axially rotating drill device for ensuring correct intraluminal passage and prevent blood vessel wall contact.

Resection – Hybrid
Multiple treatment tools use a combination of different force directions for resection purposes. A subdivision is made between devices that use an axial and radial force, and devices that use axial, radial, and tangential force for resection.
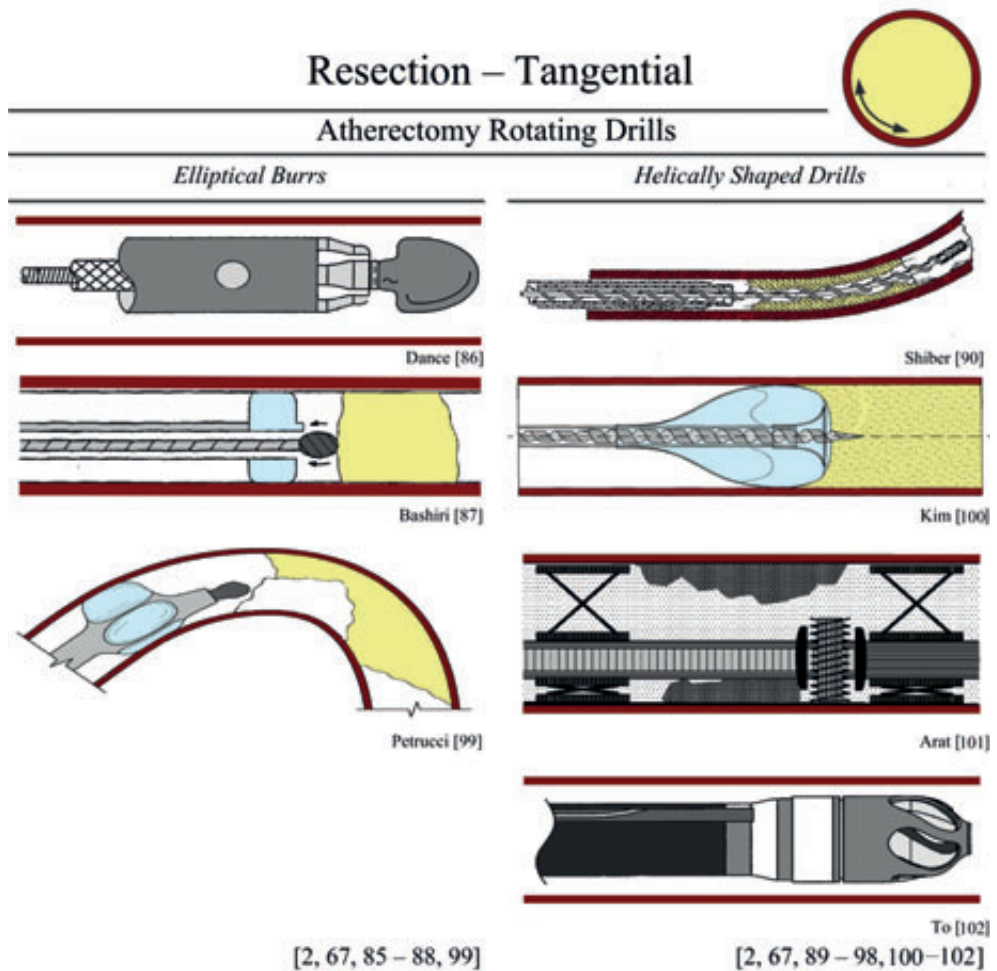
11

Figure 11.7— Resection – Tangential. Color indications in schematic pictures: Light blue = balloon. Dark red = blood vessel wall. Yellow = plaque material.

Axial and Radial Force

Resection tools that use an axial and radial force for disruption can be subdivided into four categories: (1) Push and Outward Radial Force (Figure 11.8), (2) Push & Inward Radial Force, (3) Pull & Outward Radial Force (Figure 11.9), and (4) Pull & Inward Radial Force (Figure 11.10).

(1) Push & Outward Radial Force

Pressure Chamber Resection (Proposed for peripheral and coronary chronic and acute occlusions): In pressure chamber resection, Zakai *et al.* [104] propose a proximal occlusive device that pumps saline in the space between the device and the occlusion to achieve an elevated pressure (i.e., an axial push and outward radial force) for disruption (see Figure 11.8). This elevated pressure is said to cause crack formation in weakest region in the occlusion, with crack propagation and fragmentation along the crack until the distal end is reached and the pressure drops.

Abrasive Tool Resection (Proposed for acute occlusions): In abrasive tool resection, Thompson *et al.* [105] and Jantzen *et al.* [106] propose to use abrasive elements, which are guided along the proximal side of the occlusion, resulting in an axial and radial directed resection force that is able to scrape of occlusive material. In the device proposed by Thompson *et al.* [105] an axially translating drive belt mechanism equipped with abrasive elements is proposed for clot disruption, whereas the device proposed by Jantzen *et al.* [106] consists of a flexible abrasive "rollsock" mechanism that is everted upon itself (Figure 11.8).

(2) Push & Inward Radial Force

No devices were identified in this category.

(3) Pull & Outward Radial Force

In this section, central coil, stent, and brush retrievers are discussed, since these devices apply an outward radial force during resection and an axial pull force during removal.

Central Coil Retrievers (Proposed for intracranial acute occlusions): Even though most coil retrievers are designed for distal deployment, Miller *et al.* [107] and Tsukernik *et al.* [108] propose a central coil retriever (Figure 11.9). Miller *et al.* [107] suggest a standard design as discussed in 4.2.1., whereas in the device proposed by Tsukernik *et al.* [108], the central coil retriever is equipped with sharpened edges and a distal balloon occluder to increase efficiency and prevent debris from entering the blood stream, respectively.

Central Stent Retrievers (In use for intracranial acute occlusions): Central stent retrievers are similar to permanent stent designs, with one major difference; they can be removed after treatment. Two central stent retrievers are the FDA-approved *Solitaire AB/FR Revascularization Device* (ev3, Irvine, CA) [109-113], and *Aperio Clot-Removal Device* (Acandis, Pforzheim, Germany) [111, 112]. *Solitaire* consists of a self-expandable nitinol stent structure that is able to compress and resect the thrombus from the blood vessel wall (using an outward radial force) [109-113]. *Aperio* differs from *Solitaire* in cell
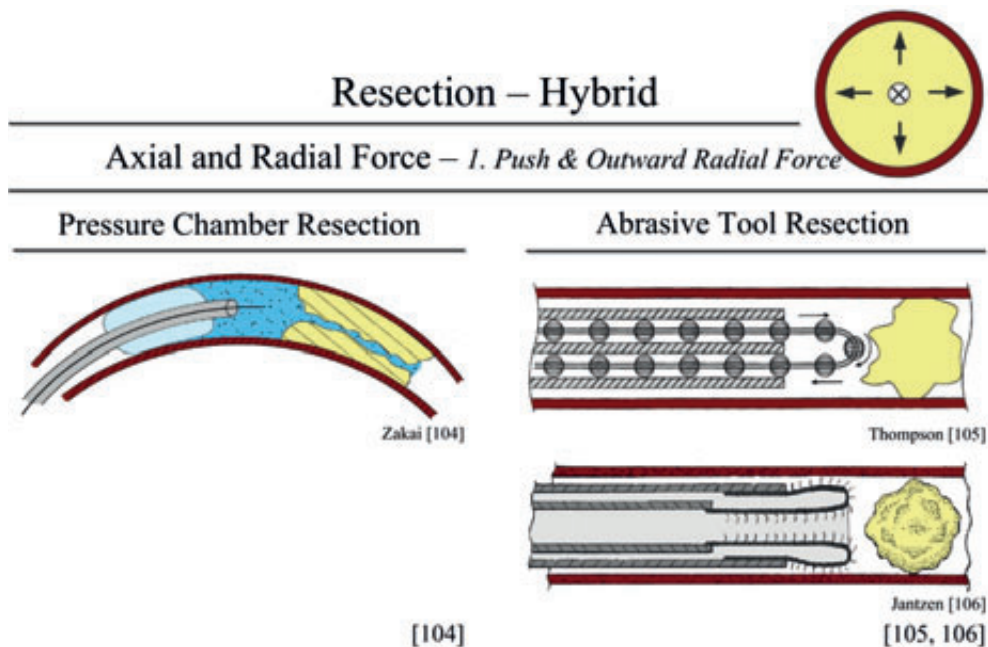
11

Figure 11.8— Resection – Hybrid – Axial and Radial – 1. Push & Outward Radial Force: treatment tools that resect the clot material from the blood vessel wall using a combined axial and radial force. Color indications in schematic pictures: Light Blue = balloon. Blue = Fluid. Dark red = blood vessel wall. Yellow = plaque material.

design, which allows for an improved clot engagement and wall apposition in comparison to the *Merci retriever* and *Solitaire* [114, 115]. Next to these devices, many different central stent retrievers are proposed [116-125] (see Figure 11.9 for an example by Voss *et al.* [119]). The designs mainly differ based on the overall shape of the retriever and cell design. One design proposed by Gerberding *et al.* [126] combines crossing, treating, and removing in one, by using an expandable cage structure that in collapsed state functions as a guidewire and in expanded state as a central stent retriever (Figure 11.9). Furthermore, to improve clot removal and prevent ischemic events, Steinke *et al.* [127] propose the addition of electrodes to help attach the thrombus to the device (Figure 11.9) and Samson *et al.* [128] a second distal stent retriever that is functioning as an emboli filter.

Central Brush Retrievers (Proposed for intracranial acute occlusions): Similar to coil retrievers, brush retrievers are in most cases designed for distal deployment. However, Ben-ami *et al.* [129], Miloslavski *et al.* [130], Cully *et al.* [131], and Kurz *et al.* [132] propose central brush retrievers, in which the radially-directed filaments directly resect the clot material from the blood vessel wall (see Figure 11.9 for the designs

proposed by Ben-ami *et al.* [129] and Cully *et al.* [132]). Furthermore, Olsen *et al.* [133] propose a somewhat different designed, unilateral brush retriever with curved radially-directed brushes located inside a hollow microcatheter that can engage and entrap the clot by axially translating the brushes forward in relation to the catheter (Figure 11.9).

(4) Pull & Inward Radial Force

Aspiration-based Resection (In use for acute occlusions): In aspiration-based resection, commonly known as thrombus aspiration, aspiration proximal to the occlusion is used to remove the clot material from the blood vessel wall using a combined axial pull and inward radial force. In almost all patents aspiration is described as a supportive means of debris removal to prevent ischemic events. However, there are some proposed devices that describe aspiration as main means of resection [134-140].

To increase the overall aspiration force on the occlusion, patents [134-136] suggest using occluders proximal and distal to the occlusion (see Figure 11.10 for an example by Barbut *et al.* [134]). Furthermore, to improve clot removal, Smalling [137] suggests
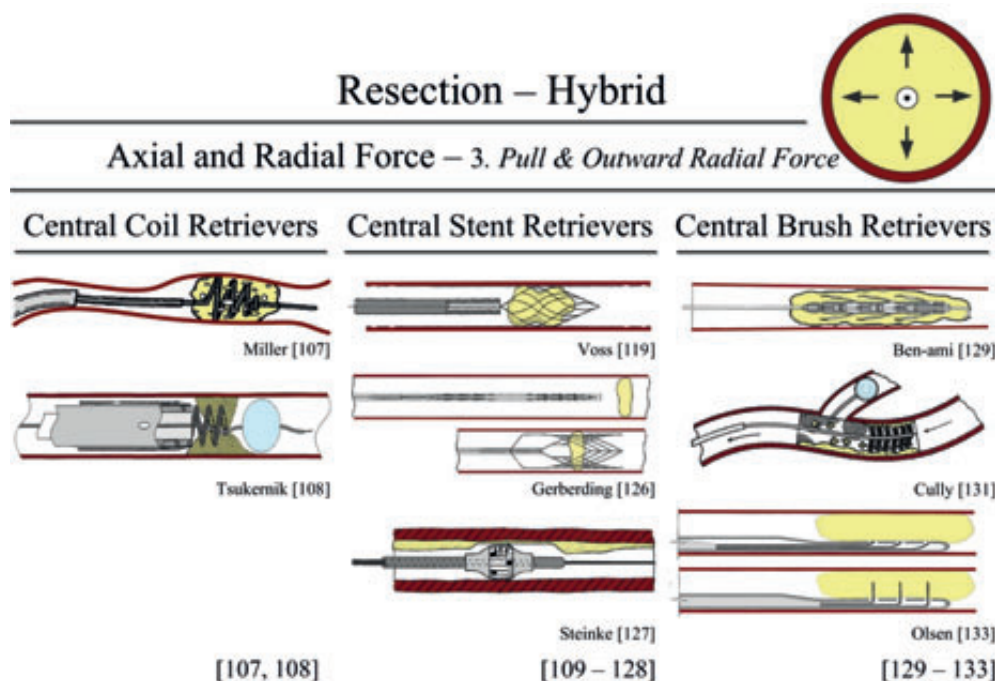

11

Figure 11.9— Resection – Hybrid – Axial and Radial – 3. Pull & Outward Radial Force: treatment tools that resect the clot material from the blood vessel wall using combined axial and radial force. Color indications in schematic pictures: Light Blue = balloon. Dark Red = blood vessel wall. Yellow = plaque material.
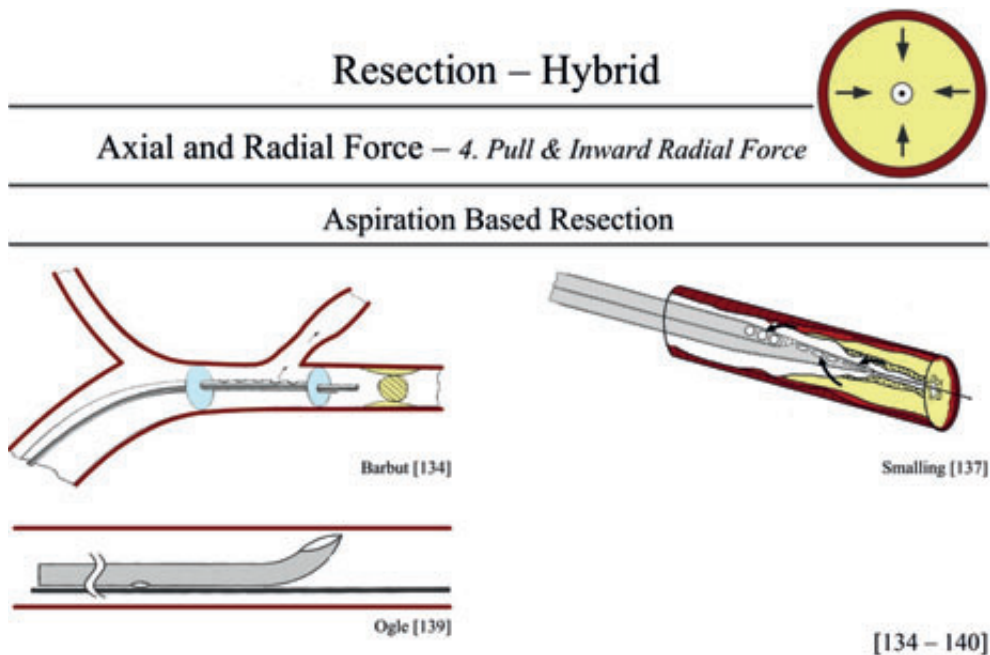
Figure 11.10— Resection – Hybrid – Axial and Radial – 4. Pull & Inward Radial Force: treatment tools that resect the clot material from the blood vessel wall using aspiration. Color indications in schematic pictures: Light Blue = balloon. Dark Red = blood vessel wall. Yellow = plaque material.

multiple aspiration ports with different sizes and a tapering distal end (see Figure 11.10), Auth *et al.* [138] an beveled distal tip, Ogle *et al.* [139] an adjustable tip angle (Figure 11.10), and Kellner *et al.* [136] and Johnson *et al.* [140] the addition of antithrombotic agents.

Axial, Radial, and Tangential Force

Combining an axial, radial, and tangential force for clot resection is proposed in two types of devices: rotatable mechanical retrievers and hybrid fluid jets (see also Figure 11.10).

Rotatable Mechanical Retrievers (Proposed for intracranial acute occlusions): To increase the resection speed of conventional mechanical retrievers, rotating [141-144] (see Figure 11.11 for an example by Hogendijk *et al.* [141]) or oscillating [145] retrievers is proposed. Furthermore, Stinis *et al.* [146], Eckhouse *et al.* [147], and Evans *et al.* [148] suggest using a rotatable expandable cutter, similar to a mechanical stent retriever, in combination with a central cutter for proximal resection of the plaque from the blood

vessel wall (see Figure 11.11 for the designs proposed by Stinis *et al.* [146] and Eckhouse *et al.* [147]).

Hybrid Fluid Jets (Proposed for acute occlusions): Two designs are proposed to obtain a hybrid jet, and thus a force, in the axial, radial, and tangential direction. In the design by Homsma [149], a tangential force component is added to axial and radial directed jets by rotating the device around its axial axis, whereas in the design by Bonnette *et al.* [150, 151] a tangential and axial force component is added to a radial jet by separating the inflow and outflow opening (Figure 11.11).

11.4.3. Conversion

Next to compressing or resecting, the clot material can also be converted into a liquid or gaseous state. Two different methods for clot conversion are distinguished: *Dissolving* and
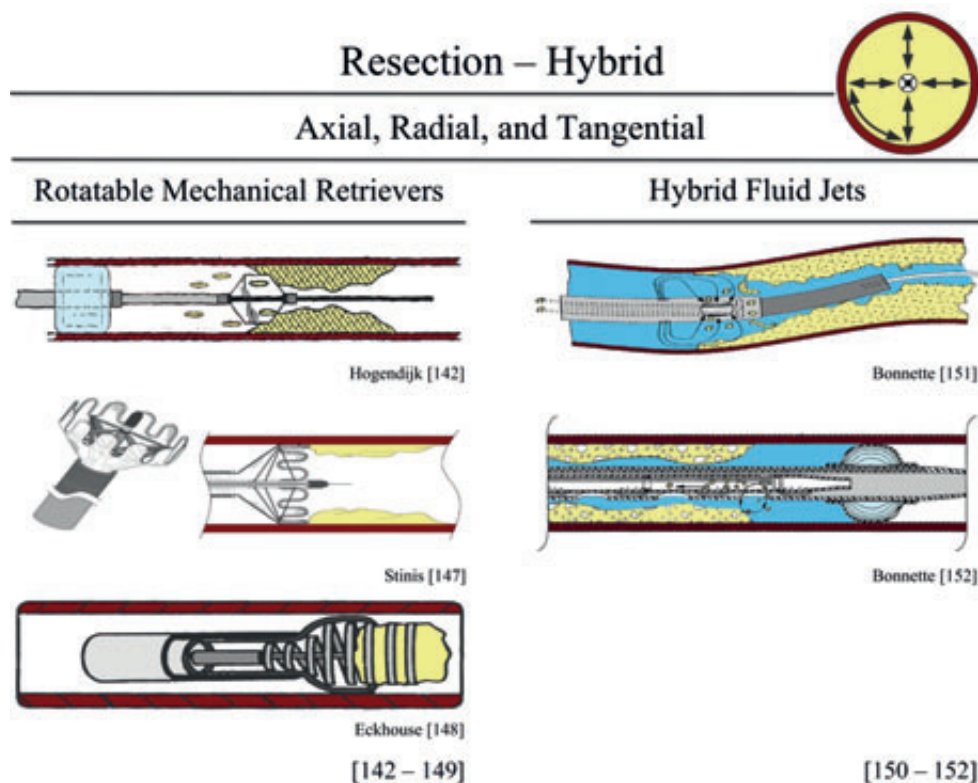

Figure 11.11— Resection – Hybrid – Axial, Radial and Tangential: treatment tools that resect the clot material from the blood vessel wall using axial, radial and tangential forces. Color indications in schematic pictures: Light Blue = balloon. (Dark) Blue = Fluid. Dark Red = blood vessel wall. Yellow = plaque material. Green = Thrombotic agents.

State Change. In the former approach, the occlusion is dissolved by breaking the cross-links in the clot material, whereas in the latter approach the state of the clot material is changed by adding sufficient energy to clot material.

Dissolving

Thrombolysis Devices (In use for chronic and acute occlusions): In thrombolysis, a thrombolytic agent is injected in the blood stream to breakdown the occlusion by severing the cross-links in the fibrin mesh. This makes the occlusion soluble and susceptible to further reduction and dissolving, until the blood flow is restored. While thrombolysis is effective in acute occlusions, it is not effective in CTOs, as calcified tissue cannot be dissolved by thrombolytic agents.

Since antithrombotic agents prevent blood clotting, they are associated with an increased risk of bleeding [152]. Therefore, several devices are being proposed to assure a maximal *localized* thrombolytic effect of the drug at the very site of occlusion to reduce the risk of bleeding. Chornenky, Herr, and Ya *et al.* [153-155] propose to use a device equipped with two occlusive balloons in between which the antithrombotic agents are circulated (see Figure 11.12 for the devices proposed by Chornenky *et al.* [153] and Herr *et al.* [154]). Additionally, Tekulve *et al.* [156] suggest using an impeller in between two expandable structures to create a fluid vortex, Evans *et al.* [157] an axially translating catheter to create turbulent flow, and Aggerholm *et al.* [158] a single distal balloon in combination with a plurality of holes to inject antithrombotic agents to increase efficiency (see Figure 11.12).

State Change

Next to breaking the cross-links of the clot material, it is also possible to change the state of the clot (i.e., from a solid to a liquid or gaseous state). Two different devices are described that change the state of the clot material: lasers and spark erosion (Figure 11.13).

Lasers (In use for peripheral and coronary chronic occlusions): A laser for plaque resection and removal was first described in 1984. A currently available laser for recanlizing CTOs is *the CVX-300 excimer laser system* (Spectranetics, Colorado Springs, CO; a pulsed xenon monochloride excimer laser, with a wavelength of 308 nm, pulse duration of 125–200 ns, a repetition rate of 25–80 Hz, and an energy level of 30–80 mJ/mm; in use for peripheral and coronary chronic occlusions) [96, 159, 160] in combination with *the Excimer Laser Coronary Atherectomy (ELCA) Laser catheter* (Spectranetics, Colorado Springs, CO) [161] or *TURBO Elite Laser Atherectomy Catheter*
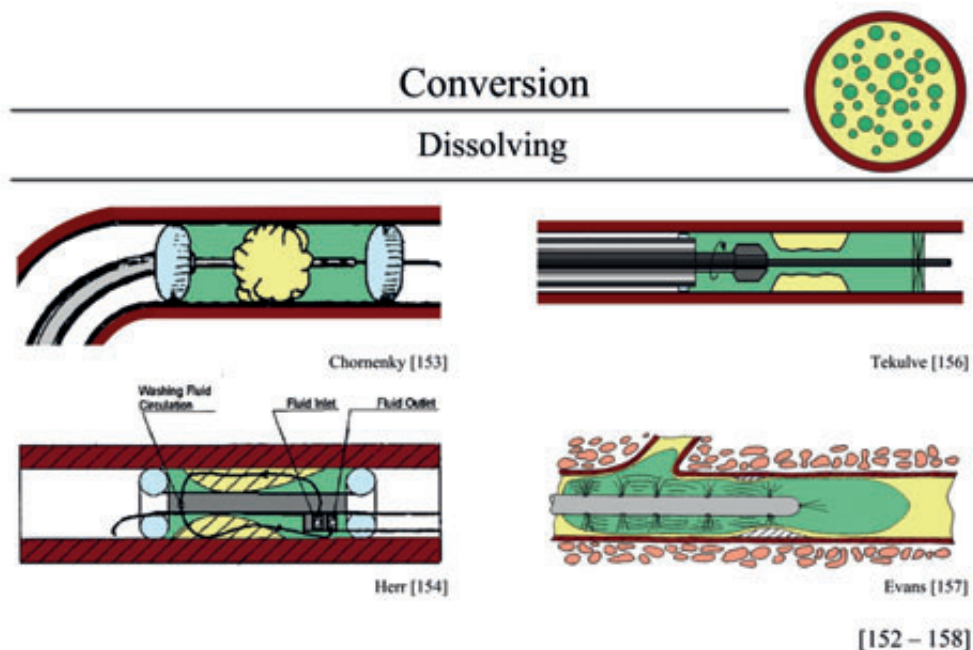
11

Figure 11.12— Conversion – Dissolving: treatment tools that convert the clot material by dissolving it. Color indications in schematic pictures: Light Blue = balloon. Dark Red = blood vessel wall. Yellow = plaque material. Green = Thrombotic Agents.

(Spectranetics, Colorado Springs, CO) (FDA approved since 2006) [7]. Furthermore, the general use of catheter-integrated lasers is described for clot disruption in [162-164] (see Figure 11.13 for a catheter integrated laser design proposed by Reiser *et al.* [162]). Other proposed lasers for recanalization include a *Nd-YAG lasers* (i.e., a flashlamp excited constant wave neodymium-yttrium aluminum garnet laser, with a wavelength of 1064 nm, pulse duration of 0.5–1 s, a repetition rate of ≤0.2 Hz, and an energy level of 5–20 J/pulse; abandoned, originally in use for peripheral chronic and acute occlusions) by [165-167], *Ho-YAG lasers* (i.e., a flashlamp excited holmium-yttrium aluminum garnet laser, with a wavelength of 2.1 μm, pulse duration of 250 μs, a repetition rate of 3.5 Hz, and an energy level of 1–1.7 mJ/mm (300–500 mJ/pulse); abandoned, originally in use for coronary chronic occlusions) by [168], and *pulsed dye lasers* (i.e., a flashlamp excited pulsed dye laser, at a wavelength of 480 nm, a repetition rate of 10 Hz, and an energy level 80–100 mJ/pulse; abandoned, originally in use for peripheral acute occlusions) by [169].
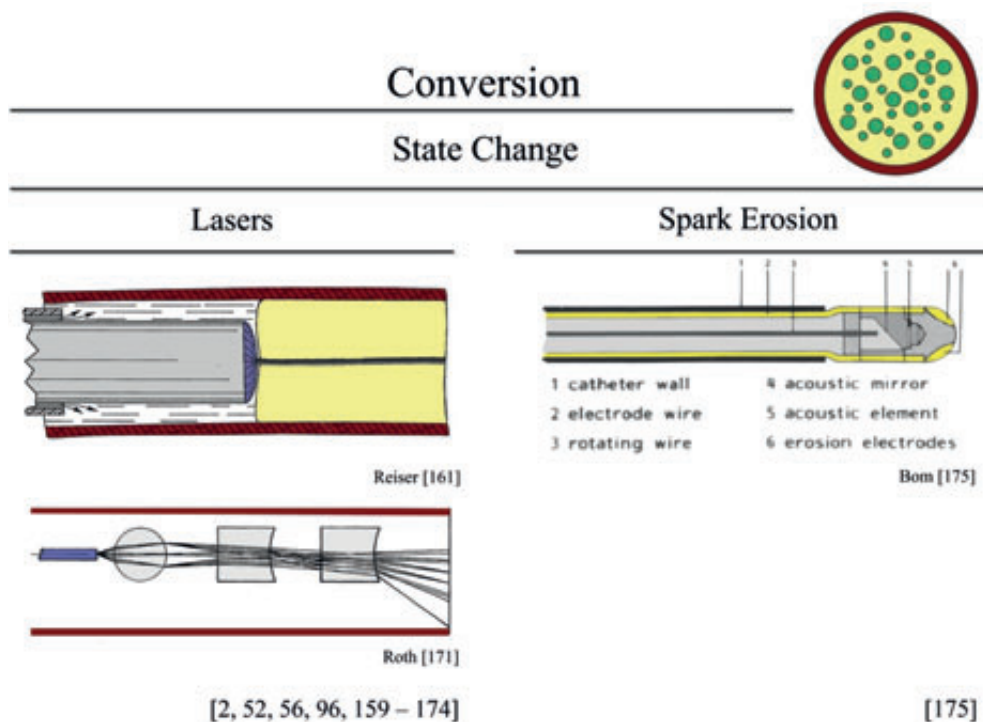
11

355

Figure 11.13— Conversion – State Change: treatment tools that convert the clot material by changing the state of the clot. Color indications in schematic pictures: Dark Red = blood vessel wall. Yellow = plaque material. Bright Yellow = Electrodes. Purple = Laser.

Currently, most laser systems are not pursued any further, such as the abandoned device *LaTIS* (LaTis, Minneapolis, MN) [53, 170], due to the high cost of these devices, the lack of clear benefit compared to conventional wires, and an increased risk of perforation due to a lack of means to direct the laser accurately [2]. To overcome these problems, Roth and Pallarito *et al.* [171, 172] suggest a miniaturized optical set-up and specialized laser tip, respectively, to focus, scatter, and direct the laser (Figure 11.13). Furthermore, Macy *et al.* [173] propose a laser that can differentiate between different tissue types by using the difference in scatter and absorbance of laser light by the tissue. Additionally, *Endovascular Photo Acoustic Recanalization* (EPAR) (Endovasix, Belmont, WA; abandoned, no further data found) is also able to differentiate between tissue types since it converts photonic energy to acoustic energy, and thus uses tissue-selective cavitation for clot disruption [53, 170, 174].

Spark Erosion (Proposed for coronary chronic occlusions): Another proposed method for CTO crossing and resecting is spark erosion [175] (Figure 11.13). In the

356

proposed device, two electrodes are placed in close proximity to the occlusion to generate an electric discharge (spark) that fragments plaque tissue in between the electrodes. Spark erosion is less suited for fragmenting calcified lesions as this method only fragments electrically conductive materials, such as fatty tissues, and thus will not fragment calcium.

11.5. DISCUSSION

11.5.1. Summary of Main Findings

In this review we identified 142 treatment devices for treating both acute and chronic total occlusions. The identified devices differ based on the treatment modality used; compression, resection, or conversion, and their specific application area (i.e., intended for use in acute or chronic occlusions in the peripheral, coronary, carotid, or intracranial blood vessels). The great majority of the identified treatment devices are found in the patented literature (120 devices). Surprisingly, only a relatively limited number of treatment devices were identified that are currently used in clinical practice: 8 devices for the treatment of chronic occlusions versus 10 devices for acute occlusions (with one device in use for both occlusion types: *Rotarex* [Straub Medical, Wang, Switzerland]).

11.5.2. Treatment Modalities versus Occlusion Type

Based on the number of patents described for both acute and chronic occlusions, there is a trend towards resection and removal of the occlusive material in the patented literature, especially in acute occlusions were the majority of the described devices falls under the mechanical retriever categories. At this point, it is important to realize that the occlusion type (acute versus chronic) has major impact on the type and effectiveness of the treatment modality as it originates from completely different pathophysiologic substrate with different mechanical and biological characteristics.

An acute occlusion is typically caused by fresh thrombus, which means that the occlusive material is relatively soft and only loosely attached to the vascular wall, which makes it easy to cross principally attractive for removal. Interestingly, the high amount of patents is in discrepancy to the limited variety of devices used in current clinical practice. Why is this? In coronary arteries, the use of thrombus aspiration is declining as it becomes increasingly obvious that the amount of removed material seems not so important and there are concerns regarding safety of the procedure [176]. Recent reports even question the clinical benefit of thrombus aspiration as such and raise safety concerns especially with respect to a possibly increased periprocedural stroke risk [177, 178]. In acute ischemic stroke treatment, there is a different scenario, as we are possibly at the verge of a paradigm shift in favor of acute percutaneous intervention as opposed to the standard treatment; intravenous recombinant tissue plasminogen activator (thrombolysis) therapy [179]. In this clinical field, there is clearly room for innovation, as the trade-offs between

11

effectiveness of thrombus removal versus the time need to perform the procedure and its technical complexity still need to be established. Clinical trials are promising with *Solitaire* shown 81% successful recanalization of intracranial acute occlusions [111]), or have been shown to be beneficial in combination with the treatment modality of choice, such as *Merci Retriever* in combination with thrombolysis [26].

Chronic total occlusions differ from acute occlusions, as the occlusive material is calcific (rather than thrombus), and thus hard like bone, making it more difficult to cross. Furthermore, it is completely embedded in the vascular wall, which renders retrieval more difficult and increases the risk of vascular wall damage and serious complications during retrieval. Due to the increased technical difficulty in treating chronic occlusions, balloon angioplasty has the advantages of being standard routine techniques, which may be perceived to carry a lower-risk in comparison to, for example, atherectomy, even though in-hospital major adverse events may exceed 5% [2]. Furthermore, the lack of familiarity with new equipment specifically designed for chronic total occlusions, such as *Frontrunner XP* and *Crosser catheter* [69], often give rise to half-hearted prematurely aborted attempts, ensuring high failure rates [2]. Nevertheless, promising success has been reported for CTO treatment using dedicated devices in peripheral arteries of the leg.

11.5.3. Treatment Modalities versus Vascular Beds

The main anatomical differences between coronary and peripheral leg arteries that are of note when it comes to the use of devices are that peripheral arteries are larger in diameter, their course is rather straight (as opposed to often tortuous coronaries), peripherals do not move during the heart cycle, and that the depending tissue is less sensitive for short periods of ischemia than the muscle of the heart; the myocardium. In consequence, from a clinical perspective devices can be somewhat larger (e.g., in coronary occlusions guidewires with a diameter of 0.36 mm [0.014 inch] are used, whereas in peripheral occlusions guidewire are usually 0.89 mm [0.035 inch] in diameter), steering of the devices is easier, as fewer bends have to be negotiated and time limitation, that is periprocedural ischemia time caused by impairment of blood flow and oxygen supply by the device itself, is less of an issue. Recently, the *Wildcat catheter* has been documented to allow for an 89% success rate in peripheral chronic occlusions [89])

11.5.4. Increasing Procedural Success in PCI of CTOs

For most interventional cardiologists, CTO angioplasty represents a challenge that might be avoided given the technical demands of the procedure with relatively low procedural success rates. As a result, patients are often managed medically or are referred for bypass graft surgery. Therefore, improvement of the current treatment devices designed for CTOs is needed to achieve a safer, faster, and more effective recanalization procedure.

Increase the Applied Force

In order to increase the maximum force that can be applied on the CTO, buckling of the guidewire, crossing, or treatment device should be prevented. Multiple buckling prevention strategies can be applied to increase the critical load. The currently applied strategies are mainly focused on increasing the stiffness (i.e., Young's modulus [*E*] and Moment area of inertia [*I*]) of the penetration tool. In the last 5 years, the introduction of stiffer, more powerful, and more supportive guidewires has steadily increased the success rate in PCIs of CTOs [2]. Unfortunately the stiffness of these guidewires alone is often not enough to prevent buckling. Therefore, a stiff support catheter, supportive "buddy" guidewire, or balloon catheter is often placed over, or close proximity to the guidewire for increased support [2, 5].

Next to these clinically applied methods, the type of load, i.e., static or dynamic, can increase the buckling resistance. Lock *et al.* [180] showed that dynamic loads, such as step loads and impulses, much in the excess of static buckling loads can be applied on the penetration tool, as long as they are removed fast enough. Therefore, the high-speed impact force tools, such as used in the axially vibrating *Vibrational Angioplasty Device* (Medical Miracles, UK), *Crosser catheter* (FlowCardia, Sunnyvale, CA; designed for peripheral chronic occlusions), and the device proposed by Rubenchik *et al.* [61], may have an increased buckling resistance over the static tools.

Another method to prevent buckling, is by changing the load direction. For buckling prevention radial or tangentially directed forces are preferable since they do not compress the treatment tool. However, from a safety point of view, radial directed forces are less preferred, since in this force direction the force is distributed over a smaller area (the circumference of the blood vessel) than in axial or tangential forces (the length of the blood vessel).

Aside from buckling prevention, where and how the force is generated can give important clues to their potential maximum magnitude. The generation of this force can be proximal, in the handle piece, or distal (locally) in the tip of the tool. If the force is generated proximally (i.e., in the handle of the device), such as in atherectomy rotating drills, high-magnitude forces can be generated. However, shape dependent friction losses will decrease the eventual force on the occlusion. On the other hand, if the force is generated locally, such as in the axially vibrating members, ultrasonic dissectors, and mechanical retrievers (amongst others), the force on the tissue is independent of the shape of the tool, but is most likely of smaller magnitude than those generated proximally. However, if it is possible to generate a sufficient force in the tip of the tool to puncture and cross the CTO, this method is preferred, since it can guarantee a specific magnitude, independent of the shape of the tool's body.

11

Decrease the Penetration Load of the CTO

The penetration load of a tissue type is dependent on the geometry of the tip of the penetration tool. Which specific tip geometry is needed to achieve the lowest penetration load is dependent on the biomechanical properties of the targeted tissue type. Sharper tip shapes, such as seen in needles, are used to penetrate elastic materials by material tearing. However, blunt shaped indenters are optimal for fracturing hard and brittle material through pulverization and chip formation upon compressive load.

The typical CTO may be classified as a mixture of both elastic and brittle materials. Even though, hard plaques are often encountered in older CTOs (>1 year), fibrocalcific regions frequently occur in CTOs < 3 months of age [1]. The specific tip geometry, and thus type of force, i.e., concentrated or distributed, of the penetration tool, should therefore, be adaptable to the consistency of the CTO. Sharper tip shapes (concentrated cutting forces) are most probably more effective on the soft plaque, whereas blunt tip shapes may be more effective in fracturing hard plaque. This can be substantiated by the fact that concentrated cutting forces, such as used in the mechanical retrievers (e.g., *Merci Retriever* and *Solitaire*) are often very effective in the treatment of acute occlusions. Furthermore, in the devices specifically designed for crossing and treating CTO, such as *Frontrunner XP, Rotablator,* and *Wildcat catheter*, and several proposed CTO crossing devices, such as those proposed by Pansky *et al*. [59], Rubenchik *et al*. [61], and Wang *et al*. [62]*,* more blunt tip shapes are used. On the other hand, it can be questioned if a totally distributed force such as used in, for example, the pressure chamber approach and aspiration, which are mainly designed for the treatment of softer acute occlusions with a weak connection to the blood vessel wall, are able to resect a CTO from the blood vessel wall, since a CTO is often a coherent tissue mass with a strong bond with the blood vessel wall.

Another method to decrease the penetration load of a tissue type is illustrated in a study of Jelinek *et al*. [181]. They showed that increasing the speed of a resection tool, in this case a biopsy blade, decreased the force needed to resect chicken liver. A similar outcome was illustrated in a study of Heverly *et al*. [182] where they inserted a 19G diamond tip needle into porcine heart at velocities between 5 and 250 mm/s and determined that the cutting force can be minimized by maximizing velocity. This effect may be researched in the high-speed impact force method (B.1.b.), such as the axially vibrating devices.

Increase Efficiency of the Intervention

To increase the efficiency of the intervention, the reaction forces on, or energy dissipation to, the environment should be minimized. This will not only increase the chance of successful treatment, but will also prevent indirect damage to the blood vessel during recanalization.

11

Minimizing the reaction force on the environment can be executed in three distinct ways: 1) by using the inertia of the occlusion to supply the needed reaction force, 2) by integrating the reaction force inside the tool or 3) by using a proximal and distal treatment tool in unison. If the inertia of the occlusion is to be used to create the needed reaction force during treatment, the resection tool should hit the occlusion with a high speed, such as seen in B.1.b. With the biomechanical properties of the CTO still largely unknown and highly age-dependent, the required speed of the tool is most probably CTO dependent, requiring an adaptable tool. If the resection tool integrates the action and reaction force during resection, the dependency on the inertia of the occlusion for delivering the reaction force, and with it the associated insecurity, is eliminated. Unfortunately, no treatment tools were found that deliver the needed reaction force for resection themselves. Lastly, if two treatment tools are used in unison, one proximal and one distal, the force loop could be confined within the occlusion. This will prevent both movement of the occlusion and forces on the environment. However, this method might be difficult to execute since previous crossing of the occlusion or crossing of the collateral vessels is required.

To decrease the energy dissipation to the environment, the applied energy in the conversion treatment modality should be contained or focused on a specific area of the CTO. This can be executed by means of occlusive balloons in thrombolysis [153-155] and focusing aids in the state change treatment modality, such as lenses [171, 172].

Finally, another important factor in determining the overall chance of successful treatment is the position of force on the occlusion. Most treatment tools are guided over a guidewire towards the distal end of the occlusion, where they are deployed. Examples of these devices are balloon catheters, distal mechanical retrievers, and central mechanical retrievers. In these devices, the inability to successfully cross the guidewire or treatment tool through the occlusion, which account for approximately 80% of the failure cases [2], causes procedural failure. Treatment devices that are deployed proximally, such as proximal retrievers, axial vibration, and ultrasonic dissection, do not require a previous crossing action, increasing both the efficiency and the chance of a successful recanalization procedure.

11

11.6. CONCLUSION

In this review we identified 142 different devices for the treatment of acute and chronic occlusions. The devices were subdivided into those that compress the clot against the blood vessel wall (compression), those that resect the plaque from the blood vessel wall (resection), and those who convert the plaque (conversion). This subdivision, combined with a further subdivision, based on the forces applied on the occlusion, has given insight into the working principles, and thus effectiveness, of these treatment tools. To increase the effectiveness of future treatment tools, and thus the chance of successful

recanalization, the force applied on the CTO or the efficiency of the intervention should be increased or the penetration force decreased. Further research into treatment devices, in particular their working principles and effect on the environment, may in time improve the success rate for the treatment of total occlusions, in particular CTOs, by the development of new, and innovative treatment tool designs.

ACKNOWLEDGMENT

REFERENCES

[1]   Stone GW, Reifart NJ, Moussa I, Hoye A, Cox DA, Colombo A, et al. Percutaneous Recanalization of Chronically Occluded Coronary Arteries. A Consensus Document Part I. Circulation. 2005;112(15): pp. 2364-2372.

[2]   Stone GW, Reifart NJ, Moussa I, Hoye A, Cox DA, Colombo A, et al. Percutaneous recanalization of chronically occluded coronary arteries - A consensus document - Part II. Circulation. 2005;112(16): pp. 2530-2537.

[3]   Sianos G, Werner GS, Galassi A, Papafaklis MI, Escaned J, Hildick-Smith D, et al. Recanalisation of Chronic Total coronary Occlusions: 2012 consensus document from the EuroCTO club. EuroIntervention. 2012;8(1): pp. 139-145.

[4]   Galassi AR, Tomasello S, Reifart N, Werner GS, Sianos G, Bonnier H, et al. In-hospital outcomes of percutaneous coronary intervention in patients with chronic total occlusion: insights from the ERCTO (European Registry of Chronic Total Occlusion) registry. EuroIntervention. 2011;7(4): pp. 472-479.

[5]   Galassi AR, Brilakis ES, Boukhris M, Tomasello SD, Sianos G, Karmpaliotis D, et al. Appropriateness of percutaneous revascularization of coronary chronic total occlusions: an overview. European Heart Journal. 2015;7(7), pp. 472-479.

[6]   Liang GZ and Zhang FX. Novel devices and specialized techniques in recanalization of peripheral artery chronic total occlusions (CTOs) — A literature review. International Journal of Cardiology. 2013;165(3): pp. 423-429.

[7]   Yalonetsky S, Osherov AB, Strauss BH, Galassi AR, Tomasello S, and Khamis H. Chronic Total Occlusions. A guide to recanalization (2nd ed.). Hoboken, NJ: Wiley-Blackwell, 2013.

[8]   Alaswad K, inventor. Thrombectomy and Balloon Angioplasty/Stenting Device. United States Patent 20100305678 A1. 2010.

[9]   Kokate JY and Dobrava EM, inventors; Scimed Life Systems, Inc, assignee. Catheter for treating vulnerable plaque. World Intellectual Property Organization Patent 03075994 A1. 2003.

[10]   Qureshi AI and Divani AA, inventors. Angioplasty device with embolic recapture mechanism for treatment of occlusive vascular diseases. United States Patent 20040006307 A1. 2004.

[11]   Wholey MH, Wholey P, and Wholey MH, inventors. Vascular catheter with expanded distal tip for receiving a thromboembolic protection device and method of use. United States Patent 20060167491 A1. 2006.

11

[12]   Loerelius L, inventor; Medical Innovation, assignee. Balloon Catheter For Canalization Of Occluded Blood Vessels," World Intellectual Property Organization Patent 9100118 A1. 1991.

[13]   Nahoom D, inventor. Methods And Devices To Remove Blood Clot and Plaque Deposit. World Intellectual Property Organization Patent 2008072243 A2. 2008.

[14]   Grancini L, Lualdi A, Boukhris M, Teruzzi G, Monizzi G, Galassi AR, et al. Balloon anchoring intraluminal tracking technique: a new application of an old technique for coronary artery chronic total occlusion percutaneous intervention. Coronary Artery Disease. 2016;27(5): pp. 429-432.

[15]   Kapur T, Malhi A, and Pruitt S, inventors; Tyco Health Care Group Lp, assignee. Apparatus and method for removing occlusive tissue. United States Patent 20130274728 A1. 2013.

[16]   Maschke M, inventor; Siemens Aktiengesellschaft, assignee. Device for removing a total vascular occlusion with OCT monitoring. United States Patent 20050222595. 2005.

[17]   Charalambous N, Schafer PJ, Trentmann J, Humme TH, Stohring C, Muller-Hulsbeck S, M, et al. Percutaneous Intraluminal Recanalization of Long, Chronic Superficial Femoral and Popliteal Occlusions Using the Frontrunner XP CTO Device: A Single-Center Experience. Cardiovascular and Interventional Radiology. 2010;33(1): pp. 25-33.

[18]   Lutsep HL. Mechanical endovascular recanalization therapies. Current Opinion in Neurology. 2008;21(1): pp. 70-75.

[19]   Kreusch AS, Psychogios MS, and Knauth M. Techniques and Results - Penumbra Aspiration Catheter. Techniques in Vascular and Interventional Radiology. 2012;15(1): pp. 53-59.

[20]   Kang DH, Hwang YH, Kim YS, Park J, Kwon O, and Jung C. Direct Thrombus Retrieval Using the Reperfusion Catheter of the Penumbra System: Forced-Suction Thrombectomy in Acute Ischemic Stroke. American Journal of Neuroradiology. 2011;32(2): pp. 283-287.

[21]   Gralla J, Schroth G, Remonda L, Nedeltchev K, Slotboom J, and Brekenfeld C. Mechanical thrombectomy for acute ischemic stroke - Thrombus-device interaction, efficiency, and complications in vivo. Stroke. 2006;37(12): pp. 3019-3024.

[22]   Guenther RW, and Vorwerk D, inventors. Apparatus for removing blood clots from arteries and veins. United States Patent 5102415 A. 1992.

[23]   Vardi G, inventor. Percutaneous Thrombus Extraction Device and Method. World Intellectual Property Organization Patent 2012068452 A1. 2012.

[24]   Gifford III HS, Simpson JB, and Brown PS, inventors; Devices for Vascular Intervention, Inc., assignee. Atherectomy Device for Severe Occlusions. United States Patent 4926858 A. 1990.

[25]   Kim D, Jahan R, Starkman S, Abolian A, Kidwell CS, Vinuela F, et al. Endovascular mechanical clot retrieval in a broad ischemic stroke cohort. American Journal of Neuroradiology. 2006;27(10): pp. 2048-2052.

[26]   Noorian AR, Gupta R, and Nogueira RG. Acute Stroke: Techniques and Results With the Merci Retriever. Techniques in Vascular and Interventional Radiology. 2012;15(1): pp. 47-52.

[27]   Sepetka I, Vu E, Nguyen D, Miller J, Pierce R, Ngo TT, and Fung N, inventors; Concentric Medical, Inc., assignee. Systems, Methods and Devices for Removing Obstructions from a Blood Vessel. United States Patent 20130253569 A1. 2013.

[28]   Henson MR, inventor. Thrombectomy System and Method. World Intellectual Property Organization Patent 2009021071 A2. 2009.

[29]   Gobin YP and Wensel JP, inventors. Clot capture coil. Australian Patent 2009212829 A1. 2009.

[30]   Martin BB, inventor. System And Methods For Removing Clots From Fluid Vessels. World Intellectual Property Organization Patent 9825656 A2. 1998.

11

[31]   Rosenbluth RF, Green GRJ, Cox BJ, Sternweiler TR, Chow SL, Monetti RR, et al, inventors. Embolectomy Catheters And Methods For Treating Stroke And Other Small Vessel Thromboembolic Disorders. United States Patent 20100145371 A1. 2010.

[32]   Engelson ET and Samson G, inventors; Target Therapeutics, Inc., assignee. Mechanical Clot Encasing and Removal Wire. United States Patent 6066158. 2000.

[33]   Maitland DJ, Iv WS, and Hartman J, inventors; The Regents of the University of California, assignee. Guide Wire Extension for Shape Memory Polymer Occlusion Removal Devices. United States Patent 20090275885 A1. 2009.

[34]   Sakai N, inventor; Wellfind Co., Ltd., assignee. Intravascular Thrombus Capturing Instrument. United States Patent 20120016407 A1. 2012.

[35]   Qureshi AI, Siddiqui AM, Suri MFK, Kim SH, Ali Z, Yahia AM, et al. Aggressive mechanical clot disruption and low-dose intra-arterial third-generation thrombolytic agent for ischemic stroke: A prospective study. Neurosurgery. 2002;51(5): pp. 1319-1327.

[36]   Gonzalez A, Mayol A, Martinez E, Gonzales-Marcos JR, and Gil-Peralta A. Mechanical thrombectomy with snare in patients with acute ischemic stroke. Neuroradiology. 2007;49(4): pp. 365-372.

[37]   Goto K, Kaneko T, Kanamaru T, Takeuchi M, and Okada K, inventors, Terumo Kabushiki Kaisha and Maruho Hatsujyo Kogyo, Ltd., assignees. Intravascular obstruction removing wire and medical instrument. United States Patent 20060 116702A1. 2006.

[38]   Asakura F, Yilmaz H, Abdo G, Sekoranja L, San Millan D, Augsburger L, et al. Preclinical testing of a new clot-retrieving wire device using polyvinyl alcohol hydrogel vascular models. Neuroradiology. 2007;49(3): pp. 243-251.

[39]   Kucharczyk J and Finitsis S, inventors; Nexgen Medical Systems, Inc., assignee. Thrombus Removal System and Process. United States Patent 20110230909 A1. 2011.

[40]   Tanaka DA and Souza AM, inventors. Vascular Thrombectomy Apparatus and Method of Use. United States Patent 20130289608 A1. 2013.

[41]   Khader M and Wilson RF, inventors; Acist Medical Systems, Inc., assignee. Thrombus removal device and system. World Intellectual Property Organization Patent 2011079111 A1. 2011.

[42]   Galdonik JA, Anderson E, Ganesan K, Boldenow G, Kirchgessner K, and Wlodarski G, inventors; Medtronic, Inc., assignee. Aspiration Catheters for Thrombus Removal. United States Patent 20120253313 A1. 2012.

[43]   Brady E, Vale D, Gilvarry M, Razavi M, and Shaughnessy JO, inventors. Clot Capture Systems and Associated Methods. United States Patent 20130144326 A1. 2013.

[44]   Demond JF, Khosravi F, Krolik JA, Ramee S, Renati RJ, Salahieh A, and Young KHK, inventors; Incept LCC, assignee. Vascular Device for Emboli and Thrombi Remove and Methods of Use. United States Patent 20110264135 A1. 2011.

[45]   Fischer JR FJ, inventor; Cook Incorporated, assignee. Mechanical Thrombectomy Device. United States Patent 20100087844 A1. 2010.

[46]   Hopkins LN, Khosravil F, Salahieh A, Demond JF, Lepak J, Ramee S, et al, inventors; Incept LCC, assignee. Vascular device for emboli, thrombus and foreign body removal and methods of use. United States Patent 20120265238 A1. 2013.

[47]   Brady E, Vale D, Gilvarry M, and Razavi M, inventors. Clot engagement and removal systems. United States Patent 20130184739 A1. 2013.

[48]   Aggerholm S, Christensen BW, Hendriksen P, Lysgaard T, Molgaard-Nielsen A, and Svendsen F. Obstruction Removal Assembly. W.O. Patent 2011/1 128 09 A1, Sept. 15, 2011.

[49]   Dubrul W and Fulton RE. Biological passageway occlusion removal. U.S. Patent 2004/0 199 202 A1, Oct. 7, 2004.

11

[50] Morsi H. Clot Removal Device and Method of Using Same. U.S. Patent 2013/0 310 803 A1, Nov. 21, 2013.

[51] Turjman A and Bernstein J. Methods, devices, and systems for postconditioning with clot removal. W.O. Patent 2014/0 084 60 A2, Jan. 9, 2014.

[52] Mordasini P, Hiller M, Brekenfeld C, Schroth G, Fischer U, Slotboom J, et al. In Vivo Evaluation of the Phenox CRC Mechanical Thrombectomy Device in a Swine Model of Acute Vessel Occlusion. American Journal of Neuroradiology. 2010;31(5): pp. 972-978.

[53] Ansari S, Rahman M, McConnell DJ, Waters MF, Hoh BL, and Mocco J. Recanalization therapy for acute ischemic stroke, part 2: mechanical intra-arterial technologies. Neurosurgical Review. 2011;34(1): pp. 11-19.

[54] Hannes R, Schneider M, Pracht H, Miloslavski E, and Monstadt H, inventors. Device for the Removal of Thrombi From Blood Vessels. United States Patent 20090198269 A1. 2009.

[55] Nakhjavan FK, inventor. Catheter for removal of clots in blood vessels. United States Patent 5772674 A. 1998.

[56] Agrawal S, inventor. Aspiration Thrombectomy Device. United States Patent 20120271231 A1. 2012.

[57] Carmeli R, Einav J, and Yonat I, inventors; Eyoca Medical, Ltd., assignee. Device and method for opening vascular obstructions. United States Patent 20120302820. 2012.

[58] Pansky A, Weizman O, and Melamud A, inventors; Oscillon, Ltd., assignee. Method and device for recanalization of total occlusions. United States Patent 20090292296 A1. 2009.

[59] Pansky A. Device for Traversing Vessel Occlusions and Method of Use. United States Patent 20110196348 A1. 2011.

[60] Nita H, and Mills TC, inventors. Ultrasound devices for ablating and removing obstructive matter from anatomical passageways and blood vessels. United States Patent 20030009125 A1. 1999.

[61] Rubenchik AM, Weber PJ, and Silva LBD, inventors; Pearl Technology Holdings, LLC., assignee. Ultrasound plaque emulsion device. World Intellectual Property Organization Patent 02083010 A1, 2002.

[62] Wang G, Sundaram S, Pant K, Feng J, and Storm P, inventors; CFD Research Corporation, assignee. Thrombectomy Microcatheter. United States Patent 20080119780 A1. 2008.

[63] Rosenschein U. Ultrasound thrombolysis: An alternative to the pharmacological approach. Journal of Interventional Cardiology. 1998;11(6): pp. 603-607.

[64] Siegel RJ, Cumberland DC, Myler RK, and DonMichael TA. Percutaneous Ultrasonic Angioplasty: Initial Clinical Experience. The Lancet. 1989;2(8666): pp. 772-774.

[65] Zander T, Rabellino M, Baldi S, Blasco O, and Maynar M. Infrainguinal revascularization using the Crosser (R) vibrational system. Minimally Invasive Therapy & Allied Technologies. 2010;19(3-4): pp. 231-236.

[66] Khalid MR, Khalid FR, Farooqui FA, Devireddy CM, Robertson GC, and Niazi K. A Novel Catheter in Patients With Peripheral Chronic Total Occlusions: A Single Center Experience. Catheterization and Cardiovascular Interventions. 2010;76(5):pp. 735-739.

[67] Schmitz-Rode T, Pfeffer JG, Bohndorf K, and Gunther RW. Percutaneous Thrombectomy of the Acutely Thrombosed Dialysis Graft: In Vitro Evaluation of Four Devices. Cardiovascular and Interventional Radiology. 1993;16(2):pp. 72-75.

[68] Owens CA. Ultrasound-Enhanced Thrombolysis: EKOS EndoWave Infusion Catheter System. Seminars in Interventional Radiology. 2008;25(1): pp. 37-41.

[69] Galassi AR, Tomasello SD, Costanzo L, Campisano MB, Marzà F, and Tamburino C. Recanalization of complex coronary chronic total occlusions using high-frequency vibrational

11

energy Crosser catheter as first-line therapy: a single center experience. Journal of interventional Cardiology. 2010;23(2): pp. 130-138.

[70] Kokov LS, Korostelev AN, Grinko AN, Ilyina MV, Solopova GV, Aiazian E, and Steum CM. Recanalization and Thrombectomy of Internal Anastomosis in a Patient With Tetralogy of Fallot Using the AngioJet Rheolytic Catheter. Catheterization and Cardiovascular Interventions. 2001;53(4): pp. 504-507.

[71] Barbato JE and Wholey MH. Use of AngioJet Mechanical Thrombectomy for Acute Peripheral Ischemia Associated wit Stent Fracture. Catheterization and Cardiovascular Interventions. 2007;70(6):pp. 795-798.

[72] Willard LK, Cassell RL, Robinson RJ, Brown BJ, Whalen MJ, and Smith SR, inventors; SciMed Life Systems, Inc., assignee. Thrombus extraction device. United States Patent 5419774 A. 1995.

[73] Drasler WJ, Dutcher RC, Jenson ML, Thielen JM, and Protonotarios EI, inventors; Possis Medical, Inc., assignee. Thrombectomy and tissue removal method. United States Patent 20040049149 A1. 2004.

[74] Wright JTM, inventors; Pioneering Technologies, Inc., assignee. Method of removing plaque from vessels. United States Patent 5135484 A. 1992.

[75] Bonnette MJ, Morris JE, Wiesel SE, Setum CM, Dutcher RC, and Drasler WJ, inventors; Possis Medical, Inc., assignee. Flexible Tip Rheolytic Thrombectomy Catheter and Method of Constructing Same. United States Patent 5989271. 1999.

[76] Boock R and Gilmartin K, inventors. Thrombus removal device. United States Patent 20020058904 A1. 2002.

[77] Nerarcher A, inventors. Hydrodynamic device for the elimination of an organic deposit obstructing a vessel of a human body. United States Patent 5135482 A. 1992.

[78] Weitzman Y, Ben-Porath A, Levitsky M, Jonas M, Gross Y, Osiroff R, and Kirshenbaum I. A Novel Technology for Large Vessel Recanalization. Innovations. 2010;5(5): pp. 381-385.

[79] Nguyen HD and Mirizzi MS, inventors; VNUS Medical Technologies, Inc., assignee. Methods and Apparatus for Thrombectomy System. World Intellectual Property Organization Patent 2008121481 A1. 2008.

[80] Delaney D, Johansson P, and Constantz BR, inventors. Catheter Devices and Methods for their Use in the Treatment of Calcified Vascular Occlusions. United States Patent 20050059955 A1. 2005.

[81] Nash JE, Walters G, Sauro DM, Eberhart M, and Fisher WT, inventors. Thrombectomy and soft debris removal device. United States Patent 20100145259 A1. 2011.

[82] Evans MA, Demarais D, Khairkhaha A, and Decicco D, inventors; Bacchus Vascular, Inc., assignee. Apparatus and method for removing occlusive material within blood vessels. World Intellectual Property Organization Patent 03097122 A2. 2003.

[83] Cragg AH and Olson EL, inventors; Micro Therapeutics, Inc., assignee. Method and apparatus for power lysis of a thrombus. Canadian Patent 2238064 A1. 1998.

[84] Saito T, Taniguchi I, Nakamura S, Oka H, Mizuno Y, Noda K, et al. Pulse-spray thrombolysis in acutely obstructed coronary artery in critical situations. Catheterization and Cardiovascular Diagnosis. 1997;40(1): pp. 101-108.

[85] Bertrand ME, Lablanche JM, Leroy F, Bauters C, Dejaegere P, Serruys PW, et al. Percutaneous transluminal coronary rotary ablation with rotablator (european experience). American Journal of Cardiology. 1992;69(5): pp. 470-474.

11

[86]   Dance CW, van den Hoek J, and Blackledge VR, inventors; Lake Region Manufacturing, assignee. Vascular Occlusion Removal Devices And Methods. World Intellectual Property Organization Patent 9300119 A1. 1993.

[87]   Bashiri M and Cornil A, inventors. Devices and methods for removing occlusions in vessels. United States Patent 20030195536 A1. 2003.

[88]   Wholey MH and Jarmolowski CR. New Reperfusion Devices: The Kensey Catheter, the Atherolytic Reperfusion Wire Device, and the Transluminal Extraction Catheter. Radiology. 1989;172(3 pt 2):pp. 947-952.

[89]   Pigott JP, Raja ML, Davis T, and Connect Trial Investigators. A multicenter experience evaluating chronic total occlusion crossing with the Wildcat catheter (the CONNECT study). Journal of Vascular Surgery. 2012;56(6): pp. 1615-1621.

[90]   Shiber S, inventors. Rotary Catheter For Removing Obstructions From Bodily Vessels. United States Patent 20130103046 A1. 2013.

[91]   Shiber S, inventors. A rotary catheter for removing an obstruction from a blood vessel. European Patent 0254414 A1. 1988.

[92]   Brown B and Smith S, inventors; SciMed Life Systems, Inc., assignee. Thrombectomy devices and methods of using same. United States Patent 5417703 A. 1995.

[93]   Consigny P, inventors. Spiral Thrombectomy Catheter. United States Patent 20130060206 A1. 2013.

[94]   Wissgott C, Kamusella P, and Andresen R. Recanalization of Acute and Subacute Venous and Synthetic Bypass-Graft Occlusions With a Mechanical Rotational Catheter. Cardiovascular and Interventional Radiology. 2013;36(4): pp. 936-942.

[95]   Duc SR, Schoch E, Pfyffer M, Jenelten R, and Zollikofer CL. Recanalization of acute and subacute femoropopliteal artery occlusions with the Rotarex catheter: One year follow-up, single center experience. Cardiovascular and Interventional Radiology. 2005;28(5): pp. 603-610.

[96]   Shafique S, Nachreiner RD, Murphy MP, Cikrit DF, Sawchuk AP, and Dalsing MC. Recanalization of infrainguinal vessels: Silverhawk, laser, and the remote superficial femoral artery endarterectomy. Seminars in Vascular Surgery. 2007;20(1): pp. 29-36.

[97]   Nash JE, Fisher WT, and DodsonJR CW, inventors; Kensey Nash Corporation, assignee. System for Opening a Lumen in an Occluded Blood Vessel. United States Patent 20080097500 A1. 2008.

[98]   Henrie RA, inventors. Catheter for removing occlusive material. United States Patent 4729763. 1988.

[99]   Petrucci G. and Khanna PK, inventors. Treating Occlusions Within Body Vessels. World Intellectual Property Organization Patent 2013134285 A1. 2013.

[100]   Kim DH and Chin R, inventors; Neo Vasc, assignee. Methods and Apparatus for Treating Vascular Occlusions. World Intellectual Property Organization Patent 2008148041 A1. 2008.

[101]   Arat V, Cohen RT, Ming TW, Lembrikov PB, and Cohen AL, inventors; Microfabrica, Inc., assignee. Atherectomy and Thrombectomy Devices, Methods for Making, and Procedures for Using. United States Patent 20100094320 A1. 2010.

[102]   To J and Danek CJ, inventors; Atheromed, Inc., assignee. Devices, systems, and methods for cutting and removing occlusive material from a body lumen. United States Patent 20110040315 A1. 2011.

[103]   Maschke M, inventors. Catheter and Medical Apparatus as well as Method for Assisting an Intervention to Remove Plaque. United States Patent 20100241147 A1. 2010.

11

[104]   Zakai A and Rottenberg D, inventors. Device and Method for Crossing a Vascular Occlusion. World Intellectual Property Ogranization Patent 2008035349. 2008.

[105]   Thompson D, Perkins DH, Johnson J, Silver M, and Mauch K, inventors; Medtronic Vascular, Inc., assignee. Obstruction Removal System. World Intellectual Property Organization Patent 2009088783 A2. 2009.

[106]   Jantzen AE and Parker FT, inventors; Cook, Inc., assignee. Everted Sheath Thrombectomy Device. U.S. Patent 20100249815 A1. 2010.

[107]   Miller J and Wilson S, inventors. Devices And Methods For Removing Obstructions From A Cerebral Vessel. United States Patent 20120123330 A1. 2012.

[108]   Tsukernik VB, inventors. Thrombectomy catheter with a helical cutter. United States Patent 20090138031 A1. 2009.

[109]   Machi P, Lobotesis K, Maldonado IL, Costalat V, Vendrell JF, Riquelme C, and Bonafe A. Endovascular treatment of tandem occlusions of the anterior cerebral circulation with solitaire FR thrombectomy system. Initial experience. European Journal of Radiology. 2012;81(11): pp. 3479-3484.

[110]   Brekenfeld C, Schroth G, Mordasini P, Fischer U, Mono ML, Weck A, et al. Impact of Retrievable Stents on Acute Ischemic Stroke Treatment. American Journal of Neuroradiology. 2011;32(7): pp. 1269-1273.

[111]   McCabe JJ, Phillips TJ, Phatouros C, Singh T, Blacker D, Hankey GJ, and McAuliffe W. Mechanical thrombectomy with the Solitaire AB device in large intracerebral artery occlusions. Journal of Medical Imaging and Radiation Oncology. 2013;57(2): pp. 149-155.

[112]   Mordasini P, Frabetti N, Gralla J, Schroth G, Fischer U, Arnold M, and Brekenfeld C. In Vivo Evaluation of the First Dedicated Combined Flow-Restoration and Mechanical Thrombectomy Device in a Swine Model of Acute Vessel Occlusion. American Journal of Neuroradiology. 2011;32(2): pp. 294-300.

[113]   Fesl G, Patzig M, Holtmannspoetter M, Mayer TE, Pfefferkorn T, Opherk C, et al. Endovascular Mechanical Recanalisation After Intravenous Thrombolysis in Acute Anterior Circulation Stroke: The Impact of a New Temporary Stent. Cardiovascular and Interventional Radiology. 2012;35(6): pp. 1326-1331.

[114]   Roth C, Junk D, Papanagiotou P, Keuler A, Korner H, Schumacher M, and Reith W. A Comparison of 2 Stroke Devices: The New Aperio Clot-Removal Device and the Solitaire AB/FR. American Journal of Neuroradiology. 2012;33(7): pp. 1317-1320.

[115]   Wenger K, Nagl F, Wagner M, and Berkefeld J. Improvement of Stent Retriever Design and Efficacy of Mechanical Thrombectomy in a Flow Model. Cardiovascular and Interventional Radiology. 2013;36(1): pp. 192-197.

[116]   Marks MP, And Que L, inventors. Intravascular Thromboembolectomy Device And Method Using The Same. World Intellectual Property Organization Patent 2013016435 A1. 2013.

[117]   Huffmaster A, inventor; SciMed Life Systems, Inc., assignee. Device for Removing a Blood Clot From a Blood Vessel. World Intellectual Property Organization Patent 2005016156 A1. 2005.

[118]   Mische HA, Ressemann TV, And Hoium SA, inventors; SciMed Life Systems, Inc., assignee. Expandable intravascular occlusion material removal devices and methods of use. United States Patent 5792157 A. 1998.

[119]   Voss L and Tremulis WS, inventors; Endovascular Technologies, Inc., assignee. Device for removal of thrombus through physiological adhesion. United States Patent 7004954 B1. 2003.

[120]   Wittens CHA, inventor; AngioDynamics, Inc., assignee. Thrombectomy Catheter And A Device Comprising The Same. United States Patent 20110190806 A1. 2011.

11

[121] Dacuycuy NJ and Ma J, inventors. Devices For Removing Vessel Occlusions. World Intellectual Property Organization Patent 2013071173 A1. 2013.

[122] Santra S, Mericle RA, Batich CD, Stanley JT, and Eskioglu E, inventors; University of Florida Research Foundation, Inc., assignee. Devices and Methods for Disruption and Removal of Luminal Occlusions. United States Patent 20100023038 A1. 2010.

[123] Porter SC, Kellett JB, and Kjos D, inventors; Stryker Corporation, assignee. Axially Variable Radial Pressure Cages For Clot Capture. World Intellectual Property Organization Patent 2012064726 A1. 2012.

[124] Ferrera D, Cragg AH, Fulkerson J, and Benjamin J, inventors; Mindfame, Inc., assignee. Thrombus Management Within Neurovasculature. United States Patent 20120316600 A1. 2012.

[125] Ferrera D, Rapaport A, Cibulski G, and Reiter A, inventors; Perflow Medical, Ltd., assignee. Method And Apparatus For Occlusion Removal. World Intellectual Property Organization Patent 2013109756 A2. 2013.

[126] Gerberding B, Jensen M, and Abrams RM, inventors; Pulsar Vascular, Inc., assignee. System and Methods for Capturing and Removing Blood Clots. World Intellectual Property Organization Patent 2012167137 A1. 2012.

[127] Steinke TA, inventor; Minnow Medical, LLW., assignee. Thrombus removal. United States Patent 20080262489 A1. 2008.

[128] Samson G and Carrison HF. Medical Clot Treatment Device with Distal Filter. United States Patent 20110082493 A1. 2011.

[129] Ben-Ami DJ, inventors; Triticum, Ltd., assignee. Device and Method for Removing Occlusions in a Biological Vessel. World Intellectual Property Organization Patent 2013105099 A2. 2013.

[130] Miloslavski E, Henkes H, Hannes R, and Monstadt H, inventors; Phenox, GmbH, assignee. Device for the Removal of Thrombi. United States Patent 20070198028 A1. 2007.

[131] Cully EH, Duncan JB, Luber KM, Montgomery WD, and Shaw EE, inventors; WL Gore & Associates, Inc., assignee. Systems For Removal of Atherosclerotic Plaque or Thrombus At A Treatment Site. World Intellectual Property Organization Patent 2013025531 A1. 2013.

[132] Kurz DR and Ferrera DA, inventors. Clot Retrieval Device. United States Patent 20040153110 A1. 2004.

[133] Olsen K, Skoedt C, Jensen AG, Christiansen F, and Elgaerd P, inventors; Cook, Inc., assignee. Thrombus Retrieval Device. World Intellectual Property Organization Patent 2010134940 A1. 2010.

[134] Barbut D, inventors; CoAxia, Inc., assignee. Medical Device for Removing Thromboembolic Material from Cerebral Arteries and Methods of Use. United States Patent 20020052620 A1. 2002.

[135] Zadno-Azizi G, Patel M, Muni KP, and Bagaoisan CJ, inventors; Percusurge, Inc., assignee. Catheter System For Containing And Removing Vascular Occlusions. World Intellectual Property Organization Patent 9838930 A1.1998.

[136] Kellner H, inventor. Endoscope for Removal of Thrombi from Pulmonary Arterial Vessels. United States Patent 4862874. 1989.

[137] Smalling R, inventors; Smalling Medical Ventures, LLC, assignee. Aspiration thrombectomy catheter system, and associated methods. United States Patent 20070161963 A1. 2007.

[138] Auth DC, Gordon LS, and Devore LJ, inventors; Boston Scientific Corporation, Inc., assignee. Percutaneous Aspiration Thrombectomy Catheter System. United States Patent 5827229. 1998.

11

[139]   Ogle MF, Webster MWI, Galdonik JA, and Boldenow GA. Thrombectomy Catheters And Other Aspiration Catheters. World Intellectual Property Organization Patent 2007022383 A2. 2007.

[140]   Johnson MS and Lalka SG, inventors; Advanced Research & Technology Institute, Inc., assignee. Thrombectomy treatment system and method. United States Patent 6719717 B1. 2004.

[141]   Hogendijk M, inventors; Novostent Corporation, assignee. Embolic Protection and Plaque Removal System with Closed Circuit Aspiration and Filtering. World Intellectual Property Organization Patent 2007011908 A2. 2007.

[142]   Bonnette MJ, Prather RR, and Thor EJ, inventors; Possis Medical, Inc., assignee. Gas Inflation/Evacuation System Incorporating A Multiple Element Valved Guidewire Assembly Having An Occlusive Device. World Intellectual Property Organization Patent 2007027563 A2. 2007.

[143]   Frisbie JS, inventors; Cardiometrics, Inc., assignee. Apparatus and Method for the Treatment of Thrombotic Occlusions in Vessels. World Intellectual Property Organization Patent 9726832. 1997.

[144]   Eli U, inventors. Implantable Device with Miniature Rotating Portion for the Treatment of Atherosclerosis, especially Vulnerable Plaques. United States Patent 20080269789 A1. 2008.

[145]   Kassab G, inventors. Thrombus Removal Systems and Devices and Method of Using the Same. United States Patent 20120316599 A1. 2012.

[146]   Stinis CT, inventor. Systems, Devices, and Methods for Removing Plaque from a Patient's Vasculature. European Patent 2670318 A1. 2013.

[147]   Eckhouse R, Sudin Y, and Eckhouse S, inventors; Rapid Medical, Ltd., assignee. Clot Removal Device with Steerable Element. United States Patent 20130325056 A1. 2013.

[148]   Evans MA, Demarais DM, Leeflang SA, and Eversull CS, inventors; Bacchus Vascular, Inc., assignee. Expansible shearing catheters for thrombus and occlusive material removal. United States Patent 20030055445 A1. 2002.

[149]   Homsma T, inventor; TMH Beheer BV, assignee. Catheter for Removing Blood Clots, has Radially Oriented Outlet Openings for Cleaning Agent Located in its Head. Dutch Patent 1034242. 2008.

[150]   Bonnette MJ, Morris JE, Wiesel SE, Bridgeman JB, Kozak DM, Beaupre RC, et al. , inventors; Possis Medical, Inc., assignee. Thrombectomy Catheter and System. United States Patent 6945951 B1. 2005.

[151]   Bonnette MJ and Le HV, inventors. IsolationThrombectomy Catheter System. United States Patent 20080275393 A1. 2008.

[152]   Nazari J, Davidson R, Kaplan K, and Fintel D. Adverse reactions to thrombolytic agents. Implications for coronary reperfusion following myocardial infarction. Medical toxicology and Adverse Drug Experience. 1987;2(4): pp. 274-286.

[153]   Chornenky VI and Forman MR, , inventors; Interventional Innovations Corporation, assignee. Systems and methods for drug delivery including treating thrombosis by driving a drug or lytic agent through the thrombus by pressure. World Intellectual Property Organization Patent 9711738 A1. 1997.

[154]   Herr M, Swaboda M, and Zagorsky M, inventors. Plaque Remover. United States Patent 20060271155 A1, Nov. 30, 2006.

[155]   Ya WD, inventor. Method of percutaneously removing a thrombus from a blood vessel by using catheters and system for removing a thrombus from a blood vessel by using catheters. United States Patent 5059178 A. 1991.

11

[156]   Tekulve K, inventor. Clot Removal System And Method. United States Patent 20130110082 A1. 2013.

[157]   Evans M and Dubrul WR, inventors; Bacchus Vascular, Inc., assignee. Thrombolysis Device. United States Patent 6508782 B1. 2003.

[158]   Steen A and Kian O, inventors; Cook Medical Technologies, LLC, assignee. Thrombus Removal Apparatus And Method. United Kingdom Patent 2498175 A. 2013.

[159]   Weber HP, Neufeldt KH, Ringelmann W, Gebauer A, Eggemann F, Heinze A, and Becker HM. Laser Recanalization of Peripheral Arteries. International Journal of Angiology. 1995;4(74):pp. 74-82.

[160]   Ambrosini V, Cioppa A, Salemme L, Tesorio T, Sorropago G, Popusoi G, et al. Excimer laser in acute myocardial infarction: Single centre experience on 66 patients. International Journal of Cardiology. 2008;127(1): pp. 98-102.

[161]   Shen ZJ, Garcia-Garcia HM, Schultz C, van der Ent M, and Serruys PW. Crossing of a calcified "balloon uncrossable" coronary chronic total occlusion facilitated by a laser catheter. A case report and review recent four years' experience at the Thoraxcenter. International Journal of Cardiology. 2009;145(2): pp. 251-254.

[162]   Reiser C, inventor. Method For Treatment Of Vascular Occlusions With Inhibition Of Platelet Aggregation. World Intellectual Property Organization Patent 03057060 A1. 2003.

[163]   Fischer FJJ, inventor. Wire Guided Thrombectomy Device. United States Patent 20100063488 A1. 2010.

[164]   Webster JR WW, inventor. Catheter for Removing Arteriosclerotic Plaque.

[165]   World Intellectual Property Organization Patent 8500510. 1985.

[166]   Lee G, Masden R, Weiss JA, Falk RL, Temes GD, Pool GE, et al. Percutaneous Peripheral laser Angioplasty: Demonstration of the clinical safety and efficacy of a new coaxial-guided laser-heated cap system. American Heart Journal. 1988;116(6): pp. 1640-1641.

[167]   Lammer J, Pilger E, Klein GE, Hausegger K, and Fluckiger F. Nd-YAG Laser Ablation of Arteriosclerotic Obstructions: Clinical Long-term Results in Femoropopliteal Artery Occlusions. Lasers in Medical Science. 1991;6(311):pp. 311-315.

[168]   Ashley S, Brooks SG, Gehani AA, Kester RC, and Rees MR. Percutaneous Laser Recanalisation of Femoropopliteal Occlusions using Continuous Wave Nd-YAG Laser and Sapphire Contact Probe Delivery System. Europese Journal of Vascular Surgery. 1994;8(4):pp. 494-501.

[169]   Geschwind H, Aptecar E, Boussignac G, Duboisrande JL, and Zelinsky R. Results Of Pulsed Laser Angioplasty Guided By Spectroscopy In Peripheral Arterial-Disease. Archives Des Maladies Du Coeur Et Des Vaisseaux. 1991;84(12): pp. 1837-1843.

[170]   Murray A, Mitchell DC, Grasty M, Wood RFM, Edwards DH, and Basu R. Peripheral Laser Angioplasty With Pulsed Dye Laser And Ball-Tipped Optical Fibres. The Lancet. 1989;334(8678-8679): pp. 1471-1474.

[171]   Edgell R and Yavagal DR. Acute endovascular stroke therapy. Current Neurology and Neuroscience Reports. 2006;6(6): pp. 531-538.

[172]   Roth LA, Herman SJ, Turnquist CR, Sinofsky EL, and Wong JY, inventors; C.R. Bard, Inc., assignee. Catheter System for Controlled Removal by Radiant Energy of Biological Obstructions. United States Patent 4817601. 1989.

[173]   Pallarito AL, , inventor. Optical Fibre and Laser for Removal of Arterial or Vascular Obstructions. United States Patent 5733277. 1998.

[174]   Macy JR WW, House MD, and Murphy-Chutorian DR, inventors; MCM Laboratories, Inc., assignee. Method and Apparatus for Detecting and Removing Plaque From Arteries by Laser. Canadian Patent 2003535. 1990.

11

[175] Berlis A, Lutsep H, Barnwell S, Norbash A, Wechsler L, Jungreis CA, et al. Mechanical thrombolysis in acute ischemic stroke with endovascular photoacoustic recanalization. Stroke. 2004;35(5): pp. 1112-1116.

[176] Bom N, Slager CJ, van Egmond FC, Lancee CT, and Serruys PW. Intra-Arterial Ultrasonic Imaging For Recanalization By Spark Erosion. Ultrasound in Medicine & Biology. 1988;14(4): pp. 257-261.

[177] Svilaas T, Vlaar PJ, van der Horst IC, Diercks GF, de Smet BJ, van den Heuvel AF, et al. Thrombus aspiration during primary percutaneous coronary intervention. the New England Journal of Medicine. 2008;358(6): pp. 557-567.

[178] Jolly SS, Cairns JA, Yusuf S, Meeks B, Pogue J, Rokoss MJ, et al. Randomized trial of primary PCI with or without routine manual thrombectomy. the New England Journal of Medicine. 2015;372(15): pp. 1389-1398.

[179] Jones DA, Rathod KS, Gallagher S, Jain AK, Kalra SS, Lim P, et al. Manual thrombus aspiration is not associated with reduced mortality in patients treated with primary percutaneous coronary intervention: An observational study of 10,929 patient with ST-segment elevation myocardial infarction from the London Heart Attack Group. JACC Cardiovasular Interventions. 2015;8(4): pp. 575-584.

[180] Berkhemer OA, Fransen PS, Beumer D, van den Berg LA, Lingsma HF, Yoo AJ, et al. A randomized trial of intraarterial treatment for acute ischemic stroke. the New England Journal of Medicine. 2015;372(1): pp. 11-20.

[181] Lock M. A study of buckling and snapping under dynamic load. El Segundo, CA: Laboratory Operations Aerospace Corporation. Report Number TR-0158 (3240-30)-3; 1967. pp. 1-55.

[182] Jelínek F, Smit G, and Breedveld P. Bioinspired Spring-Loaded Biopsy Harvester— Experimental Prototype Design and Feasibility Tests. Journal of Medical Devices. 2014;8(1): pp. 015002-1-015002-6.

[183] Heverly M, Dupont P and Triedman J 2005 Trajectory optimization for dynamic needle insertion. Proceedings of the 2005 IEEE International Conference on Robotics and Automation held at Barcelona, Spain, 18-22 April 2005. pp 1646-1651.

11

CHAPTER 12

MORCELLATOR FOR EQUINE CUSHING'S DISEASE

AIMÉE SAKES, EWOUT A. ARKENBOUT, FILIP JELÌNEK, HAN VAN DER KOLK, AND PAUL BREEDVELD.

Published in Veterinary Quarterly.

12

Abstract—A new paradigm of surgical treatment of equine Cushing's disease has been developed using the vascular system combined with a flexible morcellation instrument to reach the pituitary gland. The goal was twofold: (1) to design, prototype, and test an instrument that can reach the pituitary gland using the vascular system unique to equids and (2) to test the feasibility of the endovascular approach. The morcellator consists of a radial rotating cutting blade for tissue resection, a flexible shaft incorporating a cable drive for flexible actuation, and central morcellated tissue transportation lumen. The morcellator prototype was tested on a horse's cadaver head for the validation of the cutting blade design, actuator design, and feasibility of the endovascular approach. The overall assembled length of the morcellator tip was 13.9 mm, allowing for non-traumatic steering through the vascular system from the proximal end. The radially rotating cutting blade (barrel of Ø4 and 4.4 mm width) incorporated multiple cutting edges to deliver the action force during resection and provides the necessary grasping force to draw the tissue towards the second cutting edge of the morcellator incorporated inside the blunted cuboidal static tip element (5 mm square and wall-thickness of 0.3 mm). In the tests, the morcellator was successfully guided towards the pituitary and managed to sample pituitary tissue. Continued development of the prototype and the endovascular approach may in time improve the outcome and quality of life of horses suffering from Cushing's disease.

Keywords— Cushing's Disease, Design, Endovascular Approach, Equine, Horse, PPID, Morcellator, New Paradigm, Surgical Removal, Treatment

12

12.1. INTRODUCTION

12.1.1. Cushing's Disease

Cushing's syndrome describes the signs and symptoms associated with prolonged glucocorticoid excess. The American neurosurgeon Harvey Williams Cushing (1869-1939) was the first to describe it in man [1]. Cushing's disease refers to a pituitary-dependent cause of Cushing's syndrome rather than adrenocortical or iatrogenic glucocorticoid excess. In the equine species, a prolonged state of glucocorticoid excess is almost exclusively caused by pituitary disease and as a consequence, might be regarded as Cushing's disease per se [2]. To date, eponyms are not very popular anymore and preference is given to equine Pituitary Pars Intermedia Dysfunction (PPID) to describe the disease.

The occurrence of a pituitary pars intermedia adenoma in horses was first reported in Germany in 1932 [3]. The first description of hypertrichosis associated with a pituitary pars intermedia adenoma was in Sweden in 1956. In that report, seven kilograms of hair were combed off an 18-year-old warmblood mare [4]. Cushing's disease occurs commonly in aged horses with an average age of about 20 years [5-7]. In man, Cushing's disease predominantly occurs in women of childbearing age, but may occur at any age [8].

12.1.2. Treatment – Oral Medication Versus Surgical Treatment

In horses, treatment is aimed at controlling and reducing the severity of the clinical signs using oral medication, rather than removing the adenoma from the pituitary gland, due to the fact that to date, surgical removal has been technically impossible. Therapy in horses involves three classes of drugs: either dopamine agonists (e.g. bromocriptine and pergolide), serotonin antagonists (e.g. cyproheptadine), or a 3ß-hydroxysteroid dehydrogenase inhibitor (trilostane), acting to block adrenal steroidogenesis [10]. The prognosis of equine Cushing's disease is highly dependent on the effect of the medication, the observed clinical signs, the progression of the disease, and the willingness of the owner to properly manage the horse [5,9]. Therefore, new ways to treat Cushing's disease in horses are a necessity in order to provide a more effective treatment [5,9]. Especially so, since the incidence of equine Cushing's disease has increased over the last two decades in line with the enlargement of the population of elderly horses [11].

12.1.3. Treatment – Human Versus Horse

In humans, oral medication is not the treatment method of choice, instead surgical removal of the adenoma is commonly performed. Three significantly different surgical approaches – the transnasal transsphenoidal, transseptal transsphenoidal, and transcranial approach – provide access to the pituitary gland and allow for its removal [12].

12

Unfortunately, none of these surgical approaches are applicable for pituitary surgery in horses. If a surgical approach analogical to man was performed, such a surgery in horses would necessitate drilling through several centimeters of bone and the use of extremely long and slender instruments that are currently non-existent [13].

12.1.4. New Paradigm – Endovascular Surgical Treatment

Therefore, a new paradigm in pituitary surgery in horses was developed. In contrast to the human vascular system, the intercavernous sinus of the pituitary outflow tract can be accessed via a venous pathway unique to equids by means of the superficial facial vein midway between the anterior end of the facial crest and the ventral border of the mandible. This superficial vein can be used to guide a flexible instrument towards the pituitary gland; a procedure that has been previously described [14]. As such, this procedure was adapted for the purpose of the current design challenge.

12.1.5. Goals of this Study

The goal of this study was twofold: (1) to design, proto- type, and test an instrument that can reach and remove the equine pituitary gland using the vascular system unique to equids and (2) to test the feasibility of the endovascular approach. A previous literature survey determined mechanical morcellation as a potentially feasible removal method for the surgical treatment of Cushing's disease in horses [15]. Unfortunately, current mechanical morcellator designs such as the *Gynecare Morcellex* (Ethicon Endo-surgery, Somerville, NJ, USA) and *Truclear Ultra* (Smith&Nephew Endosurgery, Andover, MA, USA) are not compatible with the endovascular approach, necessitating redesign or complete redevelopment of these instruments for our purpose.

12.2. DESIGN PROCESS

12.2.1. Morcellator – Design Requirements

Geometry

To define the geometry of the morcellator, the dimensions of the equine vascular system, like the diameter, length, and bending radius, needed to be determined. Unfortunately, information on these dimensions was scarce, necessitating the need for cadaver experiments to deter- mine them. Therefore, three cadaver heads from adult Dutch Warmblood horses were drained of blood for dimension measurements. The drained lumens of the facial veins of the three cadavers were measured and determined as 6 mm in diameter on average. However, since the diameter of the veins decreases closer to the pituitary gland and the measured diameter was slightly larger than the actual in vivo diameter, as it was flattened due to the lack of blood, a maximum diameter of 5 mm was set as a design requirement. Subsequently, a radiopaque catheter (Ø3 mm, type 98402

12

Neoplex, Coloplast Porgès, Sarlat, France) was guided through the superficial facial vein and positioned in close contact with the pituitary gland, which was confirmed visually, to determine the minimal required length of the morcellator. The mini- mal required length was determined as 300 mm on average. However, to compensate for potential anatomical variations between horses, an extra length of 50 mm was added, setting the required total length of the morcellator to 350 mm. Finally, the minimal bending radius that the instrument needs to accommodate on route to the pituitary gland, constraining the rigid tip length, was determined and measured by taking an X-ray in the sagittal plane of the horse's head with the radiopaque catheter placed inside. It was determined that the minimum bending radius is situated just above the entry point and equals 21 mm (minimally).

Functionality

From a design perspective, using the equine vascular system as a surgical entry point to the pituitary gland will create considerable constraints for the surgical morcellator to be developed. To accommodate for the minimum bending radius and the remaining bends of the vascular system, a flexible morcellator that is capable of non-traumatic compliant steering through the vascular system is a necessity. For this purpose, and based on the minimum bending radius, a maximum rigid tip length at the distal end of the morcellator was set at 14 mm. Furthermore, since multiple simultaneous or consecutive instrument insertions are not feasible, as this would increase the chance of vascular damage, it was decided to develop a single flexible morcellation instrument able to continuously resect and remove tissue from the surrounding structures. The cutting blade should be internally force balanced, meaning that the forces associated with the cutting blade do not influence, and thus damage, the anatomical surroundings with exception of the actual tissue targeted for resection.

Size restrictions and the instrument's flexibility requirement have led to the decision for remote or proximal placement of the actuator. In order to transfer the actuator motion to the cutting blade at the instrument's tip, one flexible cable runs through the flexible shaft. Furthermore, the choice was made to develop a morcellator with radially rotating cutting blade. This design can resect in a continuous fashion, which saves time. Finally, aspiration is used for the removal and transportation of tissue debris from the operation site.

12.2.2. Morcellator – Final Design

The conceptual morcellator design was translated towards a detailed design (Figures 12.1 and 12.2), which formed the basis of the final manufactured prototype (see Figures 12.3 and 12.4). The final rigid tip design of the morcellator incorporates three functional elements: (1) a radially rotating cutting blade, (2) a static tip element, and (3) a connection

12

piece; linking the tip of the morcellator to the flexible shaft (see Figures 12.1 and 12.4). The overall assembled length of the tip is 13.9 mm, allowing for non-traumatic steering through the vascular system from the proximal end. The radially rotating cutting blade (barrel of Ø4 and 4.4 mm width, made out of high-speed steel) incorporates multiple cutting edges to deliver the action force during resection and provides the necessary grasping force to draw the tis- sue towards the second cutting edge of the morcellator incorporated inside the blunted cuboidal static tip element (5 mm square and wall-thickness of 0.3 mm). The design allows for unidirectional resection in a clockwise or counterclockwise direction.

The axially translating flexible steel cable (Ø0.3 mm), used for actuation of the cutting blade, is situated in an off-centered trapezoid slot incorporated in the cutting blade. The trapezoid slot provides a high surface area between the cable and the slot and has an automatic tightening effect on the cable. Both increase the mutual friction force during operation, and in turn provide smooth motion transfer from the cable to the cutting blade.

12
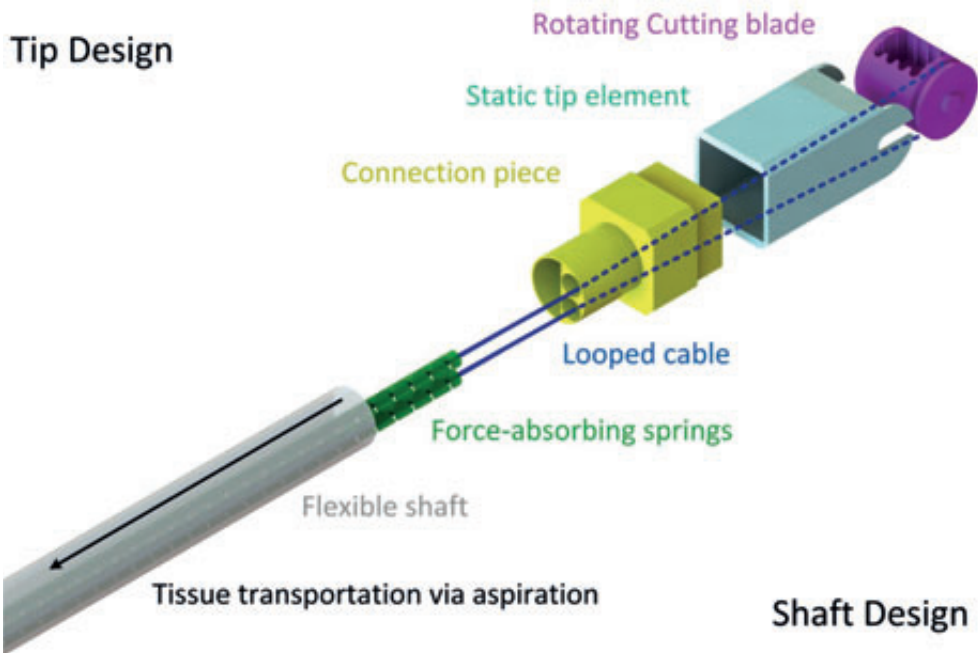
Figure 12.1— The Final Tip and Flexible Shaft Design of the Morcellator. The tip consists of the cutting blade (pink), rigid tip element (light blue), and connection piece (yellow). The shaft of the morcellator consists of the flexible cable (blue), two force-absorbing springs (green), and a flexible shaft (light gray). The black arrow indicates the aspiration force on the tissue, causing contact initiation and tissue transportation.
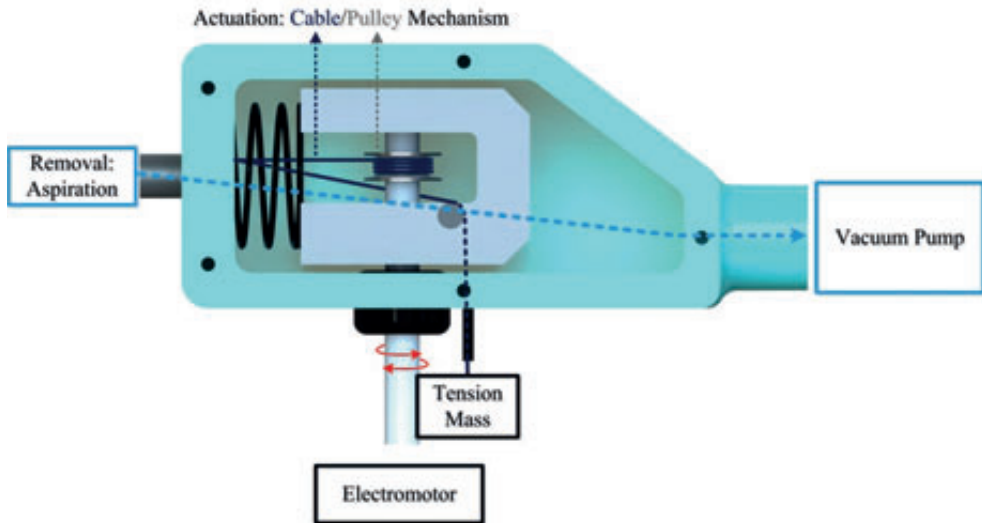
Figure 12.2— The Median Section of the Final Design of the Handle Piece of the Morcellator. The handle piece provides actuation and cable tensioning using the cable (blue)/pulley mechanism (silver) in combination with an electromotor and mass, respectively. The red arrows indicate the direction of motion of the actuator, either clockwise or counterclockwise. At the back of the handle piece, the vacuum pump is connected that removes tissue debris from the operation area (dotted light blue arrow).

The static tip of the morcellator is connected to the flexible shaft ($\varnothing_{outer}$ 5 mm, 1 mm wall-thickness, and 350 mm long), made out of polysiloxane; a common bio- compatible construction material for vascular catheters [16], by means of the connection piece. This connection piece also secures two force-absorbing springs that envelop the cable. The two main functions of these force-absorbing springs are to prevent kinking of the morcellator shaft during operation by absorbing the pulling forces and to protect the flexible shaft from damage potentially inflicted by the cable. Next to housing the cable actuator, the flexible shaft also allows for resected tissue pieces up to 1 mm in diameter to be transported towards the proximal end of the morcellator.

The handle piece (3D printed from Objet VeroBlue RGD840 material (Stratasys, Eden Prairie, MN, USA), using an *Objet Eden260V* 3D printer) is the connecting element for the actuation, cable tensioning mechanism, and aspiration mechanism of the morcellator, as illustrated in Figures 12.2 and 12.3. Actuation is achieved by connecting an electromotor with speed control (6271 DWAE, Makita, Anjo, Japan, 0–1300 rpm) to

12
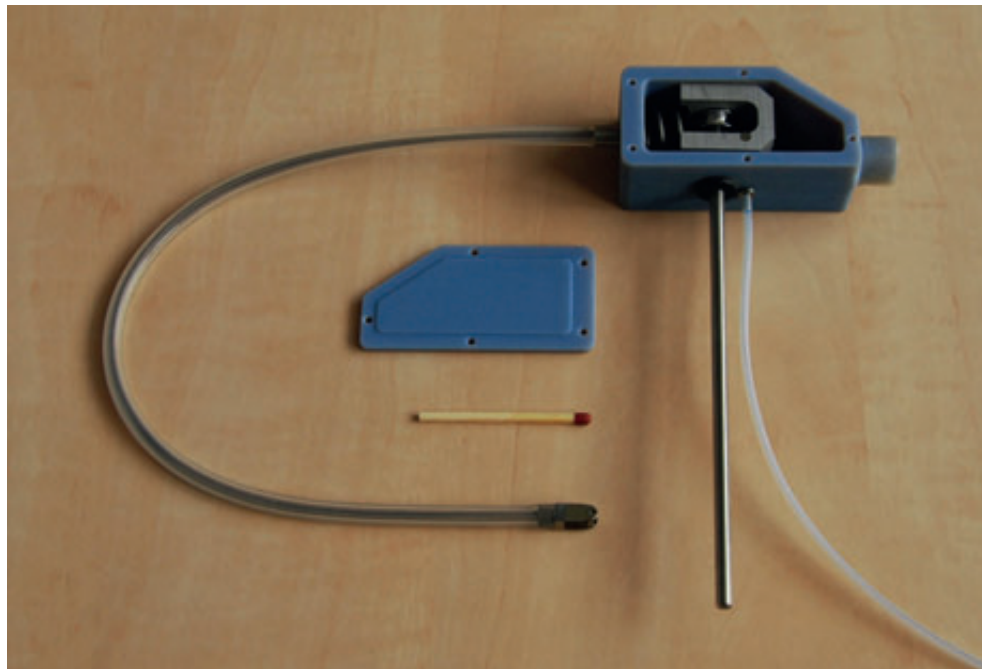
Figure 12.3— The Morcellator Prototype Including a Standard Match for Scale Purposes.

the drive axle. Cable tensioning is achieved by a mechanism consisting of a pulley, guide cylinder, and mass. In this mechanism, one cable end is connected to the pulley, whereas the second cable end is wound around the pulley, guided through the force- absorbing springs towards the cutting blade and back towards the handle piece, where it is connected to an adjustable mass that tensions the cable. Actuation of the drive axle subsequently causes the cable to rotate the cut- ting blade and at the same time to be wound around or unwound from the pulley. Finally, aspiration, and thus contact initiation and tissue transportation, is achieved by completely sealing off the handle piece in combination with the connection of a vacuum pump (TF1.5T/6651702, Brey, Memmingen, Germany, flow rate of 25 dm/min) to the handle.

12

12.3. PROOF OF PRINCIPLE EXPERIMENT

The main goals of the proof of principle experiment were threefold: (1) validating the endovascular approach for the surgical treatment of equine Cushing's disease, (2) validating the working principle of the flexible cable actuation, and (3) validating the working principle of the radially rotating cutting blade in combination with the applied aspiration. The prototype was validated using the set-up illustrated in Figure 12.5. In this
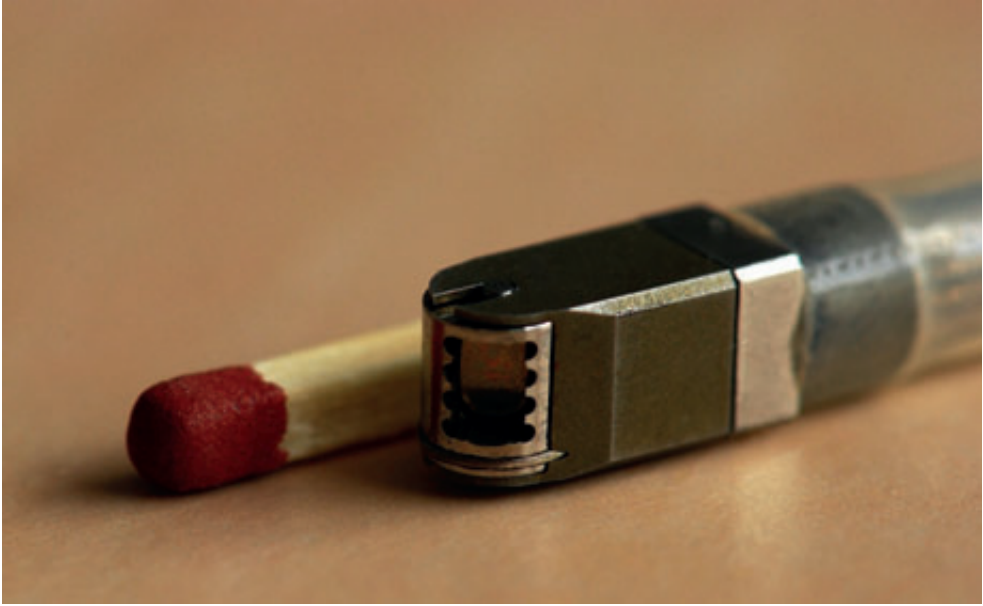
Figure 12.4— The tip of the prototype including a standard match for scale purposes.
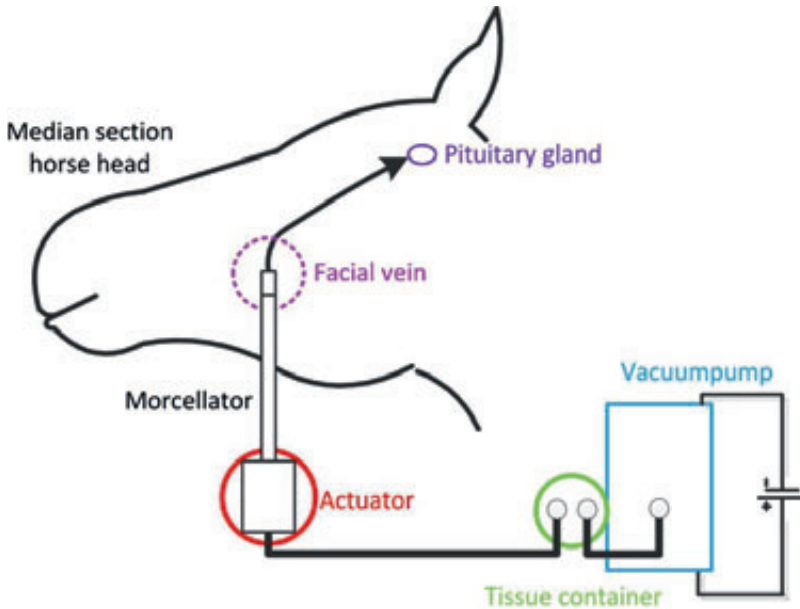
Figure 12.5— Proof of principle experiment test set-up. The morcellator is inserted in the facial vein (pink) and subsequently guided towards the pituitary gland (purple). The morcellator is actuated using a rotary electromotor (red). Aspiration is achieved by connecting tissue container (green) and vacuum pump (blue) to the morcellator and each other.

12

set-up, the morcellator was connected to the actuator, the vacuum pump, and a tissue container, after which it was inserted into the facial vein. To determine the required level of cable tensioning for smooth motion transfer from the cable to the cutting blade, the cable was tensioned with an adjustable mass until smooth energy transfer was obtained at 300 grams, providing approximately 3 N of cable tension force.

For the *in vitro* experiment, a head of a horse cadaver, which was cut into the midline for visualization of the pituitary gland, was used. A transcutaneous incision was made to expose the facial vein and gain entry to the vascular system. Subsequently, the morcellator was guided towards the pituitary gland by gently pushing it through the vascular system. After visual confirmation of the correct positioning of the morcellator with respect to the pituitary gland, the vacuum pump was turned on to initiate contact with the pituitary tissue, after which the actuator was turned on to start the resection and tissue transportation process.

12.4. RESULTS

After exposing and making an entry point into the superficial facial vein, the morcellator was successfully inserted in this vein. Passive steering through the vascular system was relatively easy to achieve with the morcellator able to reach the pituitary gland. Once positioned near the pituitary gland, the cable was capable of actuating the cutting blade without kinking or moving the flexible shaft. The friction force between the cable and the trapezoid slot proved sufficient in providing smooth motion transition of the axially translating cable to the radially rotating cutting blade, enabling the morcellator to remove a few small pieces of tissue from the pituitary gland. Furthermore, the cutting blade was able to resect pituitary tissue in the clockwise and counterclockwise direction by reversing the rotation direction of the actuator. The resection time in one particular direction was, however, limited by the cable length. In combination with the cutting blade design, the aspiration proved sufficient in providing con- tact initiation between the cutting blade and tissue. However, the aspiration proved insufficient to transport the tissue towards the tissue container.

12

12.5. DISCUSSION

The proof of principle experiment has illustrated that surgical treatment of Cushing's disease in horses via the endovascular approach is feasible. However, clinical application requires a continuation of the current research efforts. Effort should go into optimizing the design of the morcellator, determining the clinical implications of the approach, and finally towards clinical trials to determine the feasibility in multiple subjects.

12.5.1. Morcellator Design – Future Perspective

The current morcellator design should be optimized and expanded upon for clinical usage in future. At present, the morcellator has a relatively low tissue resection speed. Therefore, more research should go into optimizing the cutting blade design. Furthermore, in combination with the cutting blade design, the aspiration force on the tissue should be increased. This will not only positively affect the resection speed, but is also a necessity to prevent clogging of the shaft. Finally, a redesign of the tensioning and pulley mechanism is necessary to allow for continuous operation of the morcellator.

Expansion of the current design should go towards adding a means of visualizing the pituitary gland and surrounding structures, as well as into adding a means to actively deflect the morcellator. The visualization aid should be able to make a distinction between blood, healthy tissue, and neoplastic tissue. This is, for example, possible by using IntraVascular UltraSound or Optical Coherence Tomography. In combination with visualizing the operation area, the ability to actively deflect the tip is necessary to increase the precision with which the instrument can be operated. This will both contribute to reaching the pituitary gland without damaging the blood vessel wall and aid in more precise removal of the adenoma with minimal loss of healthy tissue.

12.5.2. Clinical Application – Endovascular Approach

The endovascular approach and its implications should also be considered. Since as of today, no surgical treatment of the equine pituitary gland has been attempted, the post-surgical results are still unclear. The chance of post-removal bleeding is present as well as the potential damage to the surrounding structures. Furthermore, the presence of the morcellator in the vascular system may potentially cause damage to the vascular system, such as the valves and vessel wall.

12.6. CONCLUSIONS

The morcellator prototype has an innovative flexible cable-actuated cutting blade design that is currently not seen in any other clinically applied flexible instrument. The prototype has illustrated the feasibility of the endovascular approach for the surgical treatment of Cushing's disease in horses. Continued development of this approach may in time improve the quality of life of horses suffering from Cushing's disease.

12

REFERENCES

[1]   Cushing H. The basophil adenomas of the pituitary body and their clinical manifestations (pituitary basophilism). Bulletin of the Johns Hopkins Hospital. 1932; 50: pp.137-195.

[2]   van der Kolk JH, IJzer J, Overgaauw PA, van der Linde-Sipman JS. Pituitary-independent Cushing's syndrome in a horse. Equine Veterinary Journal. 2001; 33(1): pp. 110-112.

[3]   Pallaske G. Some cases of rare neoplasms in domestic animals. Journal of Cancer Research. 1932;36: pp. 341-353.

[4]   Eriksson K, Dyrendahl S, Grimfelt D. A case of hirsutism in connection with hypophyseal tumour in a horse. Nordisk Veterinaer Medicin. 1956; 8(807): pp. 807-814.

[5]   Love S. Equine Cushing's disease. British Veterinary Journal. 1993; 149(2): pp. 139-153.

[6]   van der Kolk JH, Heinrichs M, van Amerongen JD, Stooker RC, in de Wal LJ, van den Ingh TS. Evaluation of pituitary gland anatomy and histopathologic findings in clinically normal horses and horses and ponies with pituitary pars intermedia adenoma. American Journal of Veterinary Research. 2004; 65(12): pp. 1701-1707.

[7]   McFarlane D. Advantages and limitations of the equine disease, pituitary pars intermedia dysfunction as a model of spontaneous dopaminergic neurodegenerative disease. Ageing Research Reviews. 2007; 6(1): pp. 54-63.

[8]   Thorner MO, Vance ML, Laws ER Jr, Horvath E, and Kovacs K. The anterior pituitary. Chapter in: Williams textbook of endocrinology (9th ed.). Philadelphia, PA: WB Saunders Company. 1998. pp. 254-255.

[9]   Grenager N. How does Cushing's disease relate to Laminitis? Advances in diagnosis and treatment. Journal of Equine Veterinary Science. 2010; 30(9): pp. 482-490.

[10]   Beech J. Treatment of hypophysial adenomas. Compendium on Continuing Education for the Practising Veterinarian. 1994; 16: pp. 921-923.

[11]   Jones WE. Questions about Cushing's syndrome. Journal of Equine Veterinary Science. 2004; 24(4): pp. 144-145.

[12]   Schwartz TH, Fraser JF, Brown S, Tabaee A, Kacker A, Anand VK. Endoscopic cranial base surgery: classification of operative approaches. Neurosurgery. 2008; 62(5): pp. 991-1005.

[13]   Riegel RJ, Hakola SE. Illustrated atlas of Clinical Equine anatomy and common disorders of the horse (1st ed.). Marysville, WA: Equistar Publications, 2004.

[14]   Irvine CHG, Alexander SL. Novel technique for measuring hypothalamic/pituitary function. Journal of Endocrinology. 1987; 113: pp. 183-192.

[15]   Sakes A, Arkenbout EA, van der Kolk JH, Breedveld P. A comprehensive overview of removal methods for the surgical treatment of Cushing's disease for human and veterinary applications. Journal of Medical Devices. 2013; 7(2): pp. 020905-1-020905-3.

[16]   Canaud B. Reducing infections associated with central vein catheters. Seminars in Dialysis. 2000:13(3): pp. 206-207.

12

CHAPTER 13

MINIATURE BIOPSY NEEDLE FOR DUCTOSCOPY

AIMÉE SAKES, KEVIN SNAAR, GERWIN SMIT, ARJEN J. WITKAMP, AND PAUL BREEDVELD

13

Abstract—The majority of the benign and malignant lesions in the breast arise from the ductal epithelium and terminal ductlobular unit. A minimally invasive procedure called ductoscopy is able to visualize these lesions as it inspects the ductal epithelium using a small micro-endoscope. Unfortunately, it is currently challenging to obtain a tissue sample during ductoscopy and reach the most distal duct. In this study we have, therefore, developed a novel miniature (Ø1.2 mm) biopsy needle that can be used during ductoscopy. This biopsy needle consists of two coaxial counter-rotating hollow blades with a distal cutout to resect lesions from the ductal wall. Three cutouts were manufactured resulting in a *beveled*, *straight*, and *reverse-beveled* blade. The blades were actuated using a novel mechanism containing two helical paths that allows for the counter-rotating motion of the blades at different velocities. In a proof-of-principle experiment, the performance of the biopsy needle was evaluated using a polymeric duct model and gelatin tissue phantom. During the experiment, the straight and reverse-beveled blades were able to obtain a sufficiently large tissue sample for histopathological examination. Based on these promising results, a second experiment was performed in which the micro-endoscope was integrated in the needle and we were able to take a biopsy from a chicken breast. In a future clinical instrument, the biopsy needle will be miniaturized and optimized to allow for an efficient, safe, and effective intraductal biopsy procedure without the need for an invasive excisional biopsy procedure.

Keywords— Biomedical Equipment, Biopsy Needles, Ductoscopy, Medical Instrument Design.

13

13.1. BACKGROUND

13.1.1. Ductoscopy for Early Cancer Detection

The majority of benign and malignant lesions (tumors) of the breast arise from the ductal epithelium (approximately 85%) and the Terminal DuctLobular Unit (TDLU, i.e. milk-producing gland) [1-3]. Current breast cancer diagnosis modalities play a vital role in primary screening for breast cancer, diagnosing lesions, treatment selection, progression monitoring, and in determining cancer recurrence. However, by the time a lesion is found by the patient herself or with the preferred population based method, namely mammography, the lesion has been growing for approximately 8 years [4]. The cancerous breast tissue is usually about 1 cm at the time it is palpable, and Ø5–10 mm when detected by mammography [4]. Early detection of breast cancer plays a vital role in increasing the survival rate of women [5].

A minimally invasive procedure called "ductoscopy", "mammary ductoscopy" or "breast endoscopy" has revolutionized breast disease diagnosis, as it is able to visualize smaller lesions (Ø0.1 mm) compared to mammography, ultrasound, and MRI, and provides surgeons direct access to the ductal epithelium [2]. Ductoscopy can be performed as an in-office or out-patient diagnostic procedure using a local anesthetic [3]. In ductoscopy, the mammary ductal epithelium is inspected using a small Ø0.45–1.2 mm fiberoptic micro-endoscope that magnifies the duct up to 60 times normal size and provides high-quality images (10.000 pixels, see Figure 13.1) [3, 6, 7]. The micro-endoscope is used in conjunction with a cannula containing 2 or 3 lumens; one for the endoscope, one irrigation lumen, and one for an additional tool, such as a (biopsy) forceps [3]. The cannula is inserted into the breast milk ducts via the nipple surface. Subsequently, the milk duct of interest is dilated using saline and the micro-endoscope is gently advanced into the duct under video guidance. After assessment of the main ducts, side ducts or branches are evaluated until further advancement is no longer possible due to the size of the cannula (Ø1.15–1.4 mm) [3].

13.1.2. Current Challenges

Although current ductoscopy instruments are effective tools for early detection of breast lesions, some limitations still need to be overcome to allow for widespread application of this technology. Due to the micro-endoscope's diameter and relatively short length (~150 mm), the current ductoscope is unable to reach the peripheral small branches of the ducts and is thus also unable to visualize the TDLU [2, 3]. Although the main central milk ducts are examined, which drain approximately 75% of the breast volume, it is unknown if these ducts represent the most common site where breast lesions arise [7]. To overcome this limitation, smaller and longer micro-endoscopes are needed [3, 6, 7].
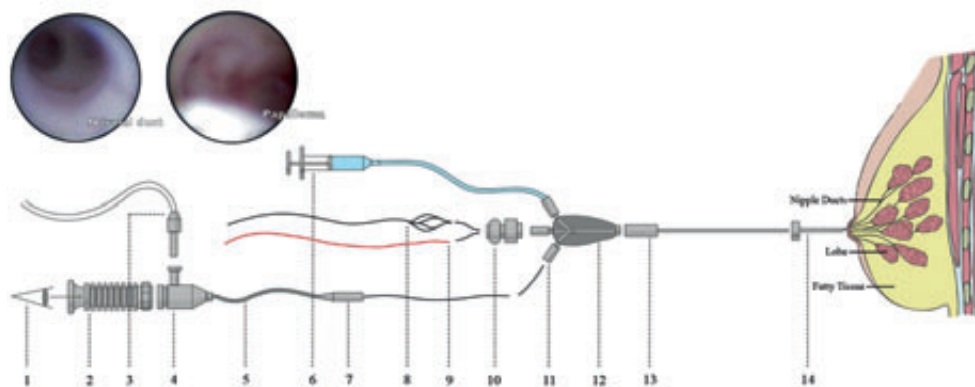
13

Figure 13.1— Overview of a Ductoscope. The ductoscope contains a cannula (Ø1.15–1.4 mm; stainless steel or Polyshaft tube (13)) connected to a hub/handle (12) to insert the micro-endoscope (7 inserted in 11), irrigation fluid (6), and other tools (such as a biopsy basket (8) and laser wire (9) via a connector (10)). During the first step of the surgery surgeon enlarges the milk duct using the lumen expander (14), followed by the insertion of the cannula (13) containing the micro-endoscope. To obtain the images, the micro-endoscope is coupled to an auto fluorescence endoscopic imaging system (3, 4, 5, and 7) via a custom-made eyepiece (2). When the milk duct is entered a salt solution (6) is used to enlarge the milk ducts diameter. During the procedure the surgeon can view the milk duct on a LCD monitor (1). After the entire breast is examined the instrument is extracted, finishing the procedure.

The second limitation that needs to be overcome during ductoscopy is related to histological verification of the findings. Unfortunately, it is not always possible to make a final diagnosis based on visual appearance of the lesion. Diagnostic accuracy based on visual appearances alone is in between 39 and 97% depending on the lesion type and visibility [2, 3]. Lesions identified during ductoscopy are most commonly assessed by ductoscopy-directed surgical removal (also known as excisional biopsy) for a definitive diagnosis of the suspicious lesion, which is a cumbersome and invasive procedure in which the entire lesion is surgically removed [3, 6]. In order to minimize the need for excisional biopsy, an intraductal biopsy instrument is needed [3]. Unfortunately, no reliable intraductal biopsy instruments is currently available capable of obtaining tissue sample suitable for histological diagnosis [3, 6]. The development of intraductal biopsy instruments has been limited by the small diameter of the working channel of the cannula, which severely limits the available space to integrate a biopsy instrument [7].

13.1.3. Goal of this Study

This paper describes the development a novel intraductal biopsy instrument that can be inserted in the cannula of a ductoscope and allows for taking a biopsy under direct guidance of the micro-endoscope. The development of an intraductal biopsy instrument is a necessity to allow for early diagnosis of breast cancer precursors and enable a histologic

diagnosis without the need for surgical excision [3]. To allow for future examination closer to the TDLUs, the biopsy instrument has been designed with further miniaturization in mind.

13.1.4. Layout of this Study

In Section 14.2, an overview of the current state of the art in biopsy devices used during ductoscopy and percutaneous biopsy is given. In Section 14.3, the design requirements and the resulting designs of the tip and handle are discussed. Section 14.4 describes the validation of the prototype biopsy needle. The results of this experiment will be discussed in Section 14.5. As the results of these experiments were promising, an ex-vivo animal test was performed and described in Section 14.6. Finally, the results of both experiments are discussed in Section 14.7 and a conclusion will be drawn in Section 14.8.

13.2. STATE OF THE ART IN BIOPSY DEVICES

As of today, ductoscopy has been combined with ductal lavage cytology, in which a double-lumen catheter is used to inject saline into the milk duct, and subsequently retrieve this using suction, to obtain cells from the epithelium and as such increase the diagnostic sensitivity of the procedure. An advantage of ductal lavage is that cells can be obtained from the TDLU even if this part cannot be reached with the ductoscope [3]. However, this biopsy method has a relatively low cellular yield and is also unable to obtain a tissue sample for histological examination.

Additionally, a variety of devices has been developed to pass down the working channel of the cannula to obtain a histologic specimen. Examples of such devices are biopsy baskets, cytological brushes, and biopsy forcipes. Biopsy baskets (see Figure 13.1) consist of flexible metallic coils, which are expanded in, or distal to, the lesion, and subsequently retracted to obtain the tissue sample, whereas a cytological brush contains radially orientated bristles (see Figure 13.2 Top Left). Two clinically available cytology brushes are the *Cellebirty Single-Use Cytology Brush* (Ø1.0–2.0 mm; Boston Scientific, Marlborough, MA, USA) [8] and the *Infinity ERCP Sampling Device* (Ø2.5–3.0 mm; USEndoscopy, Mentor, OH, USA) [9]. Biopsy forcipes resemble regular forcipes except that they are hollow to resect and, subsequently, enclose the tissue sample (see Figure 13.2 Top Right). Different tip jaws are available from smooth to toothed variants, such as the reusable *Oval Cup (with Needle)* and *Alligator Swing-Jaw* biopsy forcips (Ø1.2–2.8 mm; Olympus, Center Valley, PA, USA) [10]. Biopsy forcips are available with a rigid and flexible shaft, making them suitable for both needle and catheter interventions. During the procedure, the forceps is placed over the target tissue, after which the tip jaws are closed to obtain the tissue sample (see Figure 13.2 Top Right).

The addition of these instruments during ductoscopy results in a greater cellular yield than with ductal lavage cytology alone [3]. However, biopsy baskets and brushes

13

have been designed for collecting soft, mostly in-coherent, tissue types and not for high precision resection of high-density breast tumor tissue from the ductal wall. Biopsy forceps, on the other hand, require the micro-endoscope to be retracted during the biopsy procedure and additional room for opening the device tip, which is not always possible as space is limited in the milk duct.

If a small lesion is detected during ductoscopy and no tissue sample could be obtained using the previously mentioned methods and devices, the patient is referred for excisional biopsy (in which the lesion is surgically removed) or, on some occasions, to ductoscopy-directed core biopsy. In core biopsy, a small tissue core is removed from the patient using a special core biopsy needle, which preserves the obtained tissue architecture; enabling histological analysis. Core biopsy needles can be distinguished based on the tip design, which can be subdivided into "side cut", in which the biopsy is obtained along at the circumference of the biopsy needle or "end cut", in which the biopsy is obtained at the distal end of the needle. Side cut (also known as "Tru-cut") biopsy needles consist of an inner solid stylet with a rectangular cutout and an outer hollow cutting needle, such is seen in *SemiCut* (Ø0.9–2.1 mm; MDL, Tavani, Italy; Figure 13.2 Bottom Left) [11]. These types of needles are introduced with the stylet slightly in front of the outer cutting needle. After the stylet is advanced into the lesion, the cutting needle is advanced over the stylet resulting in the containment of the tissue inside the rectangular cutout (Figure 13.2 Bottom Left). The *BioPince* (Ø1.2–1.8; Argon medical devices, Plano, Texas) end cut design consists of three parts: a sharp inner stylet (i.e. a solid sharpened rod) surrounded by an inner hollow coring cannula and an outer cannula with a pincer [12]. During a biopsy the needle is advanced with the stylet slightly protruding from both cannulas. Near the lesion the inner coring cannula is advanced over the stylet; cutting the tissue, where after the outer cannula with pincer slides over the inner coring cannula and cuts off the core of tissue at the distal end of the needle (Figure 13.2 Bottom Right).

As of today, (core) biopsy needles have not been combined with ductoscopy. The main reason is that they do not allow for integration with the micro-endoscope. The side cut needles are solid and thus do not contain a lumen for guiding the micro-endoscope. Furthermore, both the side cut and end cut biopsy needles are currently too long to fit the 180 mm long micro-endoscope.

13

13.3. DESIGN PROCESS

13.3.1. Design Requirements

To obtain a tissue sample during ductoscopy, the biopsy needle should meet the following requirements. The biopsy structure should be able to resect all types of breast lesions that can be encountered. The Young's moduli of these lesions are reported to have
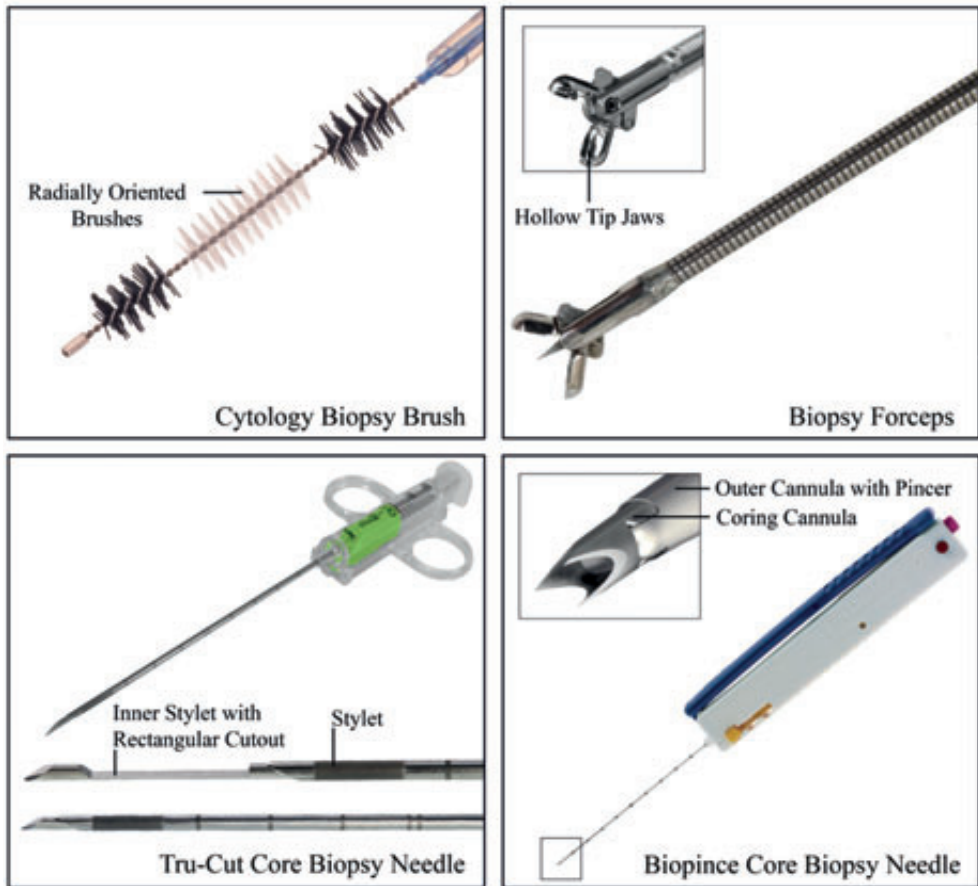
Figure 13.2— State of the Art Biopsy Needles, Forcipes, and Brushes. Top Left: *Infinity ERCP Sampling Device* (Ø2.5–3.0 mm; USEndoscopy, Mentor, OH, USA). Top Right: Biopsy Forceps *Mini Oval Rat Tooth* (Olympus, Center Valley, PA, USA). Bottom Left: *Tru-Cut* biopsy needle *SemiCut* (MDL, Tavani, Italy) using the side-cut mechanism. Bottom Right: *Biopince* biopsy needle (Argon Medical Devices, Plano, Texas) using the end-cut mechanism. Figures adapted from [9-12].

13

a value of in between 34.5–201.9 kPa [13]. To obtain a sample that is usable for the pathologist, the sample cells need to be intact and sufficiently large with a minimum number of 10 cells, which are in perfect condition. However, it is preferred to obtain a larger sample of at least 0.5 mm. Furthermore, during the removal of the instrument the tissue should be confined inside the cannula.

During insertion of the combined diagnostic and biopsy instrument into the nipple, several clinical situations can be encountered depending on the character development

stage of the lesion. At the early stage of the development of the lesion, the cells are confined within the milk duct epithelium (Figure 13.3A). At this stage the lesion is not (easily) visible during ductoscopy. When the condition progresses, the cells can protrude into the milk duct itself; partly obstructing the duct (Figure 13.3B). Finally, the entire duct can be filled with cells (Figure 13.3C). The biopsy needle should be able to take a biopsy from all these different clinical situations. When the cells fill the complete duct, the instrument needs to be able to take an end cut, while in a partially filled duct a side-cut mechanism is preferred. Therefore, the biopsy instrument should combine an end-cut and side-cut mechanism.

To allow for easy integration of the biopsy needle into the ductoscopy procedure, the device should fit into an existing cannula, which has an inner diameter of 1.2 mm, and an outer diameter of 1.4 mm. For diagnosis and visualizing purposes, the Ø0.55 mm fiber optic endoscope *LaDuScope T-flex* (Polydiagnost, Hallbergmoos, Germany) should be able to be guided through the biopsy needle and allow for an unobstructed view of the milk duct during the biopsy procedure. Additionally, for duct enlargement, an irrigation channel should be present. Finally, the biopsy needle should be able to be miniaturized towards a sub-millimeter scale to allow for inspecting the most distal milk ducts and TDLU.

13.3.2. Tip Design

Based on the design requirements, a needle tip design was developed. The tip design consists of two axially counter-rotating coaxial tubular cutting blades surrounded by an optional cannula (see Figure 13.4). The biopsy needle can be equipped with three types of cutting blades: *beveled blades, straight blades*, and *reverse-beveled blades*. The *beveled blade* design resembles a scissor and contains a triangular cutout ($L = 3$ mm, $w =$ radius of the blade r) with a blunt 95° angle between the horizontal and the cutting edge, resulting in a 10° angle between the blades (see Figure 13.4). The *straight blade* design

13

A   B   C
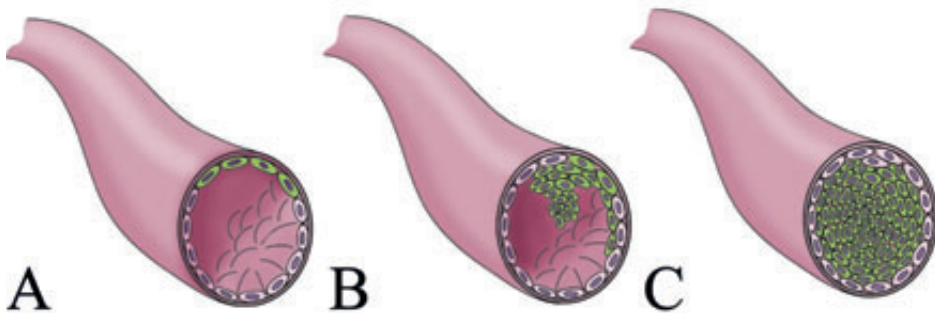
Figure 13.3— Diseased Milk duct at Different Developmental Stages. A Milk duct with cancerous cells in the epithelium (ductal wall). B: Milk duct with cancerous cells protruding into the ductal lumen. C: Milk duct completely filled with cancerous cells. The green cells represent the cancerous cells/lesion.

contains rectangular (90°) cutouts (L = 3 mm, $w = r$), resulting in axially directed cutting blades. The *reverse-beveled blade* design contains a sharp 85° angle between the horizontal and the cutting edge, resulting in a 10° angle between the blades (see Figure 13.4).

Based on the encountered clinical situation (see Figure 13.3), different modes of operation can be applied. In a semi-filled milk duct, a tangential force can be applied on the cancerous tissue by maneuvering the blades around the tissue and, subsequently, axially rotating the blades in opposite direction. In a completely filled milk duct, the blades are pushed forward into the tissue, during or after which a rotational motion can be applied.

13.3.3. Handle Design

To allow for handheld operation and actuation of the blades of the biopsy needle, a handle was designed. The actuation mechanism was designed to counter-rotate the blades at equal (but opposite) velocity, controlled by one hand. Furthermore, the cannula should be able to move over the axial axis to shield the blades during the insertion and retraction process, and expose the blades during the resection process.

The final handle design is illustrated in Figure 13.5. The handle consists of five main parts: (*A*) an outer shell, (*B*) a rotational bearing of the inner blade, (*C*) a helical tube containing two counter-rotating helical paths, (*D*) a rotational bearing of the outer blade, and (*E*) a cap connected to the cannula. The helical tube contains two helical slots; one rotating counter clockwise and the other rotating clockwise, allowing for the desired counter-rotating movement of the bearings *B* and *D* that run in these slots and that are connected to the inner and outer blade, respectively (see Figure 13.6). The handle is operated by axially translating the helical tube (*C*). The cap *E* can be translated over the outer shell *A* to move the cannula backwards and forwards for shielding the blades during insertion and retraction.

13.3.4. Prototype Design

The final design was translated into a prototype consisting of 24 parts (see Figures 13.7 and 13.8). The cutouts of the blades were manufactured using electric discharge machining, resulting in a length of 3 mm, and width of 0.5 and 0.6 for the inner and outer blade, respectively (see Figure 13.9). Subsequently the blades were sharpened using a small file. The overall length of the needle was set to 100 mm (measured from the cap *E*).

To minimize friction losses, low friction material combinations were used for the functional parts. The cannula and cutting blades were manufactured out of stainless steel. Parts (B_1), (B_2), (D_1), (D_2), (G) and (H) were made out of aluminum, whereas brass was

13

used for part (C_1) and (C_2). Two nylon rings (*F*) were fitted around the bearings B_i and D_i to prevent axial translation of the inner- and outer bearing and allow for smooth rotational motion. Figure 13.10 shows the final assembled prototype.
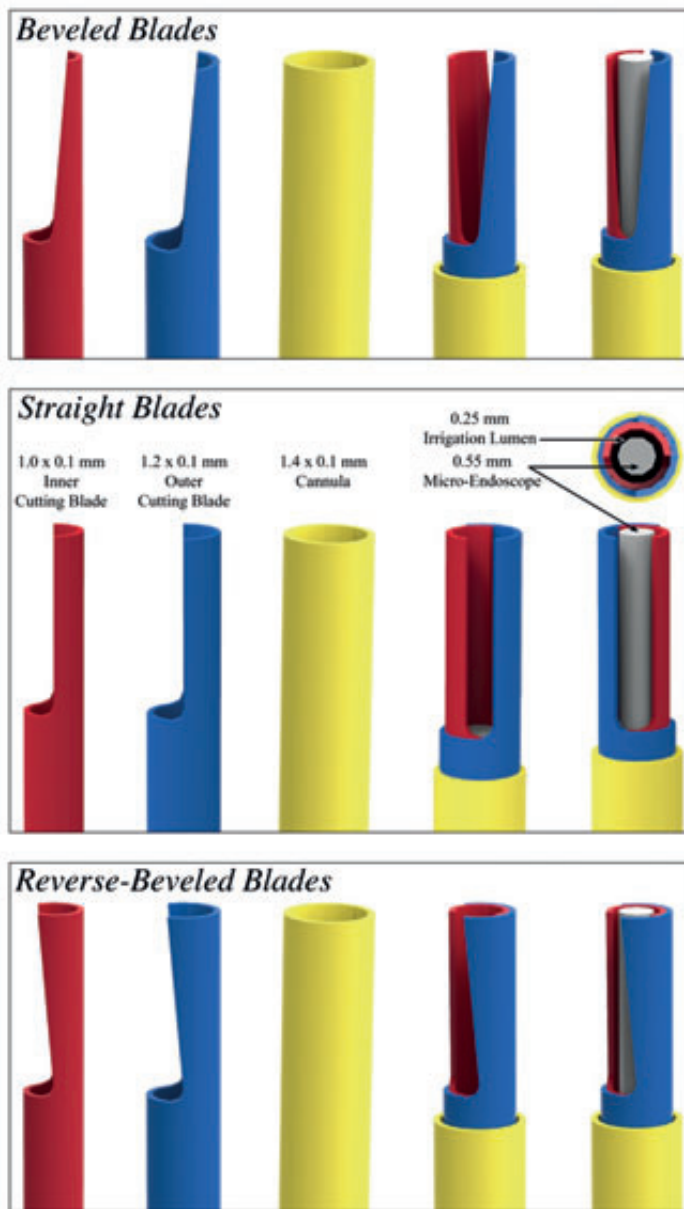
Figure 13.4— Biopsy Needle Tip Designs. The biopsy needle tip consists of three parts: an inner cutting blade (Ø1.0x0.1 mm, red), an outer cutting blade (Ø1.2x0.1 mm, blue), and an optional cannula (Ø1.4x0.1 mm, yellow). The Ø0.55 micro-endoscope can be placed in the Ø 0.8 mm lumen of the biopsy

needle, leaving room for a concentric irrigation channel. Three different blade designs have been manufactured: Top—*beveled blade* design. Middle—*straight blade* design. Bottom—*reverse-beveled blade* design. For explanation see text.
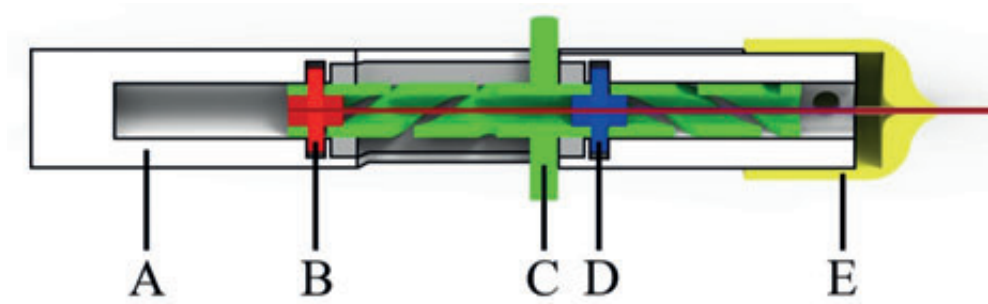
Figure 13.5— Handle Design of the Biopsy Needle. The handle of the biopsy needle consists of: A: outer shell, B: rotational bearing connected to the inner cutting blade, C: helical tube, D: rotational bearing connected to the outer cutting blade, and E: cap connected to the cannula to shield the blades during insertion and retraction.
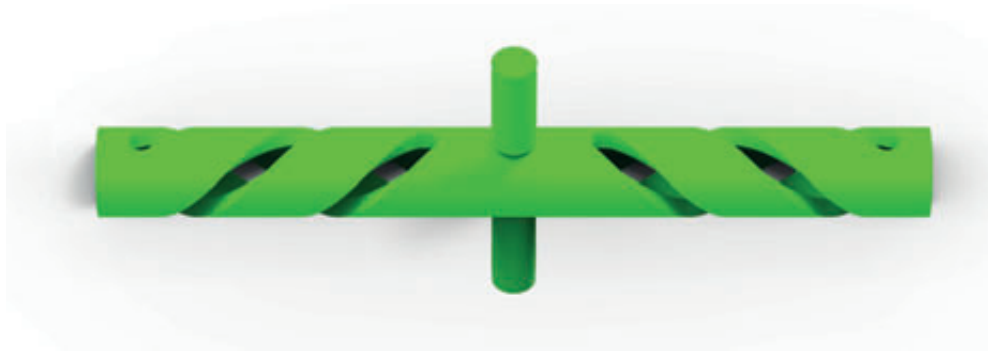
Figure 13.6— Detail of Helical Tube with Control Rods. The angle of the helical paths was set to 45° with the number of revolutions equal to one to allow for one complete rotation of the inner and outer cutting blade during a cycle.

The following steps have to be followed to obtain a biopsy with the prototype biopsy needle (see Figure 13.11). First, the biopsy needle is inserted into the milk ducts with the cannula shielding the cutting blades to prevent damage to the milk ducts.

The milk ducts are examined by the micro-endoscope inserted in the biopsy needle's lumen. Once a lesion is detected, the cannula is translated backwards to expose the cutting blades. Subsequently, the two control rods are pushed forwards or backwards to counter-rotate the blades at equal, but opposite, velocities, to obtain the biopsy. After a

13

successful biopsy procedure, the blades are covered by the cannula and retracted from the milk duct.
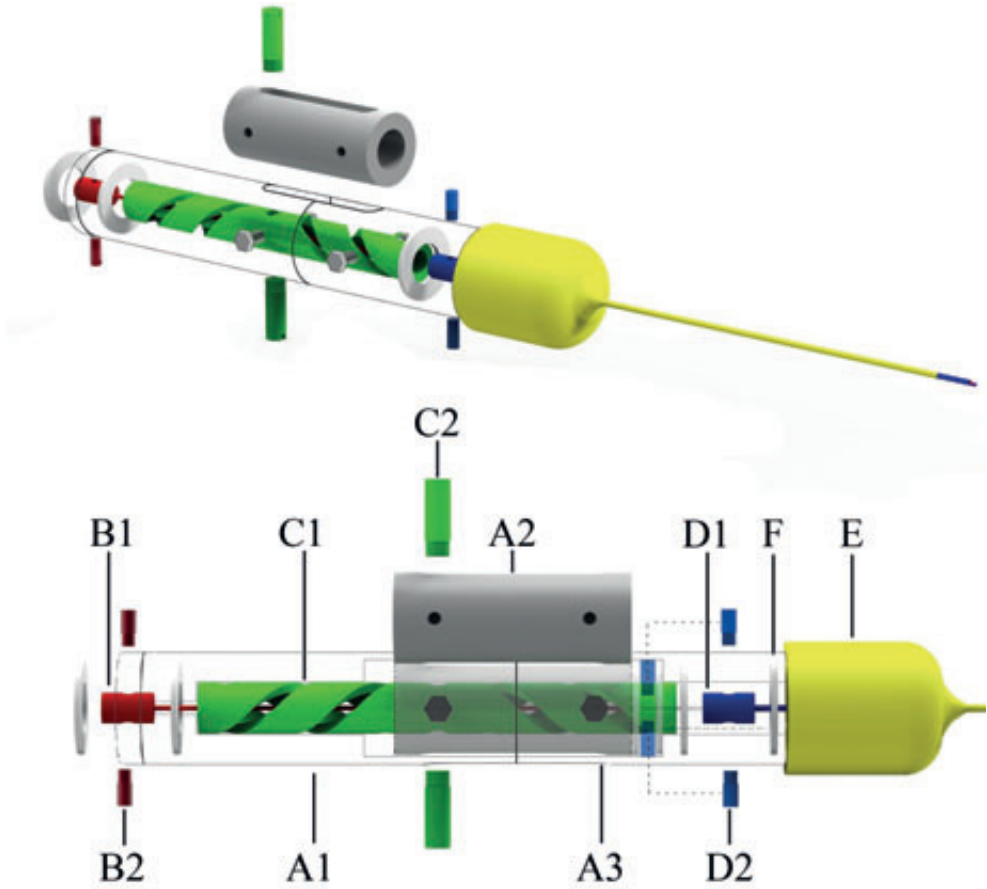
Figure 13.7— Biopsy Needle Handle Design – Exploded View. Top row: perspective view, Bottom row: side view. Letter indications: A1: bottom tube, A2: middle tube, A3: top tube, B1: inner bearing connected to the inner cutting blade, B2: cylindrical protrusions, C1: helical tube, C2: control rods (2x), D1: outer bearing connected to the outer cutting blade, D2: cylindrical protrusions, E: cap connected to the cannula, and F: nylon rings (4x).

13

13.4. PROOF-OF-PRINCIPLE EXPERIMENT

13.4.1. Experiment Goal

In order to evaluate the prototype, a proof-of-principle experiment was set up. The main goal of the experiment was to determine whether the proposed prototype is able to obtain a biopsy from a ductal wall.

Figure 13.8— Prototype Biopsy Needle showing all the parts.

13.4.2. Experimental Variables

The mechanical cutting performance of the prototype biopsy needle was evaluated based on its ability to obtain a tissue sample (Y/N) of a phantom. To give an indication about the effectiveness of the resection procedure the resection time t [s], gelatin compression until resection δ [mm], and sample size V [mm] were measured. Additionally, the operation force F [N] was measured to give an indication about the required forces to operate the prototype biopsy needle.

13

13
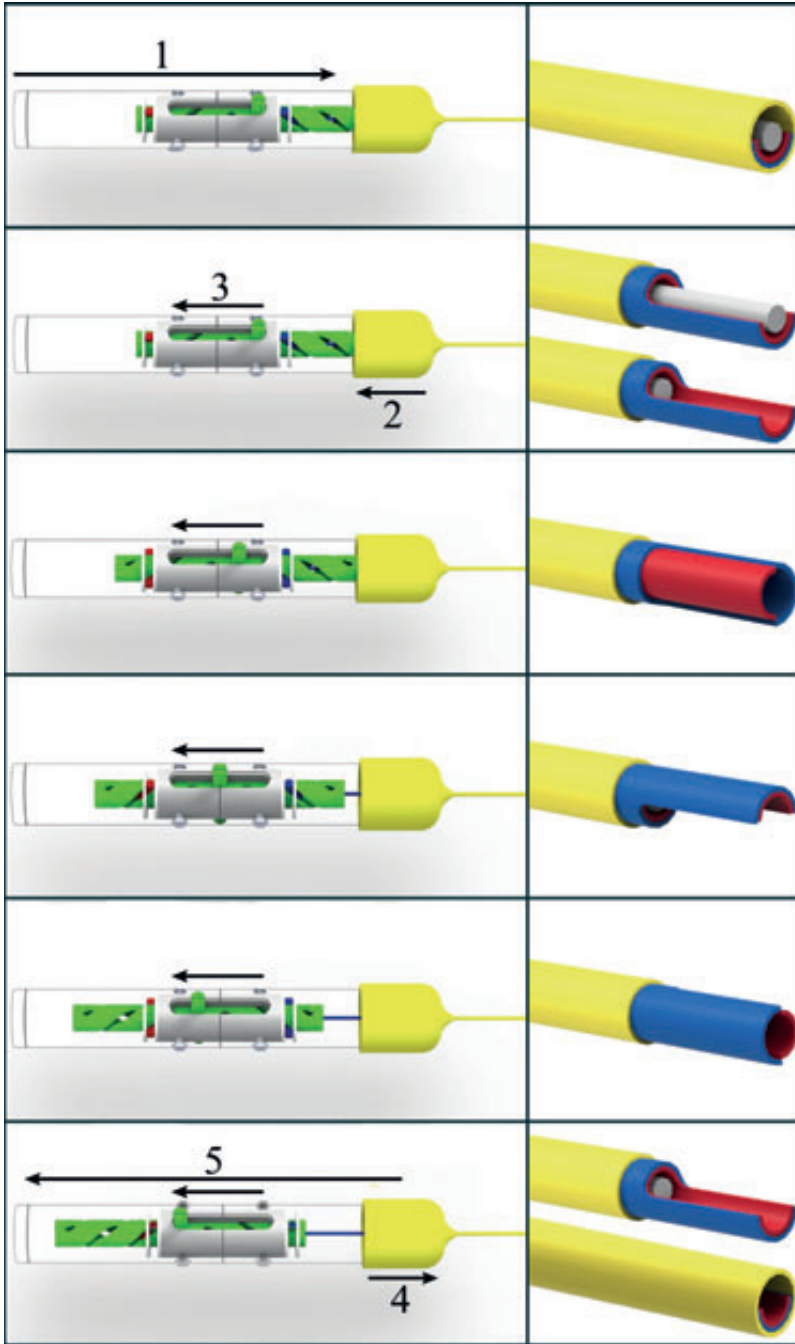
Figure 13.9— Prototype Biopsy Needle Tip Designs. Top—*beveled blade* design. Middle—*straight blade* design. Bottom— *reverse-beveled blade* design. The match is shown for scale purposes.
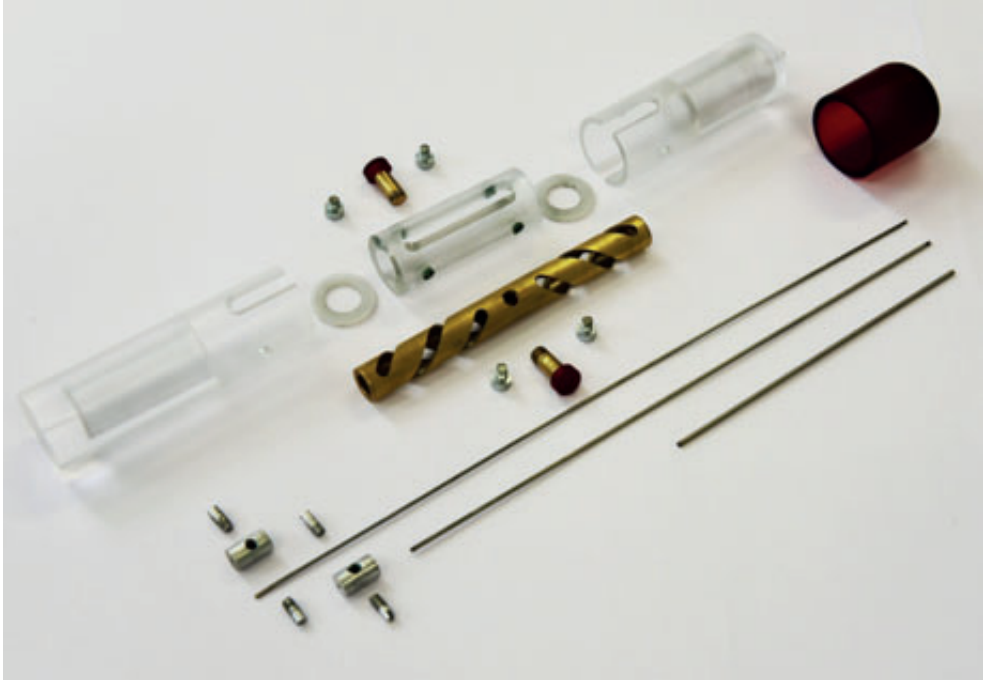
Figure 13.10— Prototype Biopsy Needle – Assembled.

13
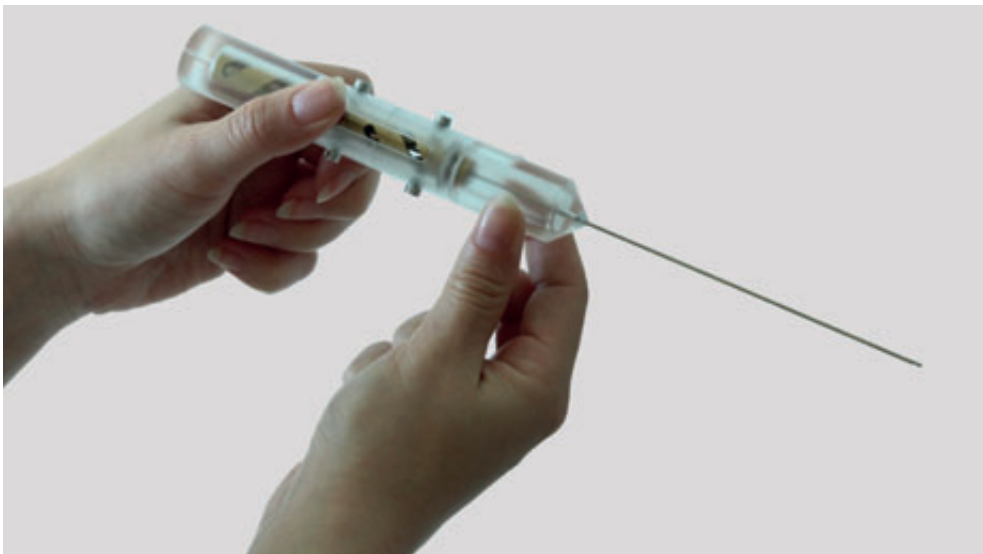
Figure 13.11— Biopsy Procedure with the Prototype Biopsy Needle. 1) Insertion of the biopsy needle in the milk duct with the cannula positioned over the cutting blades. 2) Cannula moved backwards to expose the blades. 3) Rotation of the blades to take the biopsy. 4) Repositioning of the cannula over the blades. 5) Removal of the biopsy needle from the milk duct.

13.4.3. Experimental Facility

Measurement Facility

The prototype biopsy needle was fixed in a measurement facility (see Figure 13.12). To move the blades, a U-profile was connected to the control rods (part C_2 in Figure 13.9), which in turn was connected to a linear motion stage (*Almotion LT50-TR-G8*; Almotion, Elst, the Netherlands) via a load cell (*LSB200*, Futek, Irvine, CA, USA) to measure the operation force. To initialize the linear stage and the load cell, a multifunctional data acquisition system was used (*NI USB-6008*, National Instruments, Austin, Texas, USA). The biopsy process was observed in detail using a high-speed video camera *Fastcam APX RS* (Photron, San Diego, California, USA) in combination with the *Questar QM1* (magnification factor of 11/2; Company Seven, Montpelier, MD, USA) lens. The high-speed video camera was positioned in front of the needle tip.

Milk Duct Mimicking Phantom

In order to determine the ability of the cutting blades to obtain a biopsy from the ductal wall, a transparent PMMA milk duct phantom (Ø1.7 mm) was created in which a gelatin lesion-mimicking phantom could be placed (see Figure 13.13). To mimic the properties of ductal carcinoma and papilloma, a mixture of 25wt% 250-bloom gelatin powder and water was used. When cooled down, this mixture has a similar Young's modulus as ductal carcinomas and papillomas of approximately 100–150 kPa [13].

The phantom was placed in the duct phantom just before the beginning of the experiment. The filling ratio of the duct phantom was set to 50% (see Figure 13.13) to mimic semi-filled milk ducts.

13
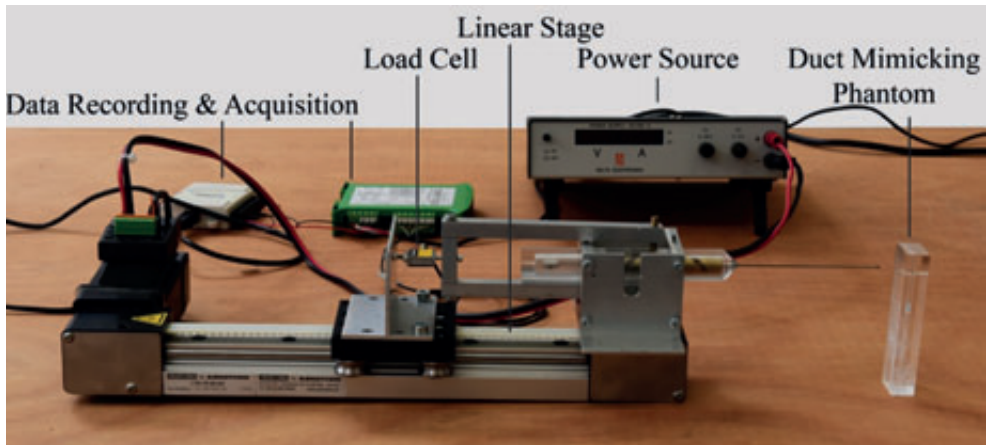
Figure 13.12— Measurement Facility. The measurement facility consisted of the prototype confined within an aluminum facility, the duct-mimicking phantom, a linear motion stage to actuate the cutting blades, a power source to power the motion stage, and data recording and acquisition boxes.
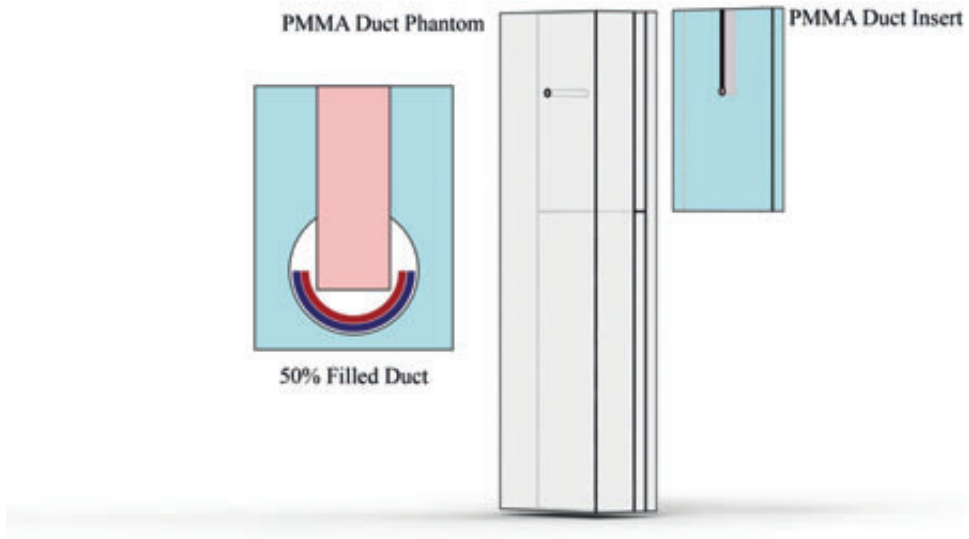
Figure 13.13— Milk Duct Mimicking Phantom. The breast-mimicking phantom consists of a PMMA laser-cut duct model through which a gelatin lesion phantom is inserted, which mimics a 50% filled duct. Color indications: Blue = Outer cutting blade, Light Blue = Rigid PMMA duct model insert, Light Grey = PMMA duct phantom, Pink = lesion mimicking phantom, and Red = Inner cutting blade.

13.4.4. Experimental Protocol

The linear motor stage was set to 0.4 mm/s, resulting in a rotational velocity of 16 rpm of the blades. All the variables were determined 3 times per phantom for each of the blade designs, resulting in a total of 9 tests. To prevent the effect of gelatin hardening over time, all the test were executed within one hour of manufacturing.

13.4.5. Data Acquisition and Analysis

Data acquisition and position control of the linear stage were achieved using a dedicated laptop equipped with Labview to initialize the data acquisition (National instruments, Austin, Texas, United States), Q-programmer feeding the linear motion stage (Moons Industries, Shanghai, China), and Photron Fastcam Viewer to analyze the camera feed.

13

13.5. RESULTS

13.5.1. Tissue Sample Obtainment

In the experiments, it became clear that the *beveled blade* design was unable to obtain a tissue sample. The gelatin breast tissue phantom was pushed forward, resulting in an

incomplete cut (see Figure 13.14). The *straight* and *reverse-beveled blades* were able to fully resect all the gelatin phantoms (see Figure 13.15). In each test, a sufficiently large tissue sample was obtained for histopathologic analysis of at least 0.5 mm, which was determined visually from the video images.

13.5.2. Effectiveness Resection Procedure

Slight differences between the *straight* and *reverse-beveled blades* were identified in terms of resection time *t* and gelatin compression *δ* (see Table 13.1). Both the resection time *t* and gelatin compression *δ* were smaller for the *straight blade* design. However, in the *straight blade* design a more "abrupt" resection procedure was seen, in which the entire tissue sample was obtained simultaneously, while in the *reverse-beveled blade* design the resection process was more constant.

13.5.3. Operating Force

The mean operation force was on average 4 N (*n* = 9) with a maximum value of 4.4 N, which allows for easy single-handed control. No significant differences between the different blade designs were found.

Figure 13.14— Incomplete resection of the gelatin phantom with the *beveled blade* design.
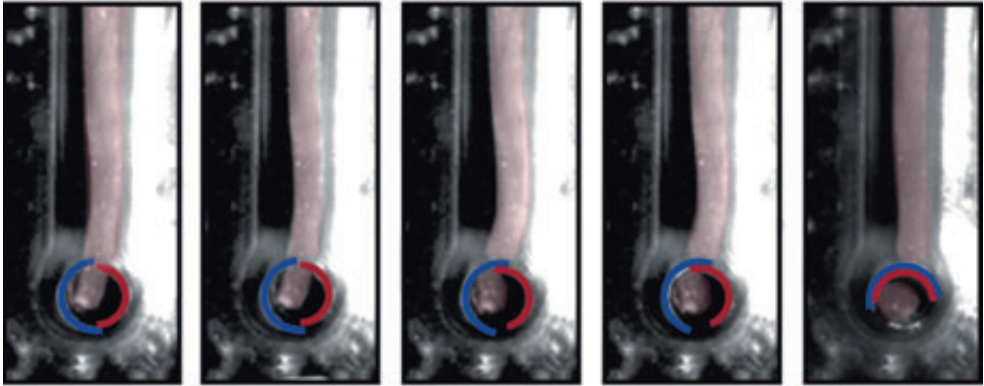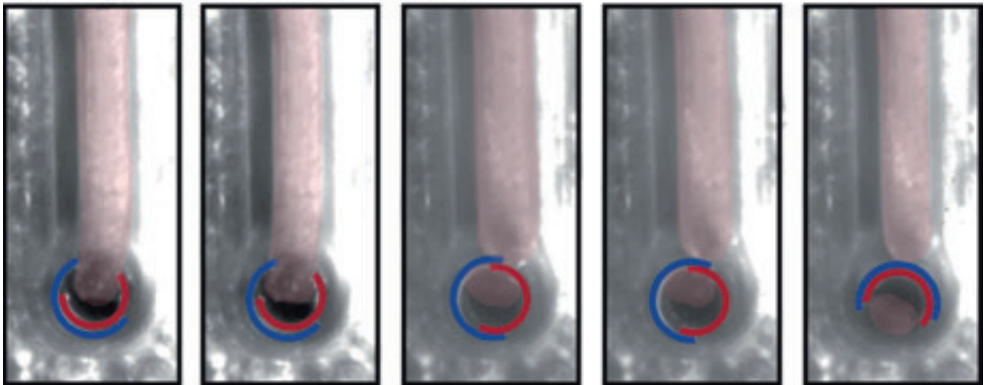
Figure 13.15— Tissue Sample Obtainment with the *Straight* and *Reverse-Beveled Blades*. Top—*Straight blade* design. Bottom—*Reverse-beveled blade* design.

Table 13.1— Measured Resection Time and Gelatin Compression for the *Straight Blade* and *Reverse-Beveled Blade* Designs (*n* = 3). The values are indicated as mean (minimum value–maximum value).

Blade design	Resection time t [s]	Gelatin compression δ [mm]
Straight blade design	4.3 (3.9–4.6)	0.04 (0.03–0.05)
Reverse-beveled blade design	6.5 (5.8–7.3)	0.09 (0.07–0.11)

13

13.6. Ex-Vivo Animal test

The biopsy needle has illustrated the ability to obtain a tissue sample in the proof-of-principle experiment. To illustrate the clinical feasibility of the biopsy needle, a second experiment was performed at the University Medical Center Utrecht (Utrecht, the Netherlands) that resembles the clinical situation more closely. In the clinical validation experiment, the Ø0.55 mm micro-endoscope (*LaDuScope T-flex*, Polydiagnost, Hallbergmoos, Germany) was inserted in the lumen of the biopsy needle (see Figures 13.16 and 13.17, as well as the supplementary video file). The biopsy needle was, subsequently, used to obtain a tissue sample from a piece of chicken breast, which resembles breast tissue [14]. Two different needle placements were investigated to determine the needle's ability to obtain a biopsy from different clinical situations (see also Figure 13.3). First, the biopsy needle was placed tangent to the outer surface of the chicken breast, resembling the situation of when a semi-filled milk duct is encountered. Secondly, to determine the ability of the needle to puncture and obtain a tissue sample from a completely filled milk duct, a small strip of 10 mm thick chicken breast was penetrated with the biopsy needle after which the blades were actuated. In both situations, the biopsy needle was able to obtain a biopsy as is illustrated in Figure 13.18. Unfortunately, as of today no suitable animal model is available for ductoscopy that allows for travelling through milk duct-type structures. In future, the biopsy needle will, therefore, be tested on mastectomy samples.

13.7. Discussion

13.7.1. Summary of Main Findings

Mechanical Validity
The biopsy needle has illustrated the ability to fully resect gelatin phantoms along the ductal wall. Three different tip geometries were tested. At the beginning of experiment, however, it became clear that one of the designs; the *beveled blade* design, was unable to fully resect the gelatin phantom, due to the forces exerted by this blade configuration, which are directed slightly forward (perpendicular to the cutting edge); pushing the tissue forward. Based on these results it was decided to abandon this tip geometry. The *straight* and *reverse-beveled blades* were able to fully resect all the phantoms from the ductal wall.

The *straight* or *reverse-beveled blades* both have their advantages and disadvantages and thus should be selected on based on the encountered clinical situation. The *reverse-beveled* blade provides a more "constant" resection procedure, as the angled blades provided high pressures, and thus relatively low forces, on the tissue during the entire process due to the sliding contact point between the blades, similar to a scissor. The *straight blade,* on the other hand, exerts a distributed line force onto the tissue for

13

Figure 13.16— Clinical Experimental Facility at University Medical Center (Utrecht, the Netherland). The experimental facility consisted of the biopsy needle integrated with the micro-endoscope connected to the imaging equipment.
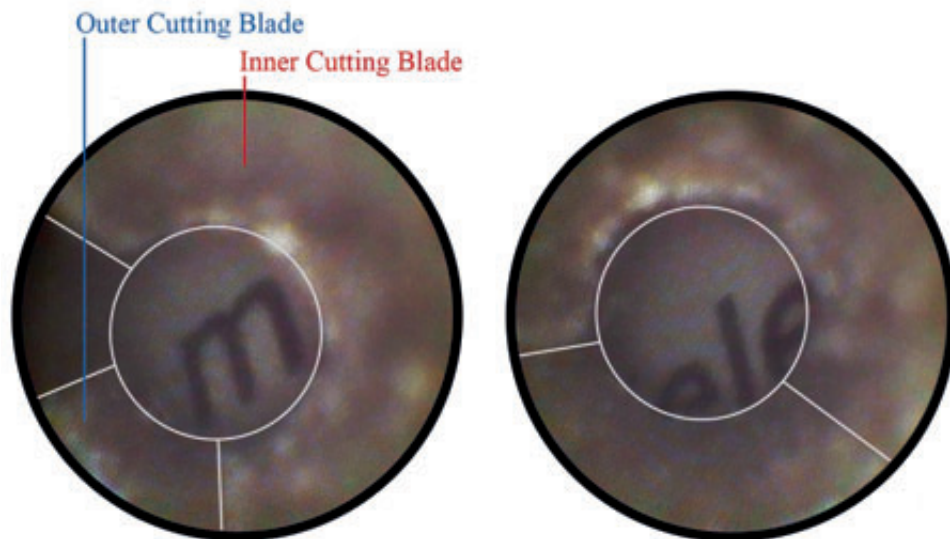
13

Figure 13.17— Micro-Endoscopic Images obtained from the Biopsy Needle. In the background a piece of text is illustrated which is imaged using the micro-endoscope.

Figure 13.18— Tissue Sample Obtainment with the Biopsy Needle from the Chicken Breast. The match is illustrated for scale estimation.

13

resection, resulting in a more "abrupt" resection process in which the entire tissue is resected at once when sufficient pressure is delivered by the blades. Furthermore, the *reverse-beveled blade* design is able to grip the lesion and pull it inward due to the inward directed cutting surface. On the other hand, the *straight blade* design was able to obtain the tissue sample faster with less gelatin compression than the *reverse-beveled blade* design, which might be beneficial for preserving the tissue structure. Furthermore,

the *straight blade* design allows for grasping larger lesions due to the larger end-point opening span of the blades than the *reverse-beveled blade* design and is less likely to cause unwanted damage the ductal wall during actuation.

The obtained tissue samples had a volume of approximately 0.5 mm, as determined visually from the video images. When it is assumed that the tissue sample of the lesion is homogeneous; containing only lesion cells, this is sufficient for histopathologic analysis.

Clinical Validity
The developed biopsy needle allowed for easy integration of the micro-endoscope. A clear and unobstructed view of the text directly in front of the endoscope tip and blades was obtained. Furthermore, the biopsy needle was able to obtain tissue sample from the chicken breast, which closely resembles human breast tissue.

13.7.2. Limitations of this Study

It is recommended that future tests will be performed on *ex-vivo* breast tissue removed during mastectomy procedures. Although the gelatin mimics the Young's modulus of the malignant cells, it is unsure how well the gelatin mimics the other tissue properties of these lesions. Furthermore, the ductal wall was mimicked using a stiff PMMA phantom, while the milk ducts are flexible. The chicken breast mimicked the clinical situation more closely than the gelatin phantom; however, it still differs significantly differs from a milk duct in human breast tissue.

13.7.3. Recommendations for Future Research

Optimization Blade Design
In a future clinical prototype, the blade design should be optimized. First, the blades should be sharpened using professional equipment, such as a wetstone or CNC drilling and milling machine. Secondly, to allow for obtaining larger biopsies in a single actuation cycle, the cutout length could be increased towards 10 mm, the maximal length of the lesions in 95% of the cases. Thirdly, different tip geometries could be researched, such as toothed blades. Finally, to prevent the obtained tissue sample from falling out of the needle during retraction it is preferred to create a slight underpressure in the shaft.

Optimization Handle Design
In a future clinical biopsy needle, the handle should allow for easy integration of the micro-endoscope, irrigation system, and a work channel. For this purpose, it is a necessity to shorten the handle, which can be executed by minimizing the blade rotation from 360° to 100° (reduction of approximately 70%), minimizing the clearance between the helical paths, and minimizing the slot diameter of the helical paths (amongst others). Additionally, we will also investigate alternative mechanisms to counter-rotate the blades that allow for the development of an even shorter handle.

13

Miniaturization Biopsy Needle Diameter

It is preferred to further miniaturize the outer dimensions of the needle towards a sub-millimeter scale to allow for inspecting the peripheral milk ducts. Due to the relative simplicity of the design this could be achieved by minimizing the diameters and wall-thickness of the cutting blades. However, miniaturization is restricted by the required inner lumen of at least 0.6 mm to allow for the insertion of the micro-endoscope and irrigation. Furthermore, miniaturization of the diameter should not impede the ability to obtain sufficiently large tissue samples. Therefore, we feel that the outer diameter of the biopsy needle should not be smaller than approximately Ø0.8 mm (with two 0.05 mm thick cutting blades), leaving sufficient room to insert the smallest Ø0.45 mm micro-endoscope, allow for irrigation, and take the biopsy.

Future Clinical Validation Biopsy Needle

In future, the biopsy needle will be tested on human mastectomy samples. During this experiment the biopsy needle will be used in combination with post-mastectomy ductoscopy for visualization of the insertion and biopsy procedure. If the mastectomy experiment has been completed successfully, we will work towards a clinical study on women with bloody nipple discharge. For this purposes, in the upcoming years the biopsy needle will be developed further into a clinical instrument, which can be easily sterilized and assembled.

13.8. CONCLUSIONS

In this study we have developed a novel Ø1.2 mm biopsy needle that consists of two counter-rotating blades that allows for taking an intraductal biopsy under direct visualization of the micro-endoscope, and thus prevents the need for a subsequent highly invasive excisional biopsy. The blades are actuated using two counter-rotating helical paths in the handle. A proof-of-principle experiment has illustrated the effectiveness of the biopsy needle in fully resecting gelatin tissue phantoms that mimic the Young's modulus of ductal carcinoma and papilloma from a stiff ductal wall model with high precision. Based on these promising results, an ex-vivo test on chicken breast was successfully performed by integrating the micro-endoscope in the biopsy needle. We will continue to develop this biopsy needle, which, in time, may improve the survival rate of breast cancer in women by early detection of suspicious lesions without the need of an invasive excisional biopsy procedure.

13

REFERENCES

[1]   Balci FL and Feldman SM. Exploring breast with therapeutic ductoscopy. Gland Surgery. 2014; 3(2): pp. 136-141.

[2]   Kapenhas-Valdes E, Feldman SM, and Boolbol SK. The role of mammary ductoscopy in breast cancer: a review of the literature. Annals of Surgical Oncology. 2008; 15(12): pp. 3350-3360.

[3]   Tang SS, Twelves DJ, Isacke CM, and Gui GP. Mammary ductoscopy in the current management of breast disease. Surgical Endoscopy. 2010; 25(6): pp. 1712-1722.

[4]   Sparks CA. Using ductoscopy to detect breast mass at an early stage. AORN Journal. 2002; 76(5): pp. 851-854.

[5]   Sree SV, Ng EY-K, Acharya RU, and Faust O. Breast imaging: A survey. World Journal of Clinical Oncology. 2011; 2(4): pp. 171-178.

[6]   Deshmane V. Intraductal approach to breast cancer: the role of mammary ductoscopy. Indian Journal of Surgical Oncology. 2011; 1(3): pp. 1228-1231.

[7]   Al Sarakbi W, Salhab M, and Mokbel K. Does mammary ductoscopy have a role in clinical practice. International Seminars in Surgical Oncology. 2006; 3: pp. 1-7.

[8]   BostonScientific. Cytology Brushes. Available from: http://www.bostonscientific.com/en-US/products/cytology-brushes.html.

[9]   USEndoscopy. Infinity ERCP Sampling Device. Available from: http://www.usendoscopy.com/Products/Infinity-ERCP-sampling-device.aspx.

[10]   Olympus. Biopsy Forceps. Available from: https://http://www.olympus-europa.com/medical/en/medical_systems/products_services/product_details/product_details_8512.jsp.

[11]   MDL. SemiCut. Available from: http://www.mdlsrl.com/en/products/interventional-radiology/light-cut/.

[12]   ArgonMedical. Biopince Full Core Biopsy Instruments. Available from: http://www.argonmedical.com/products/biopince-full-core-biopsy-instruments/.

[13]   Lee EJ, Jung HK, Ko KH, Lee JT, and Yoon JH. Diagnostic performances of shear wave elastography: which parameter to use in differential diagnosis of solid breast masses. European Radiology. 2012; 23(7): pp. 1015-1026.

[14]   Zaeimdar S. Mechanical Characterization of Breast Tissue Constituents for Cancer Assessment. M.Sc. thesis, School Mechanical and Systems Engineering, Simon Fraser University, Burnaby, Canada, 2014.

13

13

CHAPTER 14

DISCUSSION

14

14.1. MAIN FINDINGS OF THIS STUDY

The success rate of PCIs of CTOs remains undesirably low in comparison to acute lesions, resulting in high referral rates for patients suffering from a CTO. In an effort to improve the success rate of PCIs of CTOs, the goal of this thesis was to develop innovative devices that can aid the interventionist during this procedure in future. For this purpose, we aimed to solve the three major challenges encountered during PCIs of CTOs, as described in the introduction (Chapter 1) and illustrated in a study of Kinoshita *et al.* [1], by (1) adding steerability to the crossing tool to navigate and aim the catheter, (2) allow the interventionist to puncture and cross heavily calcified CTOs without buckling, and (3) allow for an easy reopening procedure of the coronary artery. In total, eight different prototypes have been developed and evaluated.

14.1.1. Improving Dexterity

Main Findings
The most common failure mode during PCI of CTOs is the inability to successfully reach the distal true lumen mainly due to two reasons: (1) the inability to actively steer the crossing tool through the CTO and (2) buckling of the crossing tool. In order to aid the interventionist during the crossing procedure, research on two steerable mechanisms has been carried out: *Accura* (Chapter 3) and *Volt* (Chapter 4). The steerable prototypes *Accura* and *Volt* increase the dexterity of the operator significantly in comparison to current passive instruments, such as guidewires and catheters, and as such allow the operator to reach behind and over obstacles, such as delicate nerves and blood vessels. Also when compared to the few clinically available steerable catheters, such as the 1-DOF *Agilis NxT* (St. Jude Medical, Saint Paul, MN, USA), the tip technology of *Accura* is advantageous, as it allows for forming complex curves, such as S-curves, at very small dimensions, which can be beneficial when circumnavigating heavily calcified regions of the CTO or navigating through tortuous anatomy. The addition of the extra DOFs also allows the tip position to be altered independently from its orientation, which is beneficial when, for example, a tissue area needs to be examined.

The design of the multisteerable tip *Accura* allows for high precision steering, with minimal loss of dexterity caused by energy absorption in the device's tip and shaft. This is mainly due to the use of incompressible elements, which prevent tip compression during actuation. The same principle is used in *Volt*, which consists of two incompressible planar joints. Furthermore, in this device, the bending stiffness of the joints is maximized by (1) placing the steering cables at the outer edge of the joint and (2) by using a steering ribbon instead of a cable to actuate the joint. The latter allows for an increase of the moment arms, while simultaneously increasing the cross-sectional area of the cable, which both contribute to maximizing the bending stiffness of the joint.

14

Future Pathways

The multisteerable tip *Accura* should be fitted with a flexible shaft in future. In order to allow for precise control of the tip independent from the shaft shape, shaft compression and cable-shaft interactions should be prevented. Shaft compression can be prevented in two main ways: (1) by constructing the shaft out of incompressible elements, similar to the ones used in the tip, or (2) by guiding closed tension springs over the steering cables to compensate for the compressive forces exerted on the shaft during tip actuation. Furthermore, in order to prevent unwanted shaft motion during tip actuation, it is imperative to prevent interaction of the steering cables with the shaft. Cable-shaft interactions can be prevented by setting the moment arms of the cables in the shaft to zero or by making sure each cable, independent from the shaft shape, encounters an equal amount of friction with the shaft.

Active control of the crossing path is imperative to treat the most calcified and tortuous CTOs. Adding additional DOF to the crossing devices, however, is only advantageous when the tip can be controlled in an intuitive manner. Intuitive control of a multisteerable tip is often challenging, as multiple steering segments need to be controlled simultaneously. This was also found in the tip of *Accura*. Furthermore, the interventionist should be able to know the exact 3D position of the multisteerable device and the shape of the CTO in front of the device tip to prevent blood vessel wall damage during the crossing procedure. In order to achieve this, the multisteerable instrument should become an extension of the interventionist's hands and eyes. Therefore, more research should go into intuitive (robotically enhanced) control of multisteerable catheters, as well as improved 3D visualization of the device tip and CTO.

In order to switch from passive to multisteerable catheters in PCI of CTOs in the near future, it is imperative to not only improve the chances of a successful procedure, but also to compete with the manufacturing costs and assembly times. Tip constructions of multisteerable instruments, such as that of *Accura,* are often quite intricate in comparison to those of passive instruments. This results in high manufacturing costs and long assembly times. Fortunately, with advances in manufacturing techniques, such as 3D printing, manufacturing costs are expected to decrease in the near future, allowing for the multisteerable catheters to compete with the passive catheters. Additionally, as the precision of 3D printing has significantly improved during the last decade, we feel that further miniaturization towards the preferred Ø1 mm scale should be achievable in the near future.

14

14.1.2. High Impact Technologies

Main Findings

Guidewire buckling is the main cause of procedural failure during PCI of CTOs. Buckling is the result of low buckling resistance of the guidewire in combination with the high

penetration load of the CTO. In order to increase the buckling resistance of the crossing tools, while leaving the geometric properties unaltered, we explored using a mechanical impulse for crossing purposes. Using an impulse for penetration is advantageous over static loading methods, as it can significantly increase the buckling resistance of the tool independent from its geometrical features. Blunt tip shapes were found to be most effective in puncturing artificial CTO models, which minimizes the chance of unwanted damage to the blood vessel wall during actuation.

Four high-speed impulse prototypes were developed: (1) *Pulze I* (Chapter 7), (2) *Pulze II* (Chapter 8), (3) *Cradle* (Chapter 9), and (4) *Wave* (Chapter 10). The four prototypes use a different means to transfer the momentum and deliver the impulse: a compression spring in *Pulze I* and *II,* a series of balls in *Cradle*, and a hydraulic pressure wave in *Wave*. Of the four prototypes, the hydraulic *Wave* catheter outperformed the other devices, as it was able to transfer high forces up to 43 N without buckling which is over 25x higher than the required static load to penetrate a CTO according to Roy *et al.* [2], did not display any shape dependency, and allowed for easy adjusting of the output characteristic. Furthermore, the hydraulic *Wave* catheter has as an additional advantage that it is simple in design and uses an existent cardiac catheter filled with biocompatible saline, which makes it relatively easy to incorporate in PCIs in the near future.

Future Pathways

The effectiveness of the developed high-speed impulse devices was tested on artificial CTO models using a single impulse strike with a specific force-time characteristic. In order to determine the optimal force-time characteristic of the impulse for puncturing real CTOs, *ex-vivo* or *in-vivo* experiments should be performed in the near future. CTO variability may have a significant effect on the required force-time characteristic of the impulse, resulting in a specific output range to which the device needs to be able to be set. Additionally, the effect of applying multiple executive strikes and (high-frequency) vibrating motions could be researched.

Next to using an impulse for penetration purposes, the impulse principle could also be used to perform other functions. The impulse principle could potentially be applied for tissue characterization, as the delivered force over time characteristic is highly dependent on the biomechanical properties of the target tissue. High peak forces are found in rigid target tissues, such as bone, while lower peak forces are found in softer tissues. If we were able to retrieve the reflected impulse signal, which is possible in the *Wave* catheter, the retrieved signal could thus be a measure for the biomechanical properties of the tissue. The use of an impulse to puncture tissues could also be beneficial for other medical application areas that require the delivery of high forces through slender shafts or for increasing the accuracy of the procedure, as using a high force low duration impulse minimizes tissue deformation during penetration by using the inertia of the tissue as a counterforce. This is substantiated by our experiments with the artificial CTOs models, in

14

which the displacement was significantly less using the impulse prototypes than the values found for the static loading method.

Similar to the impulse-principle, the *Wave* catheter could be used to perform other functions. The incompressible fluid column of *Wave,* currently in use for the impulse transfer, could also be used to sense forces, pressures, and flow in front of the catheter tip. The force information can, for example, be used to determine if the catheter is in direct contact with the CTO before commencing the crossing procedure. Additionally, by changing the tip geometry, the *Wave* catheter could also be used to cut or drill through soft tissues, take a biopsy, place leads, clips, drugs, or markers with high precision. Finally, the fluid column could be used to transfer a high-frequency current for coagulation purposes or deliver medicine to the operation area.

For future clinical application of these high-speed impulse devices, safety should be ensured. One potential risk of using the hammer prototypes is chip formation; in which small chips are freed from the CTO and can travel up the bloodstream. This can potentially lead to a stroke. For this purpose, it is recommended to use an emboli filter proximal to the occlusion and only use the catheter to puncture the most calcified regions. Furthermore, due to the rapid acceleration of the plungers there is a chance of dislodgment. In order to prevent this, and as such guarantee safe operation of the catheter, we will look deeper into ways to integrate the distal plunger with the shaft.

14.1.3. Tissue Removal Technologies

Main Findings

The final step in a PCI is the reopening of the coronary artery. For this purpose, in the majority of the cases a balloon catheter is used, which compresses the occlusion against the blood vessel wall. This final step is usually the least challenging part of the PCI. However, in a CTO, this final step can still be challenging, as the calcifications are able to resist large radial compressive forces, and thus do not allow for increasing the lumen diameter sufficiently.

In order to increase the chance of a successful reopening procedure, additional methods to reopen the coronary artery have been researched. Two additional options to reopen the coronary artery are: (1) removing the plaque material and (2) converting the plaque material (Chapter 11). As of today, there are a lot of different devices available to remove plaque tissue during PCI, such as the atherectomy drill device *Wildcat* (Avinger, Redwood City, CA, USA). Additionally, several excimer lasers, such as the *CVX-300* (Spectranetics, Colorado Springs, CO, USA), are available that evaporate the occlusive material. Unfortunately, most of these devices have illustrated no added value in comparison to standard equipment, had an increased complication rate, or require high investment costs [5-7].

14

Future Pathways

In order to simplify the reopening procedure, next to removing or converting the plaque material, another option would be to enhance plaque compression using an adapted version of the *Wave* catheter (see Figure 14.1). Impulse-aided compression allows for generating high axial and radially directed compressive forces for plaque fragmentation without the risk of buckling. Furthermore, using removal tools to resect the plaque from the blood vessel wall requires the use of sharp edges instruments, which may cause unwanted blood vessel wall damage, while in impulse-aided compression only blunt shapes are used. We are, therefore, planning to look into ways of using the impulse crossing tools for reopening purposes in the near future.

14.2. FROM SINGLE-FUNCTION TO MULTIFUNCTIONAL CATHETERS

If we consider the field of endovascular cardiovascular interventions, where space is often limited, multifunctional tools are not as readily available as one might expect. At present, CTOs are treated using three or more different single-function medical instruments: a catheter to navigate towards the lesion, a guidewire to cross the occlusion, and a balloon catheter with a premounted stent to reopen the artery. The need for a multifunctional treatment tool is high, since current devices used for endovascular treatment are often insufficient, due to the low buckling resistance and inability to actively steer. Furthermore, the instruments need to be exchanged several times during the procedure, which is not only time consuming, but also increases the risk of damaging the blood vessels [3, 4].
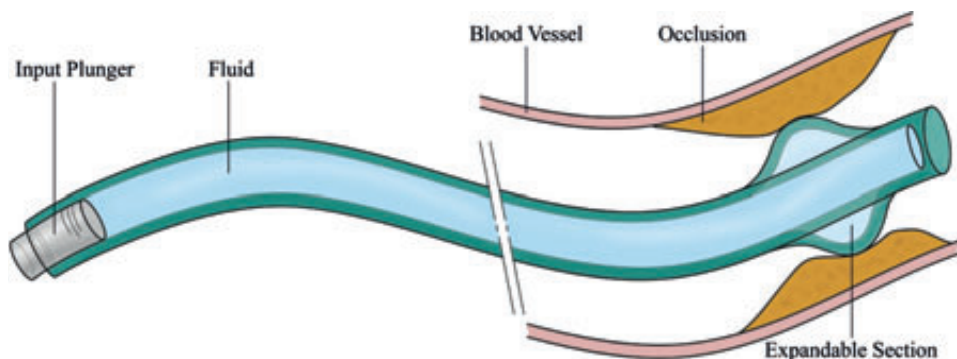
Figure 14.1– The Envisioned Wave Catheter Reopening Fragmentation Catheter.

14

417

According to a panel of 47 CTO specialists, the "ideal device" to facilitate crossing of a CTO should have the capability to combine (1) precise steerability, (2) the ability to move forward even through resistant fibrotic and calcified tissue, either through mechanical means or using an active energy source, and (3) a mechanism to detect and ensure correct intraluminal passage [5-7]. The third goal of the specialist differs from the third sub-goal drafted in this thesis. We recognize that in order to allow for navigating through the CTO, it is a necessity to add an intravascular imaging modality to the tip, as interventionists must rely on angiographic visualization in 2D (using CT fluoroscopy) to determine their position in 3D, which is challenging and can result in blood vessel wall damage. However, we did not formulate this as a major goal of this thesis, as we collaborated with the ErasmusMC, who are currently developing a Forward-Looking IntraVascular UltraSound (FL-IVUS) transducer to achieve this goal.

As of today, no devices yet exist that combine the four main functionalities as described above into one tool. Dedicated devices exist that focus on one of these functionalities, see Chapters 2 and 11 [8, 9], such as the *Ocelot* catheter (Avinger, Redwood City, CA, USA) that combines intravascular imaging with the ability to penetrate highly calcified regions. In this thesis we have made first steps to develop a multifunctional tool that integrates two of these functionalities. In collaboration with the EramusMC and Philips Research, a single-element FL-IVUS transducer and OSS fiber [10] have been fitted to the developed multisteerable tip *Accura*. First tests have proven successful in imaging a tungsten wire frame in 3D. We have chosen to focus on adding functionalities to the steerable catheter tip *Accura*, which in future can function as a main conduit through which additional tools can be guided, such as the *Wave* catheter and dedicated guidewires. The addition of the FL-IVUS transducer can ensure correct intraluminal passage and aid the interventionist in choosing the most feasible entry location in future. The OSS-fiber, in turn, allows for 3D-reconstruction of the shape of the multisteerable tip. When used in unison, the FL-IVUS transducer and OSS-fiber allowed for rendering a 3D volume in front of the device tip, which can aid the crossing procedure by circumnavigating heavily calcified regions in the CTO. Furthermore, this configuration may reduce the use of the harmful iodine contrast fluid and X-ray during the PCI in future.

The need for a multifunctional tool is high. However, if we want to use this multifunctional tool in the coronary arteries, we need to miniaturize this tool towards a sub-millimeter scale. Miniaturization by minimizing the number of parts will reach a limit beyond which scaling laws come in to play. Therefore, when designing a miniature multifunctional tool, it is a necessity to look into shared component use in which one component fulfills multiple functions. Components that are extremely suited for fulfilling multiple functions are cables. Cables are extremely versatile and can be used to steer the catheter, to power tip tools, to visualize the operation area or CTO, such as in coax

14

cables, and reconstruct the 3D-shape of the tip, such as the OSS fibers. In the future, it may, for example, be possible to use the coax cables and OSS fiber to steer the catheter tip, drastically reducing the number of cables.

14.3. ENVISIONED MULTIFUNCTIONAL CTO CATHETER

14.3.1. Design of the Multifunctional CTO Catheter

A multifunctional CTO catheter should combine the four main functionalities as described in Section 14.2: (1) precise steerability, (2) puncture without buckling, (3) easy reopening, and (4) ensuring correct intraluminal passage, into one tool. In order to create such a multifunctional catheter, the insights gained in this thesis can be used. Based on these insights, we feel that a multisteerable introducer sheath, similar to *Accura*, is the most feasible and versatile option, as it allows for guiding several tip tools, such as the *Wave* catheter, towards the operation area, while simultaneously giving information on the 3D-shape and position in order to determine the most feasible crossing path.

Figure 14.2 illustrates the envisioned multifunctional CTO catheter. The catheter consists of a 4 DOF steerable tip that allows for changing both the tip position and orientation. The multisteerable tip consists of incompressible elements, similar to the tip of *Accura*. As a means to actuate the tip, 6 axially stiff cables are used that are placed at the outer edge of the catheter to increase their moment arms. These cables can simultaneously function as a power source for the multi-element FL-IVUS transducer placed at the distal end of the catheter and for shape reconstruction. In order to prevent shape dependency, each of the cables is placed within an individual closed tension springs to create an energy neutral shaft. In the center of the catheter a lumen is present to guide a guidewire, the hydraulic *Wave* catheter to deliver high-force impulses onto the CTO, or a balloon catheter to reopen the coronary artery, towards the CTO.

14.3.2. Intended Use of the Multifunctional CTO Catheter

Figure 14.3 illustrates the envisioned use of the multifunctional CTO catheter. First, the catheter is actively guided through the vasculature towards the CTO. Once in place, the steerable tip segment is used to scan the CTO using the multi-element FL-IVUS transducer to determine the most feasible entry point. After the determination of the most feasible entry point, the hydraulic *Wave* catheter is inserted, pushed against the CTO until a small pretension is measurable from the handle side, and, subsequently, activated. Once the proximal cap of the CTO is punctured, which is confirmed by data obtained from the FL-IVUS transducer, the *Wave* catheter is retracted and a regular guidewire is used to cross the occlusion. If this remains challenging, the *Wave* catheter can be advanced during the crossing process to penetrate heavily calcified regions or compensate for guidewire deflection. Finally, the occlusion is reopened using a balloon catheter or an adjusted *Wave* balloon catheter that can assist in compressing highly resistive CTOs.
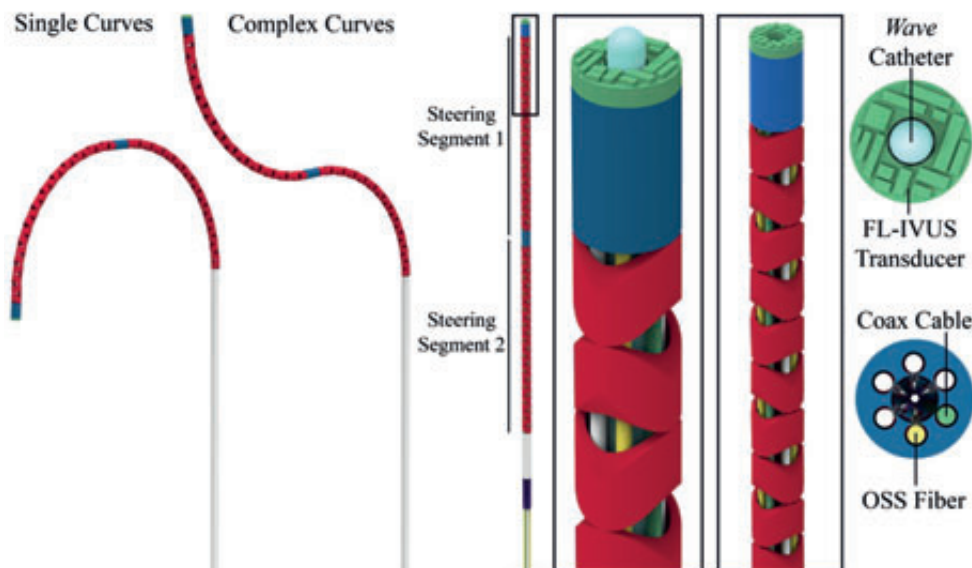
14

Figure 14.2– The Envisioned Ideal CTO Catheter Tip. The envisioned ideal CTO catheter tip is steerable in 4-DOF over 2 steering segments (red), integrates a FL-IVUS transducer (green) to visualize the CTO and determine the best entry point, OSS fiber (yellow) to reconstruct the 3D-shape of the tip, and a lumen through which several crossing tools can be guided such as a dedicated guidewire or the *Wave* catheter (light blue).

14.4. LIMITATIONS OF THIS RESEARCH

It has been proven challenging to perform experiments on *ex-vivo* CTO tissue. CTOs deteriorate immediately after dissection, and since most CTOs are currently treated using PCIs, in which they are not removed from the body, testing proved impossible in the time frame of my PhD. Unfortunately; also no realistic animal models are currently available. Developing a realistic animals model has proven challenging as simulating the CTO pathology, especially the calcification, and the inflammatory component connected to a CTO, are difficult to achieve [6]. We were, therefore, resorted to building artificial models. Even though these artificial CTO models did allow us to test our prototypes under stable test conditions, the validity of these models is difficult to determine, as information on the biomechanical properties of CTOs is limited. A representative animal model will strongly contribute to a deeper understanding of the development and biomechanical properties of CTOs and enable device investigation in an environment closely resembling that of a human CTO.

14
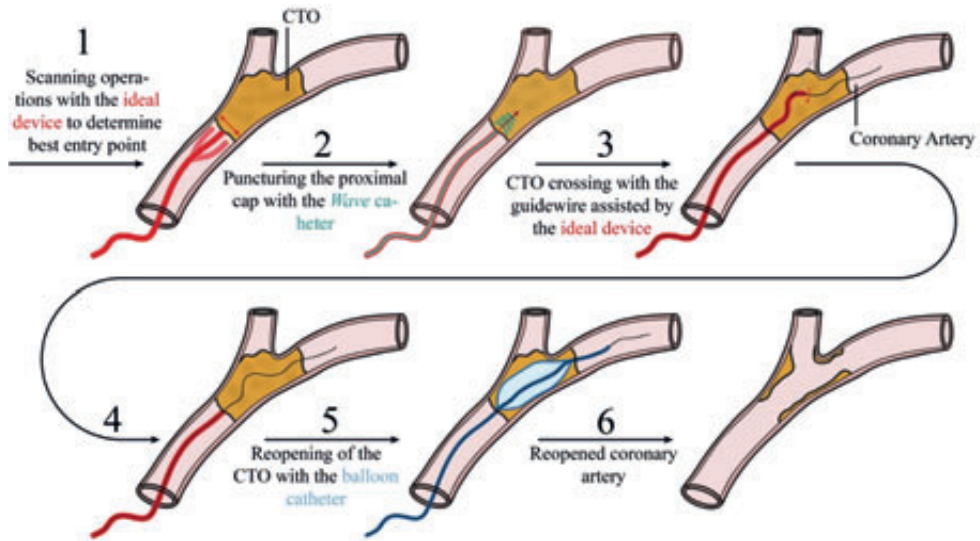
Figure 14.3– The Intended Use of the Ideal CTO Catheter. (1) The ideal CTO catheter (green) is guided towards the CTO, where it performs a scanning motion to determine the best entry point. (2) The *Wave* catheter (red) is guided through the CTO and is subsequently used to puncture the proximal cap. (3) The *Wave* catheter is retracted and a guidewire is used to cross the main CTO body. When necessary, the ideal catheter assists the guidewire. (4) The ideal catheter is retracted as the CTO is successfully crossed. (5) The CTO is reopened using a balloon catheter (blue) or, in case of highly resistive CTOs, by an adjusted radially directed *Wave* catheter. (6) The reopened coronary artery.

14.5. Recommendations for Future Research

It is recommended that in the future the prototypes will be tested on real CTO tissue. Only then definitive answers can be drawn on the effectiveness of the proposed catheters. Furthermore, in order to understand the development of a CTO in more detail, it is of importance to do more research into this area. This could lead to the development of a suitable animal model. Also, more information is needed about the biomechanical properties of the CTO. As of today only a few studies have been performed on this topic, which mainly focus on the determination of the puncture force, such as the studies of Thind *et al.* [11] and Roy *et al.* [2]. No information is available about the other biomechanical properties, such as the Young's modulus, average density, and tensile strength, of the CTO.

Advances in PCI equipment and crossing techniques have steadily increased the success rates and slowly solved the major failure modes. Unfortunately, the newest study that has investigated the major failure modes during PCIs of CTOs is from 1992 [1] and,

14

therefore, already rather dated. In 1992, the dissection-reentry technique and combined antegrade and retrograde approaches, as well as many dedicated guidewires and catheters, which have dramatically improved success rates, were not yet available. An overview of current failure modes may shed new light on challenges that are solved and those that still need to be overcome. Furthermore, it may also shed new light on the most effective crossing tools and techniques that are currently in use.

Working towards the "ideal" CTO device will still take some time. In the meantime, the most promising prototypes, such as the *Wave* catheter and the multisteerable tip *Accura*, could be developed further. Steps could be made to further miniaturize these prototypes to an acceptable Ø1 mm for coronary application. Due to the minimal complexity of the *Wave* catheter this should be easily achievable. However, for the multisteerable tip *Accura*, miniaturization could proof challenging due to the complexity of the tip parts. Next to miniaturization, it is a necessity to ensure the safety of the catheters. For this purpose, it is advised to look into alternative tip designs of the *Cradle* and *Wave* catheter in which the tip is integrated into the shaft. Furthermore, it is preferred that a steerable section is added to the tip portion of the *Cradle* and *Wave* catheter to aim the catheters and prevent unwanted blood vessel wall damage. Finally, the handles of the catheters could be redesigned to allow for easy single-handed operation, giving the interventionist full freedom to manipulate additional tools or perform other tasks with his or her second hand.

14.6. CONCLUSIONS

In this thesis important first steps have been taken to improve the devices used during PCIs of CTOs. It is imperative to continue to develop innovative prototypes that provide the interventionists with more information about the position of the crossing tool and the consistency of the CTO in front of the catheter tip, as well as an improved ability to puncture heavily calcified CTOs and actively adjust the crossing path. The developed prototypes have illustrated the ability to improve the effectiveness of current passive devices, such as guidewires and catheters, by adding one of the following functionalities: (1) precise steerability, (2) puncturing without buckling, (3) easy reopening, and (4) ensuring correct intraluminal passage. The multisteerable instruments allow for active navigation towards and through the CTO, whilst the impulse prototypes allow for delivering 170x higher forces on the CTOs without buckling than what the strongest dedicated guidewires can deliver. The addition of the IVUS transducer and OSS fiber to *Accura*, also allowed the reconstruct a 3D-volume in front of the tip, which in future can be used to ensure correct intraluminal passage. In order to simplify the reopening procedure, the impulse prototypes could be used. These prototypes will be developed further into clinical prototypes that can be used in *ex-* and *in-vivo* tests to illustrate their effectiveness, ease of operation, and safety in an environment more closely resembling

14

the actual clinical situation. Additionally, we will continue to develop the described ideal multifunctional instrument that allows for real-time intravascular imaging of the blood vessel and CTO, active control of the crossing path, and the ability to cross and remove calcified CTOs without buckling. Implementation of these prototypes in the near future, will aid even the less experienced interventionists in achieving high success rates for PCIs of CTOs, benefitting both interventionists, hospitals, and, most importantly, patients' life.

REFERENCES

[1]   Kinoshita I, Katoh O, Nariyama J, Otsuji S, Tateyama H, et al. Coronary angioplasty of chronic total occlusions with bridging collateral vessels: immediate and follow-up outcome from a large single-center experience. Journal of the American College of Cardiology. 1995; 26(2): pp. 409-415.

[2]   Roy T, Liu G, Shaikh N, Dueck AD, and Wright GA. Puncturing Plaques. Journal of Endovascular Therapy. 2017; 24(1): pp. 35-46.

[3]   Grantham JA, Marso SP, Spertus J, House J, Holmes DR, and Rutherford BD. Chronic Total Occlusion Angioplasty in the United States. JACC Cardiovascular Interventions. 2009; 2(6): pp. 479-486.

[4]   Olivari Z, Rubartelli P, Piscoine F, Ettori F, Fontanelli A, et al. Immediate results and one-year clinical outcome after percutaneous coronary interventions in chronic total occlusions: data from a multicenter, prospective, observational study (TOASTGISE). Journal of the American College of Cardiology. *2003;* 41(10): pp. 1672-1680.

[5]   Stone GW, Colombo A, Teirstein PS, Moses JW, Leon MB, et al. Percutaneous recanalization of chronically occluded coronary arteries: Procedural techniques, devices, and results. Catheterization and Cardiovascular Interventions. 2005; 66(2): pp. 217-236.

[6]   Stone GW, Reifart NJ, Moussa I, Hoye A, Cox DA, et al. Percutaneous recanalization of chronically occluded coronary arteries - A consensus document - Part II. Circulation. 2005; 112(16): pp. 2530-2537.

[7]   Stone GW, Reifart NJ, Moussa I, Hoye A, Cox DA, et al. Percutaneous Recanalization of Chronically Occluded Coronary Arteries. A Consensus Document Part I. Circulation. 2005; 112(15): pp. 2364-2372.

[8]   Sakes A, Regar E, Dankelman J, and Breedveld P. Crossing Total Occlusions: Navigating Towards Recanalization. Cardiovascular Engineering and Technology. 2016; 7(2): pp. 103-117.

[9]   Sakes A, Regar E, Dankelman J, and Breedveld P. Treating Total Occlusions: Applying Force for Recanalization. IEEE Reviews in Biomedical Engineering. 2016; 9: pp. 192-207.

[10]   Younge RG, Ramamurthy BS, Tanner N, Schlesinger RL, and Udd E, inventors; Koninklijke Philips Electronics N.V, assignee. Optical fiber shape sensing systems. United States Patent 8050523 B2, 2011.

[11]   Thind A, Strauss B, Teitelbaum A, Karshafian R, Ladouceur M, et al. A novel method for the measurement of proximal fibrous cap puncture force in chronic total occlusions: the effect of increasing age. EuroIntervention. 2011; 6(8): pp. 997-1002.

14

14

GLOSSARY

Glossary

LIST OF ABBREVIATIONS

ADP	Adenosine DiPhosphate
ATP	Adenosine TriPhosphate
BMF	Blood Mimicking Fluid
CART	Controlled Antegrade and Retrograde (sub-intimal) Tracking
CT	Computed Tomography
CTO	Chronic Total Occlusion
DOF	Degrees Of Freedom
FL	Forward-Looking
HA	HydroxyApatite
HSV	High-Speed Video
IVUS	IntraVascular UltraSound
LAST	Limited Antegrade Subintimal Tracking
MDCT	Multi-Detector Computed Tomography
MIS	Minimal Invasive Surgery
MSCT	Multi-Slice Computed Tomography
OCT	Optical Coherence Tomography
OSS	Optical Shape Sensing
PCI	Percutaneous Coronary Intervention
SMA	Shape Memory Alloy

SS	Stainless Steel
STAR	Subintimal Tracking And Re-entry
TDLU	Terminal Ductal Lobular Unit

LIST OF PCI-RELATED TERMS

Antegrade Approach   Crossing the CTO in the direction of the regular blood flow.

Collateral Blood Vessels   Pre-existing redundant blood vessels or newly formed branches between adjacent blood vessels that provide the distal part of the occluded blood vessel with oxygen and nutrients.

Dissection-Reentry   Crossing the CTO through the blood vessel wall, in between the intima and adventitia, and subsequent reentry and in the true lumen. (Reverse-)CART, LAST, and STAR are all variations of this technique.

    (Reverse-)CART   Crossing technique in which the CTO is crossed using two guidewires from the antegrade and retrograde direction, respectively. The retrograde guidewire is guided through the subintimal space.

    LAST   Crossing technique in which reentry is achieved using a guidewire with an acute distal bend.

    STAR   Crossing technique in which a knuckled (umbrella handle-shaped) guidewire is crossed subintimally until it re-enters the true lumen at the distal end.

False Lumen (Creation)   Creating a lumen inside the blood vessel wall, between the intima and adventitia, caused by the wrongful assumption that the guidewire has successfully crossed the CTO via the true lumen.

Intraluminal or Intravascular   Situated within, occurring within, or introduced into the lumen of the blood vessel.

Recanalization   The process of restoring blood flow to the blood vessel (using a balloon catheter in the majority of the cases).

Retrograde Approach   Crossing the CTO against the direction of the blood flow. For this purpose, the interventionist needs to navigate through the collateral blood vessels.

Subintimal (space)   Between the adventitia and intima.

True Lumen   The (normal) lumen of the blood vessel.

ACKNOWLEDGMENTS

Toen ik vier jaar geleden aan mijn PhD traject begon, bestond mijn opdracht slechts uit 3 zinnen. Het is leuk om te bedenken dat deze 3 zinnen zijn uitgegroeid tot dit gehele proefschrift. Het laat ook zien dat er uit slechts 3 zinnen voldoende informatie en inspiratie gehaald kan worden om tot de essentie van het probleem te komen. Deze vrijheid heeft ook erg geholpen om "out of the box" te kijken naar het probleem en zo tot innovatieve oplossingen te komen. Ik wil hiervoor met name mijn promotoren Paul Breedveld en Jenny Dankelman bedanken. Tijdens de soms ietwat chaotische, maar ook heel erg creatieve, meetings met mijn promotor Paul Breedveld kreeg ik steeds meer inzicht in wat er komt kijken bij het ontwerpen van kleine medische instrumenten. Vandaar ook sommige creatieve uitspattingen in mijn thesis.

Een van die creatieve uitspattingen is die van de ontwikkeling van de morcellator voor het behandelen van Cushing's disease in paarden. Door de grootte en anatomie van paarden zijn er soms behandelingen onmogelijk die bij mensen als normaal worden beschouwd. Ik wilde dan ook graag iets doen om de veterinaire zorg bij paarden te verbeteren. Door de openheid van Paul zijn we samen naar de Universiteit van Utrecht (UU) gegaan en daar hebben we samen met dr. Han van der Kolk en dr. Wim Back een opdracht geformuleerd. Ik wil jullie bij deze bedanken voor deze mogelijkheid. Verder wil ik ook de mensen van de snijzaal: Louis van den Boom, Guy Grinwis en Andrea Gröne, bedanken die het mogelijk hebben gemaakt dat ik mijn prototype op kadavers heb kunnen testen (iets wat nooit had gekund op de TU).

Waar ik ook veel van geleerd heb is het samenwerken met artsen. Tijdens het ontwerp proces van de prototypes heb ik zeer veel gehad aan de feedback van Arjen Witkamp, Evelyn Regar, Joost Daemen, Rob de Winter en Roberto Diletti. Bedankt hiervoor. Ook zou ik graag Dennis de Haas, Frank-Willem Jansen en Marjo de Ronde-Tillmans bedanken voor het leveren van de benodigde medische instrumenten, zoals catheters, guidewires, stents en trocars, voor het uitvoeren van de experimenten.

Naast de samenwerking met artsen heb ik ook zeer veel gehad aan de feedback van Jules Scheltes van DEAM Corp tijdens het ontwerpproces en mijn gebruikerscommissieleden Debbie Rem, Frist Mastik, Jovana Janjic, Rene Aarnink, Sandy Kalisinghi, Ton van der Steen en Thalissa Bos-Reith. Allemaal heel erg bedankt. Ook zou ik graag Merel Leistikow willen bedanken voor haar hulp met het opzetten van de experimenten bij Philips Research.

Een erg leuke bijkomstigheid tijdens mijn PhD proces was de aanvraag van een patent. Ik had er nooit bij stil gestaan wat hier allemaal bij komt kijken. Een idee dat in eerste instantie toch niet erg haalbaar leek, is uitgegroeid tot een innovatief en effectief instrument met veel potentie. Ik wil hier voornamelijk Jo Spronck voor bedanken, zonder wie dit idee nooit verder zou zijn ontwikkeld. Ook wil ik iedereen van het valorisatie centum, Los en Stigter en STW bedanken voor de steun en hulp in dit proces.

Dit patent heeft ook geleid tot de aanvraag en honoratie van de STW demonstrator grant (150K). In voorbereiding op deze aanvraag heb ik veel support en feedback gehad

Ik hoop dat jullie met veel plezier deze thesis hebben gelezen. Ik heb er in ieder geval met veel plezier aan gewerkt. Nu is het tijd voor een nieuw avontuur in de wetenschap.

Bedankt.

Aimée

CURRICULUM

VITAE

Curriculum Vitae

18 JUNE 1987

Born in Woerden, the Netherlands

1999 – 2005

Gymnasium Veenlanden College, Mijdrecht, the Netherlands.

2007 – 2011

Bachelor Mechanical Engineering at Hogeschool Utrecht, Utrecht, the Netherlands. Graduated with honors.

2011 – 2013

Master Biomedical Engineering at Delft University of Technology, Delft, the Netherlands. Graduated with honors. MSc thesis dealing with the development of an innovative endovascular morcellator for the surgical treatment of pituitary tumors in horses.

2013 – 2017

PhD candidate at the BioMechanical Engineering department at Delft University of Technology. PhD thesis dealing with the development of innovative crossing tools for improving the endovascular treatment of Chronic Total Occlusions (CTOs).

2017

Received the CVET Most Downloaded Article Award ($1.250)

Received the Medical Delta Young Researchers Award (€2.500) for her work during her PhD.

Internship at the Hamlyn Centre, Imperial College, London, UK on the development of a miniature steerable bronchoscope (June – September).

Received a STW Demonstrator Grant (€150.000) for the development and commercialization of the hydraulic pressure wave catheter.

2017 – PRESENT

Researcher at Delft University of Technology, Delft, the Netherlands on the development of an ultrathin biopsy needle for ductoscopy and the development of the hydraulic

pressure wave catheter for the improvement of the endovascular treatment of chronic total occlusions.

PUBLICATIONS

Publications

JOURNAL ARTICLES

Sakes A, Smit G, and Breedveld P. Puncturing Chronic Total Occlusions: Design of the Pulze Catheter Prototype. Plos One. Submitted.

Sakes A, Nicolai T, Karapanagiotis, J, Breedveld P, and Spronck JW. Crossing Total Occlusions using a hydraulic pressure wave: A feasibility study. Plos One. Submitted.

Sakes A, Grandia L, Lether R, Steenstra L, Valentijn MC, Breedveld P, and Spronck JW. Flexible Impulse Transfer using a Newton's Cradle Inspired Catheter: A Feasibility Study Medical Engineering & Physics. Submitted.

Sakes A, Snaar K, Smit G, Witkamp AJ, and Breedveld P. Design of a Novel Miniature Breast Biopsy Needle for Ductoscopy. Biomedical Physics & Engineering Express. Accepted for publication.

Sakes A, Ali A, Janjic J, and Breedveld P. Novel Miniature Tip Design for Enhancing Dexterity in Minimally Invasive Surgery. Journal of Medical Devices. 2017. Accepted for publication.

Sakes A, Hovland K, Smit G, Geraedts J, and Breedveld P. Design of a Novel Three-Dimensional-Printed Two Degrees of Freedom Steerable Electrosurgical Grasper for Minimally Invasive Surgery. Journal of Medical Devices. 2017; 12(1): pp. 011007-1-011007-15.

Sakes A, Van der Wiel M, Dodou D, and Breedveld P. Endovascular Crossing of Chronic Total Occlusions using an Impulse: An Explorative Design Study. Cardiovascular Engineering and Technology. 2017; 8(2): pp. 145-163.

Sakes A, Regar E, Dankelman J, and Breedveld P. Treating Total Occlusions: Applying Force for Recanalization. IEEE Reviews in Biomedical Engineering. 2016; 9: pp. 192-207.

Sakes A, Wiel van der M, Henselmans PWJ, Leeuwen JL van, Dodou D, Breedveld P. Shooting mechanisms in nature: a systematic review. Plos One. 2016; 11(7).

Sakes A, Dodou D, Breedveld P. Buckling prevention strategies in nature as inspiration for improving percutaneous instruments: a review. Bioinspiration and Biomimetics. 2016; 11(2).

Publications

Sakes A, Regar E, Dankelman J, Breedveld P. Crossing total occlusions: navigating towards recanalization. Cardiovascular Engineering and Technology. 2016; 7: pp. 103-117.

Sakes A, Arkenbout EA, Jelinek F, van der Kolk JH, Breedveld P. Design of an endovascular morcellator for the surgical treatment of equine Cushing's disease. Veterinary Quarterly. 2015; 35(3): pp. 165-169.

CONFERENCE PROCEEDINGS

Sakes A, Breedveld P, and Spronck J. The development of the hydraulic pressure wave catheter. Proceedings of the 29th International Conference of Society for Medical innovation and Technology (SMIT) held at Turin, Italy, 9-10 November 2017.

Sakes A, Dodou D, and Breedveld P. An Innovative Crossing tool for Chronic Total Occlusions. Proceedings of the Biomedical Engineering Conference (BME) held at Egmond aan Zee, the Netherlands, 26-27 Janurary 2017.

Sakes A, Dodou D, and Breedveld P. Bio-inspired Shooting Mechanism for Crossing Chronic Total Occlusions. Proceedings of the 28th International Conference of Society for Medical innovation and Technology (SMIT) held at Delft, the Netherlands, 5-8 October 2016.

Sakes A, Dodou D, Dankelman J, and Breedveld P. Buckling Prevention in Nature for Crossing Chronic Total Occlusions. Proceedings of the 27th International Conference of Society for Medical innovation and Technology (SMIT) held at Brno, Czech Republic, 10-12 September 2015.

Sakes A, Ali A, Henselmans PWJ, Breedveld P. Design of a 2mm diameter 8 DOF steerable prototype for the treatment of chronic total occlusions. Proceedings of the 5th Dutch Bio-Medical Engineering Conference (BME) held at Egmond aan Zee, the Netherlands, 22-23 January 2015.

Sakes A, Dankelman J, Breedveld P. Crossing CTO lesions: a review of the state of the art devices. Proceedings of the ASME Design of Medical Devices Conference – Europe Edition held at Delft, the Netherlands, 22-24 October 2014.

Sakes A, Arkenbout EA, van der Kolk JH, Breedveld P. Design of an endovascular morcellator for the surgical treatment of Cushing's disease in horses. Proceedings of the

26· International Conference of Society for Medical innovation and Technology (SMIT) held at Shanghai, China, 18-20 September 2014.

Sakes A, Arkenbout EA, van der Kolk JH, Breedveld P. A comprehensive overview of removal methods for the surgical treatment of Cushing's disease for human and veterinary applications. Proceedings of the 2013 ASME Design of Medical Devices Conference held at Minneapolis, USA, 8-11 April 2013.